Process Monitoring and Control during Additive Manufacturing

The University Of Sheffield.

Lova Chechik

The University of Sheffield

Department of Materials Science & Engineering

A thesis submitted for the degree of Doctor of Philosophy

June 2022

Abstract

Research in metallic additive manufacturing (AM) has been rapidly growing over the past 10 years, with increasing industrial relevance to the aerospace repair sector. Currently there is a lack understanding of how the processing parameters and the geometry affect the thermal condition of the part and hence the final microstructural/mechanical properties; without this understanding, industrial certification for aerospace will be difficult to achieve.

This work explores the range of microstructures possible that may be developed during AM of Inconel 718, a common alloy used in aerospace, and how in-situ monitoring and process control can be used to influence these structures. Two AM processes are explored: laser powder bed fusion (L-PBF) and laser directed energy deposition (L-DED). Printability is discussed with reference to nickel alloy design and the imposed conditions in both L-PBF and L-DED, concluding that there are different alloy design criteria for the two processes. The spread of Inconel 718 microstructures is shown to be distinct between the processes, confirming that the microstructural outcomes of the processes are fundamentally different, despite the processes being fundamentally similar.

Various in-situ monitoring techniques are tested in the L-DED process, with coaxial monitoring chosen for development of a simple feedback control loop. This improves both the thermal signature of the process and the microstructural homogeneity of the components. A level of intrinsic microstructural and mechanical homogeneity remains and this is further investigated. It is demonstrated that the geometry of components can have a significant effect on the heat flow, which results in a change in grain orientation. Additionally, process induced precipitation via in-situ heat treatment is proposed as a mechanism to explain the measured geometric hardness variation. Using advanced coaxial monitoring and harnessing the power of in-situ heat treatment, it is hypothesised that it would be possible to remove or reduce this process-induced variation in mechanical performance. This would bring the process closer to industrial certification.

"You don't know what you can't achieve, until you don't achieve it"

P. Foster

Acknowledgments

Firstly, a thank you to everyone who's helped me out and put up with me during my time in Sheffield, whether that be academically, emotionally or in any other way. The support has been much appreciated and needed, but I won't try to list everyone here.

I'd like to thank my supervisor Prof. Iain Todd for the opportunity to do this PhD as well as the trust he put in me, giving me the flexibility to pursue my own interests. I'd also like to give a massive thank you to Dr Kathy Christofidou for the endless enthusiasm and technical knowledge. A big thank you goes to Rolls-Royce plc., who partially funded my project and to my industrial supervisor Dr Gavin Baxter.

I'm very grateful to my whole research group for letting me bounce ideas off them and for putting up with my (irritatingly?) curious manner. They trained me on equipment, kept me motivated and were always supportive. Particularly Lucy Farquhar and Dr Felicity Freeman who, partly by proximity, got an undue share of questions and to Alex Goodall, who as my housemate, had to put up with me for more hours than most; despite which, he is still willing to advise me and projects his enthusiasm on all those around him.

I'd like to acknowledge the technical staff involved in my project, notably Dr Le Ma, Dr Oday Hussein and Dr Geoff West, for data collection in their relevant fields. Working with collaborators was greatly enjoyed and their help appreciated, notably Martin Tse, Dr Nick Boone and Dr Leigh Stanger.

Finally, a big thank you to my housemates, friends and family for supporting me through the last couple of years! To quote Joss Naylor *"To find words to express my gratitude...is beyond me. Those who know me well will sense what I want to say...thank you from the bottom of my heart."*

This work was funded by the EPSRC Rolls-Royce Strategic Partnership Grant, MAPP (grant EP/P006566/1) and EPSRC (grant EP/R512175/1).

Contents

List of Figures

List of Tables

List of Acronyms

Acronym	Full Name	Acronym	Full Name
AF	Anisotropy Factor	**HCS**	Hot Crack Susceptibility
AM	Additive Manufacturing	**IPF**	Inverse Pole Figure
APB	Anti-Phase Boundary	**KAM**	Kernel Average Misorientation
BCC	Body Centred Cubic	**L-DED**	Laser Directed Energy Deposition
BCT	Body Centred Tetragonal	**LENS**	Laser Engineered Net Shaping
BD	Back Diffusion	**L-PBF**	Laser Powder Bed Fusion
BTR	Brittle Temperature Range	**mud**	Multiples of Uniform Density
CAD	Computer Aided Design	**NE**	Normalised Enthalpy
CALPHAD	Calculation of Phase Diagrams	**NED**	Normalised Energy Density
CET	Columnar-Equiaxed Transition	**NIR**	Near Infra-Red
CLI	Common Layer Interface	**PBF**	Powder Bed Fusion
CSC	Crack Susceptibility Coefficient	**PCAS**	Primary Cell Arm Spacing
DAS	Dendrite Arm Spacing	**PDAS**	Primary Dendrite Arm Spacing
DDP	Ductility-Dip Cracking	**PHACOMP**	Phase Computation
DED	Directed Energy Deposition	**PID**	Proportional Integral Derivative
DLD	Direct Laser Deposition	**PREP**	Plasma Rotating Electrode Process
DSC	Differential Scanning Calorimetry	**QE**	Quantum Efficiency
EB-PBF	Electron Beam Powder Bed Fusion	**RDG**	Rappaz, Drezet and Gremaud
EBSD	Electron Backscatter Diffraction	**SLM**	Selective Laser Melting
FCC	Face Centred Cubic	**ST**	Solute Trapping
GA	Gas Atomisation	**TCP**	Topologically Close Packed
GAM	Grain Average Misorientation	**TGM**	Thermal Gradient Mechanism
GCM	Geometrically Close Packed	**TTT**	Time Temperature Transformation
H	Linear Heat Input	**VED**	Volumetric Energy Density
HCP	Hexagonal Close Packed		

List of Symbols

Symbol	Description	Units (Unless otherwise specified)
a	Interatomic spacing	ms^{-1}
A	Absorptivity	
A_{hkl}	Anisotropy Factor	
A_i	Area of Grain i	μm^2
b	Burgers Vector	m
C	Specific Heat	$JK^{-1}kg^{-1}$
C_0	Atomic Fraction in Original Mixture	
C_l	Atomic Fraction in Liquid	
C_p	Specific Heat Capacity	$JK^{-1}kg^{-1}$
C_s	Atomic Fraction in Solid	
C_x	Atomic Fraction of Element x	
d	Indent Diagonal	mm
d_{diff}	Diffusion Depth	m
d_g	Grain Diameter	m
D_{sub}	Subgrain Diameter	m
D_b	Laser Beam Diameter	m
D_L	Diffusivity of Solute in Liquid	m^2s^{-1}
E	Youngs Modulus	MPa
E*	Normalised Heat Input per Unit Volume	
E_{dis}	Energy Stored due to Dislocations	J
E_0^*	Normalised Energy Density	
E_v	Volumetric Energy Density	Jm^{-3}
f	Precipitate Volume Fraction	
f_l	Fraction Liquid	
f_s	Fraction Solid	
F	Fourier Number	
G	Thermal Gradient	Km^{-1}
G_s	Shear Modulus	MPa
h	Hatch Spacing	m

$\mathbf{H}$	Heat Input per Unit Length	Jm^{-1}
$\mathbf{H_f}$	Latent Heat of Fusion	Jkg^{-1}
$\mathbf{h_s}$	Enthalpy at Melting	Jkg^{-1}
HV	Hardness	HV
$\mathbf{I}$	Second Moment of Inertia	m^4
$\mathbf{K}$	Partition Coefficient	
$\mathbf{k_x}$	Solution Strengthening Constant of element X	
$\mathbf{K_0}$	Modified Bessel function of the 2^{nd} kind and the 0^{th} order	
$\mathbf{k_e}$	Equilibrium Partition Coefficient	
$\mathbf{L}$	Layer Height	m
$\mathbf{L}$	Characteristic Length	m
$\mathbf{L_h}$	Quadratic function of harmonic perturbation	
$\mathbf{L_{ppt}}$	Precipitate Spacing	m
$\mathbf{M}$	Taylor Parameter	
$\mathbf{M_d}$	Metal d-level Number	
$\mathbf{M_x}$	Weight fraction of element x	
$\mathbf{N}$	Number of Grains	
$\mathbf{N_v}$	Electron Valence Number	
$\mathbf{P}$	Laser Power	W
Pe	Peclet Number	
$\mathbf{q}$	Rate of Heat Flow	W
$\mathbf{r}$	Distance to Point Source (2D)	m
$\mathbf{r_b}$	Laser Beam Radius	m
$\mathbf{r_{ppt}}$	Precipitate Radius	m
$\mathbf{R}$	Distance to Point Source (3D)	m
$\mathbf{t}$	Time	s
$\mathbf{t_r}$	Relaxation Time	s
$\mathbf{t_v}$	Vulnerable Time	s
$\mathbf{T}$	Temperature	K
$\dot{\mathbf{T}}$	Cooling Rate	Ks^{-1}
$\mathbf{T_0}$	Initial Temperature	K
$\mathbf{T_b}$	Boiling Temperature	K

$\mathbf{T_e}$	Equilibrium Temperature	K
$\mathbf{T_l}$	Liquidus Temperature	K
$\mathbf{T_m}$	"Melting" Temperature	K
$\mathbf{T_s}$	Solidus Temperature	K
$\mathbf{v}$	Laser Velocity	ms^{-1}
$\mathbf{v_d}$	Solute Redistribution Speed	ms^{-1}
$\mathbf{V}$	Solidification Front Velocity (typically laser velocity used)	ms^{-1}
$\mathbf{x}$	Distance in x direction	m
$\mathbf{y}$	Distance in y direction	m
$\mathbf{z}$	Distance in z direction	m
$*$	Normalised Quantity	
$\boldsymbol{\alpha}$	Thermal Diffusivity	m^2s^{-1}
$\boldsymbol{\alpha_{cte}}$	Thermal Expansion Coefficient	
$\boldsymbol{\beta}$	Shrinkage Factor, $\beta = \rho_s/\rho_l - 1$	
$\boldsymbol{\Gamma}$	Gibbs-Thompson coefficient	
$\boldsymbol{\delta_n}$	Powder Layer of Layer n	m
$\boldsymbol{\Delta H}$	Specific Enthalpy	Jkg^{-1}
$\boldsymbol{\Delta H/h_s}$	Normalised Enthalpy	
$\boldsymbol{\Delta p_c}$	Critical Cavitation Pressure	Pa
$\boldsymbol{\Delta T}$	Non-equilibrium solidification interval	K
$\boldsymbol{\Delta T_e}$	Equilibrium solidification interval	K
$\boldsymbol{\varepsilon}$	Misfit Strain	
$\boldsymbol{\varepsilon}^*$	Thermal Strain Parameter	
$\boldsymbol{\varepsilon_{p,max}}$	Critical Strain Rate in the Mushy Zone	
$\boldsymbol{\theta}$	Misorientation Angle	°
$\boldsymbol{\kappa}$	Thermal Conductivity	$Wm^{-1}K^{-1}$
$\boldsymbol{\lambda}$	$2/\alpha$	sm^{-2}
$\boldsymbol{\lambda_1}$	Primary Dendrite Arm Spacing	m
$\boldsymbol{\lambda_2}$	Secondary Dendrite Arm Spacing	m
$\boldsymbol{\mu}$	Viscosity	MPa.s
$\boldsymbol{\nu}$	Poisson's Ratio	
$\boldsymbol{\xi}$	Relative displacement (in x) from laser	m

$\boldsymbol{\rho}$	Density	kgm^{-3}
$\boldsymbol{\rho_d}$	Dislocation Density	m^{-2}
$\boldsymbol{\sigma_{PI}}$	Stress Performance Index	MPa
$\boldsymbol{\sigma_y}$	Yield Strength	MPa

1. Introduction

Additive manufacture (AM) is defined as "a process of joining materials to make objects from 3D model data, usually layer upon layer, as opposed to subtractive manufacturing methodologies" [1]. In the early 1980's, AM (also known as 3D printing) was developed in the form of stereo-lithography [2], followed by fused deposition melting in 1988. The growth of 3D printing stemmed from the fact that it allowed rapid prototyping of complex parts, with minimal waste and tooling.

With the use of metallic powders and lasers, additive manufacturing of metals was first attempted in 1993 [3]. Attempts have been made to use both powder and wire as the stock material and using lasers, electron beams and electric arcs to melt the material. This thesis will focus on two main processing methods:

- **Laser Powder Bed Fusion (L-PBF)** also known as Selective Laser Melting (SLM).
- **Laser Direct Energy Deposition (L-DED)** also known as Laser Engineered Net Shaping (LENS) or sometimes Direct Laser Deposition (DLD).

AM generally has applications in biomedical, dental, auto, energy and aerospace industries [4–7], with aerospace being the focus here. Both L-PBF and L-DED are widely used for aerospace applications. L-PBF is used to create complex components such as topologically optimised brackets and fuel nozzles (e.g. GE LEAP fuel nozzle [8]), because of the light weighting benefits [6,8]. DED is mainly used for repair of components because of its ability to deposit on a previously existing part e.g. repairing turbine blisks [6,9].

There are, however, several issues with AM, these include residual stresses, anisotropy and internal defects such pores and cracks [4,6]. One of the critical challenges for AM components prior to application in aerospace is getting certification. This is due to the issues mentioned above as well as problems such as traceability of components from raw powder through printing, machining, heat treating etc. [6]. It is generally recognised that repeatability of the printing process needs to be improved, with feedback control of the process being a key part of this [9–11].

1.1. Thesis Structure

This work looks at the relationship between the inputs into the AM process and the mechanical properties produced as a result. In-situ thermal monitoring is used to analyse the thermal signature, simplifying the data processing methodology, whilst retaining sufficient information as to understand the materials response. This allows for correlation between the thermal signature and the microstructural/mechanical properties of the final part. This information is used to implement a control loop and to understand what effect this would have on component properties.

Chapter 5 looks at the definition and different ways of assessing alloy printability. Different failure mechanisms are explored and the susceptibilities of alloys to these is calculated, comparing L-PBF and L-DED. The focus of Chapter 6 is on L-PBF, looking at the thermal signals using pyrometry and analysing defects in the form of swelling.

Chapter 7 introduces the L-DED process and explores several monitoring techniques which can be used to interrogate the melt pool. These thermal signatures are related to both the microstructure and the mechanical components of the final component. Coaxial monitoring is selected as the most applicable monitoring technique for L-DED and is used going forward. In Chapter 8, thermal monitoring is shown to be insufficient on its own to explain the hardness variation measured in Inconel 718 components. The influence of imposed thermal conditions on various strengthening mechanisms present in Inconel 718 is explored, and these are investigated to determine which are responsible for the geometric variation of hardness.

A process control algorithm was developed for L-DED using coaxial monitoring, this is covered in Chapter 9. The effect of controlling the thermal signal on both microstructural and mechanical homogeneity is explored. The changes in grain structure found in Chapter 9 are covered in Chapter 10, explaining how the melt pool morphology affects the final grain structure.

Finally, Chapter 11 brings together the work done in both L-PBF and L-DED, showing the range of grain structures and mechanical properties possible using both processes. The ranges of the conditions present within both processes are compared and it is demonstrated that properties obtained using L-PBF cannot necessarily be obtained using L-DED, finally linking this back to the printability discussion initiated in Chapter 5.

2. Literature Review

Parts of this chapter are taken from the review paper published in the Journal of Materials Processing Technology by Clare et al. [12]. The full publication is available at: https://doi.org/10.1016/j.jmatprotec.2021.117358. Only sections written by L. Chechik are reused, with permission obtained from Elsevier B.V.

2.1. Additive Manufacturing

Two additive manufacturing processes are used in this work. These are both laser and powder based; L-PBF and L-DED. The differences between the main parameters can be seen in Table 2-1, which also includes other forms of additive manufacturing. Both methods require a Computer Aided Design (CAD) file to be imported, which contains the 3D model of the component to be built. Typically, L-PBF uses a narrower, lower power laser than L-DED, but with much faster scanning speeds. Overall, this results in slower production times, but the smaller laser spot allows for production of more complex components.

Table 2-1: Comparison of process parameters for DED vs PBF. Reported by DebRoy et al [4]

Process	DED			PBF	
Feedstock	Powder	Wire		Powder	
Heat source	Laser	E-beam	Electric arc	Laser	E-beam
Nomenclature	DED-L	DED-EB	DED-PA/DED-GMA	PBF-L	PBF-EB
Power (W)	100–3000	500–2000	1000–3000	50–1000	
Speed (mm/s)	5–20	1–10	5–15	10–1000	
Max. feed rate (g/s)	0.1–1.0	0.1–2.0	0.2–2.8	–	
Max. build size (mm × mm × mm)	2000 × 1500 × 750	2000 × 1500 × 750	5000 × 3000 × 1000	500 × 280 × 320	
Production time	High	Medium	Low	High	
Dimensional accuracy (mm)	0.5–1.0	1.0–1.5	Intricate features are not possible	0.04–0.2	
Surface roughness (μm)	4–10	8–15	Needs machining	7–20	
Post processing	HIP and surface grinding are seldom required	Surface grinding and machining is required to achieve better finish	Machining is essential to produce final parts	HIP is rarely required to reduce porosity	

2.1.1. Laser Powder Bed Fusion (L-PBF)

Powder bed techniques work by lowering a base plate (onto which the part is built) in constant increments, known as the layer thickness. Each time the plate is lowered, a thin layer of powder is deposited by a wiper/roller system as shown in Figure 2-1. The CAD file is sliced into thin sections, each of a layer thickness. A laser rasters across this thin powder layer in the pattern defined by the sliced CAD model, melting the required regions - bonding them; the powder bed acts as a support and conducts heat away.

This process allows for complex components (or prototypes) to be built with internal detail e.g. cooling channels or lattices. The number of processing steps required to make the final component can be greatly reduced compared to traditional manufacturing. Also, because of the near-net shape component which is removed from the printer, little or no machining is necessary significantly reducing the amount of waste material.

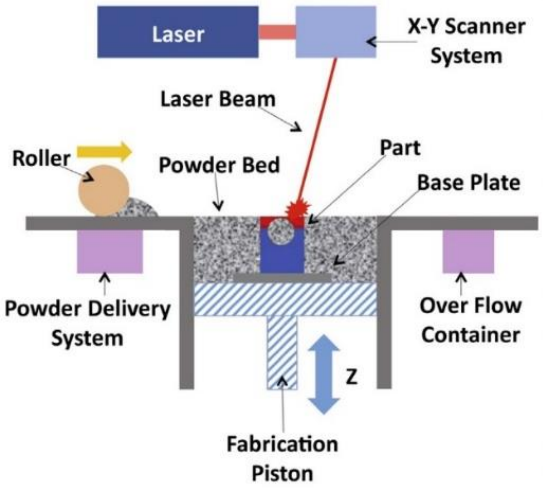

Figure 2-1: Schematic of the L-PBF process; reported by Thompson et al [13]

2.1.2. **Laser Direct Energy Deposition (L-DED)**

In blown powder methods, rather than using a bed of powder, a nozzle delivers a stream of powder (using an inert carrier gas) and focuses this at a point just above the substrate. The laser is also directed through the deposition head (which is controlled using a CNC system) and focussed at the same point as seen in Figure 2-2. The effect is that the powder is melted just above the substrate and then coalesces with the melt pool.

Due to the free movement of the deposition head this process does not require discrete layers allowing the laser to deposit continuously. Since this process is the reverse of CNC milling, 5 axis systems have been developed allowing geometries which cannot be built using powder bed e.g. overhangs and very large components. This set-up lends itself to repairs since the deposition head can build in any direction unlike the vertical restriction of L-PBF. Repairing metallic components is an enormous industry, with many turbine engine components being very expensive to replace.

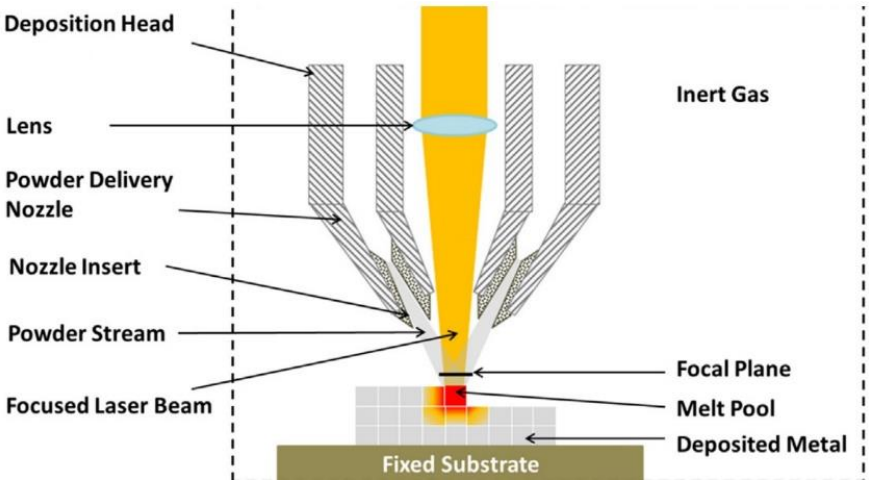

Figure 2-2: Schematic of the L-DED process; reported by Thompson et al [13]

2.1.3. **Imposed Conditions**

In conventional processing, if a component was made by casting and machining, the thermal history would be:

1. Heating of billet to the melting point
2. Pouring molten metal into preheated mould
3. First metal to touch mould will solidify rapidly
4. Remaining metal would cool at a relatively slow rate due to the thermal mass of the casting
5. Partial reheating of near-surface region due to machining

The majority of the component experiences a fairly constant, steady cooling rate, allowing for analysis using simple thermal and solidification models. The development of these models has taken decades, with many complicated issues being resolved.

In additive manufacturing, the thermal history would be:

1. Laser heats localised area to the melting point
2. Conduction from the melt pool causes a heat affected zone
3. As the laser moves, the large thermal mass of un-melted material causes the melted region to solidify rapidly
4. The subsequent layers re-melt the original region
5. Once the laser is further away (subsequent hatches), this region is reheated when the laser passes

This thermal history can cause many issues due to the multiple reheating cycles and residual stresses as will be discussed below [14–16]. The key parameters which are frequently investigated are G (thermal gradient ahead of solidification front) and V (interface growth velocity). V is often taken to be more important and is often taken to be the laser velocity. In directional solidification (which is frequently the case in AM) the cooling rate can be written as $\dot{T} = \frac{dT}{dt} = GV$ [17]. Cooling rates for different AM techniques are summarised in Table 2-2; with L-PBF being reported as $\sim 10^5$-10^6 and L-DED as $\sim 10^3$-10^4. Both are much quicker than common manufacturing processes e.g. casting (Table 2-2).

Table 2-2: Comparison of cooling rates between AM and conventional manufacturing methods. Reported by DebRoy et al [4]

Process	Cooling rate [K/s]
AM cooling rates	
DED-L	3×10^3–7×10^3
DED-L	1×10^3–4×10^3
DED-L	5×10^3–3×10^4
DED-GMA	10^2–10^3
PBF-EB	5×10^4
PBF-EB	5×10^4
PBF-L	5×10^5
PBF-L	1×10^6–6×10^6
Common manufacturing processes	
Casting	10^0–10^2
Arc welding	10^1–10^3
E-beam welding	10^2–10^4
Laser welding	10^2–10^6

The interplay between these two variables can be used in many different ways. The G/V ratio influences the stability of the solidification front and hence the microstructure. If the planar solidification front breaks down (e.g. too high a constitutional undercooling), cells and dendrites can form, as explored in Section 2.4.1 [17,18].

Rapid Solidification

If the solidification velocity is too high, this is known as rapid solidification and can cause solute trapping. Solute trapping occurs when the solidification front moves quicker than the solute atoms can diffuse in the liquid state, $V > \frac{D_L}{a}$ where D_L, diffusivity of the solute in the liquid; a, interatomic spacing.

During rapid solidification, chemical equilibrium is not reached. Instead, the composition at the interface can be calculated using a modified speed dependent partition coefficient; the form for a dilute solution is:

$$k(V) = \frac{\frac{V}{v_D} + k_e}{\frac{V}{v_D} + 1}$$

Equation 2-1

Where k, partition coefficient; V, interface velocity; v_D, solute redistribution speed (also known as the atomic diffusion velocity); k_e, equilibrium partition coefficient. At low V, $k \approx k_e$, so the interface is in equilibrium; at high V, $k \approx 1$, there is no time for diffusion and hence $C_S = C_L$ (Solid and liquid composition respectively) [19]. v_D is essentially the dendrite growth velocity and is regularly used to fit the model to known results of dendrite undercooling. Direct measurement of v_D was performed using pulsed laser melting and the value led to agreement between experiments and the dendrite growth model [20]. Limited experimental results seem to validate this rapid solidification model [21]. The speeds needed to achieve rapid solidification are said to be on the order of cm/s for localised diffusion and m/s for complete solute trapping, which would again result in planar solidification [18].

Typical L-PBF velocities are on the order of 1 ms^{-1}, so are on the boundary of solute trapping, but are frequently assumed to occur under rapid solidification conditions. Since L-DED is a slower process, with typical velocities of ~ 1 cm/s, the process is on the cusp of rapid solidification. This suggests that significant diffusion may occur in L-DED, which is not present in L-PBF due to the higher processing speeds. Despite L-PBF being under rapid solidification, steady-state growth theory applies if [22]:

$$\frac{\frac{D_L \delta V}{V \delta x}}{V_S} \ll 1$$

Equation 2-2

Harrison performs an approximation and gets a left hand side of order 10^{-6} to 10^{-4} [23]. This uses 10^{-3} s^{-1} to 10^{-4} s^{-1} as a value for $\frac{D_L \delta V}{V \delta x}$ which originates from Zimmermann with no prior justification [22].

The numerical value of the cooling rate ($\dot{T}$) is also under great debate, with suggested values varying between 10^3 Ks^{-1} to 10^6 Ks^{-1} (for both L-PBF and L-DED) although L-PBF typically seems to

be towards the higher end as summarised in Table 2-2 [4,17,24–26]. Using dendrite arm spacing (DAS), the cooling rate can be calculated and this was found to be 3×10^5 Ks^{-1}, within the values stated in literature [23]. Using relations between DAS and cooling rate [27,28] the cooling rates can be further validated.

Reheating Cycles

The AM process is further complicated by the subsequent reheating cycles. These occur both within the same layer, when the laser passes nearby and in consecutive layers, when the laser passes above the solidified region. The latter is more significant and so more frequently studied as seen in Figure 2-3 [29].

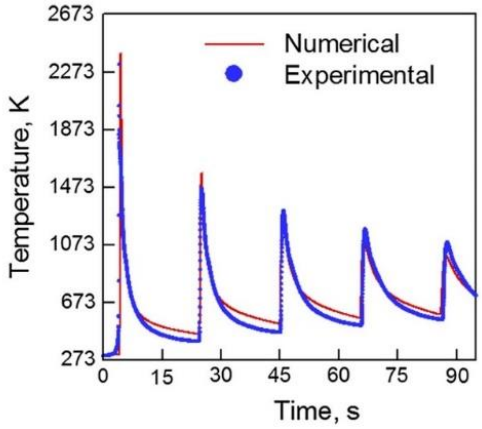

Figure 2-3: Variation of temperature with subsequent laser passes. Reported by Mukherjee et al [30]

These multiple reheating cycles cause the total heat to increase and therefore the strain experienced by the part increases with build height, this build-up of strain can be predicted using finite element modelling [30]. These high strains can cause cracking in the finished parts if they are not stress relieved. Due to the varying cooling rates, the microstructure varies with depth. This means that you might get more segregation in lower layers and hence potential for different cracking mechanisms.

2.2. Modelling of Thermal Fields

Many fundamental studies on additive manufacturing use a form of the Rosenthal equation to model the thermal fields surrounding the laser. This is an analytic equation of the steady state temperature field surrounding a moving heat source (in this case, a laser). In an infinite 3D material, the equation takes the form of:

$$T = T_0 + \frac{P}{4\pi\kappa}\exp(-\lambda v\xi)\frac{\exp(-\lambda vR)}{R}$$

Equation 2-3

where T, final temperature; T_0, initial temperature; P, laser power; κ, thermal conductivity; $1/2\lambda = \kappa/\rho C_p = \alpha$, thermal diffusivity; λ defined for convenience; ρ, density; C_p, specific heat capacity; v, laser velocity; $\xi = x - vt$, x displacement relative to laser position; $R = \sqrt{\xi^2 + y^2 + z^2}$, distance from point source [31]. However, many assumptions are made when deriving this equation:

- κ and λ are assumed to be temperature independent
- Power and velocity are taken to be constant
- The laser is assumed to be a point source

- There are no surface losses (no radiation)
- The latent heat of fusion is ignored
- No loss of material is experienced through vaporisation

Equation 2-3 is widely used as a base for complex models e.g. to predict the microstructure of a steel post laser transformation hardening. The parameters of the process were put into the Rosenthal equation, a kinetic strength for each heat cycle was calculated and hence a percentage martensite extracted; this method was shown to be accurate using hardness testing [32].

One of the larger flaws with the original Rosenthal model was the assumption of a point source, in reality all sources have a power distribution, typically between Gaussian and top-hat. Equation 2-4 was adapted to have a Gaussian profile, making the calculation more complex but the results more accurate [33,34]:

$$T = T_0 + \frac{2A\alpha P}{\kappa\pi^{3/2}} \int_{-\infty}^{\infty} \frac{exp\left[-2\frac{(\xi + vt)^2 + y^2}{{D_b}^2 + 8\alpha t} - \frac{z^2}{4\alpha t}\right]}{\sqrt{\alpha t}({D_b}^2 + 8\alpha t)} dt$$

Equation 2-4

where A, absorptivity; t, time; D_b, laser beam diameter (Gaussian).

Note that now there is an absorptivity value, which is frequently used to calibrate the models. By differentiating this thermal field, the temperature gradient, G, can be found and the interface velocity, V can be taken as the laser velocity, v, as these should be equal in steady-state. This allows for calculation of melt pool dimensions and prediction of microstructure in L-PBF using processing maps (Figure 2-13).

In L-DED, the situation is different as more material is deposited with each pass and often, thin sections are created. This is closer to a 2D situation, so the 2D Rosenthal equation applies (Equation 2-5) [31]. Modelling of the L-DED process has been extended, as the powder flow means that not all of the lasers power is absorbed by the surface (effectively reducing the absorptivity). This has been geometrically calculated for laser cladding as shown in Figure 2-4, so both the reflection of the laser from the powder and the absorption of the heat by the powder are taken into account and now the effective power is dependent on the powder flow rate.

$$T = T_0 + \frac{P}{2\pi\kappa} \exp(-\lambda v\xi) K_0(\lambda vR)$$

Equation 2-5

where $r = \sqrt{\xi^2 + z^2}$, distance from point source; K_0, the modified Bessel function of the 2nd kind and the 0th order.

As aforementioned, absorptivity (A) is hard to measure and hence used as a calibration factor. Due to the complex ray paths caused by the powder, the absorptivity of a powder is higher than that of a plain metal of the same composition (as flat surfaces are reflective), this can be calculated using complex ray simulation [35]. Absorptivity itself can be measure by scanning a surface with 2 thermocouples connected to it and measuring the differences in the temperature at the two points. This was originally used on bulk materials [36], it has since been altered to be compatible with thin layers of powder [37,38]. These studies measured different trends (against temperature and power), so cannot be directly compared especially as the latter extended into the keyholing regime.

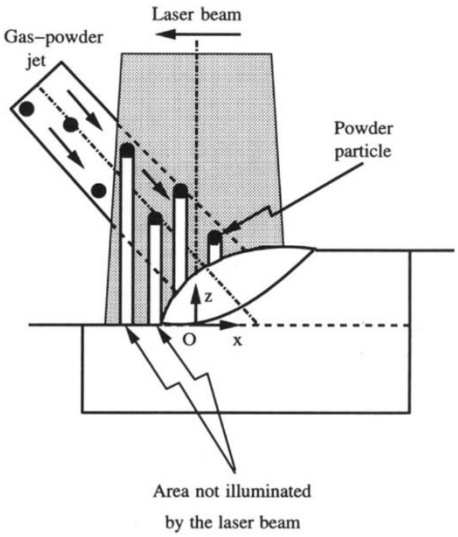

Figure 2-4: The shadowing effect of the powder, taken into account in the Picasso model. Reported by Picasso et al [39]

2.2.1. Dimensionless Numbers

Dimensionless numbers can be used to compare processes with varying conditions and see their effect on the overall process. The main numbers applicable to AM are [40]:

- **Fourier Number**: the ratio of diffusive heat rate to storage rate, $F = \frac{\alpha t}{L^2}$
- **Peclet Number**: the ratio of convection to conduction, $Pe = \frac{vL}{\alpha}$

where α is the thermal diffusivity; t is a characteristic time; L is a characteristic length and v is a characteristic velocity.

A higher Fourier number shows that heat diffuses away quicker than it can accumulate [41], this can have advantages e.g. less potential for distortion [17], however it can also lead to drawbacks e.g. lack of fusion in L-PBF [42]. Different characteristic parameters have been used, melt pool length was used as the characteristic length for both the Fourier and Peclet numbers by Mukherjee et al [17]. In this case, characteristic time can be defined as characteristic length/characteristic velocity – resulting in, $F = \frac{\alpha}{vL}$, the reciprocal of the Peclet number. A higher Fourier number is said to be desirable due to minimised distortion, which means that a lower Peclet number is desirable; this equates to saying that a conduction dominant process is desirable [17].

In other literature, the melt pool width has been used to calculate the Peclet number [43]. It is shown that the Peclet number for high density conditions is much larger than that for low density conditions. It was found that despite similar melt pool shapes (looking top down), melt pool depth varied significantly; higher energy density lead to more convection and a deeper melt pool [43].

2.2.2. **Further Modelling**

The models described above are simple and only consider heat flow, so are of limited use; more complex models do exist, but are outside the scope of this project. The current work in this field is reviewed in [44–46]. There is a common goal of being able to model the entire process on a range of size-scales and has been dubbed a 'Digital Twin' [44], so meaningful results can be gained without the need for many expensive experiments. The interlinking of the main components is shown in Figure 2-5 and are:

- Heat transfer model (FE and Lattice Boltzmann are frequently used)
- Model calculating the true absorptivity of the powder
- Solidification model including nucleation and segregation
- Development of microstructure and propensity to hot tearing
- Mechanical properties (residual stresses) of final part

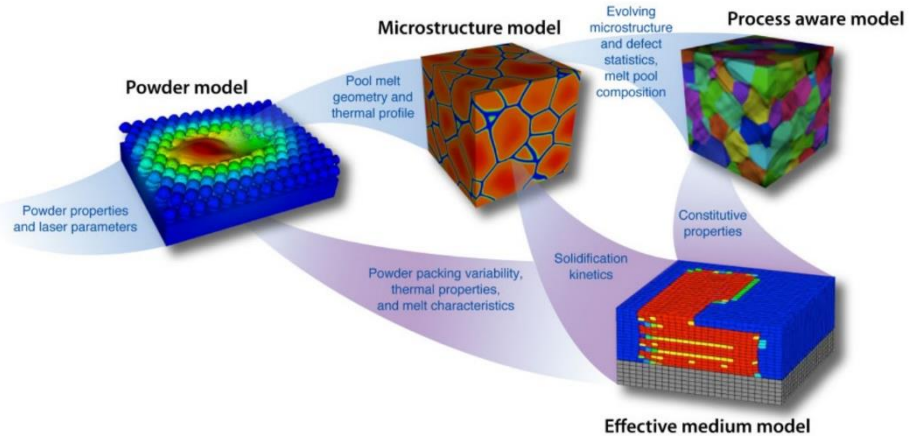

Figure 2-5: Interlinking between the different scales of modelling required for a complete 'Digital Twin'. Reported by King et al [45]

2.3. Alloy Selection for Additive Manufacturing

Many different materials have been tested in AM. Depending on the application in mind, the required materials and mechanical properties vary. Lightweight brackets for space applications may require Aluminium or Titanium, whereas components for turbine use need to withstand high stresses at temperature, so Nickel and Titanium alloys are typically chosen. For prototyping tools and moulds for the automotive industry, tool steels are normally most applicable [4,9].

For each of these families of alloys, the printability of some key alloys are summarised in Table 2-3 for L-PBF, L-DED and for electron beam PBF (EB-PBF) [12]. These are categorised into 3 levels:

- **Easily printable**; successful building widely reported in the literature. These can be built repeatedly with minimal defects; the mechanical properties of components are comparable to those conventionally manufactured (e.g. wrought).
- **Somewhat printable**; successful building reported several times in the literature. Some defects remaining, leading to inferior mechanical properties when compared to those conventionally manufactured (e.g. wrought).
- **Not printable**; unsuccessful building reported in the literature, or no reports. If printing is possible, many defects present throughout sample e.g. cracks.

L-PBF is the most widely published form of additive manufacturing, ahead of EB-PBF and L-DED [47] as seen in Table 2-3. This is especially the case for steel and aluminium components as these typically require complex shapes, which L-PBF is suited to due to its small laser spot size. Since aerospace repair is a major application of Titanium components, L-DED is best suited to this, so Titanium AM seems to be done predominantly using L-DED [4,6].

EB-PBF is not used in this thesis, but is worth briefly mentioning. When using a laser, a galvanometer must be used to physically move a mirror to move the beam. With an electron beam, the positioning is done using an electro-magnetic coil, which allows for a much quicker beam movement due to the lack of inertia [4]. This increase in speed allows for the location and size of the molten area to be better defined and hence a closer control of the cooling rate. Both G and V can be controlled closely, giving the ability to select a certain grain orientation [48]. In addition, the powder bed can be pre-heated, reducing the thermal gradients and allowing for further control. This allows for a wider range of "hard to print" alloys to be manufactured (e.g., Nickels with higher γ' content). This is shown by the improved printability of CM247LC in EB-PBF as compared to L-PBF (Table 2-3). CM247LC has a high γ' content and normally suffers from hot tearing (covered in Section 5.1.5); by using EB-PBF, the solidification rate can be controlled, reducing the driving force for cracking. This increased thermal control allows for epitaxial growth of single crystals [49,50].

However, EB-PBF also experiences some issues due to its method as well as the large up-front cost [51]. Since the powder is pre-heated and partially sintered [4], complex internal geometries cannot be achieved as the internal powder cannot be removed, also this causes EB-PBF to generally have a rougher surface finish [52]. This is not helped by the larger powder size range for EB-PBF compared to L-PBF [53] meaning that the geometric accuracy is likely inferior to L-PBF. In addition, due to the vacuum during EB-PBF, certain elements evaporate, meaning that the final composition can be different to that of the initial alloy [51]. Interestingly, despite the control of the substrate temperature (which allows for close control of cooling rates), this can cause issues in alloys such as Inconel 718 where deleterious phases can form due to prolonged exposure to intermediate temperatures [48].

Until recently, the approach has been to test pre-existing alloys using AM, despite the fact that many of these alloys were created with a specific manufacturing method in mind. E.g. CM247LC and CMSX-4 were designed for directional solidification in investment casting [49,54]. These are typically heat treated post-casting as otherwise they experience segregation; unfortunately, due to the quicker cooling rates and subsequent reheating in AM, these alloys suffer from severe cracking and are typically regarded as having poor printability. In recent years, research has turned towards designing alloys with additive manufacturing in mind. These include alloys such as Scalmalloy® (a Scandium modified Aluminium alloy) [55] and ABD-900AM (a medium γ' fraction Nickel superalloy) [56].

2.3.1. **316L Stainless Steel**

316L is a widely used stainless steel, frequently found in marine, chemical and food processing industries. It's composition is shown in Table 2-4, with carbon content reduced to hinder carbide formation during welding, which can initiate failure. In AM, 316L is often used for marine and medical applications as well as general engineering structures due to its relatively low cost [4,57]. The alloy is generally regarded as being printable [4,12] so is widely studied due to the broad range of comparable data available [58]. This allows for efficient process development.

316L produced by AM is predominantly in the FCC, γ austenite phase, with some intergranular BCC, δ ferrite present [4,59]. In L-DED, columnar dendrites form around the bottom edges of the melt pool, with some regions of equiaxed grains at the top as seen in Figure 2-6a. Grains grow in a columnar manner, through multiple melt pools, following the direction of maximum heat flow (into the baseplate). In literature, some dendritic areas are seen, but the majority is of cellular nature, with a cell spacing on the order of 1-10 μm [4,59,60].

Table 2-3: Overview of printability of materials commonly produced by AM; key below. Created by the author and adapted from [12]

		L-PBF	EB-PBF	L-DED
Steel				
	304	A	C	B
	316	A	B	A
	17-4 PH	A	C	B
	H13	B	B	B
	18Ni300	B	C	B
	2507	B	C	C
Nickel				
	Inconel 718	A	A	A
	Inconel 625	A	A	A
	Hastelloy X	A	C	B
	CM247LC	C	B	C
	CMSX-4	C	B	C
	Waspaloy	C	C	C
Aluminium				
	Al Si10Mg	A	B	B
	Al-Cu-Mg	A	B	B
	4047	A	C	B
	Scalmalloy	A	C	C
	7075	B	B	C
	6061	B	C	C
Titanium				
	Ti64	A	A	A

	CP	B	C	B
	6242	C	C	B
	5553	B	C	B
	2448	B	B	C
	Ti-6.5Al-3.5Mo -1.5Zr-0.3Si	C	C	A
	55511	C	C	B

A: Easily Printable; Widely Reported	B: Somewhat Printable; Moderately Reported	C: Not Printable; Minimally Reported

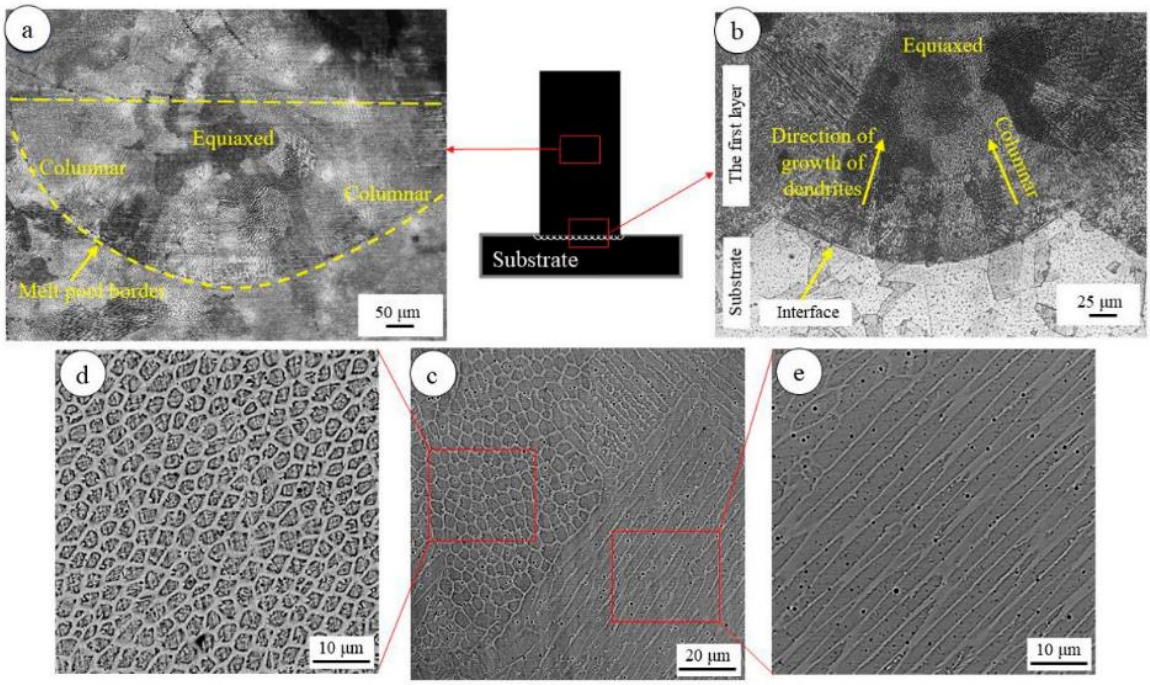

Figure 2-6: Microstructure of 316L produced by L-DED; a, b) showing structure of melt pools at different heights. c, d, e) SEM micrographs of cellular structure. Reported by Saboori et al [59]

2.3.2. **Nickel Superalloys**

A superalloy is defined as a material with exceptional mechanical properties, allowing it to be used above 540 °C or 0.7 of its absolute melting point [61,62]. These alloys can be Iron, Cobalt or Nickel based, the latter being the most appropriate for turbochargers and engines. Nickel superalloys can withstand high stresses at up to 0.9 T_m (over 1000°C). All superalloys have a face centered cubic (FCC) matrix as this increases creep resistance [63]. Nickel is FCC at room temperature, but Fe is body centred cubic (BCC) and Co is hexagonal close packed (HCP) at room temperature; both of these transition to FCC at raised temperatures. Fe and Co alloys are stabilised with FCC stabilisers (Co, Cr, Mo, W) in order to retain FCC structure at low temperatures and stabilise the FCC γ phase [61,62]. None of these alloys have a transition from FCC at higher temperatures, so these are stable to melting and hence can be used at raised temperatures. These γ stabilisers typically have a small atomic misfit to Nickel and so act to solution strengthen the alloy. Chromium also has the added

benefit of increasing the oxidation resistance, especially at high temperatures; additions of Al and Ti can further increase the oxidation resistance [63].

Original superalloys were solid solution strengthened i.e. they contained additions in the matrix, increasing strength but remaining homogeneous (e.g. Hastelloy X). These can be used at moderate temperature, but not in the components which experience the highest temperatures. It was then realised that by adding Al and Ti, precipitates can be formed, further strengthening the alloys. These are known as precipitate strengthened alloys and are more frequently used e.g. Inconel 718 and CM247LC [62,64]. Inconel 718 is very widely used in the industry and is widely regarded as the "workhorse of the aero-engine sector" [65]. The compositions of the 6 nickel superalloys reviewed in Table 2-3 can be found in Table 2-4 alongside that of 316L steel. The most common phases in Nickel superalloys are covered in Section 5.1.2.

Table 2-4: Comparison of compositions (wt%) of 316L steel and some common Nickel superalloys [62,64,66]

	Cr	Ni	Co	Mo	W	Nb	Ti	Al	Fe	Ta	C	B	Zr	Other
316L Steel	17.00	12.00	0.00	2.50	0.00	0.00	0.00	0.00	65.20	0.00	0.03	0.00	0.00	2.3Si, 1.0Mn
Inconel 718	19.00	52.77	0.00	3.00	0.00	5.10	0.90	0.50	18.50	0.00	0.08	0.00	0.00	0.15Cu
Inconel 625	21.50	62.95	0.00	9.00	0.00	3.60	0.20	0.20	2.50	0.00	0.05	0.00	0.00	N/A
Hastelloy X	22.00	49.09	1.50	9.00	0.60	0.00	0.00	2.00	15.80	0.00	0.02	0.00	0.00	N/A
CM247LC	8.00	61.42	9.00	0.50	10.00	0.00	0.70	5.60	0.00	3.20	0.07	0.10	0.01	1.40Hf
CMSX-4	6.50	64.80	9.00	0.60	6.00	0.00	1.00	5.60	0.00	6.50	0.00	0.00	0.00	N/A
Waspaloy	19.50	54.58	13.50	4.30	0.00	0.00	3.00	1.40	2.00	1.50	0.07	0.06	0.09	N/A

Mechanical Properties of Ni alloys produced by AM

The mechanical properties of as-built nickel alloys are summarised in Table 2-5. As-built properties are comparable to those produced by conventional means, with lower elongation in some cases. These can be further improved by various heat treatments as exemplified by Figure 2-7, exceeding the properties of the wrought/cast components. However, in L-DED, complex repairs are a common application, meaning that localised heat treatments are not always possible.

Nickel alloys are of great interest for aerospace application, where longevity is of utmost importance. Much work has been testing both the creep and fatigue properties of L-PBF samples. In Inconel 718, with scan strategy optimisation, a similar creep rate to wrought and a 24% increase in creep life can be achieved (in heat treated state) [67]. The elevated temperature fatigue life has also shown to be similar to wrought alloys [68], showing that printed components could be used in real-life applications. In Inconel 625, the creep strength from L-PBF exceed those of wrought samples, but with a lower ductility [69]. Overall, these creep and fatigue results show that AM can produce parts with comparable mechanical properties to wrought parts, opening the door for wider spread utilisation of additively manufactured components.

Table 2-5: Mechanical Properties of Ni Alloys produced by AM (as-built) compared with wrought

Process	Material	Yield Strength (MPa)	Elongation
Wrought	Inconel 718	1035 [70]	12
L-PBF	Inconel 718	1200 - 1213 [70]	13.1 - 30.3 [70]
EB-PBF	Inconel 718	772 – 924 [71,72]	31.5 – 40.4 [71,72]
L-DED	Inconel 718	552 [73]	16.2 [73]
Wrought	Inconel 625	513 [74]	40 [74]
L-PBF	Inconel 625	690 - 820 [74]	8 - 10 [74]
EB-PBF	Inconel 625	410 [75]	44 [75]
L-DED	Inconel 625	460 – 670 [76]	19 - 41 [76]
Wrought	Hastelloy X	367 [77]	40 [77]
L-PBF	Hastelloy X	470 – 490 [78]	39 – 41 [78]
L-EB-PBF	Hastelloy X	255 – 270 [79]	62 - 68 [79]
L-DED	Hastelloy X	800 [80]	28 [80]

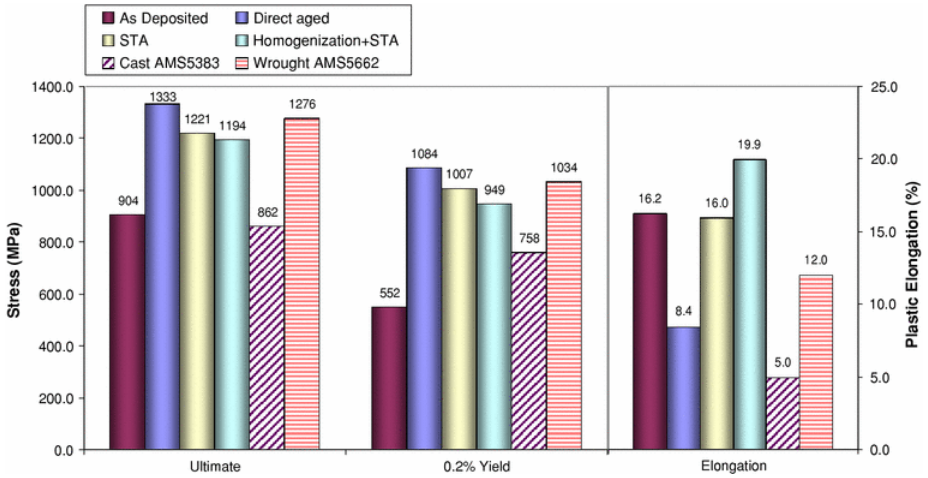

Figure 2-7: Changes in mechanical properties of L-DED manufactured Inconel 718 with different heat treatments, as compared with cast/wrought properties. (STA = Solution treatment and aging). Reported by Qi et al [73]

2.4. Energy Density and Processing Maps

To compare these parameters across machines and materials, there have been many attempts to combine the various parameters into an energy density. The simplest form is Equation 2-6, which simply calculates the volumetric energy density (VED) by dividing the power by velocity and 2 building parameters (hatch spacing, h and layer height, l) [15]. However, this ignores the machine differences, the main one being the laser beam radius, so some VEDs replace the hatch spacing with beam diameter (Equation 2-7) [81]. Neither fully captures the machine and processing parameters.

$$E_v = \frac{P}{vhl}$$

Equation 2-6

where E_v, Volumetric Energy Density [15].

$$E_v = \frac{P}{vlD_b}$$

Equation 2-7

In an attempt to overcome this, Figure 2-8 plots a normalised heat input against the reciprocal of the hatch spacing. Although this doesn't explicitly plot VED (using beam radius, r_b) against h, all the lengths are normalised by being divided by r_b, so this value is included.

The maths behind Figure 2-8 is shown in Equation 2-8 and Equation 2-9, the first showing the formula for normalised heat input, the latter showing how a normalised VED can be calculated, this will be referred to as normalised energy density (NED) throughout. Lines of constant NED (E_0^*) are shown in Figure 2-8, allowing for direct comparison between processing parameters. It allows for a quick assessment of the processing window, too low a heat input and porosity occurs due to lack of fusion, too high a heat input and swelling and/or hot tearing occur [82]. This derivation finds the volume you need to melt to avoid lack of fusion (using hatch spacing and layer thickness) and calculates the required energy to do so; in an ideal situation, E^* = 1 would lead to full melting (assuming that absorptivity, A = 0.5). In addition, if $\frac{1}{h^*} > 1, r_b > h$, so full melting should occur; it can be clearly seen that melting can occur below this threshold, but only at higher E^* values, as this has to compensate for the lack of lateral melting.

$$E^* = \frac{P^*}{v^* l^*} = \left[\frac{AP}{2vlr_b}\right]\left[\frac{1}{\rho C_p}(T_m - T_0)\right]$$

Equation 2-8

where * denotes a normalised quantity; E^*, normalised heat input per unit volume; l, layer thickness; $r_b = \frac{D_b}{2}$, laser beam radius; T_m, melting point

$$E_0^* = \frac{P^*}{v^* l^* h^*} = \left[\frac{AP}{2vlh}\right]\left[\frac{1}{\rho C_p}(T_m - T_0)\right]$$

Equation 2-9

where E_0^*, normalised volumetric energy density (NED); h, hatch spacing.

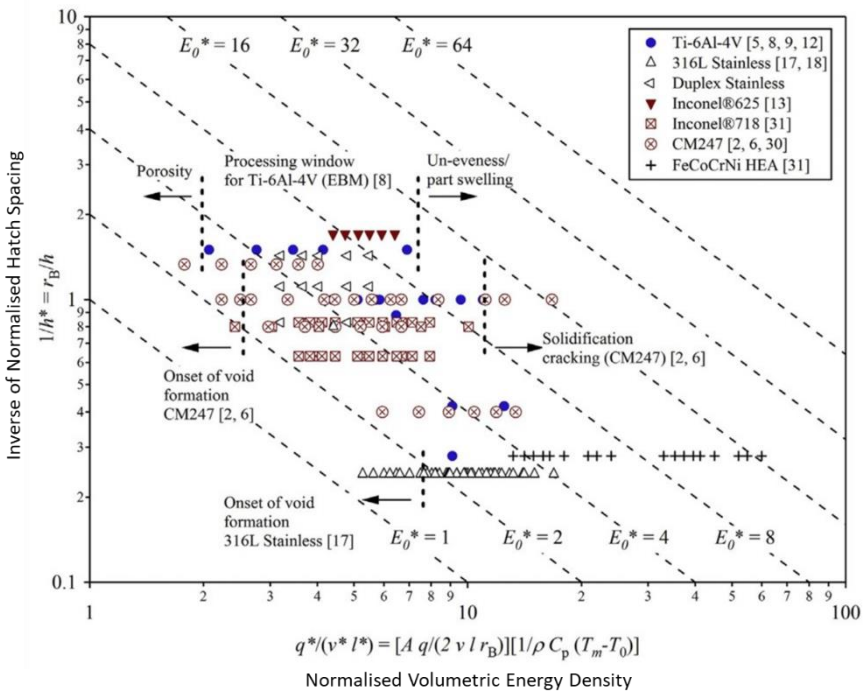

Figure 2-8: Plot of normalised heat input against 1/h showing processing ranges for different materials. Reported by Thomas et al* [82]

Lack of fusion occurs if the laser melts an insufficient thickness and so the previous layer doesn't fully bond to the new one. This can be predicted using melt pool dimensions from Equation 2-4. Figure 2-9 shows that a reduction in energy density can lead to lack of fusion porosity, however, increasing it too far can lead to keyhole porosity. Once again, there's an interplay of two defects which occur under different conditions, with a potentially narrow processing window.

Keyholing is a mode of laser welding, where part of the melt pool vaporises and forms a plasma bubble. This can entrap the photons which internally reflect, leading to near 100 % laser absorption; Marangoni flow forces this bubble deeper and so a very deep melt pool can occur despite only a small increase of power. The bubble can be trapped during solidification, increasing porosity as seen in Figure 2-9, so process parameters are typically selected to avoid keyholing [83]. Since keyholing is a cause of evaporation, it can be linked to the latent heat as expressed in Equation 2-10 for 316L steel. The second part of this forms a criterion, which can be used to predict the onset of keyholing [83,84]. This calculation looks at the energy absorbed and how far the heat can diffuse, so the volume raised above T_m can be calculated using the energy input; this leads to the key parameters being D_b and α. This is termed the normalised enthalpy (NE) and was first reported by Hann et al [84] before being extended by King et al [83]:

$$Normalised\ Enthalpy, \frac{\Delta H}{h_s} = \frac{AP}{\pi h_s \sqrt{\alpha v {D_b}^3}} = \frac{\pi T_b}{T_m} \approx 6$$

Equation 2-10

where ΔH, change in total specific enthalpy; $h_s = \rho C_p T_m$, enthalpy at melting; T_b, boiling point. This is known at the phase transition number, which itself is the inverse of the Stefan number and is frequently used in heat transfer calculations [85].

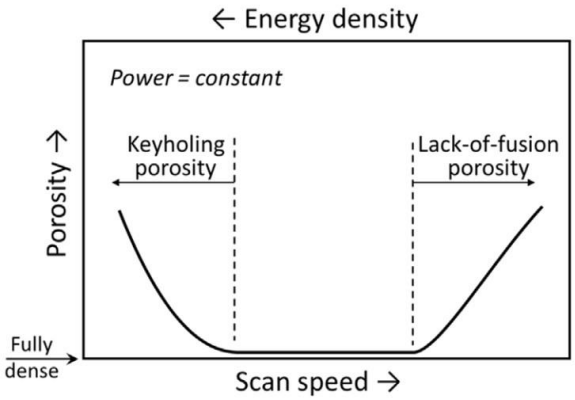

Figure 2-9: Porosity dependence on velocity, showing both keyholing and lack of fusion. Reported by Tang et al [86]

NED and NE (Equation 2-9 and Equation 2-10) are calculating a similar quantity. NED uses process parameters (hatch spacing and layer thickness); NE uses the thermal diffusivity to calculate how far the heat can diffuse. Both are interesting ways of characterising the process and can be used for different purposes e.g. normalised enthalpy can be used to characterise track welds, as they have no hatch spacing or layer thickness.

The keyhole transition can be seen if the melt pool depths are plotted against power (or VED), filled blue circles in Figure 2-10a; there is a distinct gradient change at around 70 W. This point also coincides with the sudden rise in absorptivity (black line) as explained above [38].

This step change in depth can also be clearly seen in other works [83], however not in all experiments (Figure 2-11, also 316L) [81]. The difference may be that the prior work was completed on a steel disk, whereas the latter was with a powder surface. In reality, keyholing occurs due to the formation of plasma from the evaporated metal. This does depend on the boiling point of the alloy, as considered previously [38,83,84], but can likely start below T_b, as there is a partial pressure above the surface of the melt pool.

Figure 2-11 calculates the VED using Equation 2-7, since there is no hatch spacing when scanning single tracks. No difference in trends can be seen in the transition between conduction and keyhole modes. There is clearly a correlation between depth and VED, however for different powers you get a depth variation of up to ×3, so VED isn't necessarily a good way of combining processing parameters [81]. The Rosenthal equation (Equation 2-4) can be used to predict depths and it would be interesting to see the trend in theoretical depths since they do not accommodate for the keyhole mode. Different studies find different critical NE values for the keyhole transition, this has been theoretically calculated as 6 [83], but experimentally measured at both 10 and 30 [83,84], so there is no widely-accepted keyhole threshold.

It has been determined that for each material there is a processability window – often with porosity if insufficient energy is present. Keyholes can occur if there is too high an input energy, this can also increase propensity to hot tearing due to a longer solidification time and so more time for segregation; many of the types of failure stem from excessive segregation (Section 5.1.4) [87,88].

A different form of processing map has been created for 2D situations (typically L-DED). Figure 2-12 shows a surface relating the normalised values of the melting point, the melt pool length and the deposit height. Using this allows for variation of parameters in order to maintain the melt pool volume through the build [89,90]. Similar maps have been created replacing melt pool length with both G and $\dot{T}$; both of these can be calculated using Equation 2-5 [91,92].

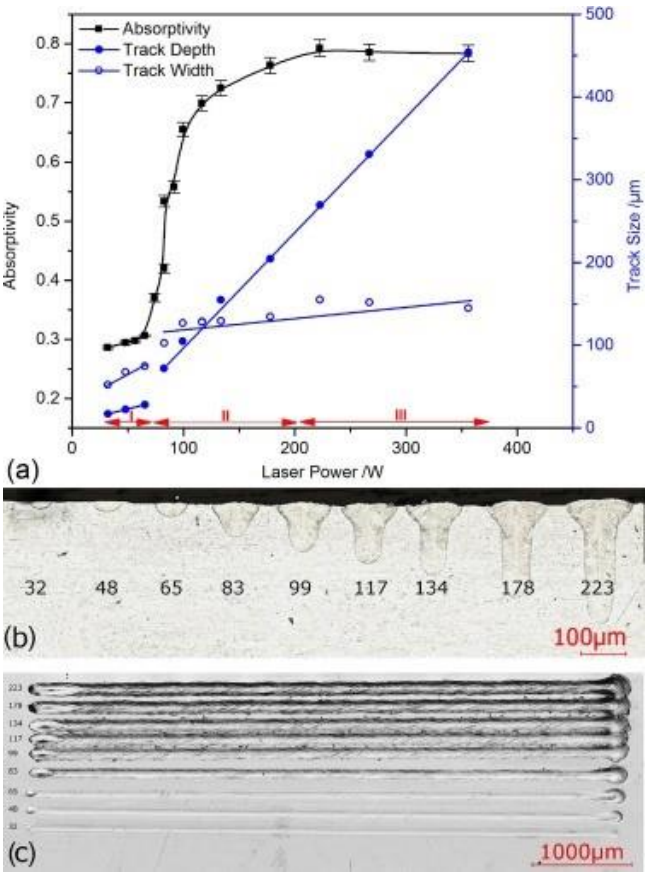

Figure 2-10: Variation of melt pool dimensions with laser power, showing 2 distinct regimes. Reported by Trapp et al [38]

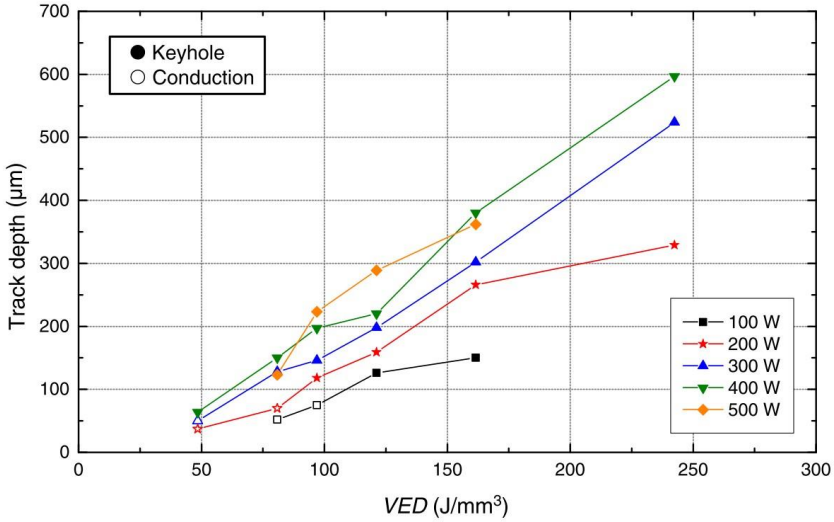

Figure 2-11: Variation of melt pool depth with VED. Reported by Scipioni Bertoli et al [81]

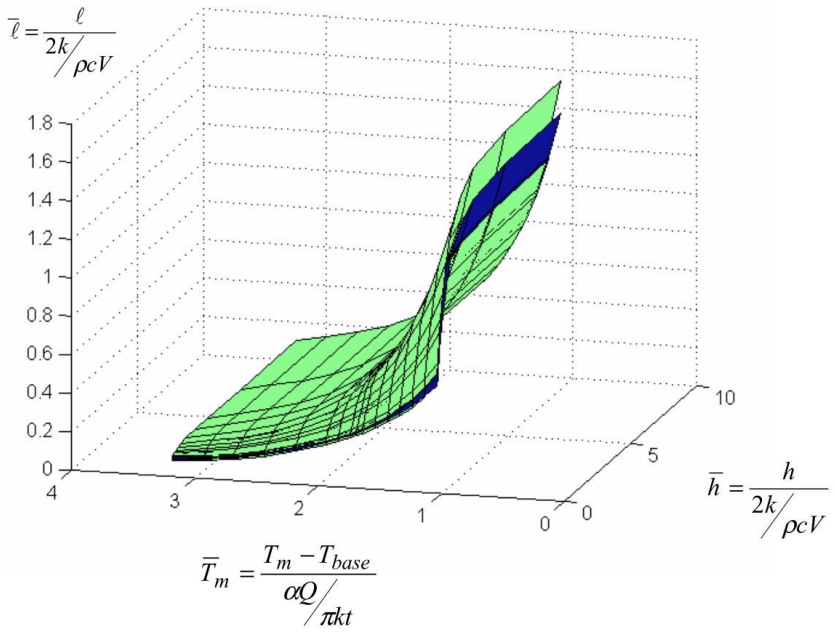

Figure 2-12: Processing map relating the melting point, deposit height and the melt pool length for L-DED. Reported by Vasinonta et al [89]

2.4.1. Solidification Structure

The solidification microstructure is directly related to the speed and stability of the solidification interface. At slow speeds, the interface is stable and in equilibrium, so planar growth occurs (very left of Figure 2-13a). The G/V ratio effectively defines the stability of this interface, the interface breaks down, first into cells and then into dendrites [18], if:

$$\frac{G}{V} > \frac{\Delta T_e}{D_L}$$

Equation 2-11

where ΔT_e, Equilibrium solidification interval; D_L, Diffusion coefficient in the liquid. This is exemplified in Figure 2-14, showing the morphology of both cells and dendrites as well as the intermediate state of dendritic cells. These occur when instabilities break down the ordered cellular nature and side-branching starts to occur.

Both cells and dendritic cells are shown to grow parallel to the maximum heat flow, which is typically perpendicular to the melt pool boundary [88,93–95]. This is shown in

Figure 2-6, which shows that the direction of the columnar structure is perpendicular to the melt pool edge. At slower cooling rates, dendrites dominate, and these are less sensitive to the direction of the maximum thermal gradient.

In AM, the left hand side of Equation 2-11 is typically significantly higher than the right, so cellular and dendritic microstructures dominate [29]. As the velocity is further increased, solute trapping may occur and may produce a planar interface (right side of Figure 2-13a).

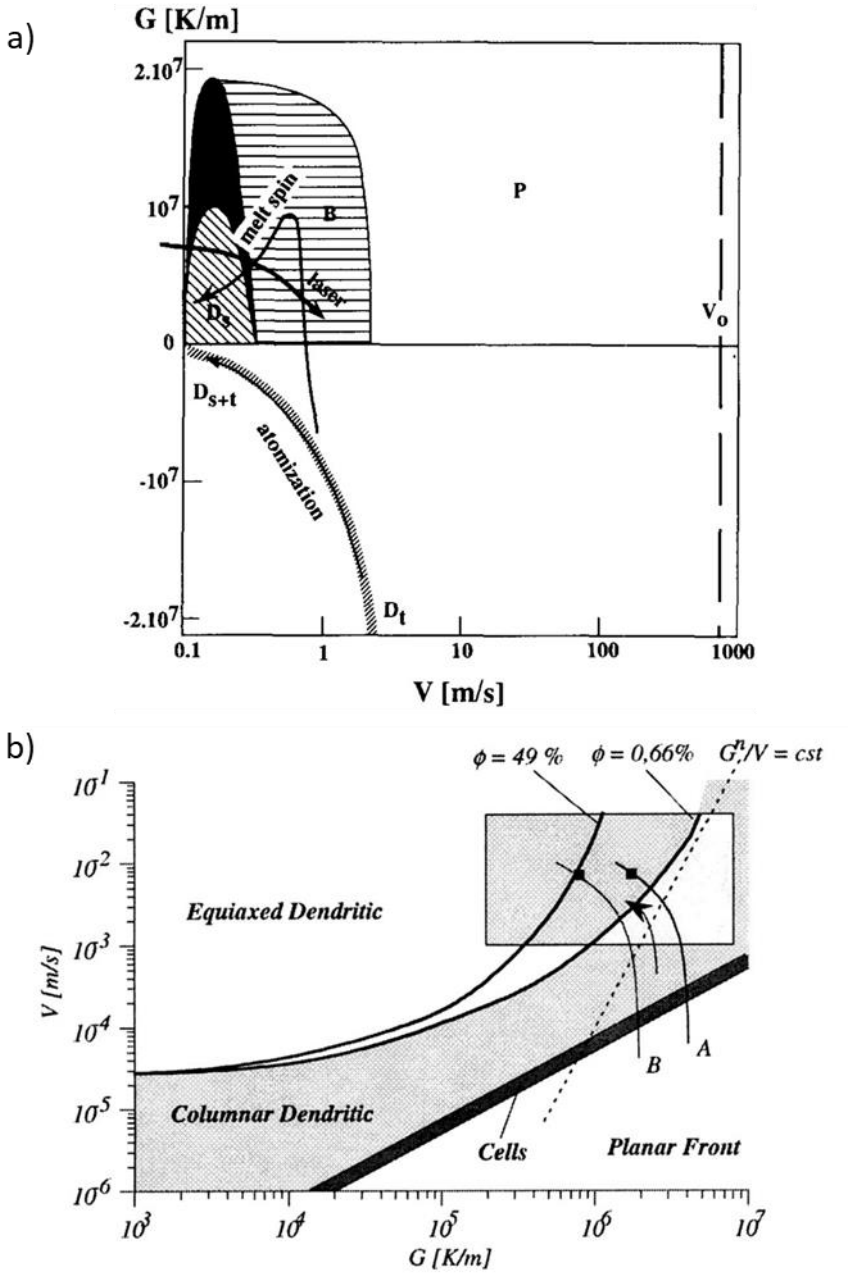

Figure 2-13: Plots of G vs V, showing the relationship between processing parameters and microstructure.

a) Different microstructures possible over wide range of solidification parameters; P, planar; D_s, dendrites (solutal); D_t, dendrites (thermal); B, banded microstructure (alternate planar and cellular); black region, cellular. Reported by Kurz and Trivedi [18]

b) A microstructure selection plot for CMSX-4, with the rectangle showing typical laser process conditions. A and B show the melt pool solidification curves for initial substrate temperatures of 20°C and 500°C respectively. Reported by Kurz et al [96]

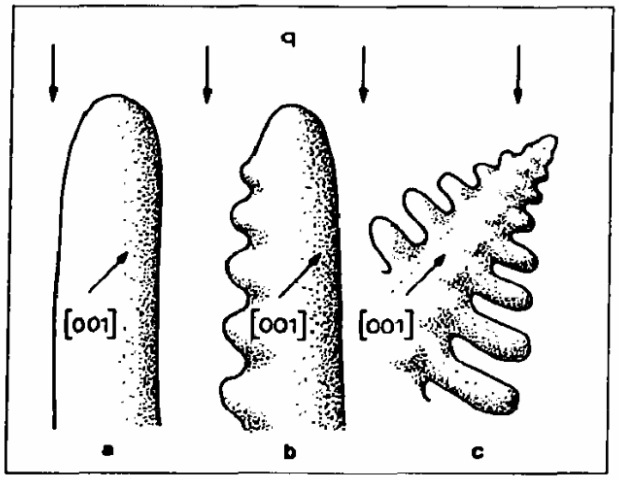

Figure 2-14: Summary of possible solidification structures. a) Cells, b) dendritic cells, c) dendrites. Directional growth can lead to all 3 formations; cells during stable growth, with perturbations/instability in the thermal field dendritic cells can form. Anisotropy of interface energies forces dendrites to grow with a preferential crystallographic direction, whereas cells grow in the direction of greatest heat flow. Reported by Kurz and Fisher [97]

Dendrite Arm Spacing (DAS)

Solidification occurs in a cellular and/or dendritic manner, typically anti-parallel to the heat flow, with regions of the similar growth direction forming grains. It has been shown that the primary dendrite arm spacing (PDAS, λ_1) can be related to both G and V. This theoretically allows for calculation of thermal conditions from the final microstructure. Two equations for PDAS were derived by Trivedi [98] and Kurz/Fisher [27]:

$$\lambda_1 = 2.83 \times G^{-0.5} \left(\frac{\Delta T_e L_h k D_L \Gamma}{V} \right)^{0.25}$$

Equation 2-12

$$\lambda_1 = 4.3 \times \left(\frac{\Delta T}{G} \right)^{0.5} \left(\frac{D_L \Gamma}{V k \Delta T_e} \right)^{0.25}$$

Equation 2-13

where ΔT_0, ΔT_e, equilibrium and non-equilibrium solidification ranges respectively; Γ, Gibbs-Thompson coefficient; L_h, quadratic function of harmonic perturbation [99].

For high laser velocities, both take the form [27,100]:

$$\lambda_1 \propto G^{-0.5} V^{-0.25}$$

Equation 2-14

The results are compared in Figure 2-15, which shows that the two criteria follow a similar trend, displaced by a factor of 1.5x and seem to act as lower and upper bounds respectively.

For the secondary DAS (λ_2), it was shown that:

$$\lambda_2 \propto \dot{T}^{-n}$$

Equation 2-15

where *n* is materials dependant, taken to be in the range of 0.2-0.4 [28,29]. The same relation has been successfully used with PDAS, but with a different constant of proportionality with $n = 0.36$ [23].

In 316L steel, cells are typically formed during AM rather than dendrites, this is also the case in L-PBF, as shown in Chapter 11. In these cases, primary cell arm spacing (PCAS) can be measured, being equivalent to the PDAS - with higher cooling rates reducing PCAS [59].

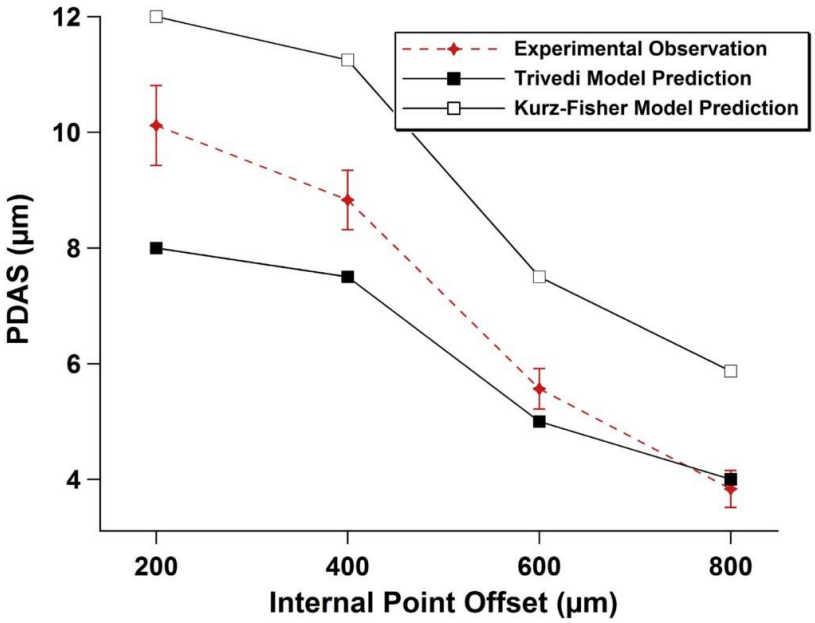

Figure 2-15: Comparison of two PDAS calculations with experimental values for varying energy input. Reported by Raghavan et al [99]

Columnar-Equiaxed Transition (CET)

As explained in Section 5.1, modern superalloys are developed to have columnar microstructure and single crystals, however these suffer greatly from hot tearing. Using AM, there are two main focuses: building single crystal components (typically using EB-PBF) [49,50] or building equiaxed structures, reducing likelihood of cracking. For an equiaxed microstructure, large-scale grain nucleation must occur which can be achieved by adding grain refiners (which initiate dendritic growth), or by increasing the undercooling, as this exponentially increases nucleation rate [33,101]. Assuming steady state growth, the columnar-equiaxed transition can be shown to occur when:

$$\frac{G^n}{V} > K$$

Equation 2-16

where *n* and *K* are materials specific (3.4 and $2.7 \times 10^{24}\ K^{3.4}\ m^{-4.4}\ s^{-1}$ respectively for CMSX-4, a single-crystal Nickel superalloy) [33,96]. Figure 2-13b shows the conditions experienced in laser processing (in the rectangle), crossing between equiaxed and columnar dendritic regions. The DAS can also be calculated using the cooling conditions as explained in Section 2.4.1.

Since laser processing occurs across the transition, it should be possible to tailor the microstructure by altering process parameters. This has been done by selecting 3 scan strategies (in EB-PBF) and spatial variation of microstructure has been achieved (Figure 2-16) [102]. In reality, the values of both G and V change throughout the process, even in different parts of the melt pool. Because of this, a range of parameters is experienced, as marked in Figure 2-13b and Figure 2-16a,

unfortunately these tend to spread across the transition, making exact microstructural prediction more difficult [96,103].

To further complicate this, due to each region being re-melted by successive layers, epitaxial growth of previous grains can occur. This can be used to carefully grow a single crystal [33]. This is a complex interplay, for example, a larger melt pool is typically associated with reducing thermal gradient [104,105], which would push the process towards the equiaxed region (Figure 2-16). However, the melt pool is also likely to be deeper, so more likely to re-melt sufficient material to reach the larger grains below, which would encourage epitaxial growth.

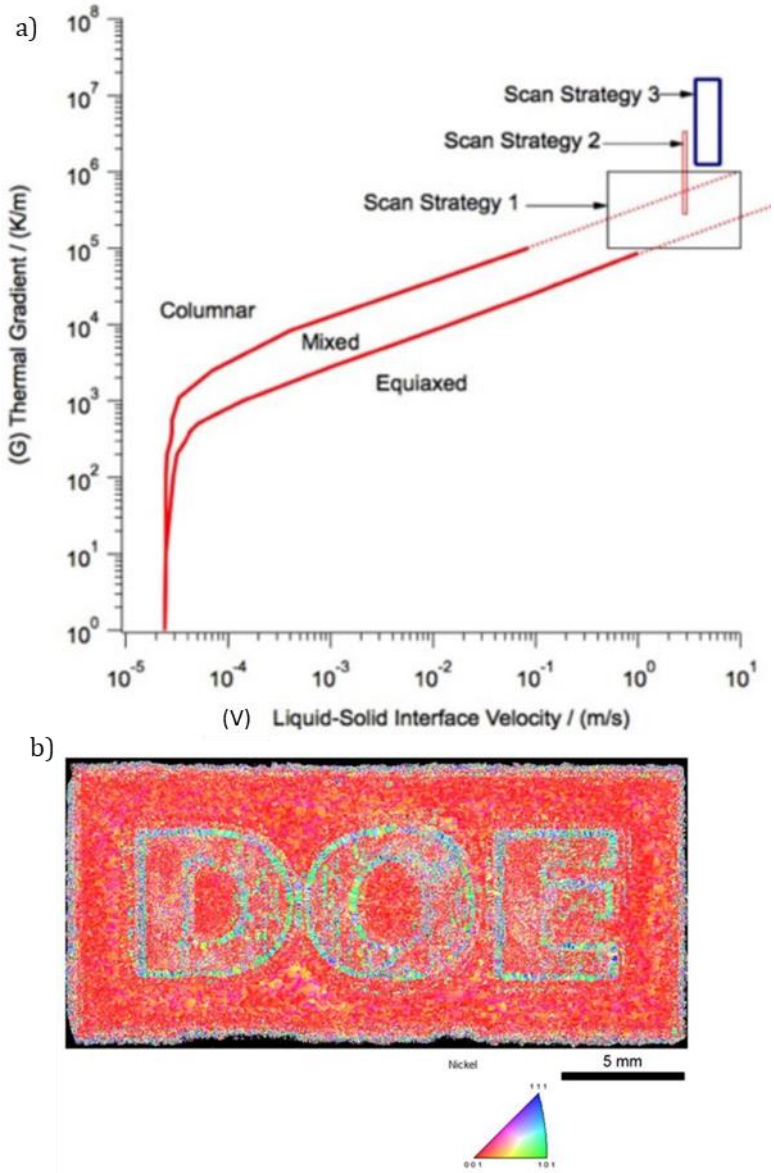

Figure 2-16: Control of the microstructure from columnar to mixed by changing scan strategy in EB-PBF. Reported by Dehoff et al [102]

a) G vs V plot for Inconel 718, with the ranges of 3 electron beam scan strategies shown

b) EBSD, showing the variation in microstructure caused by switching between scan strategies above

The rough range of G and V for both L-PBF and L-DED are shown in Figure 2-17 for Inconel 718, although similar could be plotted for other alloys. This shows that when using L-DED, both columnar and equiaxed can be achieved, whereas in L-PBF, columnar structures are more likely.

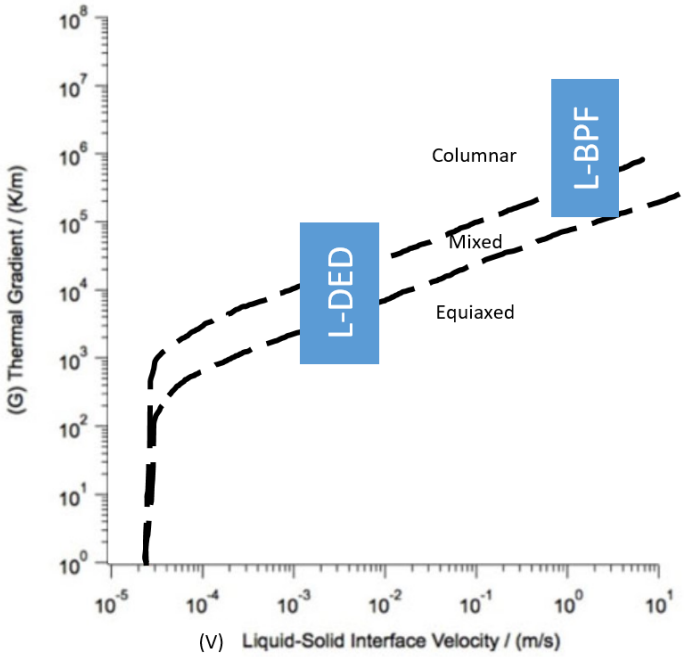

Figure 2-17: G vs V plot showing the approximate ranges covered by both L-PBF and L-DED for Inconel 718 . Adapted from Dehoff et al [102]

2.5. Comparison to Other Processes

2.5.1. Welding

The forms of failure frequently found in Nickel superalloys (Section 5.1.4) were known before the advance of AM. Much of the prior knowledge had been gained from welding. Fundamentally, welding is the same process as AM, a moving heat source melting a base component usually with some materials addition. The main differences being that in L-PBF, the laser velocities are significantly faster and that the feedstock is in powder form. When comparing to L-DED, these are even more similar, as L-DED has similar laser velocities to welding, but as it is used to build, it can create much larger components, as welding simply joins pre-built parts [4].

Analytical models (Section 2.2) were developed for welding and are now used in AM. Similar models can be found for laser transformation hardening and laser cladding.

2.5.2. Thixoforming

Thixoforming is a semi-solid processing method, where a metal is heated to the point where $f_L \approx 50\%$ and then forged in this state making the deformation require much less force. Initially, this process was developed for Al-Si-Cu-Mg alloys and for each material, a plot of fraction liquid against temperature (Figure 2-18) can be used to determine how easily processable the material will be. The key processing parameters were said to be [106]:

- Temperature at $f_L = 50\%$; $T_{fL=0.5}$
- Gradient of the curve at $T_{f_L=0.5}$; $\left.\frac{df_L}{dT}\right|_{T_{f_L=0.5}}$
- Temperature of highest 'knee' in curve; T_2
- Gradient of the curve at the solidus temperature; $\left.\frac{df_L}{dT}\right|_{T_s}$

Since then, the materials selection in steels has been investigated using DSC [107,108] and more research has been conducted into Al-based alloys [42,43]. $\frac{df_L}{dT}$ curves (both theoretical and experimental) have been plotted, analysing the thixoforming behaviour (Figure 2-18 shows a typical curve). The resulting criteria were similar, but the critical region was said to be where f_L = 0.3-0.5, i.e. where the process occurs. If the highest knee occurs here, the melting is likely to be easier to control, as the gradient above the knee is smaller than below, so melting slows. The gradients were calculated at f_L = 0.4 and a sensitivity limit of 0.03 K^{-1} was set for successful thixoforming. Finally, the freezing range was taken into account, with an approximate limit of 130 K being set [109]. The solidification curves are calculated using Scheil calculations (non-equilibrium, liquid diffusion only), unfortunately, these are not representative of the processing conditions experienced. Under solute trapping conditions (which are expected to occur), the solidification rate would be constant and so there would be no knees in the solidification curves.

In AM, similar considerations must be taken into account in order to reduce the hot tear susceptibility. Knowing the gradients of these solidification curves at very low values ($0.01 < f_L < 0.1$) allows prediction of hot tearing. The width of the freezing range is also a critical factor in both hot tearing and thixoforming. Using theoretical calculations, it should be possible to predict which alloys are likely to be resistant to hot tearing.

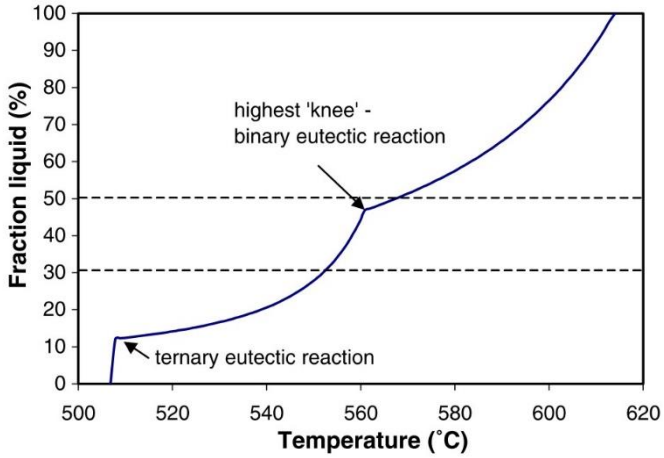

Figure 2-18: Fraction liquid as a function of temperature for a typical Al-Si-Cu alloy, showing a 'knee'. Reported by Liu et al [109]

2.6. Monitoring of Additive Manufacture

2.6.1. Introduction to thermography

Contrary to popular belief, there is no such thing as an accurate multi-purpose thermal camera. There exists a variety of different cameras with different sensors. Most everyday use cameras (DSLR or phone camera) use a Silicon sensor which are sensitive over a range of approx. 400-1000 nm [110]; these can use either CMOS or CCD sensors.

Wavelength selection

The efficiency of each sensor varies with wavelength, the proportion of photons of a set wavelength detected by a sensor is known as its quantum efficiency (QE). Example QE curve of a sensor is shown in [111]. E.g. a QE value of 50 % at 800 nm means that only half of the 800 nm wavelength photons are detected. If the QE curve is known, this can be accounted for if detecting a specific wavelength e.g. using a notch filter.

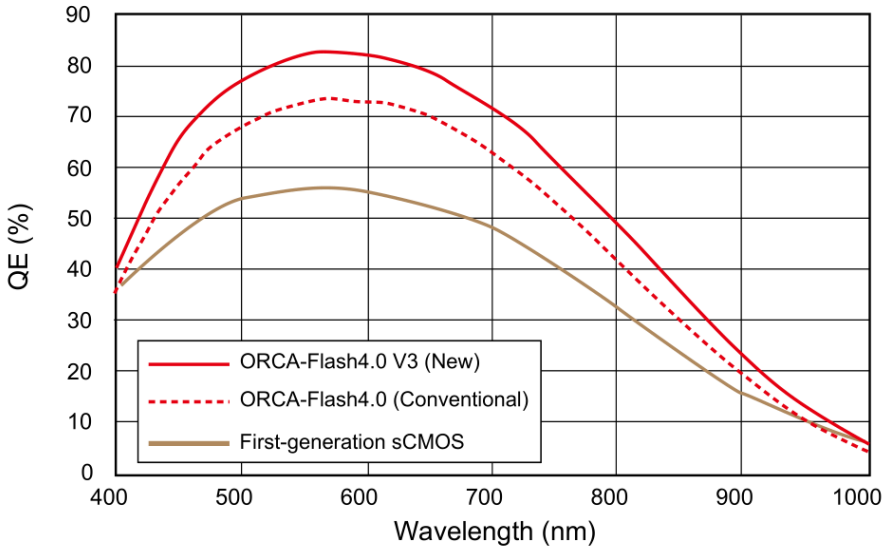

Figure 2-19: Quantum efficiency of Hamamatsu camera over wavelengths detectable by a Silicon detector. Reported by Hamamatsu Photonics [111]

As objects are heated above 825 K [112], they start emitting light e.g. hot metal glows "red hot". A black body is an idealised concept defined as not transmitting or reflecting any light, for this type of body, the intensity of radiation varies with both on wavelength and temperature (Figure 2-20). It can be seen that as temperature increases, the intensity increases, but also that the wavelength of the peak decreases towards the visible spectrum. This explains why initially, items glow red hot, then as temperatures increase, a wider range of visible spectrum is emitted, leading to a white hot appearance.

Since the melting point of most metals of interest are in the range of 1000-2000 K, minimal radiation is emitted in the visible spectrum, so even if using silicon detectors, lights is filtered above 800 nm, to limit the sensor to near infra-red (NIR) wavelengths. In reality, a silicon sensor is limited to detecting temperatures above 700 K [113]. The QE of silicon chips in the NIR range is both low and variable. We receive a single intensity value per pixel and are detecting a range of wavelengths. Since the QE is wavelength dependent, it becomes nearly impossible to determine the spectral distribution of the incoming light, let alone the temperature of the object.

The temperature range of interest can be selected by selecting an appropriate sensor; different materials are sensitive to wavelengths of different energies. If measuring the cooling rate, cooler temperatures are required and so a different sensor may be selected e.g. Indium-Gallium-Arsenide sensors have a range of 950-1700 nm so can detect cooler temperatures [104]. However, due to the sensitivity of sensors, they can only detect a certain temperature range; so if measuring the cooling rate, the melt pool itself is likely to saturate the sensor. Neutral density filters (which equally reduce all wavelength intensities by a set amount) can be used to tailor the temperature range detected.

There are several methods used for calibrating the camera to a temperature value. Often the Sakuma-Hattori equation is used for calculating a temperature once the calibration values are determined [104,114]. Using a black body furnace, this equation can be calibrated and so an accurate temperature can theoretically be measured. This assumes a constant emissivity and that the source is a perfect blackbody emitter. A guide to calibrating a camera using this method was produced by the National Institute of Standards and Technology [114]. To reduce the errors due to

poor calibration, further calibrations are performed in-situ using thermocouples in the experimental setup, but with limited success [10,115].

In reality, emissivity varies with temperature, material, phase and wavelength [116]. In the calculations described above, a constant emissivity was selected, this is a flawed assumption. Any thermal measurement which states an actual temperature is likely to have a large error associated with it, which is often not understood by the authors [4]. Dual wavelength pyrometers are an exception to this and are further discussed shortly.

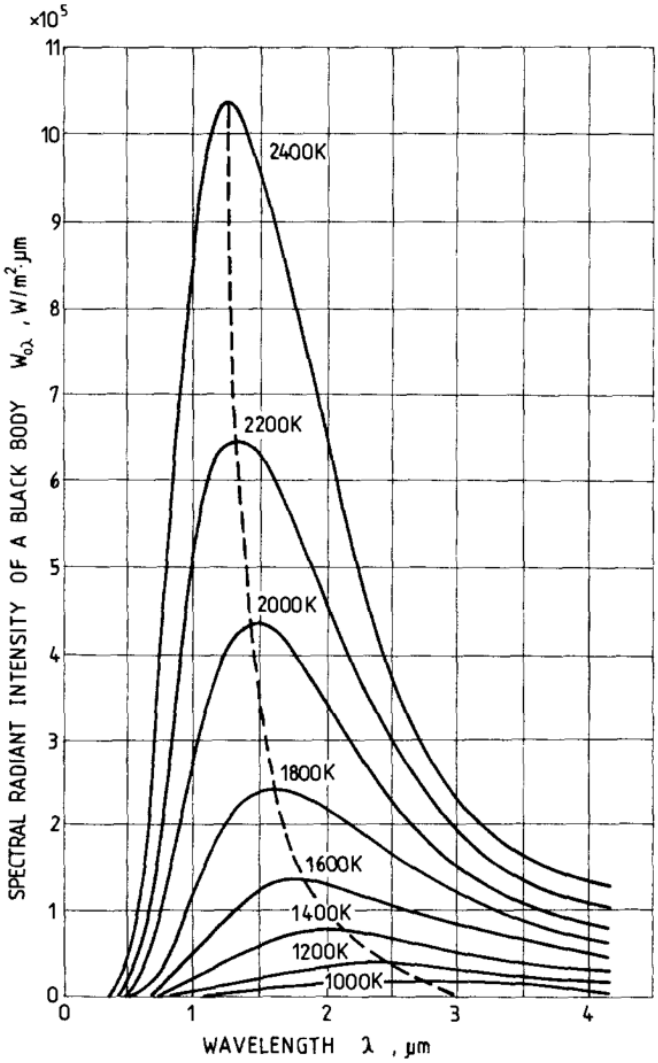

Figure 2-20: Radiation intensity as a function of both wavelength and temperature as calculated by Planck's law. Reported by Michalski et al [112]

Additional Sources of Error

An additional issue comes due to the small size of the melt pool being analysed. Imagine a situation where there is a single pixels' worth of high temperature, the rest cold. In a perfect world we would have a large count on one pixel and no count on the rest. In reality, due to electronic imperfections and diffraction within optics, some of the intensity which should be in that pixel will end up being absorbed by neighbouring pixels. This means that a small hot area will appear both larger and cooler than it is in reality [114], so neither size nor temperature of small objects can be accurately stated. Errors of up to 10% can be experienced even when measuring features 5 px in size [117].

This is overlooked by the vast majority of publications, despite its' relevance when measuring the temperature of the small melt pools.

Movement blur can create further difficulties. If a 100 µm melt pool is moving at 1 m/s (typical L-PBF parameters), it will take 100 µs to cover 100 µm, which is quicker than the integration time for a typical sensor. This must be considered when selecting a monitoring system and recording parameters.

Dual Wavelength Solution

As previously mentioned, temperature is difficult to measure accurately due to emissivity changes with temperature. However, if two sensors record concurrently at different wavelengths, then assuming constant emissivity, emissivity can be removed from the equation. i.e. the temperature is related to the ratio of the two intensities [112]. One catch is the emissivity also varies with wavelength; if the wavelengths are chosen to be similar, it can be assumed that this error is negligible [112,118]. Several studies have taken advantage of this technique and utilised it for AM monitoring [118,119].

For metals, which are opaque, Emissivity + Reflectivity = 1 [112]. A shiny metal would be more reflective, so would have a lower emissivity. This explains why a black body (which has a reflectivity of 0) has an emissivity of 1. For some alloys e.g. S235 steel, emissivity has been measured and shown to be decrease with temperature, both in solid and liquid state [120]. This, however, may not be representative of all materials.

2.6.2. **In-situ Monitoring**

In accordance to the 2013 NIST AM Roadmap [121], many in-situ monitoring techniques are being investigated, these are reviewed in [11]. The simplest method of observing the process is optically (Figure 2-21), this doesn't provide any thermal information, but shows the powder movement. In Figure 2-21a, the denudation (lack of powder) around the printed region can be seen; this process is shown in Figure 2-21b, where both ejection and entrainment take place, in this case the ejection dominates due to a large gas plume [122].

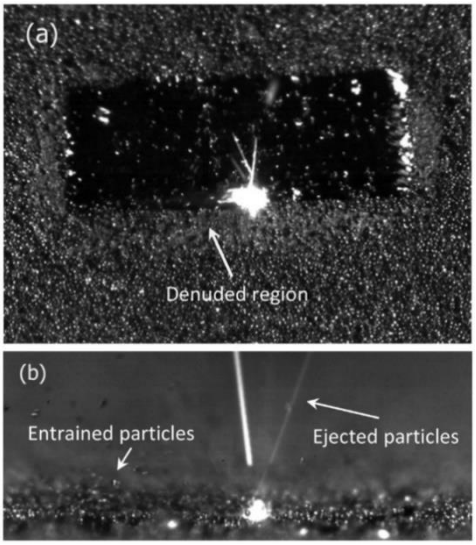

Figure 2-21: High-speed optical images showing the powder movement in L-PBF. Reported by Bidare et al [122]

More information can be gained from thermal data, either in the form of infrared (IR) cameras or pyrometers. Some measure an average radiance of a set area, resulting in a single value, whilst

others are essentially a camera [4,10,123]. These allow for identification of the melt pool and its dimensions (Figure 2-22) [124], although only on the top surface. Difficulties with calibration of thermal cameras are discussed at length in Section 2.6.1.

As previously mentioned, one way to eliminate the calibration issues due to emissivity is to detect radiance at two wavelengths concurrently and calculate the ratio of these. Assuming that the emissivity at the two selected wavelengths is similar, an accurate temperature can be calculated [118,119]. Unfortunately, these assumptions aren't always correct and due to various issues, this technique has been reported to consistently have an error of 12.8 % in a calibration setup (when compared to thermocouple measurements) [119].

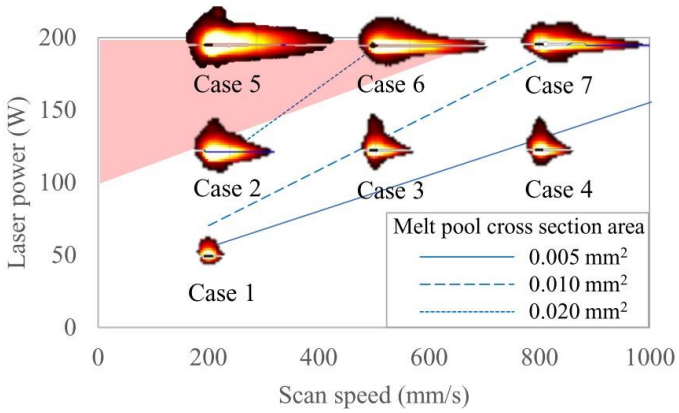

Figure 2-22: Changes in melt pool dimensions with processing parameters, measured using an IR camera. Reported by Heigel and Lane [124]

From these, values for both G and/or $\dot{T}$ can be measured [104,105,118,125] and the impact of scan strategies on G and $\dot{T}$ has been investigated [126]. Historically, much work has calculated expected temperatures and cooling rates (using Rosenthal-type calculations) and hence predicting the microstructures [127]. A recent extension of this printed different regions, some with columnar microstructures, others with equiaxed as seen in Figure 2-16b. In this case, both G and V were calculated [102]; with the advances of thermal monitoring, measurements of these will allow for close control of microstructure. In addition, the hope is that by measuring the relative temperatures in-situ, any hot-spots can be found and hence defects repaired during the build process by integrating a feedback control system [128], this would however be very machine specific.

Schlieren imaging has been used to investigate the behaviour of the gas plume, it allows visualisation of refractive index (which itself is temperature dependent). This provides information about both the gas flow out of the nozzle [129] and the movement of the gas plume during printing [122], Figure 2-23. This shows that under different processing conditions, the gas plume can be in front of, in line with, or behind the laser. This can have a significant impact, as the plume will absorb some laser power, effectively reducing the absorptivity [122].

Various spectroscopic techniques have been used to monitor the gas plume itself [113]. The basic principle is that as each element is vaporised, the plasma emits light at a wavelength which is dependent both on the temperature and on the species being vaporised. Once one species is carefully calibrated, the changes in temperature can be calculated, as well as identifying the constituents of the plasma [130,131]. These losses can be critical, as they are indicative of any compositional changes occurring due to preferential vaporisation of certain elements.

Ultrasonic resonance techniques have historically been used as a none destructive testing (NDT) method for detecting internal defects such as voids [113]. These have been extended by using

surface acoustic waves for crystallographic measurement of surfaces, this has been tested using AM parts, but cannot be performed in-situ [132]. In-situ acoustic measurements can identify nucleation/propagation of cracks, but currently requires very specific setup and results are of a qualitative nature [133]. Another way of detecting defects in L-PBF is through noticing unevenness in the recoated powder layer. Optical metrology in combination with computer vision has been shown to be able to detect and identify various types of process failure [134].

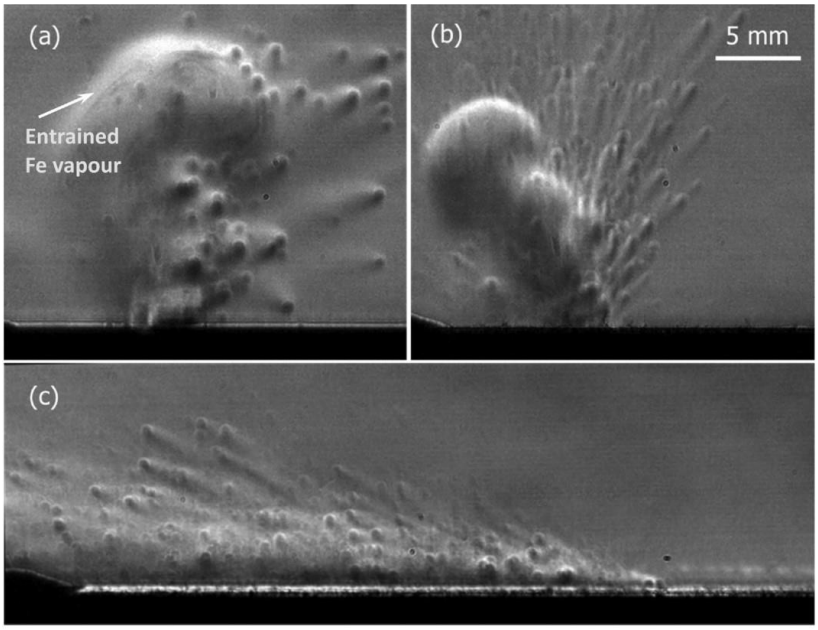

Figure 2-23: Changes in gas plume behaviour captured using Schlieren imaging. Reported by Bidare et al [122]

The final technique is potentially very useful. High powered X-rays can penetrate thin metallic regions, so by creating a thin L-PBF-like system, the process can be monitored through thickness. By taking multiple radiographs in quick succession, the development of the melt pool can be analysed. This is used to investigate the mechanism behind keyholing [135,136] and the formation of the pore was clearly demonstrated. Figure 2-24 shows how multiple radiographs can be used to give information about how a melt pool develops over time. Leung et al. used this process to investigate many features in L-PBF including Marangoni flow, particle spatter and melt pool development in the overhang condition [137]. Unfortunately, since a specific set-up was made for these measurements, it is unknown how representative these results are of an actual L-PBF process. Similar experiments have been repeated for L-DED [138,139], but again, the similarity to the real process is unknown. Additionally, the data acquisition rate is phenomenal, at roughly 3-5 GB/s [137], which means that most recordings are on the order of seconds in duration due to data transfer limitations.

2.6.3. **Control during Additive Manufacturing**

The need for process control in AM has been widely reported, to ensure part quality and repeatability [4,9]. Many methods have been attempted to control the process, typically using either melt pool geometry or by measuring a local temperature [4]. Commercial systems have started incorporating process control since around 2014, this is simpler in L-DED systems than in L-PBF systems due to the slower nature of the L-DED process [140]. The difficulties with determining temperature accurately have been covered in Section 2.6.1, with the added challenge that even with a constant temperature, the melt pool shape may change, leading to different cooling rates and/or layer morphology [141].

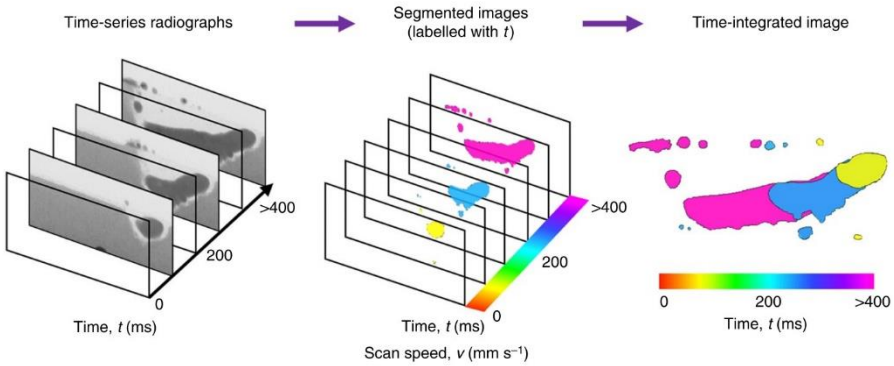

Figure 2-24: Schematic showing the processing of radiographs into a time-integrated melt pool image. Reported by Leung et al [137]

In L-PBF, the main techniques focus on either imaging the powder bed, or using a photodiode to capture a temperature snapshot, assuming that the diode signal is representative of the melt pool area [10]. Several studies have been conducted proving the capabilities of process control in L-PBF [142,143]. Due to the high speed of the L-PBF process, these control functions are normally performed once per layer.

In L-DED, process control can be both layer-by-layer [144] or live [145,146]. Control using temperature is most common, using either diodes or pyrometers to measure a value and aiming towards a pre-set target [144,145,147,148]. Along a similar line, cameras are used to measure the melt pool directly, typically coaxially. These then measure the melt pool dimensions e.g. area or width and control the process using this value [149,150]. Since the microstructure is closely linked to the cooling rate, this has recently been used as the control variable by Farshidianfar et al. [151]. Finally, other features such as the component height can be used to control the process to stop overbuilding and keeping the laser focussed on the melt pool [147,152].

2.6.4. **Avoiding Cracking**

Several ideas have been explored in order to reduce the cracking susceptibility of 'unweldable' alloys. As explained in Section 5.1.6, the amount of residual stress between a baseplate and component can be reduced by pre-heating the base-plate, which makes alloys easier to print [16,153]. In EB- PBF, due to the electromagnetic manipulation of the beam, the beam can be effectively split. This has been used to create a 'ghost' beam, which follows the melt pool and can reduce the values of both G and $\dot{T}$, hence reducing the residual stress [154].

Another way to control the residual stress (by reducing $\dot{T}$) is to shorten the length of the scan vectors by designing a smaller scale scan strategy [155]. This had been implemented several different ways, from fractal patterns (Figure 2-25) to dividing the area into small squares and printing these individually (island scan strategy). Both of these are thought to reduce the thermal gradients and residual stresses. This has been shown to reduce cracking in the printed regions, however cracks are concentrated at interfaces between islands, or at specific high stress sites in the case of fractals [155,156].

By altering the laser parameters within the processing windows, the exact microstructure can be controlled. This has been shown in both Ti-6Al-4V and Inconel 718, where the lath spacing and columnar nature can be selected respectively [157,158]. In Inconel 718, it has also been shown that the texture can be modelled from the heat flow and hence controlled [159]. This sort of work leads back to the aim of having equiaxed grains to reduce hot tear susceptibility. Other attempts have successfully grain refined Nickel superalloys (not necessarily in AM); the main methods are by

applying an oscillating magnetic field [160,161], by adding inoculants [162,163] and by applying ultrasonic vibration [164].

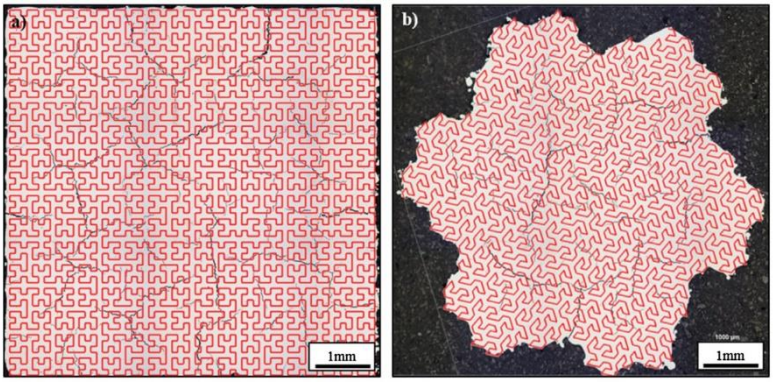

Figure 2-25: Examples of fractal scan strategies chosen to reduce residual stress. Reported by Catchpole-Smith et al [156]

Shot peening is widely using in manufacturing to compress the surface and hence enhance crack resistance and fatigue life. It has been shown that you can use a laser to shot peen (laser shot peening), reducing the surface tensile stresses (up to 1mm deep). Initially this was performed at the end of a build and improved the top surface [165], but has since been further incorporated in the process, so the sample is laser shot peened every 1, 3, or 10 layers; reducing internal residual stresses. Figure 2-26 shows the effect 3D laser shot peening has in turning the tensile stress on the surface to a compressive one, several mm deep [166].

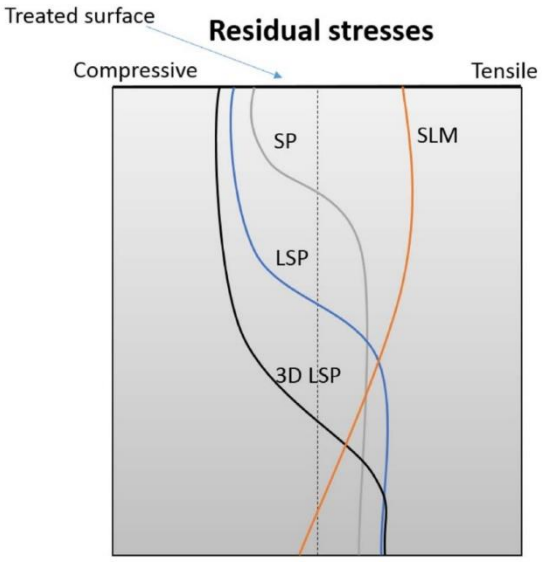

Figure 2-26: The reduction of surface tensile stress achieved by laser peening. Reported by Kalentics et al [166]

2.7. Summary

Much work has been done to develop and understand a range of AM processes. L-PBF and L-DED have been widely used both in research and commercial applications. Their reach is currently limited due to concerns over repeatability, especially in sectors such as aerospace, where accreditation is required. Nickel superalloys are of great interest in aerospace, but many of these have been developed specifically for old manufacturing processes such as directional solidification. This causes issues when using these alloys for AM, so the two solutions proposed are either developing closer control of the process, or to develop new alloys.

Since welding of similar materials is well understood and modelled, this work has been extended to AM – similar forms of cracking the segregation can be seen. However, the significant difference in thermal conditions often stops welding concepts from being directly applicable in AM. Monitoring techniques from welding have been applied to AM, but as speeds are much quicker in AM, the limits of these techniques have been reached. The rate at which data would need to be recorded for high spatial resolution of the AM process leads to an unmanageable quantity of stored data, so alternative solutions are needed.

3. Project Scope and Objective

The aim of this thesis is to analyse the root causes of microstructural and mechanical variation in components and determine if these are detectable by analysing the thermal signature in-situ. The thermal trends will be interrogated to confirm that they are representative of the conditions experienced by the component. The purpose of gaining a better understanding of these relationships is to be able to control the output and so achieve components with more consistent microstructures. The scope of this project has been defined by the following:

- What determines if an alloy will be easy to manufacture using AM? Does this depend on the process used? Can this be used to help develop new alloys?
- What can simple in-situ monitoring techniques tell us? Do the signals relate to the processing parameters?
- What advantage do advanced monitoring techniques give? Can cooling rates be accurately calculated? Can mechanical variations be explained by the thermal measurements?
- How do other factors, such as geometry, affect mechanical properties?
- Can thermal measurements be simplified? What are the key parameters which matter? By controlling these, is component homogeneity improved?
- How do the structures created by L-PBF and L-DED compare – do trends from one process follow in the other?

Both L-PBF and L-DED will be used to answer these questions. Inconel 718 is the main alloy used throughout this thesis due to its widespread use in the aerospace sector. Some initial work developing monitoring methods was done using 316L stainless steel due to the reduced cost, the printability of this alloy and its prevalence in literature.

4. Experimental Methods

This chapter covers the main equipment used for this work; for each machine, a general overview of the components and operating principles is given. Detailed parameters for various experiments will be given in the individual chapters. Where a technique is only used in a single chapter, it is covered in the relevant methods section.

4.1. Aconity3D Mini L-PBF Machine

4.1.1. Machine Hardware

The Aconity3D Mini is a research focussed L-PBF machine. The main components of the machine are labelled in Figure 4-1, although this figure is missing the pyrometers, which are located next to the galvanometer. The AconityStudio software controls the laser, galvanometer and the actuator movements. The build chamber is beneath the laser, galvanometer and the optics. Below the build chamber is a powder overflow vessel and a pipe containing the recirculating gas flow that is blown across the powder bed to remove vaporised material, which runs to a filter, removing any fine particles and stopping them from recirculating.

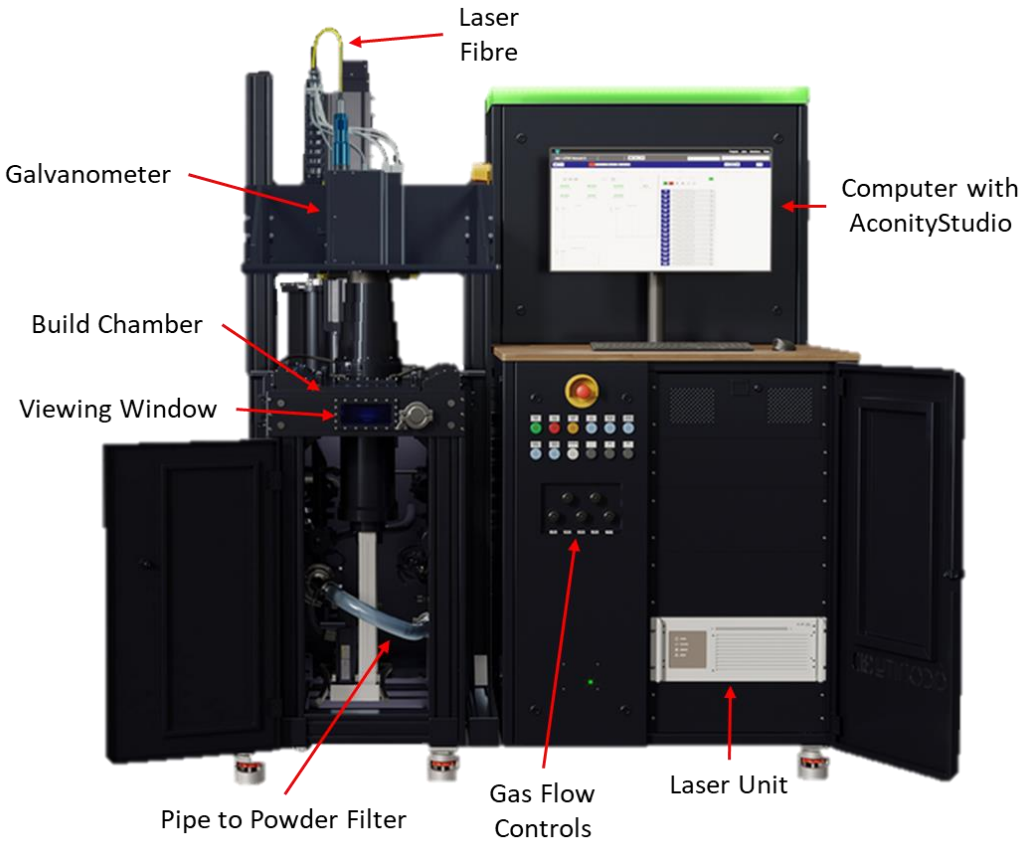

Figure 4-1: Aconity3D Mini with main components labelled; adapted from [167]

The machine contains a Gaussian IPG photonic 200 W YLR laser (1070 nm wavelength). This is a continuous Ytterbium laser with a 70 µm beam diameter. AconityStudio reads the desired laser path and sends this to the controller, which executes the movements and controls the laser timings as well as the galvanometer movement. The scan system is provided by Raylase and is the Axialscan-30, using a SP-ICE-3 control card. Two Kleiber KG 740 LO spot pyrometers (1580-

1800 nm) are connected to the laser fibre, recording at 100 kHz; these provides a radiance values of the melt pool.

Inside the build chamber are two cylindrical columns (Figure 4-2). At the start of the build, the front column is lowered and filled with powder; a baseplate is placed in the far one, as this is where the printing will occur. The wiper blade is a flat, flexible silicone rod, which moves back and forth along the build chamber. Every layer, both columns move down to allow the wiper to move to the front, the powder supplier then moves upwards by more than the layer increment (the scaling factor is normally set at 3x), the build column is lowered by a single layer thickness. The wiper blade then moves back, moving the powder to the build column, spreading it into an even layer. Any excess powder is pushed back into the powder overflow. The laser then scans the desired scan strategy before the process repeats.

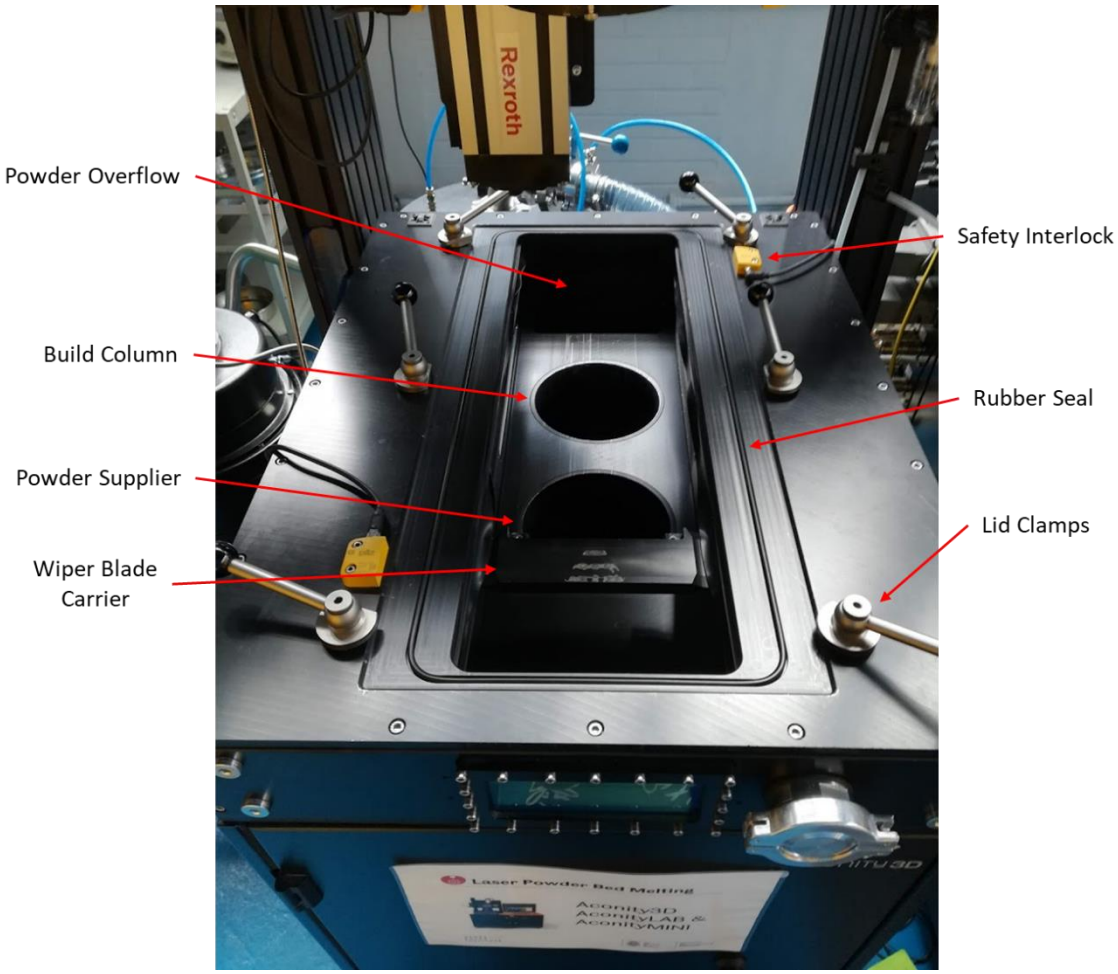

Figure 4-2: Internal components of Aconity3D build chamber

To set up the machine, the build plate must be placed flush with the build chamber, so powder can be swept onto it from the first layer. Enough powder must be placed in the powder supplier, which is typically 3x the expected build height. By manually adjusting the height of the build column and the supplier, the levels can be set so the wiper blade deposits a thin, even layer on the build plate. At this point, the machine is ready to be sealed. The lid is placed on top of the rubber seals, clamped in place and the safety interlocks are connected. The chamber must now be purged with Argon to remove any oxygen. This is done until the chamber has <2000 ppm oxygen; at this point, the recirculating gas flow is stared. Once an oxygen level <500 ppm is reached, the build can be started.

An example baseplate is shown in Figure 4-3; the diameter of these baseplates is 140 mm. Stainless steel baseplates, ~20 mm tall were used throughout this work. Figure 4-3 shows a finished build, with 31 components on it, roughly 10 x 10 x 10 mm. It can be seen that the components on the right were not successful. Early in the build, they were stopped as they were overheating. The remaining components build successfully, though some have smoother, more reflective surfaces.

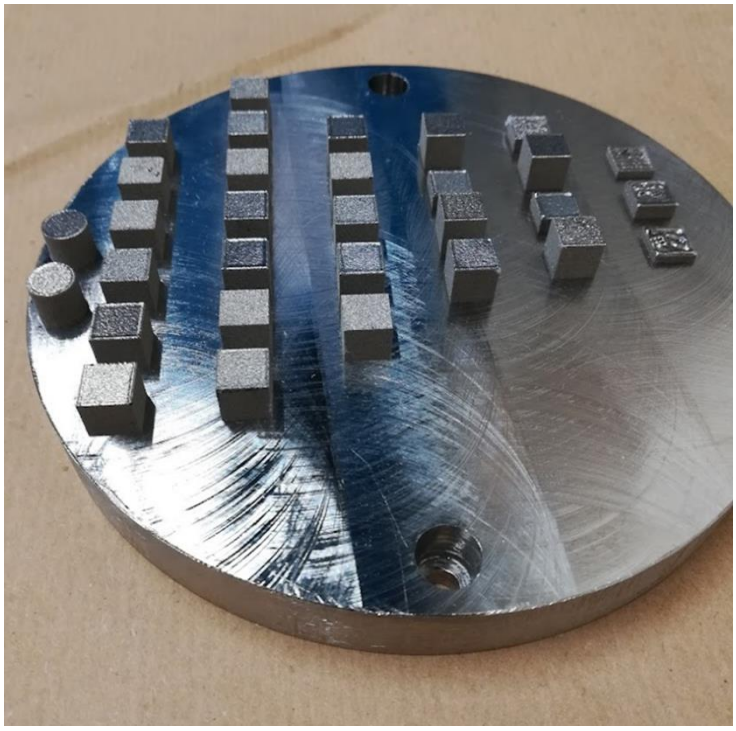

Figure 4-3: Example build from the Aconity3D Mini

4.1.2. **Build Files**

Build files need to be imported into AconityStudio in the .ilt format, which is proprietary to Aconity3D. Autodesk Netfabb can be used to create .ilt files from either imported CAD data or from basic shapes using the functionality of the software. From here, a scan strategy and laser parameters can be selected; each different component on a baseplate can be built with different settings.

4.1.3. **Powder**

The recommended powder size range for the Aconity3D Mini is 15-45 µm, although larger sizes can also be used. The powder used throughout this work was Inconel 718, produced by the gas atomisation (GA) method by LPW. GA results in powders with satellites (smaller particles) attached to them, so are not very spherical. Figure 4-4 shows a representative sample of the Inconel 718 powder used, a range of particle sizes can be seen, with some very spherical particles, but also some agglomerates of smaller powder particles.

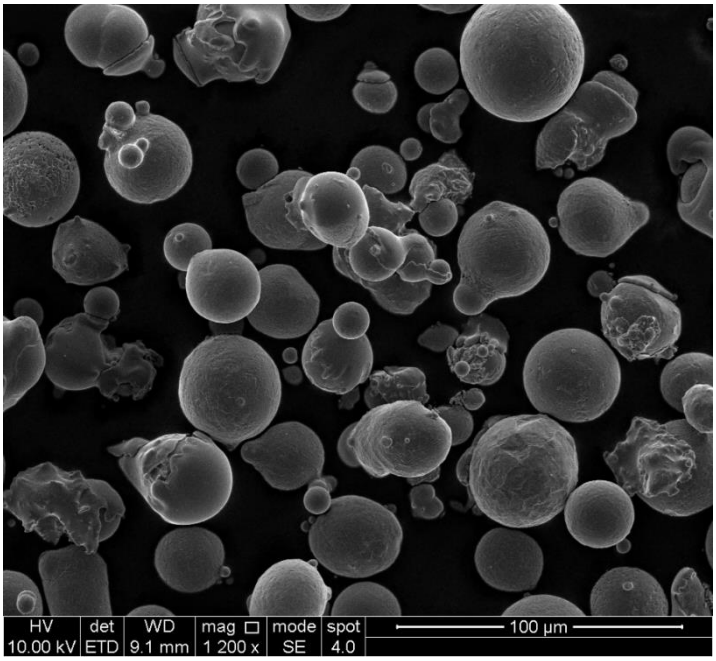

Figure 4-4: SEM image of gas atomised Inconel 718 powder

4.2. BeAM Magic 2.0 L-DED Machine

4.2.1. Machine Hardware

The BeAM Magic 2.0 is a blown powder L-DED system. A key use of L-DED systems is for repair applications, so the laser and bed need many degrees of freedom in their movement. Since the requirements are similar to a CNC machine, often L-DED machines are based on similar hardware/firmware. In the case of the BeAM, the machine is run using a Siemens Sinumerik 840D CNC automation system. Figure 4-5 shows the main components of the machine, with the electrical cabinet housing the Sinumerik system and the control panel being identical to that used for CNC machines.

There are two "tools" in the machine, a smaller 10Vx nozzle and a larger 24Vx nozzle. The 10Vx has a laser diameter of 0.7 mm, with a maximum power of 1 kW and a 3.5 mm offset between the nozzle and the component; whereas the 24Vx nozzle has a 2.25 mm diameter, with a 13.5 mm offset and a maximum power of 2 kW. All work in this thesis was performed using the 10Vx nozzle, which is quoted as having a location precision of ±0.1 mm.

The laser unit is an IPG YLS-2000 Yterrbium laser system with a 2 kW limit. At a wavelength of 1070 nm, the continuous laser has two fibres going into the machine, one for each nozzle. The powder hoppers are 3 l in volume and manufactured by Medicoat; there are 5 hoppers, each controlled independently, which theoretically allows for in-situ alloying. The movement of powder within the hopper is shown diagrammatically in Figure 4-6b. The volume of powder is controlled by the rotation speed of the steel turntable; this can be translated to a mass flow by weighing the mass of powder output over a known period of time.

Within the build chamber, the gas, powder and laser are routed through the machine head (dotted orange in Figure 4-7). This contains both the 10Vx nozzle and the 24Vx nozzle which is in the stored position. The machine head is the part which is able to move in the X, Y and Z directions, providing 3 axes of movement. The table is able to rotate in the B (around the Y axis) and the C

(around the Z axis), making this a 5 axis machine. A baseplate is attached onto the table and this is where the component is printed. The baseplate could be a component, ready to be repaired, or in our case, a 4 mm sheet of rolled material, clamped to the table.

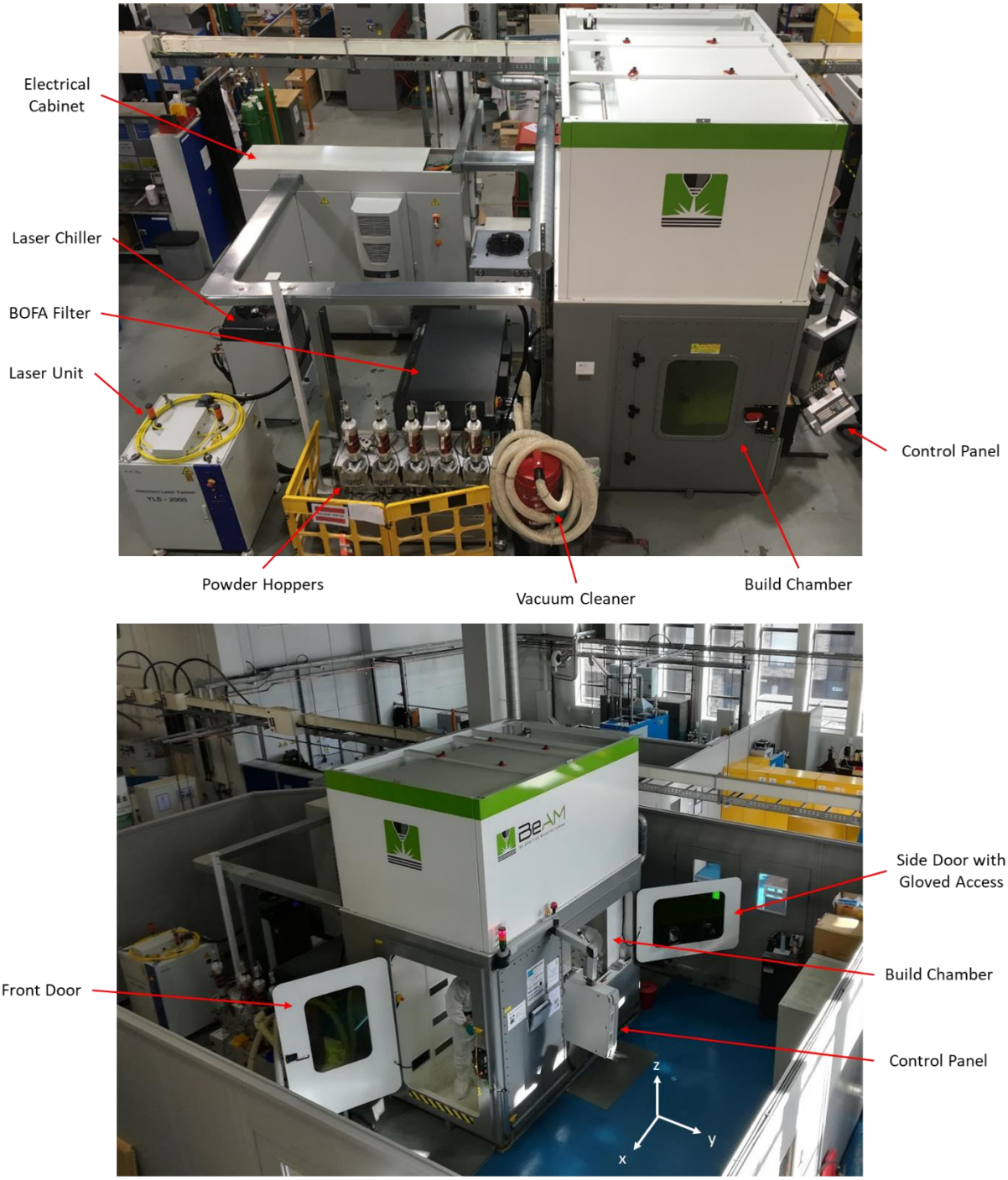

Figure 4-5: BeAM Magic 2.0 with main components labelled, machine axis labelled

The details of the nozzle are shown schematically in Figure 4-6a, where it can be seen that there are 3 incoming gas flows and 3 sections of nozzle. Since this is rotationally symmetric around the laser, there is one conical powder channel. The default argon gas flows were given by the manufacturer as central: 3 l/min, secondary: 6l/min, carrier: 3 l/min; totalling 12 l/min of argon exiting the nozzle. Additionally, there is a beam splitter on the machine head (Figure 4-7), allowing for a

coaxial cameral to be mounted and view the melt pool in-situ. In Chapter 7, the process was monitored side-in; the camera angle for this is shown in Figure 4-7.

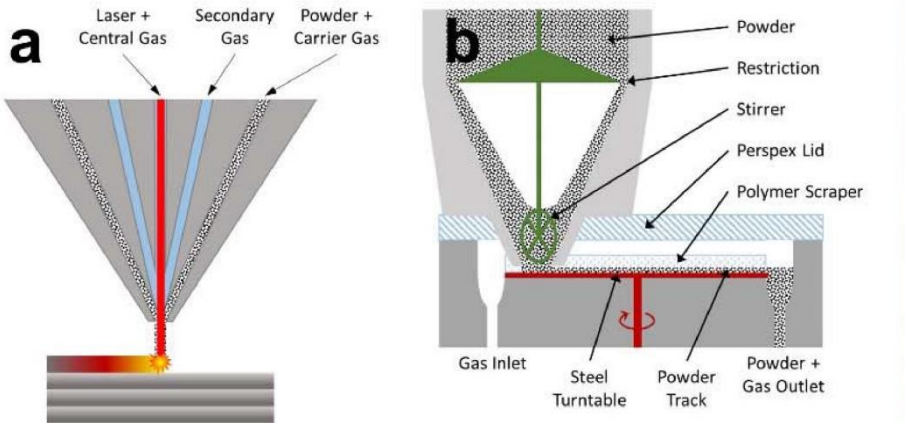

Figure 4-6: Diagram showing powder and gas flow in L-DED; through a) the nozzle, b) the powder hopper. Reported by Freeman et al [168]

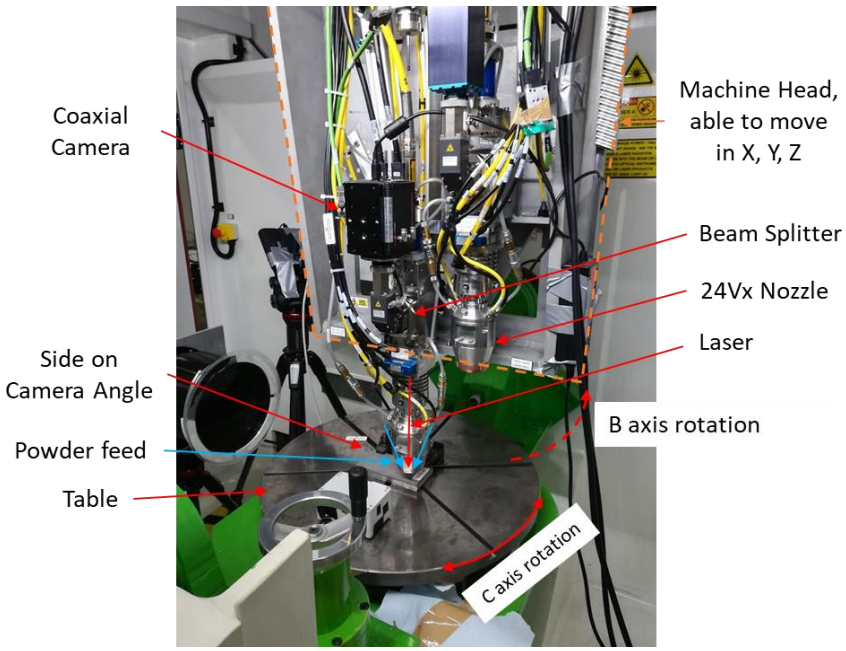

Figure 4-7: Inside the build chamber of the BeAM Magic 2.0 with the main components labelled. All 5 axes of movement are labelled, with the large frame (surrounded by dotted orange line) moving in X, Y and Z (labelled in Figure 4-5), and the table rotating in C (around z axis) and in the B (around y axis)

For builds in Steel and Nickel alloys, the local shielding gas (12 l/min) is considered sufficient to minimise oxidation and so the build chamber itself contains atmospheric air. The full chamber can be filled with inert gas (argon) for printing materials which are highly susceptible to oxidation. Once a baseplate is clamped on the table, the machine doors must be closed and the extractor turned on. Then powder mass flow tests can be done with the machine closed, by weighing the mass of a powder blown through the nozzle in a known time (e.g. 2 minutes) at a known turntable rotation rate. Once the mass flow has been set, the laser must be switched on, the gas flows started and the powder flow stabilised before the build is commenced.

Once stable, the laser can switch on and the machine head moves the nozzle as requested by the build file. Typically, the laser switches off at the end of each hatch when the machine head stops. The BeAM machine has a synchronicity between the power and velocity; so as the nozzle slows (e.g.

at the end of the hatch), the laser power decreases linearly with the velocity. Once the build has finished, the machine turns off the laser, then the powder, then the gas flow. Once this occurs, the machine must be left for at least 1 minute to allow powder to settle and the extractor to remove the fine particles, before the doors can be opened. Recordings of cylindrical builds can be seen here [169]: https://doi.org/10.5281/zenodo.6760037.

4.2.2. Build Files

G code is a widely used CNC programming language. This has been adapted for AM, with some defined functions to set the laser power and velocity and with variables written to set the gas flow rates, powder turntable rotation velocity etc. There are frequently different ways of achieving different types of movement.

For example, when building a cylinder, either the machine head can move in a circular manner in the X and Y (whilst slowly increasing Z). Alternatively, the nozzle can be placed just off-centre of the table and the table can be rotated in the C axis (around the Z), whilst the machine head slowly rises in the Z axis. Both of these examples are shown in sample videos here [169]. The latter is especially useful for side-on monitoring, as the melt pool remains almost stationary (only moving in the Z), making image analysis much simpler.

Programs like Autodesk PowerMill (designed for creating CNC paths) have additive modules, so can automatically create scan strategies. These split CAD files into short linear hatches and are written in very long, simple G code programs. Unfortunately, different machines have different line smoothing settings and interpret some commands dissimilarly, so program-created G code is hard to test and near impossible to debug.

Despite G code being a simple programming language, it does have looping functionality and can read machine variables. Using this, short programs can be easily written to crease simple shapes, such as cuboids and cylinders. Some commented examples of G code programs can be found here [170]: https://doi.org/10.5281/zenodo.6760054.

4.2.3. Powder

The recommended powder size range for the BeAM Magic 2.0 is 15-105 μm, although narrower ranges can also be used. Two powders were used in this work:

- Inconel 718, produced by the plasma rotating electrode process (PREP), provided by LPW. This powder was of a 45-150 μm distribution and is shown in Figure 4-8; PREP powder can be seen to be much more spherical and to have fewer satellites than GA powder. Composition in Table 4-1
- 316L stainless steel, produced by GA, provided by TLS Technik. This powder was of a 45-90 μm distribution. GA is typically less spherical than PREP powder, with powders typically containing more satellites. Composition in Table 4-1

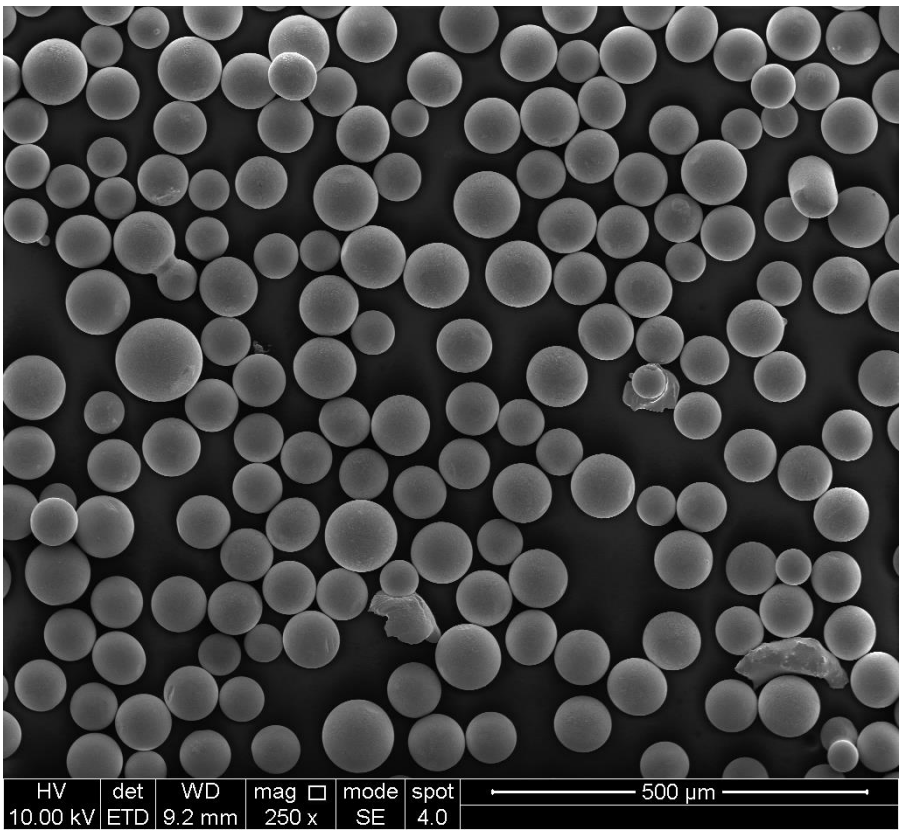

Figure 4-8: SEM image of PREP manufactured Inconel 718 powder

Table 4-1: Composition of Inconel 718 and 316L powders (wt%)

	Cr	Ni	Co	Mo	Nb + Ta	Ti	Al	Fe	Mn	Si	C	B
Inconel 718	18.72	51.85	0.03	3.0	5.12	0.80	0.52	19.91	-	-	0.05	<0.005
316L Steel	16.9	11.8	-	2.3	-	-	-	67.3	1.1	0.6	0.02	-

4.2.4. **Monitoring and Control**

The machine optics were setup with monitoring in mind, so a beam splitter was included, although the optics within were chosen by the manufacturer. Since the BeAM Magic 2.0 is based on a CNC machine, the Sinumerik software is capable of process control, however this was not implemented on the BeAM machine.

A Basler acA1440-73gm camera was chosen and set up, monitoring the melt pool coaxially; this connects to the beam splitter shown in Figure 4-7. This is a grayscale camera with a silicon detector, the region of interest is set as 500x500 px (1px = 5.4 µm, so 2700x2700 µm). A 4000 µs exposure is used and recorded at 75 fps. The images were recorded as 12-bit greyscale, the maximum pixel intensity possible to record was 4095. This was determined to be a sufficiently high spatial resolution, with the capability for a high temporal resolution, whilst minimising equipment size and cost. For each image, all the pixels were summed to give an overall thermal intensity, similarly to Baraldo et al. [171]; the code used for monitoring is available at [170]. The idea behind this thermal intensity is that the background signal of the image is significantly lower than the melt

pool region, as such, by summing the intensities of the full image, what is being captured is the size and the intensity of the melt pool itself. Figure 4-9 shows two representative images of the melt pool in a build. These are plotted with two different intensity ranges to show the level of detail available due to the 12bit nature of the images. The sum (thermal intensity) and maximum intensity are both greater in the later layer, which is to be expected due to heat accumulation. The melt pool length can also be seen to be greater, so a larger area would be expected. As well as thermal intensity, 4 other measures of the melt pool were calculated post-process (offline), these were:

- **maximum intensity:** the maximum pixel intensity value in the image
- **melt pool area:** a contour was plotted using an intensity threshold of 20; the area is the number of pixels within this contour
- **melt pool width:** the range of X values in the contour described above
- **melt pool length:** the range of Y values in the contour described above

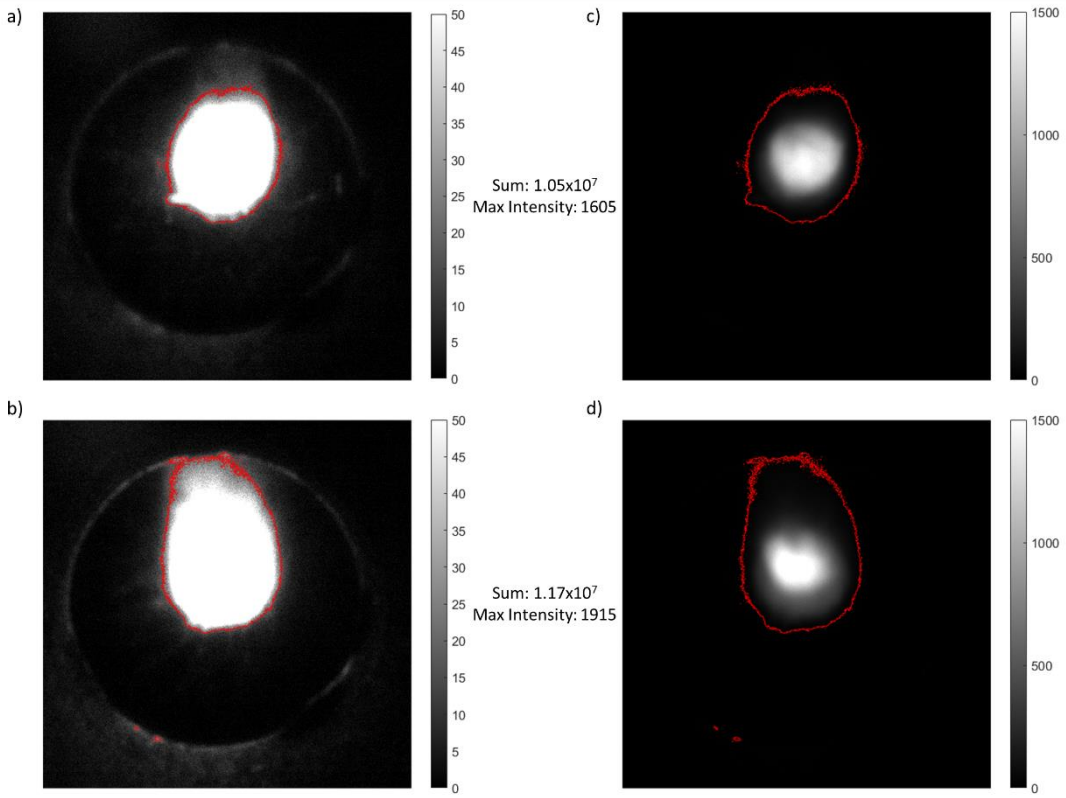

Figure 4-9: Representative coaxial images from an early layer (a, c) and from a late layer (b, d) in the 6 hatch wall. a, b) show a lower intensity than c, d), but with the same images. The sum (thermal intensity) and maximum intensity of each image is shown and contours (red) show an intensity of 20, which was used to threshold the melt pool for dimensional analysis. In all images, the laser is moving top to bottom.

The BeAM machine was purchased with a low resolution camera installed, this was upgraded to the Basler camera described above; results using this monitoring system were published by Freeman et al [168]. Process control was not implemented on this machine upon installation, during this PhD, a control system was developed, implemented and tested on the BeAM; using the Basler camera and taking advantage of the Sinumerik 840D automation system. This control system was used in Chapters 0 and 10. Figure 4-10 shows a diagram of how the BeAM and the external PC interact with one another when monitoring and/or controlling the process. A position/power log

and melt pool images can be recorded for a full build, but additionally, a feedback control loop based on the coaxial imagery can be run.

The software is written in MATLAB R2021b (Mathworks Inc); the methodology implemented by the script is:

- MATLAB waits for a BeAM program to start running
- When the program starts
  - Basler camera records melt pool imagery at 75 fps
  - MATLAB starts logging the machine position/power data at 10Hz
  - If control loop is selected, every 0.15 s the last X image intensities are averaged and compared to a target intensity (X = 5 for walls, X = 3 for triangular prisms)
    - Depending on the intensity as compared to the target, the power/velocity is adjusted
    - A control log is saved, writing the average intensity and the new power/velocity

This logic is shown diagrammatically in a flow chart (Figure 4-11).

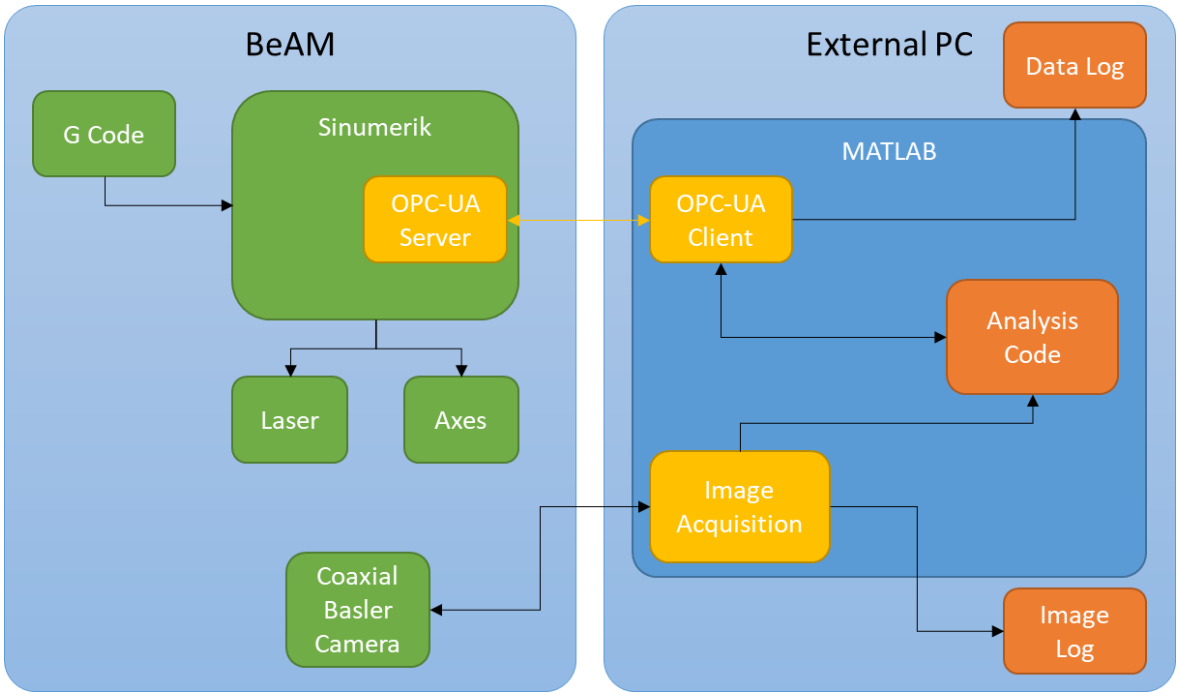

Figure 4-10: Schematic diagram showing the different components of the monitoring/control system. Diagram produced by Felicity Freeman

Simple linear relationships were used to control the feedback loop. Four successful builds were made (2 powers, 2 velocities), recording coaxial monitoring. A target thermal intensity (sum of the image) of 0.9×10^7 was used as this was the average value of the four successful builds.

When control is active, the ratio of the current thermal intensity to the target is taken (2 = twice as intense, 1 = equal intensity). The following equation is used for feedback: SF = -m·ratio+c. m was found to be 0.063 and 0.68 (power and velocity control respectively) where SF is the scaling factor. c was found to be 1.06 and 0.32 (power and velocity control respectively). These were calculated from the four builds aforementioned. The further from the target the thermal intensity, the larger the correction. For power control, the scaling factor is limited between 0.5-1.5, for velocity control, it is limited between 0.2-2.

The MATLAB code for this is available here: [170], with Camera_Recording_and_Control \0_Read_Me.docx containing finer details of the workings of the control script.

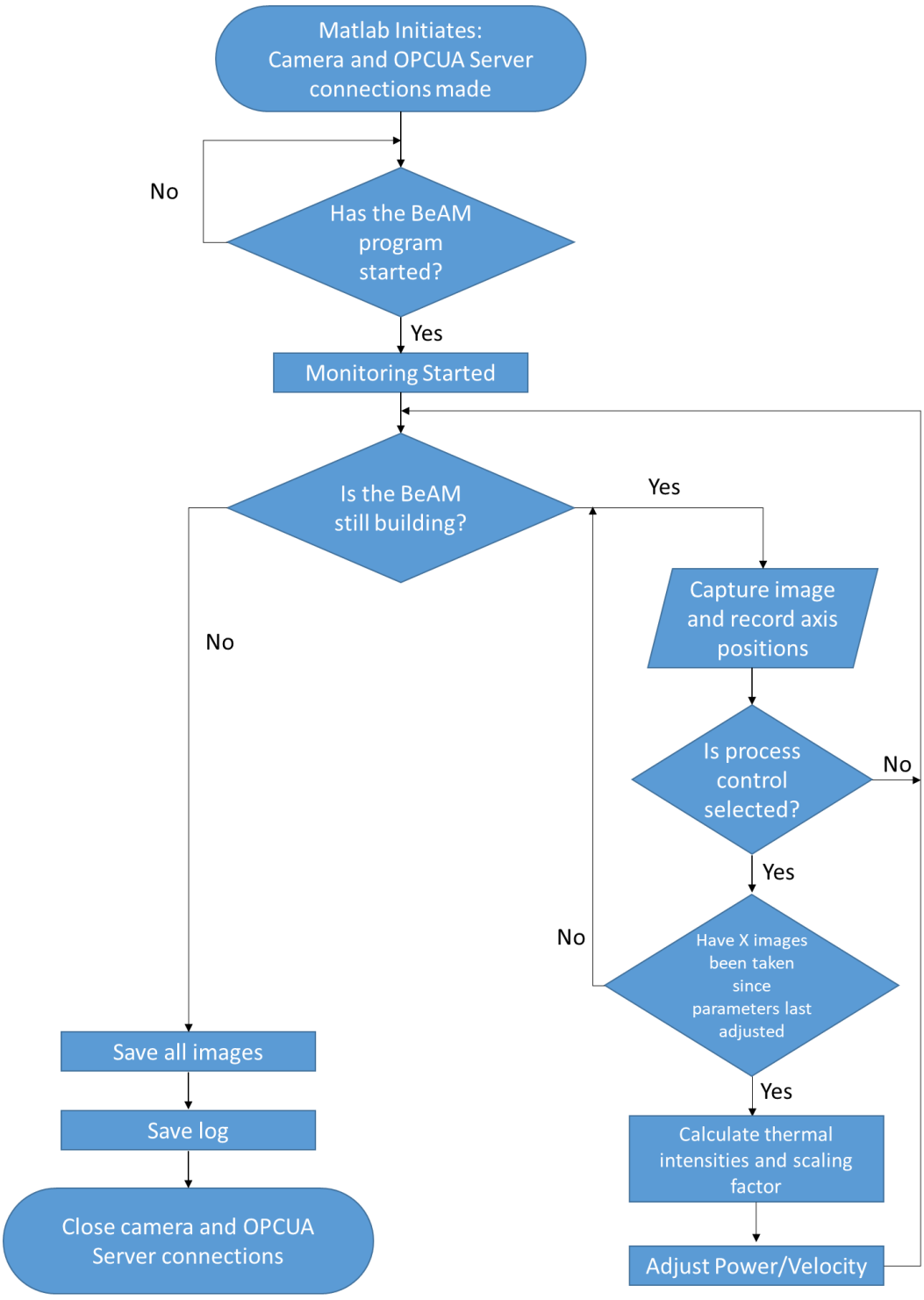

Figure 4-11: Flow chart showing logic behind monitoring/control system

4.3. Metallography

Samples were sectioned using a Struers Secotom-50 cutting machine with a Buehler AcuThin blade. They were then mounted into conductive Bakelite using a Buehler SimpleMet mounting press. Samples for EBSD needed to be very small, so were mounted in Aluminium stubs with a screw.

Samples were ground using SiC paper on a Struers Tegramin-20 machine using P240, P600 and P1200 grades (2 minutes at each). Polishing was done on the same machine, with 9 µm and then 1 µm diamond suspension (5 minutes each). Before EBSD and etching, samples were also polished using a 0.25 µm colloidal silica solution (10 minutes) before being washed with isopropyl alcohol.

4.3.1. **Etching**

Three etchants were used through this work to investigate the microstructure of the samples. Before etching, samples were polished to 0.25 µm using colloidal silica, which also has a slight etching effect.

- **Aqua Regia:** 15 ml HCl, 10 ml distilled water, 5 ml HNO_3
    - Used on 316L stainless steel samples to reveal cell/dendrite boundaries and melt pool boundaries
- **Glyceregia:** 15 ml HCl, 10 ml Glycerol, 5 ml HNO_3
    - Used on L-PBF Inconel 718 samples to reveal cell boundaries and melt pool boundaries
- **Kallings Reagent #2:** 100 ml methanol, 100 ml HCl, 5g $CuCl_2$
    - Used on L-DED Inconel 718 samples to reveal cell/dendrite boundaries and melt pool boundaries

Aqua Regia

- Pour 10 ml of distilled water into a glass beaker.
- Slowly add 15 ml HCl to the water, stirring continuously. Once added, slowly add 5 ml HNO_3, continuously stirring.
- Once the mixture is ready, dip cotton wool and swab sample.
- Angle sample to a light, a bright reflection should be visible, keep spreading etchant to get consistent etching over the surface. After 20-30 s, should see the surface start to dull; place sample into pre-prepared water bath to stop reaction.
- Remove sample and wash thoroughly using warm soapy water, once clean, rinse in water and then wash with isopropyl alcohol, blow to dry.
- Check etching under optical microscope. If underetched, swab further; if overetched, it is possible to repolish and repeat the steps.

Glyceregia

- Pour 10 ml of glycerol into a glass beaker.
- Slowly add 15 ml HCl to the glycerol, stirring continuously.
- Once added, slowly add 5 ml HNO_3, continuously stirring.
- Once the mixture is ready, dip cotton wool and swab sample.
- Angle sample to a light, a bright reflection should be visible, keep spreading etchant to get consistent etching over the surface. After 20-30 s, should see the surface start to dull; place sample into pre-prepared water bath to stop reaction.
- Remove sample and wash thoroughly using warm soapy water, once clean, rinse in water and then wash with isopropyl alcohol, blow to dry.
- Check etching under optical microscope. If underetched, swab further; if overetched, it is possible to repolish and repeat the steps.

Kallings Reagent #2

- Pour 100 ml of methanol into a glass beaker.

- Slowly add 100 ml HCl to the methanol, stirring continuously.
- Once added, slowly add 5 g $CuCl_2$, continuously stirring.
- Once the mixture is ready, dip the sample in using tongs. Submerge for 10 s, then rinse in water bath; angle to the light and see if surface is dulled, if not, dip for a further 5 s at a time.
- Once happy, wash sample thoroughly using warm soapy water, once clean, rinse in water and then wash with isopropyl alcohol, blow to dry.
- Check etching under optical microscope. If underetched, dip again; if overetched, it is possible to repolish and repeat the steps.

4.4. Optical Microscopy

Optical microscopy was captured using an Olympus BX51 microscope with lenses from 50x to 500x. The microscope is fitted with a Clemex Vision PE system, which is a motorised stage along with automation software. The automation software allows for scripts to be created; this gives the ability to automatically create large, high resolution image mosaics. Additionally, after images are captured, they can be automatically thresholded and dark regions extracted. This allows detection of cracks and defects and has been used as a method of measuring porosity throughout this work. The percentage area with intensity below the threshold is assumed to be the porosity area fraction.

4.5. Hardness

Hardness measurements were made using the EMCO-Test Durascan 70 hardness indenter (Figure 4-12). The main head has a swivelling adapter, allowing for quick switching between optical lenses and the Vickers hardness indenter. Theoretically, this means that after each indent, the optical lens can image the indent, automatically measure its' size and calculate the hardness. In reality, due to poor calibration, some indents required remeasuring manually, as the indent was not visible in the field of view. Maps of indents could be made, with maps of 120 indents taking roughly 2 hours to measure, correct and export accurate hardness values.

Figure 4-12: Durascan 70 Vickers hardness indenter, labelled, showing its' main components; adapted from [172]

For this work, a 1 kg (9.8 N) load was used for each indent, an automatically optimised approach speed was selected. The indent hold time could be selected and was left at the default value of 15 s. Within a hardness map, the relative coordinates of each indent were saved. The following equation can be used to calculate the hardness from the indent diagonal.

$HV = \frac{0.1891F}{d^2}$ [173]; where F is the force applied (1 kg = 9.8 N) and d is the indent diagonal (in mm)

Statistical analysis of hardness data was performed using Minitab 17.1.0.

4.6. Differential Scanning Calorimetry (DSC)

DSC was performed using a TA Instruments SDT Q600 in an Argon environment, scanning from 50 °C to 1450 °C and cooling back to 50 °C at a rate of 20 °C/min. The heat flows were normalised by mass for better comparison between samples. The baseline heat flow was calculated and subtracted from the measured heat flows, so when differentiated with respect to temperature – negative values represent a drop of the heat flow from the baseline.

4.7. Electron Backscatter Diffraction (EBSD) Analysis

Various SEM machines were used to capture EBSD data, the details of each machine will be covered in the specific chapters' methods section. A basic overview of the technique is given here, but more detail can be found in the literature. Once the sample is placed in a scanning electron detector, it must be tilted to 70 °. The electron beam is moved to a spot, the incoming electrons are diffracted by the atomic lattice and a diffraction pattern is detected by the detector.

The image detected is known as a kikuchi pattern. If the phase (and atomic spacing) is known, the rotation of the lattice can be calculated. By rastering the electron beam over the full area, a kikuchi pattern is recorded at each point and an orientation map can be generated. The spacing at which these kikuchi patterns are captured is known as the step size. By capturing several overlapping orientation maps, a large area mosaic can be characterised.

When analysing EBSD data, a grain is defined as an area with similar lattice orientation; typically, this is calculated using a 10 ° threshold. This means that some misorientation can be found within a grain. For each kikuchi pattern, a 3 dimensional lattice rotation is calculated, but typically, only a 2D orientation is plotted; this means that from each dataset, 3 orthogonal orientation maps can be calculated, giving the rotation of the lattice around each principal axis.

The smaller the step size, the slower the scan, but the higher the spatial resolution. Typically, step size is selected by predicting the smallest expected feature size and requiring this to contain at least 3-10 pixels. Depending on the purpose of the scan, various step sizes have been used through this work, varying between 1-10 μm.

Analysis was performed using MTEX 5.7.0, an open source MATLAB Toolbox [174]. The EBSD maps were rotated/cropped, grains were reconstructed with a threshold grain boundary misorientation of 10 °, with a minimum of 3 pixels per grain. The grain size refers to the equivalent radius calculated from the area of each grain. The aspect ratio is calculated as the ratio between the longest and the shortest principal axes.

Most measures of grain property are given as area-weighted averages. The logic behind this is that the effect of a large grain on the final property is larger than that of a small grain. If a sample has 2 grains, one 1 μm², the other 99 μm², then 99% of the area is taken up by the large grain, so their properties will not contribute equally, hence a grain size (area) weighting was chosen. Converting the grain areas into volumes (e.g. assuming spherical grains) could be done [175], but would introduce an additional source of error as the grains shapes in AM are strongly irregular. The area-weighted average of a property, P, can be calculated using:

$$\bar{P}_{area-weighted} = \frac{\sum_1^N P_i A_i}{\sum_1^N A_i}$$

where N is the number of grains, A is the grain area and i is the grain index. The area-weighted standard deviation is defined by [176]:

$$\sigma_P = \sqrt{\frac{N}{N-1} \frac{\sum_1^N A_i (P_i - \bar{P})^2}{\sum_1^N A_i}}$$

The anisotropy factor is a way of simplifying the crystal orientation of a grain into a single value. This varies between 0 for <100> directions to 1/3 for <111> directions [177]:

$$A_{hkl} = \frac{h^2k^2 + k^2l^2 + l^2h^2}{(h^2 + k^2 + l^2)^2}$$

Equation 4-1

This factor is sometimes scaled to be between 0-1, but the same trends are seen [178,179]. An anisotropy factor can be calculated for each grain. An example MTEX script, creating basic plots and performing basic calculations can be found here [170]. Anisotropy factors for 4 example points shown in Figure 4-13 are tabulated in Table 4-2. An example calculation is performed for point C:

$$A_{\bar{1}13} = \frac{(-1)^2 1^2 + 1^2 3^2 + 3^2 (-1)^2}{((-1)^2 + 1^2 + 3^2)^2} = \frac{1 + 9 + 9}{(1 + 1 + 9)^2} = \frac{19}{11^2} = 0.157 = 0.16 \ (2 \ sig. fig)$$

To calculate the average anisotropy factor for a sample, grains were calculated from the EBSD data with a misorientation angle of 10 °. Then for each point, the orientation of the grain was taken and the anisotropy factor was calculated. By averaging the anisotropy factor for each point, an overall average anisotropy factor for each sample was calculated.

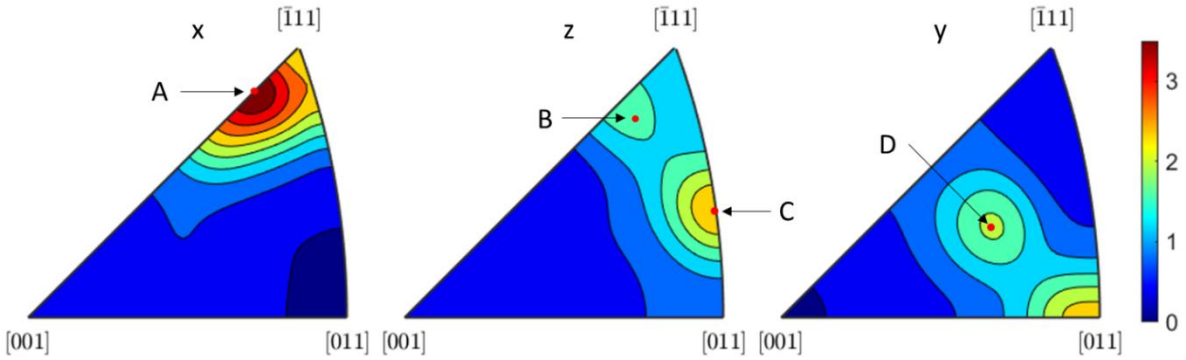

Figure 4-13: Inverse Pole Figures of 6 hatch wall, with 4 crystallographic orientations labelled

Table 4-2: Anisotropy factors calculated for key orientation and orientations marked in Figure 4-13

	h	k	l	Anisotropy Factor
[100]	1	0	0	0.00
[110]	1	1	0	0.25
[111]	1	1	1	0.33
A	-7	7	10	0.31
B	-7	8	11	0.31
C	-1	1	3	0.16
D	-3	7	12	0.22

For an EBSD dataset, a set of pole figure could be plotted, two example of these are shown in Figure 4-14. One is of weak texture, the second exhibits a strong texture (Figure 4-14a and b respectively). The scale is in units of multiples of uniform density (mud), i.e. how many more times more prevalent is an orientation than if all orientations were equally distributed. A large mud shows a strong texture, as a certain orientation is much more prevalent. There are three plots for each region, the <100>, <110> and the <111> orientations. For the EBSD quantification, the maximum of these three mud values was selected as it shows the maximum strength of texture measured. For the examples shown in Figure 4-14, the maximum mud were found to be 1.8 and 27 (for a and b respectively), so a higher maximum mud value is representative of a stronger texture, this is similar to the analysis performed by Yeoh et al [180].

The Kernel Average Misorientation (KAM) is a measure of misorientation within a grain, this can be calculated for each grain by measuring the misorientation of pixels surrounding the central spot (first order neighbours only). The misorientation for each grain can be calculated by averaging the KAM values for each grain, this is known as the Grain Average Misorientation (GAM) [181]. To get an average misorientation of each sample, an area-weighted average GAM was calculated for each sample.

For further analysis, grains within a region were split into 3 sets; small grains, medium grains and large grains. To achieve this, each grain had its' area and aspect ratio calculated and k-means analysis was performed using these. K-means clustering is a technique, were X random cluster centres are chosen (X selected by the user) and the sum of the Euclidian distances (in 2 dimension in this case) is minimised iteratively [182]. As the number of clusters is increased, each point is more likely to have a cluster centre near it, decreasing the total distance i.e. improving the clustering. Taking this to an extreme, is the number of clusters is set to the same as the number of data-points, then there will be a total distance of 0, as each point is its' own cluster. The aim is to minimise the distance (which is akin to an error), whilst having the minimum number of clusters.

An example of this is shown in Figure 4-15; k-means clustering is performed for values of X between 1-15. As expected, the total distance decreases as the number of clusters increases (Figure 4-15a). Selecting the optimal number of clusters is difficult, the aim is to find the "elbow of the curve". By taking the difference of the point-to-centroid distances (Figure 4-15b), it can be seen that increasing above 6 clusters seems to yield minimal returns. Hence 6 clusters were chosen for the k-means clustering in this case (shown by the dotted black line).

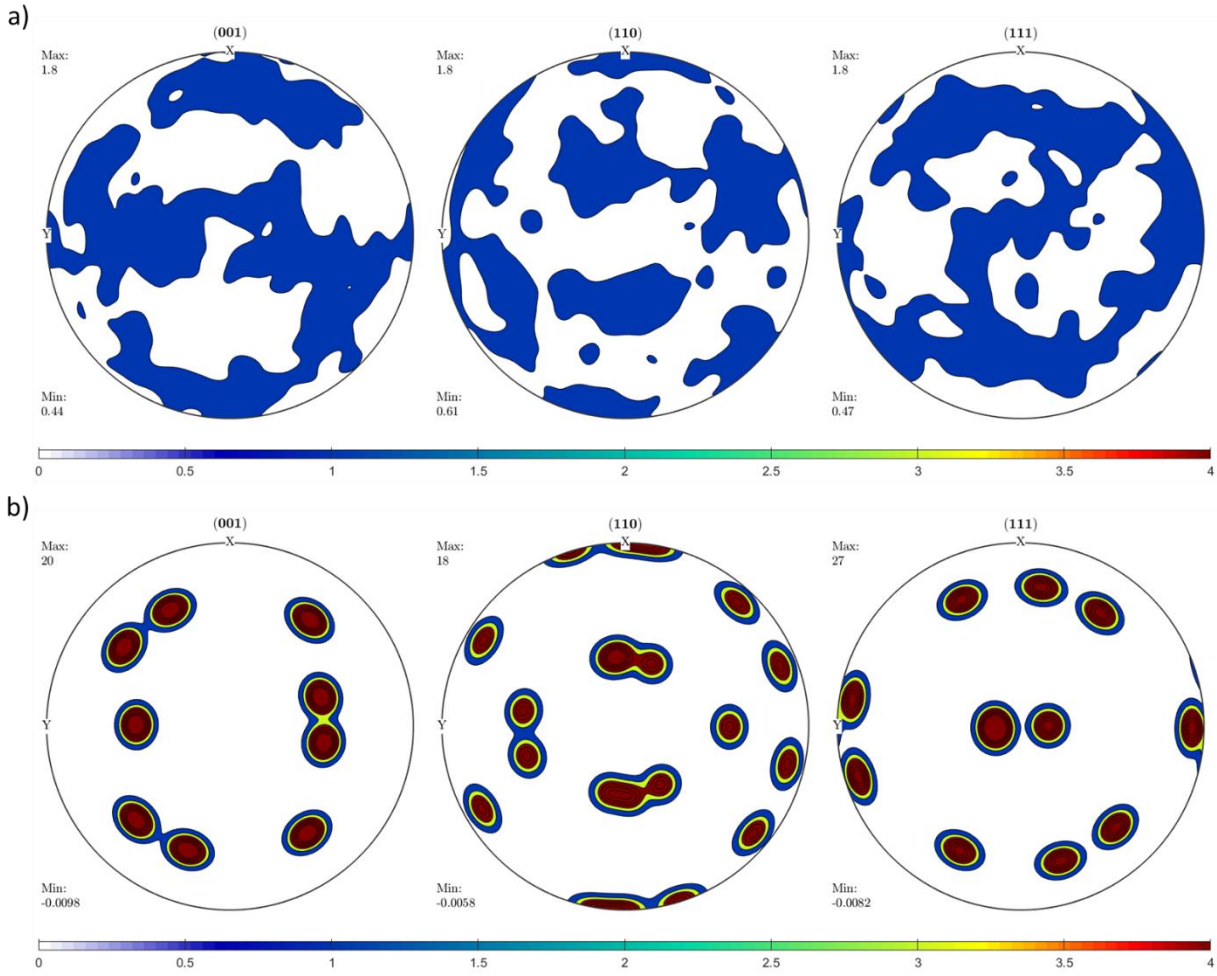

Figure 4-14: Example pole figures; a) region with weak texture; b) region with strong texture

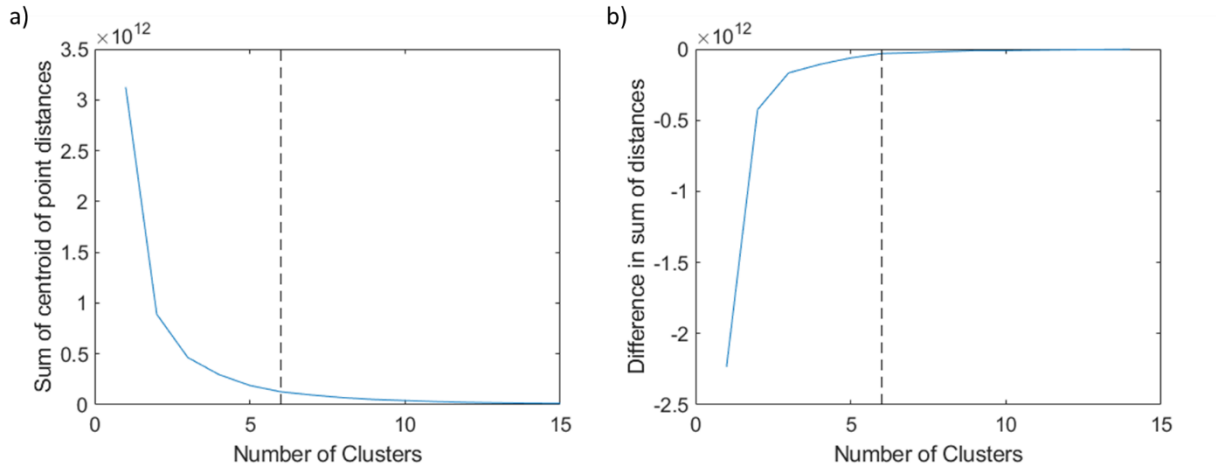

Figure 4-15: k-means distances for an example EBSD dataset; a) sum of distances between the centroid and the points; b) derivative of plot in a, showing difference in sums. Dotted black line shows 6 clusters, the chosen number of centroids for this analysis

Visually, three main types of grain can be seen in the raw EBSD (Figure 4-16a):

- Large columnar grains which typically extend a long way along the height of the map
- Small, randomly oriented grains, typically between the large columnar grains
- Remnant grains of a medium size, not equiaxed, but not columnar

The 6 clusters were manually combined into 3 sets to achieve the desired grain distributions. The cluster with the smallest grain area was taken as the of small grains, the 2 clusters with the largest grains were takes to be the large columnar grains. The remaining 3 clusters were combined to give the medium grains. These categorisations are shown in Figure 4-16b, with the three sizes of grain each represented by its' own colour; Figure 4-16a shows the original EBSD orientation map for comparison. The grains were split in the desired manner, so this methodology was used throughout this work.

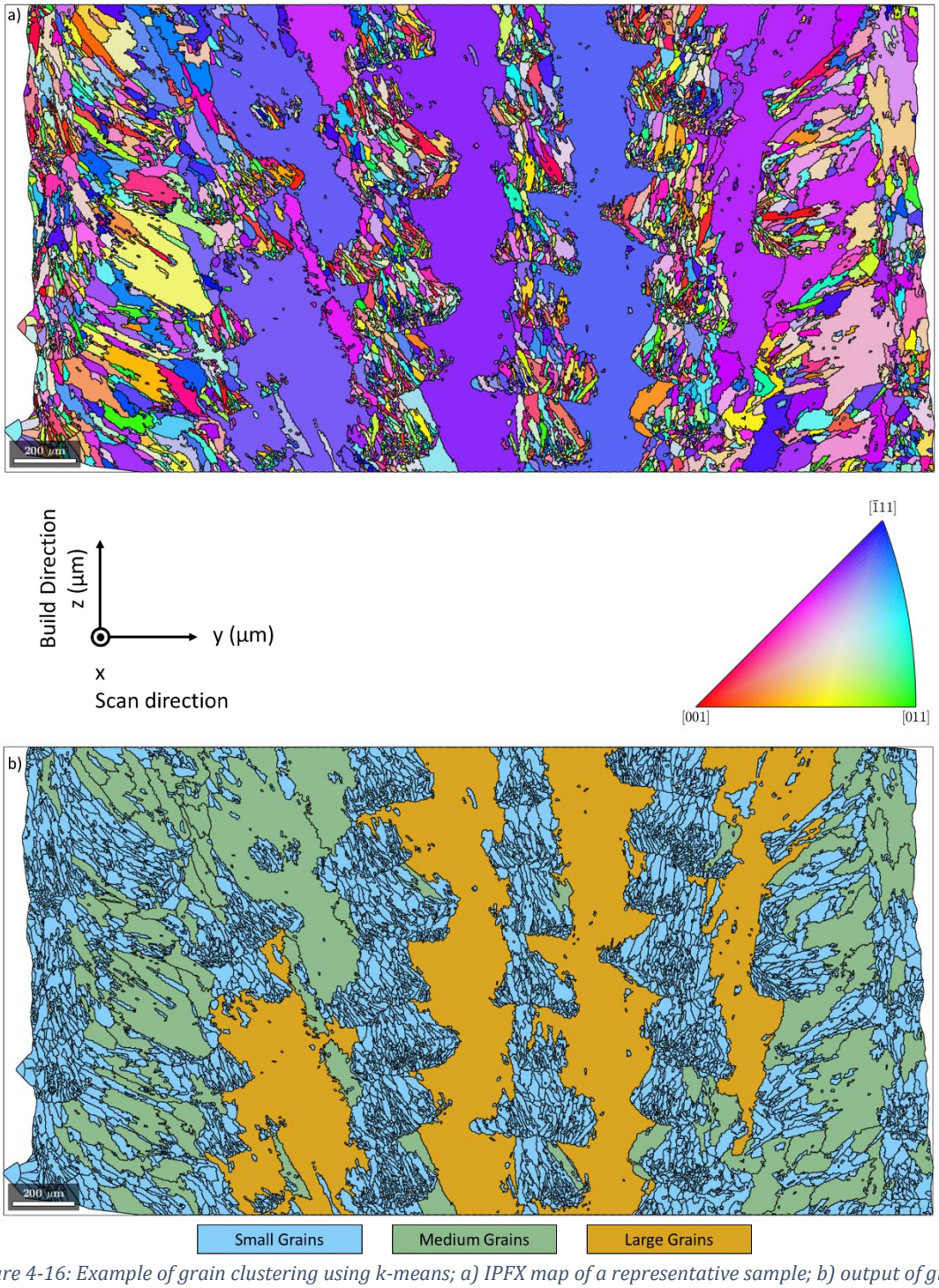

Figure 4-16: Example of grain clustering using k-means; a) IPFX map of a representative sample; b) output of grain clustering. Small, medium and large grains are shown in different colours

5. Comparison of Printability and Weldability in Additive Manufacturing

5.1. Introduction

5.1.1. History of Nickel Superalloys

Since this thesis is mainly focussed on AM of Nickel superalloys, especially Inconel 718, a background of nickel superalloy metallurgy is included. The manufacturing processes progressed from wrought alloys to directional solidification as the temperature requirements increased (Figure 5-1) [183].

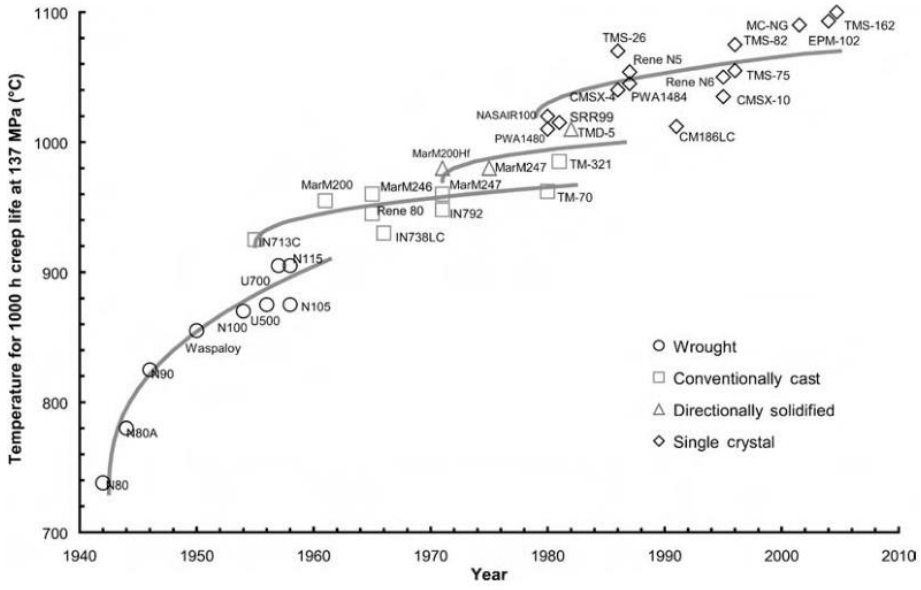

Figure 5-1: Different superalloy manufacturing processes used through the ages, showing the introduction of various new alloys. Reported by Reed [183]

Nickel superalloys have improved mechanical properties compared to the raw element, initially this was due to solution strengthening achieved by adding components [62]. After this, carbon (and later boron) was added for carbide formation, which adds further strength in the form of grain boundary pinning [62,63]. At this point, components were wrought, so excessive γ' would be too hard for hot working and γ' was avoided. From the 1960s onwards, casting took over, the γ' content increased rapidly because of the improved precipitation strengthening effects [184].

In the 1970s, engines were operating at higher temperatures and creep was becoming an issue. Investment casting took over due to the resultant columnar microstructure, the grains were oriented with the main stress direction, so weak grain boundaries were minimised in a columnar structure, making it more resilient to creep and stress rupture [61]. This allowed for the removal of carbon and other grain boundary precipitate formers, as grain boundaries were now being avoided [183]. More recently, single crystal superalloys were developed with rhenium and hafnium additions significantly improving creep life [183]. A range of Nickel superalloy compositions are shown in Table 5-1. The first 6 of these are alloys from the review by Clare et al. [12], the following 3 are alloys developed specifically for AM [56,185]. The remaining alloys are a range of Nickel superalloys, both new and old, with a range of compositions. The aim was to select a broad variety

of alloys, with different strengthening mechanisms and designed for different manufacturing processes. Having a wide range of alloys improves the likelihood of there being alloys which cover the full range of crack susceptibility for each cracking mechanism, making the analysis more robust; these compositions are used for calculating crack susceptibilities later in this chapter.

Table 5-1: Compositions of common Nickel superalloys used in aerospace applications (wt%). Process shows the manufacturing process this alloy was designed for: wrought (W), cast (C), additive manufacturing (AM), powder metallurgy (PM). Strengthening mechanisms also shown: precipitation strengthened (ppt) and solution strengthened (sol)

	Cr	Ni	Co	Mo	W	Nb	Ti	Al	Fe	Hf	Ta	Cu	V	C	B	Zr	Process	Strengthening	Ref
Inconel 718	19.00	52.77	0.00	3.00	0.00	5.10	0.90	0.50	18.50	0.00	0.00	0.15	0.00	0.08	0.00	0.00	W/C	ppt (γ'')	[62]
Inconel 625	21.50	62.95	0.00	9.00	0.00	3.60	0.20	0.20	2.50	0.00	0.00	0.00	0.00	0.05	0.00	0.00	W	sol	[62]
Hastelloy X	22.00	49.09	1.50	9.00	0.60	0.00	0.00	2.00	15.80	0.00	0.00	0.00	0.00	0.02	0.00	0.00	W/C	sol	[62]
CM247LC	8.00	61.42	9.00	0.50	10.00	0.00	0.70	5.60	0.00	1.40	3.20	0.00	0.00	0.07	0.10	0.01	C	ppt (γ')	[64]
CMSX-4	6.50	64.80	9.00	0.60	6.00	0.00	1.00	5.60	0.00	0.00	6.50	0.00	0.00	0.00	0.00	0.00	C	ppt (γ')	[62]
Waspaloy	19.50	54.58	13.50	4.30	0.00	0.00	3.00	1.40	2.00	0.00	1.50	0.00	0.00	0.07	0.06	0.09	C	ppt (γ')	[62]
ABD-850AM	18.68	52.50	17.60	1.89	4.74	0.60	2.22	1.29	0.00	0.00	0.44	0.00	0.00	0.01	0.03	0.00	AM	ppt (γ')	[56]
ABD-900AM	16.96	50.14	19.93	2.09	3.08	1.78	2.39	2.11	0.00	0.00	1.42	0.00	0.00	0.05	0.05	0.00	AM	ppt (γ')	[56]
AlloyDLD	19.00	64.87	4.00	4.90	1.20	3.00	0.00	2.90	0.00	0.00	0.00	0.00	0.00	0.04	0.05	0.05	AM	ppt (γ')	[185]
Rene41	19.00	55.30	11.00	10.00	0.00	0.00	3.10	1.50	0.00	0.00	0.00	0.00	0.00	0.09	0.01	0.00	W/C	ppt (γ')	[62]
In738	16.00	62.07	8.50	1.75	2.60	2.00	3.40	3.40	0.00	0.00	0.00	0.00	0.00	0.17	0.01	0.10	C	ppt (γ')	[62]
In713LC	12.00	72.74	0.00	4.50	0.00	0.00	0.60	6.00	0.00	0.00	4.00	0.00	0.00	0.05	0.01	0.10	C	ppt (γ')	[62]
Udimet700	15.00	53.37	18.50	5.25	0.00	0.00	3.50	4.25	0.00	0.00	0.00	0.00	0.00	0.10	0.03	0.00	W/C	ppt (γ')	[62]
RR1000	15.00	52.30	18.50	5.00	0.00	0.00	3.60	3.00	0.00	0.50	2.00	0.00	0.00	0.03	0.02	0.06	PM	ppt (γ')	[183,186]
Inconel 939	22.40	49.74	19.00	0.00	2.00	1.00	3.70	1.90	0.00	0.00	0.00	0.00	0.00	0.15	0.01	0.10	C	ppt (γ')	[183]
Haynes 282	20.00	56.34	10.00	8.50	0.00	0.00	2.10	1.50	1.50	0.00	0.00	0.00	0.00	0.06	0.01	0.00	W	ppt (γ')	[187]
In100	10.00	60.25	15.00	3.00	0.00	0.00	5.00	5.50	0.00	0.00	0.00	0.00	1.00	0.18	0.01	0.06	W/C	ppt (γ')	[62]
C263	20.00	50.79	20.00	5.90	0.00	0.00	2.10	0.45	0.70	0.00	0.00	0.00	0.00	0.06	0.00	0.00	W	ppt (γ')	[62]
Udimet720	17.90	55.55	14.70	3.00	1.25	0.00	5.00	2.50	0.00	0.00	0.00	0.00	0.00	0.04	0.03	0.03	W	ppt (γ')	[183]
MAR M002	8.00	60.70	10.00	0.00	10.00	0.00	1.50	5.50	0.00	1.50	2.60	0.00	0.00	0.15	0.02	0.03	C	ppt (γ')	[183]
ATI718+	19.00	50.21	9.00	2.80	1.10	5.50	1.75	1.45	9.00	0.00	0.00	0.15	0.00	0.03	0.01	0.00	C	ppt (γ')	[183]

5.1.2. Nickel Superalloy Phases

γ' and γ" Precipitates

In precipitation strengthened alloys, the main strengthening precipitate is typically γ'. The γ' phase is an ordered $L1_2$ FCC phase, of composition $Ni_3(Al,Ti)$. At small sizes these are spherical, but as they grow, they become cubic to maintain coherency; some alloys contain up to 60 at% γ'. The main γ' stabilisers are Al, Ti, Ta, Nb, which typically have a larger atomic misfit to Nickel [61,62]. Uniquely, the γ' phase increases flow stress with increasing temperature due to Kear-Wilsdorf locks which form due to the movement of anti-phase boundaries (APBs) through the ordered structure [189].

Some alloys (including Inconel 718) contain γ" precipitates (Ni_3Nb), which have a body centered tetragonal (BCT) structure. These experience a larger strain, however these precipitates are less stable at high temperature. Identification and analysis of these phases often requires TEM, but can be done using SEM [190].

Carbides and Grain Boundary Strengthening

Many alloys also have additions which form carbides at the grain boundaries. These are typically of the form M_6C or $M_{23}C_6$, where M can be Cr, Mo, W, Nb; Ta and Ti form TaC and TiC rather than the more complex carbides. In more recent alloys, some refractory elements e.g. Hf are added, which forms HfC. Any additions of boron or zirconia also tend to segregate the grain boundaries. These particles tend to slightly increase strength, but significantly increase grain boundary strength [61,62].

Delta, Sigma and Other Deleterious Phases

Topologically close packed (TCP) structures are universally avoided as they form brittle phases e.g. σ, μ and Laves which typically form plates. σ appears to be the worst offender and hence computational methods have been developed to predict its occurrence (PHACOMP and Sigma-Safe, Section 5.1.7).

5.1.3. Nickel Superalloy Weldability

Weldability is defined as the capacity of a metal to be welded under fabrication conditions into a specific structure and for it to subsequently perform in its intended service [191]. The main forms of failure which typically deem Nickel superalloys "unweldable" are explained in Section 5.1.4, an easily weldable alloy must be resistant to the main forms of failure.

Many different composition relationships have been plotted to describe weldability, but the main factor is the γ' volume fraction (mainly Al and Ti), which drastically decreases weldability as shown in Figure 5-2 [65,192]. Since laser AM is fundamentally a similar process to welding, printability generally correlates with weldability. This is confirmed by the more printable alloys shown in Table 2-3 being more weldable as seen in Figure 5-2.

Figure 5-2b plots a compositional measure of γ' composition on the y axis against a measure of carbide content on the x axis. Some alloys are classified as having "Fair Weldability", this implies that they can be welded in certain conditions. In reality, for a certain alloys, different processing parameters will lead to different sources of failure as seen in Figure 5-3. This means that a material can be defined as weldable, but if processed under the wrong conditions, it can crack. For Inconel 718 it can be seen that there is a relatively large weldability window, for less weldable alloys, this window will be smaller. When an alloy is said to be unweldable, it usually means that for each set of

processing conditions, you will get one form of failure e.g. either hot tearing or liquation cracking occurs.

In Figure 5-3, high velocity and power both increased the chances of a centreline grain boundary. Similarly, low velocity and high power increase propensity to hot tearing due to a longer solidification time and so more time for segregation; many of the types of failure (Section 5.1.4) stem from excessive segregation [87,88].

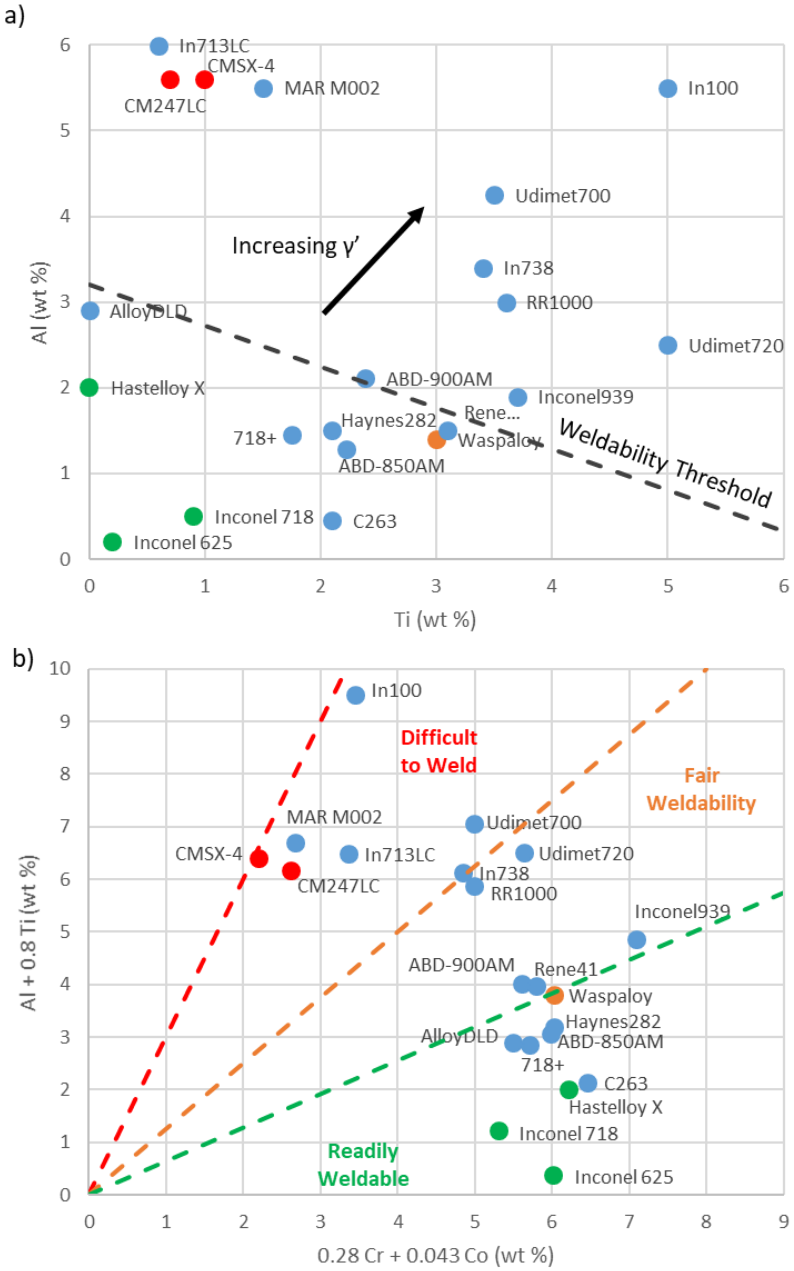

Figure 5-2: The dependence of weldability on composition for some Nickel superalloys. a) The dependence of weldability on Al and Ti for some γ' strengthened superalloys. Reported by Illston [193] *b) A different method of calculating weldability using composition. Reported by Haafkens and Matthey* [194]*. Printability of alloys to be analysed is colour-coded, with green being easily printable, red being not printable, and orange being somewhat printable (defined in Table 2-3)*

Fundamentally, superalloys are designed for their mechanical properties, with specific microstructures for increased high temperature strength. The processing method has always been selected in hindsight, with small alterations in composition to alleviate specific defect types.

Initially, superalloys were forged, but the alloys became so wear resistant that forging became very difficult and investment casting took over. Currently, in AM, the situation is different, the process is set but with some flexibility of processing parameters and an alloy must be selected to meet the industrially required mechanical properties.

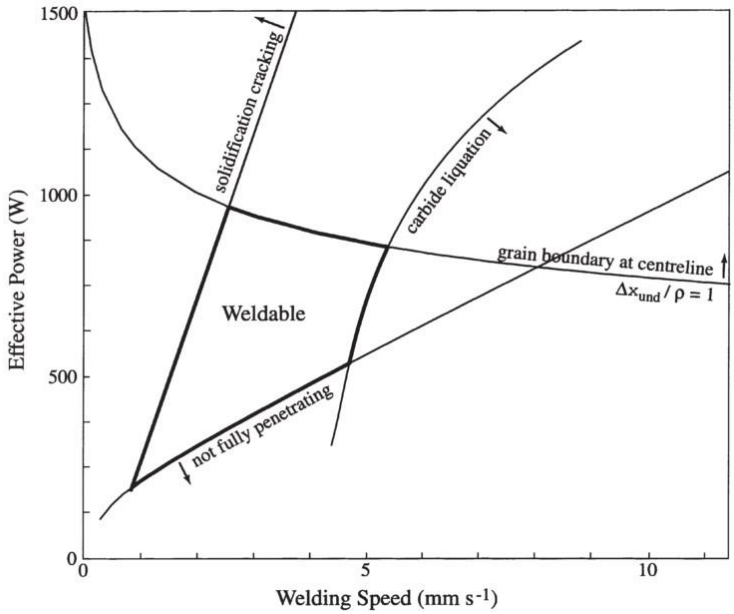

Figure 5-3: A processability map for Inconel 718, showing different causes of failures. Reported by Dye et al [195]

5.1.4. **Types of Failure**

There are many forms of failure associated with metallic components, the ones selected below are particularly applicable to Nickel superalloys but are also observed more widely. Some of these occur during solidification, others during heat treatment; the biggest issue in AM of Nickel superalloys is frequently taken to be hot tearing [196]. A lot of work is being undertaken to reduce the amount of various forms of cracking.

In Nickels, the dominant failure modes are shown diagrammatically in Figure 5-4 and are [156,192,197]:

- **Hot Tearing (Solidification Cracking)** occurs during solidification; when the dendrites are interlinked, the shrinkage due to solidification can no longer be filled by the remaining liquid
- **Liquation Cracking** occurs upon reheating of the solidified regions; where low melting point phases remelt and cannot withstand the local residual stresses, resulting in failure
- **Strain-Age Cracking** typically occurs upon heat treatment; where γ'/ γ" precipitation occurs, increasing the strength of components, but reducing their ductility. If residual stresses remain in the component but the ductility is reduced, failure can occur
- **Ductility Dip Cracking** occurs in a similar manner to strain-age cracking, but in this case, heat treatment allows carbides to grow at grain boundaries. These act as stress concentrators and can initiate failure along grain boundaries
- **Temperature Gradient Mechanism** occurs as a result of stress during solidification. This can cause cracking during the process, which manifests itself as delamination; alternatively, if/once the component is removed from the baseplate, the residual stresses can cause significant deformation

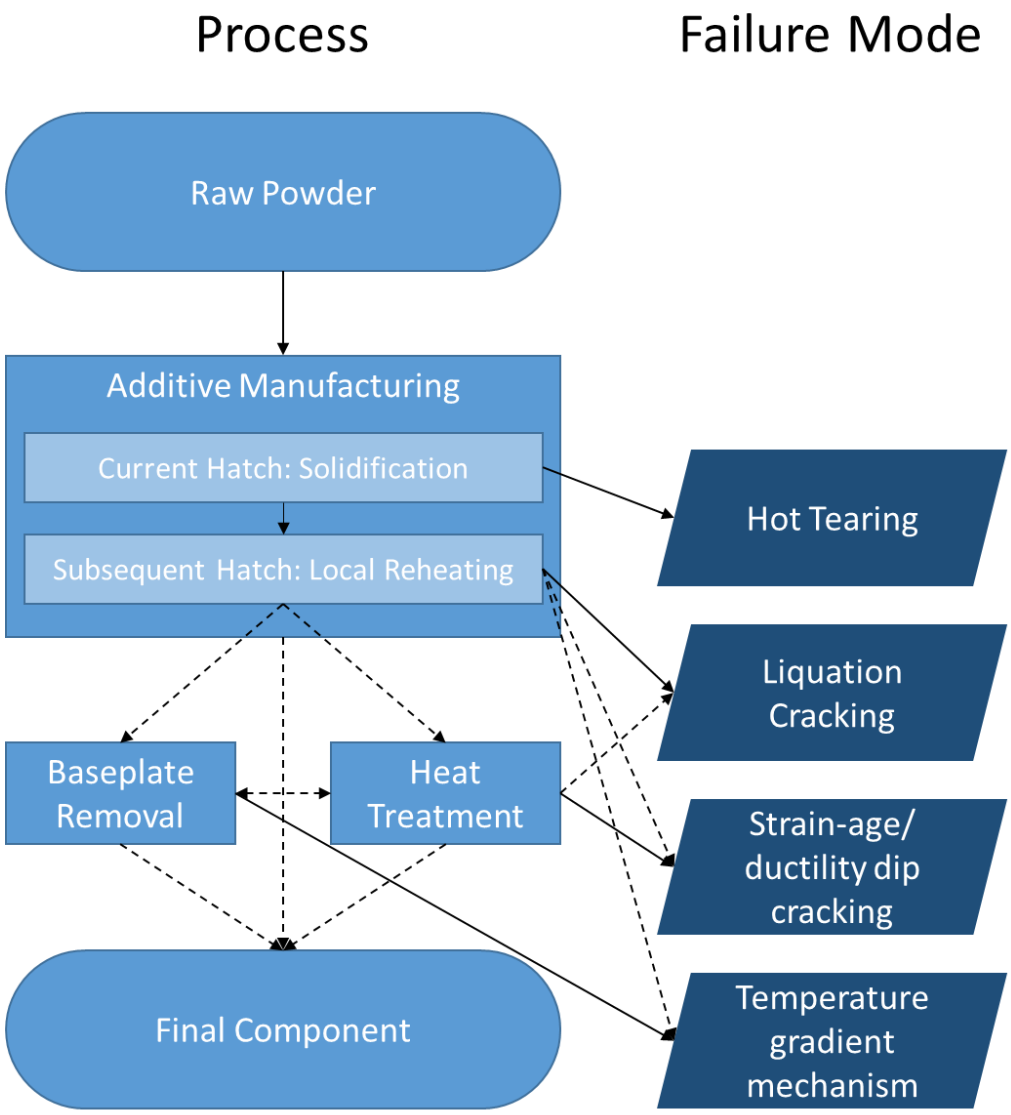

Figure 5-4: Flow-chart correlating dominant failure modes with the processing stage at which they occur

5.1.5. **Hot Tearing (Solidification Cracking)**

Hot tearing occurs during solidification and involves the formation of a tear between grains, where the last liquid was. During the late stages of solidification (fraction solid, $f_s > 0.9$) the final liquid to solidify contains all of the segregated trace elements [198]. In this mushy zone, dendrites restrict the flow of the liquid film [64] and cracks form due to the liquid not being about to accommodate the stress caused by solidification shrinkage [199]. Due to the mechanism, hot tearing is frequently called solidification cracking and it can be distinguished as it is intergranular and dendrites can often be seen on the crack face [198]; the crack faces have been shown not to match perfectly, proving that the process occurs above the solidus temperature [200]. Compositional analysis shows that there a large amount of interdendritic segregation.

Reducing the grain size and altering their shape (e.g. equiaxed grains) can reduce hot tearing as the stress on the liquid is decreased and it can flow between the grains better. By reducing the amount of trace elements and segregants, the solidification range becomes narrower and hence the liquid films solidifies quicker making the alloy easier to process without cracks [87,196]. This complex

process is dependent on both the composition of the final liquid and on the cooling during the late stages of solidification. This has led to there being two distinct ways of predicting hot tearing [201]:

- Metallurgical models, which use solidification curves and critical temperature ranges (from phase diagrams) [201]
- Thermo-mechanical models, which look at the solidification in terms of strains, strain rates and stresses associated with the shrinkage [200,201]

The former is a simpler analysis, which was developed in the 1970s [201], looking at the solidification from a global perspective, as exemplified the crack susceptibility coefficient, developed by Clyne and Davies [202]. The latter focussed more on the mechanism during the final stage of solidification and wasn't properly explored until the 1990s. More complex calculations are involved, e.g. the RDG critical strain rate developed by Rappaz, Drezet and Gremaud [203].

Clyne and Davies Model

Historically, it was assumed that simply the width of the freezing range was an indicator of hot tear susceptibility. While this is true, there are more specific regions which are critical to reducing likelihood of hot tearing. By dividing the solidification process into two main regions, the problem can be better analysed:

1. Liquid feeding, $0.6 > f_L > 0.1$. The dendritic network is formed, so no more solid movement can occur
2. Dendrites interconnected, $0.1 > f_L > 0.01$. This blocks off any liquid movement, so the dendrites have to be able to withstand the stress experienced

where f_L, fraction liquid.

The former is normal solidification and so any solidification shrinkage is fed by the remaining liquid. The time in this region, t_r is known as the relaxation time. The latter is known as the 'Brittle Temperature Range' (BTR) and is typically seen as the critical region [204]; here the dendrites are interconnected, so the dendrites have to take up any solidification strains. The time spent in this region is known as the vulnerable time, t_v; it has been shown that in this region large cooling rates are very detrimental [205]. Clyne et al. define the Crack Susceptibility Coefficient (CSC) as the ratio between these times [202]:

$$CSC = \frac{t_v}{t_r}$$

Equation 5-1

so the longer spent in the BTR, the higher the crack susceptibility.

The times spent in each region can be calculated using the Scheil model of solidification, which for binary systems takes the form:

$$C_L = C_0 f_L^{k-1}$$

Equation 5-2

where C_L and C_0, liquid and original compositions respectively; k, partition coefficient.

Next, an assumption must be made about the heat flow, this is usually taken to be constant and can be integrated between liquidus and eutectic temperatures to get an equation in terms of time [108].

The final form of this equation becomes:

$$t = \frac{\frac{H_f}{C}(1 - f_L) + (T_S - T_L)(f_L^{k-1} - 1)}{\frac{H_f}{C}\left(1 - \left(\frac{T_S - T_E}{T_S - T_L}\right)\right)^{-\frac{1}{1-k}} + (T_S - T_E)}$$

Equation 5-3

where T_S, T_L and T_E, solidus, liquidus and eutectic temperatures respectively; H_f, latent heat of fusion; C, specific heat.

When CSC is plotted against elemental addition (for binary systems) it shows a Λ shape (Figure 5-5). This model was further improved by calculating the limits rather than taking the ranges of $0.01 < f_L < 0.1$ and $0.1 < f_L < 0.6$ and the accuracy was improved [206]. The calculations involved in this model are relatively simple, in the 1970s, computation power was limited and a thorough understanding of the final stages of solidification was lacking.

Rappaz Drezet and Gremaud (RDG) Model

The second method of predicting hot tearing calculates a Hot Crack Susceptibility (HCS) using the critical strain rate in the mushy zone (mechanical effect rather than a metallurgical one). This is effectively an in-depth analysis of the mechanisms occurring in the final stages of solidification, defined as the vulnerable time by Clyne and Davies [202].

$$HCS = \frac{1}{\dot{\epsilon}_{p,max}}$$

Equation 5-4

Rappaz et al. analyse the mass balance into and out of the interdendritic region i.e. the solidification shrinkage vs the pressure on the liquid. If the solidification shrinkage is larger than the volume of liquid which can replace it, a critical cavitation pressure will be reached and a crack initiated. This critical strain rate in the mushy zone can be calculated and is [203]:

$$\dot{\epsilon}_{p,max} = \frac{{\lambda_2}^2}{180}\frac{H}{(1+\beta)\mu}\Delta p_c - V\frac{\beta}{1+\beta}H$$

Equation 5-5

where λ_2, secondary dendrite arm spacing; $\beta = \rho_s/\rho_l - 1$, shrinkage factor; μ, viscosity; Δp_c, critical cavitation pressure; V, isotherm velocity (assumed to be laser velocity); $H = \int_{T_S}^{T_L} \frac{(f_s(T))^2}{(1-f_s(T))^2} dT$; $f_s = 1 - f_L$

The results also have the Λ form (Figure 5-5), where the HCS is on a scale of 0 to 1. The maximum at 1.4 wt% Cu for the Al-Cu system is because it has the largest solidification interval (as can be seen in a phase diagram), this leads to a large value of H (Equation 5-5) due to the integral across this solidification interval. This confirms the historic idea that the larger the solidification range, the more susceptible an alloy to hot tearing.

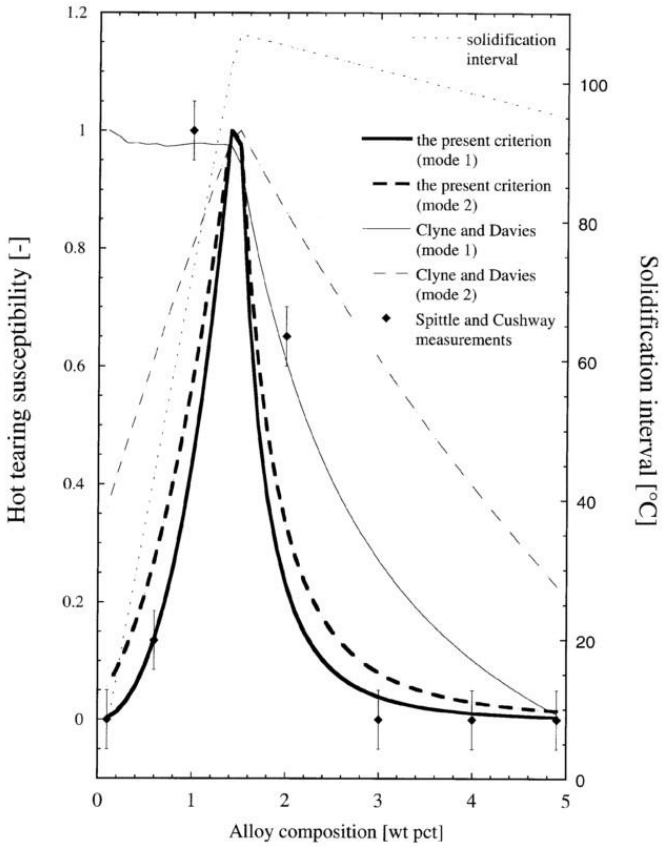

Figure 5-5: HCS values against elemental addition, comparing the RDG model with the Clyne Davies model and experimental results. Reported by Rappaz et al [203]

Kou Cracking Criterion

Kou approached this problem in an alternative manner; the maximum length of an interdendritic channel for filling to occur was calculated [207]. Assuming columnar growth of dendrites in a hexagonal array and a thin liquid layer surrounding each dendrite, the liquid feeding can be modelled. By looking at one grain boundary, the profile of the interdendritic channel can be calculated; the longer and narrower this channel, the larger the likelihood of a crack forming.

Similarly to RDG [203], columnar dendrite growth is assumed, so $f_s \propto x^2$ [207]; a critical strain rate can be calculated (Equation 5-6). For equiaxed structures, a cubic relationship has been used [208], but in AM, columnar growth is typically more representative. Looking at the driving force for crack initiation, $\left|\frac{dT}{d(f_s^{1/2})}\right| \; near \; f_s^{1/2} = 1$ increases as the interdendritic channel length increases. The longer the channel, the more difficult for feeding to occur, so cracks are more prominent [207]. Additionally, once a crack forms, the longer and thinner the interdendritic channel, the more stress will accumulate, so crack propagation will also be more likely.

$$\left\{ \begin{matrix} \frac{d\varepsilon_{local}}{dt} \\ (separation) \end{matrix} > \begin{matrix} \sqrt{1-\beta}\frac{d\sqrt{f_s}}{dT}\frac{dT}{dt} \\ (growth) \end{matrix} + \begin{matrix} \frac{d}{dz}\left[\left(1-\sqrt{1-\beta}\sqrt{f_s}\right)V\right] \\ (feeding) \end{matrix} \right\}_{\sqrt{f_s}\to 1}$$

Equation 5-6

So a larger value of $\left|\frac{dT}{d(f_s^{1/2})}\right|$ $near\ f_s^{1/2} = 1$ is indicative of a higher susceptibility to hot tearing.

Various values of f_s can be used, but a range of $0.87 < f_s < 0.94$ was used and shown to correlate well with other models for Aluminium alloys [207]. It's noted that the location of the Λ peak (Figure 5-5) varies depending on the f_s range used, but this is also the case in the RDG model [207]. The range used ($0.87 < f_s < 0.94$) gives a peak at 3.5 wt%, compared to an experimental peak of 3.0 wt%. This crack susceptibility index is said to be more useful as a qualitative measure of hot tearing rather than to calculate an optimal composition to minimise cracking [207].

If this was repeated for an equiaxed structure, $f_s \propto x^3$, the final result would come out as $\left|\frac{dT}{d(f_s^{1/3})}\right|$.

Numerically, this would be significantly different, but since the range of f_s is set and kept constant over all samples, this would lead to a systematic error. This cracking susceptibility index is used for relative comparison, so a systematic error is immaterial.

Avoiding Hot Tearing

Figure 5-5 shows a comparison of both the Clyne and Davies and the RDG models with experimental data, there are 2 modes for each model. These refer to the conditions of constant cooling rate ($dQ/dt \propto t^{-1/2}$) and constant rate of heat extraction (*dQ/dt constant*) respectively. Given how different the two approaches are, the final results are surprisingly similar, the main difference being the Clyne model overestimating the HCS at the extremes. The RDG HCS values correlate well with experimental results, however, as pointed out by the author, the HCS is for crack initiation, whereas experimental results use crack length/area and so include propagation and you wouldn't necessarily expect these to match [200,209]. One of the most important flaws in these models is that they are based on binary systems e.g. Scheil solidification; you would expect the same effects to propagate into more complex alloys, but the simple equations may not hold true.

The original assumption that wide freezing ranges lead to high HCS alloys is correct [198,210], but these equations should give a better predictor. It seems like grain structure can also affect HCS; having small (equiaxed) grains increases contact area so f_L at coherency is higher and so HCS is decreased [211]. It has been further proposed that Al, Ti and Nb are detrimental to HCS as they form γ'/γ'' phases; they do however increase susceptibility to strain-age cracking [192].

Additions of grain boundary formers (C, B, Zr) are frequently argued over, some say that they soak up solutes so reduce the HCS [212]; whereas others agree about carbon, but say that if too much is added (>0.05% B or Zr), they can be very detrimental [213,214]. Classic hot tearing models do not capture these trends, although they may be significant. Several other cavitation processes have been discussed in relation to semisolid processing and mushy zones but will not be further explored [215,216].

5.1.6. Other Forms of Cracking

Liquation Cracking

Liquation cracking is similar to hot tearing, but occurs once the bulk has already solidified. Low melting point phases e.g. grain boundary carbides or γ/γ' eutectic remelt despite being below T_m of the bulk [64]. This often occurs in welding behind the main bead; the weld heats up the grain boundary phases, creating molten pockets along the boundary in the heat affected zone (HAZ). The tensile stress due to the weld can be enough to pull the grain boundary apart, creating a liquation crack, also known as a HAZ fissure [197]. There is a fine composition balance; carbides are desirable for improved mechanical properties, yet this change in composition can decrease the

melting point of the final solidification composition. In an attempt to improve mechanical properties, susceptibility to liquation cracking can inadvertently be increased.

Strain-Age (Reheat) Cracking and Ductility Dip Cracking

Both of these forms of cracking occur below the solidus temperature (0.4-0.9 T_s) in precipitate strengthened superalloys. Post solidification, components are heat treated to relieve residual stress, this however has the side-effect of allowing γ' precipitates to precipitate and coarsen. The precipitation often occurs before the relaxation and increases the yield stress, reducing ductility. This means that material is still highly stresses, but is now more brittle and so a strain-age crack can initiate [54].

Ductility dip cracking (DDC) occurs in the same manner, but here the carbides on the grain boundaries coarsen and act as stress concentrators. DDCs occur on grain boundaries and often connect carbides as these are where the cracks initiate [217]. Both these types of crack are fundamentally caused by precipitation; if an alloy is overaged before processing, the ductility is increased and so strain-age cracking can be reduced [63,197].

Temperature Gradient Mechanism (TGM)

Laser processing of metals during AM causes very rapid heating around the melt pool, but with relatively slow cooling due to conduction. This causes a high thermal gradient, G, between the new layer and the baseplate creating a compressive stress as the new layer is constricted by the base. The raised temperature lowers the yield stress of this region allowing it to be plastically compressed, this means that there is a tensile stress in the newly printed surface layer. The solidification of the melt pool is also constrained by the solid beneath it, creating the same effect, but on a smaller scale. This increases the tensile stress on the surface; if this stress exceeds the ultimate tensile stress (at that temperature), a crack will form at the interface [23,218].

Since this stress is caused by the constriction of the new material by the baseplate, this stress is greatly reduced when the component is removed from the baseplate, so this mechanism is only active during the manufacturing process itself [218]. The thermal gradient between the baseplate and the component can be reduced by preheating the baseplate before manufacture. This decreases the stresses accumulated and so the likelihood of cracking [16].

5.1.7. **Alloy Design**

Currently, alloys are designed for conventional manufacture and then we try to manufacture them using AM [48]. Thinking about what is required of a material for it to be easily 'printable' can go a long way. Logically, we want to maximise the yield stress, σ_y, in order to have a strong material. We want to maximise thermal conductivity, κ, and minimise thermal expansion, α_{CTE} to increase the chance of a material resisting failure. These parameters can be expressed as a 'Stress Performance Index' (Equation 5-7), which needs to be maximised in order to select a good material [219,220].

$$\text{Stress Performance Index, } \sigma = \frac{E\alpha_{CTE}}{2\kappa(1-\nu)}$$

Equation 5-7

where E, Young's Modulus; α_{CTE}, thermal expansion coefficient; ν, Poisson's ratio.

Similarly, Mukherjee et al. developed a thermal strain parameter during AM [41]:

$$\text{Thermal Strain Parameter, } \varepsilon^* = \frac{\beta \Delta T}{EI} \frac{t}{F\sqrt{\rho}} H^{3/2}$$

where β is the volumetric thermal expansion coefficient; ΔT is the cooling temperature range (peak to surroundings); I, the second moment of inertia; t, the interaction time; F, the Fourier number; ρ, the density and H the heat input per unit length ($\frac{Absorptivity \times Power}{Velocity}$) [41]. This coefficient is dependent on both materials properties and the processing conditions, so may be more useful for minimising strain within an alloy (by varying processing conditions) than for alloy development.

Strain-age cracking can be related to the γ' content, the composition of which is known; so γ' volume fraction can be estimated. Al and Ti are the main γ' formers, with Nb and Ta also contributing [62,183], various equations exist to calculate a susceptibility to strain-age cracking from the alloy composition (Section 5.2.4) [56,221]. Increased carbide content can increase propensity of liquation cracking [64,221], so susceptibilities can also be calculated based on the compositions of the alloys.

PHACOMP (PHAse COMPutation) is a process which was developed in the 1960's to predict the phases formed in Nickel superalloys. By assuming that any carbon will be eaten up by carbide formers and that Al and Ti will be taken up in γ' precipitates, the composition of the final γ matrix can be approximated [222]. From this, using the electron vacancy numbers of each element, the susceptibility to form TCP phases (σ, Laves etc.) can be calculated [223]. It was originally proposed that a total electron vacancy number over 240 would suggest presence of TCP phases. Other systems were used to estimate similar properties e.g. SigmaSafe [224], however PHACOMP prevailed and is used in the aerospace industry to check that alloys are within specification [225].

The presence of TCP phases has been reported to be undesirable for both hot tearing [226] and liquation cracking [227]. By setting an arbitrary PHACOMP threshold, existing alloys were modified to improve their final mechanical properties [228,229].

Mondal et al. created a crack susceptibility index for Aluminium alloys, this considered factors such as cooling rate, crack susceptibility coefficient and the stress across the mushy zone [230]. Their final index is created by calculating the contribution of various factors using a machine learning regression. The cooling rates and solidification gradients were calculated using heat transfer models, for set processing parameters [230]. The resulting crack susceptibility index is shown to accurately predict cracking for the tested alloys, but this is not easily transferrable to new alloys and is computationally expensive.

There are some interesting interplays, so finding an optimal composition is not easy; if the amount of γ" is increased, this reduces the susceptibility to strain-age cracking, but increases the likelihood of hot tearing and liquation cracking [192]. For EB-PBF, alloy compositions have been altered to allow better control of the columnar to equiaxed transition. This was successful, but only for a certain geometry and only in the EB-PBF process [231]

Two further publications have investigated the design of new alloys, specifically for AM; these are Tang et al. (OxMet, now owned by Alloyed) [56] and Conduit et al [185]. Both of these used complex computational methods to calculate properties of large numbers of alloy compositions. As well as printability factors, mechanical properties, cost and weight had to be considered.

Tang et al. designed a medium γ' alloy to be compared with CM247LC and Inconel 939, to be tested using L-PBF [56]. Freezing range was said to be a simple indicator of hot tearing, with the Kou

cracking susceptibility (Section 5.2.1) [207] selected ahead of the RDG model. However, the Kou methodology was used over a range of regions, including $0.01 < f_L < 0.10$, compared to that used by Kou of $0.06 < f_L < 0.13$ [56,207]. Additionally, both creep life and strain-age cracking scale with γ' content; this provides an interesting compromise, as creep life must be maximised whilst avoiding cracking.

Conduit et al. considered similar criteria for their alloy selection, but were designing an alloy specifically for L-PBF (confusingly termed DLD in their paper) [185]. They used previously known materials parameters and created a neural-network to extrapolate factors such as 'processability' between them – but no details of the processability scale were given. Further, many CALPHAD (CALculation of PHAse Diagrams) calculations were performed using Thermo-Calc [232], to estimate both the γ' content and the overall phase stability. Their final alloy was gas atomised [185] and tested in AM, resulting in the required properties. However, the alloy was stated and given a 30% chance of fulfilling the requirements, so alloy development clearly still experiences high uncertainty.

In this chapter, we explore the various measures of crack susceptibility and printability - is it possible to predict which compositions are likely to experience which forms of failure? This is explored with regards to both L-PBF and L-DED, using Thermo-Calc Scheil Solidification Simulations to investigate the differences in behaviour between the processes.

5.2. Methods

5.2.1. Thermo-Calc

Thermo-Calc 2021b was used to perform classic Scheil solidification simulations of the 21 alloy compositions listed in Table 5-1, from their melting points to 99.5% solid (500 iteration limit) [232]. Thermo-Calc has recently added ability to perform the Scheil solidification simulations taking into account either back diffusion or solute trapping. Solidification with back diffusion allows for diffusion in the primary solid phase and requires a cooling rate to be input. Solidification with solute trapping allows for one phase to form dendrites in which solute trapping can occur due to high solidification speeds (which must be input). Laser scanning velocities were used as the solidification speeds [41]. TCNI8 and MOBNI4 databases were used for thermodynamic properties and element mobility's (for back diffusion) respectively.

For L-DED, a cooling rate of $5x10^3$ K/s was used and a scanning speed of 0.04 m/s (2400 mm/min). For L-PBF, a cooling rate of $1x10^6$ K/s was used with a scanning speed of 1 m/s. Further Scheil calculations were performed for the first 9 alloys in Table 5-1 (the first 6 being commonly used in AM as reviewed by Clare et al. [12], the last 3 being alloys specifically designed for AM [56,185]); for each of these, both back diffusion and solute trapping calculations were performed using both L-DED and L-PBF conditions.

From the solidification curves, several values were extracted and calculated:

- Liquidus temperature (used for viscosity calculations)
- Freezing range ($0.01 < f_L < 0.99$ used)
- Crack Susceptibility Coefficient, calculating the ratio of the vulnerable time ($0.01 < f_L < 0.1$) to the relaxation time ($0.1 < f_L < 0.6$) [202], assuming a constant cooling rate, so times can be replaced with temperature ranges
- Kou Cracking Susceptibility [207], $|dT/d(f_L^{1/2})|$ for the range $0.06 < f_L < 0.13$

Finally, equilibrium compositions were calculated at 700 °C, to estimate the expected γ' volume fraction.

5.2.2. **Viscosity**

For each alloy, a viscosity was calculated at the liquidus temperature (as calculated by Thermo-Calc); this was done by combining viscosities of various binary Nickel alloys as published by Sato [233]. Since the critical strain during solidification is inversely proportional to viscosity (RDG model) [203], a high viscosity is expected to be indicative of hot cracking susceptibility. Formulas for A and B coefficients for key elements were given in the paper, but with errors in notation, the following are the determined to be the correct equations:

$$\log \mu_{alloy} = \Sigma C_i A_i + (\Sigma C_i B_i) \frac{1}{T_l}$$

$A_{Co} = -0.607 - 0.06\ C_{Co}$ $\quad$ $B_{Co} = 2.20 - 0.20\ C_{Co}$

$A_{Cr} = -0.616 - 0.44\ C_{Cr}$ $\quad$ $B_{Cr} = 2.23 - 0.55\ C_{Cr}$

$A_{Al} = -0.609 - 0.11\ C_{Al}$ $\quad$ $B_{Al} = 2.22 - 0.75\ C_{Al}$

$A_{W} = -0.583 - 2.28\ C_{W}$ $\quad$ $B_{W} = 2.17 - 7.00\ C_{W}$

$A_{Ta} = -0.598 - 3.04\ C_{Ta}$ $\quad$ $B_{Ta} = 2.17 - 8.98\ C_{Ta}$

where T_l is the liquidus temperature (K) and C_i is the atomic fraction of the element when excluding Nickel, $C_i = C_i / (1 - C_{Ni})$ [233]. Where there were elements present which were not in this list, coefficients of the element with the nearest melting point were used [233]. The following coefficients were used for the following elements. Co parameters for Co, Ti, Fe, Cu. Cr parameters for Cr, Hf, V, B, Zr. Al parameters for Al only. W parameters for Wand C. Ta parameters for Ta and Mo.

5.2.3. **PHACOMP**

TCP phases are avoided where possible in Nickel superalloys, particular the σ phase; PHACOMP was developed by General Electric in 1966 to avoid these [62]. Using atomic compositions, the carbon is allocated to form MC and $M_{23}C_6$ equally, the boron to form M_3B_2 and γ' to form (Ni_3M). The remaining elements form the atomic composition of the final γ matrix, so this can be used to calculate an average electron vacancy number.

$$N_v^{ave} = \sum_{i=1}^{n} C_i (N_v)_i$$

Where N_v^{ave} is the average electron vacancy number, C_i is the atomic fraction of the element in the γ matrix, n is the number of elements present and N_v is the electron vacancy number of the specific element. Step by step instructions for this calculation and the elemental electron vacancy numbers are given in the SAE AS5491 standard [225].

In 1984, Morinaga et al developed a new alternative, imaginatively named "New PHACOMP" [234]. A similar process was followed, but using metal d-levels (M_d), which correlate with electronegativity and are listed in the original paper [234]. This was performed on the measured γ composition.

$$M_d^{ave} = \sum_{i=1}^{n} X_i (M_d)_i$$

In the phase allocations performed for PHACOMP [225], solutes are fully formed with no solutes remaining in the γ matrix; since this is unlikely to occur in reality, New PHACOMP was calculated using both the initial composition of the alloy and the γ composition as calculated once all other phases were formed. In reality, the composition is expected to be between these.

5.2.4. Other Cracking Factors

3 other simple calculations were performed, based on the compositions of the alloys by weight. The first two estimate the relative γ' prevalence, as a higher fraction of precipitate would reduce ductility and promote strain-age cracking. The third estimates the carbide prevalence, as more carbides could lead to increased liquation cracking.

1. $M_{Al} + 0.84M_{Ti}$ [221]
2. $M_{Al} + 0.5M_{Ti} + 0.36M_{Nb} + 0.15M_{Ta}$ [56]
3. $0.28M_{Cr} + 0.043M_{Co}$ [194,221]

Where M_i is the weight fraction of the element

Figure 5-6 shows comparison between calculation 2 (above) and the Thermo-Calc prediction of equilibrium γ' composition (at 700 °C). There is a strong positive correlation ($R^2 = 0.95$); the calculation using the alloy composition is much simpler, so this will be used going forward.

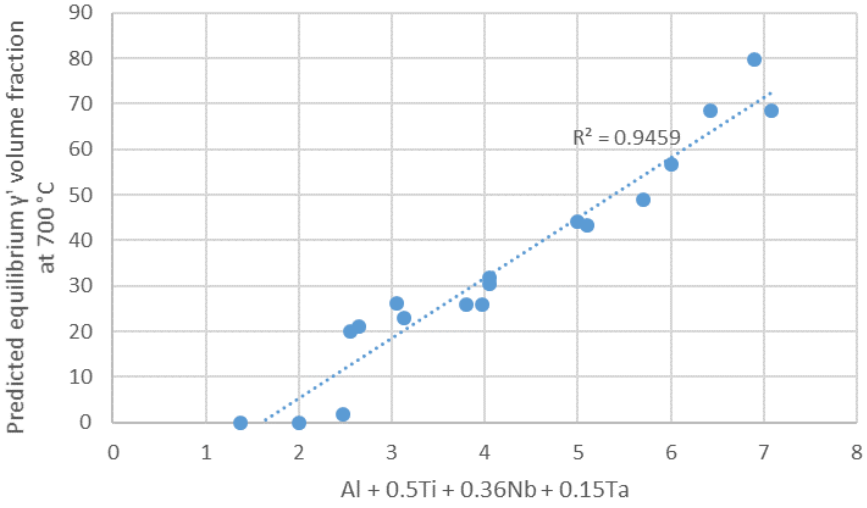

Figure 5-6: Comparison of two calculations for γ', a simple compositional analysis (reported by Tang et al [56]) against the equilibriums volume fraction predicted by Thermo-Calc

5.2.5. **Combination of Cracking Susceptibilities**

The following 10 susceptibilities have been categories into four failure modes (FM) as described above.

1. FM1: Hot tearing
    a. HT1: Crack Susceptibility Coefficient
    b. HT2: Freezing Range (K)
    c. HT3: Kou Cracking Susceptibility (K)
    d. HT4: Viscosity (mPa·s)
2. FM2: TCP Phases
    a. TCP1: PHACOMP on γ composition
    b. TCP2: New PHACOMP on γ composition
    c. TCP3: New PHACOMP on initial composition
3. FM3: Strain-age cracking
    a. SAC1: $M_{Al} + 0.84M_{Ti}$
    b. SAC2: $M_{Al} + 0.5M_{Ti} + 0.36M_{Nb} + 0.15M_{Ta}$
4. FM4: Liquation cracking
    a. LC1: $0.28M_{Cr} + 0.043M_{Co}$

Each of these 10 individual susceptibilities was normalised between 0-1, with 0 being least susceptible, 1 being most susceptible. Viscosity was the only factor which was inversely proportional, the rest were proportional. For each failure mode, a root mean square was calculated from the individual susceptibilities, this gives each alloy a single score for each failure mode – again ranging between 0-1.

These 4 failure modes were combined using root mean square, resulting in a single overall failure susceptibility score for each alloy.

5.3. Results

5.3.1. Cracking Susceptibilities

The 10 susceptibilities were calculated for each alloy, described in Section 5.1.7 and are summarised in Table A-1. These susceptibilities were then normalised between 0 and 1, with 1 being the most susceptible to failure. For viscosity (HT4), the lowest viscosity can be related to the largest hot tearing susceptibility, so this was normalised with the highest viscosity being 0 and the lowest being 1. The rest of the susceptibilities were already ranked with the highest value being most susceptible. The normalised susceptibilities are shown in Table A-2.

As explained in Section 5.2.5, for each failure mode, the susceptibilities were combined by calculating the root mean square. This gave a susceptibility for each of the four failure modes; these values were combined by calculating the root mean square to give an overall susceptibility (Table 5-2). The overall susceptibilities are plotted in Figure 5-7 for the 9 selected alloys.

It can be seen that Inconel 718 and Inconel 625 both have low overall susceptibilities, which corresponds with the literature. Hastelloy X is expected to be fairly printable, but exhibits a high overall susceptibility. CM247LC, CMSX-4 and Waspaloy are all expected to be difficult to print as reflected by the high overall susceptibility. Finally, the 3 designed alloys all have fairly high susceptibilities, with AlloyDLD being the lowest.

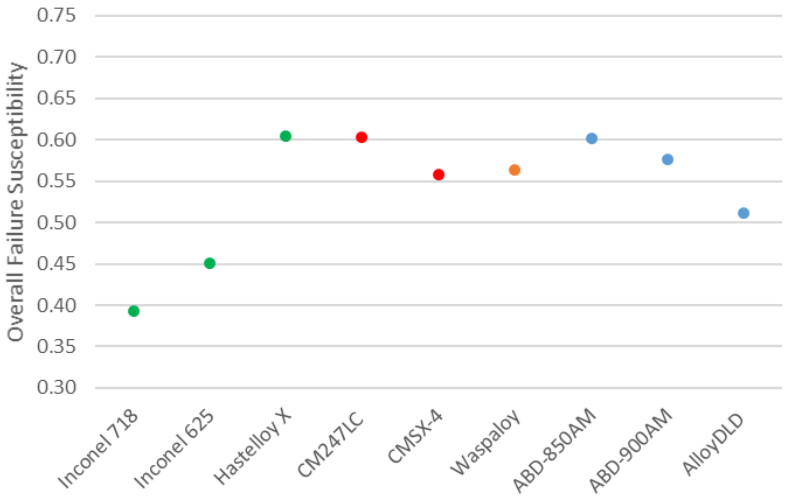

Figure 5-7: Overall failure susceptibilities of the main alloys being analysed. Colour coding continued from weldability plots in Figure 5-2; 3 new alloys have no printability attributed to them, so are coloured blue

Table 5-2: Normalised susceptibilities for the 4 failure modes for each of the 21 alloys and the overall failure susceptibility for each alloy

Alloy	FM1	FM2	FM3	FM4		Overall Susceptibility
Inconel 718	0.24	0.35	0.16	0.64		0.39
Inconel 625	0.38	0.23	0.00	0.78		0.45
Hastelloy X	0.28	0.82	0.19	0.82		0.60
CM247LC	0.65	0.52	0.87	0.09		0.60
CMSX-4	0.45	0.38	0.95	0.00		0.56
Waspaloy	0.59	0.34	0.43	0.79		0.56
ABD-850AM	0.83	0.22	0.33	0.77		0.60
ABD-900AM	0.62	0.44	0.51	0.70		0.58
AlloyDLD	0.59	0.30	0.40	0.67		0.51
Rene41	0.29	0.65	0.44	0.73		0.56
In738	0.73	0.56	0.81	0.54		0.67
In713LC	0.49	0.49	0.94	0.24		0.59
Udimet700	0.48	0.90	0.91	0.57		0.74
RR1000	0.72	0.76	0.75	0.57		0.70
Inconel939	0.58	0.65	0.58	1.00		0.72
Haynes282	0.45	0.45	0.33	0.78		0.53
Udimet720	0.34	0.84	0.80	0.70		0.70
718+	0.20	0.54	0.42	0.72		0.50

5.3.2. Thermo-Calc Scheil Calculations

Thermo-Calc recently added functionality for more specific Scheil calculations for different non-equilibrium scenarios. To analyse the effect of these on the various susceptibility coefficients, Scheil calculations were performed on 9 alloys with 5 different conditions. These were the classic calculation (no solid diffusion); back diffusion (BD) in the primary solid phase allowed (this was done using both L-PBF and L-DED cooling rates); and solute trapping (ST) in the primary solid phase (done using both L-PBF and L-DED scanning velocities).

To see how the susceptibilities change between different conditions, each of the three outputs of the Thermo-Calc calculations (HT1, HT2, HT3) as shown in Figure 5-8. The freezing range (Figure 5-8a) of the ST PBF is noticeably lower than the other calculations, the BD DED is also slightly lower – the rest of the calculations give similar results. The CSC (Figure 5-8b) results are more variable. ST PBF is the most variable, with the others closely aligned to the classic results with some

anomalies. Similar was seen in the Kou cracking susceptibilities (Figure 5-8c), with ST PBF being noticeably lower throughout but no other clear trends visible.

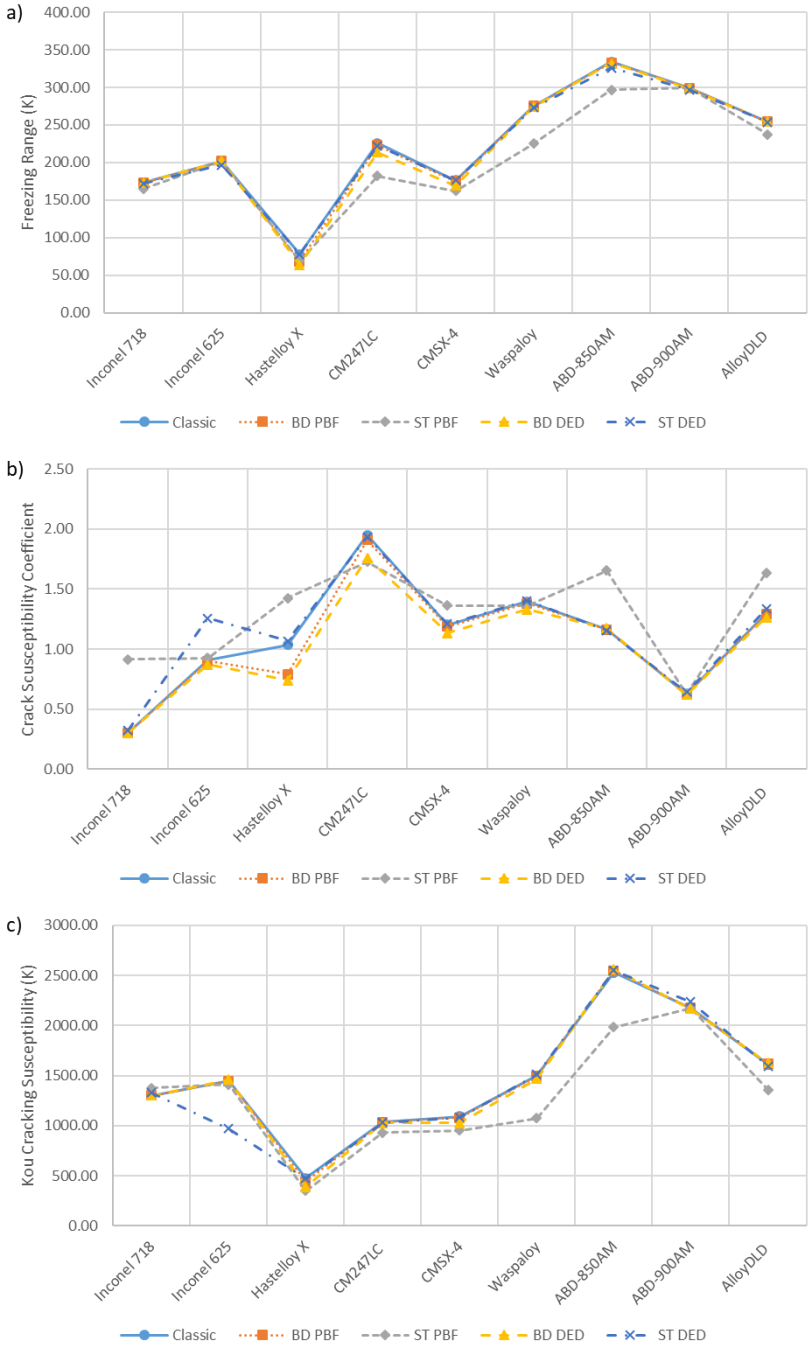

Figure 5-8: Comparison of 5 different Thermo-Calc Scheil calculations for 9 alloys; a) Freezing Range b) Crack Susceptibility Coefficient, c) Kou Cracking Susceptibility

To quantify this, for each alloy, the percentage difference between the condition and the classic Scheil was calculated (as a decimal), these are summarised in Table A-3. For example, if solute trapping was consistently different to the classic Scheil, we could deduct that Thermo-Cal predicts solute trapping to be significant under these conditions. An average of these deviations (absolute values) for each condition across all 9 alloys was taken (Table 5-3). ST PBF had the largest average deviation value for each output, as seen in Figure 5-8. These deviations were averaged over all 3 outputs; the ranking being ST PBF, BD DED, ST DED and finally BD PBF. This suggests that

Thermo-Calc expects solute trapping to be significant in L-PBF and that in L-DED, back diffusion is more significant than solute trapping.

Table 5-3: Average variation between various Scheil calculations when compared to the classic calculation; percentages reported as decimals

	Average of Absolute Percentage Differences from classic Scheil			
Calculation	**Freezing Range**	**Crack Susceptibility Coefficient**	**Kou Cracking Susceptibility**	**Overall Average**
BD PBF	0.016	0.032	0.012	0.020
ST PBF	0.088	0.375	0.137	0.200
BD DED	0.031	0.064	0.036	0.044
ST DED	0.010	0.063	0.048	0.040

5.4. Discussion

In this work, no new calculations were introduced, instead, we've looked at the various causes of defects and cracks and quantified them using as simple a method as possible. Wei et al. define printability as "relative susceptibilities to common printing defects" [227]. Here we focus solely on printability, ignoring the materials properties (which must be sufficient for aerospace accreditation), cost and density, which previous works include [56,185]. These previous attempts use complex, computationally intensive methods (e.g. neural networks) to extrapolate between known compositions. This complexity stops the method from being easily available to the wider research community.

The new calculations developed use previously published equations, mainly based upon the alloy compositions. Some CALPHAD modelling is required, using Thermo-Cal, but this was also used by previous methodologies and is fairly widely available and has an intuitive graphical user interface. The 6 alloys from Table 2-3 are roughly in printability order; Inconel 718 and Inconel 625 are both widely reported as being printable with good properties in L-PBF, EB-PBF and L-DED. Hastelloy X has been widely printed using L-PBF, somewhat printed in L-DED and not reported in EB-PBF – this doesn't necessarily mean that it's not printable in EB-PBF, it could just not be industrially relevant and so not attempted. In an ideal situation, only alloys which have been widely reported would be considered in this sort of analysis. Unfortunately, insufficient alloys have been widely printed, so this is not possible, so less-reported alloys must be included.

The equilibrium γ' content of each alloy (as calculated using Thermo-Calc) is a proxy of strain-age cracking, and the crack susceptibility coefficient is a measure of hot tearing. Both of these were calculated using Thermo-Calc and are shown in Figure 5-9. Effectively, this is an extension to the plots seen in Figure 5-2, as widely reported in literature [65,193,221]; alloys appear to cluster by their weldability/printability. Both axes use results calculated by Thermo-Calc for direct comparison, but the γ' fraction calculated using Thermo-Calc has been shown to be strongly correlated with that using the alloy composition (Figure 5-6).

CM247LC and CMSX-4 are both single crystal alloys [183], they've not been printed with much success in L-PBF, due to liquation cracking, strain-age cracking and hot tearing (different

mechanisms under different conditions) [64] and have not attempted in L-DED. AM of Waspaloy has been attempted in L-PBF and L-DED and seems to have been built successfully with each, but with minimal research interest, so few further publications are available.

The overall failure susceptibilities (Figure 5-7) should inversely correlate with printability. The lowest failure susceptibilities are for Inconel 718 and Inconel 625 which lines up with them being the most printable alloys, as implied by the fact that they're widely reported in literature. Waspaloy seems to be relatively printable, but with minimal literature published, potentially due to a lack of commercial interest. This has a much higher overall failure susceptibility, but lower than that of CM247LC and Hastelloy X.

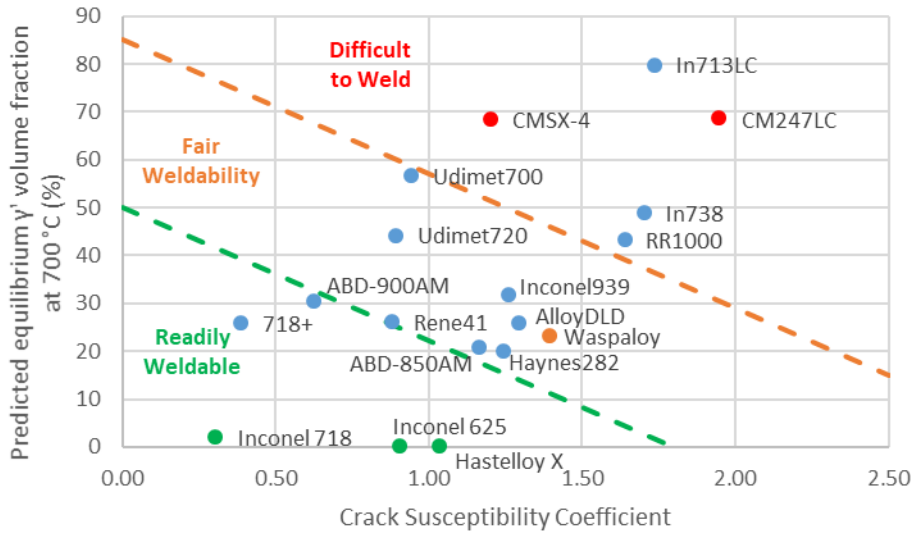

Figure 5-9: Plot showing the relationship between γ' content and the crack susceptibility coefficient, both calculated using Thermo-Calc

CM247LC and CMSX-4 are both notoriously hard to print, but are of great industrial relevance due to their use in single crystal turbine blades. This disproportionate research interest may make these alloys seem more printable than they are; the overall failure susceptibility of CM247LC is very high as expected, but that of CMSX-4 is lower – it has a very high susceptibility to strain-age cracking, but this is lost in the overall susceptibility due to the relatively low susceptibilities to the other 3 failure modes.

Finally, Hastelloy X is relatively printable according to literature, but scores very highly on the overall failure susceptibility. This is due to having two failure modes of susceptibilities around 0.8 – these are high enough to bring its' overall susceptibility to above that of CMSX-4.

Clearly the combination of the overall failure susceptibility from the four failure modes isn't perfect, but overall the correct trend is seen. It's impossible to quantify the printability of an alloy – especially due to the fact that some alloys may be more printable in one process than another e.g. printable using EB-PBF, but not using L-PBF. Attempts of quantifying printability have resulted in a stress performance index [219] and a thermal strain parameter [41], both of which require materials properties, which can't be accurately obtained before the material exists. Additionally, the latter uses the processing parameters as inputs, so is looking at the likelihood of a build failing rather than the overall printability of an alloy.

The inherent complexity of AM makes this all the more difficult. Not only is there variation within a component, with heat often accumulating with build height, heat can also accumulate within a layer

due to short return times. Calculating a thermal strain parameter for a specific material and set processing parameters would give a single value, but this would vary with geometry, so ideally, a geometric factor would also be needed. Finally, even if it were possible to integrate geometry, the cooling rate and solidification velocity vary within the melt pool. So even if the centre of the melt pool was resistant to a certain form of failure, the edge of the melt pool could experience conditions which could cause cracking. Due to this complexity, printability values should be taken as qualitative values to compare relative crack susceptibility – in an attempt to generally minimise propensity of cracking.

Most alloy compositions are given as an allowable range e.g. [188], but all calculations above are performed on a specific composition. This naturally introduces error into the calculations, as some elements have a 4 wt.% allowable range. The difference is likely to be larger in the Thermo-Calc calculations, as the final solidification path is very sensitive to composition. PHACOMP is calculated on the calculated final γ composition, where all other phases are assumed to have fully precipitated (γ' and carbides) [62,225]. Due to the rapid solidification experienced in AM, precipitation is limited due to the reduced time for diffusion. The composition of the actual γ phase is expected to be between the original alloy composition and that calculated for PHACOMP. Since the cooling rate in the L-PBF process is higher than in L-DED, less segregation is expected, so the γ composition is likely to be closer to that of the powder than during L-DED.

Combination of susceptibilities was done using the root mean square, this was chosen as a way of maintaining the normalised nature of results whilst giving the larger susceptibilities a heavier weighting. This means that four scores of 0.25 would rank lower than a 1 and three scores of 0; if we summed the susceptibilities, these would be equal. Despite the imperfect results, the general trend from literature is followed. Each susceptibility within a failure mode is weighted equally, we do not know the accuracy of these susceptibilities, so it is assumed that combining them all will help remove any anomalous results. The susceptibilities of the four failure modes are also weighted equally, as they are combined using a root mean square. Some failure modes are likely more prevalent than others, but since a single alloy can experience different failure modes under different conditions, it was decided to include all of the failure modes.

The different calculations used for hot tearing are compared in Figure 5-10. A strong positive correlation is shown between the Clyne Davies and RDG models (Figure 5-10a). It is interesting to note the outliers, two of which are new "Alloys-by-design" [56] and so are novel compositions which the hot tearing models may not be suited to. The other outliers are CM247LC and Inconel 713, both of which are notoriously susceptible to hot tearing, which suggests that the Clyne Davies model may be better at predicting Nickel superalloy hot tearing susceptibility. It is reassuring the see that simple models seem to be able to equal the performance of more complex ones. Figure 5-10b shows the positive correlation between freezing range and the Kou susceptibility [207], this shows a weaker correlation that Figure 5-10a, but a trend is still obvious. There are some unexpected results e.g. CMSX-4 and CM247LC both showing relatively low susceptibilities. However, the freezing range has widely been used as a proxy to hot tearing susceptibility; the accuracy of this is questionable.

Figure 5-10c shows the Kou susceptibility against the RDG model, one from each of the previous plots. There is a weaker positive correlation between these ($R^2 = 0.27$). However, the general trend still remains; since we do not have accurate experimental results to compare hot tearing susceptibility to, all 4 measures are calculated. Since a root mean squared of these is taken, if an alloy has a high susceptibility according to one measure, this should be carried into the overall normalised hot tearing susceptibility.

An argument could be made that FM2 (TCP phases) should be removed, as this results in poor mechanical properties rather than process failure. An adjusted failure susceptibility has been plotted in Figure 5-11, excluding FM2. This drops the susceptibility of Hastelloy X to a similar level to Inconel 625, which corresponds to reports from literature, CM247LC and CMSX-4 both remain high as expected. Waspaloy still has a high score, due to being fairly susceptible to two failure modes as explained previously.

For some of the susceptibility parameters, there are arbitrary thresholds given in literature. E.g. Morinaga et al. observe that alloys which are σ-prone tend to have M_d values above 0.915 [234]. An approach of blindly discarding any alloys above this threshold could be taken, but this seems to be an observation without any scientific reasoning. Instead, 21 alloys were selected, to cover as wide a range of compositions as possible. The idea is that this results in a more accurate susceptibility score. If we only analysed the first 6 alloys, they could all have similar scores on one susceptibility, so the highest would be given a large normalised susceptibility – whereas when looking in a more global perspective, they could all be of low susceptibility.

The crack susceptibility calculations are purposefully simple and require minimal computational intensity. The results are comparable with those in literature and appear to adequately reflect printability rankings. There is a large amount of uncertainty in the process; the composition of the alloy could be variable, the thermal conditions vary within the melt pool and across the component. These uncertainties limit the overall accuracy of the model, but should still allow a rough ranking of alloy printability. Realistically, so little is known about the actual printability of alloys, that this becomes the limiting factor. Various printability factors can be calculated, but there is no standardised method for measuring printability and very few alloys have had significant AM work performed on them. There needs to be a defined measure of printability to compare crack susceptibilities to before the efficacy of crack susceptibilities can be thoroughly assessed.

Hot tearing susceptibilities (FM1) were mainly calculated based on Thermo-Calc Scheil calculations. As explained in Section 5.2.1, as well as a classic Scheil calculation, the Scheil calculator has options to include either back diffusion in the solid, or solute trapping in the primary phase [232]. These are new additions to the software and so have had minimal testing, their reliability is unknown. However, it is interesting to see what behaviour they predict and how they'd expect this to vary between L-PBF and L-DED. Overall (Table 5-3), the deviation of the new models from the classic Scheil calculation are relatively small, once again, the simplest calculation providing sufficient accuracy for most purposes.

As shown in Table 5-3, the solute trapping L-PBF (ST PBF) calculation is the most different to the classic Scheil calculation. In Section 2.1.3, we expected L-PBF to experience rapid solidification (non-equilibrium composition) and to be on the cusp of solute trapping. L-DED is an order of magnitude slower so is on the cusp of rapid solidification. Since the ST PBF results are different to the classic Scheil, it can be deduced that solute trapping is predicted to occur at these solidification velocities. The change from classic Scheil to ST DED is much smaller, so solute trapping is unlikely to occur in DED, as predicted by literature.

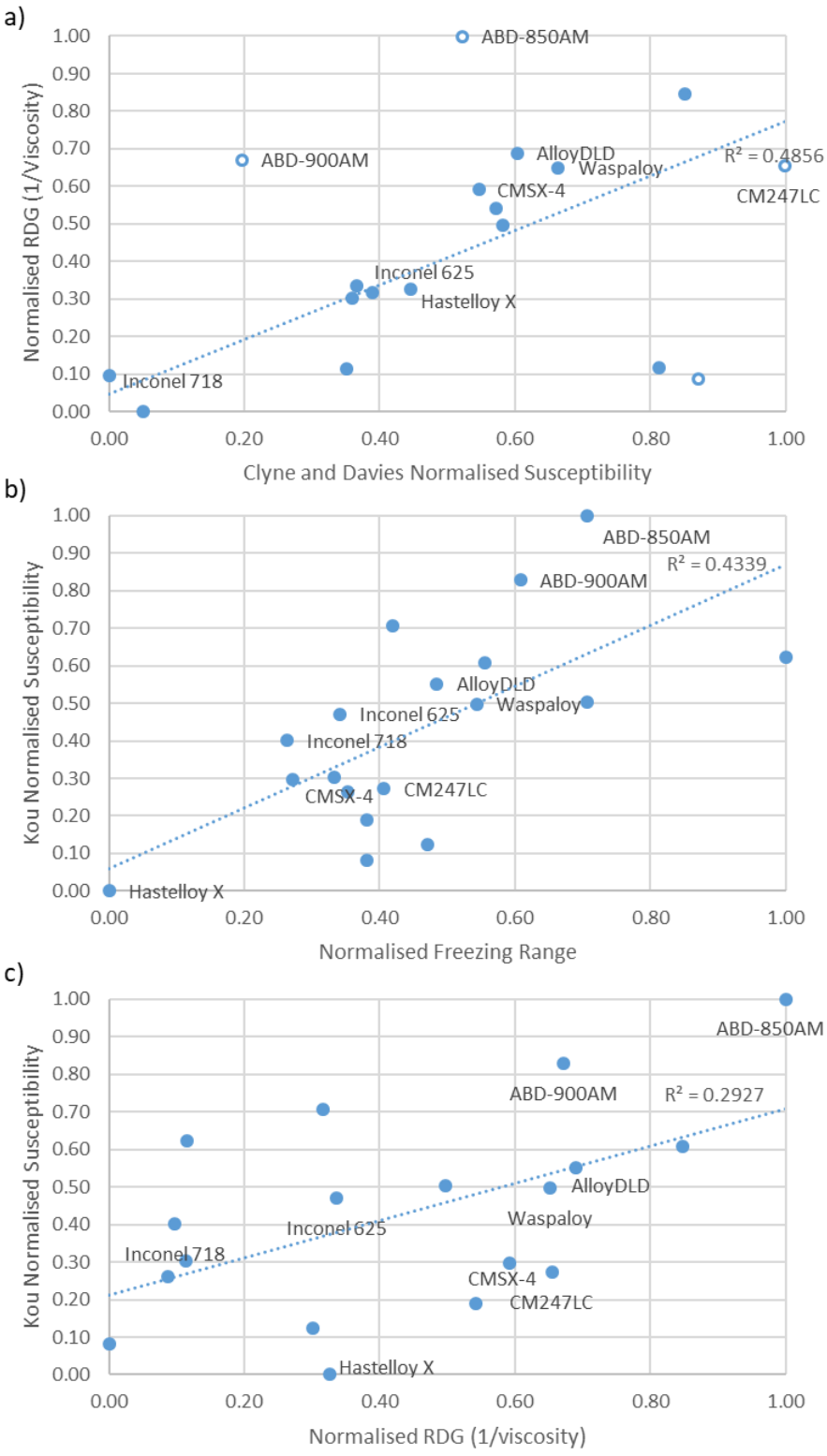

Figure 5-10: Comparison between various hot tearing susceptibilities. a) Clyne and Davies vs RDG, b) Freezing Range vs Kou, c) RDG vs Kou. Anomalous points unfilled

Back diffusion (in the solid) has a larger difference with L-DED cooling rates than with L-PBF. This can be understood when considering the time for diffusion; the quicker cooling rates in L-PBF leads to reduced time at temperature and so less diffusion. The ST PBF calculation leads to a smaller freezing range (Figure 5-8a), this means that the solidification will occur more quickly and will lead

to less segregation. This logically makes sense at the solute trapping will lock atoms in place and reduce compositional variation. On the other hand, back diffusion is expected to occur in the solid in L-DED, diffusion acts to reduce the concentration gradient, so increased back diffusion will lead to less compositional variation. Reduced segregation is expected to reduce freezing range and so reduce susceptibility to hot tearing (Section 5.1.5) – both L-PBF and L-DED have reasons for reduced segregation, so it's difficult to say that one process is likely to be less susceptible to hot tearing than the other.

L-DED is typically a hotter process, with larger and more powerful lasers than L-PBF, this typically results in the components experiencing the high temperatures for longer during the hatching. However, in L-PBF, there are more subsequent hatches in the vicinity, so the effect of reheating may be more significant. An increased time at temperature could increase precipitation and carbide formation, increasing susceptibility of both liquation cracking and strain-age cracking. From Table 2-3, it seems like some materials are more easily printable using L-PBF whilst others are easier using L-DED.

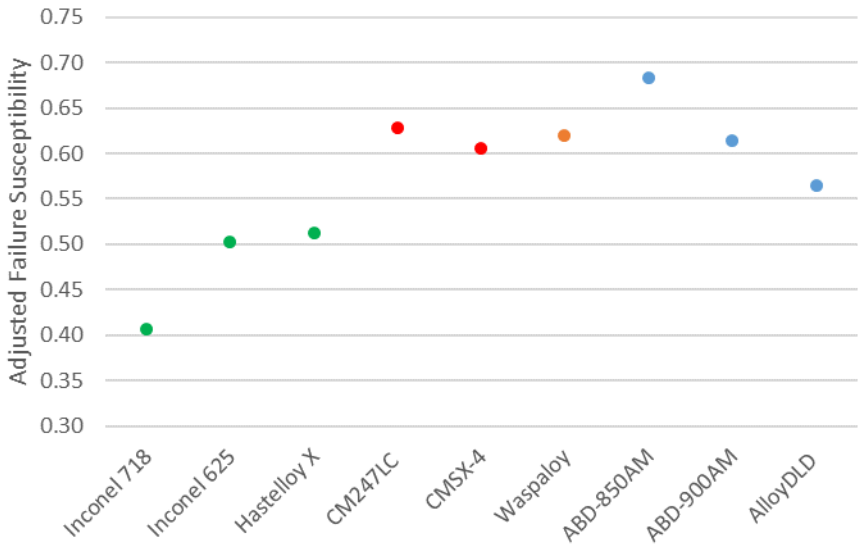

Figure 5-11: An adjusted failure susceptibility of the main alloys being analysed; excluding FM2

Unfortunately, all printability assessments are skewed by research interest, if an alloy is a C (Not Printable; Minimally Reported in Table 2-3), this could either mean that it suffers from failure during manufacture or that it's not industrially relevant, so no prolonged research attempts have been made. The ABD-900AM brochure [53] claims that it is designed to be free of solidification, strain-age and liquation cracks, the calculations above result in susceptibilities $\leqslant 0.7$, so we do not expect these to be prominent. The tests conducted on this alloy used L-PBF [53,56], but powder is also advertised for both EB-PBF and L-DED. No tests of this alloy in these processes have been reported, but by designing an alloy of "exceptional printability" [53], it is implied that this would be printable in any process.

Most development work is done using L-PBF due to the size and cost of the machine. Several trials in L-PBF can be run with as little as 5 kg of powder, which is less than that required for L-DED. In addition, the upfront cost of a L-PBF machine is significantly lower than that for a L-DED or an EB-PBF machine. The fact that tests are conducted on L-PBF machines doesn't necessarily mean that they can be manufactured using other processes.

Since L-DED and L-PBF have very different laser spot sizes and cooling rates, solidification conditions are vastly different. Conduit et al. design an alloy specifically for L-PBF [185]. Their processability property was extracted by designing a neural network from 10 known compositions. Since the processability will have been tested using L-PBF, their findings are valid for L-PBF, but they do not claim it is suitable for additive manufacturing as a whole. Alloys should be developed specifically with an application and so a manufacturing process in mind. For example, small components with intricate geometries e.g. GE LEAP fuel nozzle, L-PBF is likely the most appropriate process; for larger scale repair applications e.g. blisk repair, L-DED would be used. Once the process is decided, approximate cooling rates and solidification velocities are known, so an alloy can be better design to suit the application.

In the wider research community, there is a desire to find a magic value which solves the printability issue. Many of these solutions use dimensionless numbers or compositional analyses (e.g. Figure 5-2). Similar attempts have been made to define thresholds for keyholing, lack of fusion and other phenomena. Unfortunately, additive manufacturing is not that simple, magic numbers rarely exist. Even if we were able to calculate an accurate crack susceptibility, this would vary with the process, geometry, powder composition and the location within the melt pool. An alloy with low crack susceptibility could be developed, but due to the processing conditions chosen, the thermal gradient in a certain part of the melt pool could cause a crack to form.

It seems like a single numeric answer cannot solve such a complex problem; instead, an attempt has been made to make a more qualitative metric, one which can predict which alloys are likely to have a higher propensity to cracking. This in itself, is a useful metric to have as it gives alloy designers a starting point and warns as to which failure mechanisms may occur. As more research is conducted on a broader range of compositions, a quantitative printability scale may be developed, allowing for the accuracy of crack susceptibility models to be validated. A standardised printability measure would be needed for this; likely this would consist of either scanning weld tracks or building small, specific geometries and analysing these for cracks.

5.5. Summary

In this chapter, several published failure mode susceptibilities were combined in a simple but comprehensive manner. The final overall failure susceptibility is shown to correlate with the printability of alloys reported in literature. The printability of an alloy is difficult to define as a result of the various processes available and the range of processing conditions possible within each. A lack of successful printing reported in literature could either be due to lack of research (insufficient industrial relevance) or due to a high susceptibility of failure. As such, the proposed failure susceptibility is a good tool to check the expected printability of an alloy, but is unlikely to be instrumental in development of a new alloy.

The proposed method is simpler than currently existing methods, less computationally intensive and requires no prior knowledge of existing materials properties. It's shown that this simpler method provides adequately accurate results, limited by experimental measures of printability rather than the calculations themselves. It is reassuring that both the CSC and the classic Scheil calculation provide equivalent results to more complex calculation, confirming the approach of using the simplest methodology possible.

Both L-PBF and L-DED are shown to promote failure modes such as hot tearing, but with differing amounts of segregation. The current methodology has been to develop alloys using L-PBF, because of the lower cost associated with this. In reality, for a specific component, the most appropriate process must be decided along with required mechanical properties. Once these guidelines are set, an alloy must be tailored to fit within these and this will result in the best alloy for the specific component. Finally, a standardised measure of printability, using small scale tests is needed to quantify printability for each process.

6. Exploring Pyrometry Trends and Defect Locations in L-PBF

6.1. Introduction

One of the most widely researched processes in AM is L-PBF, first launched by EOS in 1991 [235] – the main advantage of L-PBF is the ability to print geometries otherwise unobtainable (e.g. lattices) and hence allowing the redesign of components to reduce weight whilst maintaining performance [236]. In all AM processes, the scan strategy of the heat source has a large effect on the thermal conditions experienced by the material, which in turn causes variation in the final microstructure [54]. A commonly reported scan strategy is a simple bidirectional raster, with the hatching angle rotated by 67° between layers [86,237,238]. If there is an inter-hatch defect, this rotation will stop anomalous features from occurring in the same location in each layer.

Despite the potential for AM to create complex geometries, distortion of components is common, which makes tight tolerances difficult to achieve. Distortion often occurs in the form of swollen edges (elevated by around 100 µm [239,240]), which can collide with the recoating blade, affecting the powder spreading homogeneity and potentially leading to the failure of a build. This edge swelling has been attributed to a mechanism initiated by denudation [122,239,241].

The first hatch in each layer has a fresh coating of powder which results in the formation of a complete melt track. The vapour plume generated as a result of lasing acts to blow powder particles away from the melt track, creating a denuded zone greater than the width of a single track. Some powder is entrained into the melt pool, but a denudation zone is still present [242]. Consequently when the laser returns for the next (parallel) hatch, significantly less powder is available for melting [243]. This causes the first hatch in each layer to be substantially raised above subsequent hatches. Yasa et al. confirmed this to be the occurring mechanism by placing the first hatch centrally and this is where the elevation was found [239].

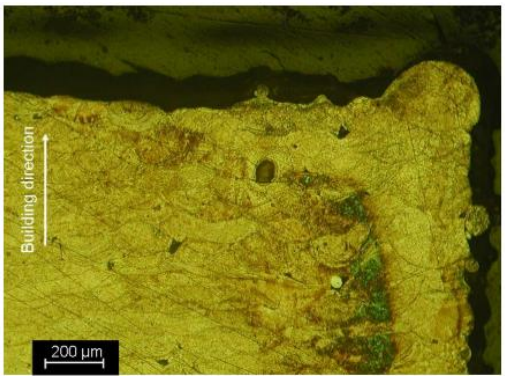

Figure 6-1: Edge swelling of a 316 steel component. Reported by Yasa et al [239]

The first hatch is almost 30 µm taller than subsequent ones as built with 904L stainless steel (Figure 6-2), but the same trend was observed in 316L [243]. In a similar manner, the laser behaviour at the end of a hatch can be altered by using 'skywriting', this allows the laser to overshoot the end of a hatch (turning the laser off at the edge), so there is not a region where the laser speed is changed i.e. deceleration. Implementing skywriting reduces the surface roughness and so can reduce the amount of internal porosity experience [244,245].

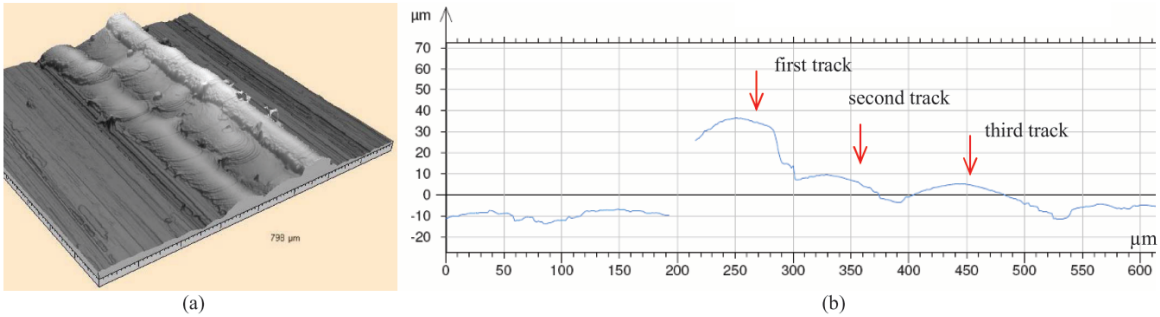

Figure 6-2: First track is found to be significantly larger than subsequent tracks in L-PBF. Reported by Yadroitsev and Smurov [243]

L-PBF staircases can be seen in Figure 6-3a, these are printed using 316L with a hatch rotation of 90°, the first layer being hatched along the x axis [246]. Figure 6-3b shows the height profile of this part; as well as the expected height increase, odd layers have an additional peak at the start of each step. This is attributed to the denudation swelling mechanism as defined above, it is worth noting that there is a large amount of noise in the data, e.g. step 8 shouldn't experience swelling but does and step 11 has no visible swelling, which would be expected.

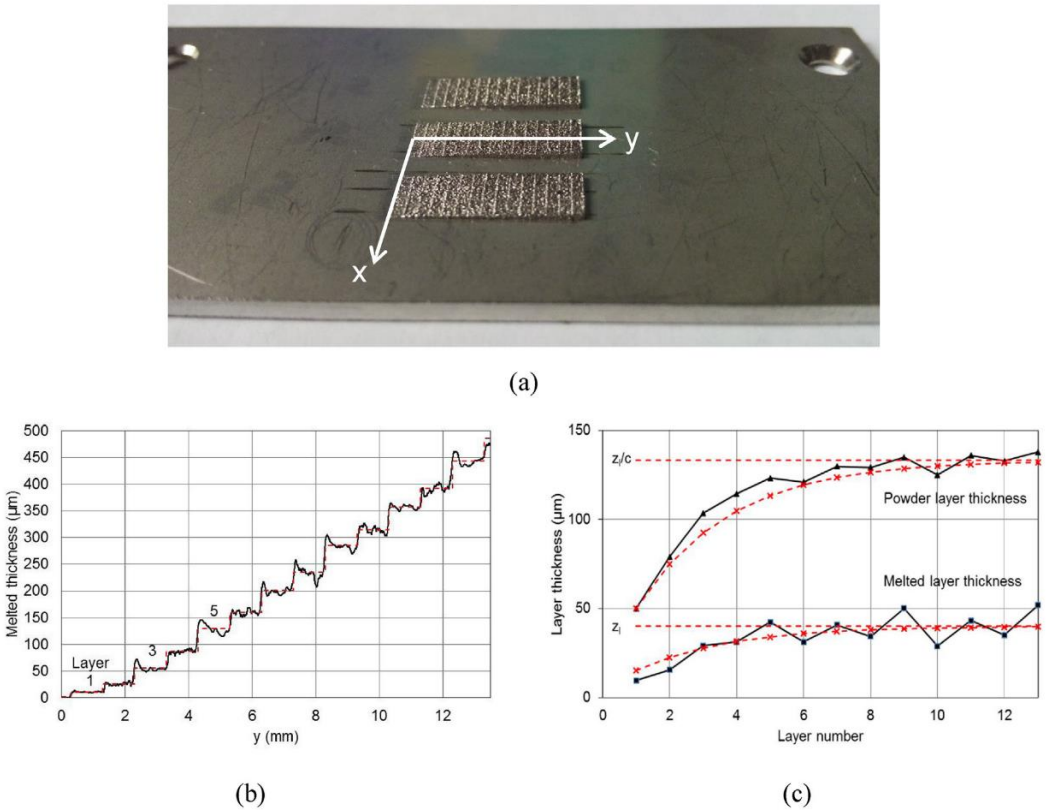

Figure 6-3: Analysis of the first few layers of a L-PBF build. a) Ladders constructed using SLM b) Height profiles showing swelling as a result of denudation c) Thicknesses of printed layers and calculation of powder thicknesses experienced. Reported by Bidare et al [246]

Further, powder has a higher laser absorptivity than consolidated metal in a conduction regime [38]. The first hatch scans a full powder layer, so more laser power will be absorbed than in subsequent hatches, which scan partially denuded regions i.e. the consolidated metal beneath. Since latter hatches absorb less laser power, the melt pool size will be smaller than the first hatch [243]. This further increases the height difference between the first and subsequent hatches. The

combination of the decreased powder availability and the decreased melt pool size will be referred to the denudation mechanism of swelling (summarised in Table 6-1).

Table 6-1: Summary of hypothesised swelling mechanisms

Reference(s)	Hypothesis	Physical Evidence Required
[239,243]	• First hatch causes denudation • Subsequent hatches surrounded by less powder ○ This reduces laser absorptivity • Subsequent hatches absorb less power and have less powder • Subsequent hatches will be smaller than first hatch This is termed the "denudation" mechanism	• First hatch in a layer experiences swelling • Effect would not occur in overhang conditions
[247]	• First hatch surrounded by powder (poor conduction) • First hatch hotter, so larger melt pool and more powder entrained ○ Subsequent hatches surrounded by solid metal, so heat conducted away • First hatch has more powder and so is larger	• First hatch in a layer experiences swelling • Effect would be more pronounced when building in overhang conditions
This Work	• Where the laser stops, solidification can occur very quickly, causing divots • These can combine, leading to raised regions at hatch ends	• Swelling occurs at hatch ends • Swelling would occur without powder present

As demonstrated by Yadroitsev and Smurov [243], when printing a single layer, the first hatch may be 30 μm taller than subsequent hatches. As this occurs on each layer, a swelling of 100 μm has been shown to accumulate [239]. This is greater than a typical top surface roughness (R_a), which is in the range of 5-30 μm [248]. The thicker the powder layer scanned, the more likely balling is to occur, so the swelling of the first hatch could have a more humped morphology [249]. Since this is a feature caused inherently by the scanning of the laser, it cannot be completely removed from the process.

Craeghs et al. attribute the increased elevation of the first hatch to it being surrounded by poorly conducting powder and so a larger melt pool being created [247]. They argue that, when the second hatch is printed a hatch already exists next to it. The new hatch only has powder on one side and the previous hatch on the other side; since the consolidated track has higher conductivity than powder, there is an increased heat flow out of second hatch. The increased heat flow restricts melt pool size, so the first hatch has the largest melt pool.

This idea of reduced thermal conductivity originates from work by Taylor et al. [250]. In the original work the laser scanned powder directly, without a baseplate. With this key difference, the introduction of a previously deposited track would have a much larger effect on heat flow than

adding a single track onto an already large baseplate. It was noted by Craeghs et al. that the first hatch was hotter than the second – this was given as evidence for increased conductivity in the second hatch [247]. The higher temperature is better explained by the increased laser absorption of the full powder layer in the first hatch, as opposed to the denuded surface of subsequent hatches. The authors consider the denudation mechanism to better explain the increased elevation of the first hatch when printing on a baseplate.

Since this swelling depends on denudation, which in turn depends on the vapour plume, the extent of denudation must be parameter dependant. Matthews et al. measured the effect of varying energy density on the width of the denudation zone [242]. Varying the laser power from 50-150 W, the width of the denudation zone increased by 50% from 200 µm, which is of similar magnitude to previous research [74]. Given that the denudation zone widens with energy input [249], the magnitude of denudation swelling must vary depending on the processing parameters.

The surface roughness is further increased by imperfections at hatch ends, such as divots, which are attributed to a high solidification rate [251,252]. These can occur at the start of a melt track, and both length and height can be on the order of 100 µm [253]. Simulations predict the presence of a vapour depression in the melt pool surrounding the laser during L-PBF [254], as confirmed by in-situ X-ray imaging [255]. Once the laser switches off, the molten metal has insufficient time to fill the vapour depression before the melt pool solidifies (~0.2 ms assuming a cooling rate of 10^6 Ks^{-1}), creating a divot. The depth of the vapour depression has been shown to increase linearly with the energy input (Figure 6-4) [255] (and normalised enthalpy, NE [136]) so one would expect the magnitude of the divots to follow the same trend. The bulge around these divots can be up to 150 µm long [254] and 50 µm high [256]. If the laser remains powered when stationary, even for a short duration, the vapour depression has been shown to become unstable and this may create keyhole porosity [255].

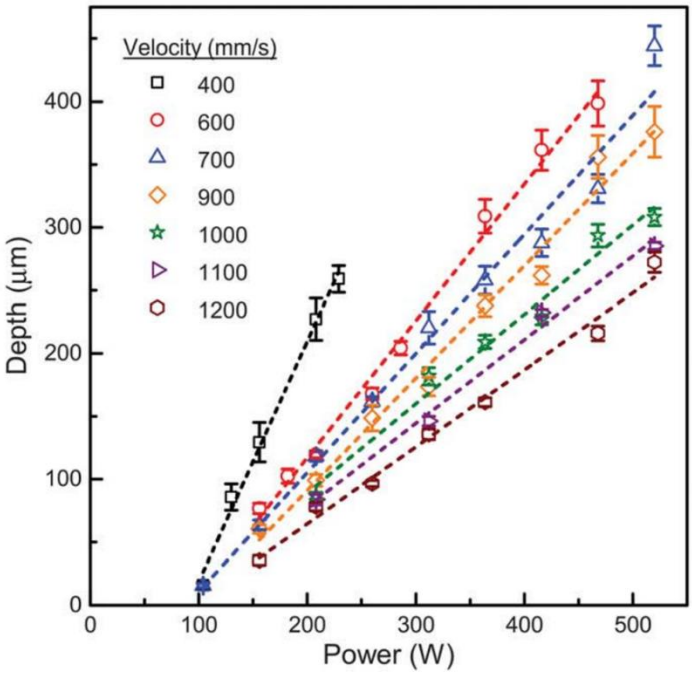

Figure 6-4: Vapour depression depth as a function of laser velocity and power. Reported by Cunningham et al [255]

The laser behaviour at the end of a hatch can be altered by using laser delays [257]. The laser delay synchronises the timings between the laser module and the galvanometer (which controls movement); examples of long and short delays are shown in Figure 6-5a and b respectively. This

can be used to force the laser to turn off before it decelerates to prevent a spike in power density at the start and end of each hatch. This concept has been explored further by ramping the power down near the turnaround point to prevent defects such as keyholes from forming [256].

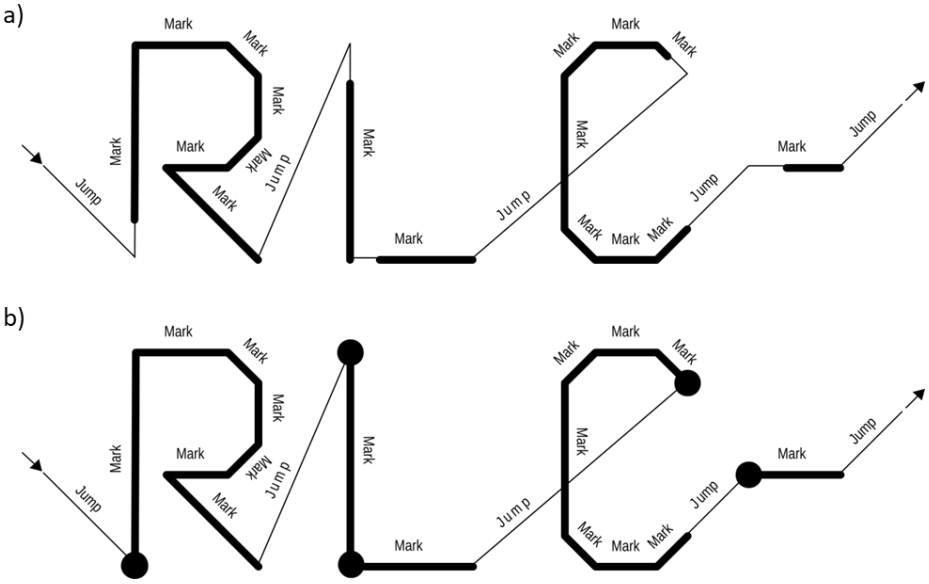

Figure 6-5: Visualisation of laser on delay; a) delay too long, so the start of hatches is missing; b) delay is too short, so laser turns on before movement occurs, causing a hot-spot at the start of every hatch. Reported by Raylase [258]

Bidare et al. observed the denudation mechanism of swelling when printing staircases with a hatch rotation of 90°. The swelling is visible in the form of additional peaks at the start of each odd step [246]. It is worth noting that the height data is noisy; general trends can be seen but quantitative analysis is difficult at this length-scale. The various swelling mechanisms described in literature are summarised in Table 6-1. The staircase geometry allowed for the observation that the first printed layers are thinner than desired [259,260]. Over the first few layers, the powder layer thickness increases, as does the consolidated layer thickness until an equilibrium is reached [246]. The result is that the properties of the first 5-10 layers are different to the bulk.

Monitoring in L-PBF has become more widely used in recent years, with various different aims, as reviewed by Everton et al [11]. Much work uses coaxial or angled cameras to observe the melt pool at a very high framerate (because of the quick nature of the L-PBF process). These allow for values such as melt pool area to be calculated, which Clijsters et al. [244] used to correlate hotspots with porosity in their samples. The technology then developed to using multiple pyrometers of different wavelengths, which removed the need for emissivity measurements and allows for direct temperature measurement [118,261]. Unfortunately, with these sorts of techniques, vast amounts of data must be stored which makes it difficult to process online and use the data to the fullest [11]. This is a much larger issue in L-PBF than in L-DED, as the laser movement speeds in L-PBF are roughly 50x quicker, with cooling rates 10^3x higher.

The alternative to optical measurement is using a spot pyrometer, where a photodiode is used to record a single intensity value per time-step. This has been used to show how trends in temperature vary within a hatch, the effect of hatch spacing [262] and the effect of the layer thickness [263]. These datasets are of a much more manageable size, but still require high recording frequency (e.g. 20 kHz [263]). Thermal datasets can be plotted in the XY plane to show the temperature distribution in the components. This is easily done for pyrometry; Figure 6-6 shows an example of this mapping, done for melt pool area [264].

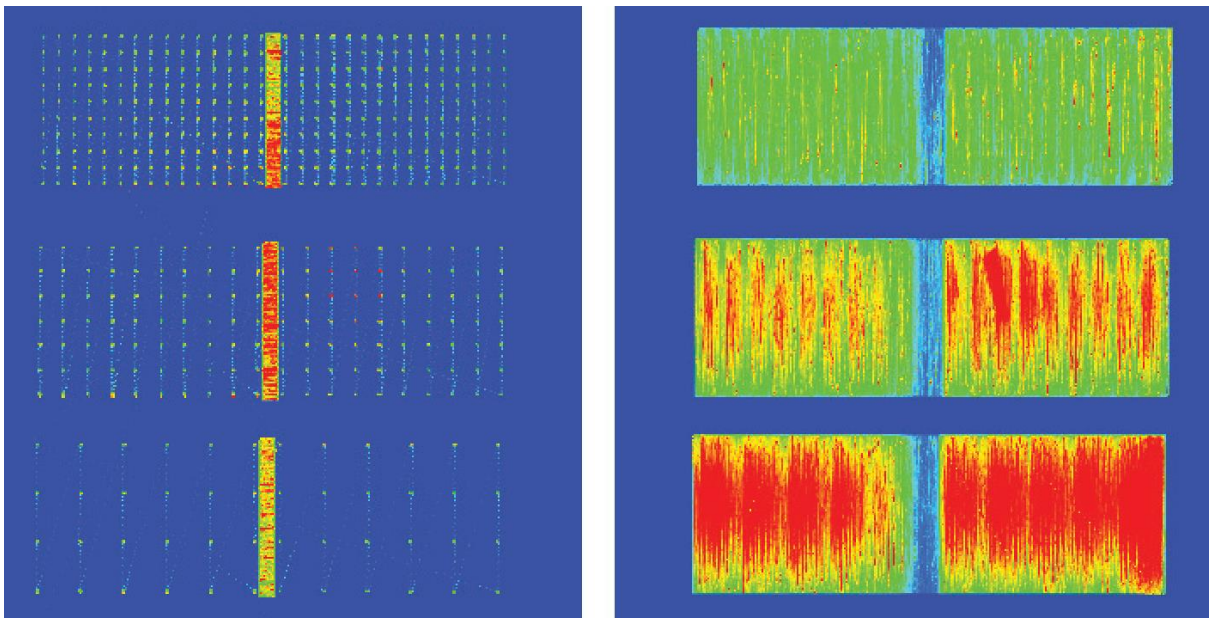

Figure 6-6: Mapping of melt pool area onto XY plane, showing components. left) supports being built, right) first overhanging layers. Note that the sparser the supports, the more overheating occur. Reported by Craeghs et al [264]

Computational modelling is currently being developed for various aspects of L-PBF, covering absorptivity, laser ray tracing, powder spreading, powder melting, microstructural development and distortion [35,41,260,265–267]. Finite element models can simulate the thermal fields experienced as a result of the laser hatching and from this, the subsequent solidification stresses and plastic strains can be calculated. The plastic strains result in displacements, which have been validated and implemented in commercial simulation packages e.g. Autodesk Netfabb [268,269].

Most models assume the powder layer to be constant and equal to the distance the baseplate is lowered, however in reality, because of the powder packing density, the initial layers are thinner than the desired thickness [240,259,260]. This is seen in Figure 6-3c, the powder layer (set at 50 µm initially then incremented by 40 µm each step) rises to 133 µm over 10 layers [246]. As the powder layer increases, so does the melted layer thickness, until it stabilises at 40 µm as expected. This means that the properties of the first 10 layers are different to the bulk and this is typically overlooked.

This chapter investigates whether a processing window in L-PBF can be developed using point source modelling, comparing various normalised parameters to determine which fits experimental results best. Previous studies have shown that features, including porosity [270] and swelling, form preferentially at component edges [239], does this adequately explain the swelling phenomena observed?

6.2. Methods

An Aconity3D Mini was used with Inconel 718 powder; the printer was fitted with a Kleiber spot pyrometer (details in Table 6-2), which output radiance in mV [271]. These values were averaged over a whole build, giving a single comparable value for each sample.

Table 6-2: Pyrometer specifications [271]

Model	**KG 740-LO**
Wavelength Range (nm)	1580-1800
Recording Frequency (kHz)	100
Emissivity	0.1 (default)

Initially, a set of 15 single weld tracks were scanned on a flat wrought Inconel 718 sample, with the parameters summarised in Table 6-3. These were cross-sectioned perpendicular to the laser scanning direction and polished with colloidal silica, before etching with Glyceregia to reveal the tracks. An Olympus BX51 microscope was used to image the tracks and subsequently the track dimensions were measured.

Table 6-3: Processing parameters of weld tracks

	Processing Parameters
Power (W)	40, 115, 190
Velocity (mm/s)	300, 750, 1200, 1650, 2100
Spacing between Tracks (mm)	2
Baseplate	Inconel 718

A series of Inconel 718 cubes (8 x 8 x 8 mm) were printed within the parameter range shown in Table 6-4. All 27 combinations of power, velocity and hatch spacing listed in Table 6-8 were printed; all with a hatch rotation of 67 ° between layers and no contour hatches. 6 samples were stopped during the build as a result of overheating, the remaining 21 were analysed. These samples were sectioned in the XY plane and polished with colloidal silica before measuring the internal porosity using an Olympus BX51 optical microscope with Clemex Vision PE.

9 samples of varying widths were printed to test the effect of geometry on Inconel 718 components. These were built with the bold parameters from Table 6-4, with a 67 ° hatch rotation between layers. The dimensions of these samples are summarised in Table 6-5.

In addition to the cubes, staircases similar to those built by Bidare et al. [246] and Chen et al. [240], were built with 15 steps over 15 layers using the bold parameters in Table 6-4. An example of a staircase is shown in Figure 6-7 together with axis definitions; all hatches were scanned in the x direction. Each staircase was 10 mm wide (x direction) and 30 mm long (y direction), each individual step was 2mm long (y direction). Staircases were scanned without powder and printed with powder.

Table 6-4: Processing parameters of samples

	Processing Parameters
Power (W)	80, **110**, 140
Velocity (mm/s)	900, **1200**, 1500
Hatch Spacing (µm)	30, **45**, 60
Layer Thickness (µm)	30
Baseplate	316L Stainless Steel

Table 6-5: Dimensions of varying thickness samples

Width, y (mm)	0.35, 0.65, 1, 2, 3, 4, 5, 6.5, 10
Length, x (mm/s)	20
Height, z (µm)	10

Figure 6-7: Example of a staircase printed with powder, hatching in the x direction as shown by orange arrows

As a result of the laser power and position being controlled by separate systems, their timings need to be synchronised using delay parameters. Manufacturer's recommended laser delay parameters were optimised for a velocity of 400 mm/s. These are referred to as old delay parameters in this work and lead to an offset between the starts and ends of hatches as shown in Figure 6-8a. These

were measured in a simple geometry and the offsets were plotted in Figure 6-9 for a variety of laser velocities and laser on delays. An improved laser on delay was determined as $L_{on} = -200\ \mu s$, compared with the default of 50 µs (Figure 6-9). The new laser on delay reduced the offset between hatch start and end points (Figure 6-8b). Both staircases were subsequently reprinted with the new delay parameters.

The final samples to be built were a series of 6 squares (single layer, horizontal hatching). These were printed on various thicknesses of powder, varying from 1 layer (30 µm) to 6 layers (180 µm).

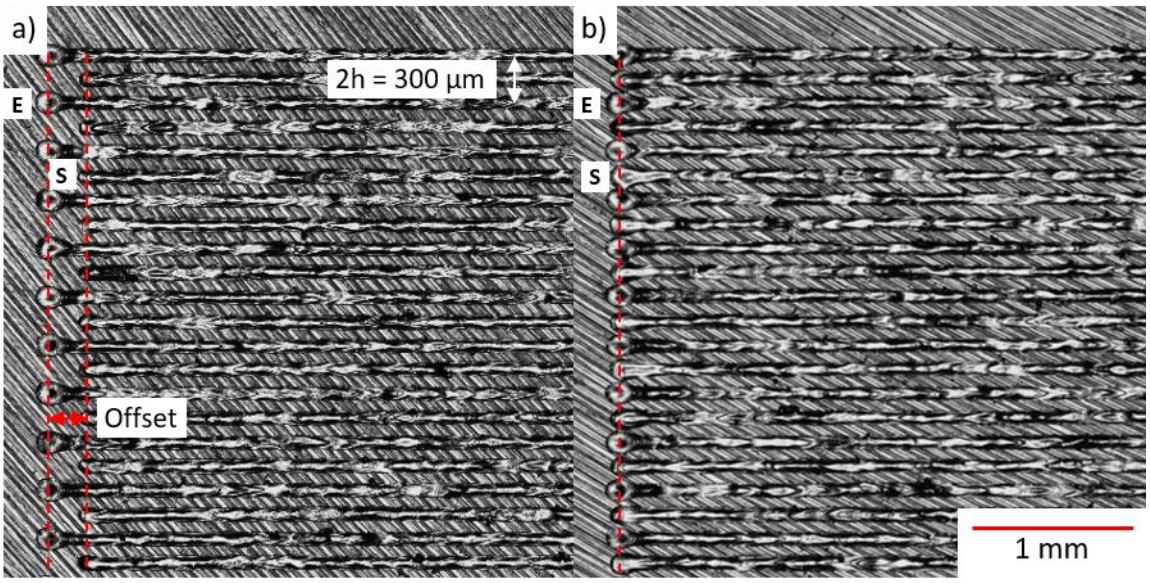

Figure 6-8: Comparison of a) old and b) new delay parameters, shown with 150 µm hatch spacing to emphasise the offsets at the ends of hatches. S marks the start of a hatch; E the end. The offset between the start and ends of hatches is clearly labelled in a) and is no longer present in b)

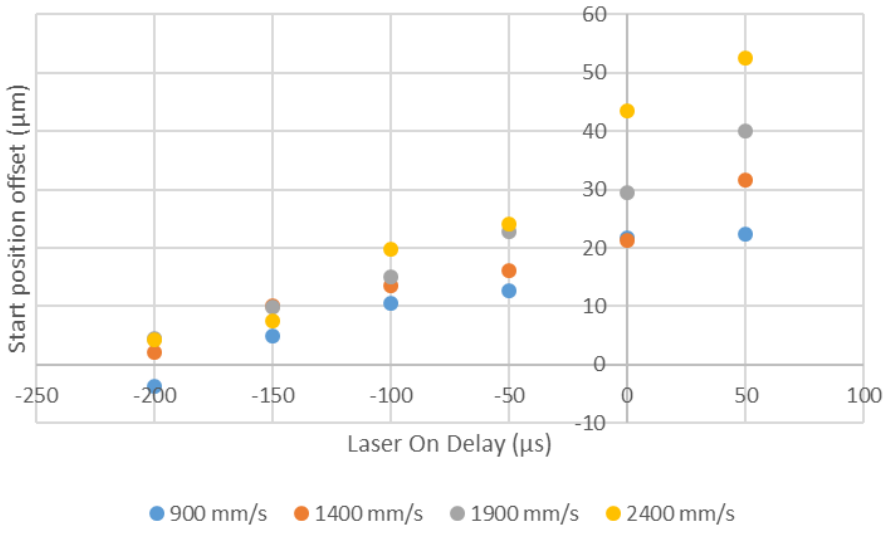

Figure 6-9: Hatch position offset with laser on delay for a variety of hatch velocities

6.2.1. **Measurement of Swelling**

Measurement of all sample surfaces was performed using an Alicona InfiniteFocusSL microscope with a 5x optical lens that uses focus variation to measure 3D surfaces. ImageFields were captured to cover each sample with a vertical resolution of 250 nm and a lateral resolution of 8 µm and saved as al3D files, which were processed using MATLAB R2019a (Mathworks Inc) [272]. Profiles were

extracted from the 3D dataset and peaks were manually identified. A script was written to level the profiles and extract the height of swelling above the build height. When swelling magnitudes were plotted, the values had a moving mean (length 3) applied to minimise the effect of inherent noise. Surface roughness (S_a) was calculated from these datasets.

6.2.2. **Visualisation of Swelling Locations**

Two programs were created using MATLAB R2019a (Mathworks). These were created to gain a deeper understanding of where the two different sources of swelling would be expected. This would highlight any key differences between the mechanisms and so help identify them in printed samples. The first looked at the denudation zone around previous hatches and identified swelling as a result of the denudation mechanism; the second recorded the positions of the ends of every hatch, to capture where melt pool divots were present.

The visualisation is summarised as follows, shown diagrammatically in Figure 6-10:

1. A square cross section is drawn using the dimensions of the cube and number of layers required. Using an initial hatch angle and interlayer hatch rotation, the hatching angle is calculated for each layer. From this the start point, for each layer can be determined. A 45 µm hatch spacing was used, as this is the central value in Table 6-3.
2. For each layer, pairs of start/end coordinates are created for each hatch using the hatch angle for that layer. The first few hatches of an example layer are seen in Figure 6-10a. For each hatch, a linear equation is calculated and coordinates are extracted every 45 µm along the direction of travel, these will be called scanned points. An array of these scanned points is built up, plotted in blue (Figure 6-10b). A 45 µm step was used, resulting in equal resolution both parallel and perpendicular to the scan direction.
3. For each hatch, these scanned points are tested to determine whether a specific swelling mechanism is present. The specifics of the testing criteria for the two models are explained in the following sections. If a scanned point is identified as experiencing swelling, its swelling value is incremented. This is repeated for every layer; some scanned points will accumulate larger swelling values than others – indicating their propensity for swelling. An inherent assumption is made that swelling mechanisms accumulate linearly and the outputs are normalised.
4. The square cross section is split into 100x100 µm squares and the swelling values of all point within each square are summed through all the layers. The result is a map of the square, showing which regions are expected to experience most significant swelling due to the selected mechanism. It is worth noting that the absolute swelling values cannot be compared between the two models, as the swelling contribution of a single occurrence of each mechanism is unknown. However, assuming that a swelling value contributes a consistent amount of swelling within a mechanism, different areas of a square can be directly compared.

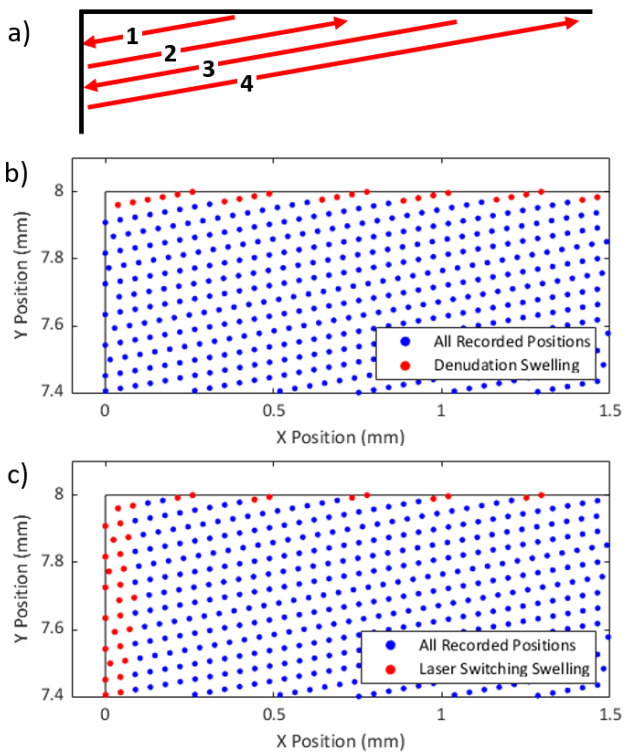

Figure 6-10: Diagrams of swelling visualisation a) first few hatches of the modelled example layer. b, c) Visualisations 1 and 2 respectively; all scanned points in blue, points determined to experience swelling in red. b) Denudation swelling is predicted in the first hatch and any points sufficiently far from previous hatches. c) Laser switching swelling is predicted for the first 2 and last 2 points in each hatch.

Visualisation 1: Denudation Swelling

In denudation swelling, the first hatch is taller than subsequent ones because of the presence of a full powder bed i.e. lack of denudation. By tracking the denuded region, any scanned points outside of this will have scanned a full power bed and therefore experience swelling of around 30 µm per layer [243]. The denudation zone for a hatch is set to include any scanned point within a set distance; two denudation width were calculated, 90 µm and 135 µm [122], which correspond well with images from literature [242].

For each hatch, all previous hatches within the layer are plotted with their denudation zones; creating a large denudation zone around the scanned hatches. Within the current hatch, all scanned points are analysed; if any of the scanned points are outside of the denudation zone, a full powder layer was scanned so this is considered a swollen point and its swelling value incremented. Any scanned points within the denudation zone are said to experience no swelling. As this is repeated for all hatches, the denudation zone increases.

For the example hatching shown in Figure 6-10a, scanned points experiencing denudation swelling are marked red in Figure 6-10b. In this case the entirety of the first hatch will be affected by denudation swelling as will the subsequent hatch ends which are furthest from previous hatches.

Visualisation 2: Laser Switching Swelling

In the second visualisation, the locations where each hatch starts and ends are recorded. It has been shown that at the start and end of a melt track, humps can form of approximately 100 µm length [254] and 50 µm height [253]. For each hatch, the locations of interest are where the laser turns both on and off. To capture this, a distance of 90 µm (2 scanned points) is set as the swollen region; this is similar to the length of the track ends visible in Figure 6-8.

For each hatch, the first two scanned points are assumed to capture the laser switching on; the last two scanned point capturing the laser switching off. These four points are affected by swelling because of the laser switching so their swelling values are incremented. The scanned points in the centres of hatches are not expected to experience swelling as a result of this mechanism.

For the example hatching shown in Figure 6-10a, scanned points experiencing swelling as a result of the laser switching are marked red in Figure 6-10c. With this mechanism, both ends of each hatch experience swelling.

Melt Pool Simulation

A point heat source model was created in MATLAB R2021b (Mathworks Inc), based on the original equation derived by Rosenthal [31], this calculates steady state thermal fields surrounding a moving point heat source using Equation 2-3. Model parameters are summarised in Table 6-6, and the model was run for power and velocity values given in Table 6-3. The same calculations were repeated using Equation 2-4, which assumes a Gaussian heat source, for comparison.

Table 6-6: Parameters used for moving heat source calculations

Parameter	**Value**	**Reference**
Step Size	5 µm	-
Thermal Conductivity, κ	9.94 $Wm^{-1}K^{-1}$	[273]
Thermal Diffusivity, α	$2.87x10^{-6}$ m^2s^{-1}	[273]
Absorption Coefficient, A	0.45	[274]
Melting Point (solidus), T_m	1643 K	[275]
Laser Beam Diameter, D_b	70 µm	-

For each output thermal field, the melt pool dimensions (using the solidus temperature) were extracted. Figure 6-11 shows an example set of thermal fields and the dimensions to be extracted. Melt pool dimensions are not expected to be numerically accurate, due to variability of materials properties, but should be comparable to one another. Additionally, it has been shown that due to constraints in growth orientation, undercooling can cause the length of the melt pool to be underestimated by calculations [88].

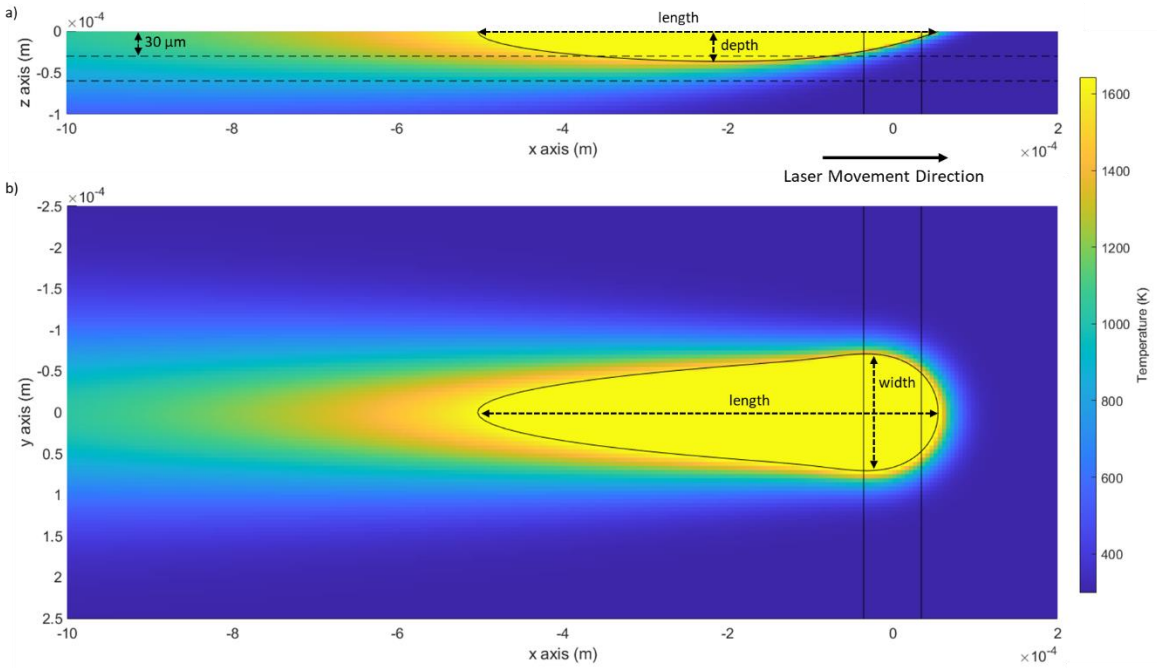

Figure 6-11: Steady state thermal fields modelling a moving Gaussian heat source at 115 W and a velocity of 1200 mm/s. a) XZ section of thermal field, b) XY section of thermal field. Melt pool length, width and depth are labelled, solidus temperature is outlined in black

Netfabb AM Simulation

Netfabb Local Simulation [269] was used to create thermal and mechanical simulations of the cube printing. The CAD component (8 x 8 x 8 mm cube) was imported, positioned on a baseplate (16 x 16 x 16 mm) and the printing parameters (Table 6-8) were set. A 5 level adaptive mesh was applied, resulting in a minimum mesh size of 83 µm. Default materials parameters for Inconel 718 were selected; the full height of the components was simulated, resulting in 36 increments which could be interrogated for results.

Outputs from these simulations include:

- Lack of fusion volume % (defined as areas below 1240 °C), this is a single value for the final component
- Hot spot volume % (defined as areas above 2000 °C), this is a single value for the final component
- Z displacement of each point in the simulation at the end of the simulation
- Interlayer temperature (after new powder layer recoated) at the end of the simulation

6.3. Results

Normalised energy density (NED) and normalised enthalpy (NE) are widely used in this chapter and are defined as (initially introduced in Section 2.4):

$$Normalised\ Energy\ Density\ (NED), E_0^* = \frac{P^*}{v^* l^* h^*} = \left[\frac{AP}{2vlh}\right]\left[\frac{1}{\rho C_p}(T_m - T_0)\right]$$

$$Normalised\ Enthalpy\ (NE)\ , \frac{\Delta H}{h_s} = \frac{AP}{\pi h_s \sqrt{\alpha v {D_b}^3}}$$

6.3.1. Weld Track Analysis

Each of the 15 weld tracks were imaged in cross-section, so their dimensions could be measured; these are summarised in Table 6-7. Figure 6-12 shows three different cross-section types, all scanned at 115 W; a) shows a keyhole, which is where a deep melt pool is formed due to internal reflection. If we define a keyhole as being deeper than it is wide, welds 10, 11 and 12 fall into this category. 12 is a transition melt pool, between conduction and keyholing. Figure 6-12b shows a representative conduction-mode melt pool, whilst Figure 6-12c shows an unstable melt pool. Welds 6, 7, 13 ,14 and 15 all had this unstable 'w' shape; this is a symptom of balling, which occurs because of the Plateau-Rayleigh instability [252]. A long melt pool (usually as a result of high power and high velocity) is more likely to become unstable, so this is where 'w' shaped melt pools are most commonly seen – this irregular melt pool shape can be the cause of lack of fusion porosity in subsequent layers [252].

Melt pool dimensions of both point heat source and Gaussian heat source calculations are tabulated in Table 6-7 and plotted in Figure 6-13, plotted against both NED and normalised enthalpy (NE). NED was developed for development of processing maps, allowing for comparison of different combinations of processing parameters in a single value [82], hence the inclusion of parameters such as the hatch spacing and layer height. It allows for blindly investigating the process, with no prior knowledge of the materials response, so is powerful for process development. NE on the other hand, calculates how far heat can diffuse and so the melt pool dimensions – it is inherently more physics based. Some important parameters, such as hatch spacing are omitted.

Given a set hatch spacing, the melt pool width can be calculated, and from this, a critical melt pool depth can be calculated [276]. The layer thickness must be below this critical depth, otherwise, the melt pools will not overlap and porosity will occur [276].

In literature, keyholing is theoretically expected to occur at NE values above 6 [83], experimentally, this transitions has been found to be 10 by Hann et al. [84] and 30 by King et al [83]; this discrepancy makes defining a global threshold very difficult. Visually, Figure 6-12has a keyhole morphology, but according to some definitions, keyholes must had a depth of at least 2x width [252], so we are seeing the transition region. One could argue that the transition in this work occurs roughly at $\frac{\Delta H}{h_s} \approx 10$, which matches the findings by Hann et al [84].

Table 6-7: Dimensions of track welds scanned compared to those predicted by both point heat source and Gaussian heat source models. A hatch spacing of 30 µm was used to calculate E_0^*

Weld	Processing Parameters		E_0^*	$\frac{\Delta H}{h_s}$	Experimental		Point heat source		Gaussian heat source	
	P (W)	v (mm/s)			Width (µm)	Depth (µm)	Width (µm)	Depth (µm)	Width (µm)	Depth (µm)
1	40	300	7.2	3.3	78	38	71	35	136	41
2	40	750	2.9	2.1	58	21	47	24	106	21
3	40	1200	1.8	1.6	54	13	38	19	92	13
4	40	1650	1.3	1.4	47	11	33	16	82	9
5	40	2100	1.0	1.2	40	8	29	15	74	7
6	115	2100	2.9	3.6	70	24	50	25	128	24
7	115	1650	3.7	4.0	80	28	56	28	134	29
8	115	1200	5.1	4.7	80	41	65	33	142	36
9	115	750	8.2	6.0	114	68	82	41	154	50
10	115	300	20.6	9.4	158	194	127	63	198	85
11	190	300	34.0	15.6	203	316	165	83	248	113
12	190	750	13.6	9.9	127	129	106	53	173	68
13	190	1200	8.5	7.8	95	79	84	42	160	51
14	190	1650	6.2	6.7	98	57	72	36	153	42
15	190	2100	4.9	5.9	99	43	64	32	148	35

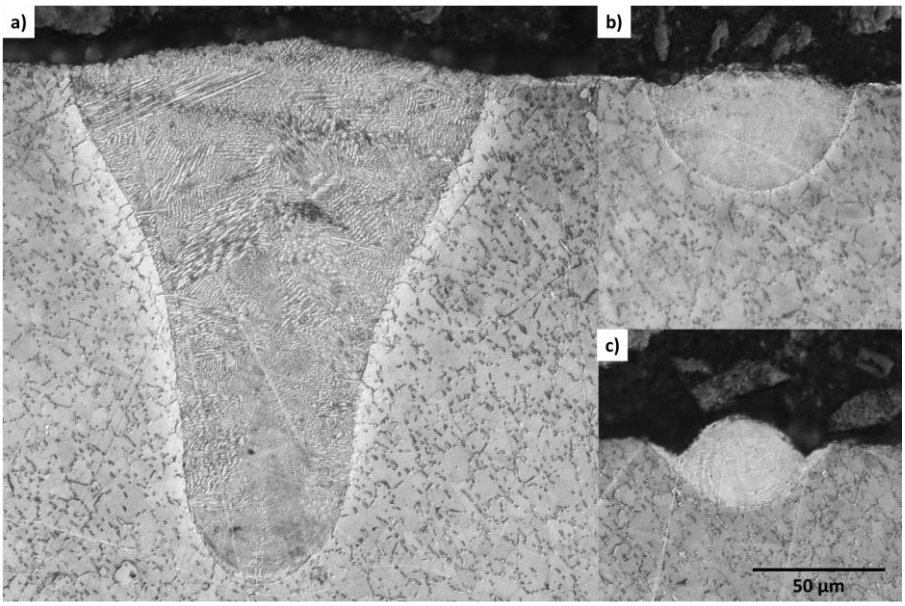

Figure 6-12: Optical micrographs of track weld cross-sections performed at 115 W. a) 300 mm/s showing a keyhole morphology, b) 1200 mm/s showing normal conduction mode morphology, c) 2100 mm/s showing a shallow melt pool with a 'w' shape

Figure 6-13 shows both melt pool depths and width plotted against both NED and NE; for a single weld track, it seems that both NED and NE fit the moving heat source models equally well. The measured dimensions correlate more strongly with NE than with NED. Figure 6-13d shows the variation of melt pool depth with NE; since depth is strongly affected by the keyhole mode, Figure 6-13e shows the same data, but limited to $0 < \frac{\Delta H}{h_s} < 9$. There is generally a positive correlation between the depth of the weld track and NE, as expected. This is also seen for both point and Gaussian heat sources; in conduction mode, the Gaussian heat source model is a better fit to the experimental data than the point heat source. Figure 6-13c and f show the weld track widths; once again, the same trend is observed experimentally as predicted by the point heat source model. For the width, the point source point heat source model fits closer to the experimentally measured values than the Gaussian heat source.

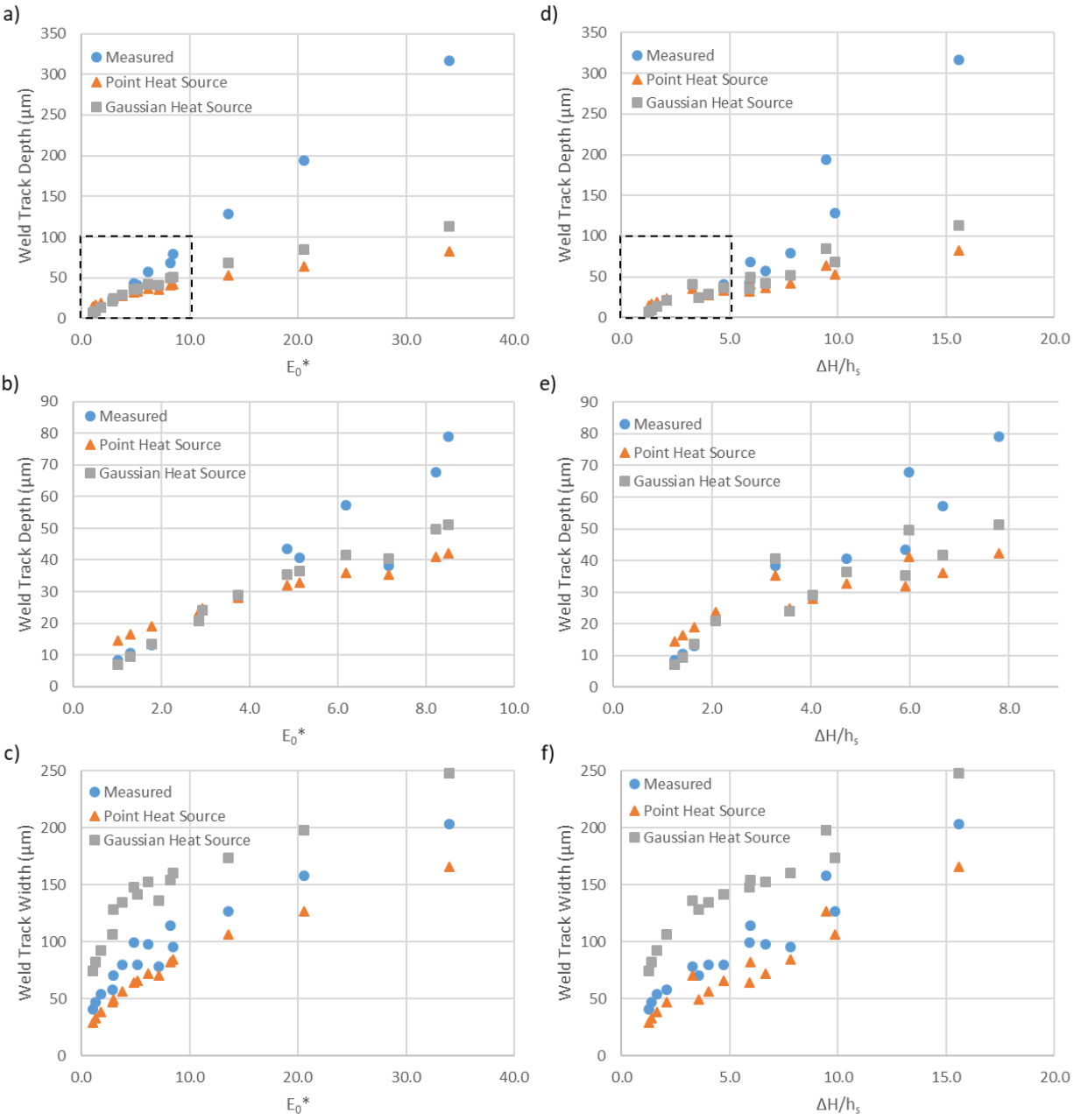

Figure 6-13: Weld track dimensions plotted against a, b, c) normalised energy density; d, e, f) normalised enthalpy, compared with outputs of both point and Gaussian heat source models. a, d) weld track depth; b, e) weld track depth excluding keyholed tracks (within dotted rectangle in a, d); c, f) weld track width

6.3.2. **Pyrometry Analysis**

To better understand the trends experienced in the pyrometry data, a larger sample was built (8 x 20 x 100 mm width, length, height respectively) using the bold parameters in Table 6-4. The pyrometry data for the first 12 hatches of a single layer is shown in Figure 6-14, with 288,500 data points recorded for a single layer, which takes only several seconds to scan. The orange overlay shows the moving average of the pyrometry signal (window 50), where you can see the signal drop to ~830mV (signal baseline) most hatches; these are hard to identify in some cases e.g. at 9000. Since the hatching is at an angle, the first few hatches are in a corner and so are not full length (shown diagrammatically in Figure 6-10a), for this reason, the duration of the first few hatches is

shorter than subsequent hatches. The pyrometry signal of the first hatches seems lower, but this could be due to the reduced hatch length.

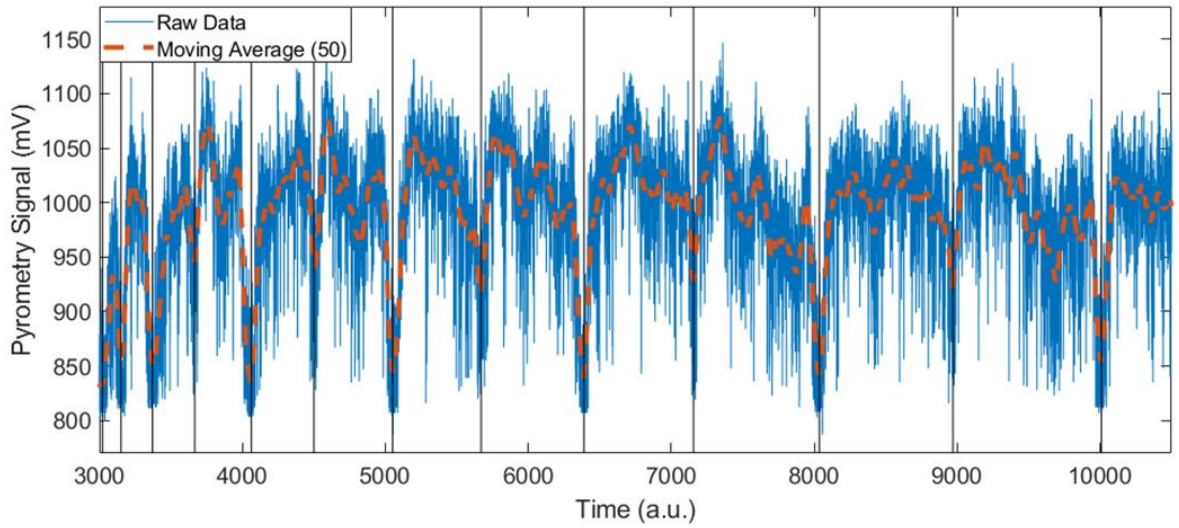

Figure 6-14: Pyrometry signal of a representative cuboid showing the first 12 hatches of a layer, orange line shows a moving average, window 50, black lines separating each hatch

The frequency of pyrometry recording results in copious amounts of data, with a relatively high noise. During the full component build (10 mm, 333 layers), 102 million pyrometry values were recorded. An average pyrometry signal per layer is shown in Figure 6-15a, with an initial pyrometry increase and then a sinusoidally oscillating value. Figure 6-15b shows the average pyrometry values for the first 50 layers. The first maximum value is reached after 8 layers, at which point the oscillation begins. There are then a further 7 oscillations by the 46th layer. Figure 6-15c clearly shows that the oscillation is dependent on the hatching angle, with the minimum pyrometry signals experienced at angles of 90 ° and 270 °.

The variation of pyrometry signal with component width is summarised in Figure 6-16. The average pyrometry signal increases with sample width up to a maximum at around 2-3 mm, above this, the signal slightly decreases and plateaus. It seems like at thicknesses above 5 mm, the thermal signature of the component is consistent.

Figure 6-17 shows a breakdown of this for the narrower samples, by layer. Figure 6-17b is included for clarity, with only the first 40 layers shown; it can be seen that the wider components experience higher pyrometry signals, which explains the general trend visible in Figure 6-16. Additionally, it seems like the wider components reach a plateau more quickly than the narrower components; little change in pyrometry signal is seen once the component width is above 2 mm. The oscillation of the pyrometry signal visible in Figure 6-15b is also visible in Figure 6-17.

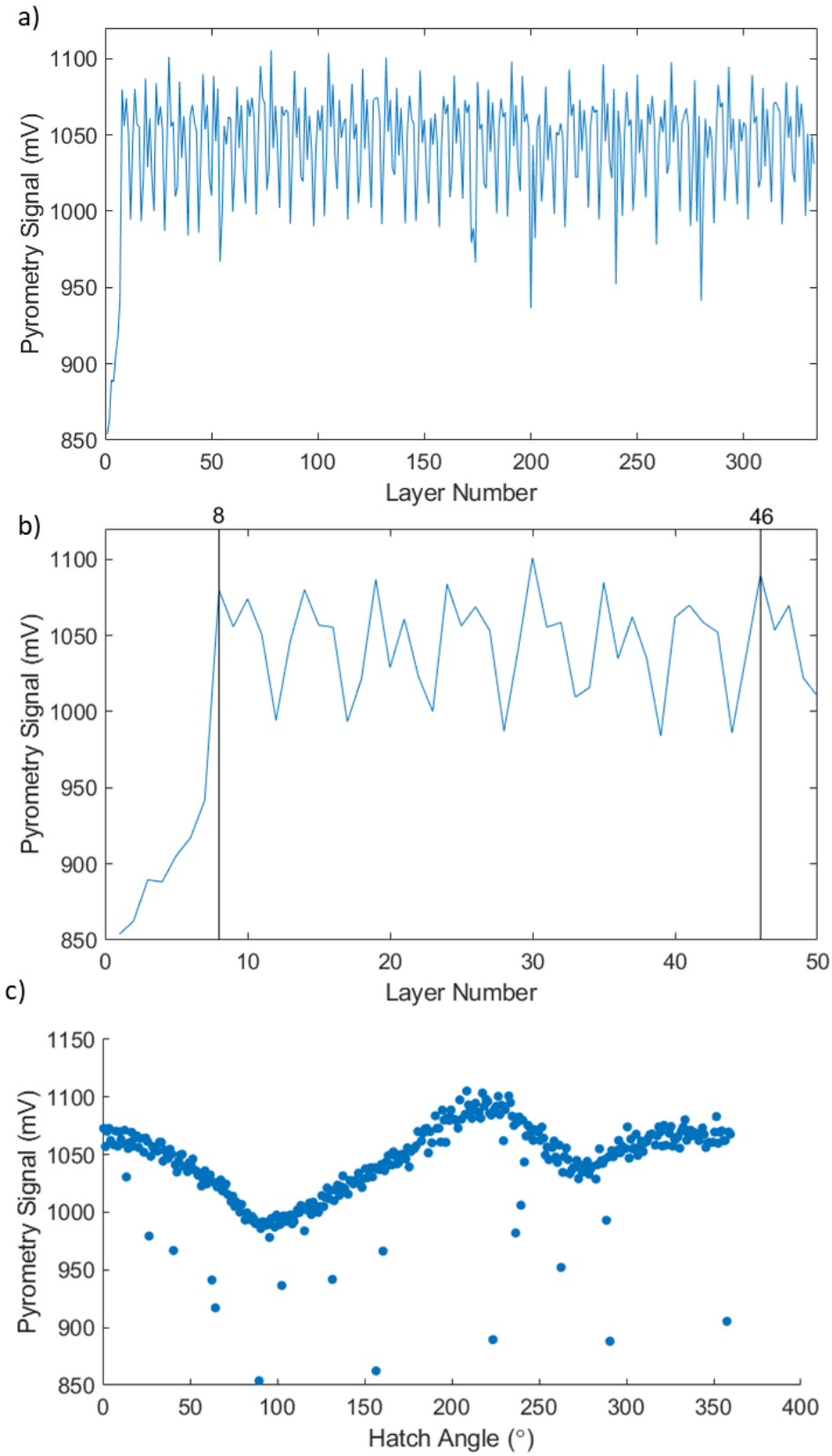

Figure 6-15: Average pyrometry signal per layer of a part. a) Full component, b) First 50 layers, black lines showing 7 pyrometry oscillations, c) Variation of pyrometry on hatching angle (clockwise from horizontal)

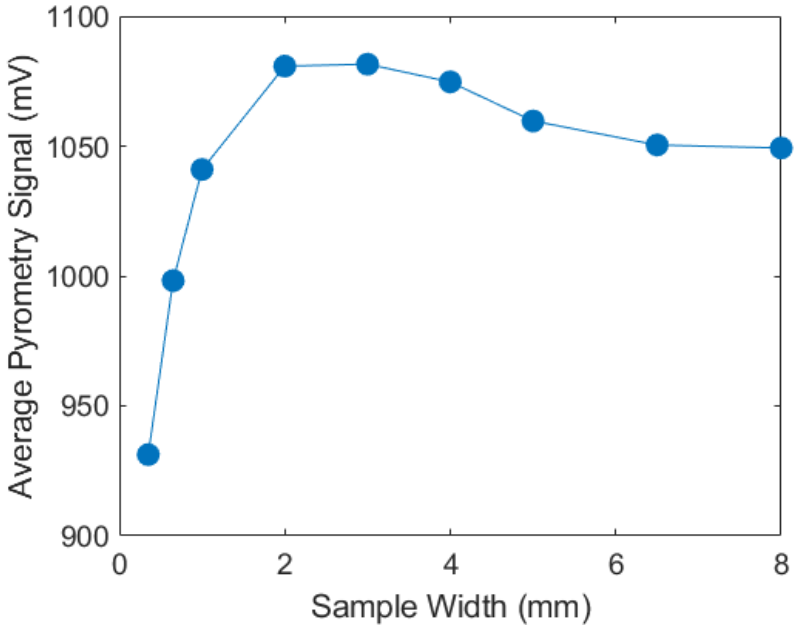

Figure 6-16: Average pyrometry signal of the varying thickness components

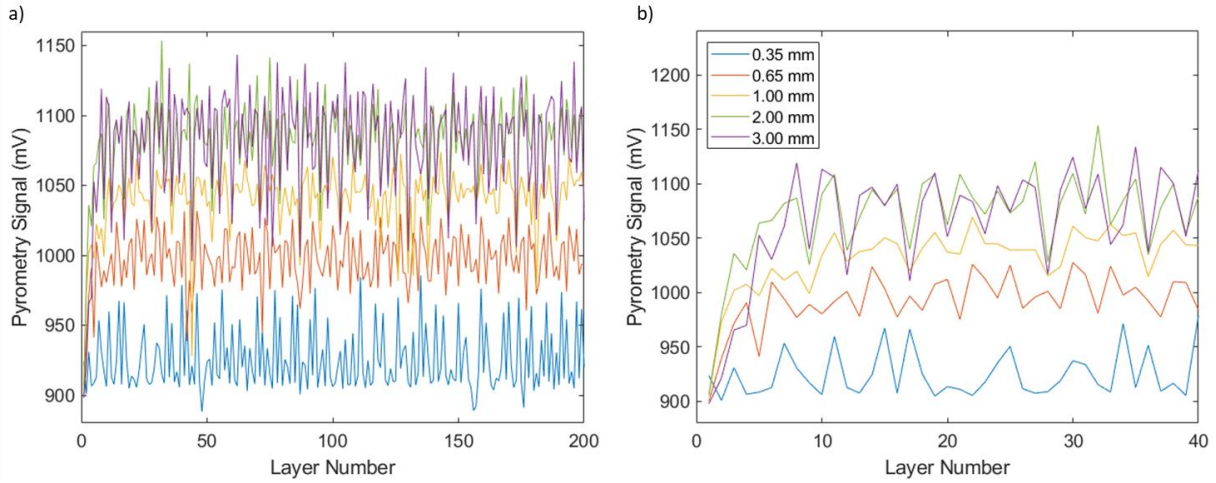

Figure 6-17: Variation of pyrometry signal with layer number for the varying width samples. For clarity, only samples up to 3 mm in width are shown. b) subset of a), showing only the first 40 layers

6.3.3. **Experimental Analysis of Cubes**

Of the 27 processing parameters tested, 21 cubes were printed successfully, full results are summarised in Table 6-8. Average pyrometry signals (mV) for the 21 successfully printed cubes are shown in Figure 6-18. As expected, they increase with NED (E_0*), proving that NED is a valid methodology for process window development. NED generally scales with NE ($\Delta H/h_s$), but some subtle changes can be seen between Figure 6-18a and Figure 6-18b. Importantly, the R^2 values of for both porosity and pyrometry are higher in Figure 6-18b, where they are plotted against NE, so NE will be predominantly used from here in.

Also shown are the area porosity values for each cube, with "nominally fully dense" being shown as 98 % density. It can be seen that at NE values below 4-5, lack of fusion is frequent, increasing porosity. However, at larger NE values the samples are fully dense over a large range of processing parameters. Porosity value, separated by hatch spacing can be seen in Table 6-9, these are shown alongside melt pool widths and depths (as predicted by the moving heat source model).

Sample	Processing Parameters			E_0*	$\frac{\Delta H}{h_s}$	Pyrometry Signal (mV)	Porosity (%)	Simulation Results			Experimental Results		
	P (W)	v (mm/s)	h (µm)					Edge Swelling (µm)	Corner Swelling (µm)	Corner/Edge Ratio	Edge Swelling (µm)	Corner Swelling (µm)	Corner/Edge Ratio
1	***80***	***900***	***30***	4.77	3.79	1037.2	N/A	6.1	10.6	1.75	N/A	N/A	N/A
2	***110***	***900***	***30***	6.56	5.21	1023.1	N/A	9.3	16.2	1.75	N/A	N/A	N/A
3	***140***	***900***	***30***	8.35	6.64	1103.9	N/A	14.5	25.3	1.75	N/A	N/A	N/A
4	***80***	***1200***	***30***	3.58	3.28	1025.3	N/A	5.1	8.9	1.75	N/A	N/A	N/A
5	110	1200	30	4.92	4.52	995.85	0.11	8.0	14.1	1.75	75.3 (12.2)	128.9 (7.0)	1.71
6	***140***	***1200***	***30***	6.26	5.75	1030.5	N/A	11.0	19.2	1.75	N/A	N/A	N/A
7	80	1500	30	2.86	2.94	987.64	3.84	4.4	7.7	1.75	34.6 (16.6)	86.2 (17.8)	2.49
8	110	1500	30	3.94	4.04	993.9	0.17	6.9	12.0	1.75	60.7 (5.2)	120.4 (27.1)	1.98
9	***140***	***1500***	***30***	5.01	5.14	1009.4	N/A	9.6	16.8	1.75	N/A	N/A	N/A
10	80	900	45	3.18	3.79	990.92	0.66	5.3	9.3	1.75	78.2 (7.4)	128.3 (4.8)	1.64
11	110	900	45	4.37	5.21	1010.6	0.06	8.0	14.0	1.75	83.4 (12.0)	164.0 (4.0)	1.97
12	140	900	45	5.57	6.64	1042.9	0.15	10.5	18.4	1.75	99.8 (8.2)	209.4 (4.4)	2.10
13	80	1200	45	2.39	3.28	969.67	1.06	4.7	8.2	1.75	34.9 (10.6)	66.6 (4.5)	1.91
14	110	1200	45	3.28	4.52	986.48	0.11	6.6	11.5	1.75	54.4 (3.5)	113.4 (21.0)	2.08
15	140	1200	45	4.17	5.75	1017.8	0.09	8.7	15.3	1.75	82.2 (7.4)	183.8 (44.0)	2.24
16	80	1500	45	1.91	2.94	954.29	3.53	4.2	7.4	1.75	24.0 (11.8)	51.6 (26.0)	2.15
17	110	1500	45	2.62	4.04	973.07	0.23	5.7	10.0	1.75	42.6 (2.2)	92.7 (2.1)	2.18
18	140	1500	45	3.34	5.14	997.5	0.10	7.5	13.1	1.75	67.5 (8.9)	164.6 (36.4)	2.44
19	80	900	60	2.39	3.79	980.13	0.55	5.1	8.9	1.75	45.5 (7.7)	81.5 (20.9)	1.79
20	110	900	60	3.28	5.21	1001.2	0.14	6.9	12.0	1.75	69.8 (6.1)	160.5 (16.4)	2.30
21	140	900	60	4.17	6.64	1048.7	0.13	8.8	15.3	1.75	90.3 (13.0)	187.0 (14.9)	2.07
22	80	1200	60	1.79	3.28	956.96	3.09	4.6	8.1	1.75	28.0 (4.3)	47.9 (14.2)	1.71
23	110	1200	60	2.46	4.52	979.74	0.33	6.0	10.5	1.75	57.4 (4.7)	106.4 (35.4)	1.85
24	140	1200	60	3.13	5.75	1006.1	0.13	7.5	13.0	1.75	62.6 (9.2)	166.7 (23.9)	2.66
25	80	1500	60	1.43	2.94	948.9	7.27	4.1	7.1	1.75	-2.2 (3.2)	50.4 (21.9)	N/A
26	110	1500	60	1.97	4.04	971.13	1.39	5.5	9.6	1.75	50.4 (4.2)	87.7 (27.2)	1.74
27	140	1500	60	2.50	5.14	997.39	0.32	6.7	11.7	1.75	58.1 (4.9)	132.5 (26.0)	2.28

Table 6-8: Summary of results for all printed samples. Samples in bold failed and were aborted during the build. Standard deviations of swelling shown; Porosity and Pyrometry errors handled in Figure 6-18

Figure 6-19 shows a Z map of the top surface of sample 14, which used the central processing parameters, measured using the Alicona. The edges of the cube are raised with respect to the centre; the corners being the highest points. The area surface roughness (S_a) of the central region was calculated as 7.2 µm. Any swelling less than this would be indistinguishable from the surface roughness.

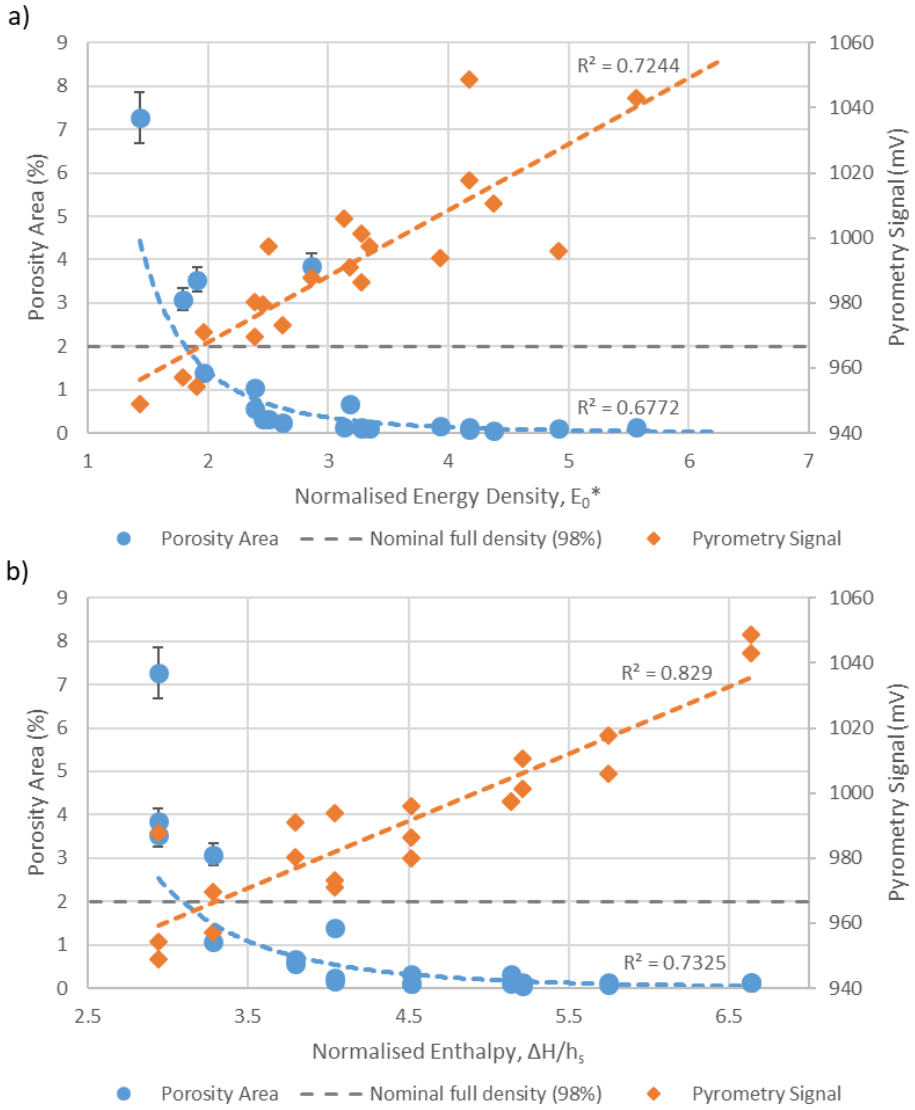

Figure 6-18: Variation of porosity and pyrometry with a) NED and b) NE. Error in porosity area calculated as 8% of the mean value as a result of image thresholding variability, linear trendlines shown with R^2 values. As a result of millions of individual points averaged for pyrometry signal value, standard errors are of the order of 0.03 mV, power trendlines shown with R^2 values

The pyrometry signal for a staircase is shown in Figure 6-20, 3 steps are shown, numbers 1, 8 and 15. All steps were hatched in the X direction, starting at minimum Y. There is a clear increase in thermal intensity with increasing step number. On step 15, the first and last regions to be scanned appear hotter than the bulk (lowest and highest Y values respectively).

For each cube, height profiles were taken in both the X and Y directions as marked by the vertical and horizontal lines in Figure 6-19. For each, a line width of 100 px (0.8 mm) was used to reduce uncertainty. Each profile had a peak at both edges of the cube, the height of this above the build height was taken to be the swelling magnitude. The 4 resultant swelling magnitudes were averaged

and the result was defined as 'edge swelling'. A diagonal profile (marked) was extracted, the average of the 2 swelling magnitudes on the diagonal is referred to as 'corner swelling'.

Table 6-9: Porosity of all printed samples, compared with melt pool widths and depths predicted by point and Gaussian heat source models

				Porosity Area % (for each hatch spacing)		
P (W)	**v (mm/s)**	**Gaussian heat source Depth (µm)**	**Point heat source Width (µm)**	**30 µm**	**45 µm**	**60 µm**
80	900	33.9	62.4	N/A	0.7	0.6
110	900	42.8	73.5	N/A	0.1	0.1
140	900	50.3	83.1	N/A	0.1	0.1
80	1200	27.5	54.4	N/A	1.1	3.1
110	1200	35.2	63.9	0.1	0.1	0.3
140	1200	41.8	72.2	N/A	0.1	0.1
80	1500	23.1	48.7	3.8	3.5	7.3
110	1500	30.0	57.3	0.2	0.2	1.4
140	1500	35.9	64.7	N/A	0.1	0.3

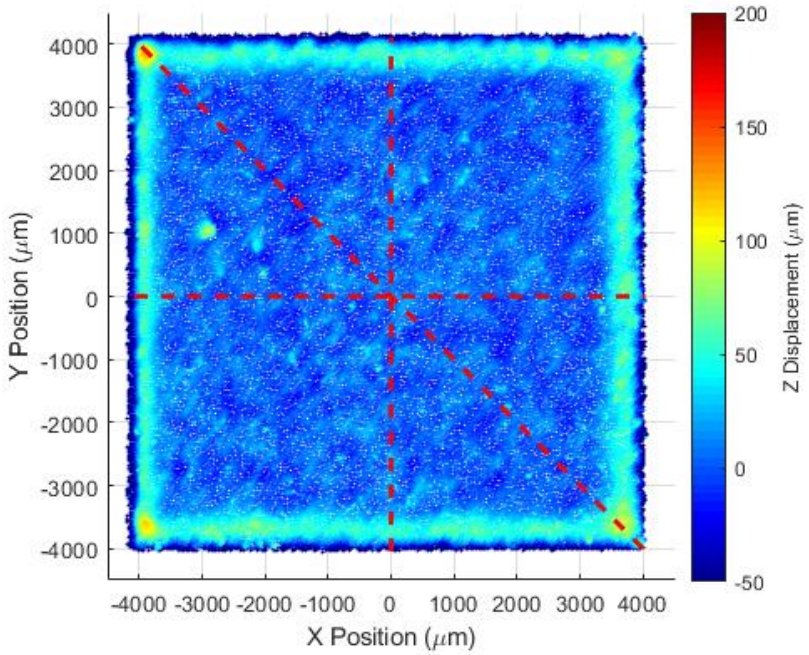

Figure 6-19: Representative Z map of a printed cube, central section used to calculate surface roughness. Red dotted lines shown profiles used to calculate swelling

Figure 6-21a shows the average values for both edge and corner swelling for all of the printed cubes. There appear to be linear trends between both edge and corner swelling with NE. Corner

swelling is observed to be more significant than edge swelling as visible in Figure 6-19. For most samples, the swelling was greater than the surface roughness (7.2 µm). Since different swelling mechanisms occur in different locations, a ratio of corner swelling to edge swelling will be taken. For the measured samples this ratio is 1.88.

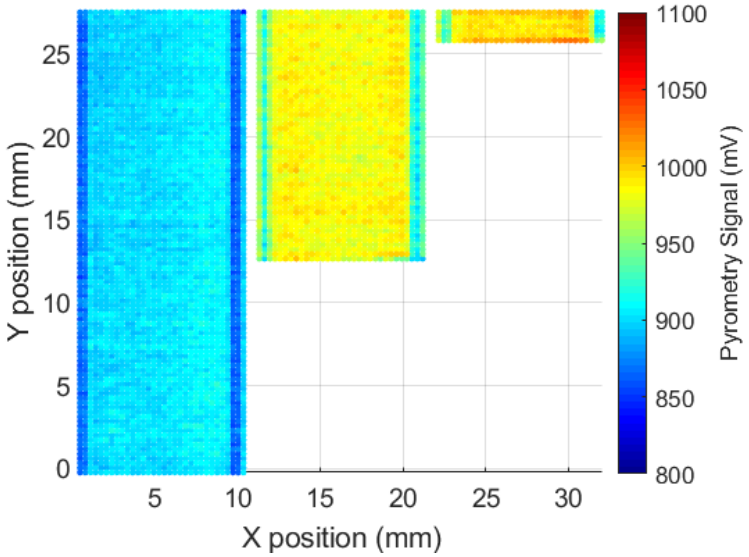

Figure 6-20: Pyrometry of staircase printed with powder (old delay parameters). Each point is the average of a 0.3 x 0.3 mm square. Shown are steps 1, 8 and 15 respectively.

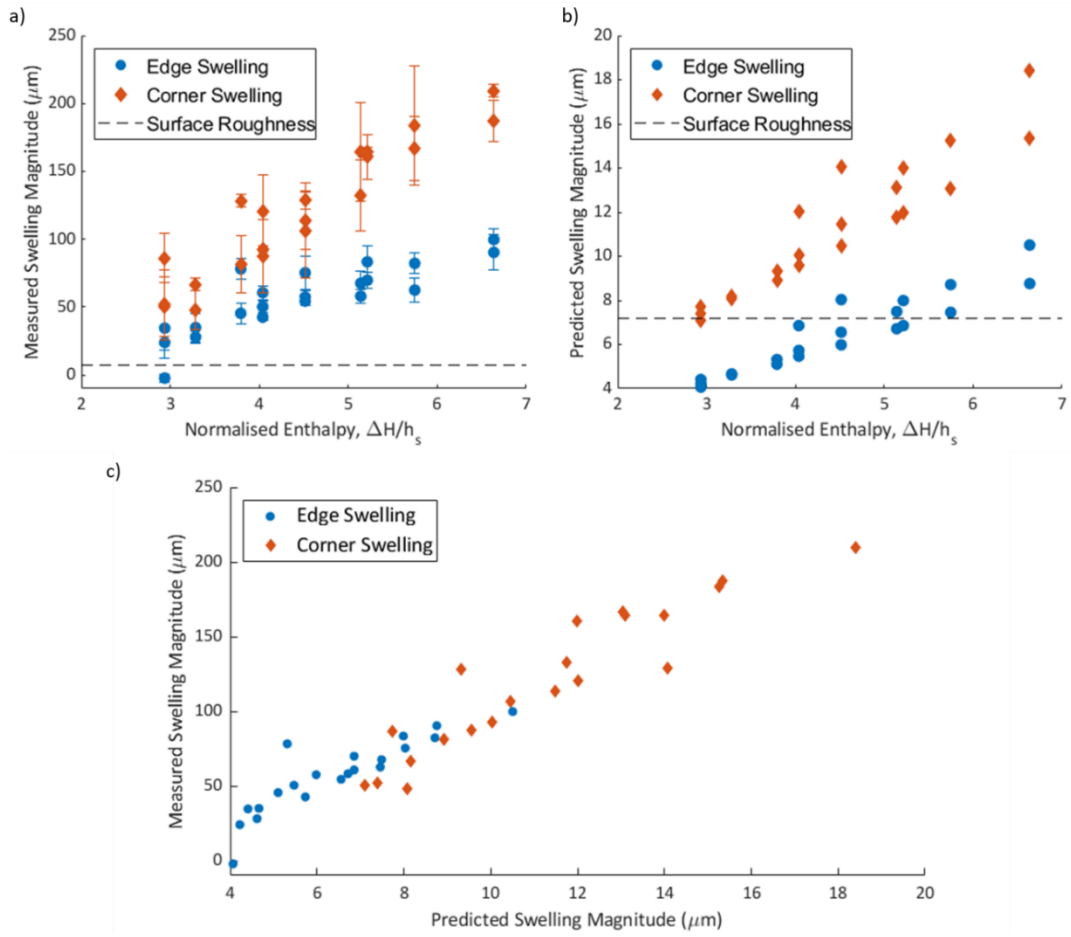

Figure 6-21: Comparison of edge swelling and corner swelling; a) measured swelling with standard deviations shown, b) swelling predicted by Netfabb Simulation, c) comparison of measured and predicted swelling

6.3.4. **Netfabb Thermal/Mechanical Simulation**

Thermal models were created using Netfabb Local Simulation to test the capabilities of the modelling. Since outputs such as lack of fusion and Z displacement were available, these outputs could be compared against experimental results. Figure 6-22a shows the geometry of the Netfabb simulation which was performed for each set of processing parameters. The simulation calculates the strain as a result of residual stresses within the geometry and hence estimates the final component geometry. The main result of interest was the Z displacement, shown both for the whole geometry (Figure 6-22a) and for the top surface of the final layer (Figure 6-22b). The simulation predicted a similar swelling pattern to that seen in Figure 6-19, with all 4 edges elevated and the corners being further raised.

The swelling values were extracted from the simulation in the same manner as the experimentally measured values. Both the measured edge and corner swelling values are plotted in Figure 6-21b. Although the trend is similar to that measured from the printed samples (Figure 6-21c), the values obtained from the Netfabb simulation are almost an order of magnitude smaller; a linear fit yields: $Measured\ (\mu m) = 13.7 \times Predicted\ (\mu m) - 32.9$. Additionally, most of the predicted edge swelling is smaller than the surface roughness of 7.2 µm. The ratio of corner to edge swelling was found to be 1.75. It seems like the model simply calculates the deformation due to plastic strain rather than taking swelling mechanisms such as denudation into account. As such, despite the trends appearing similar between model and experimental, this can be disregarded as the model does not adequately capture the mechanisms occurring – the displacement results were included due to the similarity in the trends followed, despite them not improving our understanding of swelling.

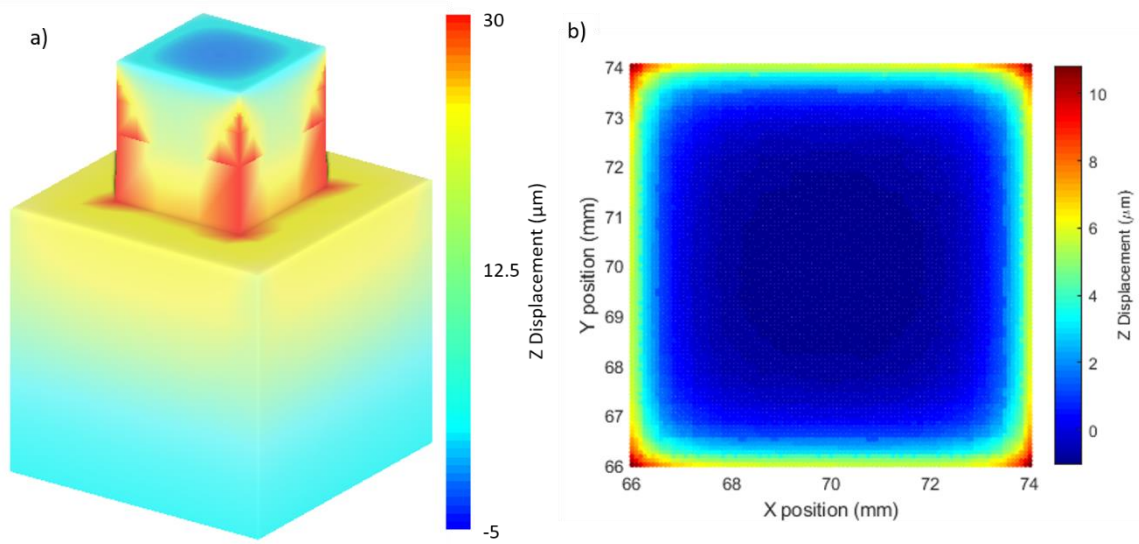

Figure 6-22: Predicted Z displacement as modelled using Netfabb Simulation. a) Full modelled geometry; b) Top surface only

For general simulation validation, three other model outputs were plotted in Figure 6-23. Both the interlayer temperature and volume fraction of hotspots (over 2000 °C) increase with NE, as would be expected. Volume fraction of lack of fusion (below 1240 °C) decreases with increasing NE, with minimal porosity expected at values of NE above 3, similar to the measured results shown in Figure 6-18. The validity of this model is unknown, but the results can be compared against pyrometry and porosity data to validate both methods.

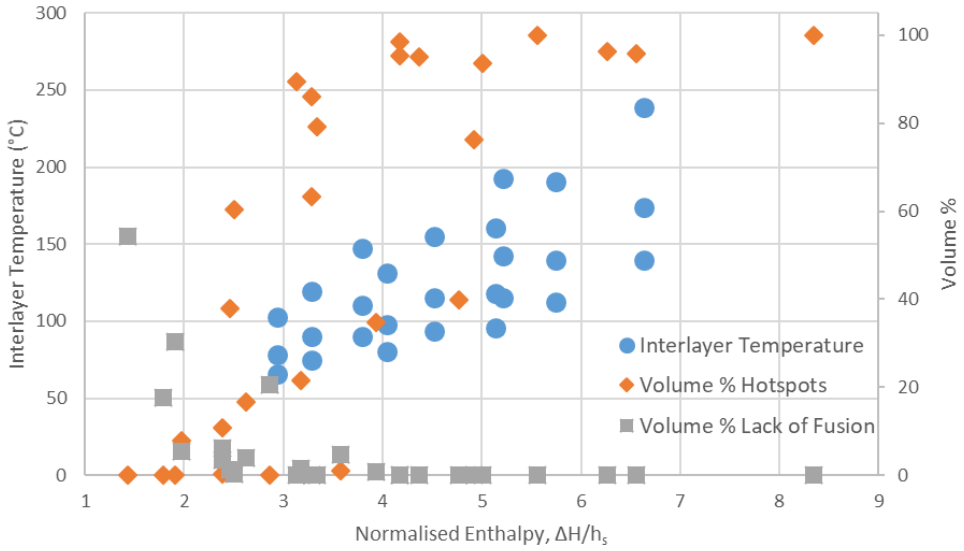

Figure 6-23: Predicted outputs from Netfabb Simulation modelling; interlayer temperature, volume fraction hotspots (over 2000 °C) and volume fraction lack of fusion (below 1240 °C)

6.3.5. Matlab Swelling Visualisations

Two visualisations were introduced in Section 6.2.2, the output being a grid of swelling values. The sums from a single square in each corner of the cube were taken and averaged to give a value for corner swelling. The swelling values of the remaining outer squares (touching the edge) were averaged to give an edge swelling value. The normalised results are shown in Table 6-10, along with the ratios of the corner/edge swelling. Assuming that a swelling value contributes a consistent amount of swelling within a mechanism, the corner/edge ratio can be directly compared.

Table 6-10: Results of swelling visualisations . Two different denudation widths were run through visualisation 1

Visualisation	Edge Swelling	Corner Swelling	Corner/Edge Ratio
1 - Denudation swelling (90 µm width)	0.045	0.186	4.11
1 - Denudation swelling (135 µm width)	0.029	0.173	6.05
2 - Laser switching swelling	0.625	1.000	1.60

6.3.6. Swelling of Printed Staircases

Figure 6-24a shows the Z height of the staircase printed with powder using old delay parameters. The Z height and swelling magnitude along lines labelled b and c in Figure 6-24a are shown in the respective subfigures. The blue line in each subfigure shows the Z height profile. In Figure 6-24b, peaks are observed at the start of each step which can be attributed to the balling, enlarged in Figure 6-25. The orange line in each subfigure shows the magnitude of these peaks. To highlight trends in the swelling magnitude data, a moving average is applied.

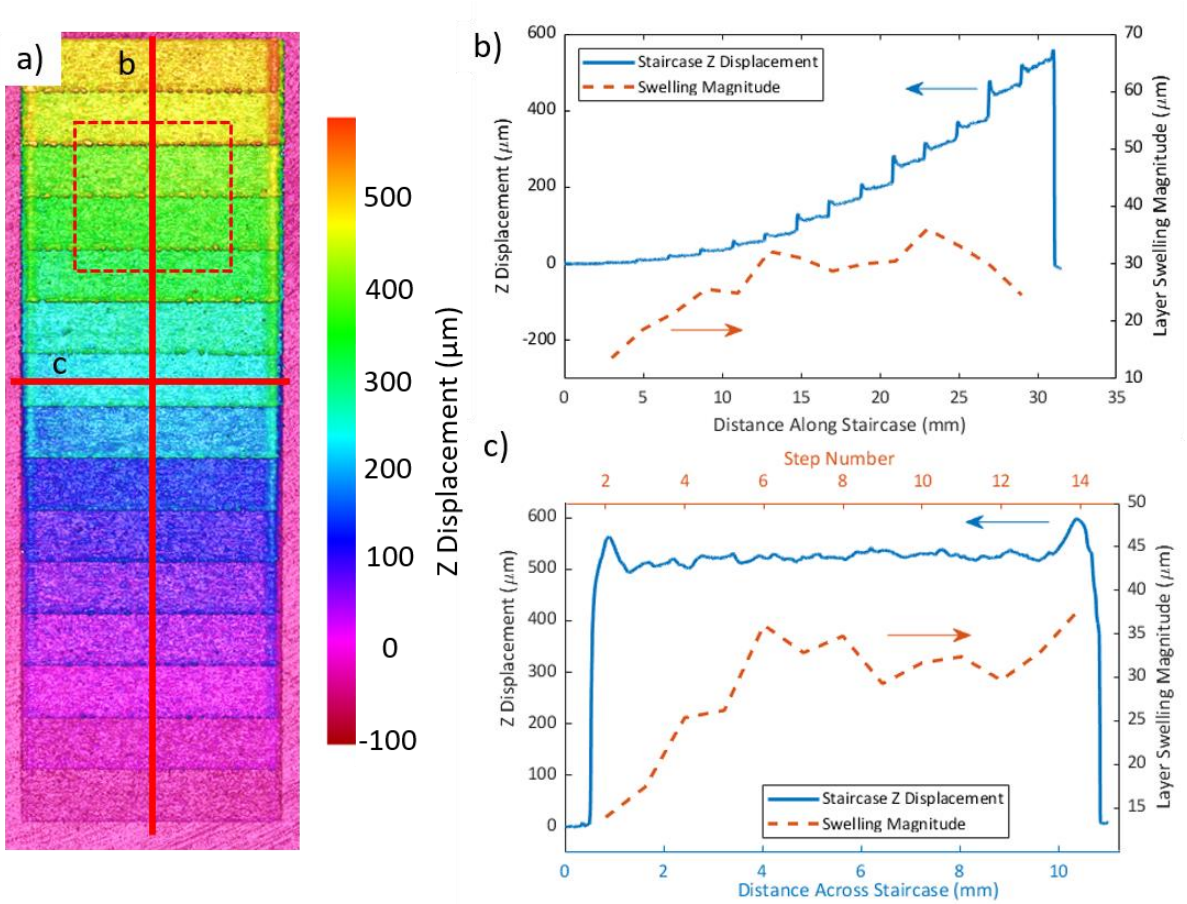

Figure 6-24: Staircase printed with powder. a) Z map, lines marked b and c show where the profiles in subsequent subfigures are taken. Dashed square enlarged in Figure 6-25

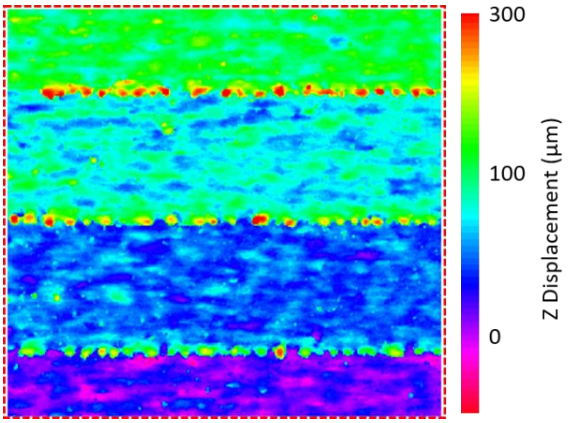

Figure 6-25: Enlarged region from Figure 6-24. 3 horizontal regions of balling can be seen; one at the bottom of each step

In Figure 6-24b, there is an initial rise in swelling magnitude over the first 10-15 mm of the staircase length. Other than this, the swelling magnitude varies between 25-40 µm with no clear trend. Figure 6-24c shows that swelling exists perpendicular to the hatch direction (along the y direction); blue line shows a representative profile. A similar profile was taken for each step of the ladder and the resulting swelling magnitudes are plotted in orange. This swelling has a similar range of magnitudes to Figure 6-24b, but increases with staircase height.

The staircases were scanned in the X direction, starting at minimum Y (at the bottom in Figure 6-24a). Because of heat accumulation, the last steps are hotter (Figure 6-20), but there isn't a

noticeable increase in pyrometry signal within each layer. This may be because of the small height of the part, allowing for quick conduction into the baseplate.

Identical measurements were taken for a laser scanning a staircase without any powder on the baseplate. As seen in Figure 6-26, there are no noticeable height differences apart from along the long edges of the staircase (y direction). The blue line in Figure 6-26b shows that discontinuities exist along the length of the staircase (y direction), but the swelling magnitude (orange line) is limited to ± 5 µm, similar to the surface roughness of the cubes. In a profile along the x direction (Figure 6-26c), it can be seen that swelling exists at the hatch ends, where the laser switches on and off. The magnitude of this swelling is observed to increase with staircase height. A maximum swelling of 35 µm is recorded with no powder present, so this must be due to melt pool dynamics rather than denudation.

The staircases were repeated with the new laser on delay. The magnitude of swelling in the y direction was measured for each staircase and the results summarised in Table 6-11 (equivalent to the orange lines in Figure 6-24c & Figure 6-26c). Table 6-11 shows that with powder, there is no change in swelling when the delay parameters are changed. Scanning without powder there is a significant decrease in swelling with the new laser delay parameters.

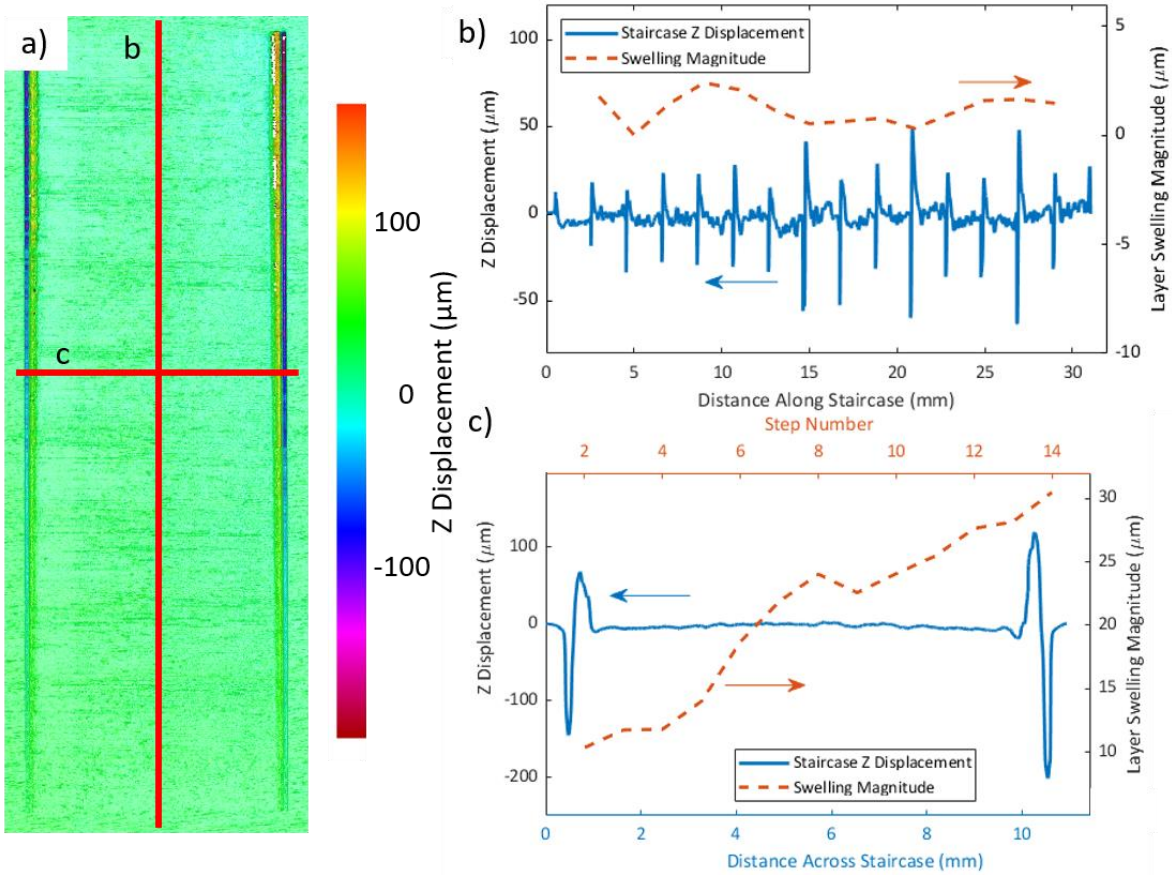

Figure 6-26: Staircase printed without powder. a) Z map, lines marked b and c show where the profiles in subsequent subfigures are taken. b) Profile along the length of the staircase, as marked in a, showing magnitude of swelling. c) Profile across the width of the staircase, as marked in a, showing magnitude of swelling

Table 6-11: Comparison of measured swelling between old and new delay parameters, showing standard errors

	Average Swelling (μm)	
	Old Delay Parameters	**New Delay Parameters**
With Powder	36.3 ± 3.1	36.4 ± 3.2
Without Powder	22.0 ± 1.8	14.8 ± 0.9

6.3.7. **Powder Layer Thickness**

The height of each ladder step was measured for the ladders with new delays (e.g. from Figure 6-24b), since the build plate was lowered by 30 μm between layers, a powder thickness for each layer can be calculated. These are shown in Figure 6-27a, the powder thickness rising from 30 μm to 120 μm over the course of 10 layers. The measured build heights are also shown to increase from 10 μm to a steady state of 30 μm over the first 8 layers.

Both sets of curves in Figure 6-27a show a predicted thickness/height – this is calculated using a 30 μm layer and assuming a powder packing density of 25% (i.e. 4:1 ratio of powder thickness to build height), using $\delta_n = \delta_{layer\ thickness} + \delta_{n-1}(1-\rho)$ [260]. Where δ_n is the powder layer thickness of layer n, δ_n is the layer thickness after n layers, $\delta_{\text{layer thickness}}$ is the set layer thickness and ρ is the powder packing density. The build height assumes full powder capture, so is found by multiplying the current powder layer thickness by the powder packing density.

The squares printed with multiple powder thicknesses were measured to get build heights, these heights are shown in Figure 6-27b. A build height of 30 μm is marked as this is the desired build thickness and can be related to a powder layer thickness of 121.5 μm.

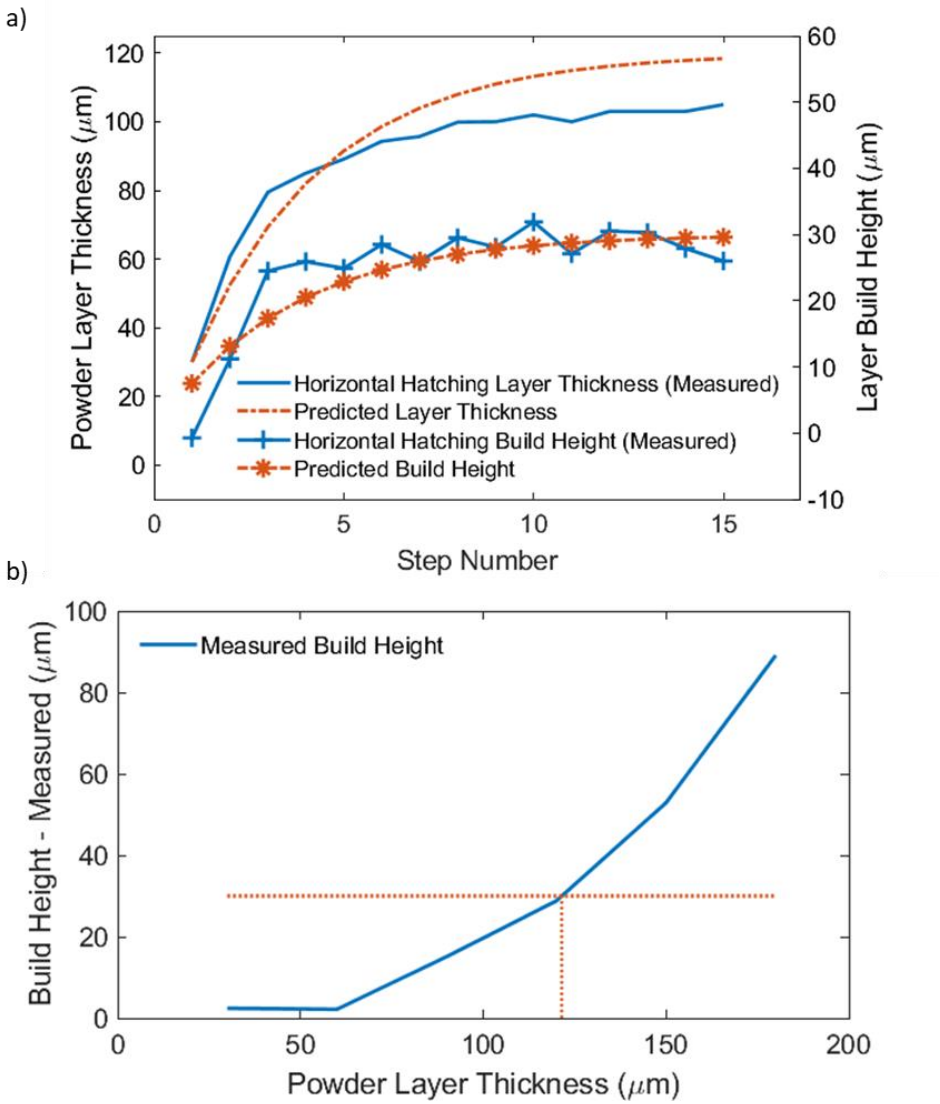

Figure 6-27: Analysis of powder layer thickness and build height; a) Changes in powder layer thickness and build height as a function of layer number b) Build heights measured when exposing set layer thicknesses to a single square hatching

6.4. Discussion

6.4.1. Melt Pool Modelling and Porosity

Simple weld tracks, printed on a bulk material (without powder) is the simplest scenario, equivalent to welding – for which much work has been conducted. Since this is the case for which the point heat source model was created, it should be fairly accurate as long as the absorptivity values are known. Unfortunately this is not a simple value to measure, so a value of 0.45 was used consistently [274].

Figure 6-12b shows the desired weld track geometry, in conduction mode – relatively wide (80 μm) and deeper than a layer thickness (41 μm). Figure 6-12a shows a keyhole shape, which has much deeper penetration, but at the risk of introducing porosity. For this reason, keyholes are widely avoided in L-PBF. The term "keyhole" has no consistent definition, with some defining it as any melt pool deeper than it is wide, others requiring depth to be double the width. Finally, Figure 6-12c shows an unstable weld track, which seems to have experienced balling and so has a 'w' shape; this unevenness in surface increases the propensity to lack of fusion porosity, as there are many small gaps which are difficult to fill.

Point heat source predictions of weld track dimensions (Figure 6-13) generally show similar trends to those measured. Keyhole depth is anomalous, so removing these points, both models closely follow the experimental results, with the Gaussian heat source model matching better – especially at low NE. The point heat source model experiences an infinite temperature spike; as a result, the power distribution through the rest of the melt pool is reduced and so depth is underestimated. The Gaussian heat source model matches the actual laser more closely so yields more accurate results. By adjusting the absorptivity, a much better fitting could be achieved. The keyholing threshold is found to be around $\frac{\Delta H}{h_s} \approx 10$, roughly matching literature [84].

The weld track widths modelled by both heat sources have a similar trend, with the point heat source being closer to the experimental values. The point source underestimates, because of the increased energy absorption at the laser spot, where infinite temperatures are reached. Again, the accuracy could be improved by adjusting the absorptivity. Figure 6-28 compares the weld track dimensions measured (for Inconel 718) with those from literature (for 316L Steel); the same trends are observed and the dimensions comparable – confirming the similarity in the thermal properties between steel and nickel alloys (further compared in Table 10-1). The weld tracks were scanned without powder; when modelling the L-PBF process, powder is present, which is likely to increase absorptivity [38]. This increase isn't known, so the models were rerun for the printed samples, using the previous absorptivity value of 0.45 (Table 6-9). For each set of parameters, the Gaussian heat source depth and the point heat source width were calculated, as these were most accurate; these are compared with porosity values for different hatch spacings. Several builds failed as a result of overheating and are marked N/A, so no porosity values were obtained.

Table 6-9 allows for an attempt at rationalising the origins of lack of fusion porosity. There are three parameter sets which would predict a layer depth of ≤30 μm (layer thickness), which are: 80 W, 1200 mm/s; 80 W, 1500 mm/s and 110 W, 1500 mm/s. All of these result in porosity values of at least 0.2 %, with the shallowest predicted melt pool experiencing at least 3.5 % porosity. Further, looking at the widths predicted by the point heat source, the same 3 parameter sets are predicted to have melt pools less than 60 μm wide. For each, there is at least a doubling in porosity between a 45 μm hatch and a 60 μm hatch. These correlations imply that if absorptivity could be

better known, using a simple point heat source model, a rough processing window could be developed to minimise the lack of fusion porosity. Bajaj et al. [276] calculated the threshold layer thickness, above which, the melt pool wouldn't fully penetrate and would causing lack of fusion porosity (taking into account lateral overlap). For a 30 µm hatch spacing, the melt pools would be deep enough to overlap fully; however, for 45 µm and 60 µm hatch spacings, the melt pool might not be sufficiently deep, which explains why they experience more porosity (Table 6-9).

Inconel 718 is regarded as a printable alloy since it is relatively straight forward to produce a nominally fully dense component by AM that is free of anomalous features such as cracks [4]. This is confirmed in Figure 6-18; cubes with densities over 99.5 % were produced with NE varying by a factor of 2. Higher energy densities produced hotter printing conditions as shown by the pyrometry signal. The mechanical properties are dependent on the thermal conditions experienced, so a range of properties can theoretically be achieved whilst maintaining full density.

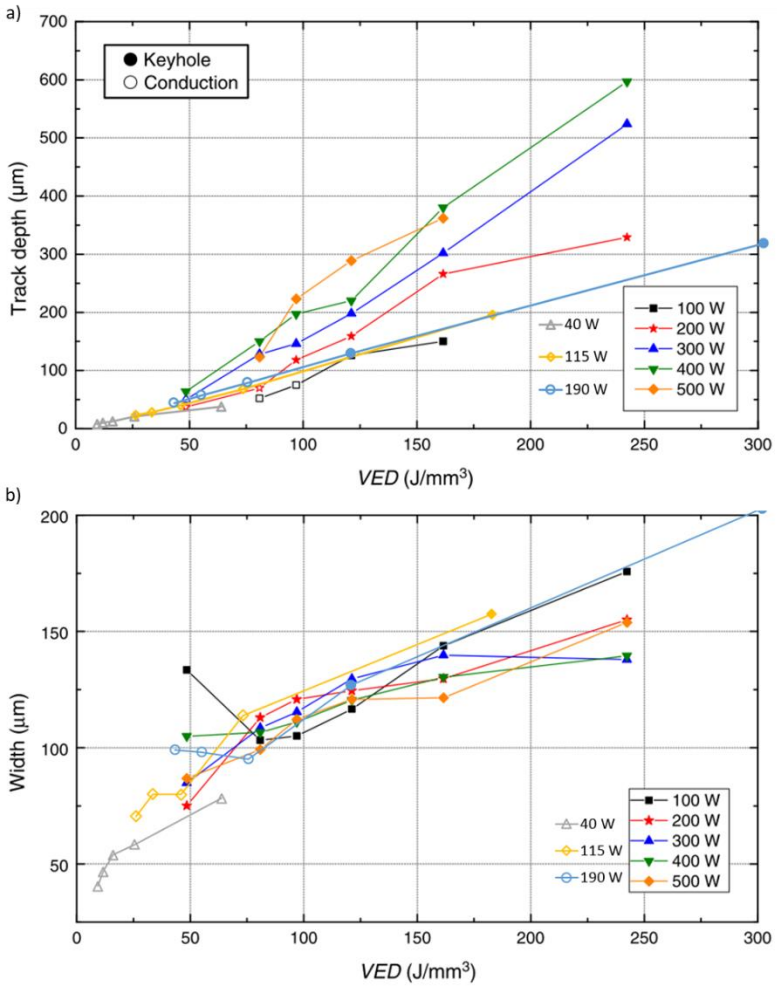

Figure 6-28: Inconel 718 weld track dimensions plotted against literature values for 316L steel; a) weld track depth, b) weld track width. Adapted from Scipioni Bertoli et al [81]

These densities have been plotted on the NED processing map, developed by Thomas et al. [82] in Figure 6-29. The densest samples cluster nicely, generally following the $E_0^* = 4$ line, however as hatch spacing decreases (1/h* increases), samples failed to build due to overheating as a result of increased melt pool overlap. As E* is reduced, porosity increases, as predicted by the processing diagram. Since NED (Equation 2-9) is effectively a volumetric energy density (Equation 2-6), $E_0^* \propto \frac{P}{vlh}$, it would be expected that temperature would scale with it as shown in Figure 6-18a.

Interestingly, plotting the same data against the NE (Equation 2-10), as shown in Figure 6-18b, actually gives a better fit, despite hatch spacing being omitted. Clearly, the hatch spacing does matter, as this has been shown to affect the porosity levels (Table 6-9), so the conclusion must be drawn that there is not yet a simple way to condense all processing parameters into a single value. Once again, the desire to oversimplify the process has resulted in inaccurate energy density calculations and so if these are used for process development, errors will be introduced.

This suggests that NE actually models the process more closely than NED. R^2 values of trendlines for both porosity and pyrometry are higher for NE than for NED, which was developed for experimental design. Neither NE and NED are perfect, they are however very useful for exploring the process window; NED can be calculated to compare initial experimental designs and finding the rough processing window. Once a processing window is defined, NE can be used to interrogate the physics and avoid defects such as keyholes.

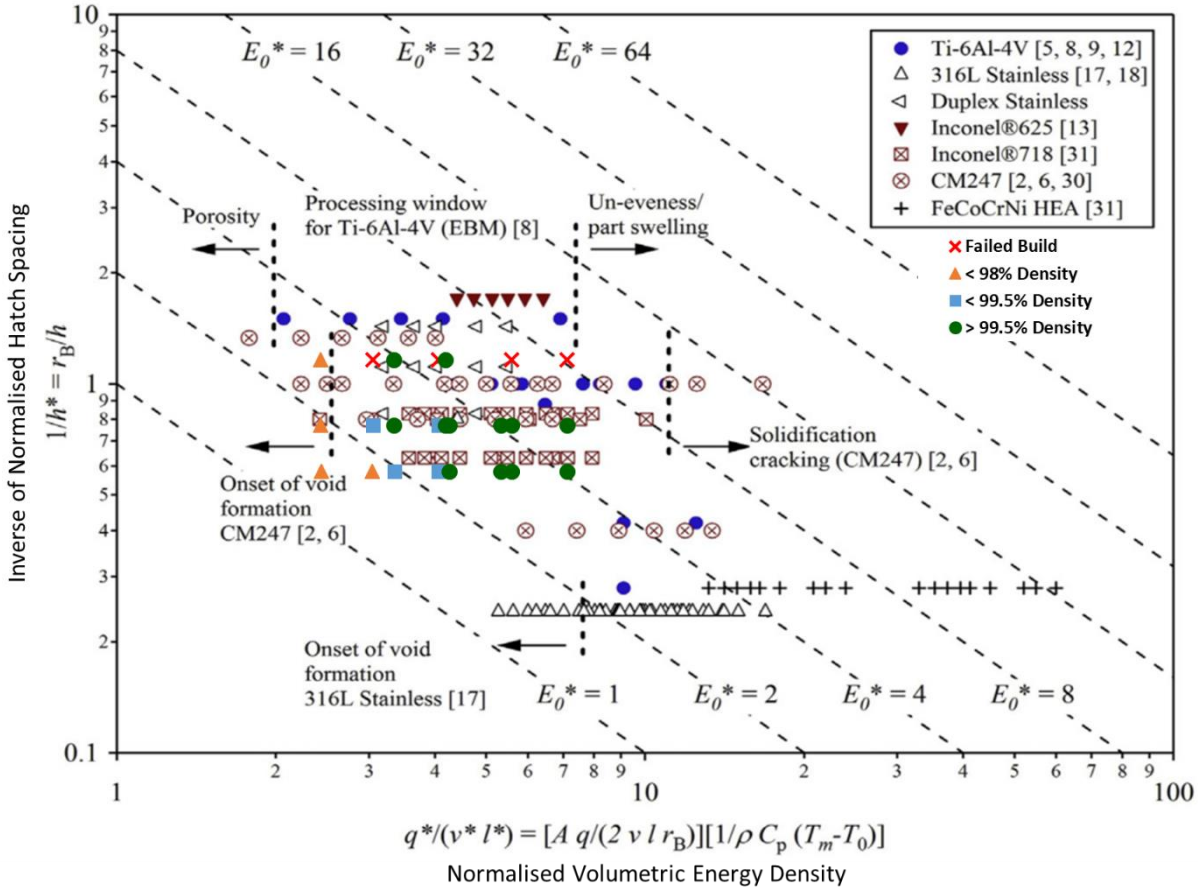

Figure 6-29: 27 sets of processing parameters overlaid on a normalised processing diagram by Thomas et al. [82]. *Different markers differentiate between cube densities*

Figure 6-30a, b show the processing parameters required to keep the melt pool area and the thermal intensity constant – for each, 6 values are shown with 4-6 sets of parameters for each [277]. This is a perfect dataset to evaluate the accuracy of both NED and NE. For each point, both $\frac{P}{v}$ (NED) and $\frac{P}{\sqrt{v}}$ (NE) were calculated. For each line of constant area/intensity, the standard deviation (as a percentage of the average value) of both $\frac{P}{v}$ and $\frac{P}{\sqrt{v}}$ were calculated, these are plotted in Figure 6-30c and Figure 6-30d respectively. It can be clearly seen that the standard deviation of NE is much lower, this was calculated as being 5x lower than that for the NED. This confirms that for L-PBF, NE is a more accurate measure than NED.

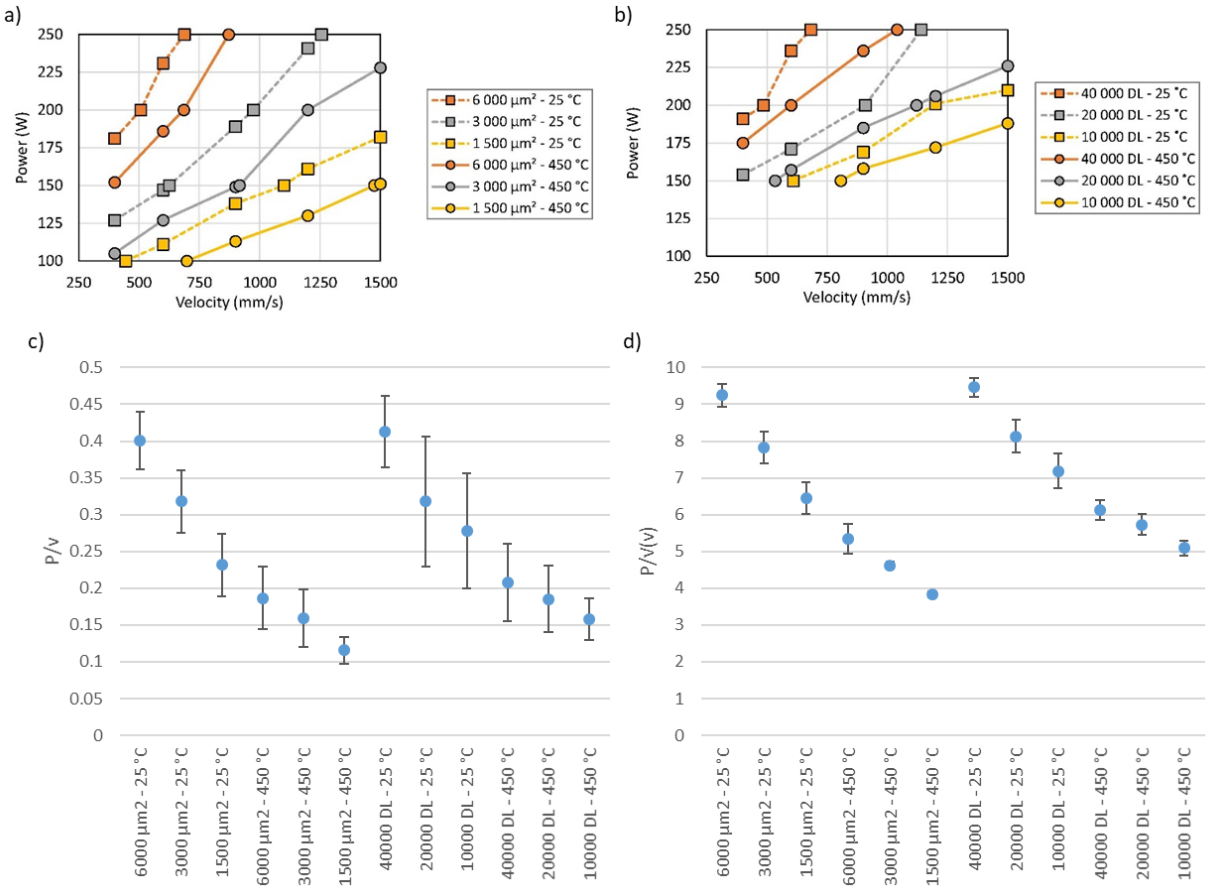

Figure 6-30: Processing maps from literature, showing parameters required to keep a) constant melt pool area (YZ), b) constant thermal intensity. Each line shows parameters leading to constant values in Ti-6Al-4V, reported by Fisher et al [277]*. c) P/v calculated for each line; d) P/√v calculated for each line; c, d) error bars show standard deviation*

6.4.2. **Pyrometry**

The output of the pyrometer on the Aconity3D Mini is a value in mV. The pyrometry is recorded throughout the build, even when the laser is off and moving between components. At these times, the pyrometry signal reduces to its baseline value, which is roughly 820 mV, however, even when the laser is off, pyrometry readings of up to 1000 mV are occasionally recorded. The pyrometry signal for a single layer of a component is shown in Figure 6-14. Since hatching rotates by 67 ° between each layer, the first few hatches are normally shorter than subsequent hatches, as shown diagrammatically in Figure 6-10. The high frequency of pyrometry recording (100 kHz) means that there is sufficient resolution to clearly see the length of each hatch and there's a large amount of pyrometry variation within each hatch. However, the noise associated with this data is very high, it could be argued that having less noisy data at a lower frequency would be better overall. Once again, a simpler, less data-heavy approach seems to contain the vast majority of the useful information.

Figure 6-15 shows the pyrometry signal for the same component, but averaged layer-by-layer. In total, 2.3 GB of pyrometry data was saved for the single component (20 x 8 x 10 mm), but realistically, Figure 6-15a seems to show sufficient data regarding the thermal trends of the component. Figure 6-15b shows the first 50 layers of this build and a clear temperature build up can be seen over the first 7-8 layers (210 – 240 µm). This correlates with results seen in literature, temperature increases with build duration until a plateau is reached. Further, a thermal oscillation can be seen, there are 7 of these oscillations seen between layer 8 and layer 46, leading to a

wavelength of 5.43 layers. Since the scan strategy rotates by 67 ° between layers, it takes 5.37 layers for a full rotation of 360 °. This is clearly shown in Figure 6-15c, where the pyrometry signal is seen to have a 180 ° periodicity when plotted against hatching angle.

A slight variation of temperature would be expected with hatch angle, as scanning along a component edge would have a much longer return time than scanning a corner at an angle. However, this would be expected to have a 90 ° periodicity. Attempts were made to align the pyrometer centrally with the melt pool by maximising the pyrometry readings. It seems that there remains a directionality effect on the pyrometry e.g. scanning in +ve x would result in a different pyrometry signal to scanning in the +ve y. This raises doubts of the reliability of the pyrometry signal. In addition, the high noise levels make data processing very difficult, especially if we were to attempt to analyse phenomena at the limit of the temporal resolution.

General pyrometry signal trends can be analysed by averaging the signal per layer, removing the high frequency noise. The intensity variation with hatch angle still remains, as seen in the regular oscillations in the wider components in Figure 6-17b. It is interesting to see that pyrometry signal increases with component width up until a maximum at a width of 2-3 mm. There is a slight decrease in pyrometry signal and then from 5 mm upwards, there seems to be a constant pyrometry signal. It is assumed that at this point, the component can be considered as a bulk component and so no further change is visible. As well as the wider walls reaching a higher pyrometry signal, they seem to reach this plateau more quickly (Figure 6-17).

In a previously reported study on L-PBF of Ti-6Al-4V, Zhao et al. [52] tested samples of 1.2, 4 and 7 mm widths. They reported a much larger difference in mechanical properties between the 1.2 mm and the 4 mm samples than between the 4 mm and the 7 mm samples [52]. This reinforces the hypothesis that at sample width above 4 mm, the component can be considered as a bulk component and so the microstructure is fairly stable. Similar samples were also created in EB-PBF, these have a similar trend, but slightly less pronounced [52]. Yu et al. showed that there were changes in both microstructure and mechanical properties between 2 mm and 4 mm wide L-PBF samples [278]. Between these studies, it is shown that (for different materials), there is more change between 1-4 mm than there is between 4-7 mm; this aligns with the findings shown in Figure 6-16.

Inclusion of a capacitor across the signal wires can be used to create a low pass filter. This reduces the noise recorded on the pyrometry data, the difference can be seen in Figure 6-31a and Figure 6-31b. The level of noise is dramatically reduced, making it much easier to differentiate between subsequent hatches; there is also a slight reduction in signal magnitude. The same effect could be achieved computationally, by running a low pass filter over the data after recording, before any further processing. If this pyrometry were to be used in process control, having a physical low pass filter (using a capacitor) would be preferential, as it would reduce the computational load required for live execution.

Additionally, the recording frequency of the pyrometer is so high that the resolution of the galvanometer becomes the limiting factor. The recorded data has several pyrometry values at each combination of X/Y coordinates, the exact location of which cannot be resolved. Having such high resolution could be useful if attempting to detect individual pores or defects, but as a macro-scale monitoring technique, such large data quantities make live processing infeasible.

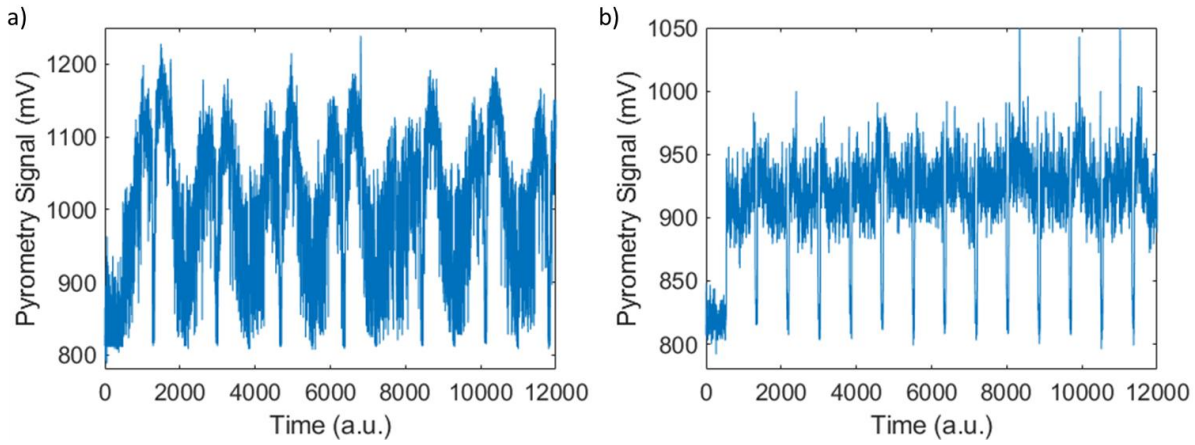

Figure 6-31: Pyrometry signal noise comparison, showing a) raw data, b) with physical low pass filter installed

6.4.3. **Modelling of L-PBF**

The results from the Netfabb Simulation (Figure 6-22) visually resemble the height maps for a printed part (Figure 6-19), suggesting that the simulation is accurately capturing the swelling phenomena which are occurring. In addition, Figure 6-23 shows the other modelling outputs available. The interlayer temperature scales linearly with NE; if the temperature just before recoating is higher, it can be assumed that the temperature during the process is also hotter. Given that the same trend is seen between the pyrometry signal and NE (Figure 6-18a) as with interlayer temperature (Figure 6-23), our confidence in the global trends recorded by the pyrometer is increased. Additionally, a higher N is shown to correlate with increased hot-spot volume and with decreasing lack of fusion volume. These are the trends which would be expected, and the lack of fusion drops to negligible amounts at values of NE above 3, matching experimental results in Figure 6-18a.

In this work, the surface roughness of the built cubes, S_a, was measured to be 7.2 µm (sample 14). Surface roughness values reported in literature, R_a, can be as high as 25-30 µm [248]. This is approximately the thickness of a single layer of powder. Given the powder size range used (15-45 µm), and a powder layer thickness of 30 µm, it is unrealistic to expect geometric accuracy better than 30 µm. Acknowledging this, a new swelling threshold of 30 µm is defined.

The maximum swelling predicted by the Netfabb simulation was 25.3 µm, this was corner swelling of a failed parameter set. Of the parameters which built successfully, the maximum value of corner swelling was 15.3 µm, and edge swelling was 8.8 µm. These are both much lower than the newly defined swelling threshold, so deformation due to plastic strain can be discounted as a key swelling mechanism in the printed cubes. Interestingly, the ratio of corner to edge swelling predicted was 1.75 which was similar to the measured value of 1.88. Unfortunately, since this deformation is as a result of plastic strain imposed by the thermal conditions, it is inherent to the process. It may be possible to reduce the magnitude of swelling by fine-tuning parameters; however, some plastic strain will always be present. Comparing the swelling values between those simulated by Netfabb and those measured using the Alicona (Figure 6-21c) reveals that the simulated swelling is over an order of magnitude smaller than those measured experimentally, with a very strong correlation (R^2=0.91).

Additionally, thickness of the powder layer increases significantly over the first 10 layers, from 30 µm (the set layer height) up to 125 µm as shown in Figure 6-27. The powder layer thicknesses plateau at 110-125 µm (3.7-4.2 times the layer thickness). This is similar to values observed in

literature, which state 4-5.5 times and most of the increase occurs in the first 7 layers, with a plateau after 10 layers [240,259,260]. By modelling this powder layer development [260], a powder packing density of 25% creates graphs which almost perfectly match our experimental results. This seems rather low, as the powder packing in L-PBF is typically assumed to be of the order of 50% [259,279]. Part of this discrepancy could be because of powder spatter, if 15-20 % of the powder is assumed to be spattered away and hence not melted [259] this increases our powder density to 31 % which is closer to that expected. Since some defects are sensitive to powder layer thickness e.g. lack of fusion porosity [280] and reduced dimensional accuracy [281], this powder thickness effect should be taken into account in future modelling.

6.4.4. Denudation Visualisation

The denudation swelling mechanism is inherent to L-PBF. The first hatch is always printed onto a full layer of unconsolidated powder and subsequent hatches scan regions with less powder as a result of the powder having been blown away. The magnitude of the swelling experienced is determined by the difference between the layer thicknesses being scanned in neighbouring hatches. As reported in literature, scanning thicker powder layers is likely to result in balling [249], this explains why the denudation swelling in Figure 6-25 has a humped morphology.

In the staircase printed with powder (Figure 6-24), swelling as a result of the denudation mechanism is observed at the bottom of each step and the magnitude of swelling increases over the first few layers. This is because the powder layer thickness increases over the first 5-10 layers until a steady state is reached when the consolidated layer thickness is equal to the layer thickness required. After 5 layers have printed, the swelling magnitude plateaus at approximately 30 μm. This corresponds well with values reported in the literature and is similar to the new swelling threshold. It is therefore possible that the denudation mechanism is responsible for the swelling observed in the cubes.

Matlab visualisation 1 identifies locations which are predicted to experience the most swelling through the denudation mechanism. Literature finds the denudation zone width to increase with energy density; increasing with power [242] and decreasing with scanning speed [249]. The expected effect of this was tested by running visualisation 1 with denudation widths of 90 μm and 135 μm. Both of these are feasible and a 50% increase was chosen to match the range measured by Matthews et al. [242]. Increasing the denudation width by 50% resulted in a 36% decrease in the swelling magnitude (Table 6-10). A wider denudation zone means that more hatches scan denuded areas, so fewer regions experience swelling. The higher the input energy, the less denudation swelling would be expected; this does not correlate with the experimental measurements shown in Figure 6-21a.

The corner to edge swelling ratio identified by the visualisations (with a 90 μm denudation zone) is 4.11 which is much larger than the measured value of 1.88 (summarised in Table 6-10). Visualisation 1 (denudation swelling only) predicts the swelling at cube corners to be significantly higher than experimentally observed.

6.4.5. Laser Switching Swelling

In Figure 6-24a, the swelling along the x direction has been accounted for by the denudation mechanism, but the swelling along the y direction (perpendicular to the scan direction, Figure 6-24c) was unaccounted for. As the number of layers increased, the swelling in this direction increased from 15-45 μm. The location of this swelling is at the points where the laser switches

either on or off. Simulations [256] and experimental [251] results identified in the literature show that the melt pool is not flat; a vapour depression is present around the laser and the expelled liquid creates a raised region around it. This can be seen in the ends of hatches in Figure 6-8. In the staircases, some regions experience laser switching in several layers which explains why the swelling magnitude increases with number of layers printed.

To isolate the effect of swelling as a result of laser switching, the staircases were scanned without any powder (Figure 6-26). As there is no significant swelling in Figure 6-26b, it can be deduced that, the denudation swelling has been removed. The swelling along the y direction remains even when scanned without powder, so it can be concluded that this swelling is a result of the laser switching on and off –it fulfils the criteria required in Table 6-1. This has been noted on a scan track level, but not considered as a swelling mechanism on a component scale.

Swelling has been reported to occur in similar locations to heat accumulation [143]. However, in this case we can show that in each step, the heat at the start and end is similar (Figure 6-20). Swelling occurs only at the start of each step (Figure 6-24), so heat accumulation does not account for the swelling in the staircases. The edges (parallel to the Y axis) are colder in all steps (Figure 6-20), this could be due to the pyrometer spot capturing cold powder at sample edge; this would artificially decrease the pyrometry signal. This would also be expected to decrease the pyrometry at the top and bottom ends of each step; since this does not occur, it is concluded that the edges of the steps are cooler due to poor synchronisation between the machine movement and the recording of the pyrometer. This time lag means that when the machine is moving, it records the pyrometry from just before the laser turned on, leading to a cold region at the start of each hatch.

The depth of the vapour depression has been shown to be linear with NE; for the experiments in Table 6-8, NE was found to vary between 2.94-6.64. In fitting these numbers to data by Calta et al. [136] and Martin et al. [136], vapour depression depths are expected to vary by a factor of 2. This doubling of depth would contribute to a deeper divot being solidified and so increased surface displacement. It can be concluded that a higher energy input would lead to a more displacement at hatch ends and so an increase in laser switching swelling magnitude.

Visualisation 2 was created to track the laser switching behaviour and determine which regions of a cube are expected to be most affected. In the powder-free staircase, the amount of swelling increased with number of laser switching events. A similar accumulation of swelling is expected to occur in a cube; swelling occurs whether or not powder is present so this swelling mechanism is irrespective of powder layer thickness. Table 6-10 shows that the corner to edge ratio predicted by this model is 1.6, which is much closer to the experimentally measured value of 1.88 than predicted by the denudation model.

As this effect is fully dependant on the behaviour of the laser at the end of the hatch, it may be possible to significantly decrease the swelling magnitude. A new set of delay parameters was selected to force the laser to turn on in the correct location; the improvement in alignment can be seen in Figure 6-8. To test the effect this had on part swelling, the staircases were reprinted with the new delay parameters (Table 6-11). Scanning without powder, the swelling magnitude was reduced by 33% suggesting that, by improving delay parameters, swelling can be reduced. However, once powder is reintroduced, the swelling magnitude did not change when the new delay parameters were used.

Much work is being completed focussing on removing porosity as a result of track imperfections. It can be seen in Figure 6-8a that the track ends have large divots which could be susceptible to keyhole porosity [256]; the offset between the track starts and end increase susceptibility to lack of

fusion porosity. Work by Khairallah et al. indicates that holding the laser stationary at the start of each hatch and ramping down the laser power over the last 100 μs can help remove the occurrence of these frozen divots [254]. This however level of control is not possible on many commercial systems, so a similar effect must be achieved using the available laser parameters. If these settings reduce the divot size, they would be expected to reduce the swelling at hatch ends, so could minimise overall swelling.

6.4.6. Interaction of swelling mechanisms

Both denudation and laser switching have been shown to be mechanisms by which swelling can form in L-PBF. Since they both cause swelling at edges and corners, it is clear that some interaction between the two mechanisms must occur. The corner to edge swelling ratios predicted by the denudation mechanism (visualisation 1, 90 μm denudation width) and the laser switching mechanism (visualisation 2), are 4.11 and 1.60 respectively. In comparison, the swelling ratio of the printed cubes was 1.88, in between the values predicted by the Matlab visualisations.

This reinforces the hypothesis that both swelling mechanisms are present and interact with one another. The corner to edge ratio predicted by visualisation 2 is significantly closer to that of the printed cubes than the radio predicted by visualisation 1. This leads to the notion that laser switching is the dominant swelling mechanism which is surprising given its lack of previous publication.

It has been argued that the denudation mechanism is dependent on the thickness of the powder layer present. Denudation swelling would be expected to occur as described in the first few layers of a build. The powder spreader keeps the top surface of the powder flat. Once swelling starts occurring, the swollen regions (mainly edges and corners) are closer to the level of the powder spreader. If the top surface of the powder is flat, this must mean that the swollen regions have a thinner powder layer than the rest of the sample. The first hatch occurs here, and it will be less prominent because of the reduced powder thickness available for consolidation (denudation swelling is proportional to layer thickness). Once initial swelling occurs, the contribution from denudation swelling would be expected to decrease. This explains why the denudation mechanism plateaus at a swelling magnitude of 30-40 μm in the staircases.

The swelling as a result of laser switching has been shown to increase linearly with number of laser switching events, rising to 40 μm within the 15 layers of the staircase. Laser switching occurs on each layer and is independent of powder layer thickness, this swelling is expected to accumulate more consistently than the denudation swelling. It is hypothesised that in the initial 5-10 layers, the denudation mechanism is significant. However, this is typically only 3-4% of a build, so in a build of full height, the laser switching mechanism will be dominant. This explains why the corner to edge ratio of the printed samples is much closer to the laser switching model than to the denudation model.

The magnitude of swelling has been shown to increase linearly with energy input. A higher energy density would be expected to lead to an increased temperature, which is confirmed by a larger pyrometry signal (Figure 6-18 and Table 6-8). Laser switching swelling is expected to increase with energy input as explained previously. Denudation swelling is expected to decrease with increasing energy input. Experimental results show that swelling increases with energy input. This reinforces the authors conclusion that the laser switching swelling mechanism is dominant.

6.5. Summary

Various different strands of the L-PBF process have been explored in this chapter. It's been shown that simple moving heat source models could be used for initial process map development, and that with measurement of absorptivity values, their accuracy can be improved. Pyrometry has been shown to create phenomenal amounts of noisy data, but it seems like global trends can be trusted, more detailed analysis would, however, be difficult. For process window identification and general component scale monitoring, significantly lower resolution data would suffice and this would likely result in less noisy data.

L-PBF simulation results have qualitatively been shown to be representative of experimental results. However, the numeric values output by the simulations vary significantly from those measured experimentally. AM simulation is in its' early days, with models constantly being improved; currently it seems that results from models should be used qualitatively, but not quantitatively.

A L-PBF swelling mechanism has been discussed, caused by the laser switching on and off at the ends of each hatch. This has been shown to be the dominant mechanism on a component scale, when previously it had only been noted on a single scan level. It is hypothesised that this source of swelling can be minimised through the optimisation of laser ramping parameters.

It has been noted that of the two interacting swelling mechanisms aren't currently incorporated in simulations. Since both swelling mechanisms have been previously observed, visualisations were created to predict which areas will suffer most from both denudation and laser switching related swelling and these could be easily adapted to analyse different geometries. The dependence of the different swelling mechanisms on energy input is proposed, explaining the observed trends. A qualitative explanation of how the two main swelling mechanisms has been given, but further experimentation is required to quantify this.

7. Side-On Thermal Monitoring of 316L Steel in L-DED

Parts of this chapter are taken from the journal paper published in the Additive Manufacturing Journal by Chechik et al. [104], which is permitted under the CC-BY license. The full publication is available at: https://doi.org/10.1016/j.addma.2020.101806

7.1. Introduction

The focus of this chapter is blown powder L-DED of 316L stainless steel. Cooling rates in L-DED are estimated on the order of 10^3-10^4 K/s, with the microstructure being dependent on the cooling rate and the thermal gradient; slight variations in the process or part geometry are unavoidable, which makes it difficult to achieve the high level of microstructural control required [25].

To reduce both time and materials waste when optimising a process, significant effort has been invested in thermal modelling of various laser processes, including welding and L-DED [88,282]. The melt pool width in L-DED is typically 1 mm, much larger than that in other laser AM processes e.g. 0.1 mm in L-PBF [105,283]. Due to the large melt pool size, the maximum heat flow and so the solidification direction lies in the plane tilted between the build direction and the laser movement direction [284,285]. Depending on the laser raster pattern and the processing parameters, this angle is 45-60° above the horizontal [284,286] (this is further explored in Chapter 10). Welding solidification models predict grains to sweep radially from the melt pool edges. With higher input power, these grains get swept along the laser movement direction. Where these sweeping grains from the edges meet, a centreline can be formed [88,287].

In L-DED, this centreline is predicted to contain many small grains with long grains spanning between adjacent laser centre locations [282]; compared to larger epitaxial grains growing out of the back of melt pool centres in L-PBF [93,94]. As velocity is increases in L-DED, the centreline region widens, changing the texture [282]. A strong texture is found in the build plane perpendicular to the laser movement, as explained by elongated grains growing between laser centrelines. Secondary texture is found between the laser movement direction and the build direction, corresponding to the maximum thermal gradients. In a bidirectional raster system, this will lead to a less intense texture, as there are two equally significant crystal directions [286,287]. This phenomenon is commonly referred to as a solidification fibre texture [285,286,288].

Due to the change in heat flow conditions with build height, the cooling rates change and a different microstructure is achieved [289,290]. This variation of mechanical properties with height has been reported through mechanical testing including hardness [149]. Additionally, when subsequent layers are printed, the deposited material is reheated multiple times. This leads to the bulk experiencing similar conditions, but a different microstructure in the final 1-2 mm of the build due to lack of reheating [291]. Aversa et al. [292] measured a variation of Oxygen content throughout the build, generally increasing with height. By building in a N_2 filled chamber, they reduced the Oxygen content by a factor of ~2 when compared to using a local N_2 shielding; this had the effect of increasing yield strength by 12 % [292].

Mechanical properties of a part are controlled by the grain structure e.g. both hardness and elastic modulus vary by 20 % depending on the crystal orientation [178]. Stinville et al. reported hardness

to increase linearly with the anisotropy factor in polycrystalline 316L [178]. Similar findings have been found in another austenitic stainless steel (301LN), with a higher variance [179].

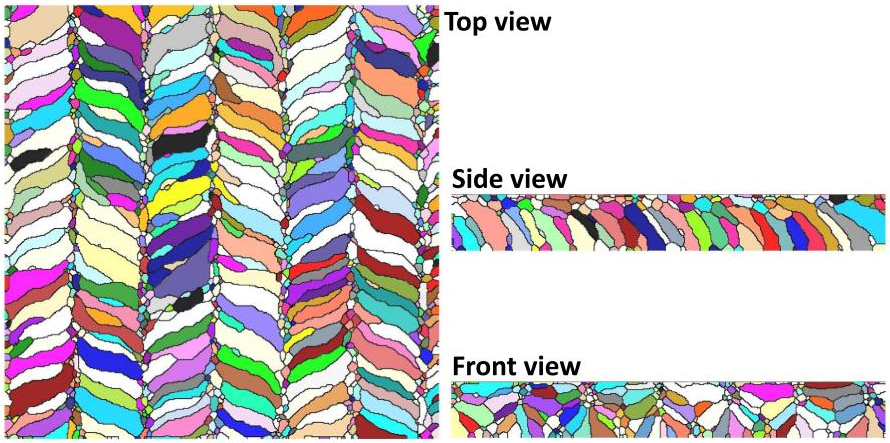

Figure 7-1: Predicted morphology of grain structure for L-DED deposited 304L steel; the higher velocity parameters resulted in finer grains, but in a similar structure. Reported by Li and Soshi [282]

In literature, Schmid factors have been used to correlate hardness to microstructure for a Berkovich indenter. Specific slip plane observations were required, limiting the transferability of this technique, but by combining 6 Schmid factors, a good correlation was achieved (using nanoindentation of individual grains) [293]. Care must be taken when comparing absolute hardness values due to the indentation size effect, which causes measured hardness to decrease as indenter load increases [294]. When macroscopic properties are of interest, larger indents are more representative due to the averaging of multiple grains, although this likely reduces the hardness difference between measurements. To the authors' knowledge, the dependence of hardness on grain orientation has not been extended to areas covering multiple grains by creating cumulative anisotropy factors.

The final microstructure strongly depends on the thermal conditions experienced during solidification; cooling rate being the key factor [4,125,295]. Cooling rate is difficult to measure in-situ, so work has been published relating cooling rate to melt pool dimensions. A linear log-log relationship has been shown between cooling rate and melt pool length in Figure 7-2 [105]. Hence research has focused on measuring melt pool dimensions [296,297] and relating the dimensions to the microstructure [149].

As explained in Section 2.6.1, calibrating temperature accurately is extremely difficult, so measuring melt pool dimensions is not trivial. Common practise is to define an intensity/temperature (uncalibrated) threshold and to use this to extract the melt pool shape; even if not numerically accurate, the correct trends are expected, with larger melt pools leading to slower cooling rates and so coarser microstructure. If we were wanting to monitor the melt pool shape accurately, measuring the melt pool every 10 μm in L-PBF is desired [298], this roughly translates to monitoring at ~100 kHz. For L-DED, the melt pool is an order of magnitude larger, and accounting for the laser velocity, a monitoring rate of ~300 Hz would be desired.

The quantity of data associated with these measurements is phenomenal; for L-PBF, it is estimated that ~75 GB of images would be generated [298]. This is a processable amount, but if storing the raw data for analysis post-build it soon becomes unmanageable; generation of 600 MB/s has been reported [11]. The obvious solution is to process the data live and only save the outputs of this rather than saving the raw data [298,299]; this can reduce data storage requirements by a factor of 10^4 [298]. However, selecting what melt pool properties to calculate is not trivial; melt pool size can

be correlated with cooling rate, but this is not the only factor affecting build quality. Concept Laser save the melt pool area and intensity as well as the laser position; this allows for data recording at 10-50 kHz [299].

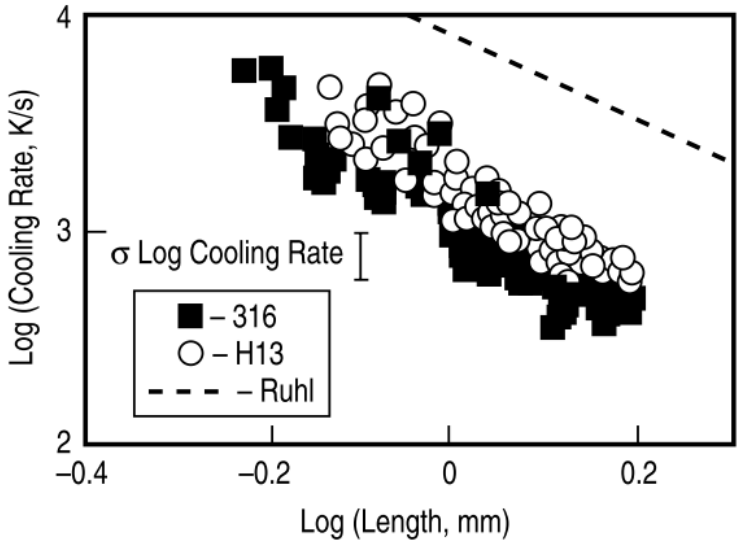

Figure 7-2: Linear relationship shown between the cooling rate and the melt pool length for L-DED (on a log-log plot), error bar shows standard deviation of cooling rate. Reported by Hofmeister et al [105]

The melt pool size and dilution are sensitive to the processing parameters such as power, velocity and mass flow [66]. Increasing power or decreasing velocity typically leads to a larger melt pool [300]. Linear heat input (H) is used as a parameter which encompasses both the laser power and velocity, where linear heat input, $H = P/v$ [4]. Even with a constant H, as the build height increases the heat flow behaviour changes. Conduction to the baseplate is reduced as distance from the baseplate increases, leading to increased melt pool temperature and size through the build [289]. Using coaxial measurement, the melt pool area has been shown to increase by factors of 1.1-3.0 through a build [149,296,300,301]. Changes in the melt pool size lead to dimensional variation in the component [296,297].

Previous work has shown there to be differences in thermal signature when varying processing parameters and through the height of a build. The final mechanical properties are affected, but no direct relationship between the microstructure and mechanical properties has been reported for L-DED. What are the capabilities and limitations of melt pool monitoring in L-DED? In this chapter, the capabilities of different monitoring setups were tested and a wide processing window was probed. The effect of changing the heat input on grain structure was explored and the capabilities of melt pool monitoring were investigated. The feasibility of using coaxial monitoring to predict cooling rate, microstructure and mechanical properties was tested for L-DED.

7.2. Methods

The experimental work was performed on a BeAM Magic 2.0 DED machine using gas atomised 316L stainless steel powder; maintained in the range 6.5-7.5 g/min.

7.2.1. Cylinder Build

A cylinder of 50 mm radius was built on a 4 mm thick stainless steel baseplate. This was built by rotating the table (shown by red arrow in Figure 7-3), so the laser (and melt pool) remained static. A helical scan strategy was used, increasing in Z (height) by 0.22 mm every 360 ° rotation. A height of 36 mm (with a short pause after 15 mm) was built directly onto the baseplate, so the melt pool was not obstructed in the camera view; 17 parameter sets were tested, summarised in Table 7-1. All parameters were built directly on top of the previous, with roughly 8-10 minutes between each parameter set. Example recordings of camera modes in bold (Table 7-1) are available [302], visualised at 25 fps.

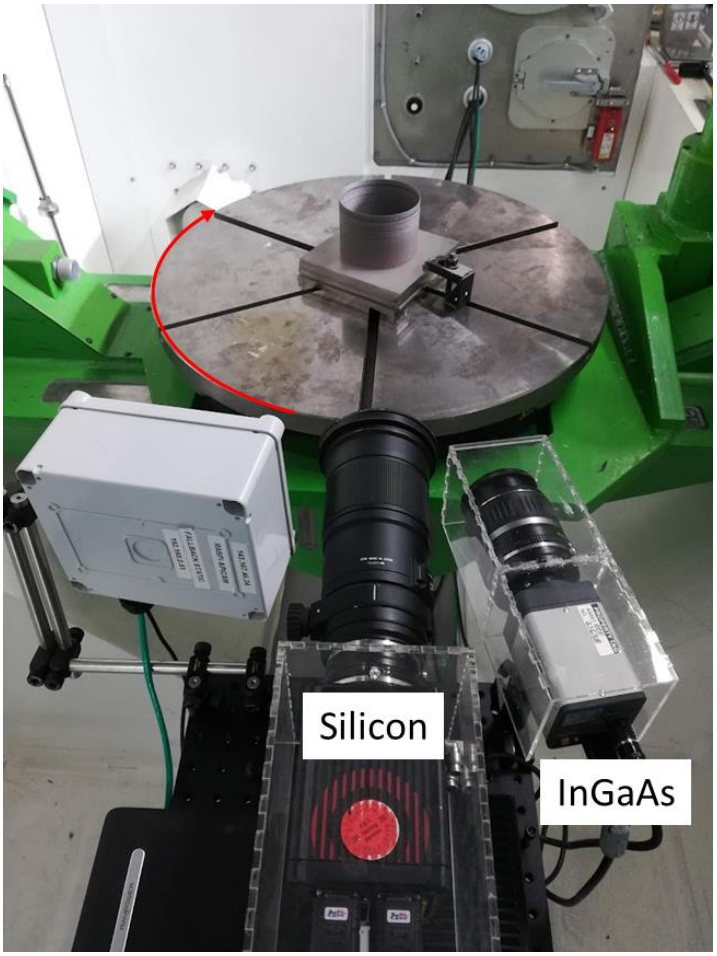

Figure 7-3: Setup of cylinder build; showing table rotation and camera setup

The cylinder was sectioned and a small sector was extracted. This was in essence a thin wall with parameter sets incrementing with height; once mounted and polished, cross sectional images were taken using an Olympus BX51 microscope. Figure 7-4 shows the cross section of two parts of the cylinder; Cyl_8 has a very variable width, whilst the width of Cyl_base is much more consistent. To capture this, both inner and outer widths were measured for each sample, as seen in Figure 7-4, from which both an average width and a standard deviation could be calculated.

Table 7-1: Processing parameters used for cylindrical build; recordings of bold camera modes available [302]

Sample	Power (W)	Velocity (mm/min)	Z Step (mm)	Build height (mm)	Silicon Capture Mode	InGaAs Capture Mode
Cyl_Base	296.8	2000	0.22	36	N/A	N/A
Cyl_1		2000		2.5	Silicon_100	InGaAs_60
Cyl_2		2500		2.5	**Silicon_100**	InGaAs_60
Cyl_3		1500		2.5	Silicon_100	InGaAs_60
Cyl_4		1500		2	Silicon_100	N/A
Cyl_5		1000		1	**Silicon_400**	**InGaAs_60**
Cyl_6		2500		1	**Silicon_400**	**InGaAs_60**
Cyl_7		1750		1	**Silicon_400**	**InGaAs_60**
Cyl_8		1000		2	**Silicon_100**	InGaAs_60
Cyl_9		3000		2	Silicon_100	InGaAs_60
Cyl_10		1750		2	**Silicon_100**	InGaAs_60
Cyl_11		1000		0.5	N/A	N/A
Cyl_12		1000		2.5	N/A	InGaAs_30
Cyl_13		1750		2.5	N/A	InGaAs_30
Cyl_14		2500		2.5	N/A	InGaAs_30
Cyl_15	200	1750		2.5	N/A	**InGaAs_30**
Cyl_16	400			2.5	N/A	**InGaAs_30**
Cyl_17	300			5	N/A	**InGaAs_30**

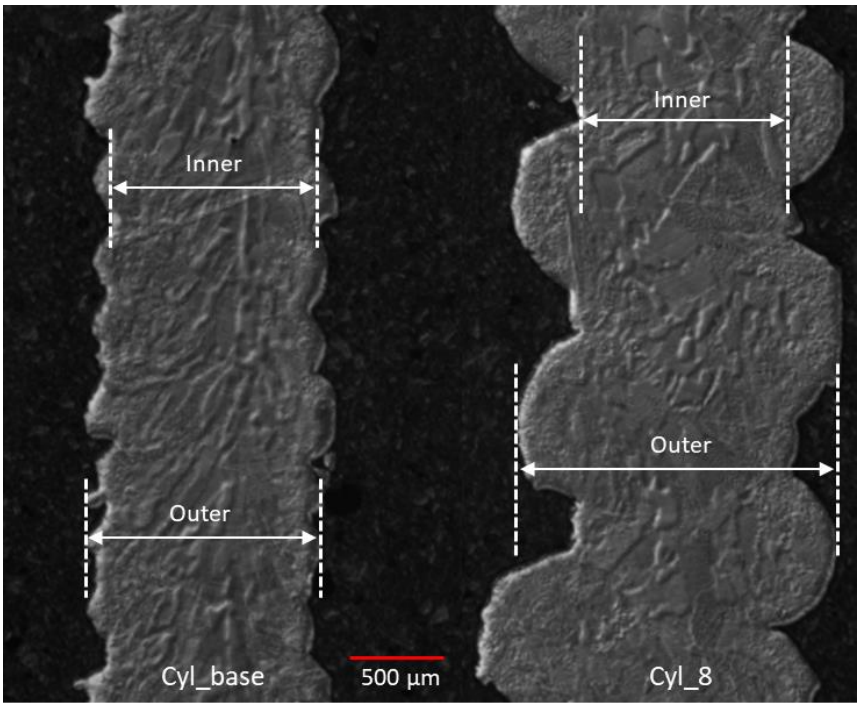

Figure 7-4: Cross sections of Cyl_base and Cyl_8; the measurement of inner and outer wall widths is shown

Hardness indents were taken using a Durascan 70 Vickers indenter with a 1 kg load, with 2 indents taken at each height. 156 indents were taken in total along the full height of the wall, with at least 6 indents per parameter to allow for an uncertainty calculation. Sections of samples Cyl_12, Cyl_13 and Cyl_14 were analysed for their Oxygen content using LECO by AMGSuperalloys.

In-situ monitoring of Cylinders

All samples (excluding Cyl_base) were monitored side-on using a variety of cameras (Figure 7-3). Two cameras were used, a Hamamatsu C12741-03 InGaAs camera [303] (referred to as InGaAs, due to the Indium Gallium Arsenide sensor it contains) and a Hamamatsu Orca-Flash4.0 [111] (referred to as Silicon, due to the Silicon sensor it contains. The Silicon sensor is sensitive to light of 400-1000 nm [111], whilst the InGaAs sensor is sensitive to light of 950-1700 nm [303]. As explained in Section 2.6.1, this longer wavelength allows for measurement of cooler temperatures, as at lower temperatures, the black body emission curve shifts to the right (Figure 2-20). Table 7-2 summarises the different camera setups used to monitor the builds, these capture modes will be referenced throughout this chapter. All images were saved as 16-bit grayscale tif images, calibration of InGaAs_Tele is covered in Section 7.2.2. The set frame rate is specified for each capture mode; some frame rate variability was experienced. Additionally, Table 7-2 shows the pixel resolution of each camera mode, along with the data acquisition rate.

Table 7-2: Summary of various capture modes used to monitor builds

Capture Mode	Frame Rate (fps)	Exposure (ms)	Imaging Region Width, X (px)	Imaging Region Height, Y (px)	Pixel Resolution (µm/px)	Data Acquisition Rate (MB/s)
Silicon_100	100	5.01	2048	1024	13.8	369
Silicon_400	400	2.50	2048	256	13.8	388
InGaAs_60	60	16.7	640	512	198.8	37
InGaAs_30	30	33.3	640	512	198.8	18
InGaAs_Tele	60	16.8	640	256	374.4	18
Aconity_Pyro	100,000	0.009	N/A	N/A	N/A	2-2.5

All image processing was performed using MATLAB R2021b (Mathworks Inc). Figure 7-5 shows example melt pools using various camera modes, with melt pools outlined. The images are greyscale, with the value of each pixel showing the intensity detected by the sensor at that location. E.g. the InGaAs sensor records the intensities as 14-bit values [303], so the maximum possible range of greyscale values is 1-16384 (2^0-2^{14}). Higher values indicate that the sensor received a higher intensity input, but due to the variable quantum efficiency of sensors and the range of wavelengths present, this cannot be easily converted into a temperature (discussed in Section 2.6.1). The variation of emissivity with temperature/phase adds another difficulty, but very generally, a higher temperature will result in a higher greyscale value and a brighter image.

Images using the Silicon sensor have significantly better contrast variation, so melt pool dimensions were identified manually. For the InGaAs sensor, simple image thresholding could be used to plot a melt pool outline. By plotting a bounding box around the melt pool outline, both the length and depth could be calculated.

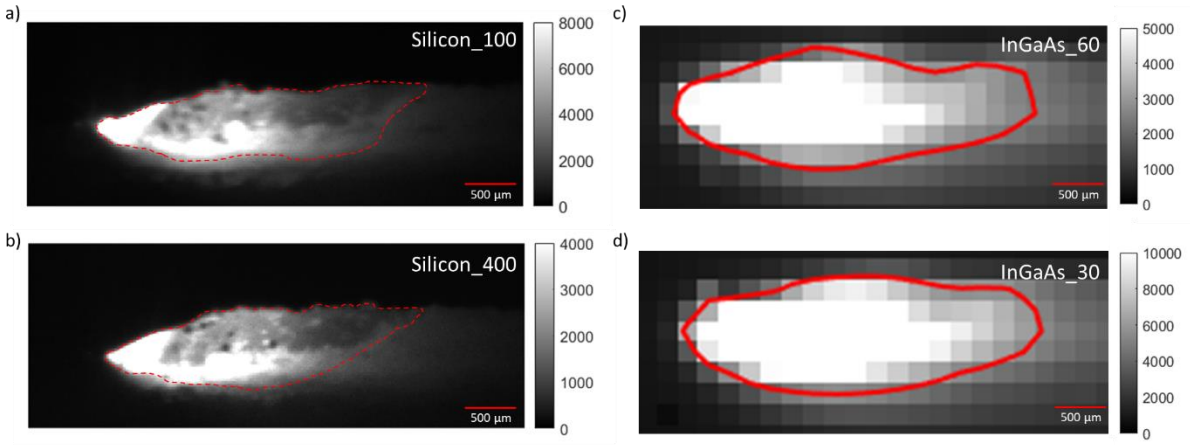

Figure 7-5: Example melt pools using the first 4 capture modes, scale bars show pixel intensity, laser moving right to left. a) melt pool captured using Silicon_100 setup, melt pool manually outlined; b) melt pool captured using Silicon_400 setup, melt pool manually outlined; c) melt pool captured using InGaAs_60 setup, melt pool extracted using a threshold of 2500; d) melt pool captured using InGaAs_30 setup, melt pool extracted using a threshold of 5500. Recordings using all four camera modes available here [302]

7.2.2. Rectangular Walls

Table 7-3 shows the parameters used to deposit 5 rectangular walls on a 4 mm thick 316L baseplate. Two velocities and two powers were used to provide a factor of 2 range in linear heat input (H); Wall A was duplicated to check repeatability. Figure 7-6a shows the geometry of the printed parts; these axes definitions will be used throughout. The walls consisted of 6 bidirectional hatches scanned in the X (laser movement) direction, with 450 µm hatch spacing (in the Y) and 200 µm Z step between layers. 49 layers were printed, with the laser returning to the same start point between layers (3.6 s interlayer time).

Table 7-3: Processing parameters used for rectangular walls

Sample	Power (W)	Velocity (mm/min)	Hatch Spacing (µm)	Z Step (mm)	H (J/mm)
Wall A1	300	2750	450	0.2	6.5
Wall A2		2750			6.5
Wall B		2250			8.0
Wall C	500	2750			10.9
Wall D		2250			13.3

YZ wall sections (defined in Figure 7-6) were polished before hardness was measured using a Durascan 70 Vickers indenter with a 1 kg load (5 s hold). Between 27-30 measurements were taken for each sample, in a 3 x 9/10 array (Y and Z respectively). Polished samples were etched with aqua regia before being analysed optically for porosity using ImageJ.

Electron Backscattered Diffraction (EBSD)

EBSD was performed on polished samples using an FEI Apreo FEG scanning electron microscope. Scans used a 10 µm step size, an accelerating voltage of 20 kV and a probe current of 13 nA. EBSD

scans were in the YZ plane. For walls A1, B, C, D (Table 7-3) scans were taken in the centre (in both Y and Z); Walls A1 and D had further scans taken at the top and bottom (both central in Y).

EBSD scans were cropped to 2 hatches wide (900 μm) and 2 mm tall. Grains were reconstructed with a threshold grain boundary misorientation of 10°, with a minimum of 3 pixels per grain. Grain sizes refer to the equivalent radius calculated from the area of each grain. Schmid factors were calculated in the normal (X) direction.

Thermal Monitoring

The thermal imaging setup consisted of a Hamamatsu C12741-03 InGaAs camera [303] and a Thorlabs MVTC23005 telecentric lens. The use of a telecentric lens afforded a thermal image undistorted by perspective, resulting in an isometric projection of the scene. The exposure was set to 16.7 ms, the frame rate fluctuated in the range 40-60 fps due to data bottlenecks, as summarised for "InGaAs_Tele" in Table 7-2. A series of optical filters was used to achieve a working wavelength range of 1500-1700 nm, giving a radiance temperature range of 595-1635 K. The filters used were 2 Thorlabs NENIR10B OD2 neutral density filters, a Thorlabs FEL1500 1500 nm long pass filter and a Thorlabs NF1064-44 44 nm wide notch filter with a 1064 nm centre wavelength. The notch filter was used to provide extra blocking at the laser wavelengths, to remove any reflected light which would be erroneously measured as thermal emission. A 4 mm acrylic window was also mounted to the front of the lens to protect it from spatter.

The setup was calibrated with a Land Instruments Landcal 1200b blackbody furnace and an Isotech miliK with a UKAS calibrated type R thermocouple. This was accomplished by capturing a series of images of the calibration furnace at approximately 100 K increments between 923K and 1423 K. The Sakuma-Hattori method was then used to fit a model to these calibration temperature points [304]. This model was used to perform the conversion of raw images from the camera in DLs (Digital Levels), into thermal images. The reported images are in radiance temperature, K_{rad} (i.e. temperature assuming a constant emissivity of 1). The radiance temperature is always lower than the actual temperature, but the scaling is non-linear as described by Planks Law.

The decision to use radiance temperature for analysis steps is considered good practise when working with infrared thermal data because of the large uncertainties associated with emissivity calculation [305]. Where required, emissivity can be applied after any analysis steps which will reduce the error in the final value [306]. The emissivity of molten material and material undergoing phase changes during a measurement are especially difficult to calculate. This could be due to impurities in the material or changes in the materials surface such as the forming of oxide layers. This is likely the reason for the wide range of emissivity values seen in literature for similar steels [116,305,307,308].

An emissivity value of 0.14 with an uncertainty of ±0.1 was chosen in this work for sections where it was felt that converting to an absolute temperature was necessary, this is referenced as K_{em} and uncorrected radiance temperatures as K_{rad}. This is lower than values in the literature but was chosen based on obtaining a realistic melt pool size from the images. The comparison between K_{em} and K_{rad} is seen in Figure 7-6d, along with the error in K_{em}, associated with the uncertainty in emissivity.

Thermal images (Figure 7-6b) were further analysed using MATLAB R2019a (Mathworks Inc). The final hatch of each layer was the closest to the camera, this was used to analyse melt pool characteristics. For each layer, a frame was manually identified with the melt pool in the centre of

the last hatch. Thermal data was only captured for 30 % of Wall B, so this will be omitted in further analysis.

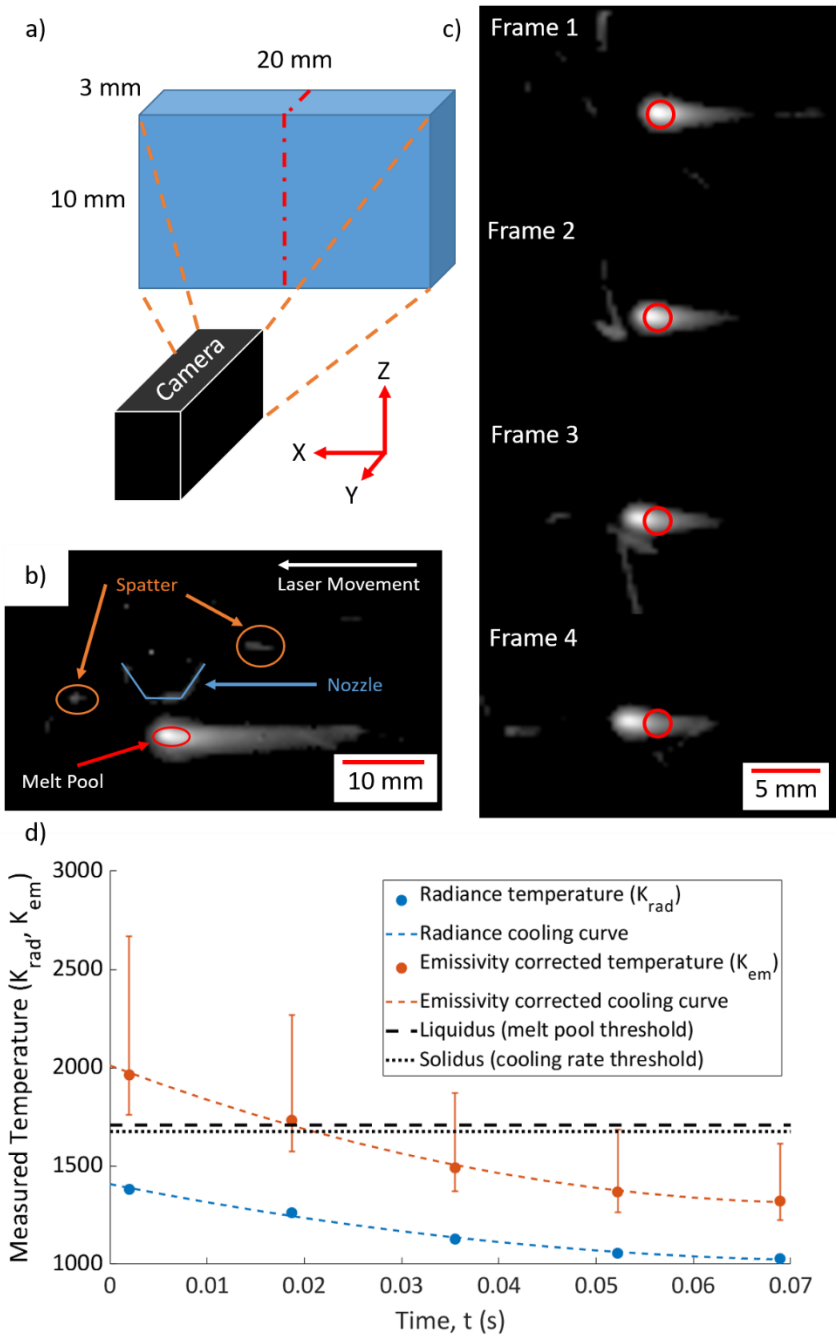

Figure 7-6: L-DED build geometry and calculation of cooling rates; a) Schematic of deposited walls, showing approximate dimensions and axis definitions. b) Representative thermal image showing key features. c,d show extraction of cooling rate. c) time series of images showing same field of view, temperature taken from centre of red circle. d) Schematic of cooling curves comparing radiance temperature (K_{rad}) with emissivity corrected temperature (K_{em}). Error bars show the uncertainty originating from the emissivity value. Cooling rates calculated at emissivity corrected solidus temperature

Melt Pool Dimensions

In the last hatch, the melt pool moves right to left, allowing the depth and length of the melt pool to be measured (Figure 7-6). Since the emissivity (0.14) was selected to ensure that all analysed images captured a melt pool of a realistic size, the emissivity corrected liquidus (1708 K_{em} [309]; 1249 K_{rad}) was used as the melt pool threshold. The melt pool depths calculated with this threshold were 0.88 ± 0.37 mm (standard deviation), similar to the laser diameter.

A contour at the threshold was assumed to be representative of the melt pool. The melt pool area (mm^2), length (mm) and depth (mm) were calculated for each layer. Spatter could be above the melt threshold (Figure 7-6b). To avoid this being counted, only the contour with the longest boundary was selected. With a scaling of 1 px = 0.37 mm, an uncertainty of 0.37 mm is associated with the distance measurements.

Extracting Cooling Rate

To calculate the cooling rate, the centre of the melt pool was found. The location of this pixel was saved along with its temperature. To capture the cooling, the temperature of the same pixel was extracted in subsequent frames (Figure 7-6c). Since the frame rate is known, this results in a plot of temperature against time (Figure 7-6d). The nearest temperature values either side of the solidus (1675 K_{em} [309]; 1231 K_{rad}) were found and a cooling rate was determined by dividing the temperature difference by the time difference. A cooling rate was determined for every layer of every wall. In the case that the recorded temperature never reached the solidus, no cooling rate was recorded.

As the laser passes, a plateau of maximum temperature is often experienced before cooling occurs. At high cooling rates, the maximum temperature may only be experienced in one frame. This peak may be an average of the plateau and the start of cooling, or the end of the heating period overlapping with the plateau. If the peak temperature is used in the cooling rate calculation, the error would be increased as the accuracy of the peak point is unknown. Low H samples experience the lowest peak temperatures, so will have the highest cooling rate errors. Finally, the smallest melt pool depths are 2-3 pixels; the pixel analysed for cooling rate calculation is bound to be near a melt pool edge. Due to melt pool fluctuations, the melt pool may deviate outside the tracked pixel leading to an inaccurate cooling rate.

7.3. Results

7.3.1. Melt Pool Dimensions of Cylinder build

The longer the exposure time of a camera, the further the melt pool will move within a single frame, which can lead to motion blur. Consequently, the most accurate images will be those captured with the shortest exposure, with the best spatial resolution. Referring to Table 7-2, it can be seen that Silicon_400 is the most accurate camera mode, where an image is taken every 73 µm (at 1750 mm/min). An example of this is shown in Figure 7-5b, where melt pool details can be seen, the full recording is available here [302] (Si_400_297_1000). The bottom of the melt pool is brightest, with a darker oxide shell (grey) on top; a few black spots can be seen, which are likely to be (relatively) cool powder particles. Due to the dark nature of the oxide, the melt pool can be seen by eye but cannot be computed using a simple threshold; melt pool dimensions were manually measured and extracted; three measurements were taken for each parameter set and are summarised in Table 7-4.

Table 7-4: Melt pool dimensions extracted from Silicon_400 images; standard deviations shown in brackets

Sample	Power (W)	Velocity (mm/min)	Melt Pool Length (mm)	Melt Pool Depth (mm)
Cyl_5	296.8	1000	3.25 (0.13)	0.83 (0.01)
Cyl_7		1750	3.14 (0.12)	0.62 (0.02)
Cyl_6		2500	1.38 (0.07)	0.28 (0.02)

Due to the longer exposure and lower resolution of the InGaAs modes, automatic thresholding could be used to measure melt pool dimensions. To check for repeatability, Cyl_5 and Cyl_8 (identical parameters) were both recorded using InGaAs_60 and are compared in Figure 7-7. The melt pool dimensions are relatively similar to one another, with variations much smaller than those experienced by varying velocity (Figure 7-8). For the case of InGaAs_60, the melt pool moves 487 µm (at 1750 mm/min) during the capture of each frame.

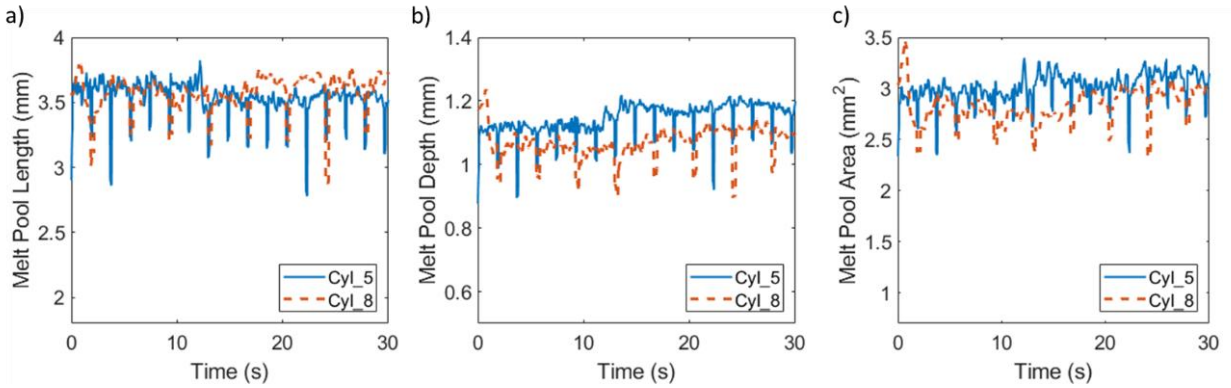

Figure 7-7: Comparison of Cyl_5 and Cyl_8 melt pool dimensions using InGaAs_60; a) melt pool length; b) melt pool depth; c) melt pool area

Melt pool dimensions extracted from InGaAs_60 and InGaAs_30 images are summarised in Figure 7-8 for 3 velocities. Length, depth and area are all similar between the camera modes, with melt pool size decreasing as velocity increases. InGaAs_60 melt pool dimensions experience a drop in melt pool size roughly every 2 secs.

To gain an estimate of the third melt pool dimension, the width of the wall was measured for each set of parameters, as demonstrated in Figure 7-4. Both the inner and outer wall widths were measured and the average width calculated (Table 7-5). The variation of melt pool dimensions with parameters is shown in Figure 7-9, melt pool size generally decreases with increasing velocity and with decreasing power. This is true for both the dimensions from the thermal imagery (Figure 7-9a,c) and for the physical width measurements (Figure 7-9b,d). For the width measurements, errors increase significantly with width; looking at Figure 7-4, for Cyl_8, the large melt pool can be seen which seems to move between two alternative (left and right) positions resulting in a wall with alternating bulges. Looking at the recording of Cyl_16, using 400 W, available: [302], the fluctuation of the melt pool is clearly visible after an initial stable period. This fluctuation causes the variable width and explains the increased variability in the larger melt pools.

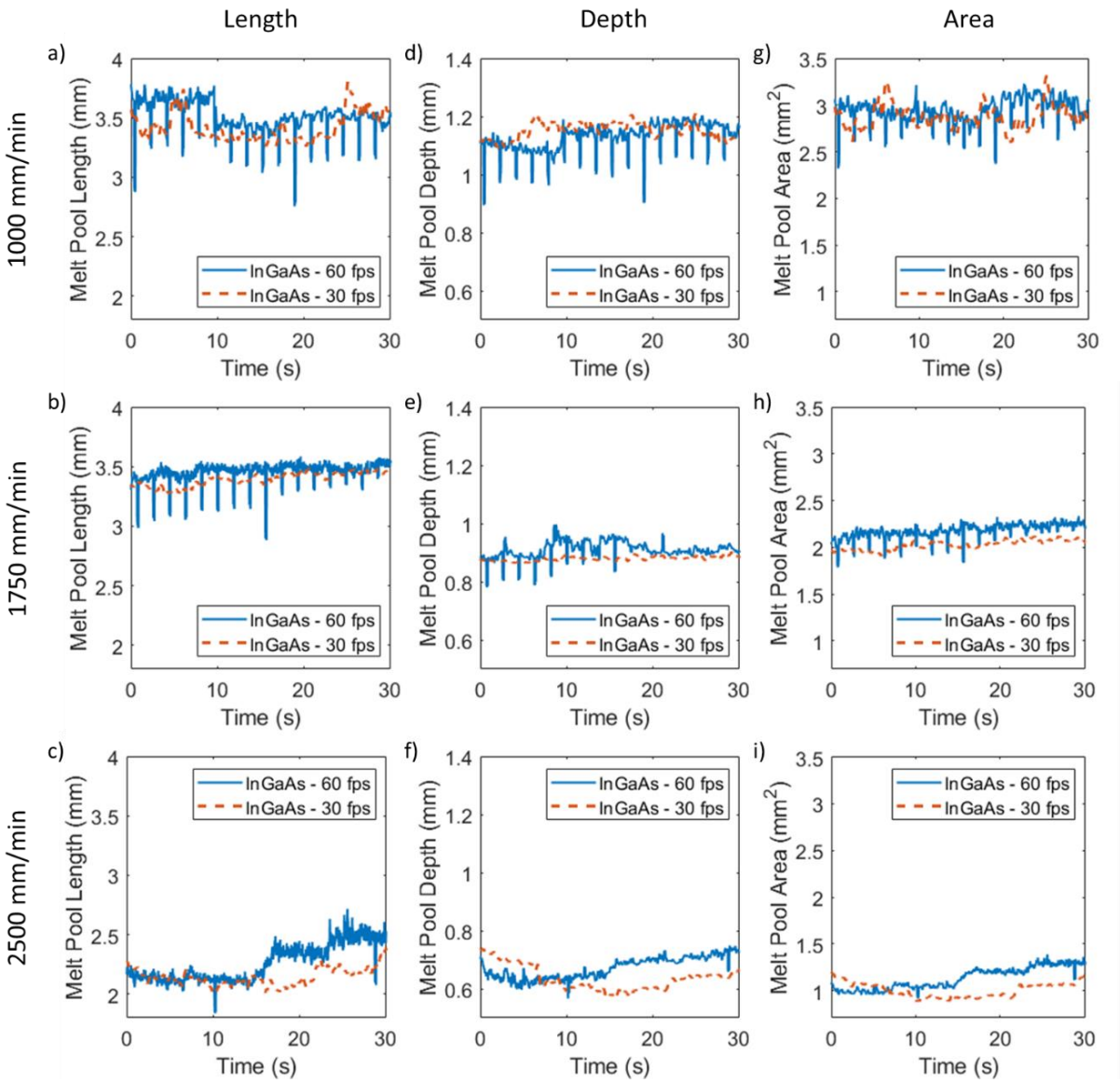

Figure 7-8: Comparison of melt pool dimensions between InGaAs_60 and InGaAs_30 modes. a, b, c) melt pool length; d, e, f) melt pool depth; g, h, i) melt pool area. a, d, e) 1000 mm/min; b, e, h) 1750 mm/min; c, f, h) 2500 mm/min

Table 7-5: Measurement of wall widths for various sets of processing parameters. Inner and outer widths defined in Figure 7-4

Power (W)	Velocity (mm/min)	Inner Width (µm)	Outer Width (µm)	Average Width (µm)	Standard Deviation of Width (µm)
296.8	1000	679	1005	842	177
	1500	644	793	719	93
	1750	667	752	709	49
	2000	616	759	687	79
	2500	625	733	679	63
	3000	625	625	625	0
200	1750	538	680	609	100
300		620	763	692	101
400		642	1038	840	280

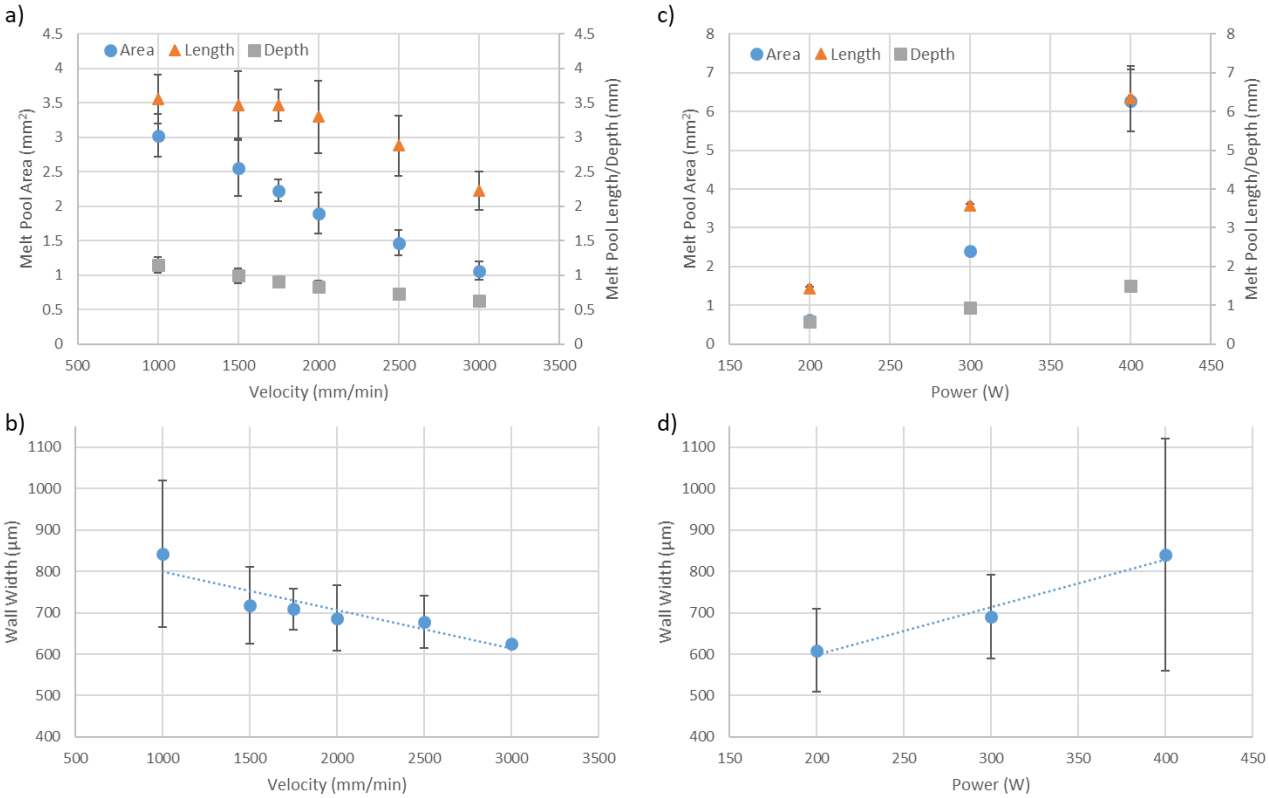

Figure 7-9: Dimensions of melt pool plotted against processing parameters; a, b) varying velocity; c, d) varying power); a, c) area, length and depth as measured using InGaAs_60, averaged over 1000 frames, standard deviations shown; b, d) average wall widths (Table 7-5), standard deviation shown

7.3.2. **Hardness of Cylinder build**

The hardness variation of the initial build (Cyl_base) is shown in Figure 7-10, the hardness is higher near the baseplate, but decreases with distance for roughly 5 mm before settling to a stable value. The black line in Figure 7-10 shows the point where the build was paused, no change in hardness can be seen directly after this. Figure 7-11a shows that hardness increases with velocity, with some hardness error within each velocity set. Figure 7-11b shows the variation of hardness with power,

no obvious trend is visible, but only 3 power values were used. For this reason, only the trends from the velocity variation will be investigated further.

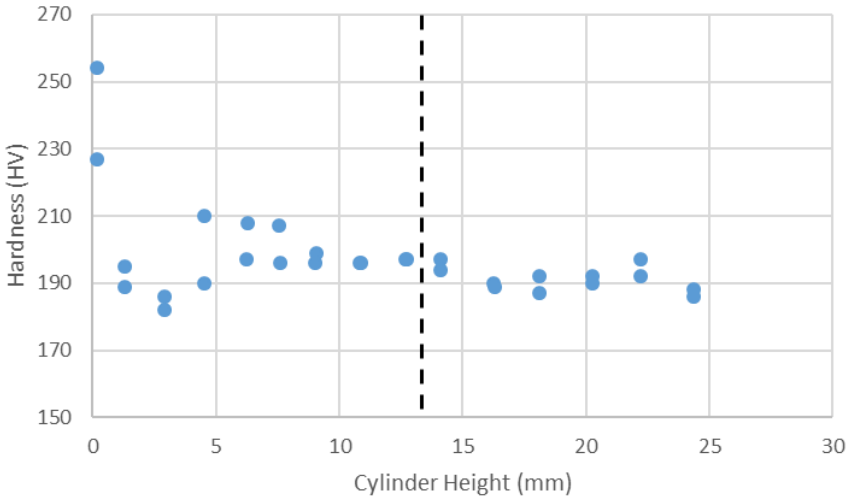

Figure 7-10: Hardness variation with height with Cyl_base parameters. Black dotted line shows the location at which the build was paused

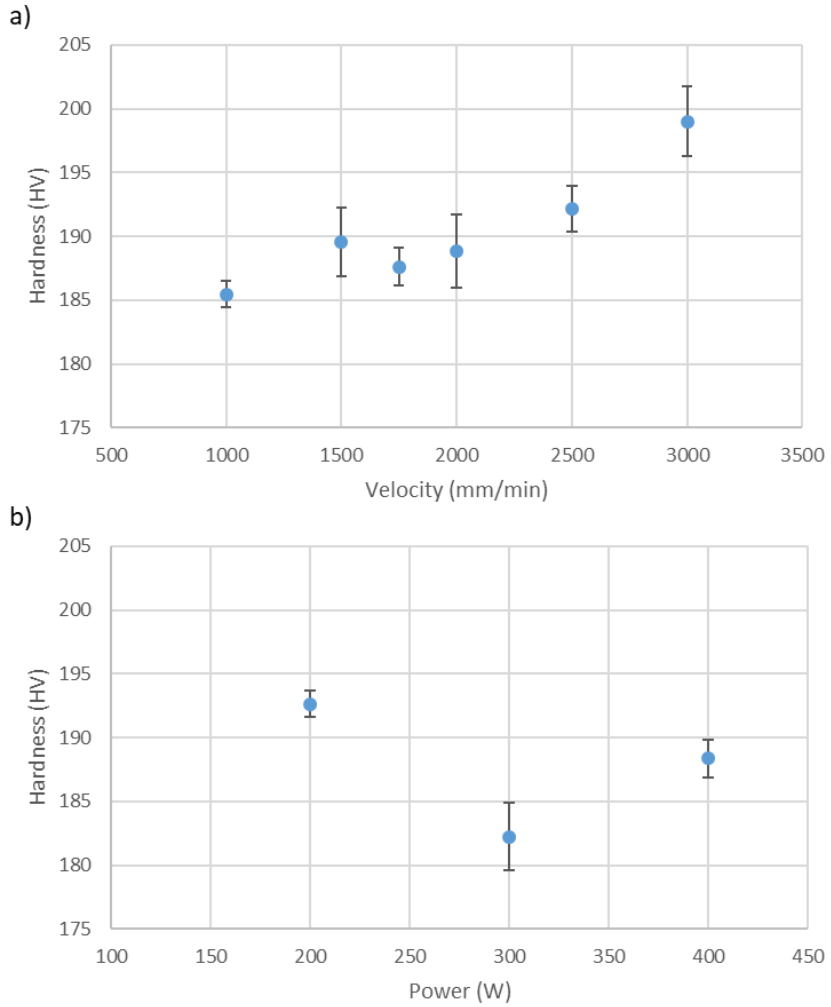

Figure 7-11: Variation of hardness with processing parameters a) velocity; b) power. Error bars show standard error

The hardness was plotted against the various melt pool dimensions in Figure 7-12. It is clear that the hardness decreases as melt pool size increases, this is shown by all 4 measures of melt pool size. Linear trendlines have been plotted for each measure of melt pool size; the hardness correlates best with the melt pool length, with $R^2 = 0.94$ (Figure 7-12).

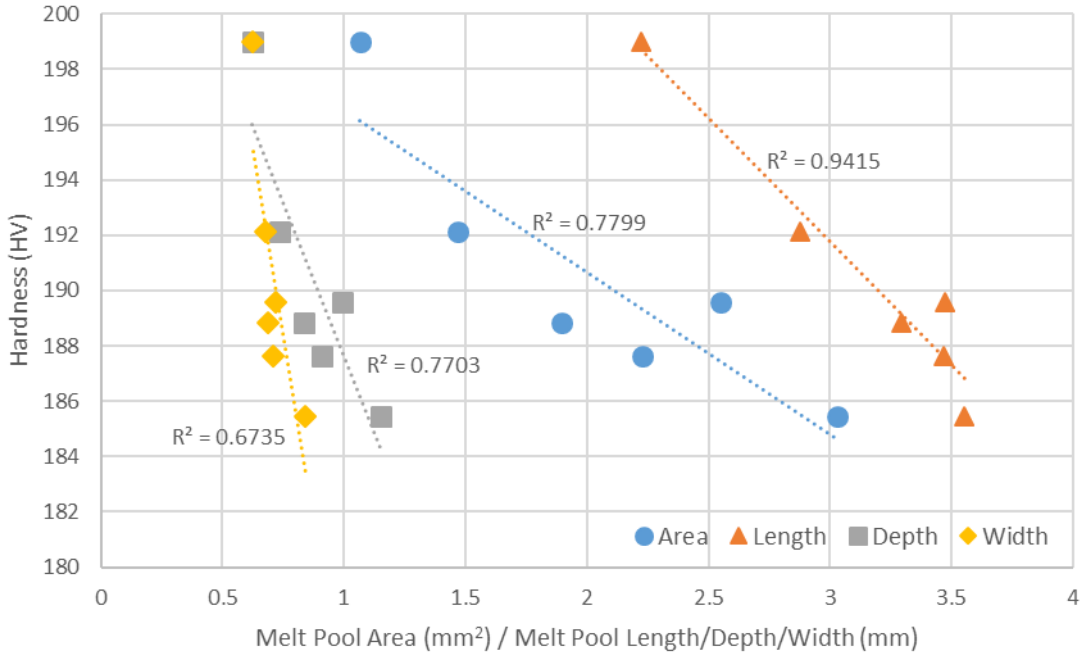

Figure 7-12: Variation of hardness with melt pool dimensions; error bars excluded for clarity (shown in Figure 7-11); linear trendlines and R^2 values shown for each melt pool dimension

For three processing parameters, the oxygen content of the walls was measured, summarised in Table 7-6; a measurement uncertainty of 5% was given by AMGSuperalloys who performed the analysis. The oxygen content increases with velocity; also the oxygen content decreases with increasing melt pool area (Figure 7-13a). Consequently, it can be seen that hardness increases as oxygen content increases (Figure 7-13b). Again, this was only measured for three parameter sets.

Table 7-6: Oxygen content of three sets of processing parameters ; measurement uncertainty (5%) in brackets

Sample	Power (W)	Velocity (mm/min)	Oxygen Content (ppm)
Cyl_12	296.8	1000	1152 (58)
Cyl_13		1750	1315 (66)
Cyl_14		2500	1346 (67)

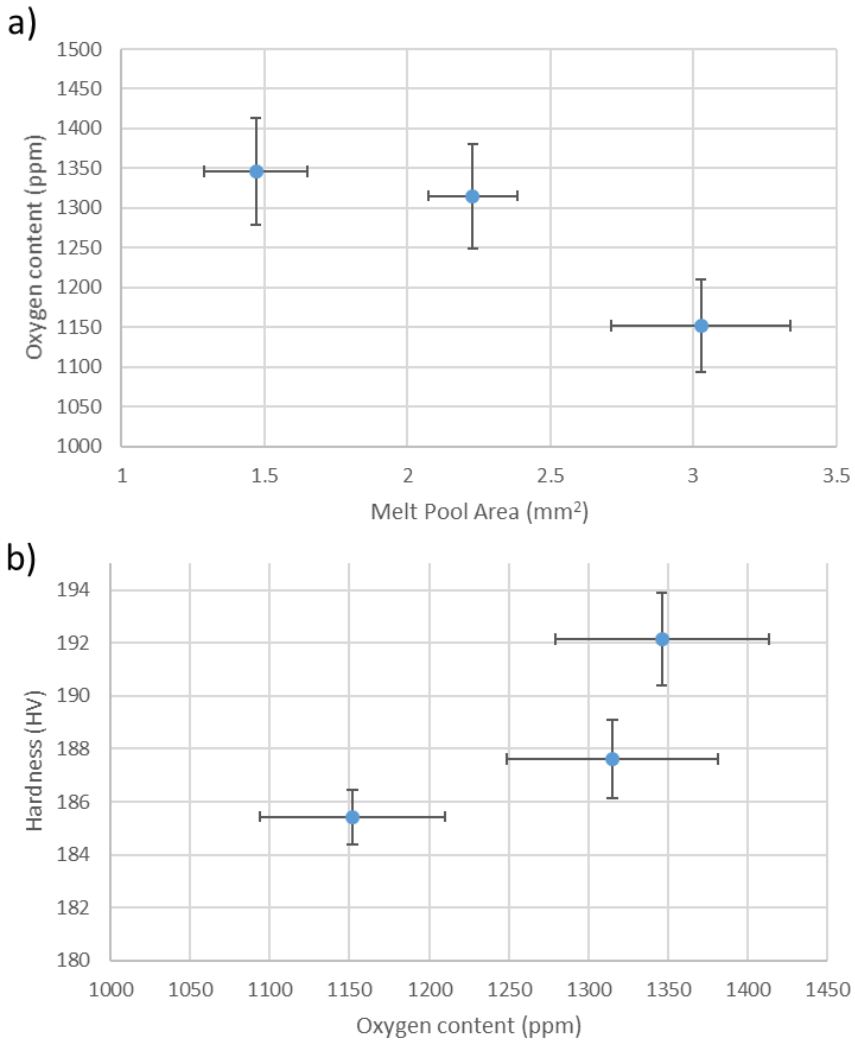

Figure 7-13: Analysis of oxygen presence in L-DED; a) dependence of oxygen content in the samples with melt pool area; b) variation of hardness with oxygen content

7.3.3. **Physical Properties of Walls**

Micrographs were taken of etched samples, approx. 6 layers high and one hatch wide (Figure 2). Figure 7-14a shows Wall A1 (low H, where linear heat input, H=P/v), with porosity visible between the central and the right hand hatches (circled). With a high H (Figure 7-14b) no porosity is visible, however, elongated grains can be seen along the centre of the hatch (outlined). The average porosity of a wall decreases with increasing H (Table 7-7). Average hardness values are shown for each wall and are similar to literature values [178]; walls with a low H have higher hardness. The higher H walls (Walls C and D) have a greater uncertainty in measured hardness, suggesting that hardness is variable within the sample.

Splitting the hardness average into 5 regions, each 2 mm tall, shows the variation of wall hardness with height. Low H samples (Walls A1, A2 and B) have a consistent hardness of 205-210 HV through the full height (Figure 7-15). The increased hardness variability observed in Walls C and D is due to a significant decrease in hardness with wall height. The hardness at the base of all walls is similar; the Wall D (highest H) shows the largest change and experiences an 8 % decrease in hardness with height.

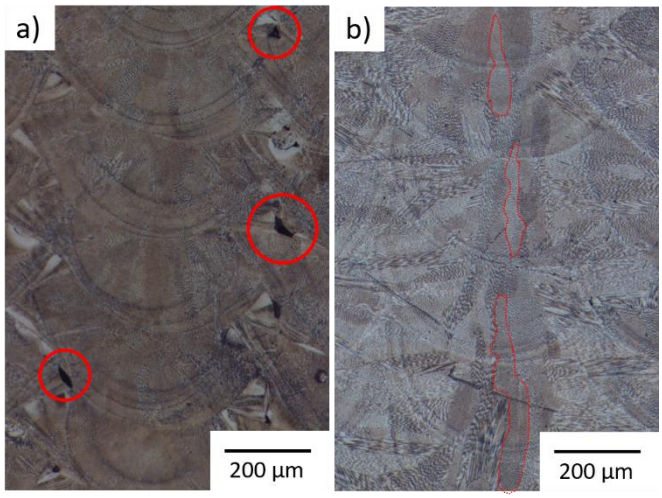

Figure 7-14: Optical micrographs of YZ plane of walls etched with aqua regia. a) Wall A1 with examples of porosity circled, b) Wall C with several columnar grains highlighted

Table 7-7: Porosity and hardness measurements of walls. Hardness values include a 95 % confidence interval

Sample	H (J/mm)	Porosity (%)	Average Hardness (HV)
Wall A1	6.5	0.301	207.6 ± 2.5
Wall A2	6.5	0.259	207. 9 ± 2.2
Wall B	8.0	0.182	208.4 ± 2.6
Wall C	10.9	0.081	200.1 ± 3.7
Wall D	13.3	0.105	190.0 ± 3.9

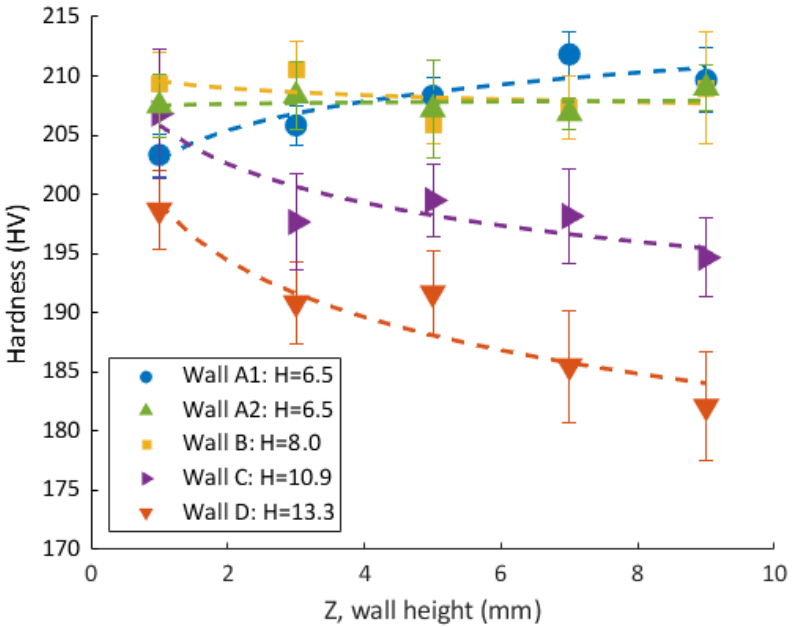

Figure 7-15: Hardness variation with wall height. Error bars show standard deviation

7.3.4. **Thermal Measurement of Walls**

For low H walls, the melt pool area increases by a factor 2 through the height, plateauing ~0.5 mm^2 (Figure 7-16a). Melt pools in high H walls are larger from layer 1, both Walls C and D experiencing a melt pool area increase by a factor of 6. This is the inverse of the relationship seen with hardness.

Cooling rates in low H walls vary between 7,000-10,000 K_{rad}/s, with quicker cooling typically lower in the walls (Figure 7-16b). High H walls have lower cooling rates initially (6,000-7000 K_{rad}/s) and drop more significantly with wall height, ending at 2,000-3,000 K_{rad}/s. Cooling rates in the low H walls have a large scatter, with outliers generally lower than the trend. In high H walls, the cooling rates have significantly less variability.

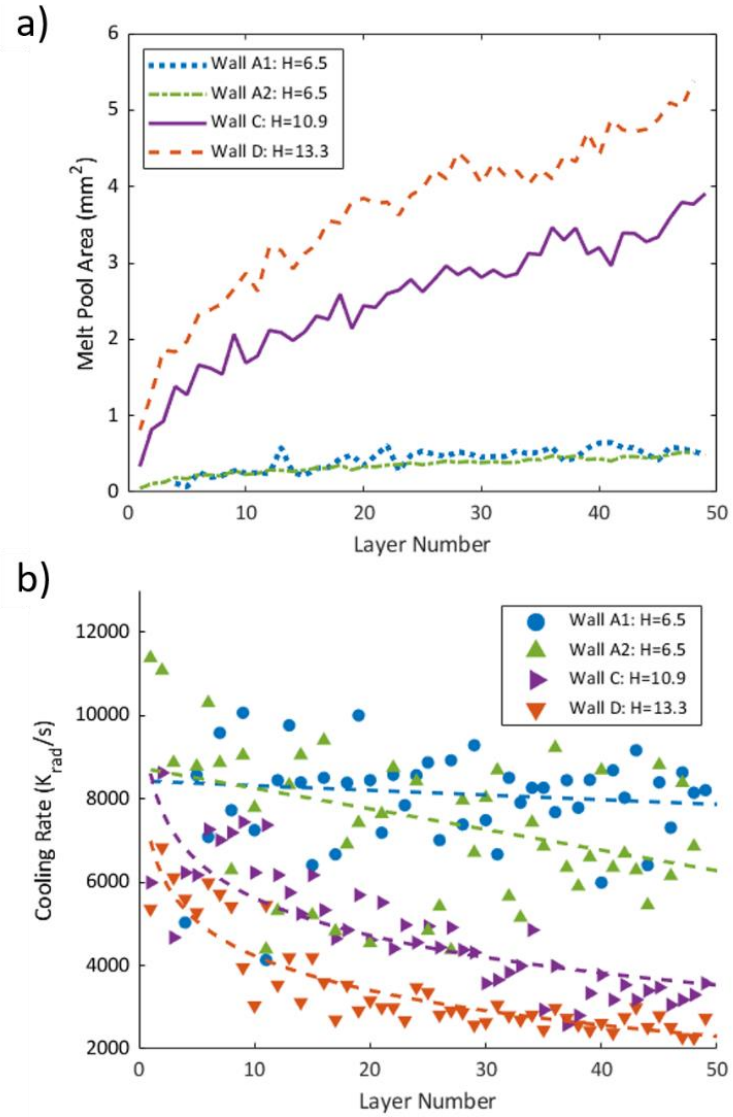

Figure 7-16: Thermal variation through layers; a) melt pool area; b) cooling rate, dashed lines indicating general trends

7.3.5. **Grain Structure and Texture of Walls**

Inverse pole figure (IPF) maps in the X direction (laser movement) are shown for a high H and a low H wall (Figure 7-17). There is a stark difference between these; in the low H walls (Figure 7-17a) the grains are fine with little noticeable texture. Some grains sweep into the centreline of the hatches, but few grains are elongated. No crystal orientations are dominant; there is no visible

change in microstructure through height. The high H wall (Figure 7-17b) shows distinct elongated grains along the Z direction in the centre of each hatch. These tend to be between the <100> and the <111> orientations and become larger and more prevalent towards the top of the wall. Between the hatch centres are wide grains aligned in the Y direction, some of these sweep into centreline grains. Very few grains have a <111> orientation.

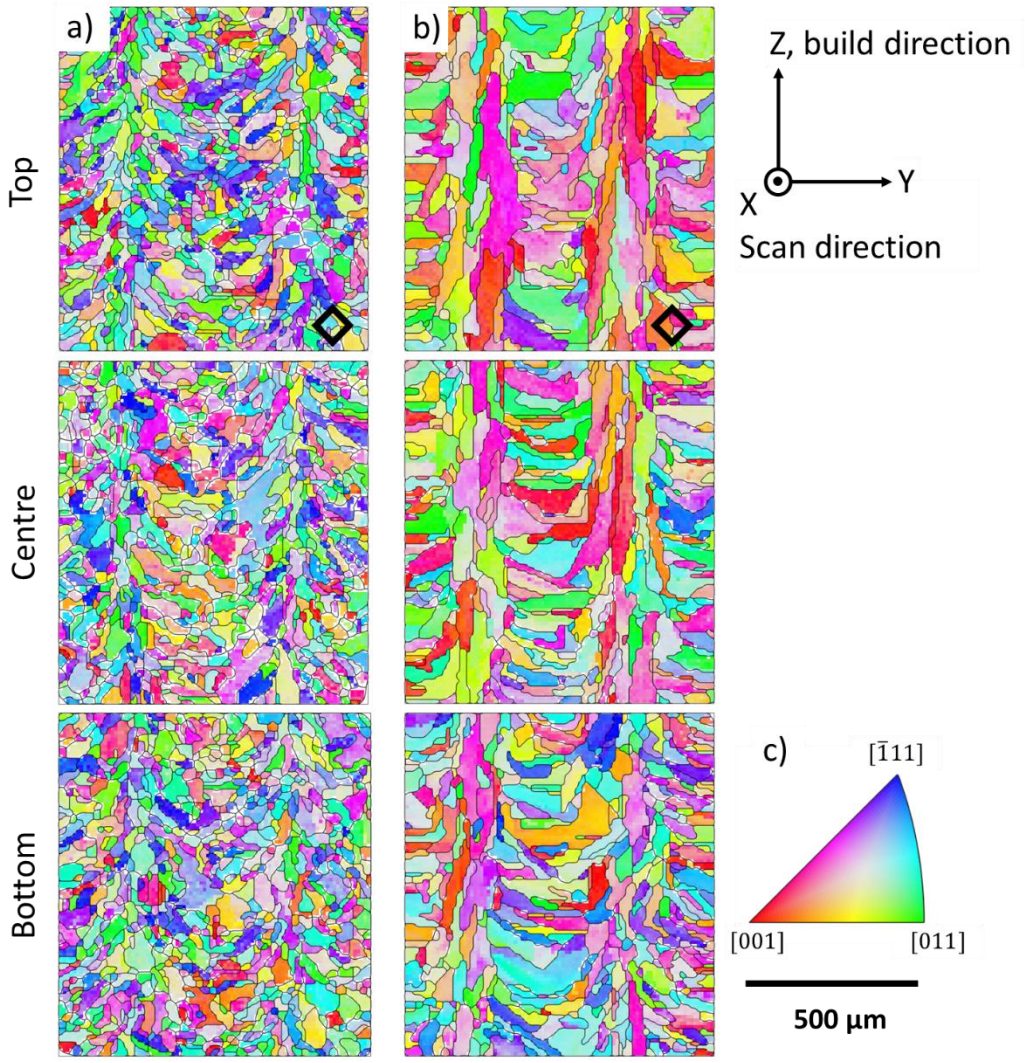

Figure 7-17: Inverse pole figure (IPFX) maps of walls; a) A1 (low H); b) D (high H). A top, centre and bottom section of each c) IPF key. Indentation size shown in bottom right corner of each map

There is a large variation in grain size between samples, Walls A1 and B (low H) have smaller average grain size and less variation than high H walls (Table 7-8). Grain size tends to increase with wall height and heat input. The maximum grain size in the centres of low H walls is 20 µm smaller than in the high H walls.

For each wall, inverse pole figures are shown for the X, Y and Z directions (Figure 7-18), axes defined in Figure 7-6. Since grains are irregular shapes and their crystallographic orientations have three components, the inverse pole figures for the three principal directions can vary significantly. For low H walls (A1, B), there is little texture, the maximum being 2 multiples of uniform density (mud). No texture is in the <001> directions; this could be linked to the largest cooling gradients which occur at an angle to the defined axes. In high H walls (C, D), the Y direction is heavily textured, which corresponds with literature [282,285]. In the X and Z directions, there is texture in the <113> direction (between <001> and <111>, circled in Figure 7-18D-C). This equates to 65°

above the horizontal. Wall D (highest H), has the strongest texture in both the <100> direction in the Y orientation and the <113> direction in the X and Z orientations, this behaviour is discussed further in Chapter 10.

Table 7-8: Average grain sizes from EBSD scans. For the centre of 4 walls and 3 heights in walls A1 and D

	Grain Size (Equivalent Radius, µm)	Grain Size Standard Deviation (µm)
Centres		
Wall A1	18.8	8.2
Wall B	19.4	8.7
Wall C	23.2	12.5
Wall D	26.7	16.0
Wall A1		
Top	18.1	8.3
Centre	18.8	8.2
Bottom	17.6	7.9
Wall D		
Top	27.8	17.2
Centre	26.7	16.0
Bottom	23.4	13.0

Averaging the anisotropy factor (Equation 4-1) for each scanned point within an IPF map, a cumulative anisotropy factor was calculated for each wall in each orientation (Table 7-9). Due to the strong <100> texture in the high H walls (in the Y orientation), these have a low average anisotropy factor of 0.13 and 0.10 for Walls C and D respectively. The other orientations on these walls all have anisotropy factors of 0.18-0.19. In low H walls, the average anisotropy factors are 0.21-0.23 in all orientations.

The ratio between the maximum and minimum anisotropy factors for each wall will be referred to as anisotropy variation (Table 7-9). Low H walls may have higher anisotropy factors, but the anisotropy variation between orientations (within a single IPF map) is minimal. Whereas the high H walls have lower anisotropy, but this varies more between the 3 orientations. The anisotropy factor is not seen to change significantly with height in the low H Wall. There is a noticeable reduction in the anisotropy factors of high H walls with increased height (in all orientations). By taking a ratio of the highest anisotropy factor to the lowest for walls A1 and D (for all three heights), global anisotropy variations can be defined. The global anisotropy variation in Wall A1 (low H) was 1.1, compared to 2.0 for Wall D (high H).

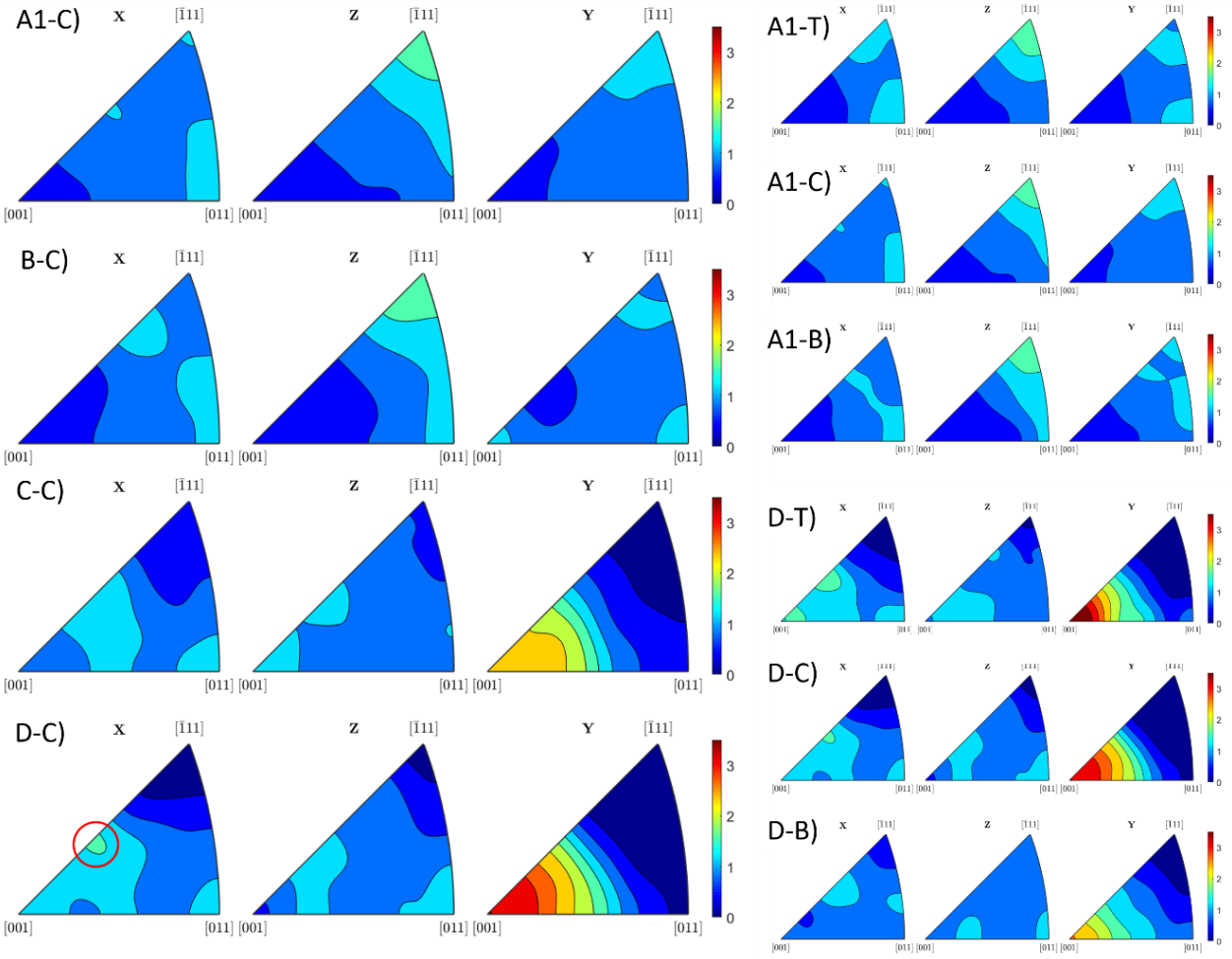

Figure 7-18: Inverse pole figures (IPFs) revealing texture of the centre of each wall (left, walls labelled). IPFs of walls A1 and D at the top, centre and bottom (T, C, B resepctively). Scale in multiples of uniform density (mud)

Low H walls have little texture in any orientation, with a maximum texture of 2 mud. For high H walls, the texture in the Y direction is much higher than the other directions, with this texture increasing with H, up to 3.4 mud. At the bottom of both walls, there is little texture in the indentation (X) direction (Figure 7-19), equiaxed grains dominate; the hardness of both walls is similar in this region. The texture in the Y direction of high H walls increases with height. In the low H wall, there is little microstructural variation through the build height, hardness is constant and texture minimal in all three directions.

Table 7-9: Average anisotropy factors for 4 walls

	Average Anisotropy factor (standard deviation)			Anisotropy Variation
	X	Z	Y	
Centres				
Wall A1	0.21 (0.08)	0.23 (0.08)	0.22 (0.08)	1.1
Wall B	0.22 (0.08)	0.22 (0.08)	0.21 (0.09)	1.1
Wall C	0.18 (0.08)	0.19 (0.09	0.13 (0.08)	1.5
Wall D	0.18 (0.08)	0.19 (0.08)	0.10 (0.07)	1.8
Wall A1				
Top	0.22 (0.08)	0.23 (0.08)	0.22 (0.08)	1.0
Centre	0.21 (0.08)	0.23 (0.08)	0.22 (0.08)	1.1
Bottom	0.22 (0.08)	0.23 (0.08)	0.22 (0.08)	1.1
	Wall A1 Global Anisotropy Variation			**1.1**
Wall D				
Top	0.17 (0.08)	0.18 (0.08)	0.11 (0.07)	1.6
Centre	0.18 (0.08)	0.19 (0.08)	0.10 (0.07)	1.8
Bottom	0.20 (0.08)	0.19 (0.09)	0.15 (0.09)	1.4
	Wall D Global Anisotropy Variation			**2.0**

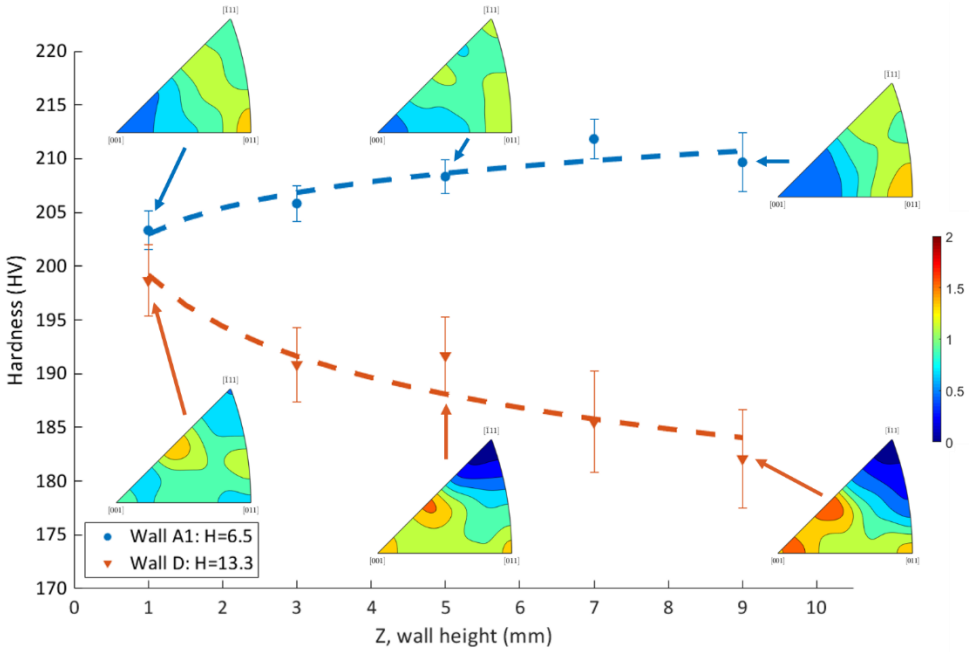

Figure 7-19: Variation of hardness through height of walls A1 and D, showing change of texture (in the X direction)

7.4. Discussion

7.4.1. Melt Pool Changes with Processing Parameters

The general trends of melt pool dimensions are as expected, the melt pool size decreases as the velocity increases (Figure 7-9 and Table 7-4). And when increasing power, the melt pool size increases (Figure 7-9); both of these trends occur for each of the melt pool dimensions (length, depth, width and area). The fact that the trends can be logically explained and are measured using both Silicon and InGaAs sensors increases confidence in the results. Literature states that a shorter melt pool experiences a higher cooling rate and experiences increased mechanical properties [105]. Figure 7-11a shows that the cylinders with the highest velocities have the higher hardness, which follows as they have smaller melt pools and so would be expected to have faster cooling rates. There is not an obvious trend of hardness with power (Figure 7-11b), but only 3 measurements were made. The hardness is inversely proportional to the melt pool dimensions (Figure 7-12), with the best correlation occurring with melt pool length. For monitoring purposes, if wanting to predict hardness from melt pool imagery, melt pool length would be the most useful measure as previously reported [105]. Melt pool width has the worst correlation with hardness, however this was measured ex-situ, so it could be due to systematic measurement error.

Several other melt pool observations were made; looking at the physical widths, the slowest speeds yielded the largest melt pools (Table 7-5). However, these also have the largest variation, as seen in Figure 7-4; the melt pool is unstable, so geometric accuracy is reduced. On the other end of the scale, small melt pools have been shown to have higher oxygen content (Figure 7-13a), which can be detrimental to mechanical properties [292]. In this case, hardness seems to increase with oxygen content (Figure 7-13b), but this is likely to the underlying trend in melt pool size and so the varying cooling rate.

Melt pool area generally decreases as velocity increases (Figure 7-8g, h and i); however, this linear decrease is not reflected in both the melt pool length and depth. Between 1000 mm/min and 1750 mm/min, the melt pool length is constant, but the depth is reduced. Whereas in the velocity change between 1750 mm/min and 2500 mm/min, there is a much larger decrease in melt pool length than in melt pool depth. It is interesting that it seems that the melt pool length plateaus somewhere at velocities below 2500 mm/min.

Figure 7-10 shows that the baseplate has a significant effect on mechanical properties; unfortunately, due to the baseplate being clamped to the table, melt pool monitoring could not be performed for the Cyl_base sample. The hardness is shown to drop in the first 5 mm of height and then a plateau seems to be reached. Even when the build was paused (black line in Figure 7-10), the hardness didn't fluctuate. This suggests that once away from the baseplate, a steady state is quickly reached and so hardness is constant; this reinforces the methodology used for the subsequent cylindrical parameters.

As explained previously, camera mode Silicon_400 has both the best spatial and temporal resolution so will yield the most accurate image of the melt pool. As shown in Figure 7-5b, many details can be seen in the melt pool. The base of the melt pool is white, of highest intensity, but further back, the top actually seems to have relatively low intensity which would suggest a lower temperature. It has previously been shown that oxidation of surfaces can affect thermal readings [310], likely due to a change in emissivity from the base alloy. In this case, it seems the oxide has a lower emissivity and so appears darker than the molten material. Due to the higher melting point of

the oxide, it likely forms a solid shell, which flows along the melt pool surface as seen in [302] (Si_400_297_1000). Dark (unmelted) powder particles can be seen moving along this oxide layer.

These high resolution images are very useful for fundamental analysis of phenomena, but generate over 350 MB/s (Table 7-2), which limits recording durations to 2-3 minutes at a time. Additionally, due to the high spatial and temporal resolution, the different parts of the melt pool can be distinguished with their varying emissivity; this means that melt pool thresholding cannot be automated and must be done manually. The results of this are shown in Table 7-4, but unfortunately, doing this analysis on a large scale or live is not feasible. A small melt pool will have a larger surface area/volume ratio, so one would expect it to have the highest oxygen content as confirmed by Table 7-6 and Figure 7-13.

Using the InGaAs sensor, both the temporal and spatial resolutions are reduced (Figure 7-5c,d). However, the advantage of this is that the details are blurred and so a simple threshold can be used to extract the melt pool size. This has been shown to be repeatable by monitoring the same parameters twice (Table 7-7). It is interesting that the melt pool area can be increased by just one of the dimensions increased e.g. an increase in the depth of the melt pool in Cyl_8 at 12 s (Table 7-7b) is reflected by an increase in melt pool area (Table 7-7c). Figure 7-8 shows that by using different thresholds, similar melt pool dimensions can be extracted from camera modes InGaAs_60 and InGaAs_30. One would expect that doubling the exposure would lead to each pixel having double the intensity, and so the threshold would need to be doubled. The thresholds used for these calculations are 2500 and 5500 respectively. The threshold is slightly over double, but seems to be measuring similar melt pool dimensions; this discrepancy could be due to the non-linear QE curve of the InGaAs sensor [303].

Selecting the correct exposure is a difficult balancing act; if the exposure is too long, the sensor receives too much signal and will read at its' maximum value. The image will be saturated and no detail will be resolvable in the hottest region. However, if exposure is low, the intensity readings will be lower; this means that the temperature resolution will be decreased and since the signal is lower, there will be a lower signal/noise ratio. Natural density filters can be used to reduce the intensity, so the strength of these can be used to bring the signal into the correct range.

The inter-relation between data acquisition rate and resolution is summarised in Figure 7-20. To get an overall resolution, both the spatial (pixel) resolution and the temporal resolution (frame rate) were combined. This was done as follows (assuming a laser velocity of 1750 mm/min):

$$Distance\ moved\ between\ subsequenct\ frames\ (px) = \frac{laser\ velocity \times pixel\ resolution}{frame\ rate}$$

The smaller the distance moved by the laser between frames, the higher the temporal/spatial resolution of the camera. Typically, a greater acquisition rate accompanies the higher the resolution. In the case of the Basler coaxial camera (Section 4.2.4), the coaxial configurations means that there is no melt pool movement within the field of view, so a small region with high spatial resolution can be captured. At the resolution captured by the Silicon camera modes, continuous recording was not possible due to the data volume recorded; if this were to be analysed, it would have to be offline (Figure 7-20). Both the InGaAs and the Basler cameras record melt pool images which can be processed automatically (unlike the Silicon) and at data acquisition rates which can be processed online. Further, if data processing was performed online and only the output values were stored (as opposed to the raw images, as done by Concept Laser for L-PBF), the data storage volume would be further reduced. For industrial applications, the key aim is to extract the maximum useful information from the monitoring, whilst retaining the minimum storage footprint,

as this minimises cost; as such for industrial applications, online calculations must be performed and only output value stored.

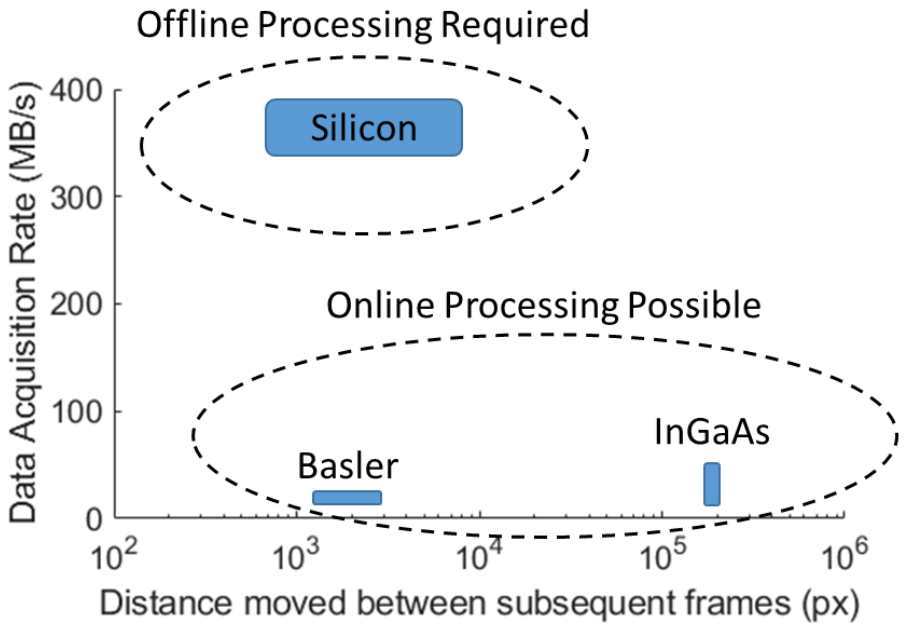

Figure 7-20: Comparison of data acquisition rates with the resolution of various cameras. Note that the number of pixels moved during a single frame captures both the spatial resolution and the temporal resolution (assuming a velocity of 1750 mm/min)

The pyrometer on the Aconity3D Mini L-PBF machine records data at a rate of roughly 2-2.5 MB/s, which is an order of magnitude smaller than the InGaAs sensor and two orders of magnitude less than the Silicon sensor (Table 7-2). Similarly to the Concept Laser L-PBF machine [298,299], the pyrometer records only a single value, rather than the raw image, this makes the data quantity manageable, but reduces the resolution of the data. The spot-size of the pyrometer is unknown and since only a single value is recorded, no spatial resolution can be calculated (hence its' omission from Figure 7-20). As previously mentioned, the Silicon sensor provides images of great detail, but this is not useful for live in-situ monitoring, as the data volume is unmanageable. The results are of similar resolution to X-ray imaging, but showing a side-on view rather than through the melt pool; as with X-ray image (Section 2.6.2), this cannot be used for live analysis, but is very useful for detailed phenomenon analysis.

The InGaAs sensor saves data at a much more reasonable rate, but the processing is still difficult. As a result of the increased exposure time, the melt pool can move almost 1 mm during the recording of one image (at 1750 mm/min) when using InGaAs_30. This reduces spatial resolution; the melt pool is static in the image, so the melt pool dimensions shouldn't be affected. This long exposure increases the blur of the image, so any details will be averaged out – resulting in the low resolution images when compared to the Silicon sensor. Interestingly, when recording using the InGaAs_60 (Figure 7-8 and blue lines in Figure 7-9), an oscillation can be seen, where the melt pool size reduces regularly. The cause of this is unknown, but the spacing is likely to correspond with the rotation velocity. It is interesting that this is seen in InGaAs_60 images, but not InGaAs_30 images – because of the increase temporal resolution of the InGaAs_60 images.

The data acquisition rate of the InGaAs sensor makes online processing possible; the melt pool moves through the image making data automation more difficult. Simple analysis would, such as the melt pool size, would still be possible to calculate online. More complex calculations such as cooling rates are more difficult to calculate live, but potentially still possible to compute in-situ. For

the cylindrical builds, the laser was kept stationary whilst the table was rotating – this kept the melt pool static in the cameras field of view (in the XY plane). Data analysis, especially of cooling rates, is much simpler when lateral melt pool motion is removed from the equation. Unfortunately, cylinders are the only geometry which can be printed in this manner with a static laser; in most builds, the nozzle moves. This means that sometimes there will sometimes be solid in the line of sight between the camera and the melt pool, blocking the field of view. As such, side-on monitoring is limited by the geometry being printed, this can be improved by raising the camera and recording at an increased angle of incidence. This can lead to issues with the nozzle blocking the field of view and means that perspective correction is required; as a result of these reasons, coaxial monitoring is often preferred.

7.4.2. Correlation of Thermal Signatures

Over the first 20 layers, cooling rates of high H (where linear heat input, H=P/v) walls decrease to a plateau (Figure 7-16b), this is less pronounced in low H walls. This is attributed to the change in heat conduction mode; initially the baseplate is near and conducts heat away quickly, similarly to Cyl_base (Figure 7-10). As the wall height increases, heat builds up in the wall and there is a much smaller conduction area – the area of the wall rather than the baseplate. This increases the base material temperature and reduces the cooling rate. Walls A1 and A2 were built with the same parameters but cooling rates appear to have a large amount of scatter as explained in Section 7.2.2. Due to the rapid heating and cooling in this process, the peak temperature likely captures part of the cooling, leading to a measured value lower than expected. This decreases the measured value of the cooling rate when the peak value is near the solidus temperature. Since this is more likely in low H walls, there are anomalous cooling rates for walls A1 and A2 which are much lower than the general trend (Figure 7-16b).

Due to the large uncertainty in emissivity corrected temperature (Figure 7-6d), these were not used to calculate cooling rates. Radiance temperature values were used for cooling rates, this assumption is common in such circumstances [311], resulting in units of K_{rad}/s. Emissivity corrected cooling rates would have yielded larger values, but by less than a factor 2. The cooling rates experienced are comparable to literature, where values of the order 10^3-10^4 K/s are reported [4,105].

High H walls experience a large decrease in cooling rate through height (Figure 7-15) and have the most significant decrease in hardness. This drop in hardness is similar to that experienced in the cylindrical build (Figure 7-10). Conversely, the low H walls have a more consistent melt pool area and a constant hardness throughout. Hardness increases with cooling rate and decreases with melt pool dimensions (as shown in Figure 7-12 for the cylinder build), the hardness has the strongest correlation with melt pool length, so this will be used. The gradient of 1.05 on a log-log plot shows that the relationship is $\frac{dT}{dt} \propto MP^{-n}$ where MP is the melt pool length (Figure 7-21). This was plotted for wall D, as the largest melt pools and highest temperatures yield lower uncertainties. From Figure 7-21, n was calculated to be 1.05, compared to 2.02 reported by Hofmeister et al. as shown in Figure 7-2 [105]. Numerically, the measured gradient is different, but the same trend is seen; due to the potential differences in thermal calibration, emissivity calculation, laser type, laser diameter and build geometry, measuring the same gradient would be unlikely. The relationship between cooling rate and melt pool length is however, confirmed.

Since the melt pool length has units of distance, this relationship is equivalent to Chvorinov's rule, which states that freezing time is proportional to $(Volume/Area)^n$ where n is 1.5-2 [312]. 1.05

doesn't fit within the range set by Chvorinov's rule, however this was established for casting and as mentioned, the cooling range value will change dependant on the emissivity chosen.

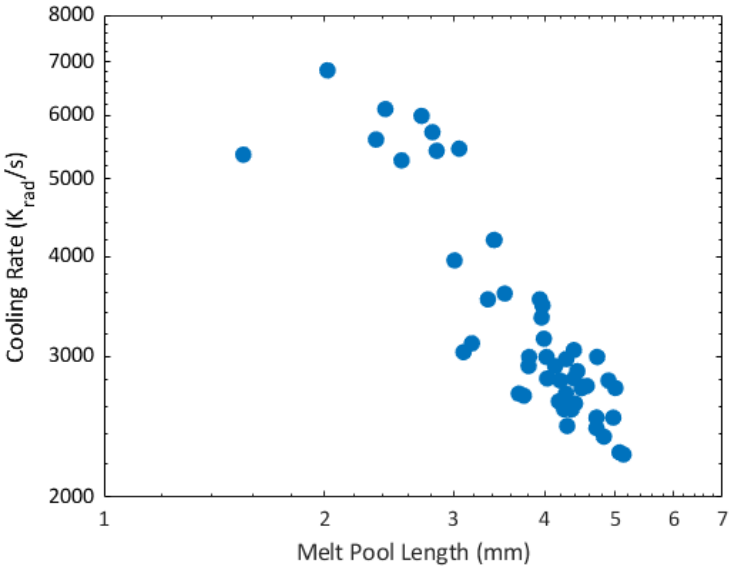

Figure 7-21: Cooling rate vs melt pool length for Wall D (log scales)

Since melt pool length is monotonic with cooling rate, it can be used as a proxy for cooling rate; which is beneficial, as cooling rates are difficult to measure in-situ. The standard deviation of cooling rates from the line of best fit is found to be 15.5 %. Given the melt pool length uncertainty of 0.37 mm and a trendline gradient of -1.05, the melt pool size uncertainty leads to a cooling rate error of 10.4 %, which is similar to the scatter. These calculations were performed for wall D to reduce cooling rate errors due to the measurement limitations, but the conclusions should hold more generally. In the case of InGaAs_60 recording, a threshold was picked without temperature calibration; the melt pool length shows the expected trends with hardness (Figure 7-12), so even using uncalibrated pixel intensities can be sufficient to estimate simple mechanical properties.

The data acquisition rate of the InGaAs_Tele camera mode is 18 MB/s; this is a rate which can be stored continuously. Due to the physical movement of the melt pool when printing the rectangular walls, the melt pool analysis is difficult to perform online. Static melt pool (using the table rotation) is only possible when printing cylinders, but is not transferrable to other geometries. Because of the response rate of the BeAM machine, if feedback control were to be implemented, the quickest response that could be expected would be ~10 Hz. It can be seen that having cameras recording at 50-100 fps could be beneficial, but much higher than this seems redundant for the L-DED process.

From coaxial measurement, literature has reported that the melt pool areas increase with build height. A similar observation has been made in this work but using side-on measurement, showing that the two measurement approaches agree. However, it was also observed that the increase in melt pool area with build height was more pronounced for high H builds compared with low H builds, by a factor of around 3 (Figure 4a). This suggests that, even for a fixed geometry, the degree of thermal variation through a build (change in melt pool size with build height) is itself dependent on the build parameters. To the authors' knowledge, this has not been reported previously.

7.4.3. Grain Structure

L-DED models predict a microstructure containing elongated grains in the Y direction producing the texture seen in high H walls (Figure 7-18). There is debate as to what occurs along the centreline. Laser welding literature expects grains to sweep into the centreline and result in elongated grains which lie at 60° between the X and the Z directions, i.e. along the highest thermal gradient [88,284]. These explain the <113> direction texture seen in high H walls. Other L-DED models predict equiaxed grains along the centreline, with the equiaxed region expanding at higher velocity (lower H) [282]. This is taken to the extreme in the low H walls, which are mainly equiaxed, with some centreline alignment.

7.4.4. Effect of Anisotropy on Hardness

The anisotropy factor was developed as a measure of crystal orientation, as <111> orientations have higher Young's moduli than <100> orientations [177]. This gives a measure of expected mechanical properties for each grain. The hardness indents were performed in the X direction, the average anisotropy factors in this direction were further explored (Table 7-9). The average anisotropy factor can be shown to scale linearly with both melt pool size and cooling rate.

The Schmid factor describes the ease with which slip will occur; this is calculated for all active slip planes, with the largest Schmid factor being shown (Table 7-10). Previous studies have found Schmid to show a weak relationship to hardness; Table 7-10 shows the Schmid factor to have a strong correlation with hardness, similar to the anisotropy factor.

Table 7-10: Comparison of Schmid factors between centres of walls and through the height of Walls A1 and D (standard deviations indicated)

	Schmid Factor	Average Anisotropy Factor (X direction)	Hardness (HV)
Centres			
Wall A1	0.451 (0.042)	0.21 (0.08)	208.3 (1.6)
Wall B	0.450 (0.041)	0.22 (0.08)	205.8 (1.5)
Wall C	0.461 (0.034)	0.18 (0.08)	199.5 (3.0)
Wall D	0.464 (0.028)	0.18 (0.08)	191.7 (3.6)
Wall A1			
Top	0.449 (0.042)	0.22 (0.08)	209.7 (2.7)
Centre	0.451 (0.042)	0.21 (0.08)	208.3 (1.6)
Bottom	0.450 (0.042)	0.22 (0.08)	203.3 (1.8)
Wall D			
Top	0.466 (0.028)	0.17 (0.08)	182.1 (4.6)
Centre	0.464 (0.028)	0.18 (0.08)	191.7 (3.6)
Bottom	0.456 (0.038)	0.20 (0.08)	198.7 (3.3)

The anisotropy factors and hardness's for all of the EBSD scanned regions are in line with literature values (Figure 7-22) [178]; anisotropy factor was used because it allows direct comparison to literature. Each hardness indent deforms multiple grains because the indent diagonal is 90-100 µm (Figure 7-17), the resultant hardness is an average hardness across the individual grains. Since literature vales were for individual grains, no errors in A_{hkl} were stated.

A small indent allows for analysis of individual grains so a larger hardness difference may be measured between distinct regions; this detail is lost when using a larger indent due to averaging of multiple grains. However, this work focuses on anisotropy differences on the macro-scale, so the large indent is sufficient to provide global trends in hardness and to relate these to the average anisotropy factor.

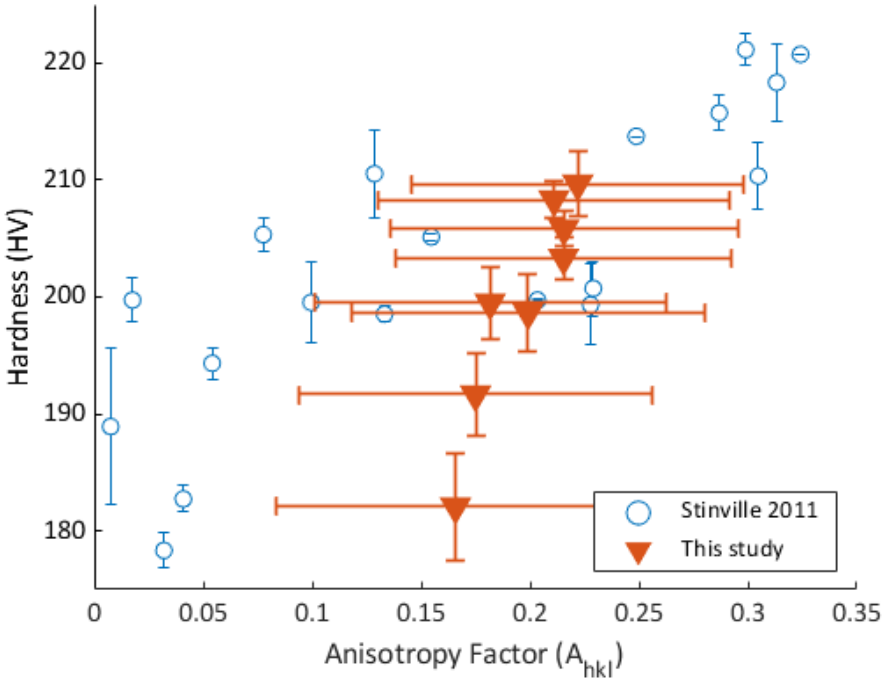

Figure 7-22: Change in hardness with anisotropy factor, compared to literature values [178]*. Error bars show standard deviation*

High H walls have a larger average grain size (Table 7-8), so fewer grains are deformed by the indenter. This means indents in high H walls deform fewer grains and are less representative, which increases the uncertainty magnitude. The indentation sizes in literature are an order of magnitude smaller than used in this work; so the literature values may overstate the hardness due to the indenter size effect.

Low H walls experienced small melt pools and high cooling rates. Models predict these to experience more equiaxed grains, which have little texture. Since there is no fibre texture, the anisotropy factor is higher and so the walls are harder (Figure 7-23). High H walls have larger melt pools, slower cooling rates and larger, more orientated grains. This leads to a more pronounced texture and so a lower anisotropy factor as confirmed by the reduced hardness in the X axes as compared to low H walls (Figure 7-23).

Similar variations are seen through the build height. Low H walls have constant melt pool size and cooling rate; this is reflected in a consistent anisotropy factor through build height. The equiaxed nature is shown by the small anisotropy variation. In the high H wall, the melt pool size increases with build height, reducing the cooling rate. This leads to an increase in grain size and a more

pronounced texture with build height; the anisotropy factor decreases with height leading to a lower hardness at the top of the walls.

The hardness in each orientation of the wall depends on the average anisotropy factor in that orientation. The severe global anisotropy of the wall could be estimated by taking a ratio between the maximum and minimum anisotropy factors for each wall (Table 7-9). The low H walls were found to be very isotropic (10 % maximum difference in anisotropy factor between orientations in any location). High H walls were found to have a much larger variation (up to 100 %), so the mechanical properties in one direction are inferior to those in the other directions. This could create significant issues when producing components of industrial relevance, as there are often stringent limits of mechanical properties.

The stark microstructural difference between the low H and the high H walls suggests there was a significant difference in heat flow during manufacture. All walls were built with the same hatch spacing, so the inter-hatch porosity experienced in the low H walls must be due to differences in melt pool width (Figure 7-14). The pores between hatches could change the way the heat conducted away from the melt pool. Despite low H walls having better mechanical properties, having regular pores could be an initiation point for mechanical failure, which would not be captured in the hardness data.

The optimum wall would have no inter-hatch porosity, like the high H walls, but the isotropic hardness properties of the low H walls. Using a narrower hatch spacing and a closed loop control this could be achieved. It has been shown in this work that the hardness is dependent on the microstructure, which itself is dependent on the cooling rate as summarised in Figure 7-23. Since melt pool length/area are monotonic with cooling rate (Figure 7-21), control of these would suffice. A coaxial camera would be able to capture this data and so would be the simplest way of achieving these optimal properties.

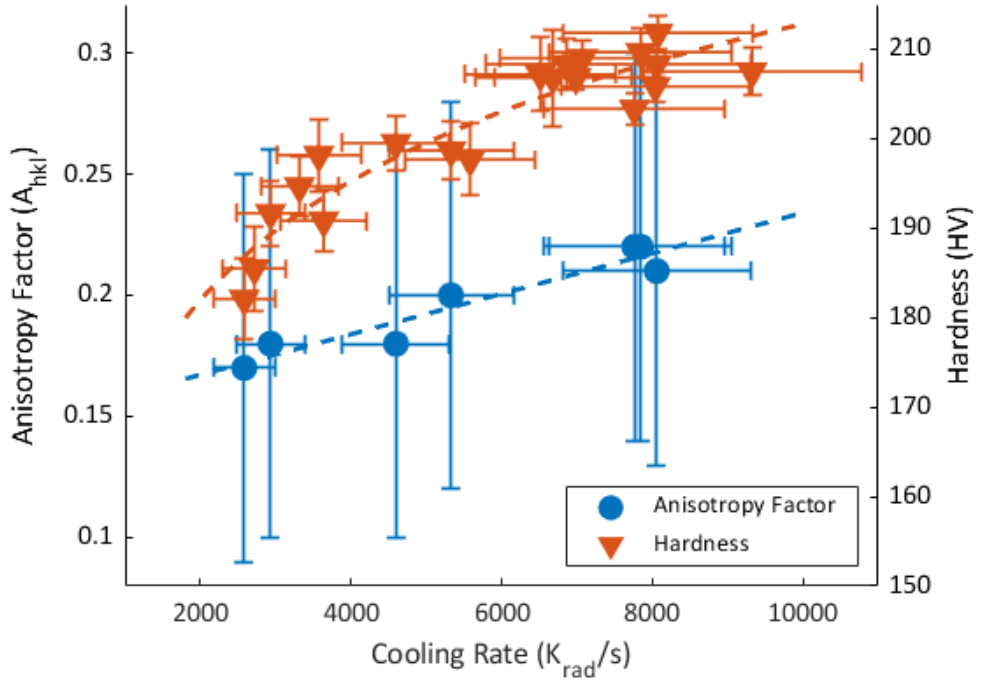

Figure 7-23: Variation of anisotropy factor and hardness with cooling rate. Error bars show standard deviation

7.5. Summary

Several cameras have been used to record the L-DED process from side-on, looking at the melt pool during printing. Using a Hamamatsu Orca-Flash4.0 Silicon camera, very high resolution images can be captured at 400 fps, but this leads to unmanageable data storage issues. For live monitoring, lower frequency, lower resolution imagery would be sufficient and much easier to manage; essentially, it's a process of gaining the maximising amount of useful data for the minimum storage/processing cost.

Imagery from the Hamamatsu C12741-03 InGaAs is of a much more manageable volume for online processing; and once processed, if only output values are stored, the storage requirements are greatly reduced. This is the equivalent of what is being recorded by the pyrometer in Chapter 5, whose data acquisition rate is and order of magnitude lower than that for the side-on monitoring in this chapter, despite it having by far the highest frame rate. Unfortunately, side-on monitoring comes with geometric difficulties; the line of sight between the camera and the melt pool will be interrupted for most geometries.

It is shown that the melt pool length is a good predictor of hardness and that melt pool size strongly affects the final component properties; with large melt pools sacrificing geometric accuracy and small melt pools increasing oxygen intake in the component. Further, the inverse relationship between melt pool size and cooling rate has been confirmed. High linear heat input walls are shown to have slower cooling rates, which leads to a more textured grain structure. By calculating the anisotropy factors of individual grains, the measured hardness can be explained through the grain structure which itself is dependent on the cooling rate.

Low linear heat input walls are shown to have both higher hardness and to be more isotropic in terms of their grain structure, with minimal variation through height. High linear heat input walls have an increasing thermal signal with height; this increased temperature creates local anisotropy. The increase in temperature with height is much more significant in the high H walls, so this creates further anisotropy throughout the sample.

The ability to predict the hardness from the thermal signal opens the possibility to tailor mechanical properties throughout a component by controlling thermal signatures. This is of high importance for acceptance into industrial repair applications, as thermal monitoring can increase confidence in the final components without the need for further testing.

8. Hardness Variation of Inconel 718 in L-DED

8.1. Introduction

Inconel 718 is a nickel superalloy widely used in critical aerospace components with operating temperatures up to 650 °C [65,313]. The main strengthening mechanisms are precipitation and order strengthening due to the body centred tetragonal γ", Ni_3Nb, phase [180,313–315], with a small strengthening contribution from the γ', $Ni_3(Al,Ti)$, phase. The γ" phase adopts a DO_{22} structure[316], often forming a disk morphology [183] – with a larger mismatch in the c direction than in the a direction [317]. One of the benefits of Inconel 718 as an alloy in the wrought condition is that it can be age-hardened, i.e. peak precipitation strengthening is only achieved once the component shape is finalised. The volume fraction of γ" precipitates in cast and wrought Inconel 718 is 15-20 % [315,318] with up to 5 % γ', which is low compared to higher temperature capable alloys e.g. CM247LC, which have γ' precipitate volume fractions of up to 65% [319]. It has been shown that Nickel superalloys can experience significant anisotropy with Young's modulus variation of over 2x between the <100> and <111> directions in single crystals [320].

Numerous thermal studies have been performed, analysing the precipitation behaviour of Inconel 718. Often, the precipitation of γ' and γ" are analysed together due to them forming at similar temperatures [313,314]. However, as the γ" accounts for 70-80 % of precipitates in Inconel 718 [190,313], it is believed that these studies are indeed representative of the γ" precipitation behaviour in Inconel 718. Differential scanning calorimetry (DSC) cycles show peaks at temperatures where precipitation occurs. For γ", this is best seen at a heating rate of 20 °C/min and is found to be in the range 840-890 °C [321], which is within the short-term aging temperature range of 700-900 °C identified by Slama and Abdellaoui [313]. Time temperature transformation (TTT) curves for Inconel 718 show a combined γ' and γ" precipitation window with a minimum time for transformation of the order 0.1 s and sub second transformation times roughly between 650-900 °C as seen in Figure 8-1 [314].

The majority of precipitation work has been completed with heat treatment of wrought material in mind, 720 °C for 8 hours being a representative γ" aging cycle [322]. Although the morphology of the precipitates in wrought and AM material may be similar, the AM process occurs at much higher speeds with cooling rates around 10^3-10^4 °C/s for L-DED [4], with sub-second holding periods within the precipitation range. The TTT curve reaches 0.1 s, which suggests that precipitation could occur during L-DED, but the precipitation kinetics cannot be directly transferred. γ" has been identified in as-build AM samples both using L-DED [323] and EB-PBF [315]. TTT curves of Inconel 718 vary by orders of magnitude in literature, reducing confidence in them [314,324–326], the nose of the γ" is always at quicker times than that for δ. Additionally, the exact composition can significantly alter the time required for precipitation [327].

Due to its wide applicability in industry as well as the age-hardenable behaviour of Inconel 718, it is particularly popular for manufacturing using additive processes. γ" is typically found in the interdendritic regions of AM samples [227], as these contain up to four times more Nb as a result of segregation during solidification [328]. The kinetics of γ" precipitation are an order of magnitude quicker in these interdendritic regions compared to the dendrite cores [327]. Tian et al. hypothesise that on initial solidification, Nb-rich eutectic products are formed interdendritically [316]. In subsequent hatches/layers, these low melting point eutectics remelt, allowing for Nb diffusion away from them, it's in these areas that γ" can precipitate and then grow [316]. Kumara et

al. extend this by saying that these high Nb concentrations in the interdendritic regions form Laves phases upon solidification [327]. During subsequent hatches, Nb diffuses back out of these Laves phases and γ" forms nearby the Laves phases [327]. These theories explain why γ" is predominantly found in the interdendritic regions [227] and explain the observation by Yeoh et al. that hardness increases with local Nb content [180].

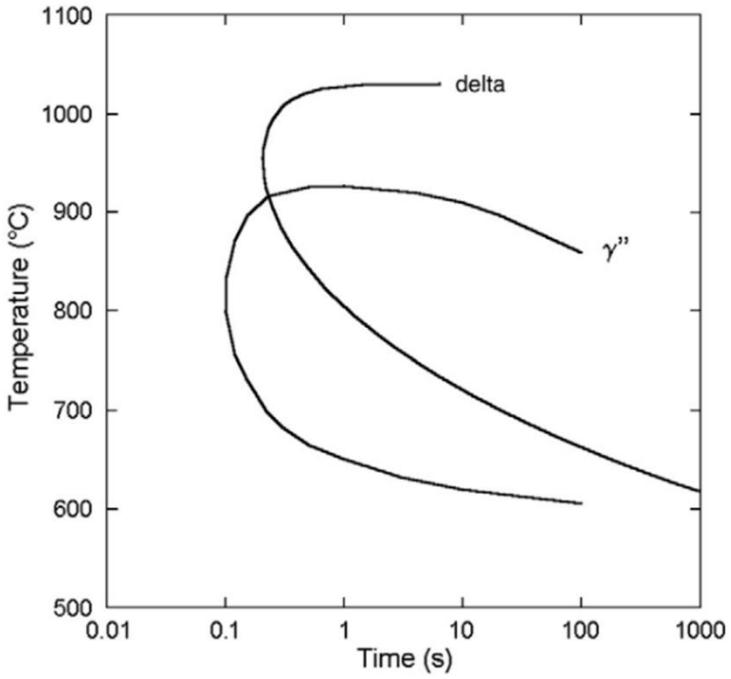

Figure 8-1: Time temperature transformation (TTT) curve for Inconel 718. Original caption contradicts figure in terms of the γ" curve, we believe the caption to be correct. Reported by Niang et al [314]

During AM, multiple reheats occur in the subsequent hatches and layers, which allows for more time in the precipitation temperature range. However, γ" can transform to δ at temperatures above 900 °C [313,314], which is a geometrically close packed (GCP) phase and can be deleterious to mechanical performance due to its' brittle nature. Despite this, it has been shown that γ" is retained when aged samples are held at 1100 °C for 1 s and subsequently cooled at 10 °C/min (total of 21 mins above 900 °C) [314]. Tian et al. [316] hypothesised that more γ" was found at the bottom of an as-build L-DED sample which would explain the decrease in hardness observed with height. The cause of this was speculated to be due to growth and precipitation of γ" in subsequent hatches and layers as allowed by Nb segregation as shown schematically in Figure 8-2 [316]. Hardness was shown to increase with height, but no quantification of temperature cycles to precipitation kinetics was attempted [316].

EB-PBF has been used to show that by holding the baseplate at high temperatures, the amount of precipitates (including both γ' and γ") can be increased [329]. This method was used to recreate standard heat treatments (1-8 hrs), which were shown to retain both γ' and γ". The resultant hardness values of these samples was 478±7 HV, significantly higher than samples built without the in-situ heat-treatment and comparable to those achieved in the peak aged wrought alloy [315]. In addition, 2 further cooling rates were tested by Sames et al, with the slower one resulting in a higher hardness, which would be expected due to the increased time in the precipitation range [315].

In the literature, there are several attempts to utilise in-situ heat treatment for microstructural control. As reported in Nature, Kürnsteiner et al. printed a martensitic steel using L-DED to recreate a layered "Damascus" steel [330]. This utilised inter-layer holds to allow martensite formation after certain layers, forming a layered structure. Several studies have investigated in-situ heat treatment of Titanium alloys, both using L-PBF [331] and EB-PBF [332]. Chen and Qiu printed Ti-6Al-4V using L-PBF; martensite forms upon solidification, however, by rescanning (without remelting), (α + β) bands could be formed [331]. Li et al. printed Ti-55511 using EB-PBF; by varying the baseplate temperature, the fraction of secondary α could be increased by 5x [332]. Finally, Sames et al. controlled the cooling of Inconel 718 in EB-PBF, by both controlling cooling rate and keeping the sample at heat treatment temperatures. The latter resulted in much increased γ" precipitate size and so increased hardness [315].

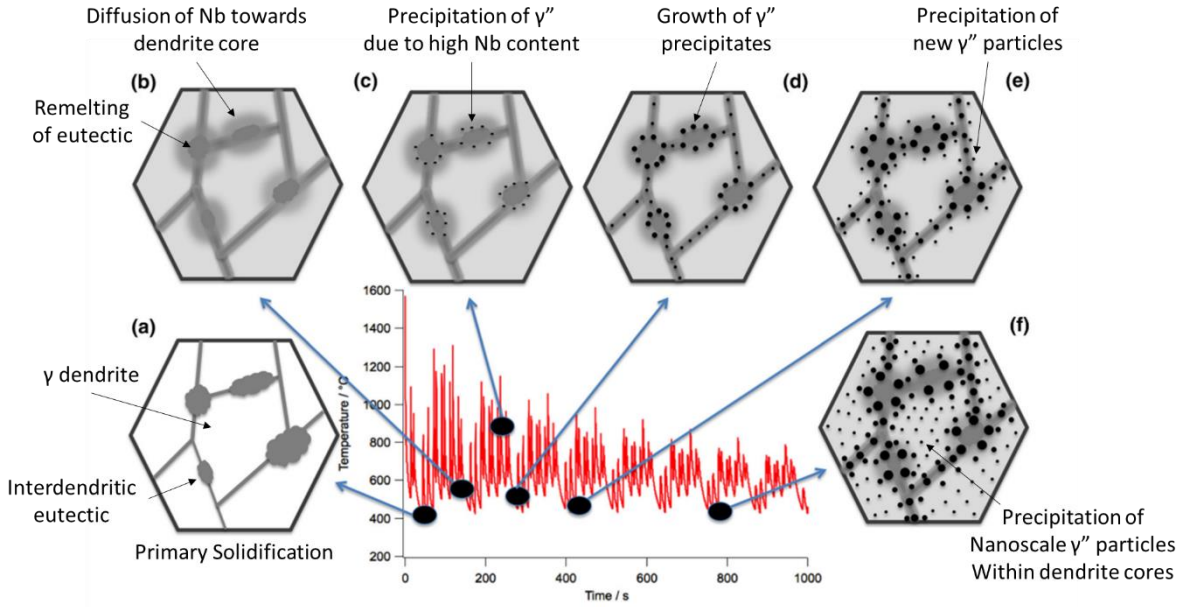

Figure 8-2: Schematic showing evolution of γ" precipitates in Inconel 718 through the DED process. With subsequent hatches/layers reheating the solidified material, each schematic shows a later stage in the process, explaining the growth of precipitates with thermal cycles. Adapted from Tian et al [316]

The density of dislocations has been related to the yield stress of components in L-DED [333], with $\sigma_y \propto \sqrt{\rho_d}$, where ρ_d is the dislocation density [334,335]. The geometrically necessary dislocation density can be approximated using EBSD data [336–338]; the grain average misorientation (GAM) being reported as being proportional to the dislocation density [338,339]. There are some reports of this being an underestimate, but the trend of $\sigma_y \propto GAM$ remains [340]. The dislocation density has been shown to be proportional to yield strength in both L-DED [333] and L- PBF [334]; the reports for L-DED showing a strength variation with build height [333].

Juechter et al. calculated several critical velocities, to determine how quick the power source would have to be moving to interact in different directions [341]. I.e. how quick would the laser have to move for the subsequent hatch to return before the heat from the current hatch dissipated to the extent that it no longer promoted melting. The thermal diffusion depth, $d_{diff} = \sqrt{4\alpha t_{int}}$ where α is the thermal diffusivity and t_{int} the thermal interaction time. d_{diff} was defined as 3 layer depths; this diffusion length should be a characteristic distance of how far the heat diffuses in time t. Since this definition is vague, Juechter et al. have chosen a distance of 3 layer depths, this is arbitrary, but should be of the scale of the heat affected zone. Looking at the definition of the Fourier number,

$F = \frac{\alpha t}{L^2}$ (Section 2.2.1), the definition of their thermal diffusion depth is actually setting F = 0.25, signifying that heat is accumulating in the system.

Critical velocities were then calculated for several types of thermal interaction/conduction; local interaction being the interaction between the laser and the powder and hatching interaction being the thermal losses whilst the laser returns to the same point on the neighbouring hatch. For the laser interaction $t_{int} = \frac{D_b}{v}$, where D_b is the beam diameter and v the scan speed. The critical scanning velocity for local interaction is $v_{crit.local} = \frac{4\alpha D_b}{d_{diff}^2}$ [341]. This is a process dependant parameter, so geometry independent. For the hatching interaction, the interaction time can be calculated as $t_{int} = \frac{L}{v}$ where L is the hatch length. This gives a critical scanning velocity for hatch interaction of $v_{crit.hatch} = \frac{4\alpha L}{d_{diff}^2}$ [341]. Hypothetically, this could be extended to a layer return time by calculating the distance to be hatched within a full layer.

For EB-PBF, the critical hatch interaction velocity was calculated as 10 ms^{-1}, so Juechter et al. conclude that at scanning velocities quicker than this, "heat from previous lines can be used for melting" [341]. The idea is that if there is more remnant heat, then a lower energy density can be used to reach the same temperature. However, a threshold for this cannot be set; in reality, at high scan velocity, increasing the velocity further will decrease return time and so heat will accumulate quicker. But the concept of having heat available for melting, as stated by Juechter et al. is misleading [341]. The fact that increasing velocity is typically thought of as reducing energy density, but can have the effect of increasing heat within the component is an interesting paradox.

As discussed in Section 2.6.1, accurate temperature monitoring is very difficult in AM. Sames et al. used a thermocouple attached to the baseplate [329], but this is not representative of the thermal cycles experienced in the build; this can however, be used to estimate the precipitation occurring during the build. For the precipitation events occurring in subsequent hatches/layers, temperature measurement within the component would be required, which is not currently possible. A simple measure of melt pool size/temperature can be gained by imaging the melt pool coaxially using a greyscale camera and calculating a measure such as the image sum [171] or the melt pool dimension(s) [342]. This is the most common monitoring method on industrial L-DED machines and is most commonly used in process control research [141,343], likely due to the simplicity of the set-up.

The as-built hardness heterogeneity of Inconel 718 is yet to be fully explained. Can simple melt pool modelling be used to estimate the precipitation kinetics in Inconel 718? The hardness trends in as-built L-DED components were explored and the source of hardness variation analysed.

8.2. Methods

Samples were printed in Inconel 718 on the BeAM Magic 2.0 L-DED machine. Samples were built on an Inconel 718 substrate, with the nozzle placed 3.5 mm above the substrate.

Walls of six different thicknesses (controlled by number of hatches) were built, ranging from 1 hatch (1.1 mm thickness) to 8 hatches (3.6 mm thickness) all with consistent build parameters as summarised in Table 10-3. These were sectioned at the midpoint in the YZ section as shown by the orange line in Figure 8-3a, which includes axis definitions. In addition, two triangular prisms were printed with equilateral triangular bases of length 27.5 mm; the hatching strategies were from base to tip and from tip to base, as shown schematically in Figure 8-3b. These were sectioned in the YZ

plane along the midpoint of the triangular section. One extra wall was built for DSC analysis; this was 15 mm tall and was sectioned in the YZ.

Table 8-1: Parameters used for both wall and triangular prism samples

Sample	Wall Thickness (mm)	Power (W)	Velocity (mm/min)	Hatch Spacing (µm)	Z Step (µm)	Mass flow (g/min)
1 hatch Wall	1.1	300	2250	400	200	6-6.5
2 hatch Wall	1.3					
3 hatch Wall	1.7					
4 hatch Wall	2.1					
6 hatch Wall	2.8					
8 hatch Wall	3.6					
10 hatch Wall (DSC)	4.3	300	2000	400	200	6.5-7.5
Base to Tip Triangular Prism	N/A	275	2000	350	225	6.5-7.5
Tip to Base Triangular Prism	N/A	275	2000	350	225	6.5-7.5

Coaxial melt pool monitoring was performed using a greyscale Basler acA1440–73gm camera, filtered to a 660-1000 nm range. Images were recorded at 75 fps using an exposure time of 4000 µs for all builds listed in Table 10-3. The resultant 12-bit images (500 x 500 px) were analysed in MATLAB R2021b (Mathworks Inc), scripts available [170]. For each image, all the pixels were summed to give an overall thermal intensity, similarly to Baraldo et al. [171]. This was compared to both the maximum intensity in a single image and to the melt pool area (calculated using an intensity threshold of 20) as seen in Figure 8-4 for the 6 hatch wall. These plots are linear at intensity sums of above $0.2x10^7$ (marked by the black line), which suggests that the intensity sum (thermal intensity) can be used as a proxy of melt pool temperature/size. The images with sums below $0.2x10^7$ were ignored as they indicated where the laser is off or ramping up/down at the hatch edges. Representative images, thermal intensities and contours are shown in Section 4.2.4.

For each of the walls, one half was polished to a 1 µm finish, these were used for hardness indentation. The other half was further polished using 0.25 µm colloidal silica in preparation for EBSD. The triangular prisms were sectioned along the orange line shown in Figure 8-3a. One half had the top (XY) surface and the other half had the internal YZ section polished to 1 µm diamond suspension, both for hardness indentation.

Hardness was performed using a Durascan 70 Vickers indenter with a 1 kg load, 15 s hold and the indent automatically measured using a 40x optical lens. Walls were indented with an array of

indents in the YZ section, spaced 0.25 mm in the Y axis and 0.75 mm in the Z axis. Triangular prisms were indented with square arrays of 1 mm spacing in both the XY and YZ cross sections.

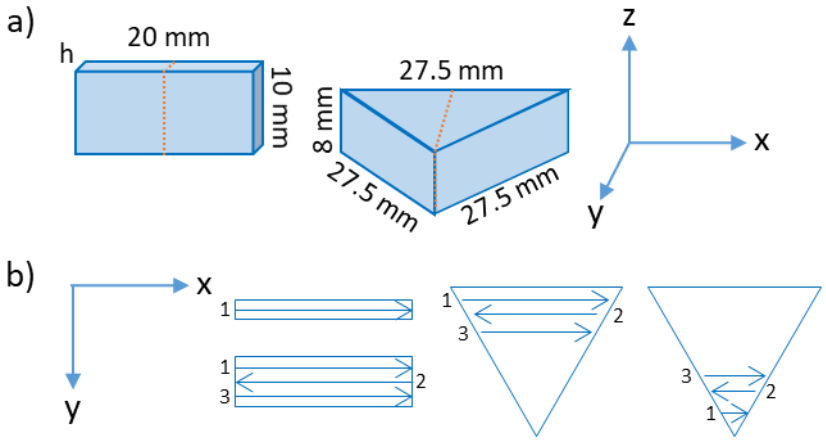

Figure 8-3: Geometries of components built. a) dimensions of both walls and triangular prisms along with machine axes; h is the number of hatches. orange lines show sectioning direction b) view from above showing hatching strategies for 1 hatch wall, 3 hatch wall and triangular prisms. Both base to tip (left) and tip to base (right) hatching shown

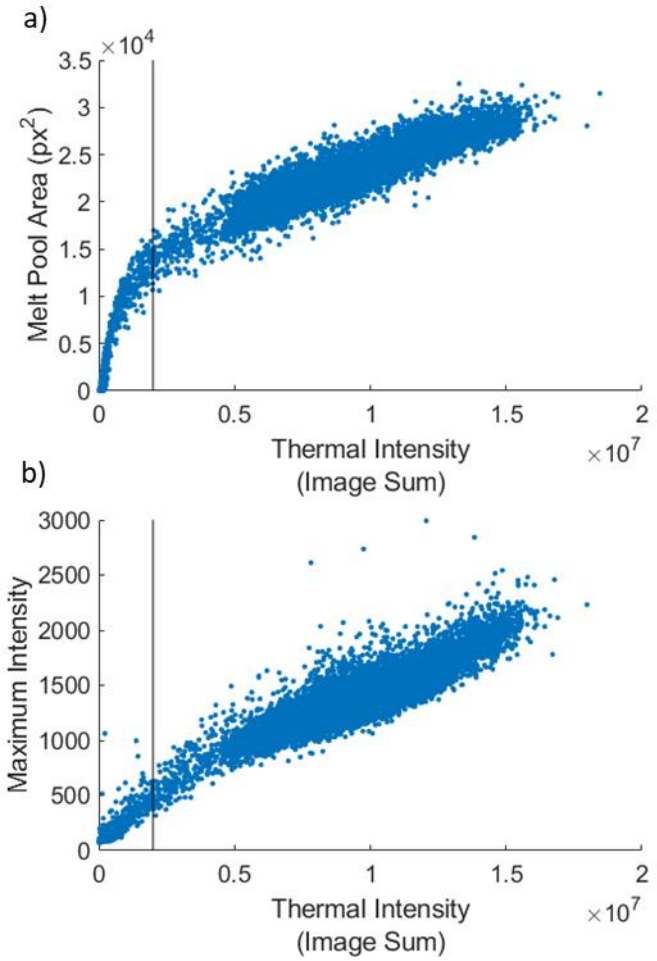

Figure 8-4: Coaxial melt pool data for 6 wall hatch; a) Linear relationship between melt pool area and image sum (above 0.2x10⁷, marked) b) Linear relationship between maximum intensity and image sum

EBSD of the walls was performed using a Jeol 7900F with an Oxford Instruments Symmetry EBSD detector. A 3 µm step size was chosen with a 13 mm work offset and a ~ 90 nA probe current. Walls were scanned with the area covering the full thickness (Y axis) with height of 1.5 mm (Z axis). EBSD

analysis was performed using MTEX 5.7.0, an open source MATLAB Toolbox [174]. Grains were calculated using a threshold grain boundary misorientation of 10°, with a minimum of 3 pixels per grain.

As explained in Section 4.7, area-weighted averages were used for comparison of EBSD data because of the large spread of grain sizes found in L-DED samples; as such, the grain area had to be measured to calculate the weighted averages. Additionally, due to the directional columnar nature of many larger grains, it was decided to plot grain area rather than grain size (for which an equivalent grain diameter is normally reported). The calculation of grain size assumes an equiaxed grain structure, so by stating a grain area we are avoiding using this invalid approximation. Two perpendicular grain sizes could be stated, but this adds complexity as the grains aren't perfectly aligned so it would be difficult to define the axes along which to measure the grain size. Finally, if a grain size was stated, the reader would automatically imagine a spherical grain of that size, to avoid this misinterpretation, the grain area was used throughout.

For each sample, an average calculated anisotropy factor, A_{hkl}, was calculated [104], which varies between 0 for <100> directions to 1/3 for <111> directions: $A_{hkl} = \frac{h^2k^2+k^2l^2+l^2h^2}{(h^2+k^2+l^2)^2}$ [178]. Anisotropy factors are further explained in Section 4.7 with example calculations. Schmid factors were computed for each scanned point (in the X direction) and the maximum Schmid factor at each point was averaged for each sample. Average grain average misorientation (GAM) was calculated for each sample and was calculated for vertical strips (250 μm wide in Y) to allow for an analysis of GAM variation with sample width.

Two samples (cuboids of 1-2 mm edge length) were removed from the 10 hatch wall, both at mid X section, one from the top surface (maximum Z) and the other from halfway up; these will be referred to as tip and centre respectively. DSC was performed on these samples (Section 4.6), calculating a differentiated heat flow, where negative values represent a drop of the heat flow from the baseline.

8.2.1. Precipitation Potential Model

As hypothesised by Tian et al. and Kumara et al., precipitate nucleation and growth occurs not only during solidification, but mainly during reheating from subsequent hatches and layers [316,327]. To capture this effect, the time within the γ" precipitation temperature range was calculated by using a moving Gaussian heat source model (Equation 2-4) [33]. The Gaussian heat source is a reasonable approximation to the BeAM's top hat beam [33]. Parameters used for these calculations are summarised in Table 8-2, scripts available [170].

The output from the model is a steady state temperature field from which the melt pool can be extracted by drawing a contour at the solidus temperature (Figure 8-5). The precipitation temperature range was taken as 700-900 °C, in line with literature values [314,321,322], with dissolution occurring between 900 °C and the solidus temperature. It is assumed that precipitation kinetics are constant in the temperature range analysed, which is supported by TTT curves by Niang et al (Figure 8-1) [314].

Table 8-2: Parameters used for the Gaussian heat source calculations

Parameter	Value	Reference
Step Size	5 µm	-
Thermal Conductivity, κ	9.94 $Wm^{-1}K^{-1}$	[273]
Thermal Diffusivity, α	2.87x10^{-6} m^2s^{-1}	[273]
Absorption Coefficient, A	0.45	[275]
Melting Point (solidus), T_m	1643 K	[275]
Laser Power, P	300 W	-
Laser Velocity, v	2250 mm·min^{-1}	-
Laser Beam Diameter, D_b	0.7 mm	-

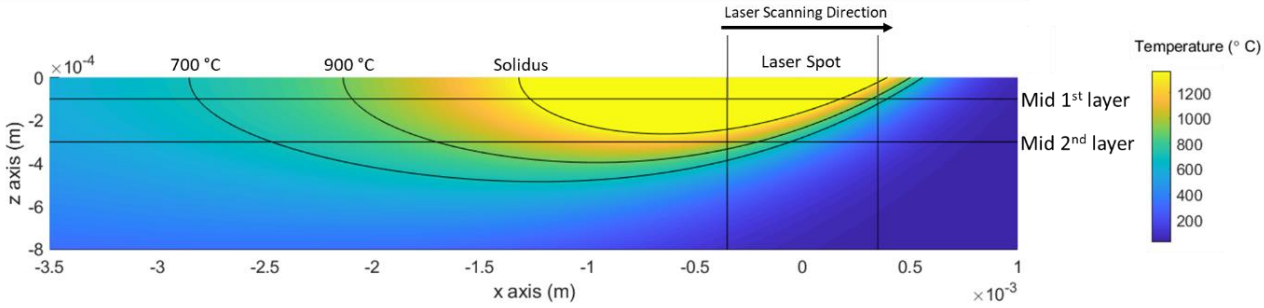

Figure 8-5: Temperature field output from moving laser source model; side on (XZ) view showing the laser position and contours at the solidus temperature, 700 °C and 900 °C. Horizontal lines shown halfway through subsequent layers

The light blue temperature regions in Figure 8-6 show the precipitation zone, which is of interest in this analysis. The length of the zone was measured, and by knowing the laser velocity, the duration in the precipitation zone could be calculated. The temperature range within the dark blue regions were such that no microstructural changes were expected to occur. The temperature of the green region was above the precipitation zone, such that transformation or dissolution may occur and finally, the yellow temperature regions were above the solidus temperature, and were assumed to be molten. For simplicity, the centre point of each hatch was taken to be representative of the whole hatch (marked by red dots in Figure 8-6d).

P1 (Figure 8-6a, b) shows the precipitation during solidification – directly behind the melt pool. The subsequent hatch remelted this material and then precipitation occurred in the region marked P2; the following hatch never heated the region into the precipitation region (marked as the bottom horizontal line in Figure 8-6b). As the next layer is deposited (Figure 8-6c), when the laser is directly above the hatch of interest, precipitation marked by P3 occurred, so some precipitation occurred, then dissolution occurred in the region marked D1 and finally more precipitation (again, P3). In addition, the neighbouring hatch in this layer also heated the hatch of interest, marked P4.

Figure 8-6d shows the yz section of a melt pool and where the temperature field for each hatch was extracted. Three hatches were marked in red as worked examples. The one on the left hand side at height 1.8 mm was remelted by the subsequent hatch (marked P2), which caused dissolution of any precipitates formed during solidification, but re-precipitation occurred due to P2. Then in the

subsequent layer, it experienced precipitation due to P4 and P3 as marked – by summing the time spent in these precipitation regions, the cumulative precipitation potential could be calculated.

For the hatch of interest at z=2.1 mm on the right side, there was no subsequent remelting, so precipitations due to P1 was retained; then on the following layer, precipitation during P3 and P4 occurred. Finally, for the hatch of interest at x=2.2 mm, the P2 hatch remelted it, so no P1 precipitation was present. In the following layer, as well as being heated by the hatch directly above it (P4), there were 2 neighbouring hatches (both P3) which contribute to the precipitation.

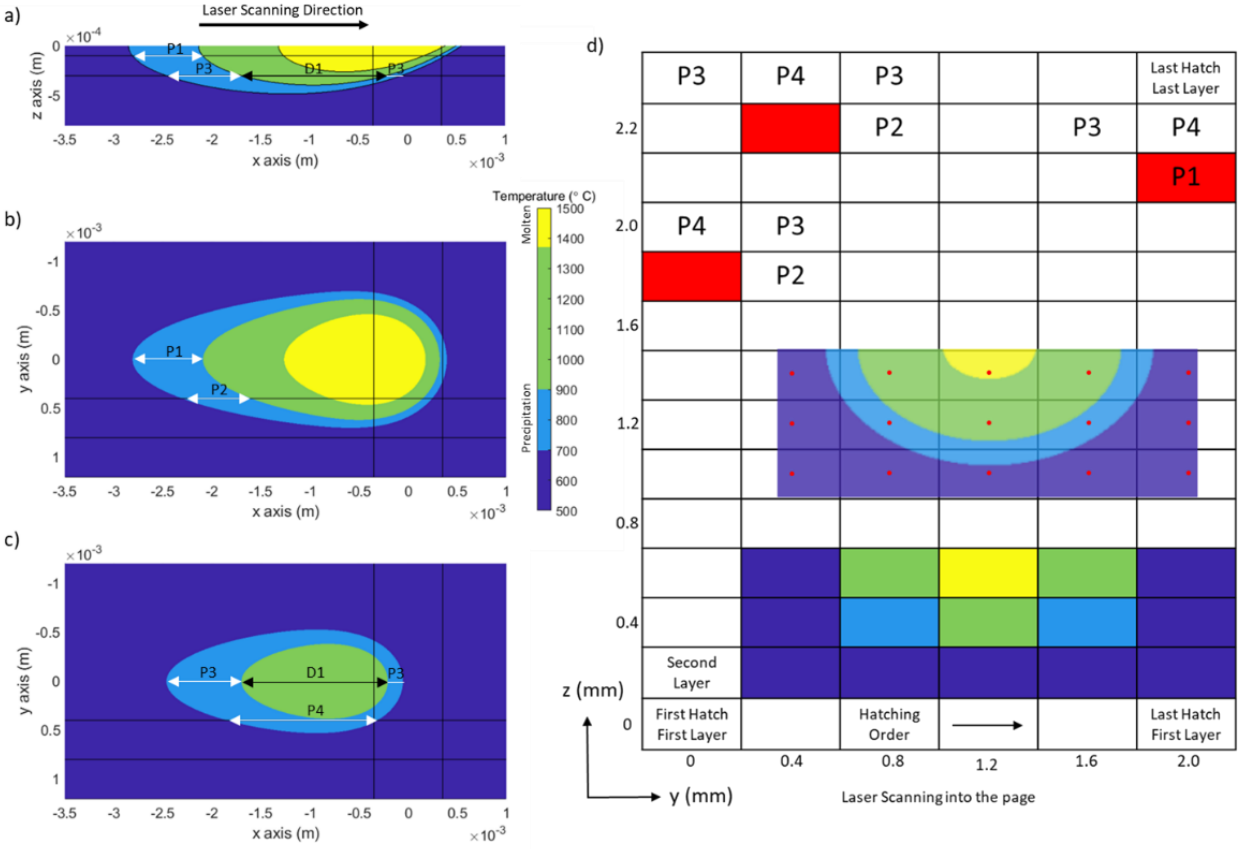

Figure 8-6: Diagram showing the calculations for precipitation potential during L-DED. a) xz section at maximum length of melt pool, as in Figure 8-5, colour scale set to show different key regions during cooling. b) xz section at mid-1st layer (as marked Figure 8-5), precipitation regions shown for the current hatch (P1) and the subsequent hatch (P2). c) xz section at mid-2nd layer (as marked in Figure 8-5), precipitation regions shown for the next layer (P3) and the subsequent hatch in the next layer (P4). d) yz cross section of a 6 hatch wall, laser scans into the page, hatching order from left to right. Shown in red are 3 example hatches with precipitation regions from subsequent hatches marked. Also shown is a yz section of the melt pool with the red dots showing the centre points at which analysis was undertaken

8.2.2. **Precipitation Hardening**

The hardness increase due to precipitation is difficult to calculate. γ", due to its ordered nature, increases hardness both using traditional particle strengthening mechanisms as well as order strengthening [334]. When small, γ" particles are coherent with the matrix, they can be cut by dislocations. The main strengthening mechanism at this stage is coherency strengthening, with the precipitate mismatch causing a strain, which hinders dislocation movement [344]. In γ", the misfit strain varies with orientation and temperature, but in ambient conditions, the misfit strains are 0.0014 and 0.033 for the a and c axes respectively [317]. Coherency hardening is expected to increase the shear strength according to the following equation [344]:

$$\tau = \sqrt{\frac{3k^2\varepsilon^3 {G_s}^2 f r_{ppt}}{2\pi b}}$$

Parameters used in the calculation are summarised in Table 8-3, calculations were performed for the a and c axes independently. Due to the larger misfit in the c axis, when the precipitates grow, coherency is lost in the c axis first. At this point, coherency strains no longer apply, so the dislocations have no option, but to bow around the precipitate. The Orowan dislocation bowing model was used to calculate this [345,346]:

$$Shear\ strength, \tau\ = \frac{G_s b}{L}$$

Parameters used in the calculation are summarised in Table 8-3. L is the precipitate spacing, which is calculated assuming a constant distribution of spherical precipitates [347], the larger particle radius of 25 nm being used in this case. Shear stress can be converted to yield stress using $\sigma_y \sim M\tau$ [334]. M is the Taylor parameter, this is typically reported to be ~3 [345,346]. Hardness is often stated to be related to yield stress (MPa) by the rule of thumb HV ~ σ_y /3 [348,349].

As the precipitate grows, the energy required for cutting increases, whilst that for bowing decreases, such that bowing takes over. For low γ' nickel superalloys, the γ' precipitate size at which bowing dominates is of the order of 200 nm [350]. In reality, due to the incoherent nature of the precipitates in the c axis, Orowan bowing can be taken as the dominant mechanism along the c axis. In the a axis, initially, coherency strains will dominate, but as they grow, Orowan bowing will take over. The hardening effect will therefore be between that due to coherency strengthening and that due to Orowan bowing for the a axis.

Precipitation of γ" removes elements from the solid solution, reducing the effect of solid solution strengthening. Since this predominantly occurs interdendritically, the initial powder composition isn't representative. Instead, a Scheil solidification calculation was run using Thermo-Calc 2021b [232] to determine the composition of the interdendritic regions. The powder composition (Table 4-1) was input and the composition was calculated at f_s=0.65; this was chosen as the average between f_s=0.4, where there is still mass movement and f_s=0.9 where there is an interdendritic film only [202]; the results are summarised in Table 8-4.

Table 8-3: Parameters used in precipitation strengthening calculations

Parameter	**Value**
Shear Modulus, G_s	77.2 GPa [351]
Burgers Vector, b	0.254 [352]
Precipitate Radius, r_{ppt}	25 nm in a, 5 nm in c [183,314,316,322]
Precipitate Volume Fraction, f	5 – 20 % [190,315,318,346]
Numerical Constant, k	3.5 [344]
Misfit strain, ε	0.0014 in a, 0.033 in c [317]
Precipitate Spacing, L	$L = 2r\left(\sqrt{\frac{8}{3\pi f}} - 1\right)$ [347]
Taylor Parameter, M	3 [345,346]

Table 8-4: Interdendritic composition of alloy as calculated by Thermo-Calc and the strengthening constants as used to calculate solid solution strengthening effect [353]

Element	Cr	Ni	Co	Mo	Nb	Ti	Al	Fe
Scheil composition at 65% fraction solid (at. %)	20.65	50.45	0.03	2.12	4.40	1.23	1.12	19.56
Strengthening Constant, k [40]	337	-	39.4	1015	1183	775	225	153

8.3. Results

8.3.1. Thermal Monitoring

Coaxial melt pool imagery was recorded throughout all builds and a thermal intensity for each frame calculated by summing the pixel intensities in the frame. The data acquisition rate was 17.6 MB/s, similar to the InGaAs_30 camera mode (Section 7.2), despite recording at more than double the frame rate. As shown in Figure 8-4, thermal intensity values below $0.2x10^7$ were excluded. For the base to tip triangular prism, the thermal intensities are shown in Figure 8-7, with an overview of the full build shown in Figure 8-7a (smoothing applied), the thermal intensity can be seen to increase over the first 6-7 layers and then a plateau being reached, with significant variation within a layer. Figure 8-7b shows the thermal intensity for a layer in the plateau without any smoothing or frame removal. Each hatch can be seen as the thermal intensity drops to 0 between hatches and the hatch length can be seen to decrease as the tip is approached, with the thermal intensity increases near the tip.

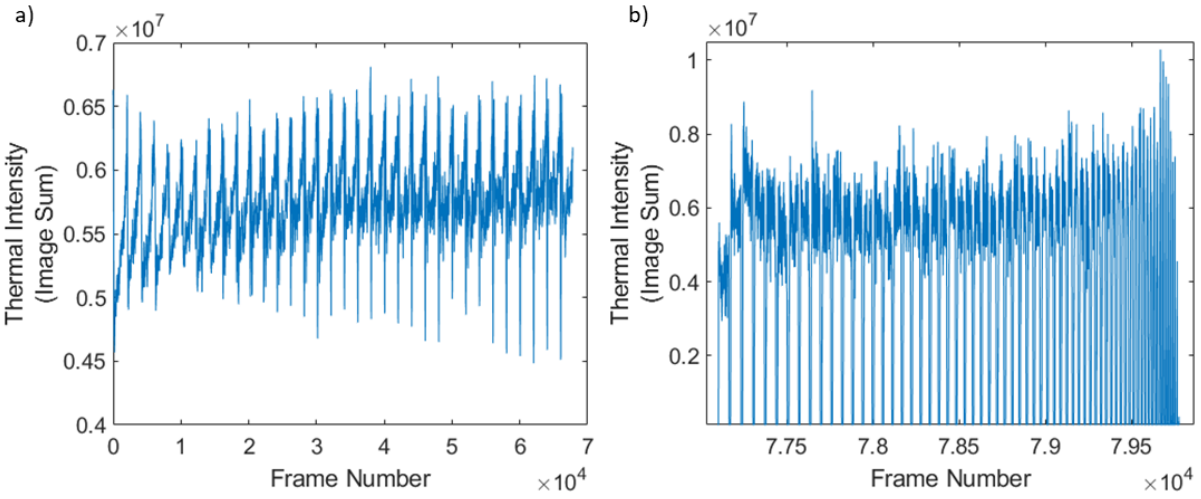

Figure 8-7: Thermal data from base to tip triangular prism showing the thermal intensity with frame number; a) full build, values below 0.2x10⁷ removed and a moving mean of width 100 points applied b) single layer without any data filtering/smoothing

Similar plots are shown for the 6 hatch wall in Figure 8-8, again with the overall intensity shown to increase with build time, but in this case, more layers were required before the plateau was reached, potentially due to the shorter layers. Figure 8-8b shows the thermal intensity of 2 layers, exhibiting a clear trend with the central hatches having higher thermal intensity than edge hatches.

The average intensity for each wall (excluding points below 0.2x10⁷) is shown in Figure 8-9. The thermal intensity increases with hatch number up to 3 hatches, above this, the thermal intensity drops until a plateau at a thickness of 8 hatches.

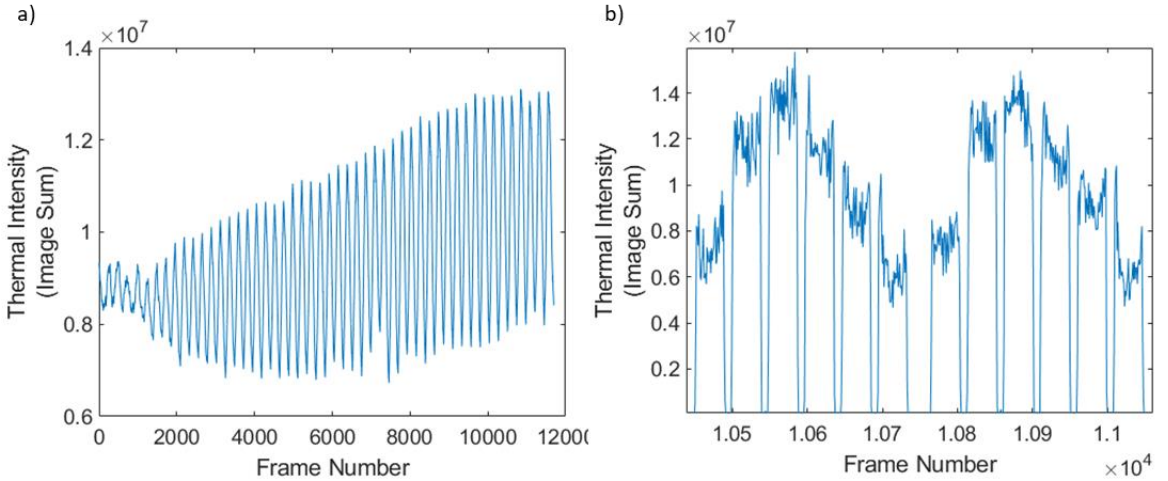

Figure 8-8: Thermal data of 6 hatch wall showing the thermal intensity with frame number; a) full build, values below 0.2x10⁷ removed and a moving mean of width 100 points applied b) two layers without any data filtering/smoothing

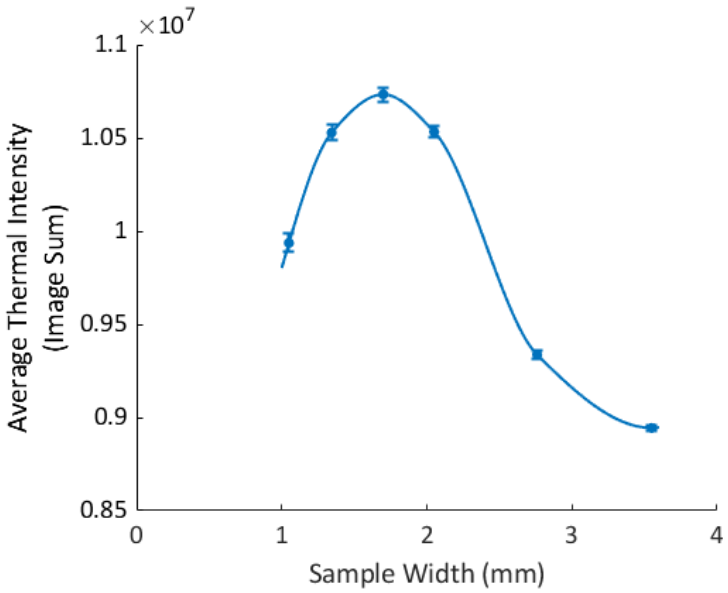

Figure 8-9: Average thermal intensity (<0.2x10⁷ removed) for each wall, error bars showing standard error

8.3.2. **Hardness Analysis**

Hardness maps were taken from two sections of the triangular prisms as shown in Figure 8-10a and b. The slanted and bottom edges of the XY section were observed to be softer than the bulk (unfilled in Figure 8-10a) and Figure 8-10c shows that the edges (along the Y axis) are softer than the bulk. A longer drop-off is seen at larger y values, which is where the tip of the triangular prism is.

The hardness distribution in the walls is summarised in Figure 8-11a shows the hardness variation in the y axis. For most walls, the peak hardness is at the centre, with notable hardness drop-offs within 1 mm of the edge. For this reason, the peak hardness increases with wall thickness until the 6 hatch wall after which there is minimal change. Figure 8-11b shows the variation with height within the 6 hatch wall, which is representative. The indents closest the substrate were hardest, with a steady decrease, before a drop at the final indent. Figure 8-11c shows the average hardness for each wall with respect to sample thickness. Again, the average hardness increases with sample thickness until 2-3 mm at which point the hardness plateaus. Table 8-5 shows the average hardness for each section of each sample. The bottom row of indents (in z) was disregarded, because of the heat-sink effect of the substrate. For each section, a single indent along each external edge of the sample were selected; these were called the edge hardness' and the remaining indents were classed as centre hardness' as summarised in Table 8-5. Unpaired 2 sample t-tests (α=0.05) were performed for each sample between the centre and the edge to test whether the hardness values were significantly different and the results are shown in Table 8-5.

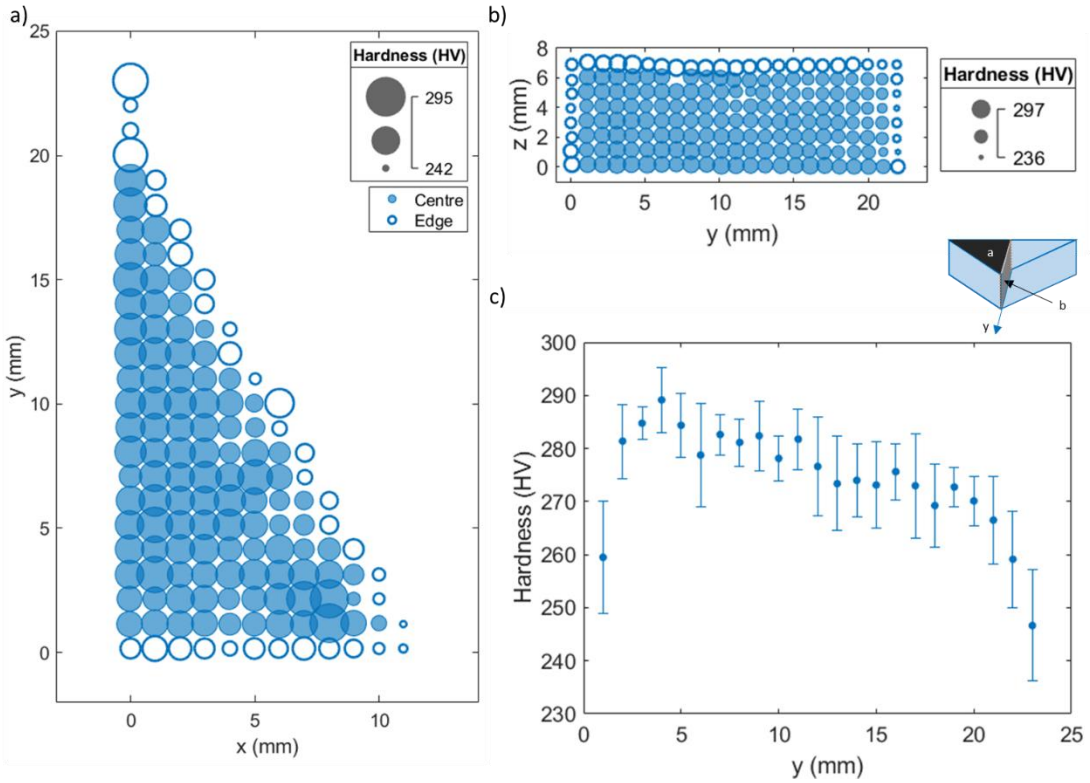

Figure 8-10: Hardness distribution for base-tip triangular prism; a) XY section b) YZ section c) average hardness along Y direction as calculated from yz section, standard deviation shown. Inset shows cross-sections taken and positive y direction

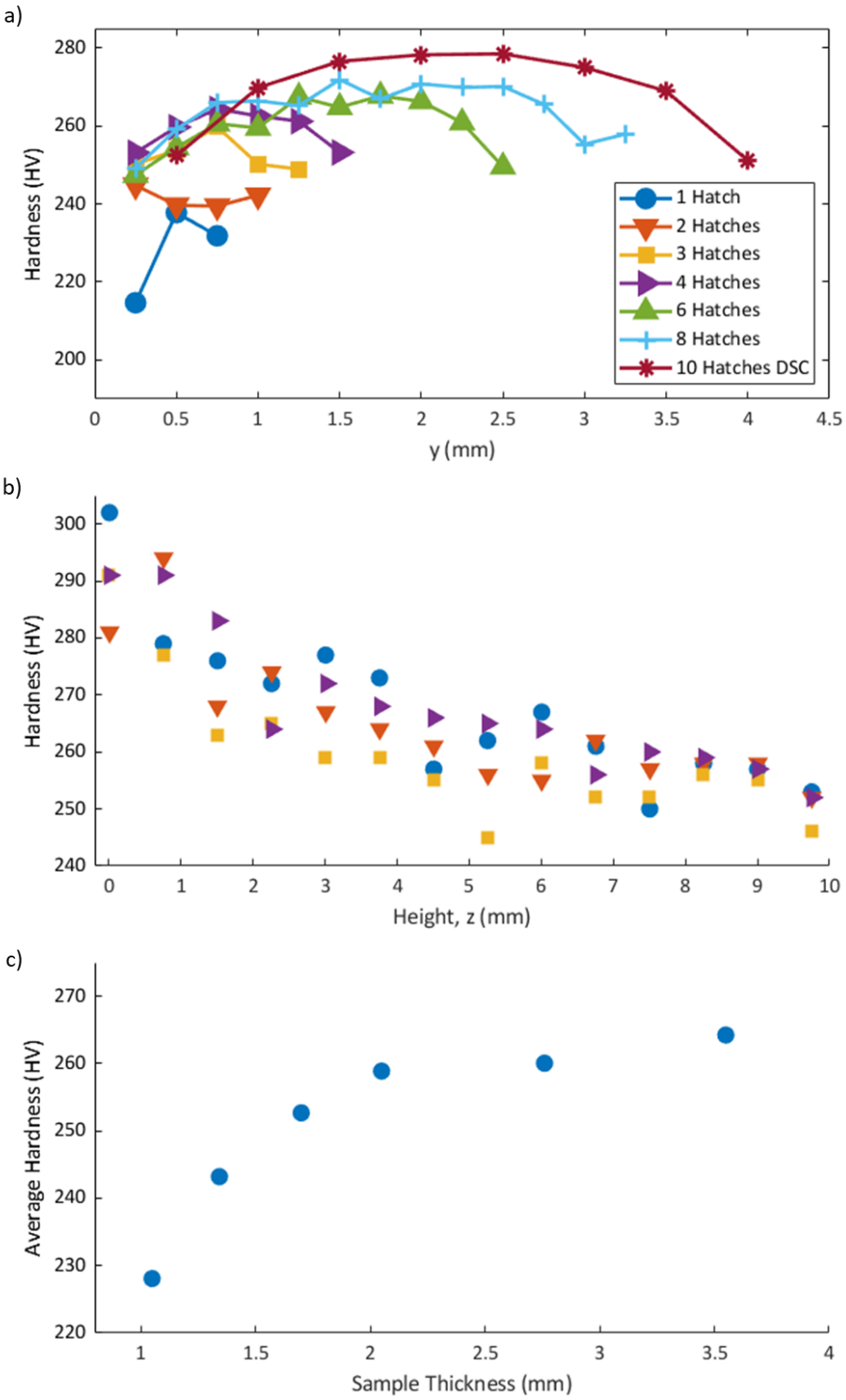

Figure 8-11: Hardness plots of walls; a) with thickness (y axis), showing maximum hardness at centre of the wall b) Hardness values along four central columns of indents in 6 hatch wall c) average hardness of walls plotted against sample thickness

Table 8-5: Table summarising average hardness values for all walls and triangular prisms. Showing centre and edge value separately to test whether these are significantly different (two sample t-tests were used to determine statistical significance using $p<0.05$)

			Average Hardness - HV (Standard Error)			Statistically significant difference between centre and edge hardness
	Sample	No. Indents	Full Sample	Edges	Centre	
	1 hatch wall	36	223.3 (3.3)	218.9 (3.8)	233.6 (5.2)	Yes
	2 hatch wall	52	243.2 (2.6)	240.1 (3.7)	239.9 (2.9)	No
	3 hatch wall	68	250.1 (2.2)	245.4 (3.7)	253.6 (2.0)	Yes
	4 hatch wall	84	256.6 (2.0)	249.1 (3.6)	261.2 (1.5)	Yes
	6 hatch wall	136	257.8 (1.6)	246.7 (3.5)	261.6 (0.8)	Yes
	8 hatch wall	176	262.6 (1.4)	252.9 (3.4)	265.2 (0.5)	Yes
	10_DSC wall	128	267.8 (1.7)	253.2 (3.4)	274.0 (0.5)	Yes
Base to Tip Triangular Prism	YZ section (rectangular)	184	273.4 (0.9)	264.3 (2.7)	276.0 (0.8)	Yes
	XY section (triangular)	142	264.6 (0.9)	254.3 (1.6)	267.9 (0.9)	Yes
	Combined	326	272.7 (0.7)	259.3 (1.6)	272.3 (0.6)	Yes
Tip to Base Triangular Prism	YZ section (rectangular)	184	275.6 (0.9)	274.0 (2.9)	276.1 (0.9)	No
	XY section (triangular)	155	260.8 (0.9)	251.3 (1.3)	263.5 (0.9)	Yes
	Combined	339	268.3 (0.7)	262.3 (2.1)	269.9 (0.7)	Yes

8.3.3. **EBSD Analysis**

EBSD maps of the YZ sections of the walls were used to understand the grain structure. Maps were constructed through the full thickness (Y) and a height of at least 1.5 mm (Z) (Figure 8-12). The results indicated that the single hatch was symmetrical, with grains growing from the edges downwards towards the centre and a variety of orientations were present. Samples with 2 and 3 hatches were progressively more oriented along <100> with more grains aligned in the growth direction and some large grains in the 3 hatch sample. Samples consisting of 4, 6 and 8 hatches were all predominantly near the <111> orientation (blue/purple) with long grains growing along the height of the walls.

Small equiaxed grains with no dominant orientation were found to form where the laser had passed. Between these centres, there are grains which propagate through many layers, forming large elongated grains. The average hardness values are plotted against the anisotropy factor [178] for the 6 walls in Figure 8-13. No clear trends are visible, with 1-3 hatch walls decreasing in

hardness with increasing anisotropy factor, whereas wider walls show little variation in either hardness or anisotropy factor.

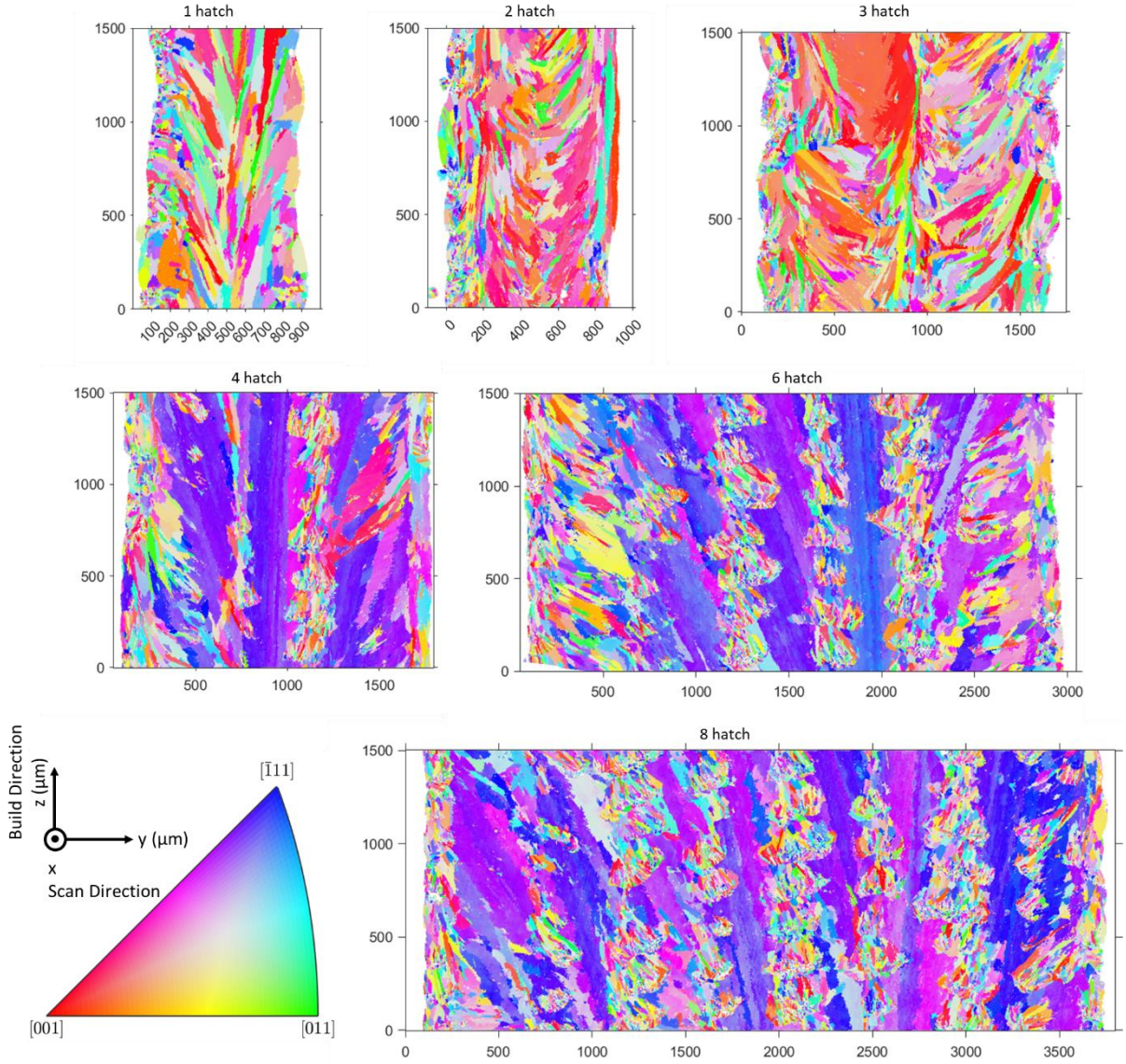

Figure 8-12: Inverse pole figure (IPFX) maps of YZ section of walls from 1 - 8 hatches showing full thickness (Y) and 1500 µm height (Z) at the midpoint of the height

Figure 8-14 shows the distribution of GAM for each grain in the 6 hatch wall; the large grains appear to have the highest GAM values. There seems to be no clear trend between the edges and the centre of the sample. The average GAM for each wall was calculated and is shown in Figure 8-15; there is a monotonic relationship, with the GAM increasing with wall width. The distribution of GAM values with width are shown in Figure 8-16; this confirms that wider walls have higher GAM values. Also, the wider walls (which have more columnar grains) have a stronger variation of GAM; for some samples, the edges seem to show a lower GAM value, but this is not a universal trend.

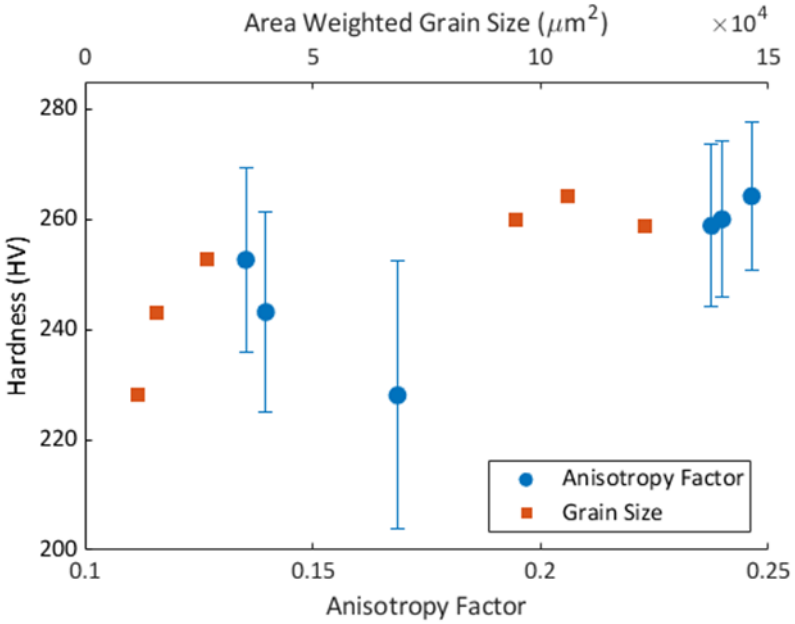

Figure 8-13: Plot of hardness against anisotropy factor for the 6 walls of varying thicknesses shown on bottom axis (blue). Standard deviations of hardness shown; labels show number of hatches. Top axis shows the variation of hardness with area weighted grain size (orange) for the same six walls

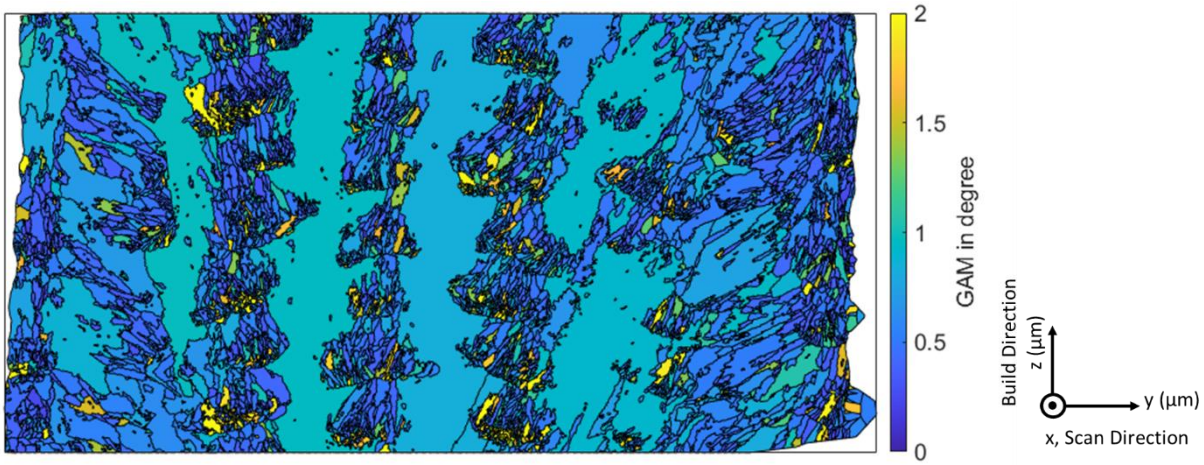

Figure 8-14: Grain average misorientation (GAM) of the 6 hatch wall

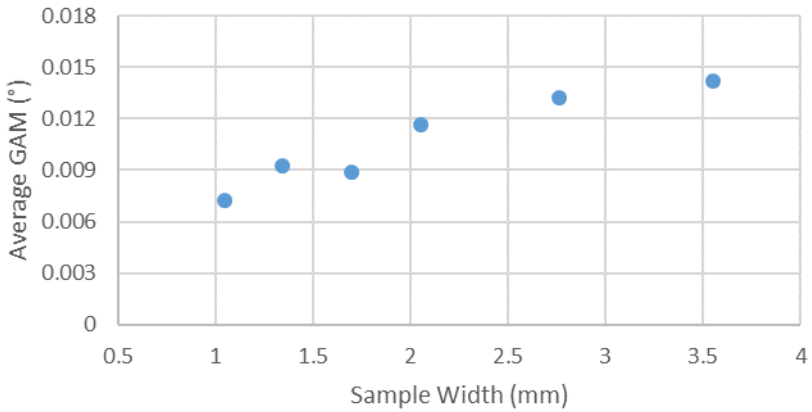

Figure 8-15: Average GAM for each wall

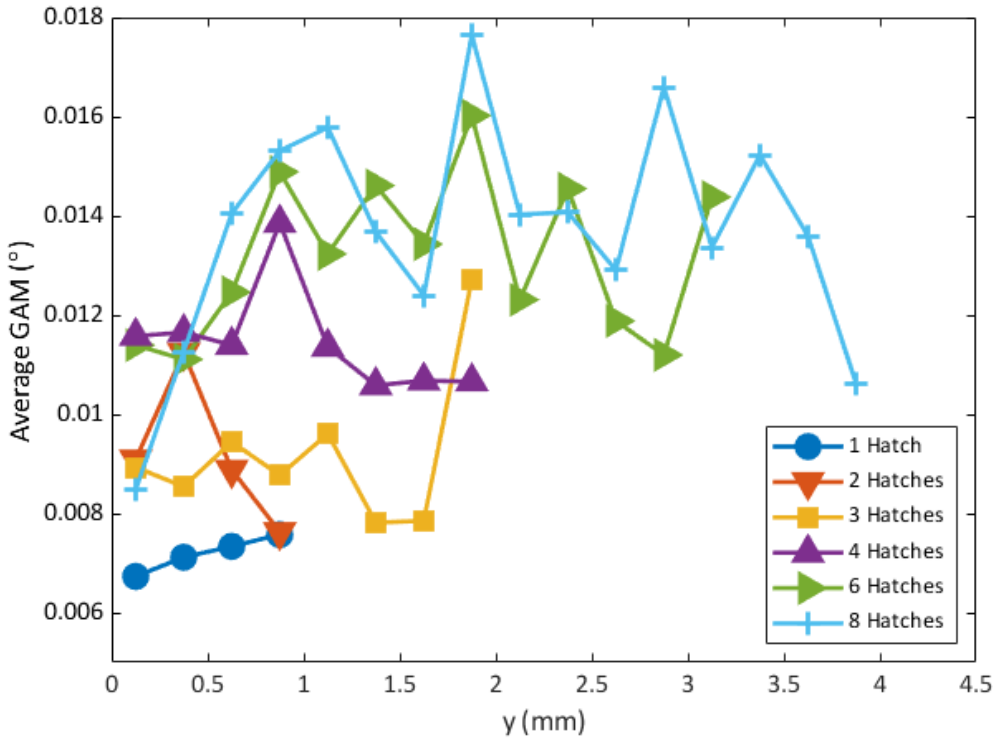

Figure 8-16: Variation of average GAM with sample width

For each sample, the Schmid Factor was calculated as a point average, this is summarised in Table 8-6. For thin walls (1-3 hatches), this is 0.46; for the wider walls, this decreases to ~0.41. In addition, MTEX was used calculate the principal axes for each grain [23]. The short principal axis can be taken as the shortest path that an average dislocation would take before encountering a grain boundary. An area weighted average minimum grain diameter was extracted. This was averaged for each wall, so an expected yield stress change due to the Hall-Petch effect was calculated using $\sigma_y = \frac{k}{\sqrt{d}}$ [31], where d is the grain size (µm – equivalent diameter) and k is a constant (750 MPa µm^{-1} [31]), Table 8-7. A small hardness difference was observed with the number of hatches, with the largest hardness increase in the narrowest walls.

Table 8-6: Schmid Factors calculated for each wall

Hatches	Schmid Factor
1	0.46
2	0.46
3	0.46
4	0.41
6	0.42
8	0.41

Table 8-7: Expected hardness increase as a result of grain size effects using Hall-Petch effect

Hatches	Average Minimum Principal Component Axis (µm)	Calculated Yield Stress Increase (MPa)	Calculated Hardness Increase (HV)
1	23.5	155	52
2	23.9	153	51
3	36.3	124	41
4	77.7	85	28
6	65.6	93	31
8	71.3	89	30

8.3.4. **Precipitate Analysis**

DSC experiments were conducted to characterise which precipitates were present in the as-built samples. DSC was performed at a rate of 20 °C/min for both a central sample and one at the tip of a 10 hatch sample. The raw data is plotted in Figure 8-17a, showing both the heating and cooling cycles, both normalised by weight for comparison. The γ" phase is typically formed in the 700-900 °C range, with DSC thermal arrest reported in the 840-890 °C range [321]. Figure 8-17b shows the rate of change of heat with temperature (having removed the heating baseline). Heat is absorbed during precipitation which would be seen as a drop to negative values in Figure 8-17b.

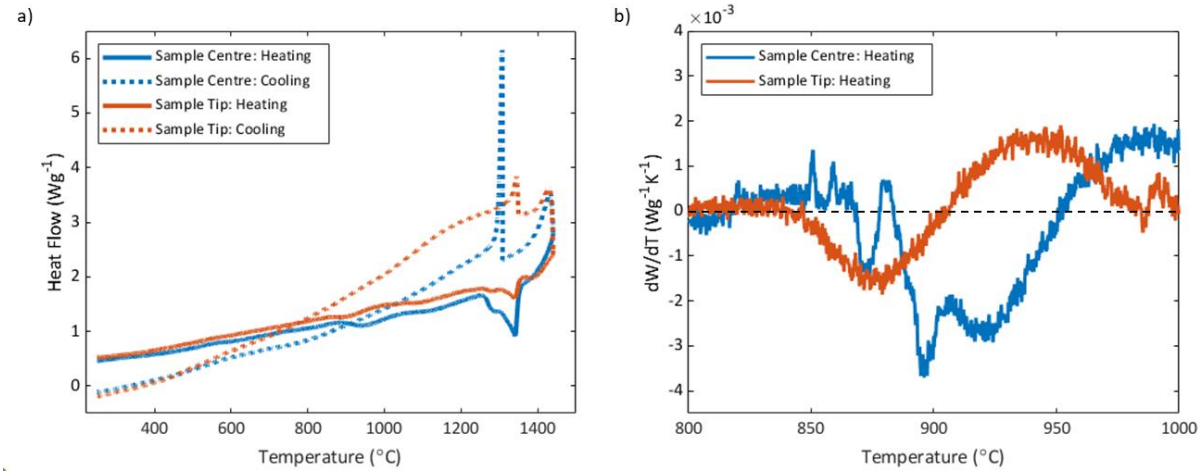

Figure 8-17: DSC results comparing the centre and the tip of the 10 hatch sample; a) Heat flow (normalised for mass) for both samples during heating and cooling cycles b) heat flow of heating cycles removed from heating baseline, differentiated with respect to temperature. Negative values show a drop from the heating curve, i.e. heat being absorbed by the sample

For the sample tip (orange), deviation from the baseline in the range between 850-900 °C is observed, as expected. In the sample centre (blue), there is more noise, with a slight dip around 870 °C and then a much wider dip centred on 920 °C. The area between the curve and the x-axis is the heat absorbed, which can be used to provide an indication of the relative fraction of the precipitate. Although this cannot always be quantitatively compared due to sample differences, it provides a qualitative measure suggesting higher fraction of γ" in the centre sample when compared with the tip of the sample (area 2.5x in the centre compared to the tip).

Hardness increase calculations were performed at 2 % increments in precipitate volume fraction between 5 – 15 % and for 20 % as heat treated samples are reported with volume fractions up to 20 %, but this is unlikely in an as-built AM sample. The hardness was found to increase with

volume fraction for both the Orowan and coherency strengthening mechanisms, whilst the solid solution strengthening decreases (Table 8-8). If there are two competing strengthening mechanisms, the one with the smaller strengthening increase will dominate, as the dislocation requires less energy to behave in this manner.

Table 8-8: Outputs from precipitation strengthening calculations

	Hardness Increase (HV)			
Volume Fraction γ" (%)	**Solid Solution Strengthening**	**Orowan Bowing**	**Coherency strengthening (a axis)**	**Coherency strengthening (c axis)**
5	259	126	36	5853
7	257	158	43	6925
9	254	189	49	7852
11	252	221	54	8681
13	248	252	58	9437
15	244	284	63	10137
20	229	370	75	11705

8.3.5. **Precipitation Potential**

For each hatch, the total time in the precipitation temperature range was calculated, which effectively represents the precipitation potential of the sample. Since precipitates can dissolve/transform above 900 °C, dissolution time was also calculated and subtracted from the precipitation time. These total times are plotted in Figure 8-18a, with longer precipitation times in grey and shorter times in blue. It can be clearly seen that the top surface experiences the least time in the precipitation zone, followed by the outside edges. The bulk of the samples experiences the longest time in the precipitation zone, which is estimated to be ~0.095 s.

Since dissolution rates are not accurately known, the same calculations were repeated, but without subtracting dissolution times (i.e. sum of precipitation times only). This is shown in Figure 8-18b with similar trends but an increased maximum duration of 0.14 s.

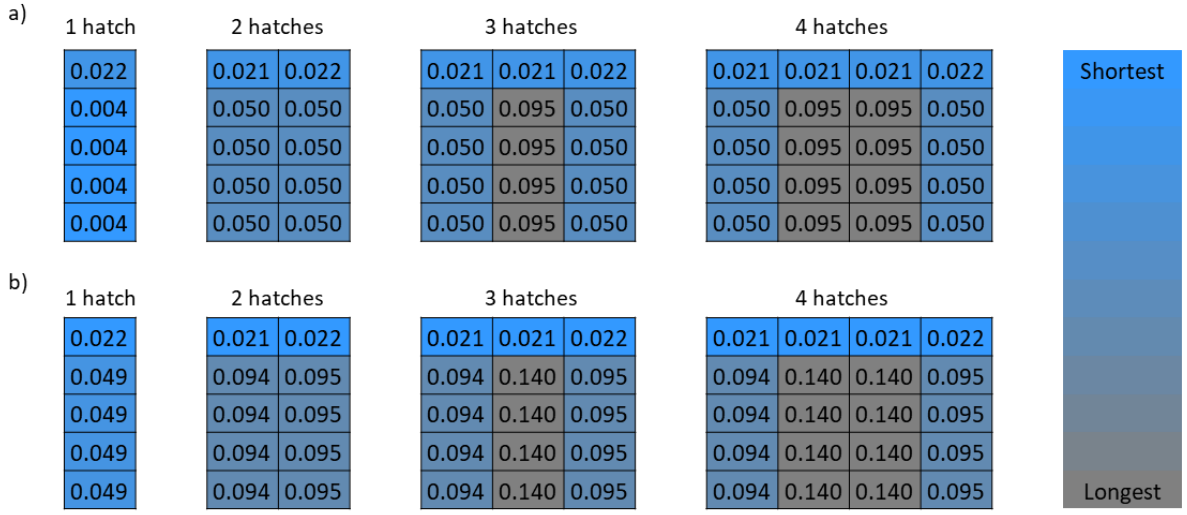

Figure 8-18: Precipitation times (s) output from the precipitation potential model, showing YZ section. For walls wider than 4 hatches, the same edge pattern remains. a) sum of time in precipitation regions, subtracting time in dissolution zone. b) sum of time in precipitation regions, assuming dissolution is negligible

8.4. Discussion

The hardness maps of the triangular prisms (Figure 8-10a) show that the external edges are softer than the centre. The same pattern can be seen in the walls, with maximum hardness at the wall centres (Figure 8-11a). It could be expected that this would be derived from the melt pool morphology. Figure 8-8b shows the thermal intensity, which has been shown to be representative of the melt pool size (Figure 8-4). The same pattern can be seen, with the edges having a lower thermal intensity corresponding to the lower hardness.

However, when looking at the average thermal intensities for the walls, the maximum thermal intensity is for the 3 hatch wall, with dropping intensity either side (Figure 8-9). The average hardness values for walls increases with thickness until a plateau is reached following 4 hatches. Since the overall hardness' of the walls doesn't correlate with the thermal intensities, it can be concluded that the measured hardness values are not directly dependant on the melt pool morphology. Coaxial monitoring is found to be simpler to analyse than side-on monitoring, due to the static position within the field of view; the temporal resolution is lower than that used in Chapter 7, however, the information captured is sufficient to determine average melt pool dimensions, whilst being easy to process live.

At a data acquisition rate of 18 MB/s, roughly 30 GB are stored for each of the wider wall builds. The image intensities can be calculated live and stored without saving the raw images, similarly to the Concept Laser L-PBF [298,299]. If storing only the calculated data and laser positions, then the data storage rate is reduced to 3.7 KB/s. This is a 5000x storage reduction, of a similar order to that reported by Spears and Gold [298]. In this case, only the overall melt pool intensity was stored (which is comparable to the pyrometry signal on the Aconity3D machine), but more dimensions such as melt pool length and width could be recorded with minimal data storage increases. At this point, the difficulty becomes calculating melt pool dimensions; number of pixels above a threshold is a relatively simple calculation, but for a length, a contour must be drawn, which is more computationally demanding.

When compared to the side-on monitoring methods discussed in Section 7.2, the combined spatial and temporal resolution of the Basler coaxial camera is comparable to that of the side-on Silicon camera (Figure 7-20). As previously discussed, the coaxial nature of monitoring keeps the melt pool static in the field of view and a high spatial resolution can be achieved. However, since the beam splitter on the BeAM Magic 2.0 was preinstalled, the Basler camera is routed through optics which may not have been designed with this in mind. When considering process control, coaxial monitoring is advantageous due to the simpler processing associated with a static melt pool. The spatial and temporal resolution are sufficiently high for accurate process monitoring, whilst retaining low enough data volumes for online processing to be feasible.

A decrease of hardness with height has previously been reported in Inconel 718 [316] and is confirmed in Figure 8-11b. Also seen is that the highest indent typically experiences a more significant hardness drop-off. To quantify the hardness differences between the edges and the centres of samples, the hardness indents were classified as follows:

- Indents in the bottom row (z, closest to substrate) were removed
- Indents in the top row and nearest indent to any other external face were classified as edge indents
- The rest of the indents were classified as centre indents.

Two sample t-tests show that for both triangular prisms, there is a statistically significant ($p<0.05$) decrease in hardness in the edge indents when compared with the centre (Table 8-5). The decrease in the YZ section of the tip to base triangular prism was not statistically significant, but when combined with the XY section, then the whole part was significantly harder in the centre. Walls were built with different numbers of hatches to simplify the geometry and identify the source of the hardness variation.

For 6 of the 7 walls, the centre was statistically significantly harder than the edges (Table 8-5). The 2 hatch wall shows no trend, but since the 1 and 3 hatch walls both experience the hardness variation, the 2 hatch wall can be treated as anomalous, potentially due to the hardness map being poorly centred on the sample. There is some hardness variation remaining through the bulk of the samples (Figure 8-11), despite constant processing parameters being used; this could potentially be reduced using process control.

EBSD maps of the walls were analysed (Figure 8-12); visually, it seems like the narrower walls have smaller grains. Whilst the wider walls have a few very large grains, which occupy roughly 50 % of the sample. Normally, when calculating average grain size, each grain size is weighted equally and a simple mean is taken. However, the result of this is shown in blue in Figure 8-19, where apparently the 1 hatch wall has the largest grains.

In this work, we are correlating the microstructure with the hardness values measured; as such, we assume that the hardness indenter is equally likely to hit each point on the same. This means that there is a much higher chance of a large grain being indented (as they take up such a large fraction of the area). As such, area weighted grain averages have been used as this accounts for the increased likelihood of the large grains being indented.

Similar methodologies have been applied to non-standard grain size distributions for correlation with yield stress [175]. The Hall-Petch effect correlates the yield to the grain size; the model considers dislocations originating at the centre of a grain and building up at the grain boundaries. The smaller the grains, the higher the stress build up. Since the grain diameter is used to calculate the average distance from a dislocation to the grain boundary, this assumes both spherical grains and that all the grains are of a similar size [354,355].

In order to compensate for an uneven grain size distribution, Lehto et al. calculated a volume-weighted grain size [175]. In our case, we know that our samples are anisotropic in all 3 dimensions (Figure 4-13 and Figure 4-14), so scaling the area by a power of 3/2 to get a volume would not be representative. Since the likelihood of every grain being indented is proportional to its' area, an area-weighted average was used. This is shown in orange in Figure 8-19; the results are very different to the simple average. These results look more representative, with the wider samples showing the largest area-weighted grain size, so it seems that this has had the desired effect of accounting for the grain area. The fact that this is required, reiterates how complex the microstructure of AM components is.

Area weighted averages were used throughout this work, including the calculation of average anisotropy factor (Figure 8-13). In the 3 thicker walls, the predominant texture is near the <111> orientation (purple in IPF map). For the narrower walls, there is more significant variation, but with a noticeable tendency towards the <100> orientation (red). The anisotropy factor, a_{hkl}, is a simple way of condensing the orientations into a single number, with <100> being 0, <110> being 0.25 and <111> being 0.33. Since literature reports that Young's modulus should increase in the same manner, $E_{<100>} < E_{<110>} < E_{<111>}$ [320], and hardness being proportional to Young's modulus [348,349], it would be expected that hardness would correlate with the average anisotropy factor.

This is not the case as shown in Figure 8-13, so the hardness cannot be directly explained by the crystallographic structure [180]. The Schmid factors of the narrow walls (Table 8-6) are higher than for wider walls; this makes slip in these samples easier, which could partly explain the lower hardness.

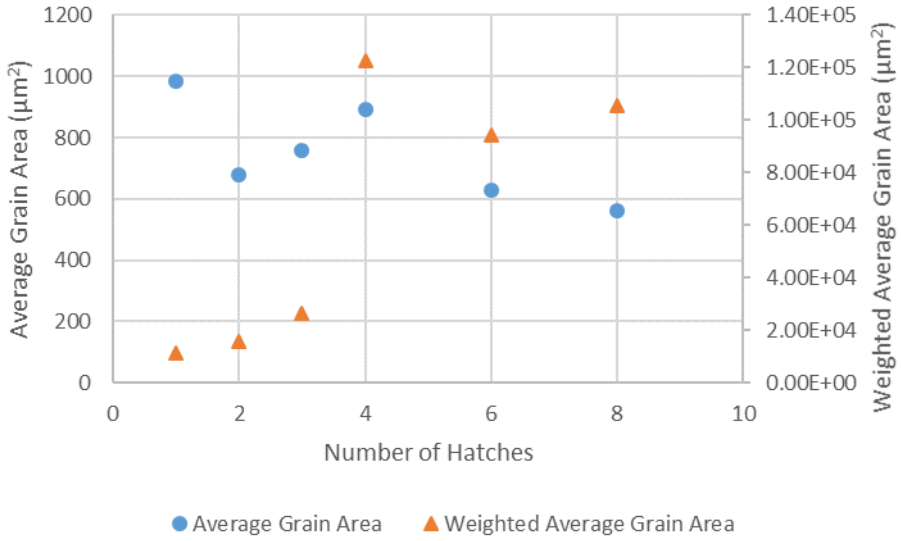

Figure 8-19: Comparison of average grain area and area weighted average grain area for the walls of varying thicknesses

Due to the Hall-Petch effect, a finer grain size would be expected to lead to a higher hardness, this is the opposite trend to that shown in Figure 8-13. There is variation with hardness with width (Figure 8-11a), however, the hardness indent spacing was purposefully offset from the hatch spacing, so the regular patterns in grain size (Figure 8-12) cannot be used to explain the trend in hardness. The large grains, however, have a higher average GAM (Figure 8-14), and so a higher dislocation density. This partially explains the variation in GAM with width (Figure 8-16), however, there is no consistent decrease in GAM at component edges, so this cannot be concluded to be the dominant mechanism behind the hardness trends observed. There is a monotonic increase in GAM with sample width (Figure 8-13), similar to hardness (Figure 8-11a), so there may be some underlying effect of dislocation density on the component hardness.

A hypothesis was formed that the hardness differences could be due to a change in γ" precipitate fraction and/or size. Hardness variation in the YZ section of the triangular prism (Figure 8-10c) varies between 247-289 HV, so ~40HV range is encountered. When taking walls into consideration, similar peak hardness value of 290-300 HV were seen, but with hardness values as low as 215 HV in the narrow walls (Figure 8-11a). This overall range of 80 HV comes from averaged values, so is not a result of outlier values.

Simple precipitation hardness calculations were performed to determine whether or not the γ" precipitates could be responsible for the hardness increases measured experimentally. Very simplistically, if a dislocation is heading for a γ" precipitate along its a axis, due to the coherency of the precipitate, it is likely to be cut, as the coherency requires less energy to overcome than bowing would require. In this case, coherency strengthening is the major strengthening mechanism, with some order strengthening (which is being ignored for simplicity). As these precipitates grow, bowing becomes more likely, so Orowan bowing may occur. If a dislocation reaches the γ" precipitate along the (incoherent) c axes, it is unable to cut the precipitate (hence the very high coherency strengthening increase in Table 8-8), so bowing will occur, with Orowan bowing considered the dominant strengthening mechanism.

Using these two edge cases and assuming that dislocations are equally likely to approach from both the a and the c directions, the average hardness increase can be calculated by:

$$\sigma_{overall} = \sigma_{solid\ solution} + \frac{\left(\sigma_{coherency,a} + \sigma_{orowan}\right)}{2}\ where\ HV \approx\ \sigma_y/3$$

This is the minimum expected hardness increase due to the precipitates because we are ignoring order strengthening and other strengthening additions. The overall expected hardness increases are shown in Table 8-9. As expected, hardness increase due to precipitation outweighs the decrease in hardness due to the reduction in solid solution strengthening (Table 8-8). On average, a 4 % increase in volume fraction γ" leads to a 30 HV increase in hardness and given the range of volume fractions reported in literature of 5 – 20 %.

Strengthening calculations were repeated for precipitate diameters of 25 nm and 75 nm (originally 50 nm was used). In both cases, the overall hardness increased with precipitate fraction, although at larger precipitate sizes, the hardness increase is reduced. This increases confidence in the hypothesis, as we do not know the precipitate size and realistically, there will be a range of precipitate sizes.

Table 8-9: Overall calculated hardness increases as a result of γ" precipitation

Volume Fraction γ" (%)	**Overall Hardness Increase, $HV_{overall}$**
5	340
7	357
9	373
11	389
13	403
15	418
20	452

To check for the presence of γ" precipitates, DSC was performed on a 10 hatch sample which had a statistically significant difference in hardness between the centre and the edge (Figure 8-17). Both the centre and tip samples showed a drop in heat flow around the 850-890 °C that would be expected due to the dissolution of γ" precipitates (Figure 8-17b). The centre sample has a small dip in the expected range and a wider one continuing into hotter temperatures. Changes in precipitate size and fraction could both change the exact temperature of the transformation. The transformation to delta has been reported to be as high as 920 °C [314], and the delta thermal arrest is reported to be centred around 990 °C. Since the larger dip starts at 890 °C and doesn't reach the delta temperature (990 °C), it seems that this also corresponds to γ" dissolution.

The area under the heat flow curve (in the γ" dissolution range) in the central sample is 2.5x larger than that in the tip sample. A larger area under the DSC curve shows that the centre of the sample required more energy to dissolve the γ" precipitates, which may suggest a larger volume fraction γ". If the central region contained more γ", as suggested by the DSC, this would explain the increased hardness observed. For example, if the edge of the sample contained 5 % γ", and the centre 13% γ" (2.6x more, similar to DSC), we would expect a 63 HV increase (Table 8-9). This is an underestimate, so these calculations could explain the 80 HV increase in hardness observed.

The yield strength of a material is the point at which elastic deformation is replaced by plastic deformation via the movement of dislocations in the lattice [356]. Any impedance to dislocation motion increases the energy required for dislocation movement and so increases the yield stress, which is correlated with the materials hardness [348,349,357]. Solid solution strengthening occurs due to the strains caused by the atomic size mismatch between the base alloy and the substitutional alloying additions [356]. These are on an atomic scale, so occur in all non-elemental phases. If the precipitate spacing is of the order 50-150 nm and the grain length of the order 100-300 μm, dislocations are much more likely to experience hardening due to the precipitates as a first order effect. This strengthens the argument of the hardness being influenced by the γ" precipitates.

The next obstacle to dislocation movement is the grain boundary; due to the misorientation between grains, dislocations cannot easily pass from one grain to another [356]. The Hall-Petch effect describes how this increase in grain boundary area increases the yield strength of the material. To get a measure of grain size, the short axis of the grains principal components was used, as this is the shortest average distance from anywhere in the grain to a grain boundary. An area-weighted average of this short axis length was used as a representative grain size to input into the Hall-Petch equation. From this, a yield stress increase was calculated and a hardness increase was estimated (Table 8-7).

Comparing the predicted hardness increase due to the grain size effect (Table 8-7) with the hardness of the walls (Table 8-5), there is a negative correlation [180]. This suggests that the hardness of the walls is not well explained by the grain size effect. Martin [344] showed that after specific aging conditions, the Hall-Petch equation is followed, yet for others, the yield stress cannot be explained by the grain size alone. The argument follows that once a certain precipitate volume/hardening has been experienced, this becomes dominant and therefore grain size is not the dominant mechanism [344]. Assuming this is the case in as-built Inconel 718, it can be concluded that the grain size and orientation are not the dominant mechanisms in determining material hardness, instead, the γ" precipitation was concluded to be dominant.

A moving Gaussian heat source model was used to calculate the time spent in the precipitation temperature range (700-900 °C) for the walls. These models, albeit not numerically accurate, give a realistic temperature distribution around the melt pool; for this reason, this is referred to as a precipitation potential rather than attempting to estimate precipitate volume fractions. Time spent above 900 °C but below the solvus promotes either transformation to the delta phase, or dissolution of the γ" precipitates. Assuming this dissolution rate is equal to the precipitation rate, the time in this temperature range can be simply subtracted from the time in the precipitation zone (Figure 8-18a). The top surface spends up to 4.5x less time in the precipitation zone than the bulk, which would explain the lower hardness, with the external edges spending 2x less.

However, there are reports of samples being heated to 1100 °C and cooled at 10 °C/min, so spending 21 mins in the dissolution range, yet still with large amounts of γ" retained [314]. For this reason, it was decided that the dissolution would be ignored and calculations would only consider the time in the precipitation temperature range (Figure 8-18b). A similar trend was observed, but with a larger variation between centre and edge (up to 6.7x). The maximum precipitation time was 0.14 s, greater than the 0.1 s "nose" of the TTT curve [314]. The times are of the correct order to experience precipitation and the variation is in the expected positions, with edges and top surfaces having shorter times in the precipitation zone and so less precipitation is expected, leading to a softer material.

As shown by Kumara et al. [327], γ" precipitation in the interdendritic regions can be an order of magnitude quicker than at the dendrite core due to local segregation, so feasibly, 0.01 s in the temperature range 700-900 °C would be sufficient for precipitation to occur. The large uncertainty in location of TTT curves (Figure 8-1) was mentioned in Section 8.1, which is increased by the changes in composition caused by segregation during solidification. However, DSC results (Figure 8-17) show that both samples contain γ", and calculations predict that the samples are in the precipitation temperature range for ~0.1 s (Figure 8-18). Despite the variation in TTT curves in literature, the experimental results in this chapter suggest that the γ" TTT curve in Figure 8-1 is reasonable.

The maximum precipitation potential increases from 1 hatch to 3 hatches, which would explain the increase in centre hardness with thickness as observed in Figure 8-11c. The precipitation range used was 700-900 °C, but there is sub-second precipitation down to ~650 °C (Figure 8-1). The precipitation at this temperature would be slower, but would still increase the total time spent in the precipitation zone. The Gaussian heat source model calculates the scanning of a single laser hatch, but it is known that during the build the component retains heat. This would increase the temperature of the component and likely increase the melt pool size, importantly, it would also increase the time spent in the precipitation zone. Both of these effects would increase the precipitation potential in all parts of the sample, but would not affect the distribution of precipitation potentials. The analysis focusses on the central point of each hatch, this snapshot will not be numerically accurate for the whole sample e.g. slightly above the centre, the melt pool and precipitation regions will be larger and slightly below, they will be smaller. The centre points should be representative of the bulk and any error would be systematic, hence this should not affect the results of the model.

A simple thought experiment based on the Juechter et al. critical hatch velocity could be conducted to see if this could account for the heat accumulation expected [341]. For the BeAM Magic 2.0, the critical hatch velocity would be 0.64 m/s for the walls, so the laser velocity would have to be quicker than that for the heat from the previous hatch to contribute to the melt pool temperature. This is an order of magnitude quicker than the velocity used in these experiments, but it is well known that heat accumulation does occur with build duration. This comes back to the concept of using heat for melting – at much higher velocities, the heat retained would be much more significant.

The parameters used in all the samples are identical, so the local interaction time doesn't change, so this cannot be responsible for the hardness variation. The length of the wall, and so the hatch return time, are also equal throughout the experiment, so this value also doesn't change. Since the wider walls experience a longer return time between layers, we expect an increased heat loss occurring. This means that less heat accumulation would be expected in the wider samples and so less precipitation. In reality, the peak hardness of the wider samples is the highest (Figure 8-11c). Looking at the both hatch and layer return times is too simple to explain the hardness effects seen as the effect of subsequent hatches is critical.

Previous work by Tian et al. [316] and Kumara et al. [328] concluded that the first step to γ" precipitation is interdendritic Nb segregation which occurs during solidification (Figure 8-2). Subsequent heat treatment allows for nucleation and further growth of γ" precipitates, which increases the components hardness. In this work, this hypothesis has been confirmed and extended to quantify how the subsequent hatches and layers cause the precipitation and growth of these γ" precipitates. The amount of time spent in the precipitation temperature range would allow for both nucleation of new precipitates and growth of current precipitates.

It has been shown that these effects occur within a layer as well as with build height, causing hardness variation on the component scale. When printing complex geometries, both wide and narrow sections would be expected. The walls show a 35 HV hardness difference between a 1 mm and a 3.5 mm section with the tip of the triangular prism being 40 HV softer than the centre. Since the tip is narrower, the hatches are shorter and so the time at temperature will be decreased. This explains why there is a drop-off in hardness in the last 3 mm of the triangular prism (Figure 8-10c).

Figure 8-11a shows that in any component, a region of ~1 mm around the edges is softer than the centre. This is critical as when components are being repaired, consistent properties are required. In addition, any components narrower than 2-3 mm never reach peak hardness. These factors affect the design process for printing complex shapes in L-DED. For consistent mechanical properties, sections should be designed to be wider than 3mm, with 1mm on the edges removed post process; alternatively, the design must account for the fact that sections thinner than 3mm will have dissimilar mechanical properties.

Alternatively, the idea of precipitation kinetics could be used to create a build strategy which would result in a homogeneous component. For example, if the edge of the sample is in the precipitation zone for 0.5 s, compared to 1.4 s in the centre, then theoretically, the edge needs a subsequent 0.9 s precipitation for a consistent hardness. Using a moving heat source model, an in-situ heat treatment (reheating the sample without melting it) could be calculated and applied. This is similar to the application of in-situ heat treatment to EB-PBF by Sames et al [315]. The same technique could be used to increase the hardness of a thin sample by rescanning it and so creating an as-built thin sample with the higher hardness experienced in a wider sample.

Since the thermal intensity is related to the melt pool area, the melt pool dimensions of the moving heat source model can be adapted depending on the current melt pool monitoring. It would be possible to create a variety of melt pools in the moving heat source model and select appropriate ones depending on the current thermal intensity. This way, a live calculation of precipitation time could be made and an adaptive in-situ heat treatment could be automated. This would allow for building of right-first-time complex components with constant hardness in L-DED.

We have shown that there is an unavoidable in-situ heat treatment intrinsically associated with L-DED. This produces variation across the component even when constant parameters are used. To accurately control the final microstructure, attempts have been made to use in-situ heat treatment; frequently involving lengthy holds and/or rescans [315,330–332]. These are currently proof of concept builds; they cannot be properly implemented until a full understanding of the intrinsic heat treatment experienced during the process. By developing a better understanding of the as-built variation, this variation can then be reduced/removed and the full sample heat treated in-situ to produce as-built samples with the desired properties.

8.5. Summary

It has been shown that in as-built Inconel 718, there are significant hardness variations in both the build plane and the build direction. The presence of γ" has been confirmed and the increased precipitation/growth of γ" precipitates caused by the materials being in the precipitation temperature range can be related to the increased hardness. Coaxial monitoring was introduced and the data acquisition rate was shown to be low enough for online calculations to be performed, unlike some of the higher resolution monitoring introduced in Chapter 7. Common factors such as melt pool morphology, dislocation density and crystallographic structure have been shown not to be cause of the hardness variation.

A precipitation kinetic model based on a Gaussian heat source model has been created to calculate the time different sections of the component spent in the precipitation temperature range. The time spent in the precipitation temperature range is shown to correlate with the hardness, suggesting that the increase in hardness is caused by γ" precipitation. This could be used to calculate in-situ heat treatments, which would result in consistent hardness in complex components. Further, using the coaxial monitoring, an in-situ control algorithm could be used to homogenise each component directly after being built. There is still remnant hardness variation in the centre of the components, but this could be reduced by introducing a process control algorithm.

9. Effect of Process Control on Inconel 718 components in L-DED

9.1. Introduction

The applicability of L-DED to component repair has been widely reported [358], however process consistency is still lacking [9]. There is a need for adaptive process control in L-DED to achieve accurate component geometries and remove defects such as porosity [359]. Certification issues are reported as being the main barrier to L-DED being more widely integrated in the aerospace industry [6,360]. Currently, there is a large variation in mechanical properties e.g. hardness, produced using AM, both within and between components [361,362]. Due to these difficulties in validating AM components, research has turned toward process control. If the process were better controlled, this could increase component reliability and process control could become a part of the certified manufacturing method [6].

Several comprehensive reviews on process control in AM exist in literature [10,141,363–365], so only the main relevant methodologies and results are covered here. Most work in literature focusses on improving the dimensional accuracy of components i.e. removing unevenness at corners/edges [141,147,296,366]. Some research focusses on control of the work offset (dependent on component height) [147,367,368] and powder deposition rate [25]. These studies successfully improve dimensional accuracy and surface finish of components. Inconel 718 is generally regarded as being printable, geometric issues are no longer a key issue; in this work, the main interest is in improving microstructural and mechanical homogeneity. The cameras used are expensive and the control algorithms complex and require fine-tuning; the focus of this work is to develop a simple, low-cost alternative and to test its' capabilities.

There are many different ways to achieve process control, we will focus on methodologies monitoring the melt pool and using that as an input for feedback control. Common sensors reported in literature are photodiodes/pyrometers and optical/thermal cameras. Using a photodiode/pyrometer [145,296], a single value is output at each time step, the control loop can use this as an input and compare it against a target. Using a camera (either temperature calibrated or uncalibrated), an array of pixel values is recorded, comparing this against a target is more difficult. The main methodologies identify melt pool area [105,301,366], melt pool width [149] or the temperature of a specified point [147,300,369]. Baraldo et al. attempted to reduce a coaxial image to a single numeric value by calculating the sum of the pixels in the image [171], in the same way as thermal intensity is calculated (Section 4.2.4). This single value gives a measure of the current state of the process so it can be determined whether or not the process needs adjusting.

A controller compares the current state to the desired state and decides the adjustment of processing parameters required. This can be as simple as a linear equation (Section 4.2.4), or a more complex control function [146]. Frequently proportional integral derivative (PID) controllers are used, but these require numerous runs to optimise gain constants [149,370]. The nature of the controller determines how quickly the target is achieved and how much the target value may be overshot by.

Several source of error are discussed by Bi et al [296]:

- if the work offset varies, the melt pool may become out of focus which would change the intensity of the image. The control loop would adjust parameters to correct this and so change the melt pool temperature/dimensions, reducing the accuracy of the control loop [296]
- oxides are reported to have a different emissivity to the molten metal [296,371]; if a region has a higher oxygen content but the same temperature, it may be reported to be of a different temperature due to the difference in emissivity [296]

These phenomena are unavoidable, but must be considered when reporting monitoring work of this nature, as they may reduce accuracy.

In L-DED, two variables are frequently adjusted to control the process, these are the laser power [145,149,204] and velocity [151,366,370]. There is no consensus in literature as to which is superior and rarely any justification as to why one is chosen. Most work in the field of process control in L-DED is unexpectedly qualitative, with images being described verbally rather than quantifying the data and checking for statistical significance. Hofman et al. demonstrate that by controlling laser power to keep a constant melt pool width, the hardness variation along the component length can be reduced [149]. They compare hardness without control to hardness with control (without any calculation of variance) [149], whereas most studies omit analysis of components built without control (with constant processing parameters), so it cannot be concluded that the control loop had any effect.

There are several studies published in literature by Farshidianfar et al [151,370], which are most relevant to this work. By looking at a spot in the image as the melt pool moves through it, they calculated an uncalibrated cooling rate; this was compared to a target using a PID controller and the velocity was adjusted towards a target cooling rate [370]. The images were recorded at 30 fps, and the delay in control was reported to be 0.9 s [370]. In previous work, they showed that increasing the velocity led to an increased cooling rate [125]. Initially, their work succumbed to the widespread flaw of claiming to show hardness and microstructural consistency whilst failing to show results without the control loop [370] i.e. not showing that process control improved process consistency.

The latest work by Farshidianfar et al. showed micrographs for both open loop (no control) and closed loop (velocity control); they conclude “the parts’ microstructure and overall geometry are much more uniform for the closed-loop state” [151]. However, this is not as obvious as the author leads us to believe as shown by the micrographs in Figure 9-1. Both open and closed loop samples show variation from the first layer to the 5th layer, with no noticeable uniformity increase once control was implemented; Figure 9-1 shows the central set of parameters, but similar trends were visible in all samples. Dendrite arm spacing plots are shown and seem to show a decrease in variability, but once again, a simple analysis of the variance would quantify this. On the mechanical properties side, they claim to show that they decrease hardness variability by introducing velocity control [151]. Unfortunately, it seems like this is true for 2 of the 3 cases, with the third sample having more variability once control was introduced.

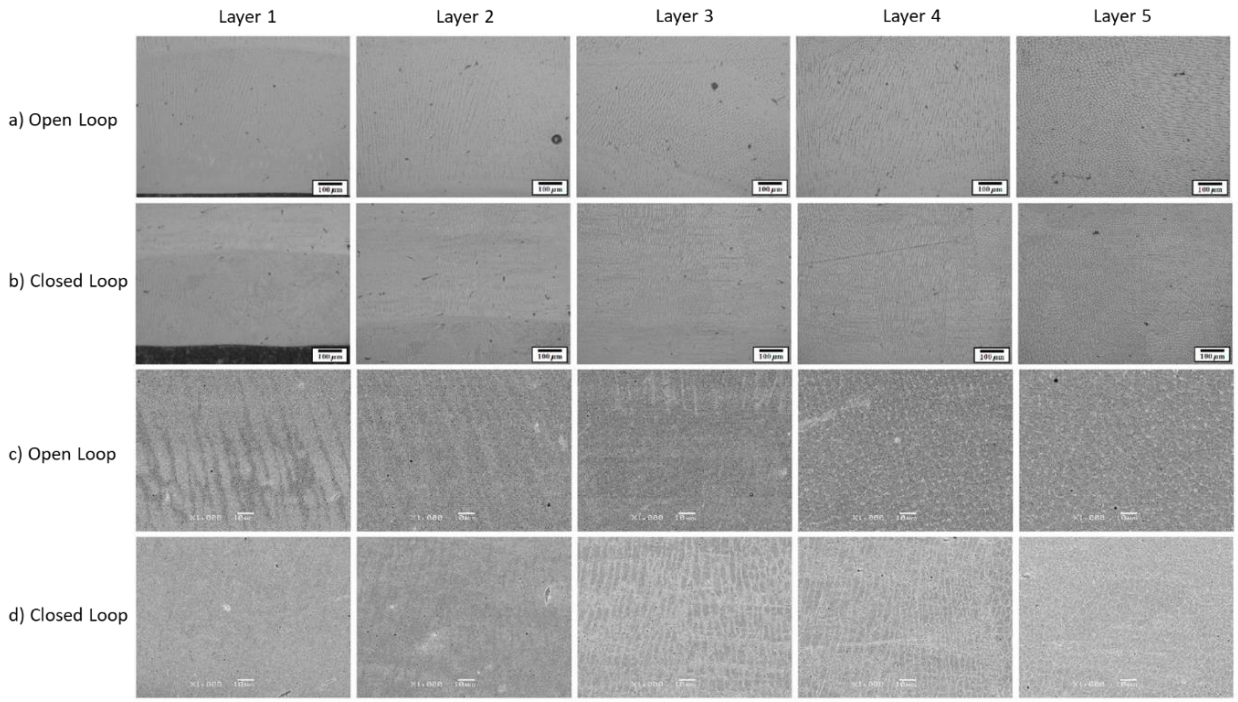

Figure 9-1: Effect of closed loop control on microstructure. Comparison of a, c) open loop (no control, 800 W, 200 mm/min) sample, with b, d) closed loop (cooling rate controlled at 1100 K/s) sample. a, b) Optical micrographs, c, d) SEM images. Adapted from Farshidianfar et al. [151]

Despite the vast amount of research published surrounding process control in L-DED, there is no convincing data showing that the decrease in thermal/melt pool fluctuations translates to improved mechanical homogeneity. Does a consistent melt pool shape lead to a more consistent microstructure and hence reduced mechanical anisotropy? This chapter investigates this argument and aims to determine whether microstructural and mechanical variability are reduced by implementing process control.

9.2. Methods

Samples were printed using Inconel 718 powder on the BeAM Magic 2.0 L-DED machine, on Inconel 718 substrates, with a 3.5 mm work offset. This chapter investigates process control, using coaxial imagery as an input to the control loop. Details of the monitoring and control, using a Basler acA1440-73gm are covered in Section 4.2.4. Three different thicknesses of wall (30 mm long, 15 mm tall) were printed; 3 6 and 10 hatches wide (roughly 1.5 mm, 3 mm and 4.5 mm respectively). Each of these was printed using constant processing parameters (no control, sample names appended with “N”), with the power being controlled in response to thermal intensity (power control, sample names appended with “P”) and with the velocity being controlled in response to the thermal intensity (velocity control, sample names appended with “V”). The initial parameters are shown in Table 10-3 with the dimensions and hatching being shown diagrammatically in Figure 8-3. These walls were sectioned at the midpoint in the YZ section as shown by the orange line in Figure 8-3a.

Additionally, two triangular prisms were printed with equilateral bases of length 27.5 mm; the hatching strategies were from base to tip (sample names include “BT”) and from tip to base (sample names include “TB”), as shown schematically in Figure 8-3b. These were sectioned in the YZ plane along the midpoint of the triangular section. Both of these were reprinted with power control (sample names appended with “P”).

As explained in Section 4.2.4, thermal intensities of each image are calculated, the raw images being acquired at 75 fps. If process control is required, then every 0.15 s, the last 5 thermal intensities are averaged if each of their sums is above $0.2x10^7$ (this is changed to 3 thermal intensities for the triangular prisms). This average thermal intensity is compare to the target of $0.9x10^7$ and the power/velocity is adjusted accordingly, scripts available [170]. As well as thermal intensity, maximum intensity, melt pool area, and melt pool length/width were calculated post-process (offline), as described in Section 4.2.4.

Table 9-1: Parameters used for both wall and triangular prism samples; initial processing parameters are shown, control will alter the power/velocity parameters respectively

Sample	Hatching Details	Sample Width (mm)	Power (W)	Velocity (mm/min)	Hatch Spacing (µm)	Z Step (µm)	Mass flow (g/min)	Control
3N	Wall; 3 hatches wide	1.6	300	2000	400	200	6-7	No Control
3P	Wall; 3 hatches wide	1.6						Power Control
3V	Wall; 3 hatches wide	1.4						Velocity Control
6N	Wall; 6 hatches wide	2.7						No Control
6P	Wall; 6 hatches wide	2.7						Power Control
6V	Wall; 6 hatches wide	2.7						Velocity Control
10N	Wall; 10 hatches wide	4.3						No Control
10P	Wall; 10 hatches wide	4.3						Power Control
10V	Wall; 10 hatches wide	4.4						Velocity Control
Tri_BT_N	Base to Tip Triangular Prism	N/A	275	2000	350	225	6.5-7.5	No Control
Tri_BT_P	Base to Tip Triangular Prism							Power Control
Tri_TB_N	Tip to Base Triangular Prism							No Control
Tri_TB_P	Tip to Base Triangular Prism							Power Control

For each of the walls, one half was polished to a 1 µm finish, these were used for hardness indentation. The other half was further polished using 0.25 µm colloidal silica in preparation for EBSD. The triangular prisms were sectioned along the orange line shown in Figure 8-3a. One half had the top surface (XY) polished to 0.25 µm colloidal silica and the other half had the internal YZ section polished. The YZ section was then sent to the Warwick Manufacturing Group (WMG) for EBSD, once this was done, both sections had hardness maps captured.

Hardness was performed with a 1 kg load, 15 s hold and the indent automatically measured using a 40x optical lens. Walls were indented with an array of indents in the YZ section, spaced 0.5 mm in the Y axis and 1.0 mm in the Z axis. Triangular prisms were indented with square arrays of 1 mm spacing in both the XY and YZ cross sections. For each set of hardness's, tests of two variances were performed to see whether the process control decreased the variance of hardness (α=0.05); additionally, two sample t-tests were performed to determine whether the hardness values were significantly different (α=0.05).

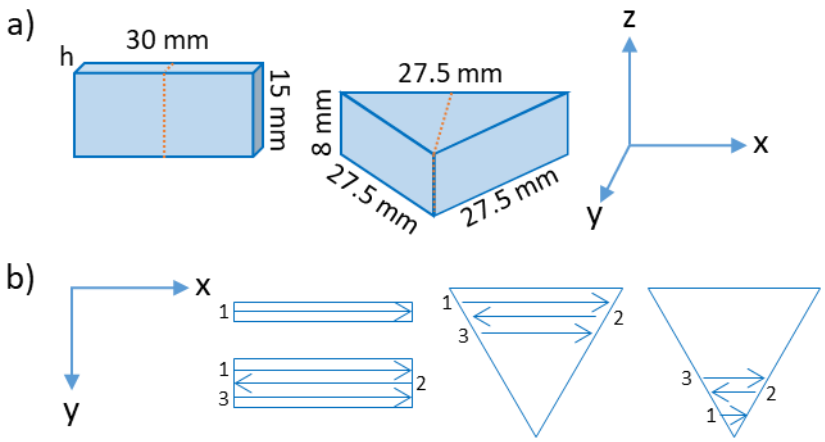

Figure 9-2: Geometries of components built. a) dimensions of both walls and triangular prisms along with machine axes; h is the number of hatches. Orange lines show sectioning direction b) view from above showing hatching strategies for 3 hatch wall and triangular prisms. Both base to tip (left) and tip to base (right) hatching shown

The walls were then re-polished and etched with Kallings Reagent #2. Low resolution optical micrographs were taken of all 9 samples, allowing for melt pool dimensions to be measured. Melt pool dimensions were measured from the top row of melt pools, as these were not remelted by subsequent layers.

EBSD of the walls was performed using a Jeol 7900F with an Oxford Instruments Symmetry EBSD detector. A 3.5 µm step size was chosen with a 13 mm work offset and a ~ 90 nA probe current. Walls were scanned with the area covering 1 mm (Y axis) in the central section of the sample (Y axis) with a height of 12 mm from the baseplate (Z axis). EBSD of the Tri_BT_N and Tri_BT_P triangular prisms was performed at the WMG using an FEI Versa 3D Microscope with an Oxford Instruments Symmetry 2 EBSD detector. A 5 µm step size was chosen, with a 20 kV accelerating voltage. For each of the 9 walls, the EBSD map was split into four 3 mm tall sections to quantify the changes with distance from baseplate. For each of these sections, the grain area and anisotropy factor were calculated, both weighted by grain area.

Subsequent analysis was focussed on the 3 hatch and 10 hatch walls. Grains from the top and bottom quarters of all 6 walls (3N, 3P, 3V, 10N, 10P, 10V) were combined and k-means clustering using grain area and grain aspect ratio was performed as explained in Section 4.7. The grains were clustered into 6 clusters to minimise variance within clusters. From these, clusters were combined into 3 sets as these represented small, medium and large grains. For each of the samples, the fraction area of each grain size was calculated as well as the anisotropy factor, aspect ratio and the maximum mud. For the two triangular prisms, the central regions were extracted (20 x 5 mm; Y and Z respectively), this was split into 5 rows, each 1 mm tall (20 mm) wide. For each of these, area weighted grain area, anisotropy factor and aspect ratio were calculated.

9.3. Results

In this section, the effect of process control is investigated. As such, most analysis compares a “normal build” (no control, constant processing parameters) with a controlled build (process or velocity control).

9.3.1. **Processing Parameters**

When processing without control, the pre-set power and velocity values were used throughout the build. Once power or velocity control were introduced (corrections performed at an interval of 0.15 s), the power/velocity values were adjusted to hit the target thermal intensity. Figure 9-3 shows the processing parameters used for all 9 walls; for no control walls (blue), the parameters were constant, so stay at 100 % for the duration of the build. The power control walls (orange) show that the power required to hit the thermal intensity target was lower than the pre-set value, reducing to 91 % for the 3P wall. Figure 9-3b shows that for the 6 hatch walls, there is a smaller difference than in the 3 hatch walls, and in Figure 9-3c, the 10 hatch wall needed a decrease in power, but of a smaller magnitude.

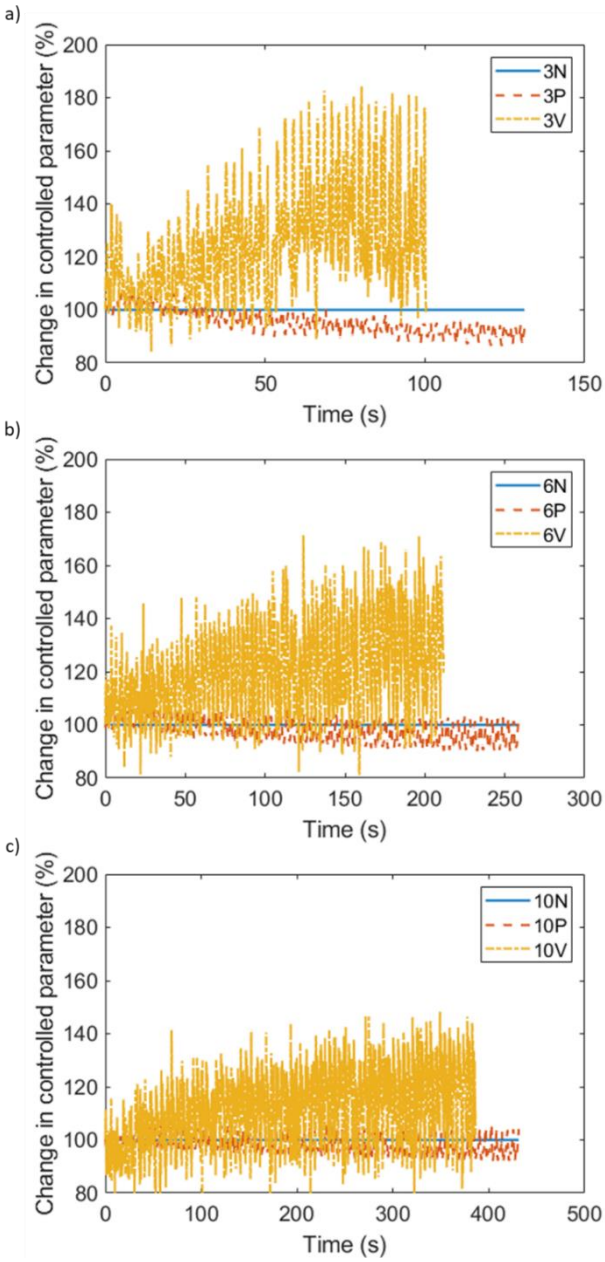

Figure 9-3: Required parameter changed for the control algorithm. A value of 120% means that 1.2x the original power/velocity was needed to achieve the target thermal intensity. Shown for a) 3 hatch walls, b) 6 hatch walls, c) 10 hatch walls

The velocity control walls (yellow) show that the control loop increased velocity to keep thermal intensity constant. The 3V wall (Figure 9-3a) showed an increase of velocity to ~129 %, with the wider walls requiring less adjustment. Since the velocity of the laser was increased, the processing time was decreased; this could be useful in industrial applications, where a reduction in cost is associated with reduced manufacturing time. Additionally, there appears to be a larger variation in the velocity adjustment than there does with the power adjustment.

9.3.2. Thermal Monitoring

The control algorithm used thermal intensity as the target; Figure 9-4 shows the thermal intensity throughout the build for all 9 walls. Figure 9-4a shows the variation for 3 hatch walls; with no control, the intensity increases with time, appearing to plateau near the end of the build in a similar manner to that seen in Chapter 7. For both power and velocity control, the thermal intensity is maintained near the target of 0.9×10^7; once again, the velocity controlled build is completed in a shorter duration. Figure 9-4b and c show the same trends for the 6 and 10 hatch walls respectively; within these samples, the wider walls show the smallest increase in thermal intensity through the build.

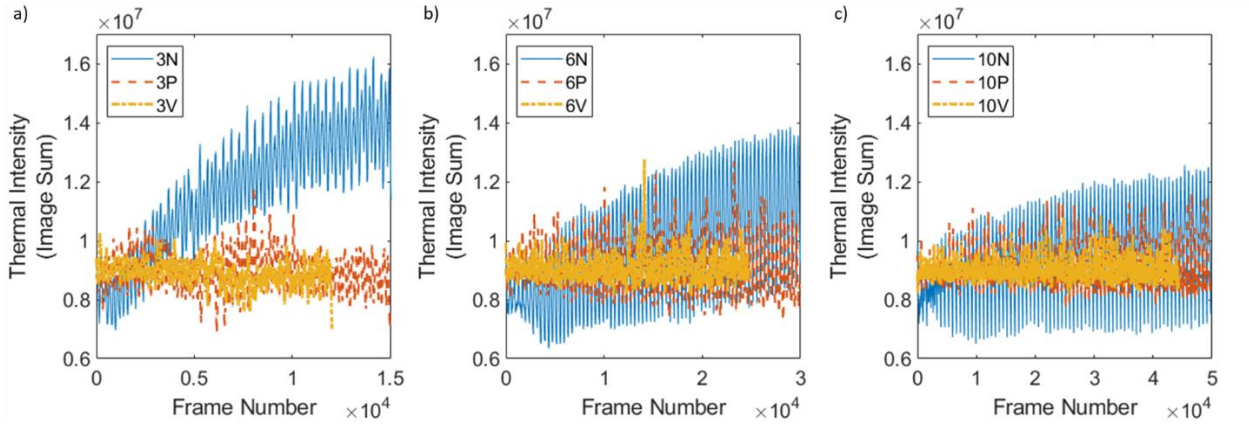

Figure 9-4: Thermal intensities during the build of 9 walls, a moving mean of window 100 points applied; a) 3 hatch walls, b) 6 hatch walls, c) 10 hatch walls

The thermal intensities along with their associated standard errors are summarised in Table 9-2. Additionally, the other melt pool measures (maximum intensity, melt pool area, melt pool width and melt pool length) are also shown in Table 9-2; triangular prisms are included for comparison. Both power and velocity control consistently reduce the standard error in the thermal intensity when compared to the no control build.

Figure 9-5a shows the trend of thermal intensity with wall thickness; it can be seen that without control, the thermal intensity decreases with width. Both power and control result in thermal intensities very near to the target of 0.9×10^7. Generally, the narrowest walls experience the largest variation, as seen by the large change in thermal intensity experienced by 3N (Figure 9-4a). This trend is explicitly shown in Figure 9-5b, where the standard error of thermal intensity is shown. It can be seen that wider walls have a lower standard error. Both power and velocity control decrease the standard error in thermal intensity, but power control more strongly. It can be concluded that power control is more successful than velocity control, as the average thermal velocity is closer to the target and it experiences less variation.

Similar plots are shown in Figure 9-6 for the remaining 4 melt pool measures from Table 9-2. Figure 9-6a shows that the maximum intensity follows the same trend as the thermal intensity

(Figure 9-5a); the control function was not controlling maximum intensity directly, so the maximum intensities are not identical across sample widths in the power/velocity controlled samples. The thermal intensity of the 3N was largest, so it's unsurprising that the melt pool area is also largest (Figure 9-6b). The area of velocity controlled melt pools is consistently larger than that of power controlled melt pools.

Table 9-2: Different measures of melt pool and thermal analysis for the walls and triangular prisms, comparing the different types of control. Standard errors (SE) included

	Average Thermal Intensity	Thermal Intensity SE	Maximum Intensity	Maximum Intensity SE	Melt Pool Area (px²)	Melt Pool Area SE	Melt Pool Width (px)	Melt Pool Width SE	Melt Pool Length (px)	Melt Pool Length SE
3N	1.17E+07	2.48E+04	1605	3	27312	36	176.1	0.1	213.3	0.2
3P	8.97E+06	1.48E+04	1277	2	24088	20	165.8	0.1	201.2	0.2
3V	8.89E+06	1.75E+04	1361	3	24409	30	162.9	0.1	208.2	0.2
6N	9.75E+06	1.43E+04	1339	1	23537	17	167.7	0.1	191.9	0.1
6P	8.98E+06	9.98E+03	1258	1	22602	12	165.1	0.1	187.3	0.1
6V	9.06E+06	1.09E+04	1369	1	23006	14	166.2	0.1	193.3	0.1
10N	9.38E+06	8.70E+03	1253	1	23014	10	168.0	0.1	189.0	0.1
10P	8.97E+06	6.42E+03	1257	1	22447	8	167.0	0.1	186.3	0.1
10V	9.01E+06	7.15E+03	1301	1	22705	9	168.9	0.1	189.5	0.1
Tri_BT_N	5.73E+06	4.10E+03	961	1	18517	6	156.2	0.1	169.4	0.1
Tri_BT_P	8.94E+06	6.62E+03	1273	1	22687	10	176.1	0.1	187.5	0.1
Tri_TB_N	5.42E+06	4.48E+03	945	1	18022	6	153.2	0.1	165.5	0.0
Tri_TB_P	9.10E+06	7.11E+03	1270	1	22640	9	174.4	0.1	186.1	0.1

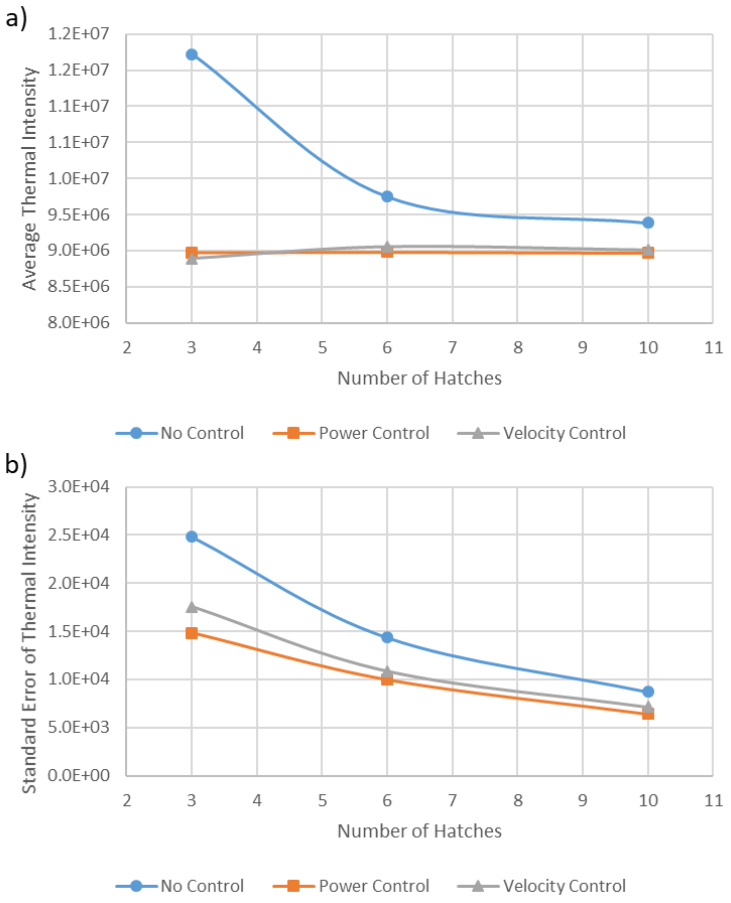

Figure 9-5: Effect of process control on thermal intensity; a) average thermal intensities for 3, 6 and 10 hatch walls, with no control, power control and velocity control; b) standard error of the thermal intensities in a)

Melt pool width (Figure 9-6c) again shows a similar trends to the maximum intensity, with the 3N sample having the largest melt pool width. The remaining walls display a range of melt pool widths, with the width of the velocity controlled melt pools increasing with sample width. Finally, the melt pool length (Figure 9-6d) is longest for the 3 hatch samples, with shorter melt pools in wider walls. In the previous melt pool dimensions, both power and velocity control have been closest to one another, with no control having a larger melt pool. Figure 9-6d shows that for the melt pool length, velocity control seems not to change the melt pool length from the no control scenario, whereas power control does decrease melt pool length.

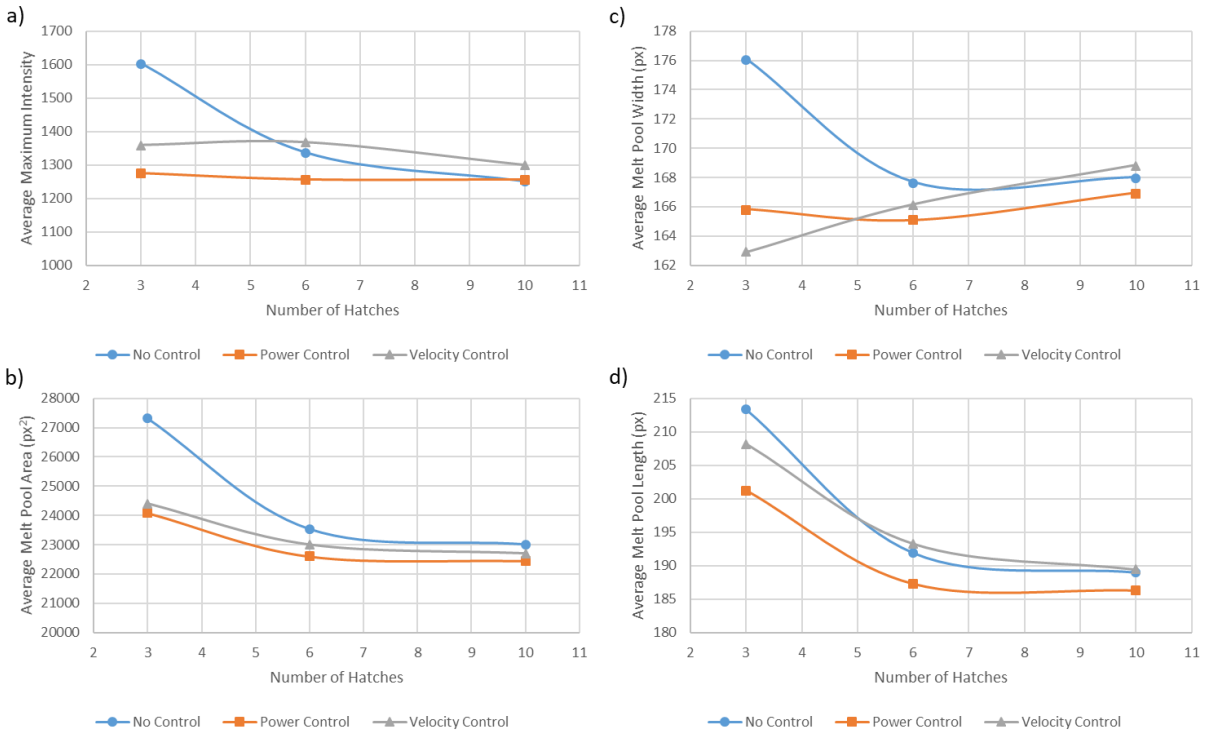

Figure 9-6: Plots showing the effect of different control systems on thermal measures; a) average maximum intensity, b) average melt pool area, c) average melt pool width, d) average melt pool length

9.3.3. **Hardness Analysis**

For hardness measurements, edge effects have been shown to occur (Chapter 8), so a row of hardness indents was discarded from each sample edge. Average hardness values for the 9 walls are summarised in Table 9-3 along with their associated standard errors. For 3 hatch walls, both power and velocity control were found to increase hardness, and to slightly decrease the standard error. For the 6 hatch walls, power control slightly decreased the hardness, whilst velocity control slightly increased it; both showed decreased standard error when compared to the no control wall. In the 10 hatch wall, there was minimal change in hardness when power/velocity control were implemented, with standard errors increasing by a small amount.

Table 9-3: Average hardness values for walls, standard errors included

	Average Hardness, HV (Standard Error)		
Hatches	**No Control**	**Power Control**	**Velocity Control**
3	254.4 (2.7)	263.1 (2.6)	265.5 (2.3)
6	271.5 (1.5)	268.5 (1.1)	283.5 (1.4)
10	274.0 (0.8)	274.0 (0.8)	274.4 (0.9)

In the triangular prisms (Table 9-4), there is less hardness difference when power control is introduced as compared to the walls, both in average hardness values and in their standard errors. In the YZ sections, the hardness variance is slightly decreased, whereas in the XY sections it is increased. Overall, the latter dominates, so the standard error of hardness increases slightly when power control is introduced.

Table 9-4: Average hardness values for triangular prisms, standard errors included

		Average Hardness, HV (Standard Error)	
Component	**Section**	**No Control**	**Power Control**
Tri_BT	YZ Section	276.0 (0.8)	275.4 (0.7)
Tri_BT	XY Section	267.9 (0.9)	265.3 (0.9)
Tri_BT	Combined	272.3 (0.6)	271.2 (0.6)
Tri_TB	YZ Section	276.1 (0.9)	276.8 (0.7)
Tri_TB	XY Section	263.5 (0.9)	262.7 (1.4)
Tri_TB	Combined	269.9 (0.7)	270.2 (0.9)

Statistical tests were performed to quantify whether these changes were statistically significant. Each controlled sample was compared against the equivalent sample manufactured without control (Table 9-5), for each:

- a test of two variances was performed to determine whether the change in standard error was significant
- a two sample t-test was performed to determine whether the change in average hardness was significant

Both of these tests used $\alpha=0.05$ as the threshold significance value. Table 9-5 shows that despite slight changes in standard error, these changes were not statistically significant for any sample. The hardness however did change in a statistically significant manner in three cases, 3P, 3V and 6V. This suggests that hardness in narrower walls is more sensitive to processing conditions. Since velocity control causes a larger hardness change in the 3 hatch walls (Table 9-3) and causes a significant hardness difference in the 6 hatch wall, it could be argued that velocity control has a larger impact on hardness than power control.

Table 9-5: Tests for statistical significance between no control hardness values and controlled hardness values. Changes in the average value were tested for significance as well whether the variance has changed

				Test for Statistical Significance	
Sample A	**Sample B**	**Subset?**	**Control being tested**	**Change in Hardness**	**Change in Hardness Variation**
3N	3P	-	Power	Yes	No
3N	3V	-	Velocity	Yes	No
6N	6P	-	Power	No	No
6N	6V	-	Velocity	Yes	No
10N	10P	-	Power	No	No
10N	10V	-	Velocity	No	No
Tri_BT_N	Tri_BT_P	YZ Section	Power	No	No
Tri_BT_N	Tri_BT_P	XY Section	Power	No	No
Tri_BT_N	Tri_BT_P	Combined	Power	No	No
Tri_TB_N	Tri_TB_P	YZ Section	Power	No	No
Tri_TB_N	Tri_TB_P	XY Section	Power	No	No
Tri_TB_N	Tri_TB_P	Combined	Power	No	No

9.3.4. EBSD Analysis

Orientation maps for the 9 walls are shown in Figure 9-7, with the full 12 x 1 mm region visible; the samples were later split into 4 sections each, labelled A-D (bottom to top). The 3 hatch walls all have small, randomly oriented grains at the bottom, near the baseplate, but with height, the grain size increases. The 3N wall has some very large, red grains (<100> orientation) towards the top of the sample; along the centre of the y direction, there are fine grains along the full height of the build – these are where the centre of the laser scanned, similar to Section 7.1. The 3P and 3V orientation maps show similar trends, but generally with smaller grains at the top. In these orientation maps, there are more lenticular grains in the higher sections, which are angled diagonally away from the centreline.

For the 6 and 10 hatch walls, the <111> orientation is dominant, causing the purple colour. In both 6N and 6P, tall elongated grains occur early on, again with small grains along the centrelines. In 6V, there is less dominance by these tall elongated grains; instead, a large number of small, randomly oriented grains are retained higher up the wall. A similar trend is seen in the 10 hatch walls, with

10N and 10P both containing large, elongated grains near the top; some large grains are found in 10V, but there are larger regions of equiaxed grains along the full height.

Orientation maps for the rectangular YZ sections of the two triangular prisms are shown in Figure 9-8, the edges have been cropped, so only the central region is shown. This is a bulk sample and <111> orientations dominate, as seen by the dark blue/purple background colours. In both samples there are many clusters of small, randomly oriented grains. Tri_BT_N appears to have more of these randomly oriented clusters, with a background oriented somewhere between <100> and <111>, whilst Tri_BT_P seems to have fewer of these small grains and a background orientation closer to <111>.

As described in Section 9.2, each of the walls shown in Figure 9-7 was split into 4 sections along the z direction (build height), these are labelled A-D (bottom – top respectively). For each of these sectors, an area weighted average grain area and anisotropy factor are shown in Figure 9-9. The grain area tends to increase with build height, this being most pronounced in the narrowest walls. The largest change in grain area occurs in no control walls, with both power and velocity control decreasing the variance; velocity has the most consistent grain area along the height of the walls.

The trend in anisotropy factor is less pronounced. For a 3 hatch wall (Figure 9-9d), anisotropy factor decreases with height; the largest change is seen in the no control wall, power and velocity control experience a change of similar magnitude. For 6 and 10 hatch walls, the change in anisotropy factor is smaller than for the 3 hatch walls, there is some change in anisotropy factor with height, with the 10 hatch wall showing the least variance.

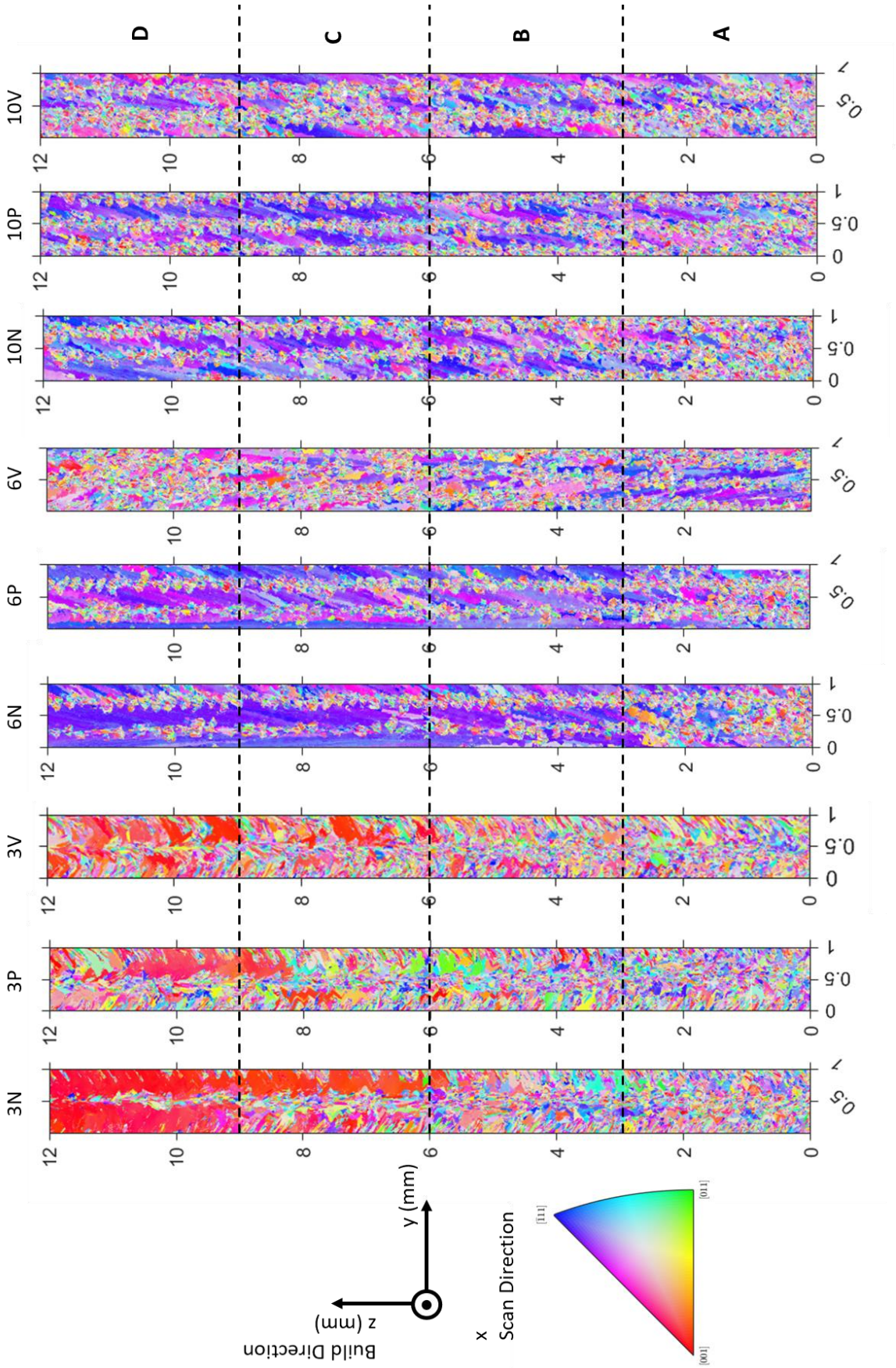

Figure 9-7: Inverse pole figure (IPFX) maps of 9 walls, showing axis directions. Four sections with height, A-D, shown

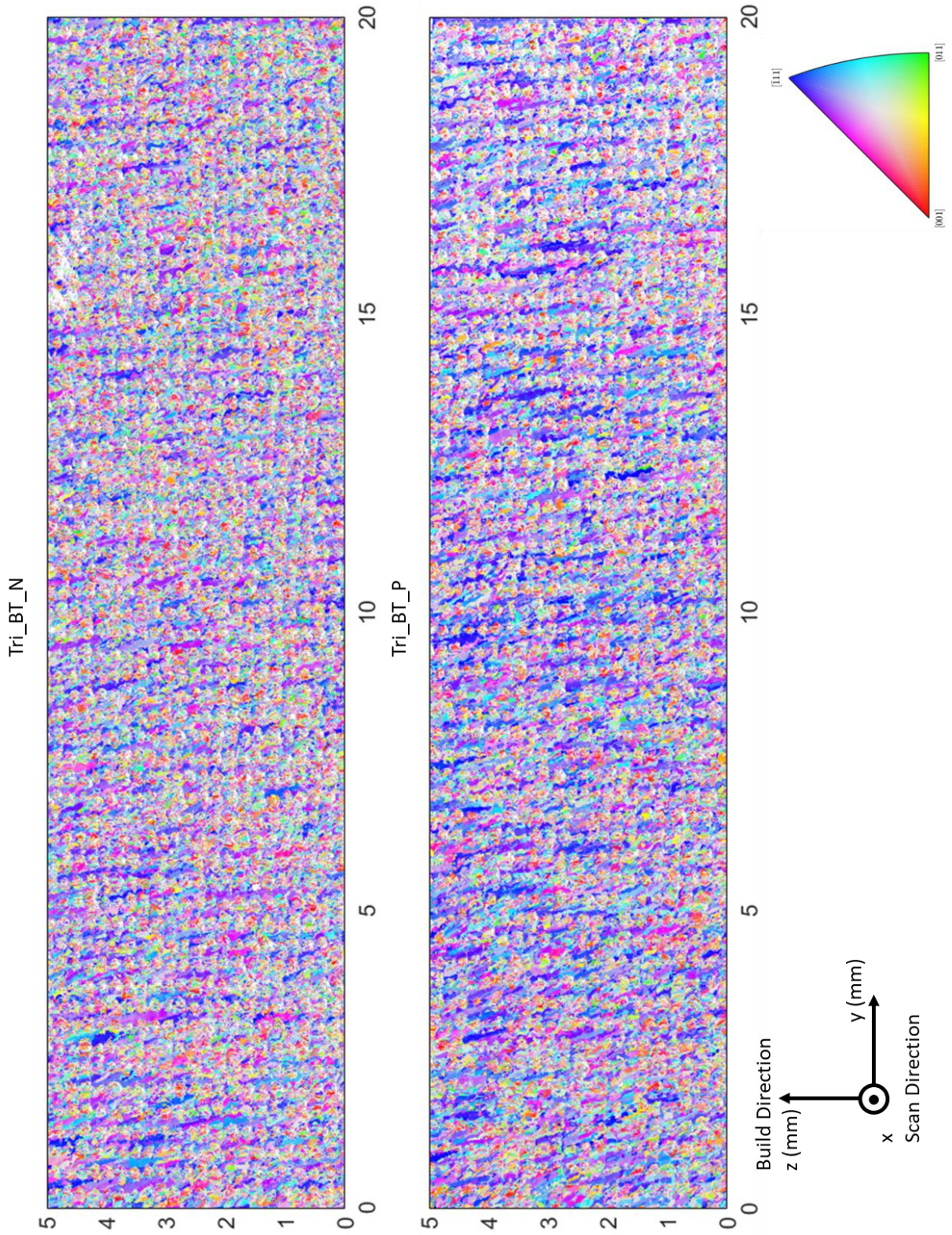

Figure 9-8: Inverse pole figure (IPFX) maps of Tri_BT_N and Tri_BT_P triangular prisms, cropped to show only the central region

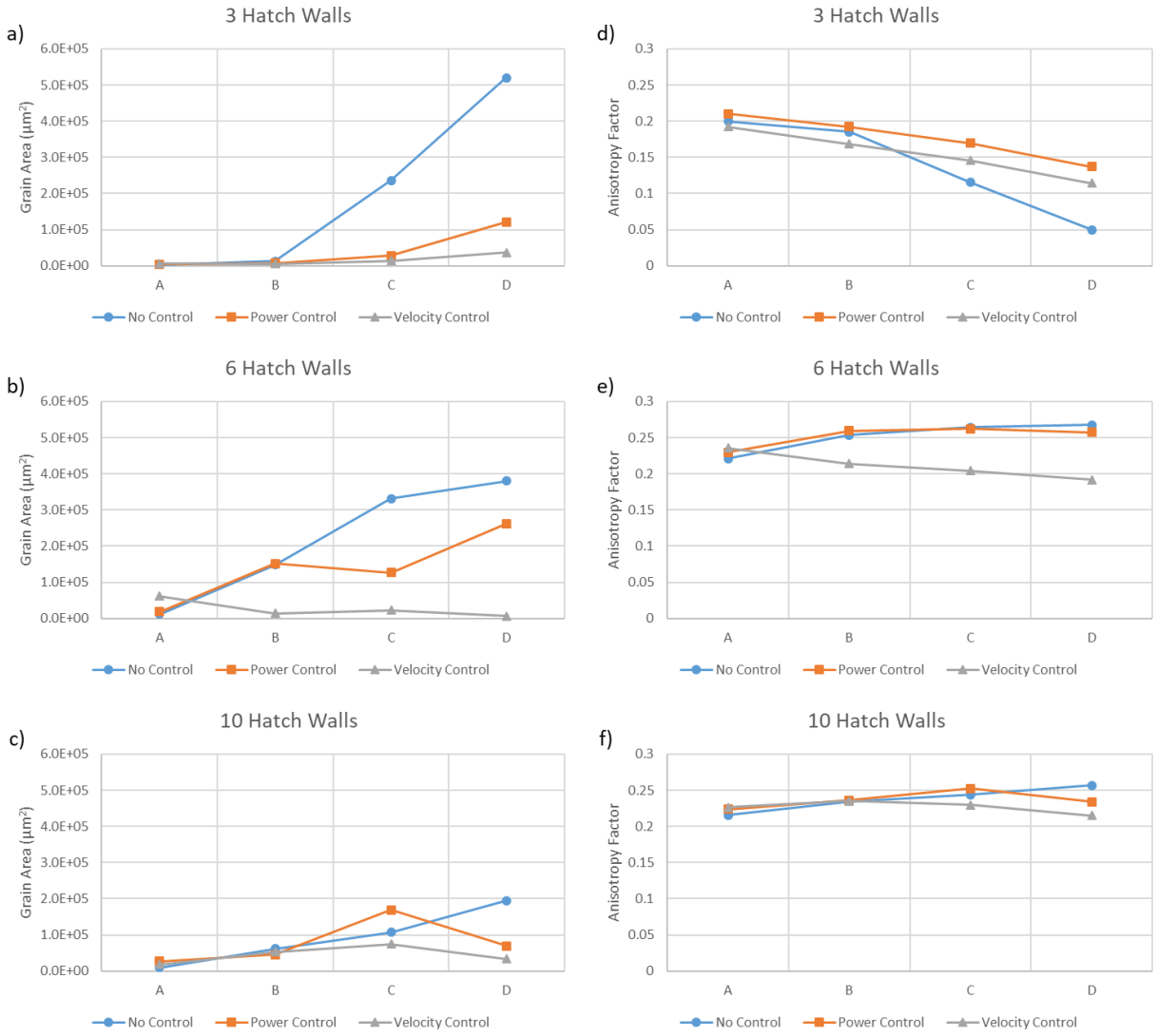

Figure 9-9: Breakdown of EBSD with each wall split into quarters, comparing grain area (a-c) and anisotropy factor (d-f), both weighted by area; a, d) 3 hatch walls, b, e) 6 hatch walls, c, f) 10 hatch walls. In each plot, no control is compared to power and velocity control

Once the average value for each quarter was calculated (Figure 9-9), the variation with height can be calculated by taking the standard deviation of these 4 values for each wall; these are summarised in Figure 9-10. With no control, the narrowest walls have the largest variation with height for grain area, anisotropy factor and maximum mud. These variations decrease as wall width increases, but no control walls always experience higher variance in these measures than power and velocity control. As concluded from Figure 9-9a-c, velocity control has the largest effect on grain area, reducing the variation of grain area with height as well as reducing the variation in aspect ratio (Figure 9-10c). Variation of anisotropy factor and maximum mud (Figure 9-10b and d) both decrease with number of hatches, both power and velocity control reducing the amount of variation when compared with no control. Both seem to have a similar effect, it could be argued that power control yields the most consistent anisotropy factor (Figure 9-10b).

Since the changes occur over the full height of the walls (Figure 9-9a-c), it was decided to compare region A with region D, as there would be the largest difference between these. Generally, the 3 hatch wall had more variation than the 6 and 10 hatch walls, with 10 having the least variation (Figure 9-10). Sections A and D were selected within the 3 and 10 hatch walls, for all 3 control

types; these grains were processed using k-means clustering, labelling each grain as either small, medium or large. Examples of grain identification is shown in Figure 9-11 for 3N and 10N (A and D for each). The clustering seems to have sensibly separated the grains into the 3 classes; the bottoms of both samples (A) are dominated by small grains (blue), with some medium grains (green) appearing near the top. The tops of both samples (D) have large regions of medium and large grains (green and yellow respectively), with streaks of small grains along the centrelines.

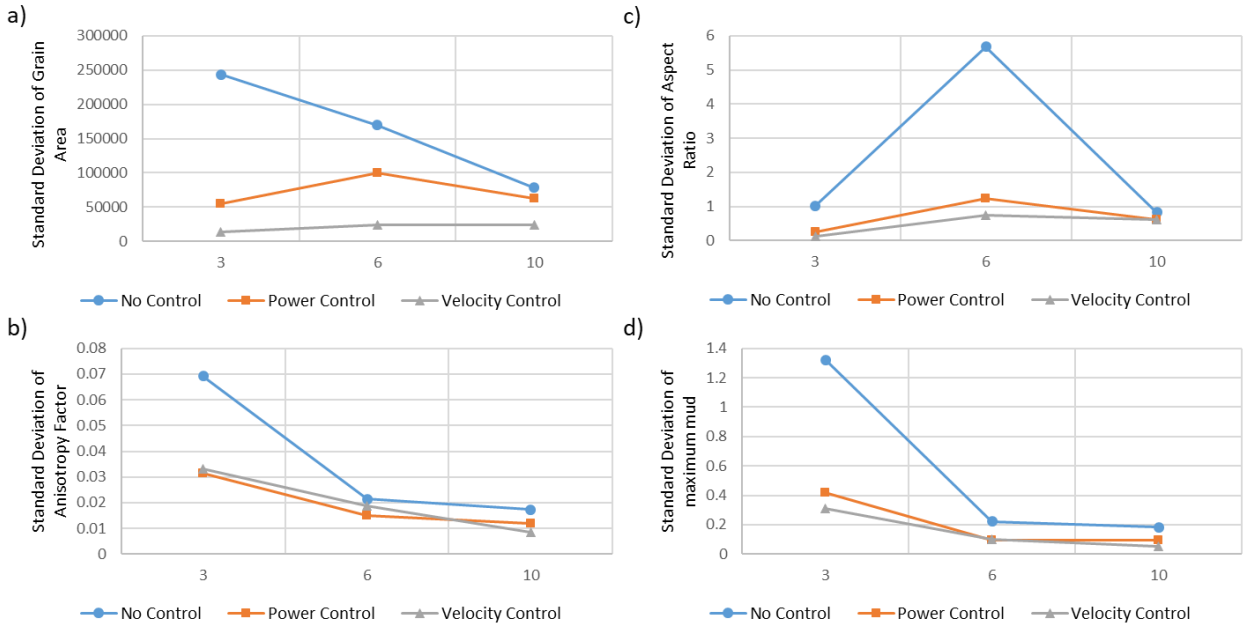

Figure 9-10: Standard deviation of EBSD measures; a) grain area, b) anisotropy factor, c) aspect ratio and d) maximum mud with height. An average value was calculated for each quarter of the sample and the standard deviation of these averages is shown

The area fraction of each grain type for each sample are shown in Figure 9-12. Typically, the small grains account for the majority of the area. Comparing the bottom of each wall to the top (A and D respectively), it can be seen that the area fraction of small grain decreases, being replaced with medium and large grains. There are very few large grains overall, with a maximum of 3 large grains within any region. Comparing 3 hatch walls to 10 hatch walls, 10 hatch walls have less variation from the bottom to the top; 3 hatch walls typically have a bigger area fraction of small grains at the bottom than 10 hatch walls, but by the top, the 10 hatch walls have a bigger area fraction of small grains than 3 hatch walls.

The change in area fraction for each grain type was calculated and the maximum of these is shown in Figure 9-13a; a large change in maximum area fraction change suggests that the grain size distribution is changing. As seen in Figure 9-12, the 3 hatch wall experiences more change than the 10 hatch wall, and the power and velocity control experience less change with height than the no control wall. Velocity control has the least variation with height for both the 3 and 10 hatch walls, similarly to Figure 9-10a. Small grains typically have the largest area fraction, Figure 9-13b shows the decrease in small grain area fraction with height. The same trend is seen in Figure 9-13a, the 3 hatch wall changes more than the 10 hatch wall and velocity control experiences the least variation with height.

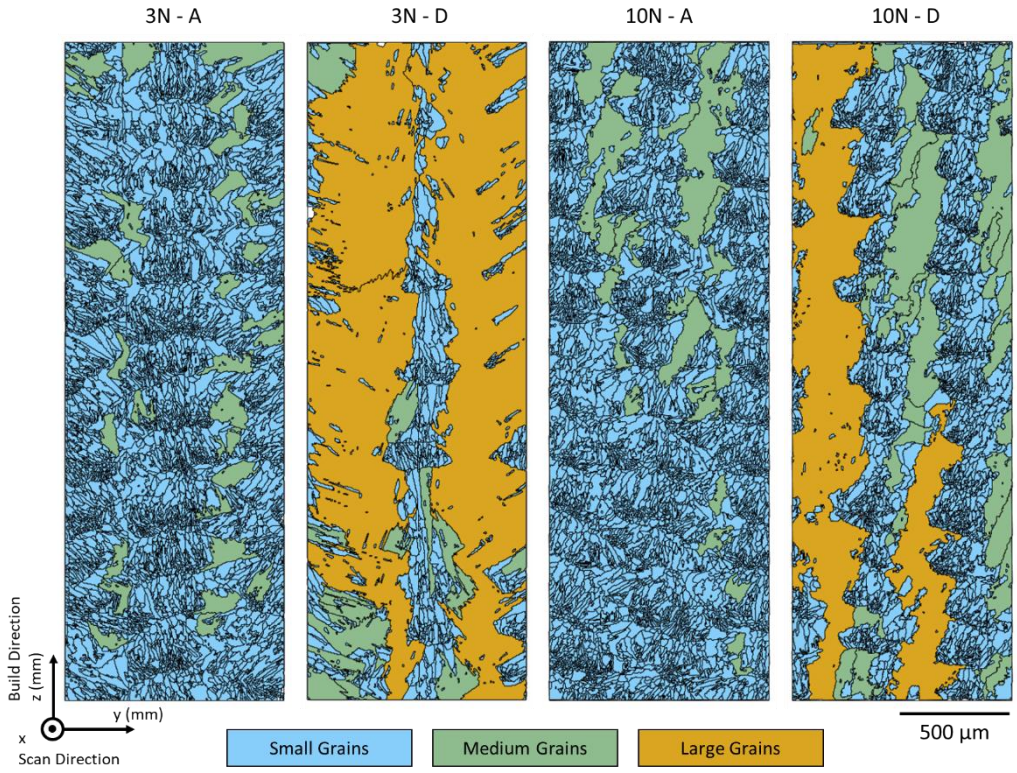

Figure 9-11: Clustering of grains into small (blue), medium (green) and large (yellow) shown for both 3N and 10N walls (A and D; botton and top quarters respectively)

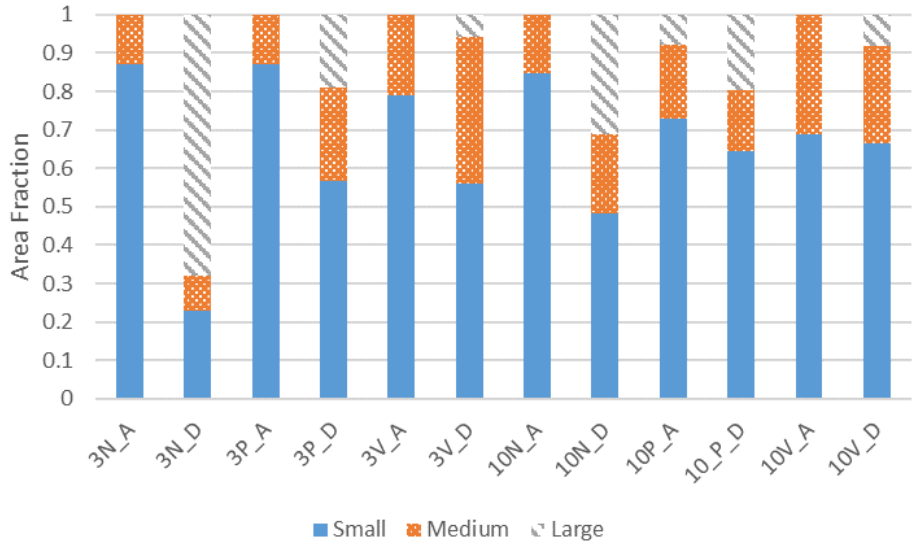

Figure 9-12: Breakdown of grain area fractions across the walls. A being the bottom quarter, D being the top quarter; comparing 3 and 10 hatch walls across all control types

There were so few large grains in the selected regions that they were discarded; even if we included them, no conclusions can be drawn from 2 grains. Changes in height (between top and bottom) for anisotropy factor, aspect ratio and maximum mud were calculated (Figure 9-14). For each measure, there is more change in the medium grains than in the small grains; the small grains are typically equiaxed in nature and randomly oriented, so the changes in the medium grains will be analysed. Figure 9-14a and d shows that power control leads to the least change in anisotropy factor of the 3 control methods. The maximum mud is the other measure of texture and in the 3 hatch wall, power control decreased mud variation, which is not the case in the 10 hatch wall (Figure 9-14f), where

mud variation increased with both power and velocity control. Finally, the change in aspect ratio decreased for the velocity control for both 3 and 10 hatch walls, for power control, there was no consistent change.

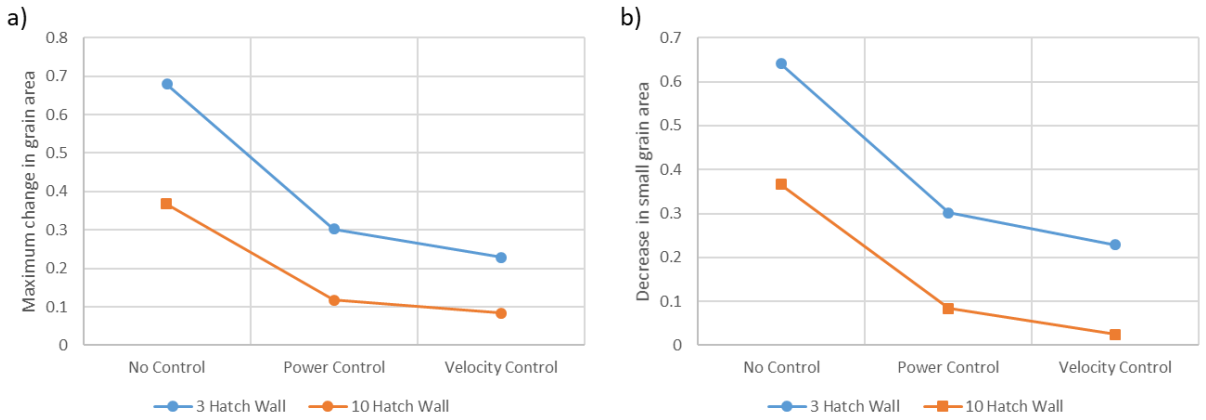

Figure 9-13: Change in grain size distributions (between D and A) depending on wall thickness and control method. a) maximum change in area fraction of a grain size (out of small, medium and large grains); b) decrease in area of small grains between A and D

The various measures of grain shape/orientation for the triangular prisms are summarised in Figure 9-15 for the Tri_BT_N and Tri_BT_P samples. In the triangular prism, Figure 9-15a shows that average grain area increases with height (z); the change is more pronounced in the sample with power control than with no control. There is minimal variation in aspect ratio with height, although the no control sample has more variation. Anisotropy factor increases with height, again, more so when built with power control (Figure 9-15b); with no control, there is minimal change in maximum mud, but some variation is introduced in the sample with power control.

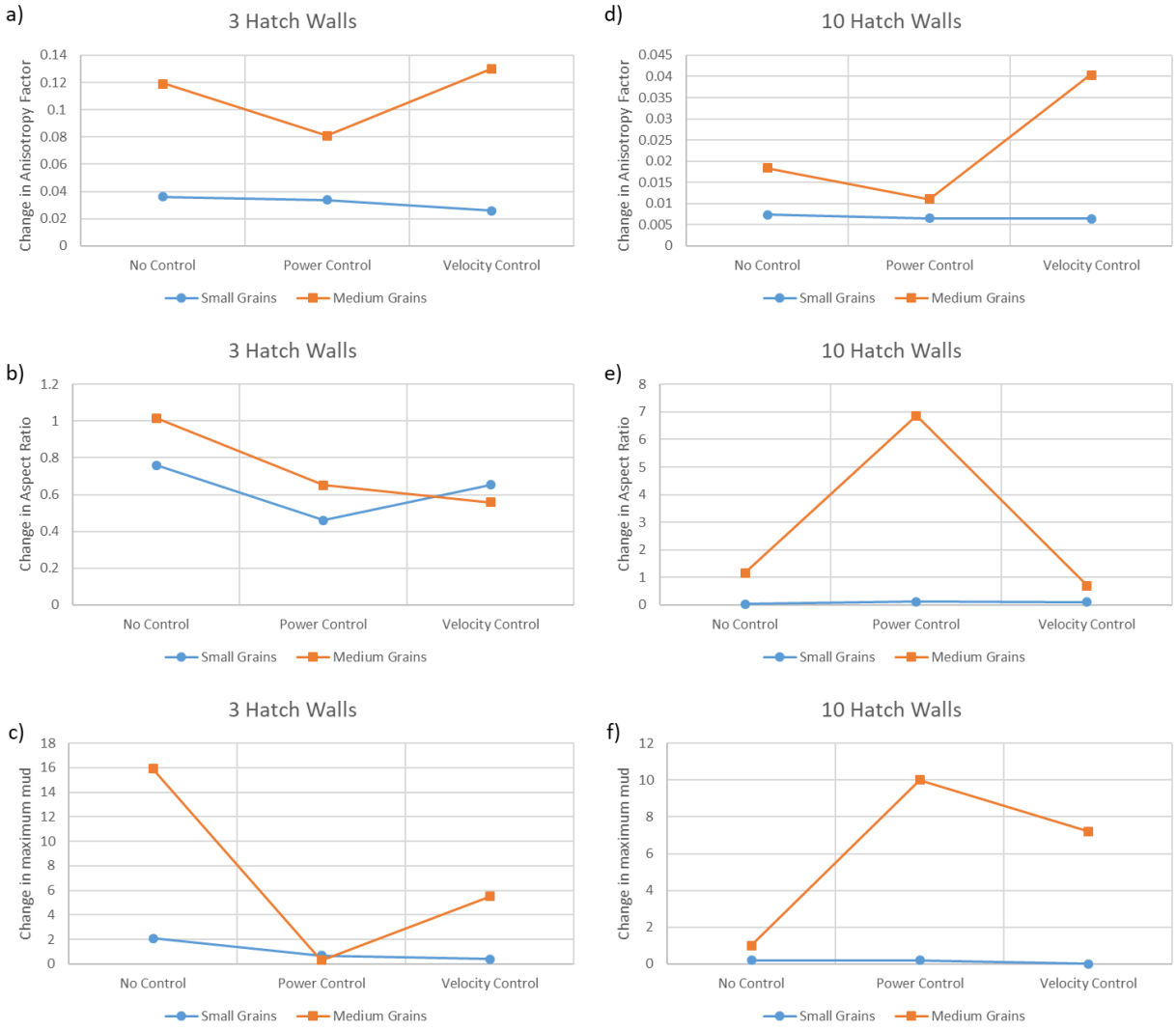

Figure 9-14: Differences in various microstructural measures between top and bottom (D and A) in walls. a, b, c) 3 hatch walls, d, e, f) 10 hatch walls. a, d) change in anisotropy factor; b, e) change in aspect ratio; c, f) change in maximum mud. Small and medium grains shown for each wall

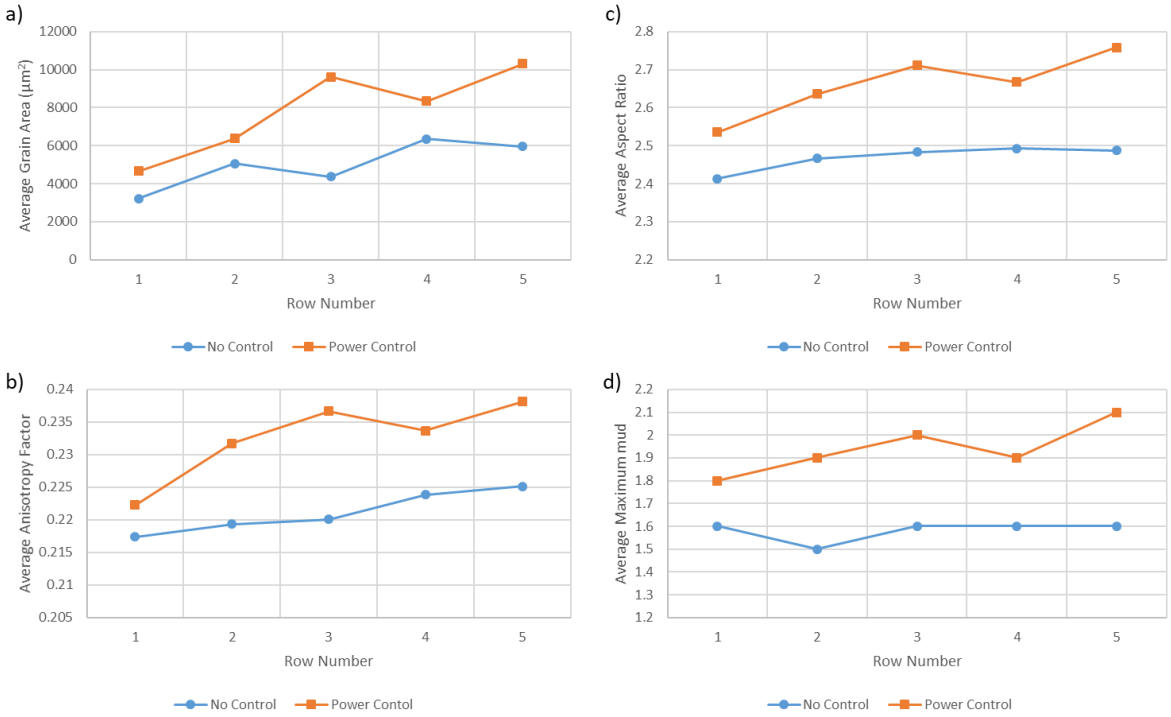

Figure 9-15: Grain variation in triangular prisms, comparing Tri_BT_N to Tri_BT_P; each split into 5 rows, with row 5 being at the top. Comparing a) grain area; b) anisotropy factor; c) aspect ratio; d) maximum mud

9.3.5. **Optical Microscopy**

For each wall, several melt pool dimensions were measured (only one for the 3 hatch, as the edge melt pools were not representative). The depths and widths were averaged for each type of control, Figure 9-16a and c show that the melt pool is both narrower and shallower when either form of control is implemented. This is more significant for velocity control, despite the same target being used for both power and velocity control. There is no visible trend of melt pool width with sample width, however, the melt pool depth is shallower in the 10 hatch walls than in the narrower walls (Figure 9-16d).

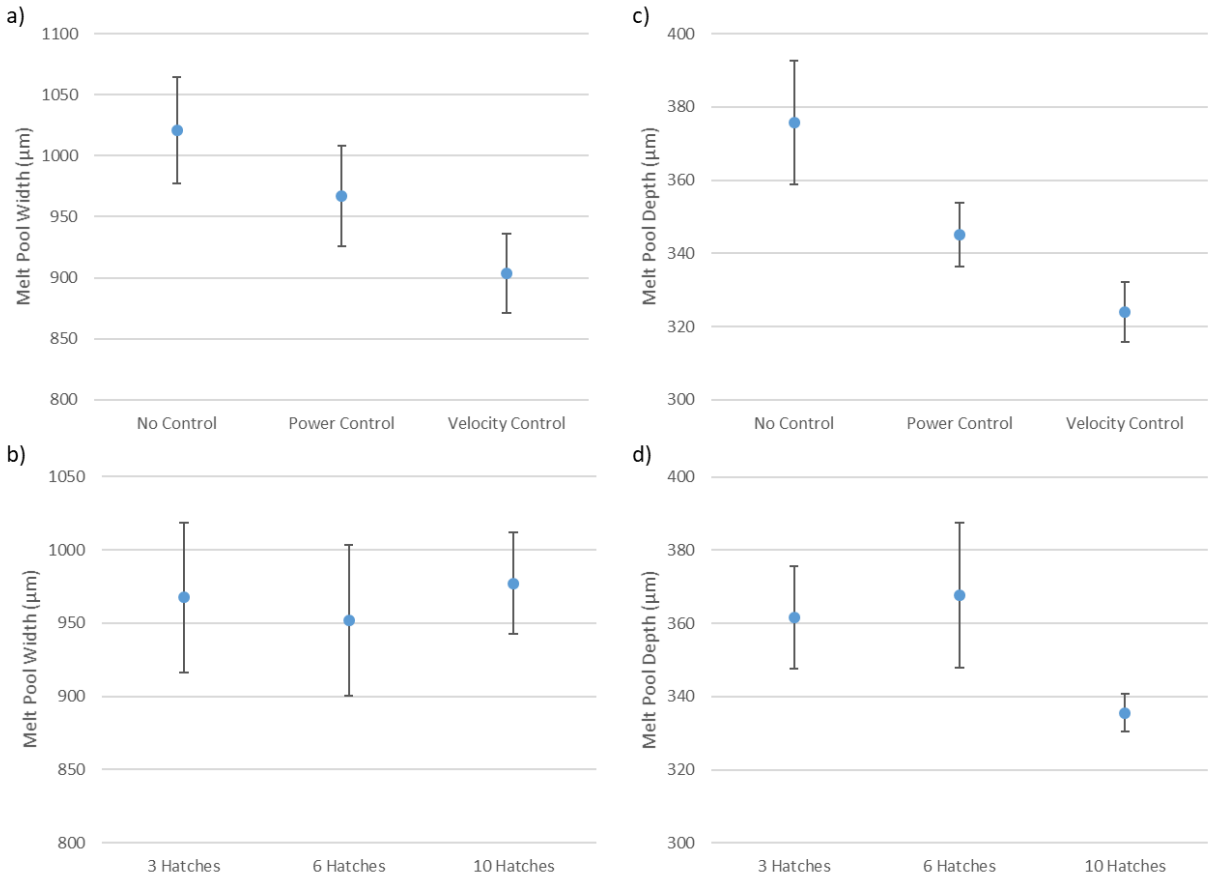

Figure 9-16: Melt pool dimensions of 9 walls. a, b) melt pool width; c, d) melt pool depth; a, c) comparing different control types; b, d) comparing wall widths. Standard errors shown

9.4. Discussion

9.4.1. Process Control

Process control is widely researched in the field of AM due to the variability in the process currently experienced. For a variety of reasons such as component geometry, powder size distribution and heat accumulation, even if a component is printed many times with identical processing parameters (power, velocity), there will be significant scatter in the final components mechanical properties. The idea behind process control is as follows:

- consistent and predictable mechanical properties are desired
- these are (at least partially) controlled by the microstructure of the component
- component microstructure is dependent on the thermal conditions in the process e.g. G, V

It follows that if the thermal conditions are kept constant, then one would expect the microstructure to be homogenous. This would in turn reduce the variability in the mechanical properties of the component.

The difficulty then becomes defining "thermal conditions", in a way that we can measure online (in-situ) and allowing us to adjust the input parameters (power and velocity) to change the conditions in a controlled manner. Provisional experiments show thermal intensity to be well correlated with both maximum intensity and melt pool area (Figure 8-4). Melt pool area requires a contour to be plotted at a threshold value which is computationally expensive; maximum intensity takes a single value, so is prone to error if any sensor anomalies occur. For these reasons, thermal intensity was used as the measure of "thermal conditions" to be controlled, similarly to Baraldo et al [171]. The control script ran at ~6 Hz and averaged the thermal intensities of 5 images and MATLAB R2021b (Mathworks Inc) was able to process this online.

The melt pool area and thermal intensity both vary with processing parameters in the expected manner, however, we have no confirmation that we are actually observing the melt pool. It has been reported that vaporised metal can cause a plume, which can obscure the coaxial view of the melt pool [171]. As explained in Section 4.2.4, four builds were initially performed and these showed that increasing power or decreasing velocity both increased thermal intensity. This logically makes sense and these experiments give us confidence in being able to change thermal intensity in a controlled manner. Even if the melt pool is being partially obscured by a plume, we are getting sufficient variation in coaxial imagery to detect changes in material behaviour. Simultaneous side-on monitoring and coaxial would allow for direct comparison of the melt pool length; however, at the time Chapter 7 was performed, the coaxial Basler camera sensor was faulty and so being replaced.

Figure 9-4 shows without control, thermal intensity started below the target, but quickly rose above the target of 0.9×10^7. For the 3 hatch wall there was the greatest change in thermal intensity with height, whereas the 10 hatch wall experienced the least change in thermal intensity. Both power and velocity are shown to bring the thermal intensity close to the target from the very start and maintain it; there is some variability, but significantly less than that in the no control wall. This is shown in Table 9-2, where the average thermal intensities of the controlled walls is between 0.889×10^7-0.906×10^7 (maximum standard error in a sample is 0.2 %).

The standard error of thermal intensity was decreased by 45 % in the 3 hatch walls and by 25 % in the 10 hatch walls (Figure 9-5b). This is definitive evidence that the process control achieved its

desired function – the thermal intensity was brought to the target value of $0.9x10^7$ and the variation of thermal intensity was greatly reduced. Figure 9-5a shows how well the controlled walls hit the target, irrespective of wall thickness; it is interesting to note that the natural variability in the 3 hatch wall is much larger than that of the 10 hatch wall. Particularly, the thermal intensity changes more with height in these narrower walls and the thermal intensity reaches greater values. It takes much longer for the hotter 3N wall to reach a plateau than the cooler 10N wall, a similar phenomenon to that seen in Chapter 7.

Figure 9-3 shows the required change in processing parameters to keep the intensity constant in the walls. In all cases, without control, the thermal intensity was above the target, so when using control, either the power was decreased or the velocity was increased. Since the 3 hatch wall had the most fluctuation without control, it required the largest adjustment in parameters. The power control decreased to 91 % by the end of the build, whereas velocity had to increase to 129 % to counteract the increase in thermal intensity. The increase in velocity required is much larger than the decrease in power required, this in itself casts doubts as to the accuracy of normalised energy density (NED) as an overarching quantity, where the ratio $\frac{P}{v}$ is widely used (Section 2.4).

Normalised enthalpy (NE), however, uses a ratio of $\frac{P}{\sqrt{v}}$ [84], so for an equal change in process, one would expect to need a larger change in velocity than the change in power required. Chapter 6 found that NE resulted in a better fit to experimental results for L-PBF than NED. Testing the two sets of controlled parameters in the NE form, using power control: $\frac{P}{\sqrt{v}} = \frac{0.91}{\sqrt{1}} = 0.91$ and for velocity control, we get $\frac{P}{\sqrt{v}} = \frac{1}{\sqrt{1.29}} = 0.88$ (all process parameters are a ratio of the no control parameters). These values are 4x closer to one another than the values of 0.91 and 0.78 which would be calculated using NED, so NE is much more representative of the process than NED. This has been shown for L-PBF in Chapter 6 and now for L-DED, so the $\frac{P}{\sqrt{v}}$ relationship is better at representing the physical phenomena occurring in AM. This confirms that AM processes are much more sensitive to power than velocity.

A greater percentage change in velocity is needed to control the thermal intensity (compared to power change required) as seen in Figure 9-3. They yield similar thermal intensity variances as process is less sensitive to velocity control. As a result of this increased sensitivity, even if the target intensity is only slightly below target, this would yield to a large increase in velocity as seen in Figure 9-3; the gradient of the response function for velocity is 10x larger than that for power (Section 4.2.4).

The aim of process control in this case was to reduce melt pool variation, to create a homogenous component. A thermal intensity target was used, and the variation of thermal intensity was greatly reduced. However, maximum intensity and melt pool dimensions (area, width, length) could equally be used to describe the melt pool. As such, to quantify the overall variability in melt pools, the standard errors presented in Table 9-2 were recalculated as percentages of the average value. For each type of control, there were 5 melt pool measures for 3 samples (3, 6, 10 hatches), all 15 standard errors were summed to give the combined standard error presented in Table 9-6.

Table 9-6 shows that both power and velocity control reduce the melt pool variation. Power control is shown to have a greater total reduction of melt pool variability. Velocity control was shown to reduce variability in thermal intensity (which was the original target) in Figure 9-5b. However, a change in melt pool area/length was experienced in the velocity controlled sample (Figure 9-6b and d), reducing its' overall success at minimising melt pool variance. The melt pool length is

always greater in velocity controlled walls than in power controlled walls. This can be rationalised, as the velocity increases, so the laser heats a longer length of material per unit time.

Table 9-6: Combined standard error for each type of control; calculated by summing the standard error (as a percentage of the average) of all five measures from Table 9-2, for all 3 sample widths

	Combined Standard Error (%)
No Control	1.40
Power Control	1.09
Velocity Control	1.38

9.4.2. **Effect of Control on Microstructure and Mechanical Properties**

Figure 9-7 shows the EBSD orientation maps for the walls, the 3N wall has a clear difference between the bottom and the top. The bottom mainly consists of small, randomly orientated, equiaxed grains, whilst the top is mainly made up of large <100> oriented grains, with some small randomly oriented grains along the centreline. To quantify these changes, the EBSD maps were split into 4 sections (vertically). Figure 9-9 shows that the narrow wall (3 hatch) experiences the biggest changes with height, both in terms of grain area and in terms of anisotropy factor.

Both power and velocity control tend to decrease this variation in microstructure with height. Figure 9-10a shows that velocity control leads to the greatest reduction in grain area variation with height. It is difficult to know the accuracy of aspect ratio measurements, as the tall grains have the largest aspect ratios, but due to the EBSD map being cut into 4 regions, these grains will likely be cut off, reducing the measured aspect ratio. It seems like both power and velocity control reduce the texture variation (anisotropy factor and maximum mud) for all walls (Figure 9-10b, d). There is much more microstructural variation in the 3 hatch wall than in the 10 hatch wall, as was the case with thermal intensity. The 10 hatch walls were shown to have shallower melt pools (Figure 9-16d), which is linked to a faster cooling rate, which could explain the columnar structure of the component (Figure 9-7) using the G-V plot in Figure 2-17.

To analyse the change in grain size more closely, grains were clustered into 3 categories: small, medium and large. k-means clustering was performed on regions A and D of the 3 and 10 hatch walls; the final result is shown in Figure 9-11. Calculating the area fraction of each grain size yields some interesting results (Figure 9-12). By calculating the change in each of the area fractions between the bottom and top, we can see that both power and control reduce the variation of grain size with height, with velocity control showing greatest reduction in variation (Figure 9-13a). The most obvious trends is observed in the area fraction of small grains, Figure 9-13b shows the area of small grains decreases with height for all samples (more small grains at the bottom than at the top). Once again, velocity control yields for the most consistent grain size for both 3 and 10 hatch walls. Additionally, Figure 9-10c and Figure 9-14b and d show that the variation in grain aspect ratio in velocity control samples is equal to or less than that for the no control walls.

Power and velocity control both decrease the standard deviation of both anisotropy factor and maximum mud for all 3 walls. It could be argued that power control results in the least variation in anisotropy factor (Figure 9-10b), whilst velocity control has more effect on maximum mud (Figure 9-10d). When clustering the grains, there were very few large grains (maximum of 3 in a region), so

these were not further analysed, as an increase from 1 grain to 3 grains cannot be said to be conclusive. The small grains were described as being equiaxed and randomly oriented, so when looking at variations in texture, only the medium grains were analysed (orange in Figure 9-14). Power control has the smallest change in anisotropy factor (medium grains) for both 3 and 10 hatch walls (Figure 9-14 a and d) and the least change in maximum mud for the 3 hatch walls (Figure 9-14c).

Overall, it seems both power and velocity control decrease the thermal and microstructural variation of the walls. Power control was shown to yield the most consistent melt pool shape, whilst velocity control elongated the melt pool. Velocity control appears to yield the most consistent grain area/shape whilst power control appears to control the texture slightly better than velocity control.

During velocity control, the velocity of the process is increased and is being adjusted. Figure 2-17 shows that as the interface velocity is increased, the propensity for equiaxed grains increases (from columnar grains). So as we increase the velocity, we are pushing the process towards equiaxed grains; this explains the increased retention of equiaxed grains at the top of the wall visible in 10V when compared to 10N (Figure 9-7). Additionally, Farshidianfar et al. showed that an increased velocity lead to a higher cooling rate [125]; a higher cooling rate naturally leads to a finer grain size. Since the bottom regions of the walls naturally have a fine grain size due to the effect of the baseplate, decreasing the grain size in the rest of the wall results in a more homogenous grain size throughout the component.

As explained in Section 2.4.1, the crystal orientation of a grain is dependent upon the direction of the thermal gradient. This is exemplified by the zig-zag grain pattern visible in bi-directional hatching strategies [284,285,372]. As such, the shape and size of the melt pool can affect the texture of the component. During power control, the smallest variation in melt pool area is experienced (Table 9-2), but the power is decreased, which reduces the melt pool depth (Figure 9-16c). As we change power and hence the melt pool depth, there will be a change in thermal gradient direction and so a change in crystal orientation is expected. Velocity control reduces the melt pool depth further(Figure 9-16c), however, the melt pool length is also elongated (Figure 9-6d). It seems like the increased cooling rate due to increased velocity affected the grain morphology more than the change in melt pool depth affected the grain orientation.

Even when the melt pool image looks comparable using coaxial monitoring, the melt pool depth can be significantly different as shown in Figure 9-16. This causes the structure of the components to differ, despite the melt pools being consistent in the XY plane. A similar observation was made after modelling work by Raghavan et al, finding that a similar XY section could have a very different melt pool depth [43]. It may be possible to gain an insight into the melt pool depth by analysing the temperature distribution within the melt pool. Alternatively, using modelling to estimate the melt pool dimensions could be used to improve input parameters.

Both power and velocity control decrease texture variation in the component (anisotropy factor and maximum mud), but since power control resulted in the most consistent melt pool shape (Figure 9-6), it is unsurprising that power control lead to the smallest variation in component texture.

The concept of a 2D component is introduced in Equation 2-5, these are generally thin components where conduction does not dominate as a heat flow mechanism [89]. Additionally, it has been noted that with height, a 3D component can start behaving in a 2D manner, this is due to the distance from the baseplate and hence the reduction in thermal condition to the baseplate [300]. The Peclet

number, defined in Section 2.2.1, is a dimensionless number used to study various transport phenomena; in this case, we are using it to characterise the nature of the heat flow. $Pe = \frac{vL}{\alpha}$, which effectively is a ratio of convection to conduction; Peclet number is proportional to the characteristic length, for which we use the melt pool length, as this is the dimension which varies most between walls whilst being calculable online. The melt pool in a 3 hatch wall (3N) is longer than the 10 hatch wall (10N), this suggests that the narrower wall experiences less conduction and so is more 2D in nature, which follows with literature [89]. Since our aim is to maintain constant thermal conditions through the build, that should include maintaining a constant Peclet number and so constant melt pool dimensions. Power control experienced least variation in melt pool area, so in terms of thermal conduction, we would it expect component built with power control to show least variation.

Essentially, the aim of process control is to reduce variation in mechanical properties, as required for industrial certification. Hardness indentation maps were taken of each wall as a simple proxy for mechanical properties. Chapter 8 showed that the edges of Inconel 718 samples are softer than the bulk due to in-situ precipitation, to avoid this, only central hardness indents were considered (a row of indents was removed from each edge). For both 3 and 6 hatch walls, the standard error of hardness was reduced by both power and velocity control (Table 9-3). For the 10 hatch wall, the initial variation was already low, and the control algorithms slightly increased the standard error. Despite some decreases in standard error being observed, no change in hardness variation was determined to be statistically significant using α=0.05 (Table 9-5).

In terms of absolute hardness values, velocity control increased the hardness of the 3 hatch wall more than power control. 3P, 3V and 6V were all found to have statistically significantly different average hardness values compared to 3N, 3N, 6N respectively (Table 9-5). This suggests that velocity control had a larger effect on the component hardness than power control.

It is interesting to find that despite a noticeable change in grain size and orientation, there is no significant reduction in the hardness variation. It could be that the magnitude of microstructural changes incurred was insufficient to cause a change in mechanical properties. Alternatively, it could be although hardness is unchanged, the variability of other mechanical properties is reduced. Tensile properties [373], crack growth behaviour [374], fatigue [375] and creep [67] have all been shown to be dependent on the grain size and orientation. Hardness is typically correlated with the youngs modulus which is known to be an intrinsic property (constant, independent of microstructure), however, it could be that more in-depth mechanical characterisation is required to determine the effect of process control.

9.4.3. **Triangular Prisms**

Triangular prisms were printed with no control and with power control to determine whether the observations made on the walls hold true in more complex geometries. The thermal intensity of the 10 hatch wall had much less variation than narrower (3 hatch) walls, this was further reduced in the triangular prisms (Table 9-2). Introducing power control brought the thermal intensity close to the target (0.89×10^7 and 0.91×10^7), however it actually increased the standard error in thermal intensity. This is likely due to the changing hatch length; e.g. at the end of a layer, the shortest hatches are being scanned, so the laser power is accustomed to short hatches and the first hatch of the next layer is long again, so the parameters are wrong.

Figure 9-15 shows the analysis of grain orientation and size for the Tri_BT_N and Tri_BT_P components. Both triangular prisms follow similar trends, grain area increases with height, as does

anisotropy factor; in both cases, the variation is slightly larger in the power controlled component. Power control slightly increases the variation in aspect ratio and of maximum mud. It seems that power control does not homogenise the grain size/orientation of larger components. It must be noted that only the central regions of the triangular prisms were analysed, all edges were removed due to the edge hardness effect. Roughly 3 mm of EBSD data is removed from both edges in the Y direction and one of these edges is the tip of the triangle, a narrow section, equivalent to the narrow walls. There was less effect of control visible in the 10 hatch walls than the narrower walls and the triangular prism is larger than the 10 hatch walls, so it is not surprising that the bulk of the triangular prism experiences no microstructural homogenisation.

In terms of hardness, no statistically significant change in either hardness or hardness variation was seen in the triangular prisms (Table 9-5), similar to the 10 hatch walls. 2 sections were taken of the triangular prism, a triangular XY section and a rectangular YZ section (of which the EBSD map is taken). The hardness variation seems to reduce slightly in the rectangular YZ sections when power control is introduced. However, the hardness variation in the triangular XY sections slightly increases, so no overall trend is seen.

Thinner components appear to be more sensitive to process control, where the microstructural variation is reduced. This effect was not observed in bulk components. Figure 9-10 shows that for 3 hatch walls, the grain size/orientation changes are most significant, whilst for the 10 hatch wall, there is minimal change in microstructural measures. The 6 hatch wall (~3 mm wide) experiences a more significant homogenisation than the 10 hatch wall, so it can be concluded that process control is most effective in sections less than 3 mm wide.

9.4.4. Additional Sources of Uncertainty

There are various phenomena which could affect the accuracy of the process control algorithms. In literature, the presence of oxides was reported as a potential impact factor on the emissivity; in this work, the powder batch was kept constant and the Argon flow was kept constant at 12 l/min. By controlling these factors, the likelihood of environmental changes was reduced. Additionally, in literature, the oxide defects were visible to the naked eye; no such defects were noticeable in components printed in this work. A variable work offset was mentioned as a secondary cause of process control inaccuracy. In this work, the work offset was set to 3.5 mm and at the end of each build, a similar work offset was observed. Further, by minimising the size of the aperture on the coaxial camera, the depth of field was increased to over 1 mm, which would stop any defocussing in the case of minor work offset fluctuations.

A very simple linear control function was used, however, Figure 9-4 shows that the target intensity was reached very quickly and was maintained relatively well. In literature, PID algorithms are typically used as controllers for process control, but these require many experiments to optimise the gain parameters. In the creation of this system, it was decided that simplicity was key and so a simpler control function was chosen. The linear control function only requires 4 components to be built to calibrate both the power and the velocity components. As aforementioned, the fluctuation in the velocity values used is quite large (Figure 9-3), this is due to the greater change in velocity required for a change in thermal intensity. Using an optimised PID controller could dampen the control and reduce the amount of overshooting; however, the linear control reduced the thermal variation sufficiently for the microstructural properties to be homogenised. In more complex geometries, a PID controller may be required for thermal intensity variation to be reduced.

A constant mass flow was used irrespective of the control algorithm used. As velocity is increased, the mass flow per unit length decreases; if less cold powder is entering the melt pool, this could allow the melt pool size to increase. There is a balance, as increasing velocity has the following effects:

- energy density decreased, so a smaller melt pool would be expected
- laser moves further per unit time, which could elongate the melt pool
- mass flow per unit length decreased, which could elongate the melt pool

It is not obvious which of these effects will dominate, and this could be dependent on the component geometry. Power control could be used to avoid this uncertainty, but increasing power will increase the melt pool size. Given that the powder capture efficiency is <100 %, a larger melt pool will capture more powder. These phenomena are unavoidable, but by being aware of them, we can comment on their potential effect rather than assuming that the mass flow is constant.

9.5. Summary

In this chapter, process control was implemented using a cheap coaxial monitoring setup. It has been shown that both power and velocity control can successfully regulate the thermal intensity, even when using a simple control function, reducing the variation in thermal intensity in narrow components. Narrow components experience significantly more thermal and microstructural variation when printed with no control; this naturally means that the process control has more effect on these. It was shown that the L-DED process is more sensitive to power than velocity; NE ($\frac{P}{\sqrt{v}}$) was found to be more accurate than NED ($\frac{P}{v}$).

Coaxial monitoring was found to be easier to implement due to geometrical constraints. Power control was shown to maintain the overall thermal signature of the component with the greatest consistency, likely due to the melt pool elongation experienced in the case of velocity control. With no control, 10 hatch walls experienced minimal microstructural variation, however, the microstructural variation of 3 and 6 hatch walls was greatly reduced by using both power and velocity control.

Velocity control is hypothesised to increase cooling rate by elongating the melt pool, leading to a finer grain size. Power control was hypothesised to alter the melt pool shape and so the direction of the thermal gradients, changing the grain orientation and altering the texture. Despite the fact that the variation of grain size/orientation was reduced by power and velocity control, the variation of hardness in these components was not significantly reduced. The grain structure was altered, and this change in grain size/orientation would be expected to affect other mechanical properties such as tensile properties and fatigue life.

The triangular prisms behaved much like the 10 hatch walls, showing minimal variation when power control was applied. The results analysed suggest that process control does have an effect on components of up to 3 mm width, but have no real effect in larger components. Real life components, such as turbine blades, do have sections less than 3 mm wide, so being able to control the component homogeneity in these extremities would be advantageous. Even with process control implemented, the melt pool depth varied with sample width, which explains the microstructural changes between samples of different widths. This could be improved by a detailed analysis of the temperature distribution within the melt pool, which could lead to a more advanced parameter being used as the input to the control algorithm.

Inconel 718 is known for being a very printable alloy with a wide processing window; if another alloy was more susceptible to changes in thermal gradient and/or cooling rate, the effect of power/velocity control may be more pronounced. Work has previously been done on Ti-6Al-4V [376] and Fe-19Ni-5Ti [330] alloys, creating banded structures, either by allowing the material to cool between layers [330], or by changing the energy density [376]. Since both of these alloys have a strong microstructural response to a change in processing parameters, these alloys may be a good choice for testing the capability of process control as they would better determine the feasibility of reducing variability in mechanical properties of components by using process control.

10. Analysis of Grain Size and Orientation Distributions in Inconel 718 produced by L-DED

10.1. Introduction

Additive manufacturing yields notoriously complex component microstructures. Much work has been focussed on understanding grain orientation, in an attempt to achieve consistent structures, specific structures or single crystal components [33,180,372,377–379].

10.1.1. Heat Flow in AM

Much work is focussed on modelling of AM, this is needed for a better understanding of the heat flow during the process and hence the final component texture. In full component models, conduction is found to account for around 90 % of cooling (conduction∝T) [105,380]. Along the top surface, convection is shown to be constant (convection∝T), radiation is of similar magnitude to convection, but increases by a factor 3 in the melt pool (radiation∝T^4) [380]. It must be noted that these models ignore heat flow from the front/back faces. As reported by Heigel, including convection increases the accuracy of thermal models, Figure 10-1 shows the effect of varying the convection coefficient; different coefficients fit better at different times in the process [381]. By fitting the convection coefficient to the data and modelling forced convection (which increases cooling), Heigel was able to reduce thermal error to 5 % [381]. This is a similar situation to emissivity calibration for thermal monitoring, most work published in literature uses a single value for simplicity, but this introduces error into the measurement.

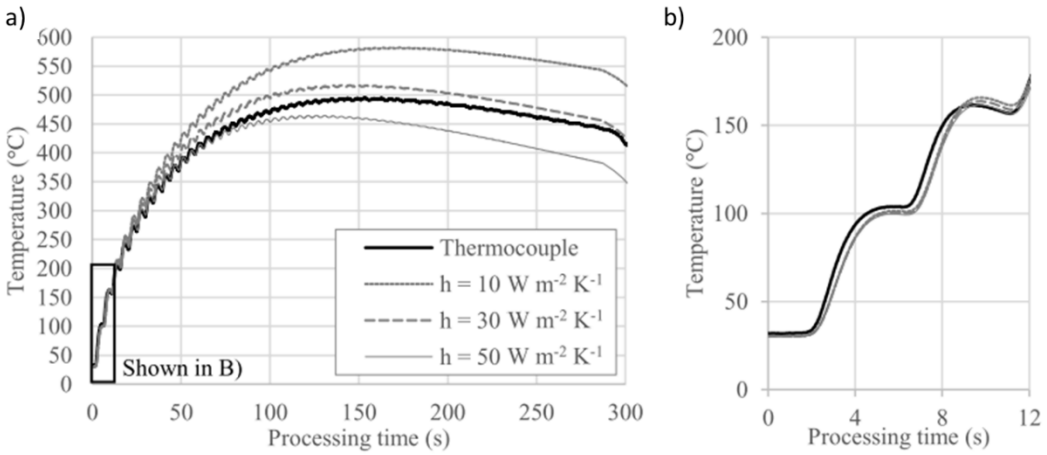

Figure 10-1: Effect of varying convection coefficients on the accuracy of thermal models for L-DED; b) shows the initial rise from a). Reported by Heigel [381]

Vasinonta et al. created processing maps using both 2D (thin wall) and 3D (bulk) point heat source models [89]; these allow for prediction of a normalised melt pool size from processing parameters. Since conduction is restricted in the thin wall due to reduced volume, the melt pool is predicted to be 65 % longer than in the bulk scenario when printing with the same parameters [89]. In reality, due to the larger surface area and longer melt pool, radiative cooling would also become more significant [381], so the cooling rate is likely underestimated. There is also a reduction in conduction with build height, which leads to a temperature increase with height [105]; thermal

monitoring and modelling both show the temperature rising over initial layers before plateauing, as seen in Chapter 7 [89,300].

Heat flow conditions vary significantly depending on the geometry being printed and will vary starkly in different parts of a component [95]. For repeatable, homogenous components to be printed, the variation of the melt pool with part cross-section needs to be better understood, as this directly influences the microstructure.

10.1.2. Grain Orientation in PBF

There is more work regarding the origin of grain orientation in L-PBF than in L-DED in the literature. Sun et al. report that by increasing energy, density keyhole mode is reached (Figure 10-2d) [93], the increased roundness of the bottom of the melt pool means that grains predominantly grow diagonally (as shown by the green arrows) and so no columnar grains occur. In Figure 10-2c, large columnar grains are visible in the conduction mode melt pools, the authors claim that a flatter melt pool allows for growth of the columnar grains, as the melt pool shape dictates the thermal gradients and so the texture [93]. 316L steel has an FCC structure (as does Inconel 718) and the materials properties are relatively similar to that of Inconel 718 (summarised in Table 10-1, with Ti-6Al-4V included for comparison), hence similar microstructural phenomena are expected as with Inconel 718.

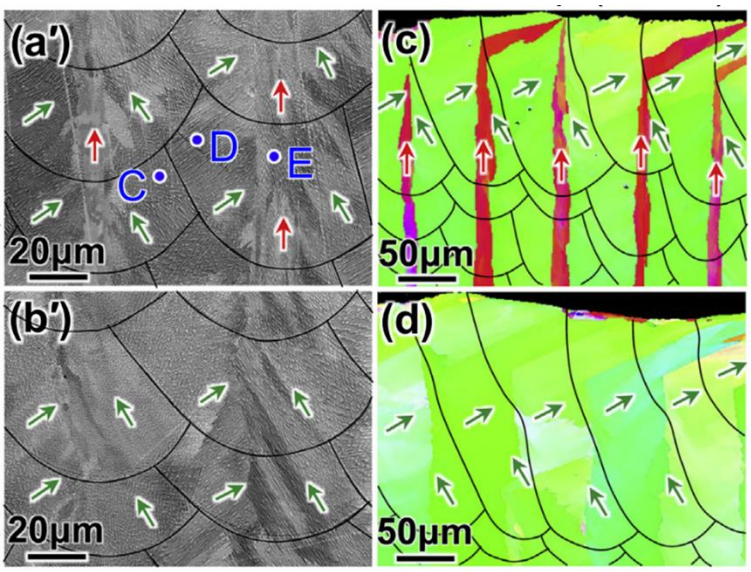

Figure 10-2: Microstructure of L-PBF manufactured 316L steel. a', b') optical micrographs; c, d) inverse pole figure maps; a', c) low energy density; b', d) high energy density. Laser scans into/out of page; reported by Sun et al [93]

A similar transition was reported by Gokcekaya et al. [94], however, in this case, it was achieved by increasing the velocity (which decreases energy density). They claim to perform a thermal diffusion analysis and that the results of this predict a vertical maximal heat flow direction in the low velocity case (Figure 10-3a'); unfortunately, no modelling details are given, so it is now known how well the modelled melt pool shapes match those seen experimentally [94]. Jodi et al. manipulated the melt pool shape using a top-hat laser profile, allowing for epitaxial growth of pure Nickel [379]; since the melt pool was wide and flat, grains grew vertically, propagating in the <100> orientation. In EB-PBF, Pistor et al. found that a low solidification angle (flat melt pool) lead to coarse columnar grains [378]; this follows the hypothesis made by Sun et al. [93] that the melt pool shape can be taken as a proxy for the maximal heat flow direction, as accurate modelling is difficult.

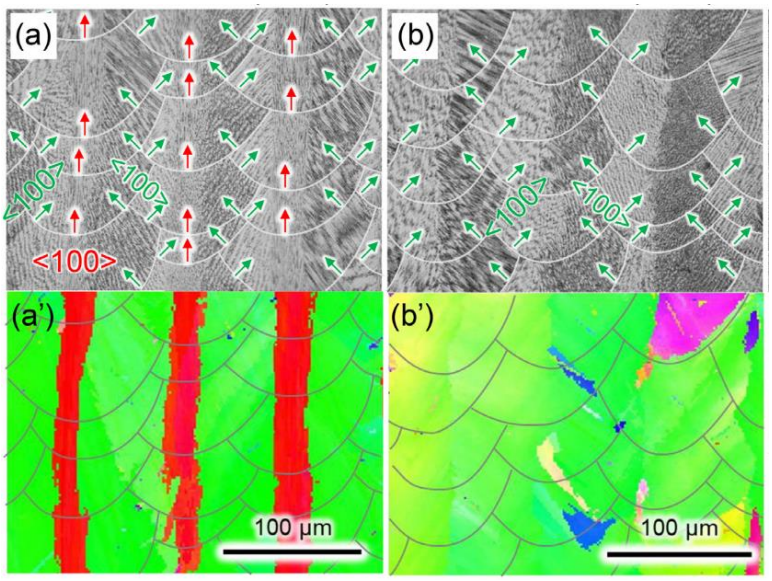

Figure 10-3: Microstructure of L-PBF manufactured Inconel 718; a, b) optical micrographs; a', b') inverse pole figure maps; a, a') lower velocity; b, b') higher velocity. As reported by Gokcekaya et al [94]

Table 10-1: Comparison of materials properties of 316L, Inconel 718 and Ti-6Al-4V

	316L	**Inconel 718**	**Ti-6Al-4V**
Crystal Structure	FCC	FCC	HCP
ρ, Density, kgm^{-3}	7800 [4]	8100 [4]	4000 [4]
κ, Thermal Conductivity, $Wm^{-1}K^{-1}$	16.3 [95]	9.9 [273]	6.63 [4]
α, Thermal Diffusivity, m^2s^{-1}	$4.07x10^{-6}$ [95]	$2.87x10^{-6}$ [273]	$10.7x10^{-6}$ [382]
ΔT, Freezing Range, K	40 [4]	76 [4]	50 [4]

10.1.3. Grain Structure in L-DED

Generally, it has been shown that grains grow anti-parallel to the maximum heat flow direction [377], as shown to be the case in L-PBF; for the γ phase (FCC), the <100> orientation is the fastest growing direction [285,377]. In L-DED, dendritic solidification is shown to occur, where heat flow is not the only factor in the growth direction (Figure 2.4.1), as there is a high energy cost associated with the nucleation of dendrites [159]. Figure 10-4a shows the direction of the beam movement and how the maximum heat flow (perpendicular to melt pool boundary) leads to a solidification velocity at an angle from the laser movement direction. In the example by Wei et al. (L-DED), this is calculated to be 60 ° (Figure 10-4c) and so the dendrites are expected to grow at this angle (Figure 10-4 d, e); this is confirmed experimentally for Inconel 718 in Figure 10-5a.

Similarly, Guévenoux et al. hypothesised that the angle at the bottom of the melt pool determines the observed crystal structure as shown in Figure 10-6 [95]. In this case, the grain orientation was vertically aligned, however, when an inter-layer dwell was introduced, the zig-zag pattern was observed. The extra cooling time was said to elongate the melt pool and hence create an angled interface which results in diagonal grain growth (55 °). In L-DED, much EBSD is done XZ sections

(e.g. Figure 10-5); if looking in the YZ plane (melt pool moving into/out of page, similarly to Figure 10-3), a vertical (columnar) grain would appear as <100> orientation, whilst a diagonal grain will have an orientation far from <100> (towards <110> or <111>, depending on the 3 dimensional orientation of the grain).

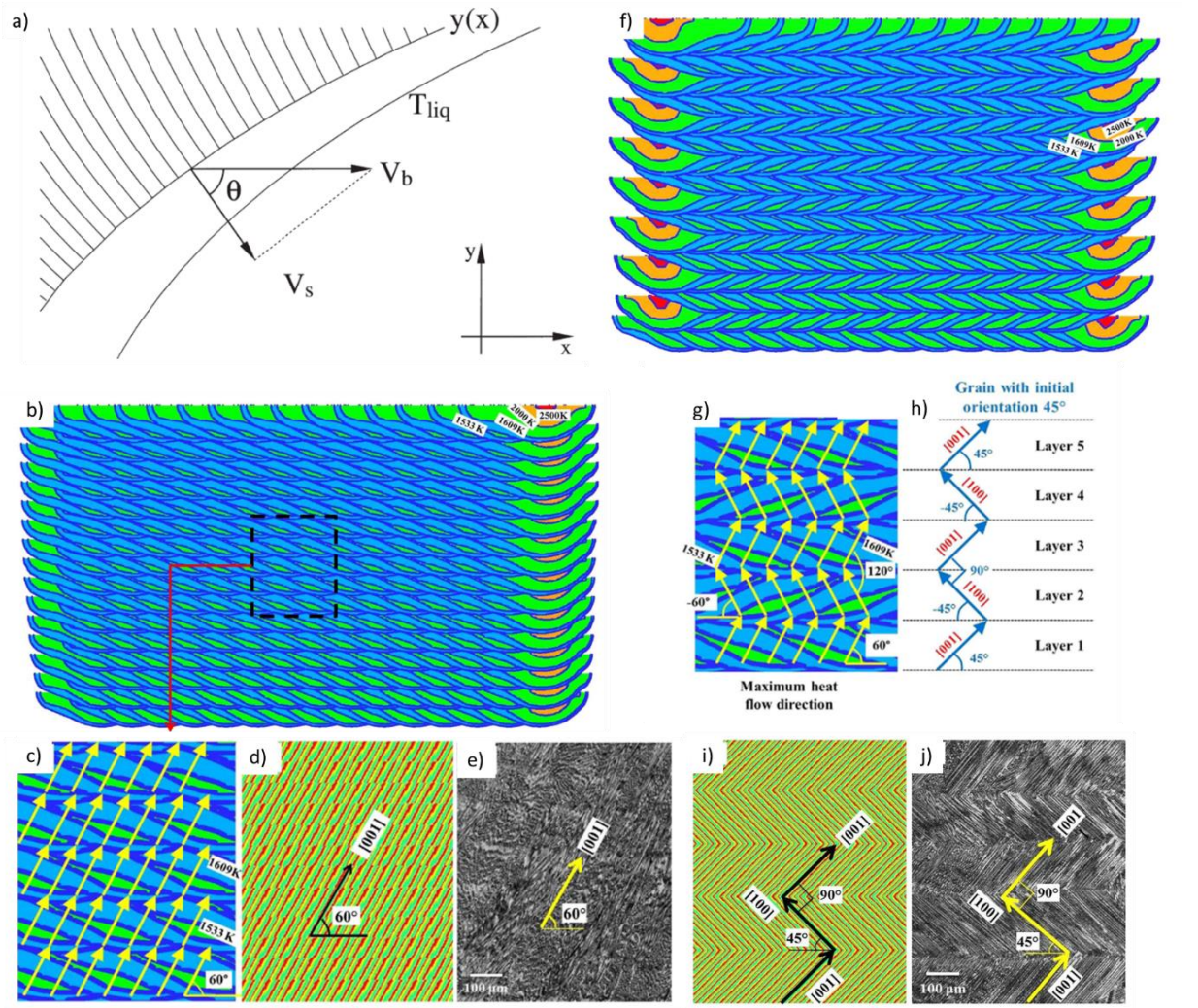

Figure 10-4: Grain growth direction explained through scan strategy and heat flow direction. a) Corner of a modelled melt pool, with solid in the top left, V_b shows the beam velocity and V_s shows the direction of the solidification velocity; b) overlapping melt pools in a uniaxial scan strategy, showing multiple layers of the build; c) maximum heat direction overlaid on b), resulting in d), the predicted dendrite solidification pattern; e) 60 ° dendrite angle shown for Inconel 718; f) overlapping melt pools in a biaxial scan strategy, showing multiple layers of the build; g) maximum heat direction overlaid on f), h) schematic showing a 45 ° grain growth; i) the predicted dendrite solidification pattern; j) 45 ° dendrite angle shown for Inconel 718. Adapted from Hunziker et al [88] *and Wei et al* [159]

The case is more complex if the hatching direction is alternated (Figure 10-4f). If one grain grows at 60 °, then the next layer would grow at -60 °, 120 ° between them (Figure 10-4g); this is energetically unfavourable. If dendrites grow at 45 ° from the laser movement direction, the maximum heat flow remains at 60 °, so there is a 15 ° mismatch. However, in the next layer, if dendrites grow at -45 °, then there is a 90 ° angle between layers (Figure 10-4h); this allows for secondary dendrites in one layer to grow into primary dendrites in the subsequent layer [159]. This removes the need for nucleation of new dendrites and so reduces the overall energy required; this reduction is sufficient for the dendrite growth to consistently grow at 15 ° from the maximum heat flow direction (45 ° growth compared to a 60 ° heat flow). Figure 10-4j and Figure 10-5b show that a 90 ° orientation change does occur between layers, confirming that the heat flow isn't the only factor in determining the dendrite orientation. This would lead to the appearance of tall,

continuous grains (when looking in the YZ plane), although for different reasons than those that occur in L-PBF; in L-PBF, vertical epitaxial growth occurs, in L-DED, zig-zag growth occurs, but from the YZ plane, these appear to be of a constant orientation. Similar phenomena are occurring in both processes, but due to the different melt pool scale and different solidification structures, direct parallels cannot always be drawn.

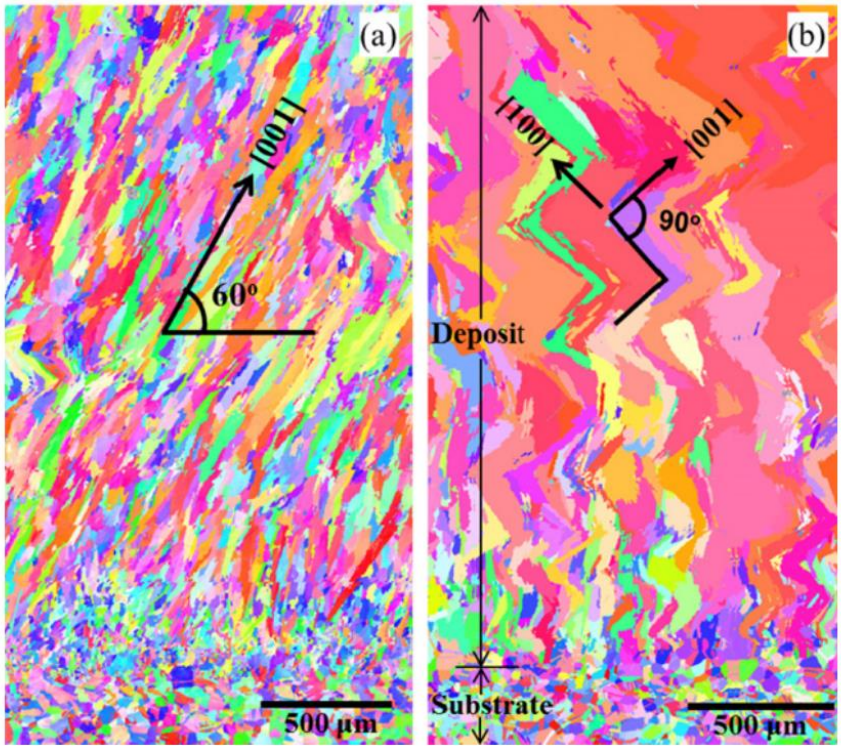

Figure 10-5: Inverse pole figure maps of Inconel 718 manufactured using L-DED. a) unidirectional scan strategy; b) bidirectional scan strategy. Laser movement axis is left to right, reported by Dinda et al. [285]

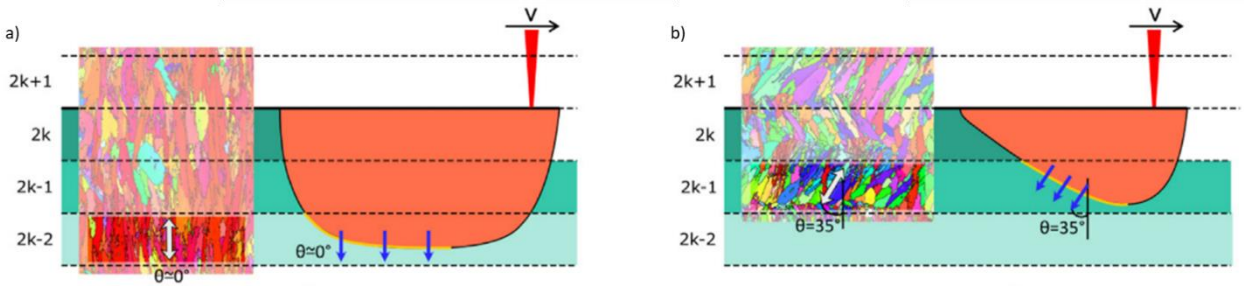

Figure 10-6: Melt pool shapes and EBSD maps of Inconel 718; a) no interlayer dwell; b) 10 second interlayer dwell. Reported by Guévenoux et al. [95]

Figure 10-7 shows the expected transition from columnar to equiaxed grains with G and V; constructed for Inconel 718 by Dehoff et al (for EB-PBF) [102]. A black arrow has been overlaid, using the laser velocity for these experiments as the interface velocity and showing a range of cooling rates from 10^3-10^4 K/s. It has been reported that a small melt pool is associated with having a faster cooling rate [104,105]; Figure 10-7 shows that this would in turn lead to a more columnar structure [102].

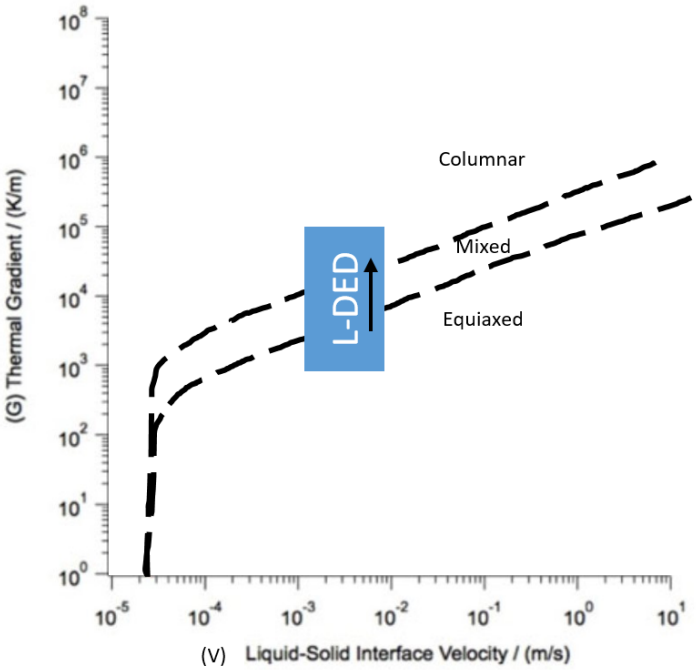

Figure 10-7: Plot of G vs V, with the black arrow showing the approximate range of conditions experienced, direction shows increasing cooling rate. Reported by Dehoff et al. [102]

10.1.4. Effect of Grain Orientation on Mechanical Properties

As microstructure has a strong effect on the resulting mechanical properties of a component, understanding the microstructure formation during AM is critical for predicting the mechanical properties. In literature, both grain size and orientation have been reported to affect the mechanical properties of components; summarised in Table 10-2. Overall, it is shown that changes in processing conditions, sample orientation and scan strategy have a large effect on the mechanical properties, and these effects are maintained post heat-treatment. As concluded in Chapter 9, keeping consistent thermal conditions is critical for both microstructural and mechanical homogeneity.

A large change in grain orientation was observed with sample thickness in Chapter 8 and Chapter 9, what causes this change in grain structure? In-depth optical/EBSD analysis is performed in this chapter and the cause of the orientation change is explored. If melt pool monitoring cannot capture this change in grain structure, does this negate the use of coaxial monitoring for process control?

Table 10-2: Summary of mechanical property dependence of Inconel 718 on the microstructure

Primary Author	Process	Change in Microstructure	Change in Mechanical Properties
Kirka [373]	EB-PBF, HIP, Heat Treatment	Equiaxed vs Columnar Parallel and Perpendicular to build direction	Order of magnitude difference in low cycle fatigue. 20% difference in σ_y
Ghorbanpour [374]	L-PBF	Small vs Large Grains (3.5x increase) Parallel and Perpendicular to build direction	35 % difference in E 20 % difference in HV 2.75x difference in crack fatigue threshold
Gribbin [375]	L-PBF (some HIPed)	Horizontal vs 45 ° angle	15 % difference in high cycle fatigue stress threshold (at which failure did not occur)
Sanchez [67]	L-PBF, Heat Treatment	2x change in grain size (changing scan strategy and orientation of tensile bar to baseplate)	2.5x change in creep life 4x change in elongation to failure
Alhuzaim [383]	L-DED	4x change in grain dimensions by varying laser power. 4x change in PDAS	15 % change in micro-hardness
Tabernero [384]	L-DED	Change in scan strategy. Microstructural change not quantified	55 % change in UTS

10.2. Methods

Samples were printed in Inconel 718 on the BeAM Magic 2.0 DED machine on an Inconel 718 substrate, with the nozzle 3.5 mm above the substrate. Walls of six different thicknesses (controlled by number of hatches) were built, ranging from 1 hatch (1.1 mm thickness) to 8 hatches (3.6 mm thickness) all with consistent build parameters, as summarised in Table 10-3. These were originally introduced in Section 8.2. Additionally, two walls were printed with power control, 3 and 10 hatches wide respectively (Section 9.2). Finally, one triangular prism was printed, hatching from base to tip, as introduced in Section 8.2; the scan strategies and axes are defined consistently throughout, as defined in Figure 8-3. During the process, coaxial monitoring was recorded as described in Section 4.2.4, calculating average thermal intensities and melt pool measures for each component.

Table 10-3: Parameters used for both wall and triangular prism samples; all samples previously introduced in Chapter 8 and Chapter 9

Sample	Power (W)	Velocity (mm/min)	Hatch Spacing (µm)	Z Step (µm)	Mass flow (g/min)
1 hatch Wall	300	2250	400	200	6-6.5
2 hatch Wall					
3 hatch Wall					
4 hatch Wall					
6 hatch Wall					
8 hatch Wall					
3P (power control)	300	2000	400	200	6-7
10P (power control)					
Base to Tip Triangular Prism	275	2000	350	225	6.5-7.5

EBSD was performed on all of the samples; the details of the various thickness walls and the triangular prism EBSD capture are described in Section 8.3.3. EBSD of the power controlled walls was performed using a Jeol 7900F with an Oxford Instruments Symmetry EBSD detector. A 3.5 µm step size was chosen with a 13 mm work offset and a ~ 90 nA probe current. Walls were scanned with the area covering 1 mm (Y axis) in the central section of the sample (Y axis) with a height of 12 mm from the baseplate (Z axis). The average grain area (weighted by area) was calculated for each component.

All the grains from the 6 walls were combined to perform k-means clustering (as described in Section 4.7) for further analysis. This involved clustering the grains into 6 clusters, by grain area and aspect ratio; these were then combined into three grain types: small, medium and large. All the grains from the two power controlled walls were also clustered, with each grain being assigned to its nearest cluster centroid, as calculated above. The YZ section of the triangular prism is rectangular, roughly 21 x 7 mm (Y and Z respectively); this was split into 21 slits, each 1 mm slits along the Y direction, so the effect of the component thickness (in X) on microstructure could be analysed. Each of these 21 slits has their grains clustered using the pre-calculated centroids. For each set of grains within each component, area percentage, anisotropy factor, aspect ratio and maximum mud were calculated.

Once polished, the walls of various thicknesses were etched with Kallings Reagent #2 to reveal the underlying microstructure. Optical micrographs were then taken to measure the melt pool dimensions and the primary dendrite arm spacing (PDAS). Since subsequent layers remelt previously printed material, the top layer of melt pools is the only one which can be used to measure an accurate melt pool depth. To analyse the melt pool shape, an outline was manually drawn from the optical images and the line was fitted with a 6^{th} order polynomial. This allowed for calculation of the melt pool angle, so the fraction of "flat" melt pool could be calculated. In EBSD, a grain threshold angle of 10° is typically used, a section of melt pool was defined as flat if the angle was ±5 ° from horizontal.

10.3. Results

10.3.1. Thermal Monitoring

Coaxial monitoring was recorded throughout the builds, and this is shown for several components in Figure 10-8. The thermal intensity for the 3P wall is shown in Figure 10-8a, b, raw data and with intensities below $0.2x10^7$ removed respectively. This reduces the noise due to the laser turning off and makes it easier to compare the thermal intensity of walls. Figure 10-8c shows the variation in thermal intensity throughout the 3 and 8 hatch walls. They start with a similar thermal intensity, but the intensity of the 3 hatch wall increases rapidly, whilst the intensity of the 8 hatch wall only slightly increases over a longer duration. Both 3 and 8 hatch walls have an increase in thermal intensity variation with build height. The average thermal intensities for the walls of varying width are summarised in Figure 8-9.

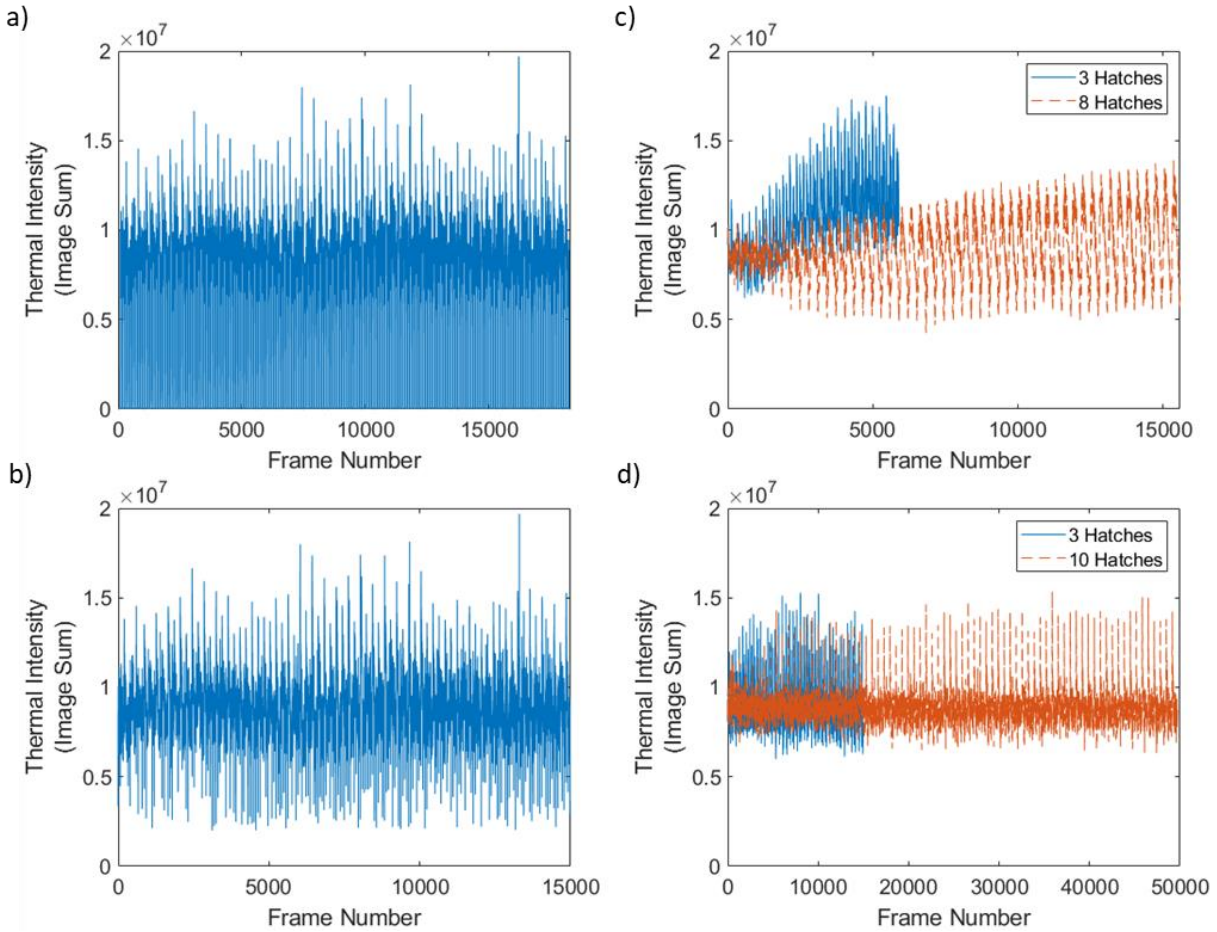

Figure 10-8: Thermal intensities of walls; a) 3P wall, b) 3P wall (removing points with intensity below $0.2x10^7$), c) 3 hatch and 8 hatch walls (removing points below $0.2x10^7$, moving average with window 10), d) 3P and 10P walls (removing points below $0.2x10^7$, moving average with window 10)

Figure 10-8d shows that with power control, both 3 and 10 hatch walls (3P and 10P) have a consistent thermal intensity, centred around the target intensity ($0.9x10^7$). The average thermal intensities of the 3P and 10P walls are summarised in Table 10-4 along with the other melt pool measures. The average thermal intensities, maximum intensities, melt pool widths and melt pool areas are very similar, with the difference between the two walls being less than the standard deviations. The average melt pool length of the 3P wall is 15 px longer than the 10P wall, which is less than the average standard deviation but is the largest difference between the melt pools.

Table 10-4: Comparison between 5 coaxial monitoring measures for the 3P and 10P walls. Standard deviations are shown in brackets

	3P (14989 frames)	**10P (49724 frames)**
Thermal Intensity	8.97 (1.8) x 10^7	8.96 (1.43) x 10^7
Max Intensity	1277 (218)	1257 (172)
Melt Pool Width (px)	166 (9.7)	167 (13.4)
Melt Pool Length (px)	201 (20.5)	186 (12.8)
Melt Pool Area (px^2)	24088 (2470)	24470 (1809)

10.3.2. **EBSD Analysis**

Figure 10-9 is a duplicate of Figure 8-12, included for ease of reading, it shows the orientation maps of the 6 walls of various thicknesses. Generally, it seems like narrow walls (1-3 hatches) are made up of smaller, fairly equiaxed grains, along with some larger diagonal grains, which do not seem to have a preferred crystallographic orientation. The 3 hatch wall has some larger grains and more of a tendency for the larger grains to be oriented in the <100> orientation.

The wider walls (4-8 hatches) have regions of small, randomly oriented, equiaxed grains running along the laser centrelines. Between these, there are large columnar grains, these have a strong tendency to be somewhere between the <100> and <111> orientations; generally centred on <112>.

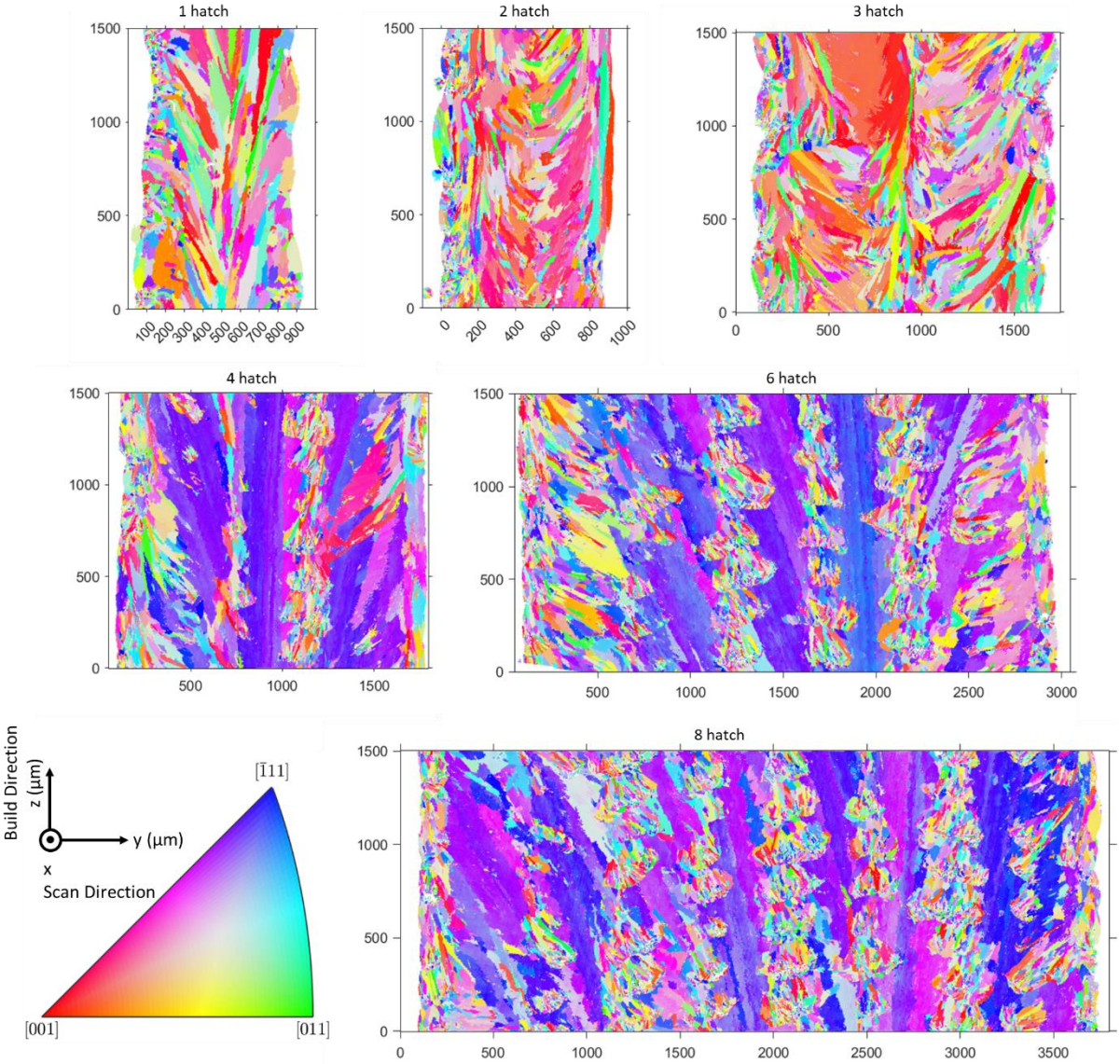

Figure 10-9: Inverse pole figure maps (IPFX) of yz section of walls from 1 - 8 hatches showing full thickness (y) and 1500 µm height (z) at the midpoint of the height. This is a duplication of Figure 8-12, reproduced for ease of reading

The equivalent figures for the 3P and 10P walls are shown in Figure 10-10; these are 1 mm wide, but 12 mm high (from the baseplate). The orientation maps in Figure 10-9 are full sample width, but only 1.5 mm tall – this height is shown in Figure 10-10 for reference. Similar trends are observed, 3P having mainly small, randomly oriented, equiaxed grains; towards the top of the

sample, some larger <100> orientation grains appear. The 10P wall has centreline regions of fine grain sizes, similar to the wider walls in Figure 10-9; with tall, columnar grains, again, oriented around the <112> orientations.

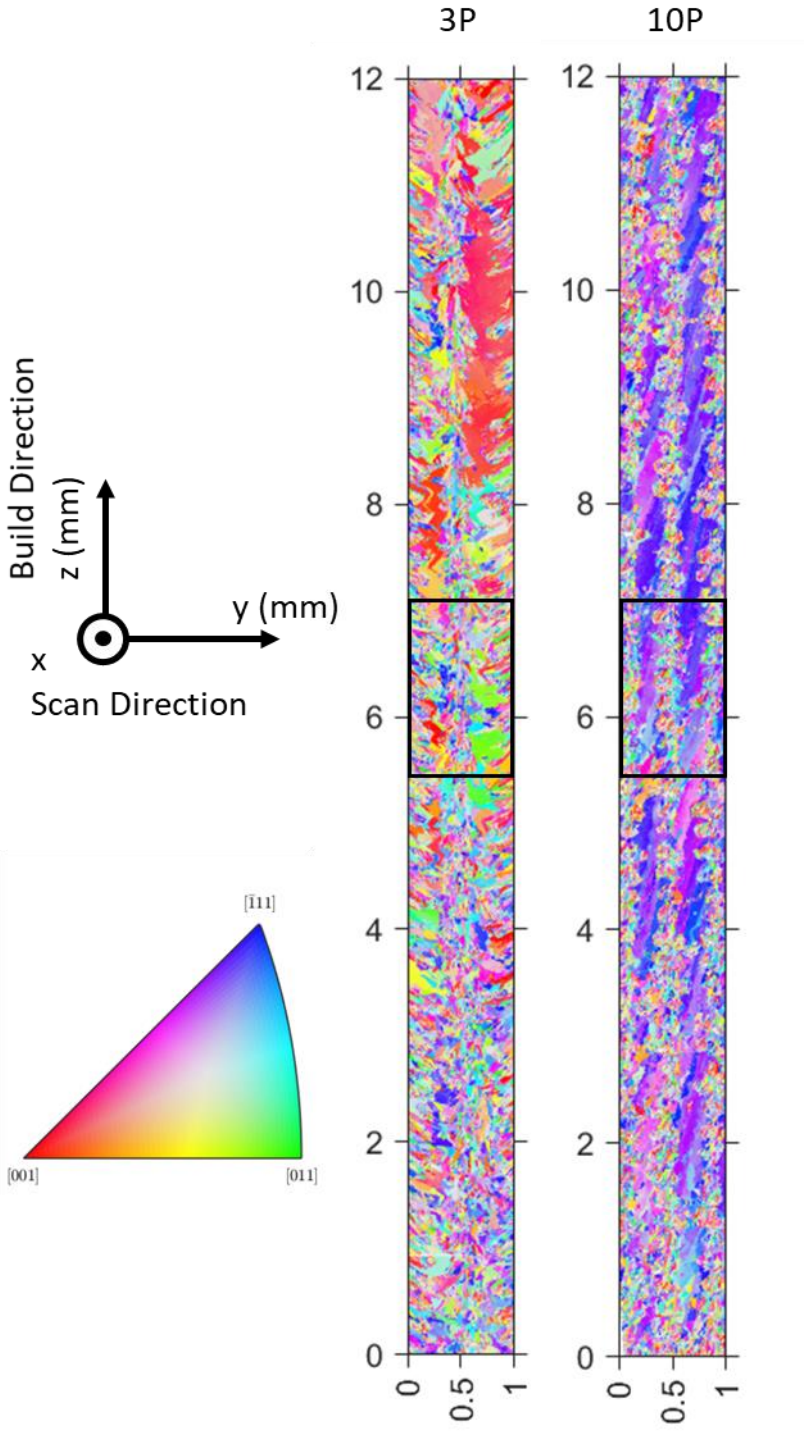

Figure 10-10: Inverse pole figure (IPFX) maps of 3P and 10P walls, showing axis direction. Black boxes show equivalent region captured of the various thickness walls

The inverse pole figure map of the YZ section of the triangular prism is shown in Figure 10-11. Three 1 mm strips are highlighted to show the notation used later; the tip of the triangular prism is at y=0. The grain structure of this section is dominated by small, randomly oriented grains; the

background is definitely a blue/purple colour. There is a preference toward grains oriented in the <112> orientations; few large columnar grains are seen.

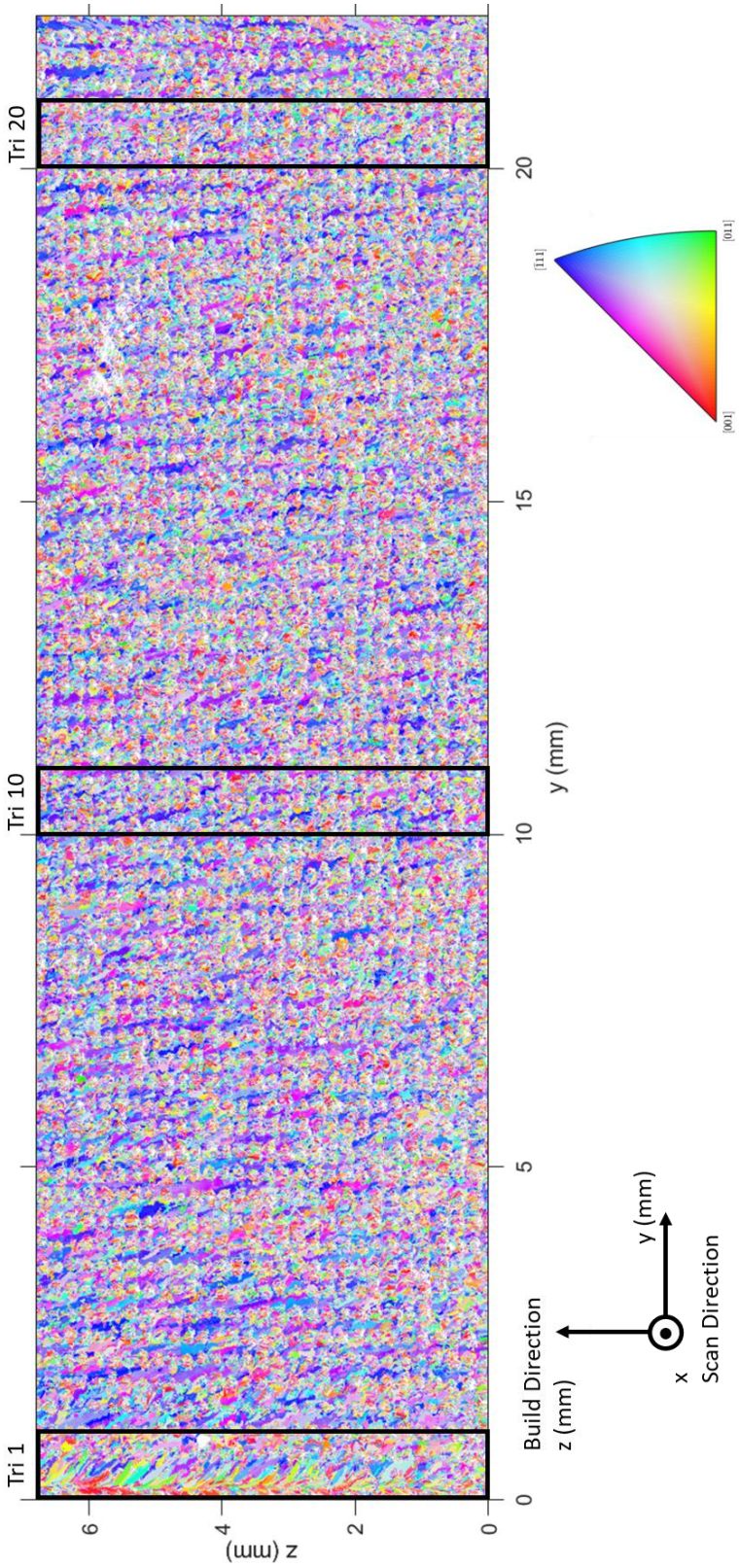

Figure 10-11: Inverse pole figure (IPFX) map of triangular prism YZ section

For each of the walls, the grain area was averaged (weighted by grain area), which is shown in Figure 10-12. The narrower walls have significantly smaller grains than the wider walls, with a sharp transition between 3 and 4 hatches. The 3P and 10P walls include the full height of the wall, which includes some larger grains at the top, but are included for comparison. There is still an increase in grain area with hatch number, but the 3P wall has a much larger grain area than the 3 hatch wall.

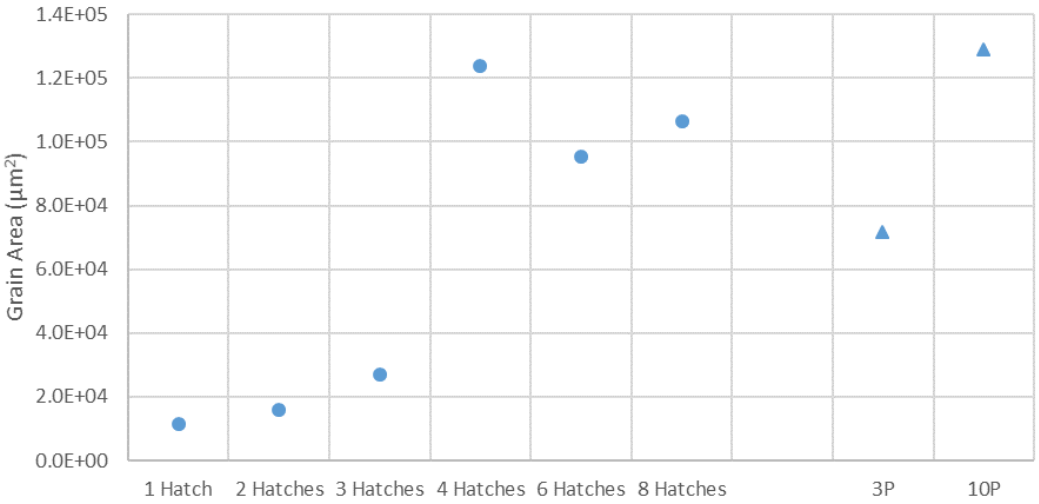

Figure 10-12: Area weighted average grain areas for each wall, including 3P and 10P

The grains were clustered into small, medium and large grains, this is shown in Figure 10-13. Visually, the clustering seems to have performed the desired function, there are few large grains, but these are typically columnar. Medium grains are more prevalent in the narrow walls, being diagonally oriented towards centrelines; small grains are typically along grain centrelines and are present in all samples.

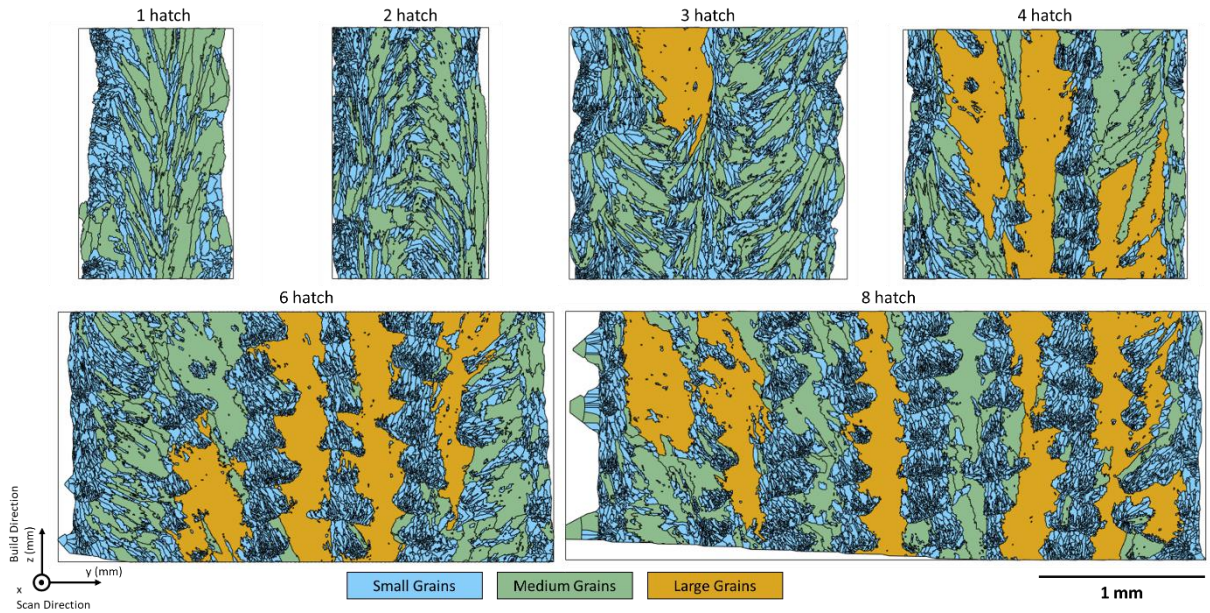

Figure 10-13: Clustering of grains into small (blue), medium (green) and large (yellow) clusters, shown for 6 walls of varying thicknesses

Pole figures for the different grain sizes of the 1 hatch wall are shown in Figure 10-14. The small grains are fairly randomly oriented, with a maximum mud of 1.8; the maximum mud of the medium grains is 9.4; there are no large grains present.

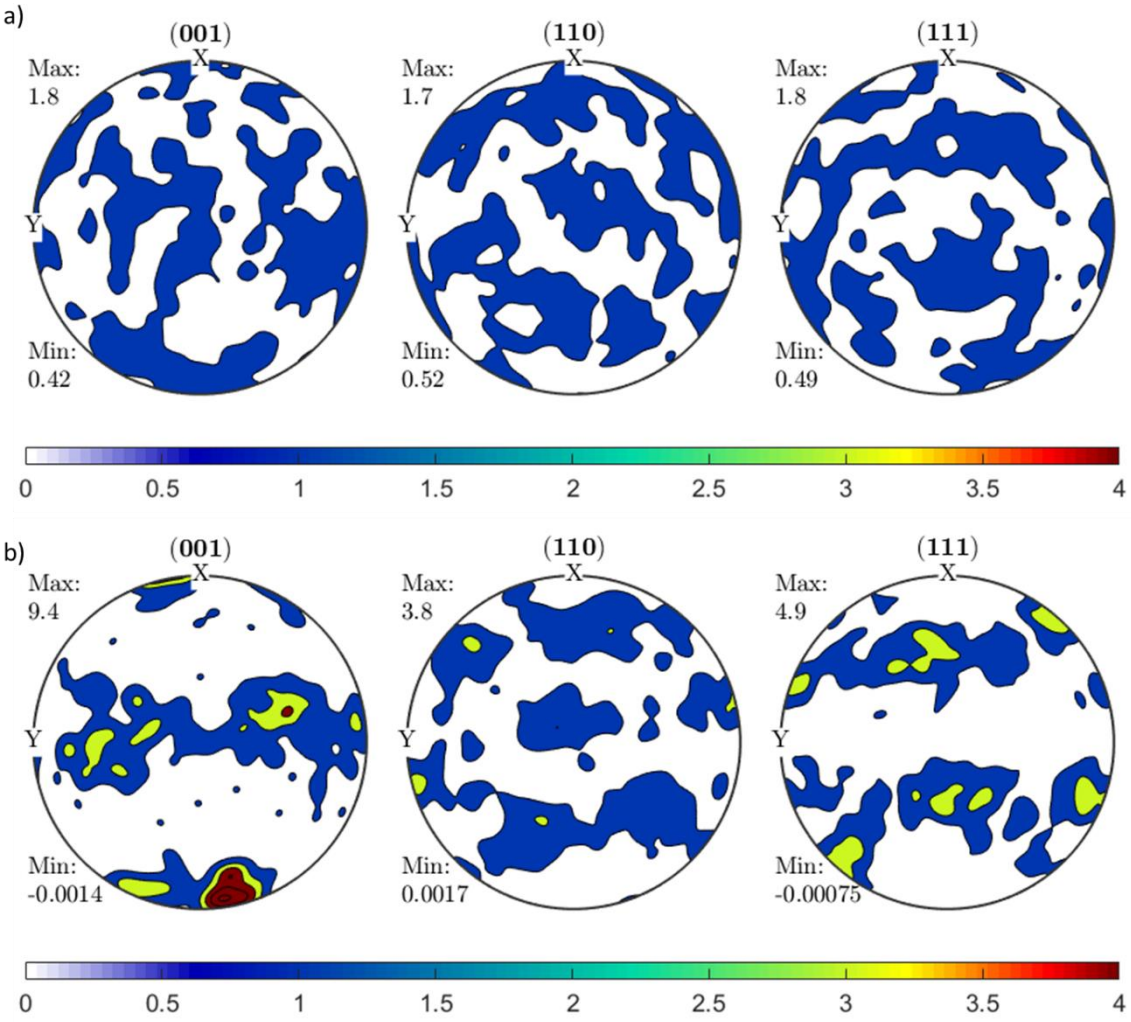

Figure 10-14: Pole figures for 1 hatch wall; a) small grains, b) medium grains

Pole figures for the three different grain sizes of the 6 hatch wall are shown in Figure 10-15. The small grains are fairly randomly oriented, with a maximum mud of 1.6; the maximum mud of the medium grains is 5.1. Large grains have the largest mud of 22, which is representative of a strong texture, the peaks on the <111> plot in Figure 10-15c are near the centre, so it can be determined that the large grains in the 6 hatch wall are near the <111> orientation (i.e. <112>).

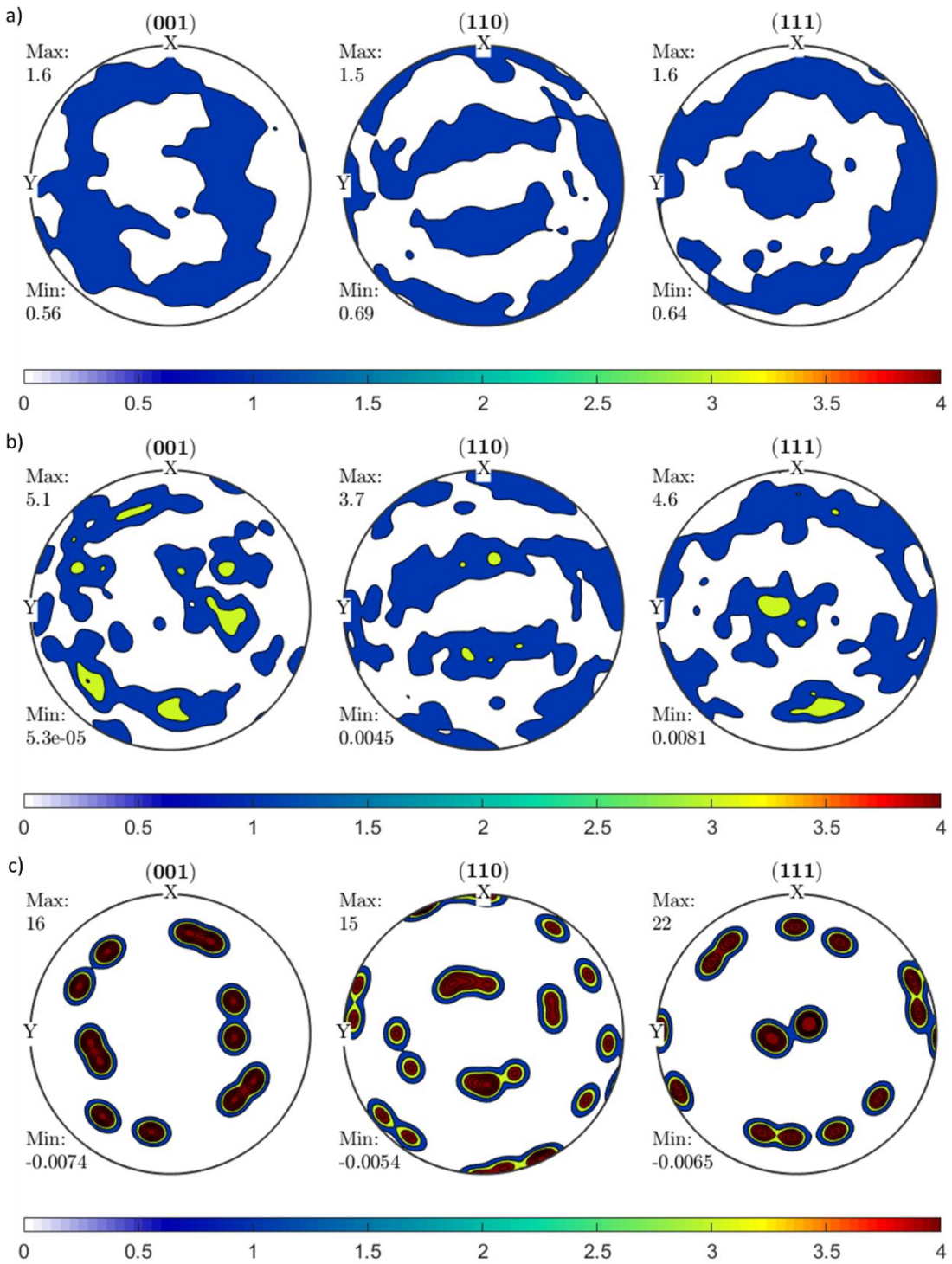

Figure 10-15: Pole figures for 6 hatch wall; a) small grains, b) medium grains, c) large grains

The distribution of different grain types in each wall is summarised in Figure 10-16. For narrow walls (1-3 hatches), there are roughly 50 % small grains and the rest are medium (with 1 large grain in the 3 hatch wall). For the wider walls (4-8 hatches), small grains account for less than 50 % of the area, with the rest slightly dominated by large grains. Comparing the 3P and 10P walls, the 10P has more, larger grains, so the grain size generally increases with wall width. Finally, in the triangular prism, near the tip (Tri 1) the majority of grains are small, with some medium grains; in the bulk (Tri 11), there is a greater number of smaller grains.

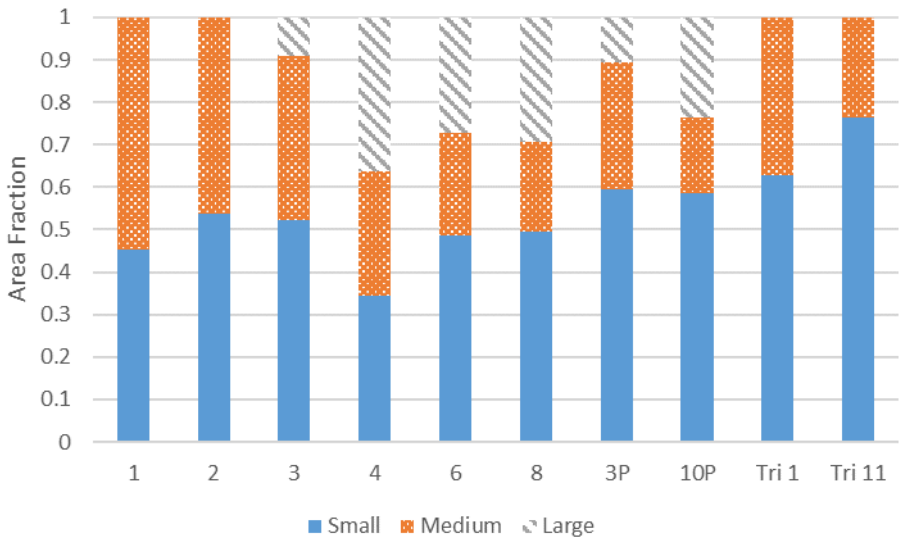

Figure 10-16: Breakdown of grain area fractions for various thickness walls, 3P and 10 P walls and 2 sections of the triangular prism

A detailed comparison of the different sized grains for the different walls is shown in Figure 10-17. The anisotropy factor (Figure 10-17a) of all small grains is 0.15-0.2, irrespective of the wall. In the narrow walls (and 3P), the anisotropy factor of large grains is smaller than that of medium grains, which is itself smaller than small grains. This reduction in anisotropy factor tells us that the larger grains in the narrow walls are the closer to the <100> orientation (as this has the minimum anisotropy factor of 0). The opposite trend is seen in wider walls (and 10P), where the larger grains experience a greater anisotropy factor (i.e. further from <100>).

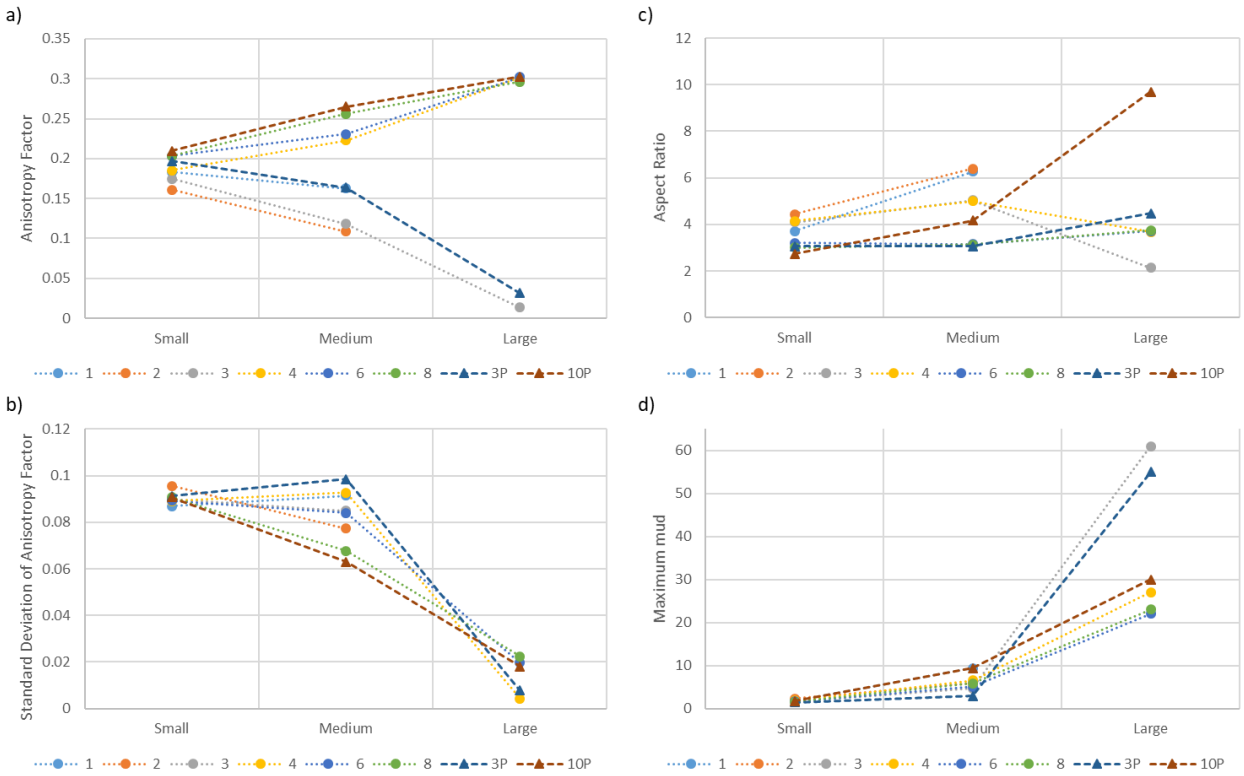

Figure 10-17: Analysis of grains, clustered by size; for various thickness, 3P and 10P walls; a) anisotropy factor; b) standard deviation of anisotropy factor; c) aspect ratio; d) maximum mud

The standard deviation of anisotropy factor is shown in Figure 10-17b; this is high for small grains, which confirms that they have no preferential orientation. For medium grains, the deviation in narrow walls is relatively high, which confirms the observation from Figure 10-9, that the medium grains have random orientations. Whereas for wider walls, medium grains have a smaller deviation, so are more textured; the large grains in all walls have little deviation in anisotropy factor. The maximum mud is a measure of texture and shows that for all walls, the texture is greater in large grains than in small grains (Figure 10-17d); in narrow walls, the large grains have the greatest maximum mud, but this is due to the fact that there were only 1 or 2 grains of this type.

The aspect ratios of grains is shown in Figure 10-17c, all small grains have a relatively low aspect ratio. In narrow walls, the aspect ratio increases in medium grains and they have very few large grains. In wider walls, the aspect ratio of large grains is highest, but not by much, this could be because the EBSD regions are limited to 1.5 mm in the Z direction, which is the direction in which the grains are elongated. The EBSD map of the 10P wall was 15 mm high, so this allowed grains to be captured in full height, hence the larger aspect ratio observed.

An analysis of the grain structures in the triangular prism is shown in Figure 10-18; there were very few large grains, so these were excluded from the analysis. Figure 10-18a shows the anisotropy factor variation with height; the lowest anisotropy factor was in the Tri 1 section (nearest the tip as shown in Figure 10-11), after this, a plateau is reached, the medium grains experiencing a higher anisotropy factor than the small grains. Maximum mud (Figure 10-18c) shows a similar trend, the small grains exhibiting minimal texture through the full width, whilst the medium grains have little texture in Tri 1, but with more texture in the rest of the triangular prism. The aspect ratio of small grains is constantly small (Figure 10-18b), for medium grains, this is slightly higher; for both grain sizes, in Tri 1 there is a greater aspect ratio than in the rest of the component.

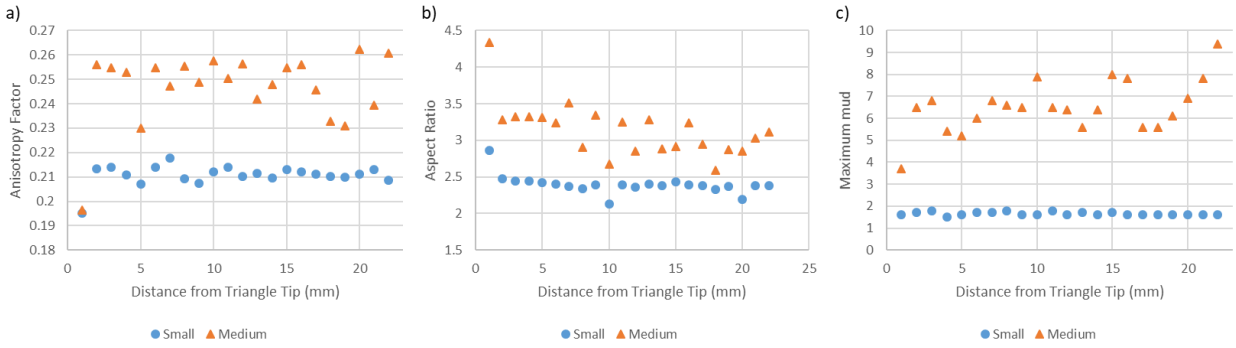

Figure 10-18: Variation of grain structure in the triangular prisms, with distance from the tip; a) anisotropy factor; b) aspect ratio; c) maximum mud

10.3.3. Optical Microscopy

The walls of various thicknesses were etched with Kallings Reagent #2 and optical micrographs were taken. Since the top melt pool was never remelted, its dimensions could be measured (Figure 10-19), the melt pool width and depth for all 6 walls of varying thicknesses were measured and are summarised in Table 10-5. The Peclet number was calculated for each wall (using the melt pool length) and is included in Table 10-5. The melt pool dimensions are plotted in Figure 10-20; melt pool width is shown to be relatively consistent, with widths between 840-961 µm. The melt pool depth, however, varies with number of hatches; the narrowest walls have the deepest melt pools

(826 µm). The melt pool depth decreases until 4 hatches wide, where a depth of 342 µm is recorded; in wider walls, little change in melt pool depth is experienced.

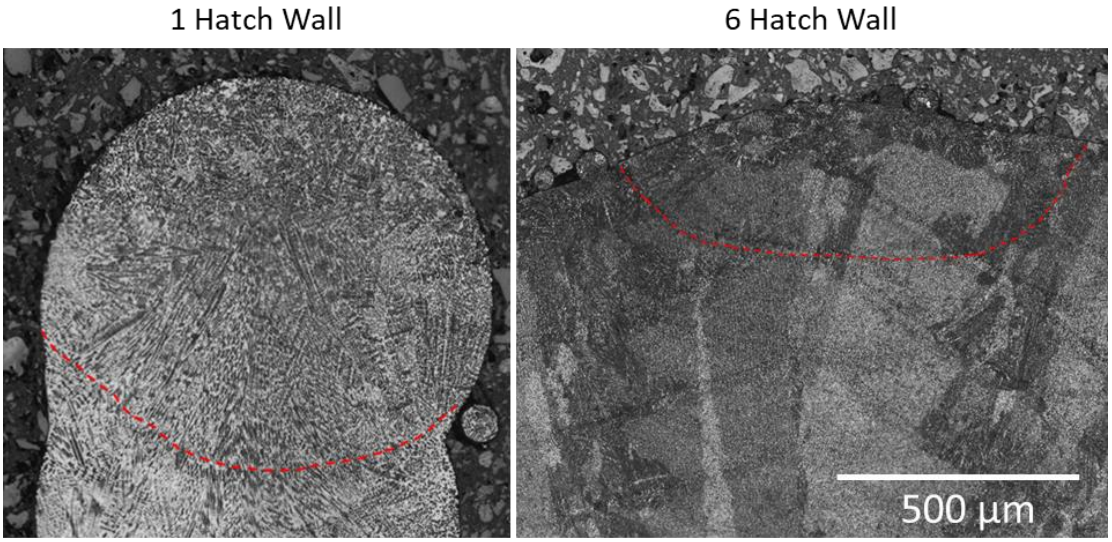

Figure 10-19: Optical micrographs of 1 and 6 hatch walls, etched with Kallings Reagent #2. Top melt pool outlines shown

Representative optical micrographs of the YZ section of the walls are shown in Figure 10-21; the cellular/dendritic nature of the structure can be seen. If the cells/dendrites grew in the YZ plane, they will appear as long rod-like structures, if they are perpendicular to the plane, then they appear as dots, if they are angled from the plane, then they appear as short rods. In the 1 hatch wall, long rod-like structures can be seen, throughout; in the 2 hatch wall, there are sections of long rods and sections of shorter rods. The 3 hatch wall has a roughly 50-50 split of long rod-like sections and end-on/short sections. In 4, 6 and 8 hatch walls, the most of the structures are seen end on, with some small sections of elongated cells/dendrites. From these micrographs, PDAS were measured, these are plotted in Figure 10-22; due to the dendrites in wider walls being end-on, the PDAS measurements may be less representative of the bulk. Narrower walls were found to have a greater PDAS, however, from 4 hatches upwards, there was little change in the scale of the microstructure.

Table 10-5: Dimensions of top melt pools measured from optical micrographs; Peclet number calculated using melt pool length

	1 Hatch Wall	**2 Hatch Wall**	**3 Hatch Wall**	**4 Hatch Wall**	**6 Hatch Wall**	**8 Hatch Wall**
Top Melt Pool Depth (µm)	826	665	441	342	330	316
Top Melt Pool Width (µm)	927	836	961	922	946	840
Peclet Number	10.8	8.7	5.8	4.5	4.3	4.1

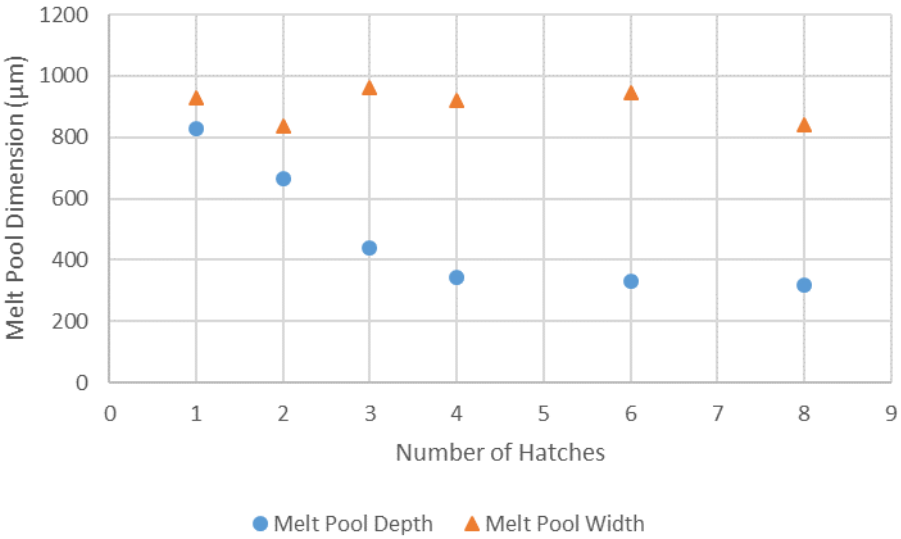

Figure 10-20: Variation in the dimensions of the top melt pool with number of hatches

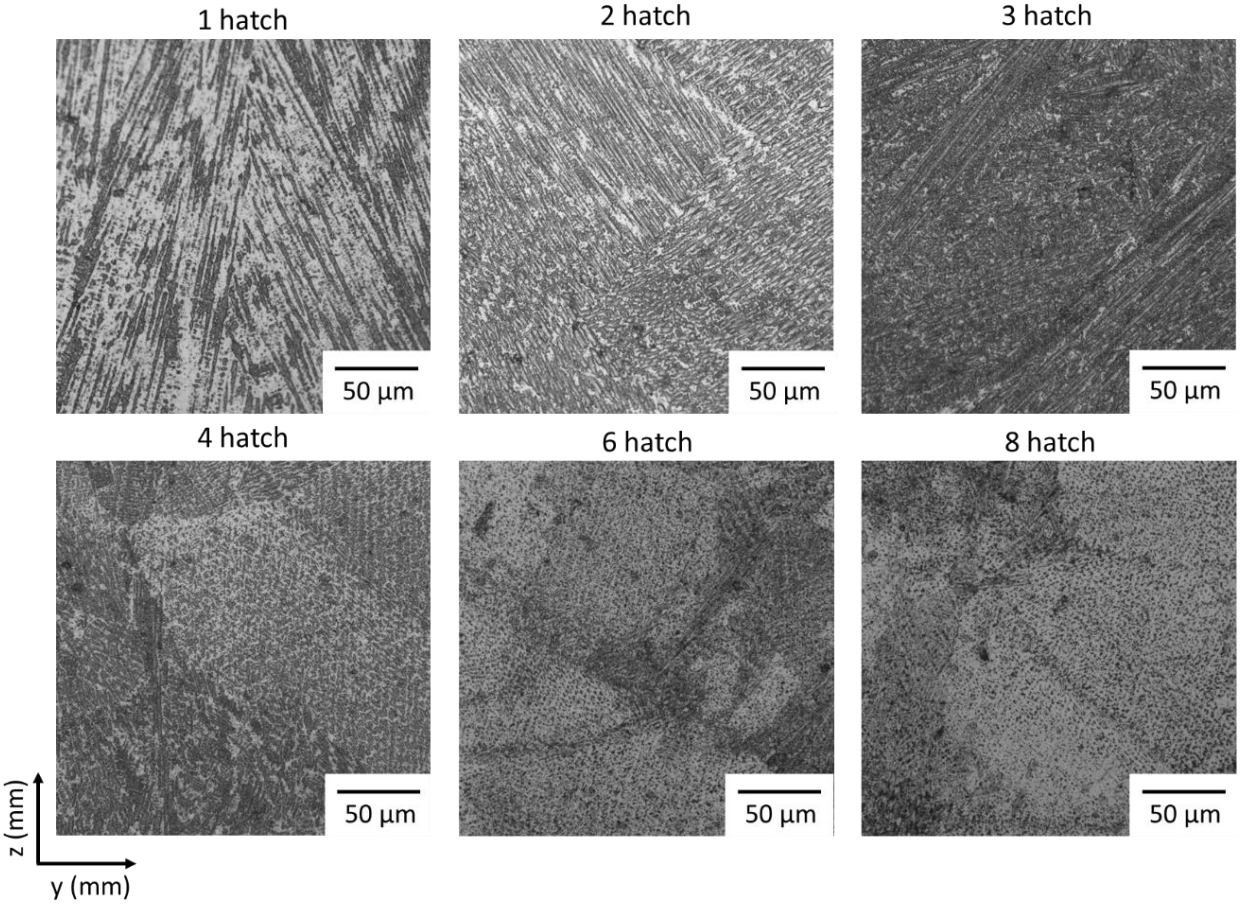

Figure 10-21: High resolution optical micrographs of 6 walls of varying thickness

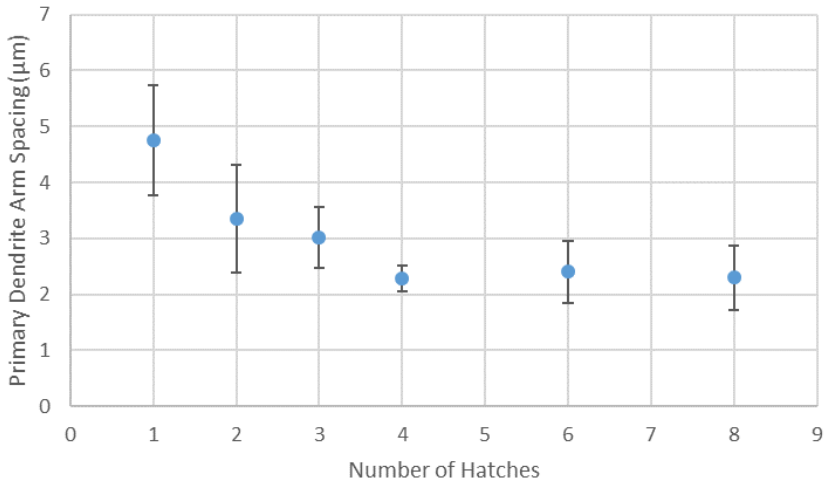

Figure 10-22: Primary dendrite arm spacings (PDAS) for samples of varying width; measured from optical micrographs

10.4. Discussion

There is a clear step change in crystal orientation between 3 and 4 hatches, with narrow walls being predominantly red (<100> orientation dominating), whilst wider walls are predominantly purple (orientation closer to <111>; these grains are typically centred around the <112> orientation), as seen in Figure 10-9. The same trend holds in Figure 10-10, where different parameters are used; this sharp transition appears to occur at a width of roughly 2mm. The narrower walls tend to be composed of small equiaxed grains along with some larger grains running diagonally away from the laser centre, this is similar to the structure observed in 316L steel in Chapter 7. The wider walls have large columnar grains running parallel to the build direction, with small equiaxed grains visible at the laser centrelines; the average grain size is much larger than in the narrow walls (Figure 10-12). The large grains have a very strong texture, which is shown by the high maximum mud (Figure 10-15) and the low variation in anisotropy factor (Figure 10-17b). The pole figures (Figure 10-14 and Figure 10-15) clearly show that small grains have no preferential orientation and that the texture of medium grains is stronger in the narrow wall than the wide wall.

The power controlled walls (3P and 10P) follow a similar microstructural trend; the 3P wall has a much larger average grain size than the 3 hatch wall. This can be explained as the 3P orientation map covers the full height of the sample and the top of the walls have larger grains, whilst the orientation map of the 3 hatch wall was taken at a central height. Since wider walls have long columnar grains, they would be expected to have the maximum aspect ratio, however, this is not the case (Figure 10-17c). This can be rationalised by the fact that the scans were only 1.5 mm along the z direction (which is the long axis of the grains); these long grains are roughly 400 µm wide, so even if they were the full height of the scan, this would only be an aspect ratio of 4. Figure 10-13 shows that every long grain detected was cut off on at least one end, without this measurement artefact, the aspect ratios in wide walls would likely be much closer to that of the 10P wall.

To compare the grain orientations in the triangular prism, the a YZ section was taken (perpendicular to laser movement); this rectangular section (Figure 10-11) went from narrow (left) to wide (right) allowing for it to be compared with the walls. The comparison is not perfect, as

in the walls, the width being varied was the number of hatches, whereas in the triangular prism, the hatch length was the factor being varied. Either way, the surface area of the triangular prism is much greater (per time) at the tip, similar to the narrow walls. Figure 10-18 shows the variation of grain structure with distance from the tip of the triangular prism; there is a clear trend showing that the edge 1 mm is consistently different to the bulk. The grain structure in the rest of the component is relatively consistent, it is interesting to note that in the triangular prism, 1 mm on the edge is different. The narrow walls, which have a different grain structure to the wider, bulk structures, are up to 2 mm wide – 1 mm from the edge on each side.

For comparison of triangular prisms to the walls, Figure 10-17 was modified to include the triangular prism (Figure 10-23); Tri 1 shows the structure within 1 mm of the tip, whilst Tri 11 shows the centre of the triangular prism, which is representative of the bulk. The behaviour of the Tri 11 section is similar to the wide walls in terms of anisotropy factor and maximum mud. The Tri 1 section is similar to the narrow walls, however the anisotropy factor is higher (Figure 10-23a), this is between the narrow and wide walls, potentially due to the narrow nature of the tip, but the large heat sink being present in the form of the triangular prism. There are no large grains present in the triangular prism, and the aspect ratios of the grains aren't as high as expected. There is no obvious reason for the lack of columnar grains, these could potentially be explained by the slightly increased Z step (225 µm compared to 200 µm). If less material is remelted, it could be that the previous layer melts less, so growth from the previous grains cannot occur; instead, new dendrites must nucleate, forming new grains.

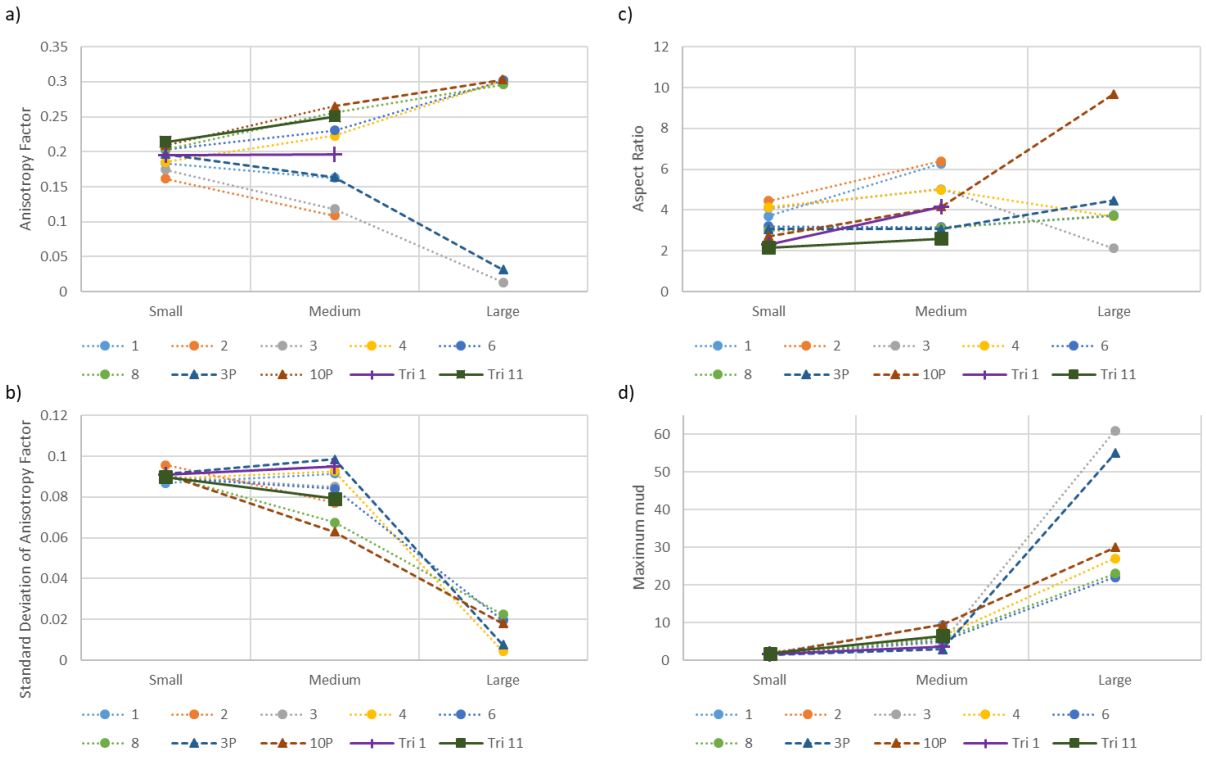

Figure 10-23: Analysis of grains, clustered by size; replication of Figure 10-17, but with addition of 2 sections of the triangular prism; a) anisotropy factor; b) standard deviation of anisotropy factor; c) aspect ratio; d) maximum mud

There is a variation of thermal intensities of the walls of varying thicknesses (Figure 10-8c), this could be expected to control the microstructure of the component. Using power control, the thermal intensity of 3 and 10 hatch walls was kept consistent (Figure 10-8d); this also had the effect of keeping a constant the XY melt pool profile between the two walls (Table 10-4). The stark

microstructural difference between the 3P and 10P walls (Figure 10-10) shows that even controlling the XY shape intensity of the melt pool is insufficient for a constant microstructure.

YZ cross-sections were taken of the walls and examples of the 1 and 6 hatch walls are shown in Figure 10-19; the final hatch is not remelted by subsequent layers, so melt pool dimensions of these pools were taken, for wider walls, the central region was chosen. It is clear that the wider walls have much shallower melt pools, despite the melt pool width remaining fairly constant (Figure 10-20) and it seems like there is little variation of melt pool dimensions in the walls wider than 4 hatches. This reinforces the trend seen in Figure 9-16, where the widest walls were found to be the shallowest. The laser width is reported to be 0.7 mm and the melt pool widths are slightly wider than this (0.9 mm), which seems reasonable.

Now that we know that narrow walls have much deeper melt pools, but similar XY sections, we can conclude that the melt pool volume is much larger. Literature shows that the larger a melt pool, the slower the cooling rate [104,105]; despite using constant processing parameters, it seems that the geometry is greatly affecting the melt pool depth and so very different thermal conditions are being experienced. These observations are in line with the calculations made by Vasinonta et al. [89], who observed that melt pool dimensions were much larger in a thin walled component when compared to a bulk component; in that case, it was the melt pool length which was being reported. Assuming that the wide walls (shallow melt pools) have higher cooling rates, this would increase the thermal gradient and move them along the arrow shown in Figure 10-7; this results in a more columnar structure [102]. This theory lines up with the observations made from the EBSD analysis; wider walls have a much higher tendency to have tall columnar grains, whilst narrow walls have more small grains with no orientation preference.

The Peclet number represents the influence of convection in the process; this is shown in Table 10-5, using the melt pool depth as the characteristic length. In literature, melt pool width and length are used as the characteristic length [17,43], but this is due to ease of measurement, using the melt pool length is equally valid. In literature, Peclet number is shown to scale with energy density [17] and it is reported that laser velocity is a key factor in determining the convection behaviour is important [227]. The general approach is that we control how much heat enters the component using processing parameters, this changes the melt pool morphology and the Peclet number, which determines the heat leaving the component. However, we show that we can change the heat flow properties of the component by changing the geometry. This means that whilst using constant parameters, we observe a 2.5x change in Peclet number simply by altering the component thickness. As well as being able to change the Peclet number by altering the heat input, we can change it by altering the geometry, which affects the cooling of the component.

The high Peclet numbers suggest that convection is the dominant heat flow mechanism, with the narrow walls experiencing more convection than wider walls. In reality, radiation is also present and significant in thin components; it might be better to think of the Peclet number as the ratio of radiative and convective cooling to the conductive cooling. Looking at Figure 10-24, which is the output of a simple heat flow model for these walls (explained and discussed in Appendix B), it can be seen that convection and radiation combined make up a large proportion of the overall heat loss in narrow components. At these narrow widths, less conduction is possible and so heat accumulates in the part, because as convection/radiation struggle to dissipate the heat. This high Peclet number is indicative of a low Fourier number (Section 2.2.1), confirming that more heat is being stored than is being diffused away; this explains the longer duration taken for a temperature plateau to be reached. As the width of the wall exceeds 2 mm, conduction dominates and a bulk steady-state is reached as sufficient heat can be dissipated.

There is a thin layer of fine grains visible on the outer edges of the components; this is best visible on the left hand side of the walls in Figure 10-9. At these points, conduction is minimal, and so convection and radiation dominate, resulting in the different grain structure at the edges. This layer is roughly 100 µm wide, so will affect the surface properties of as-built components.

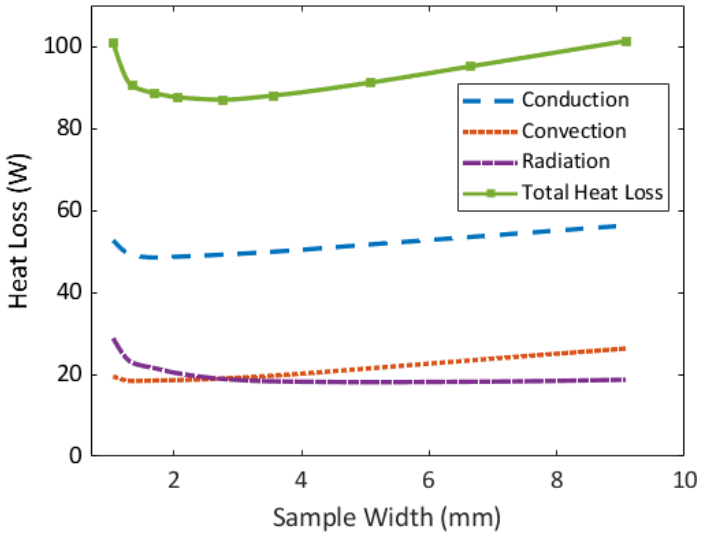

Figure 10-24: Breakdown of calculated heat flows, workings explained in Appendix B

In L-PBF, Sun et al. claim that the melt pool shape "largely determines the thermal gradient direction" [93], and use this to explain the tall columnar grains. An outline of the melt pools reported was drawn and the horizontal fraction was calculated (±5° from flat); Table 10-6 shows that the lower energy density wall contained flatter melt pools (larger horizontal component) and that this had the columnar structure reported. The same conclusion could be reached for the micrographs in this work, the 6 hatch wall contains 30.7 % horizontal melt pool and a columnar structure, compared to 8.6 % in the one hatch wall, which showed a more equiaxed structure. Gokcekaya report a similar phenomenon and perform thermal heat flow calculations to show that they would expect columnar growth in the slower velocity [94]. The melt pool shape in this case does not follow the hypothesis above, as the less horizontal melt pool yields the columnar structure (5.7 % compared to 4.4 %).

It seems like the melt pool shape correlates with the columnar nature of these L-DED components, but this may not in itself be sufficient to explain the columnar structure. In L-DED, the larger melt pools result in a centreline, which contains small grains, and the large columnar grains are found between the laser hatches (unlike L-PBF where they follow the centreline). The melt pools in the wide walls (Figure 10-19), are sufficiently wide that the columnar regions are still partially found below the section of melt pool. Generally, dendrites are less affected by the heat flow direction when compared to cells (Section 2.4.1), and as discussed in Section 10.1.3, there is a tendency to reduce energy by reducing the need for nucleation. Dendrites will grow at an angle away from the maximum heat flow if this is energetically preferential. This could help explain the large columnar grains seen in the wider walls, as the grains could grow epitaxially despite thermal gradients being slightly misaligned. Due to 90 ° rotation in the zig-zag structure shown in Figure 10-5b, this could appear as a single columnar grain if sectioned in the YZ plane.

The EBSD maps (Figure 10-9) are taken in the YZ plane, perpendicular to those shown in Figure 10-6. A zig-zag structure would result in dendrites growing diagonally out of the page in the YZ plane, which was observed in the optical micrographs of wide walls (Figure 10-21). The narrow

walls experience more vertical growth and so the grains are aligned with the Z axis, resulting in dendrites visible along their length in Figure 10-21. This in turn results in a <100> structure when looking at the YZ orientation maps, hence the red dominance in narrow walls. By contrast, grains growing at an angle will be somewhere around <112>, resulting in a purple dominance in wider walls.

Table 10-6: Summary of melt pool flatness from literature compared to this work

Authors	**Material**	**Mode**	**Horizontal Melt Pool (%)**	**Columnar structure?**
Sun et al. [93]	316L Steel	Low energy density	10.9	Yes
Sun et al. [93]	316L Steel	High energy density	7.5	No
Gokcekaya et al. [94]	Inconel 718	1000 mm/min	4.4	Yes
Gokcekaya et al. [94]	Inconel 718	1400 mm/min	5.7	No
This work	Inconel 718	6 hatch (wide)	30.7	Yes
This work	Inconel 718	1 hatch (narrow)	8.6	No

In wider walls, there is a much longer return time to the same point (due to a longer scan length within the layer), this is similar to the 10 second hold sample (Figure 10-21). The longer return time allows for more cooling and so a cooler sample is expected. The cooler a sample, the smaller the melt pool, which is what was observed in Figure 10-19. A longer return time would lead to a higher cooling rate, using the G-V plot (Figure 10-7), a more columnar structure would be expected in the wider walls. The grain orientation is a result of many factors, but in this case, it seems that both the thermal gradients and the melt pool shapes explain the grain structure, both in terms of grain orientation (<112> for wide walls) and in terms of the columnar structure experienced in the wide walls. The average PDAS (Figure 10-22) are larger in the narrow walls, which have a deeper melt pool and a slower cooling rate, which follows the expected trends [27,98]. Walls which have 4 hatches (~2 mm) or more have a consistent PDAS, so it can be concluded that in wider walls, the cooling rate no longer changes significantly, this aligns with the point at which the grain orientation changes. It can be concluded that at this width, the sample structure is no longer dependent on the width, so the sample can be considered bulk.

It is very interesting to see that despite having very similar XY melt pool profiles, the grain structures of the 3P and 10P walls were not similar. This is explained by the melt pool depths varying despite being comparable coaxially [43], which could also explain why power and velocity control struggled to tightly control the microstructure (Chapter 9). The stark microstructural change at 2 mm seems to be due to an increase in conductive cooling with width. Figure 10-25 shows the trends in thermal intensity with width for both L-DED (BeAM) and L-PBF (Aconity) processes, these are from taken from Figure 6-16 and Figure 8-9 respectively. The pyrometer in L-PBF captures a single value, which represents the signal incident on the sensor, for L-DED, the thermal intensity is calculated by summing all the pixels in the image – fundamentally replicating the pyrometer. In both processes, there appears to be a peak in thermal intensity (and pyrometry) in samples of 2-3 mm width; in both cases, samples above 5 mm seems to experience minimum fairly constant bulk conditions, with minimal change in wider samples. The L-PBF process appears to be more stable in terms of thermal signal once a width of 2 mm is surpassed.

Narrower samples can be referred to as 2D in nature, with conduction not necessarily being the dominant heat flow mechanism. In L-PBF (Ti-6Al-4V), it was reported that thinner samples experience the highest cooling rates [52], which would explain why they show the lower pyrometry signal. It is interesting that both L-PBF and L-DED seem to show a similar overall trend in thermal signature, despite the melt pool dimensions being different by an order of magnitude. It seems, however, that the transition from thin component to bulk component may be process agnostic, although this may be a coincidental observation.

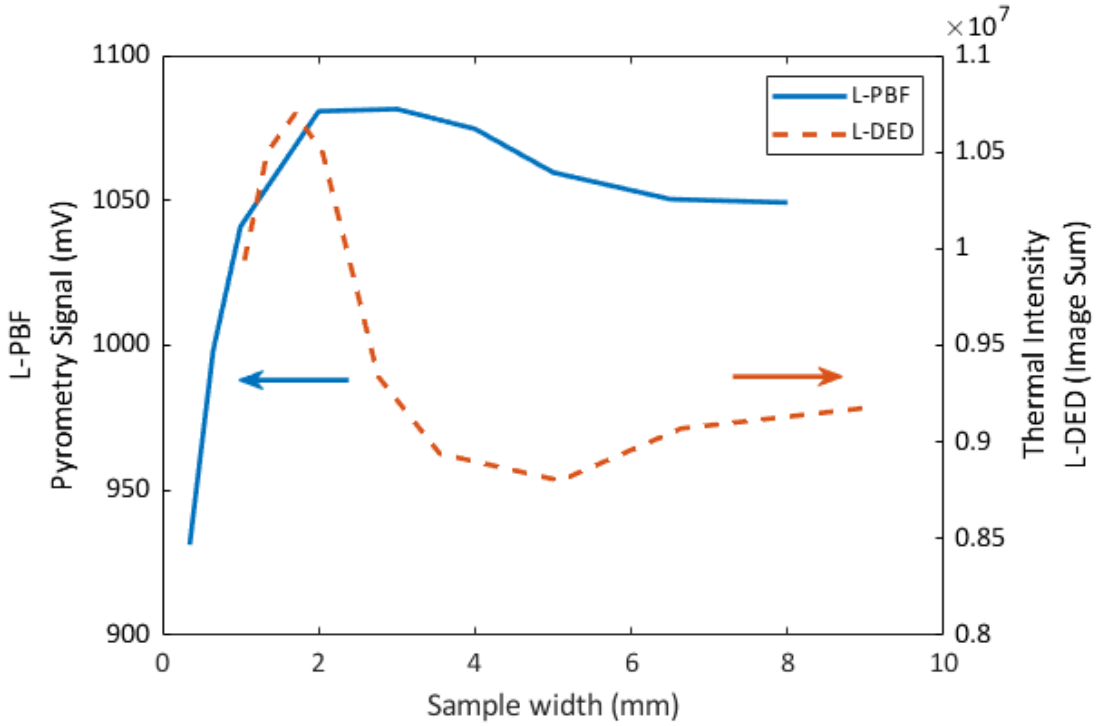

Figure 10-25: Comparison of BeAM thermal intensity with wall thickness against Aconity pyrometry signal variation with sample width

At the peak of the thermal intensity (Figure 10-25), the heat flow mechanisms are changing, with wider walls experiencing more conductive cooling. This leads to a change in melt pool shape and the heat flow, resulting in very different microstructures either side of this thickness. These microstructural differences can have a profound influence on the mechanical properties of the component; creep life, crack propagation and tensile properties can all be affected by grain orientation/size, as summarised in Table 10-2 [67,373,374].

Since this microstructural change could cause the mechanical properties to be insufficient for industrial requirements, this change in structure with thickness must either be accepted or combatted. This could include adapting the geometry to reduce thin sections, or to thicken the geometry and require more machining post-process. It could be possible to create thermal models which output carefully designed scan strategies, which adjust the processing parameters in a location-sensitive manner. In order for process monitoring to be more representative, coaxial monitoring has been shown to be insufficient. However, side-on monitoring can be obscured by the newly build material, so this solution is not better; a combination of cameras around the L-DED chamber could triangulate the melt pool, but this is extremely complex.

It may be possible to extract a measure of melt pool depth from the coaxial imagery. This would likely require monitoring the same build both side-on (where depth is visible) and coaxially. A thorough analysis may be able to extract thermal gradient trends in the coaxial monitoring which

can be related to melt pool depth. Alternatively, a secondary technique, such as laser-induced spectroscopy could be used and it may be possible to use the combination of these signals to predict the melt pool depth. Coaxial melt pool analysis can still be used for general melt pool monitoring, but the fact that it cannot determine the melt pool depth is something which must be kept under consideration. Despite the limitations of coaxial monitoring, the process control demonstrated in Chapter 9 improves thermal homogeneity, so it would be beneficial to use this control algorithm over a process with no control.

10.5. Summary

There seems to be a step change in microstructure occurring when the thickness of components is increased; this change occurs at roughly 2 mm (4 hatches) as observed in Chapter 8 and Chapter 9. We have shown that this change correlates with a decrease in melt pool depth; the depth decreases with increasing wall width, until a plateau is reached at a wall width of 2 mm. This change in melt pool depth will affect the overall melt pool morphology and so the direction of the thermal gradients will also change. The PDAS plateaus at this point as well, likely due to the thermal gradient change. This change in melt pool shape and thermal gradient direction are sufficient to cause the change in grain structure observed.

Generally, the narrow walls tend to experience deeper melt pools, these have a slower cooling rate, so small equiaxed grains are formed. A higher Peclet number is experienced, so convection and radiation are significant within the process. Grains are typically oriented around the <100> direction, likely due to the very steep trailing edge of the melt pool. The wider walls have shallower melt pools, with grains growing in the <112> orientation, as a result of a more angled melt pool trailing edge. The grains are tall and columnar, growing through many layers, because of the flat melt pool and the higher cooling rates experienced; these walls represent bulk 3D components, where conduction is the dominant heat flow mechanism.

A similar grain orientation trend is seen in more realistic geometries such as the triangular prism. The narrow tip section has a different grain structure to the rest of the bulk component. These differences in microstructure have been shown to hold, even if the coaxial monitoring determines the melt pool shape to be nearly identical. These changes in grain orientation and size are sufficient to create noticeable differences in mechanical properties, so must be considered when designing components. Since coaxial monitoring is insufficient to detect these changes, either more complex, multi-perspective monitoring is needed, or complex modelling is needed to predict these melt pool changes and so adapt the process parameters in advance.

11. Comparison Between Microstructure and Hardness in Inconel 718 produced by L-PBF and L-DED

11.1. Introduction

The microstructure of Inconel 718 produced by L-DED has been summarised in Chapter 9 and Chapter 10. The wide range of grain structures possible was explored and it was shown that both the grain size and the texture can be greatly varied, simply by changing the component size. A similar range of grain structure has been shown for L-PBF for Inconel 718 by Gokcekaya et al. by varying laser velocity (Figure 10-3) [94] and by Serrano-Munoz et al. by varying the scan strategy (Figure 11-1) [385].

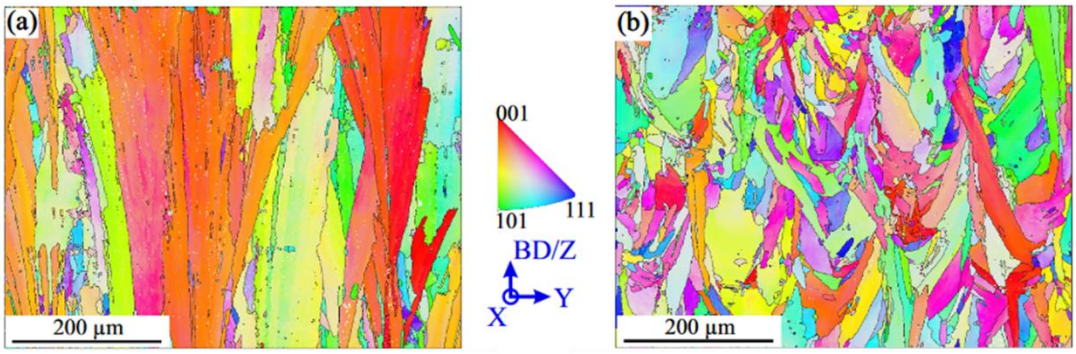

Figure 11-1: Range of grain structures possible by varying the scan strategy when printing Inconel 718 using L-PBF. Reported by Serrano-Munoz et al [385].

As explained in Section 10.1.2, 316L steel forms an FCC matrix, similarly to that of Inconel 718, so fundamentally, we would expect the two materials to exhibit similar structures. Heiden et al. show the range of crystal structures possible by varying the processing parameters (Figure 11-2) [280]. This covers the range of parameters from lack of fusion porosity with small, randomly oriented grains, to fully dense components, with large columnar grains and a dominant <100> orientation. Such a comprehensive study has not been published for Inconel 718, but it is assumed that a similar range of structures must be possible.

What range of grain structures is possible in AM and do these overlap for the two processes? By analysing the grain structures and hardness in L-PBF and L-DED, the feasibility of knowledge transfer between the two processes is explored.

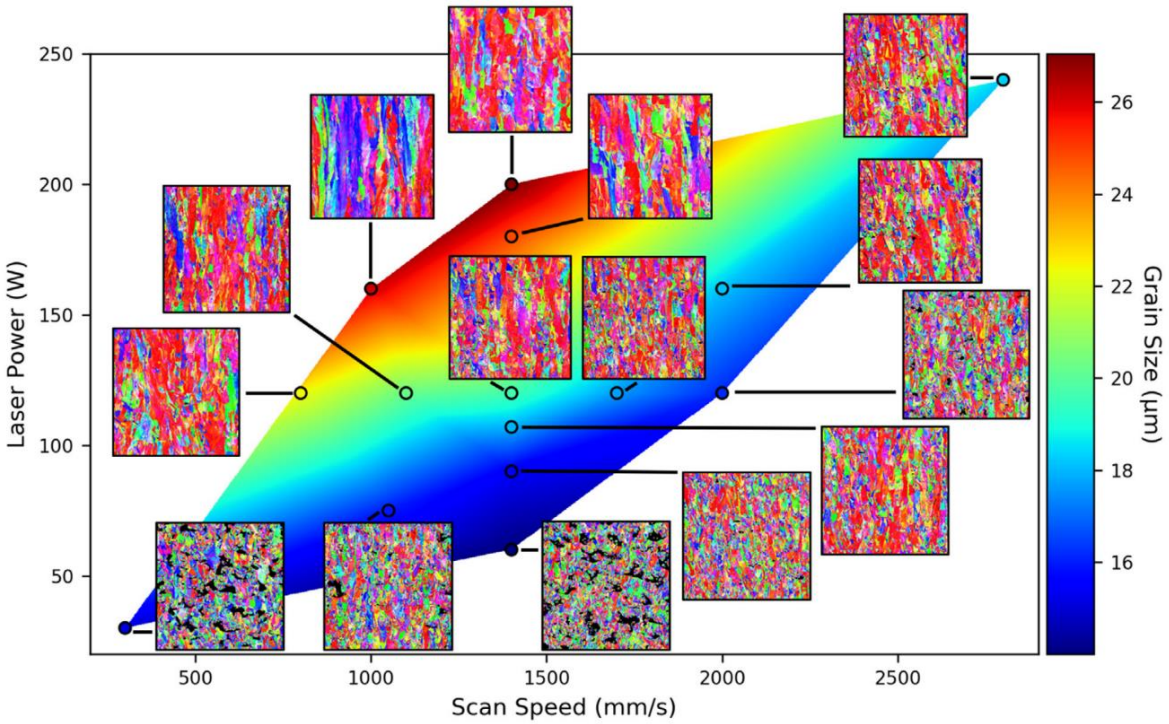

Figure 11-2: Processing map for L-PBF of 316L steel showing the possible grain structures. Reported by Heiden et al [280].

11.2. Methods

In this chapter, samples were made in Inconel 718 using both the Aconity3D Mini (L-PBF) and the BeAM Magic 2.0 (L-DED). The L-DED samples were made using the hatch strategy showed in Figure 8-3, 3 hatches wide (20 mm long, 9.8 mm tall). The L-PBF samples were printed to replicate these, with hatching along the length of the wall and dimensions of 2.95 x 20 x 9.8 mm (width, length, height respectively). The processing parameters for both processes are summarised in Table 11-1.

Table 11-1: Summary of processing parameters used for both L-PBF and L-DED samples

Process	Power (W)	Velocity (mm/s)	Hatch Spacing (µm)	Z Step (µm)	Mass flow (g/min)	$\frac{P}{v}$ (Jm^{-1})	$\frac{P}{\sqrt{v}}$ (Js$^{-1/2}$m$^{-1/2}$)	Name
L-PBF (Aconity)	95	1000	45	30	-	95	95	-
	130					130	130	Aconity_H
	95	1500				63	78	Aconity_L
	130					87	106	-
L-DED (BeAM)	223	33.3	400	200	5.5-6.5	6690	1221	-
	359					10770	1966	BeAM_H
	223	50				4460	997	BeAM_L
	359					7180	1605	-

The range of processing parameters was purposefully extended to see the variety of possible outcome grain structures. For L-PBF, there was a 1.7x spread in $\frac{P}{\sqrt{v}}$ values (2.1x spread in $\frac{P}{v}$ values); for L-DED, there was a 2.0x spread in $\frac{P}{\sqrt{v}}$ values (2.4x spread in $\frac{P}{v}$).

For each printed sample, thermal monitoring was recorded. For L-PBF, this was the pyrometry signal through the component, to remove background noise, any signal below 850 mV was removed; these were averaged for the second half of the build to give an average signal per component (as this removed the heat build-up). For L-DED, coaxial monitoring was performed, calculating the thermal intensity from the Basler camera. These were plotted with a moving average (window width of 100) to show the change in intensity with component height; again, the second half was averaged to get an average thermal intensity per component.

The extreme set of parameters were defined as Aconity_L and BeAM_L for low heat input and Aconity_H and BeAM_H for high heat input. These 4 samples were further analysed. Hardness maps were taken of the YZ sections with a 0.5 mm step size in both directions. These allowed for both a measure of hardness variation within each component and a comparison of the average hardness values. 2 sample t-tests were performed (α=0.05) to determine whether or not the average hardness values were significantly different from one another.

EBSD analysis was performed using a Jeol 7900F with an Oxford Instruments Symmetry EBSD detector and a 13 mm work offset, with an accelerating voltage of 20 kV. Different step sizes were used for each sample, depending on the time available for each scan, these are summarised in Table 11-2. For each sample, a region of 750x5000 µm (Y and Z respectively) was extracted and was further analysed for grain size, aspect ratio, anisotropy factor and maximum mud. Additionally, the grain average misorientation (GAM, which is an average of the kernel average misorientation, KAM) was calculated to get an estimate of dislocation density, as introduced in Chapter 8.

Table 11-2: Step sizes of EBSD scans

Name	**Step Size (µm)**
Aconity_L	1.66
Aconity_H	1.20
BeAM_L	1.00
BeAM_H	1.20

Aconity_L and Aconity_H samples were polished and etched with Glyceregia; BeAM_L and BeAM_H samples were polished and etched with Kallings Reagent #2. Both low and high resolution optical micrographs were taken of all 4 samples, allowing for melt pool dimensions and cell/dendrite spacings (these will jointly be referred to as PDAS) to be measured. Melt pool dimensions were measured from the top row of melt pools, as these were not remelted by subsequent layers; for L-PBF several melt pools were measured and so could be averaged; for L-DED, since only 3 hatches were printed, the dimensions of the central melt pool were taken. PDAS was manually measured in a variety of locations within each sample and averaged.

11.3. Results

11.3.1. Thermal Monitoring

Pyrometry signal is used as the thermal monitoring technique in L-PBF, for each layer, all signals below 850 mV were assumed to be background noise and were removed. The rest were averaged, showing the variation of pyrometry signal with height (Figure 11-3). It can be clearly seen that the samples built with higher power have higher pyrometry signals and that increasing velocity decreases the pyrometry signal. All four samples reach a temperature plateau within 2 mm of height, but the samples with lower pyrometry signals reach their plateau more quickly.

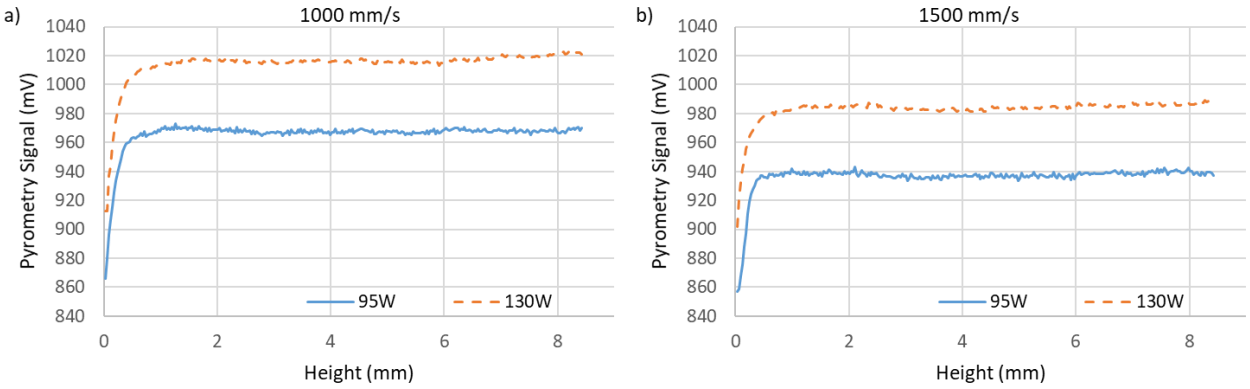

Figure 11-3: Variation in pyrometry signal with component height for samples built using L-PBF; a) 1000 mm/s; b) 1500 mm/s

To get an average pyrometry signal for each component, the average layer signals were averaged for the top half of the build; by this point, the plateau was reached and so the pyrometry signal was representative. To compare the accuracy of NED ($\frac{P}{v}$) and NE ($\frac{P}{\sqrt{v}}$), both of these were plotted against the average pyrometry signal as seen in Figure 11-4. Both $\frac{P}{v}$ and $\frac{P}{\sqrt{v}}$ show strong positive correlations, but the latter has a stronger (R^2=0.996).

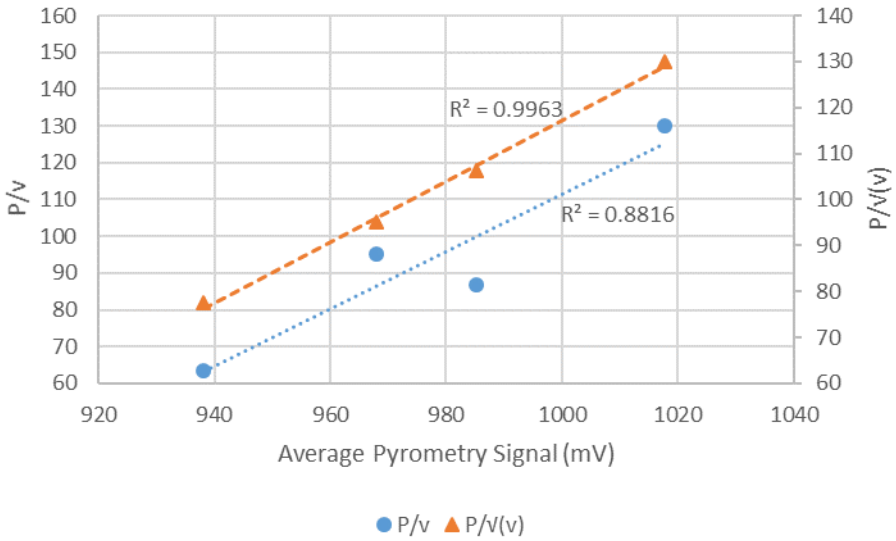

Figure 11-4: Correlation of the average pyrometry signal with P/v and $P/\sqrt{v}$, for the second half of the build. R^2 values included

Thermal intensity is used as the thermal monitoring technique in L-DED, which is a measure of the total signal over an area; this is effectively the same as a spot pyrometer. All thermal intensity values below 0.2×10^7 were removed and the rest were plotted against the frame number (which increases with build height) as seen in Figure 11-5. It can be seen that the samples built with higher power have higher thermal intensities and that increasing velocity decreases the thermal intensity. It is hard to determine whether any of the L-DED samples reached a thermal plateau.

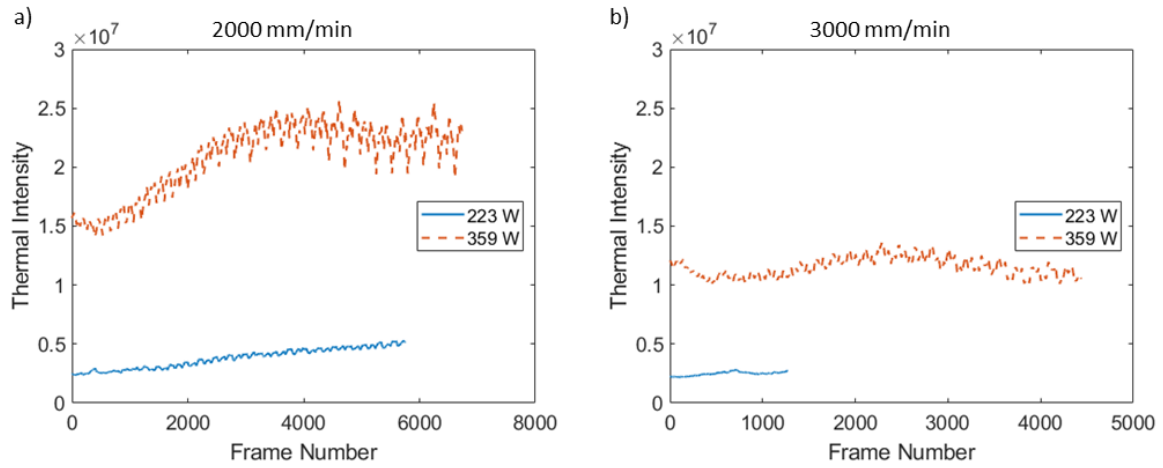

Figure 11-5: Variation in thermal intensity with component height for samples built using L-DED; a) 2000 mm/min; b) 3000 mm/min. A moving mean with a 100-point window was applied

To get an average thermal intensity for each component, the average layer intensities were averaged for the top half of the build to be consistent with the L-PBF analysis. $\frac{P}{v}$ and $\frac{P}{\sqrt{v}}$ were plotted against the average thermal intensity (Figure 11-6). Both $\frac{P}{v}$ and $\frac{P}{\sqrt{v}}$ show strong positive correlations, but the latter has a stronger correlation (R^2=0.959).

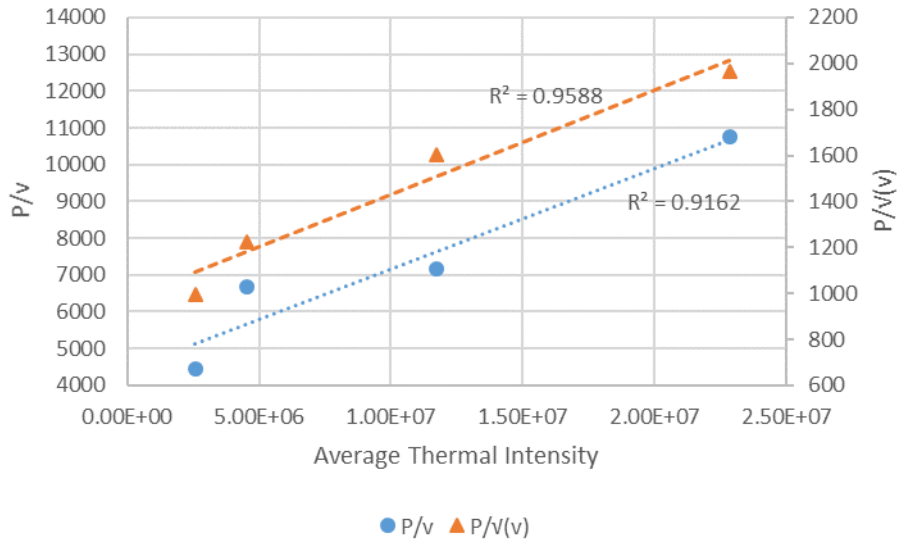

Figure 11-6: Correlation of the average thermal intensity with P/v and $P/\sqrt{v}$, for the second half of the build . R^2 values included to show the strength of the correlation

11.3.2. Hardness Analysis

Chapter 8 showed that a significant hardness variation is found within L-DED components. The bulk was found to be significantly harder than the edges; there was no such variation found in the L-PBF samples. BeAM_L was the smallest sample, as the low heat input resulted in a thinner component, the hardness map contained 18 indents. The Aconity samples were largest, so 45 indents were performed on each of these. The average hardness and variation of this are shown in Table 11-3; the hardness of Aconity samples is much greater than that of BeAM samples. Aconity_H was found to be harder than Aconity_L, whilst BeAM_L was found to be harder than BeAM_H.

Table 11-3: Comparison of hardness values between L-PBF and L-DED

Sample	Average Hardness (HV)	Standard Error
Aconity_L	323.4	3.1
Aconity_H	342.6	0.9
BeAM_L	276.4	3.6
BeAM_H	246.4	3.0

The standard deviation of both BeAM samples was constant at around 16 HV, whilst the Aconity_L sample experiences a much larger hardness variation than the Aconity_H sample. Pairwise 2 sample t-tests were performed and each sample hardness was found to be significantly different from each other sample (using α=0.05).

11.3.3. EBSD Analysis

EBSD orientation maps are shown in Figure 11-7 for both low and high heat input samples for both L-PBF and L-DED. Figure 11-7a, b are L-PBF samples and both appear to be predominantly <100> orientated. Aconity_H has large columnar grains with a strong texture; Aconity_L appears to have much smaller grains than Aconity_H, with clusters of small, randomly oriented grains. In L-PBF, discrete columns of melt pools can be seen, with some epitaxial growth through multiple layers resulting in some larger grains (these are dominant in Aconity_H). These can be explained by the vertical heat flow and the preference of cells to grow anti-parallel to the heat flow, as discussed in Chapter 10. In BeAM_L (Figure 11-7c), there are large clusters of small grains located at roughly the z-step interval (200 μm), due to the large melt pool size (~ 800 μm wide), we can likely see only the width of one melt pool. Different step sizes in the range 1.0-1.6 μm were used for different EBSD scans (Table 11-2); this is significantly smaller than the typical grain size, so this variation in step size is not expected to have any effect on the final results.

The grain orientations in BeAM_L are free of any texture, whilst those in BeAM_H seems to have a tendency towards the <100> orientation; the grains in BeAM_H are the largest of any of the 4 samples. The GAM for each grain is plotted in Figure 11-8; the Aconity (L-PBF) samples both have higher GAM than the BeAM (L-DED) samples. The Aconity_L sample has some grains of high misorientation, whilst in Aconity_H, the larger grains generally have higher GAM values. In the BeAM_L sample, some small grains have high GAM, but the majority of the sample has a low GAM value; in BeAM_H, there are few grains, but these are larger and have greater GAM values, taking up the majority of the area.

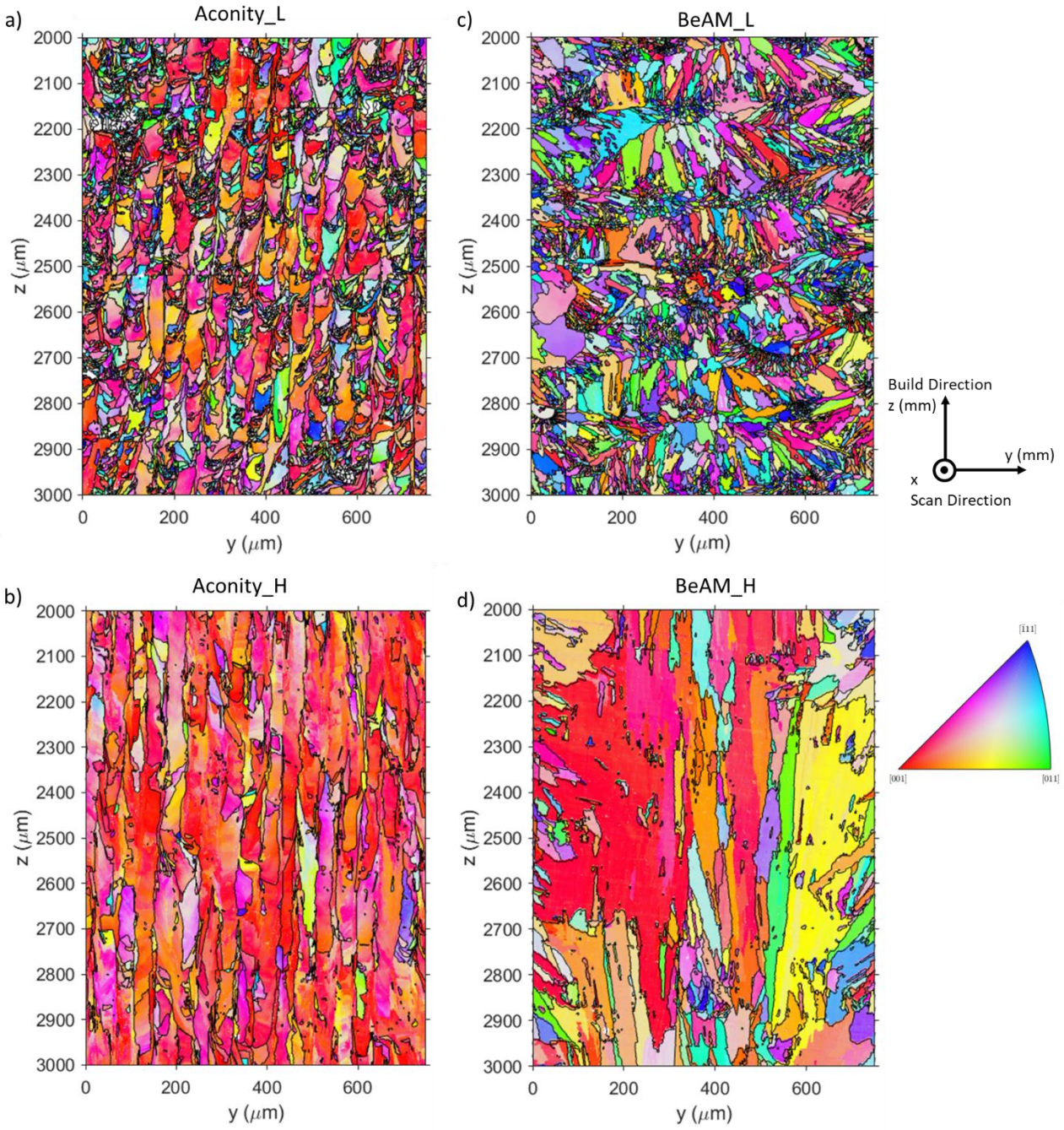

Figure 11-7: EBSD orientation maps (IPFX) of the YZ sections. a) Aconity_L; b) Aconity_H; BeAM_L; BeAM_H

Overall, of the L-DED samples, BeAM_H has a noticeably higher average GAM than BeAM_L. Additionally, in Aconity_H, there are large grains with misorientations of 1.5-2 °, whilst in Aconity_L, there are some grains with very large GAM values, but the majority of the sample has a GAM of around 1 °. Figure 11-9 shows the comparison between average GAM values and area-weighted average GAM values (calculation details covered in Section 4.7). Area weighted GAM values line up with the trend explained above, as the Aconity_H has a larger GAM than Aconity_L, but by a smaller margin than when using a simple average. Additionally, using area weighted GAM leads to a larger difference in GAM between BeAM_L and BeAM_H. As such, area weighted averages will be used, by similar logic to that for grain areas in Section 8.4.

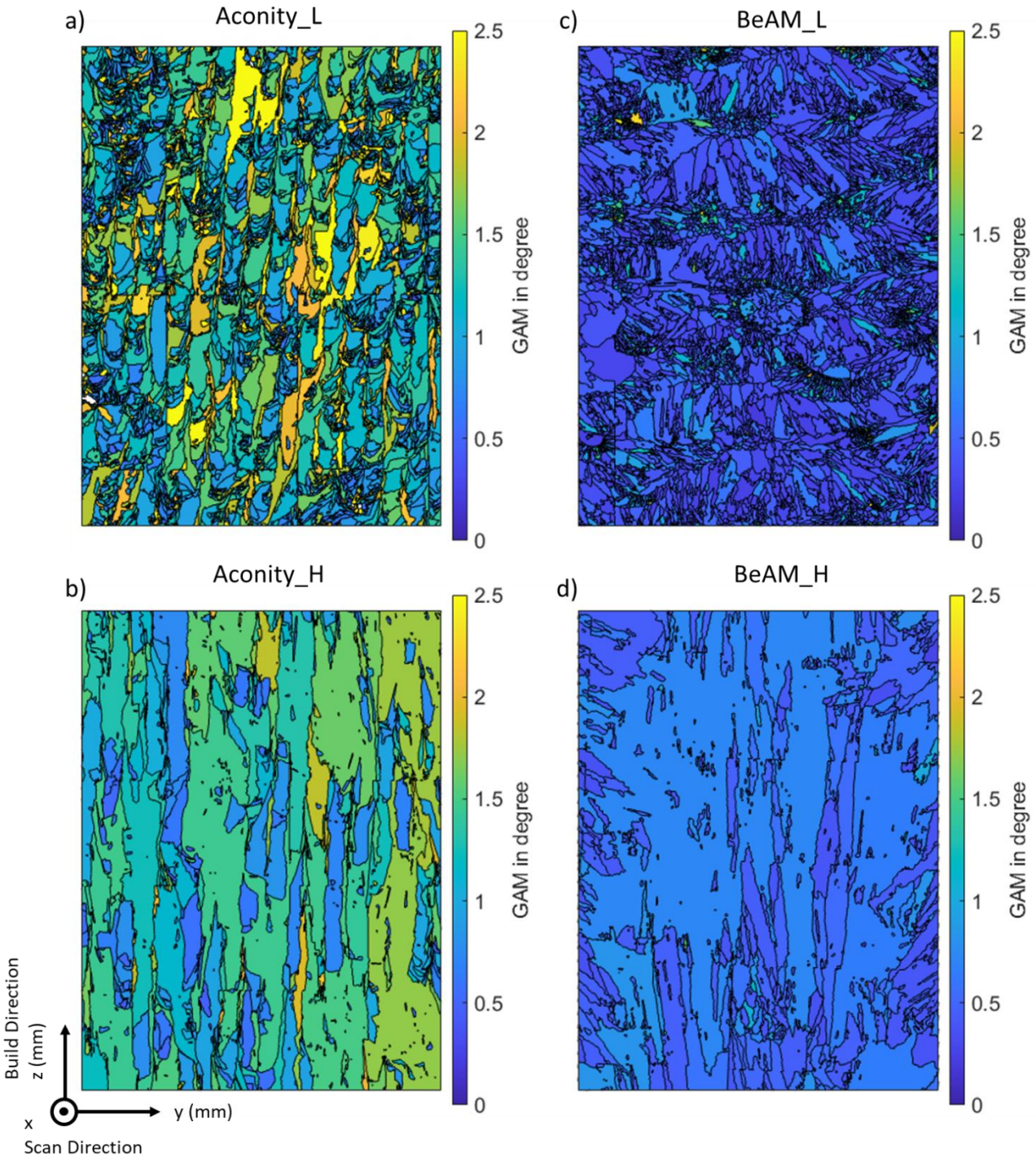

Figure 11-8: Maps of the grain average misorientation (GAM) in the YZ sections. a) Aconity_L; b) Aconity_H; BeAM_L; BeAM_H

A comparison of various grain properties between L-PBF and L-DED is summarised in Figure 11-10; for both processes, the range of measured values is shown. For each parameter, the area weighted average is calculated. In the high heat input samples, the average grain area is found to be much smaller for L-PBF than for L-DED, however in low heat input samples, the L-DED samples showed a smaller average grain size. The aspect ratio of L-PBF samples is generally larger although both processes can experience columnar grains. The anisotropy factor is a measure of the average orientation of the sample, this is lower for L-PBF, so the L-PBF process has a tendency towards

grains near the <100> orientation. The range of anisotropy factor values is however larger for L-PBF so there is a larger possible spread in grain orientations.

Within a sample, L-PBF has a larger maximum mud, which suggests than L-PBF samples experience stronger texture than L-DED samples. As seen in Figure 11-8 and summarised in Figure 11-10, L-PBF samples experience a larger grain average misorientation than L-DED samples; this can be linked to a higher dislocation density (Chapter 8).

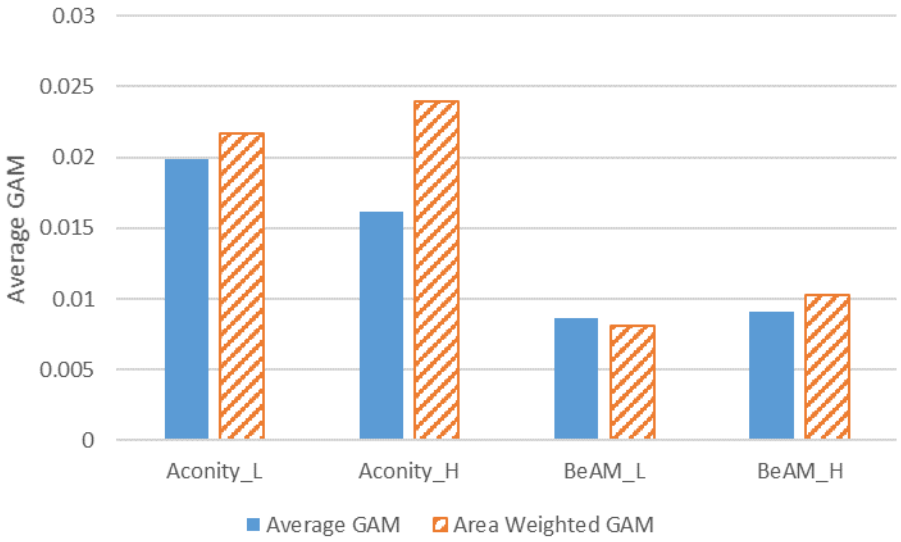

Figure 11-9: Difference between average GAM and area weighted average GAM

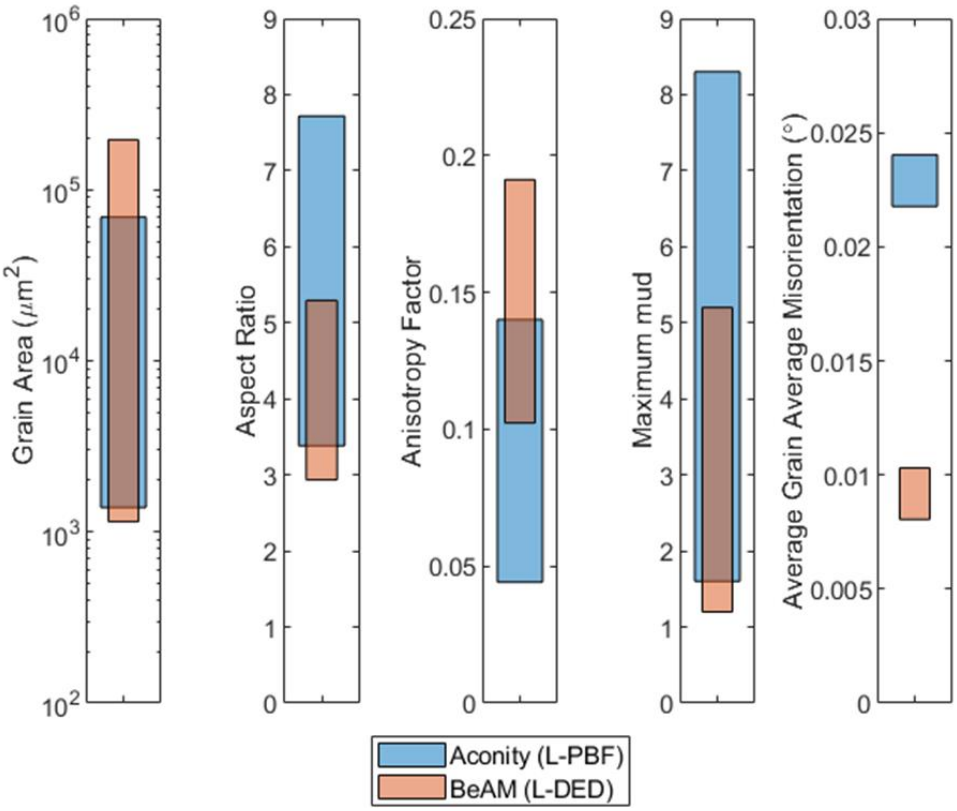

Figure 11-10: Comparison of the ranges of grain properties between the L-PBF and L-DED processes

11.3.4. Optical Microscopy

Example optical micrographs of L-PBF and L-DED samples are shown in Figure 11-11, with melt pools highlighted. The top layer of the build shows the full depth of the melt pool, which is not visible in lower layers due to remelting. The melt pool width in L-PBF is on the order of 100 μm, whilst those in L-DED are of the order of 1000 μm.

High resolution micrographs (Figure 11-12) show regions with striped patterns, these are regions where the cells/dendrites are oriented in the plane of the page and so the PCAS/PDAS (which will jointly be referred to as PDAS) can be measured. This is typically done by measuring the width of a larger number of cells/dendrites e.g. 15 and calculating the average width. In the L-PBF samples (e.g. Figure 11-12a), the cells are typically linear with no perturbations; however, in L-DED samples (e.g. Figure 11-12b), some perturbations of dendritic nature (perpendicular to the primary growth direction) can be seen.

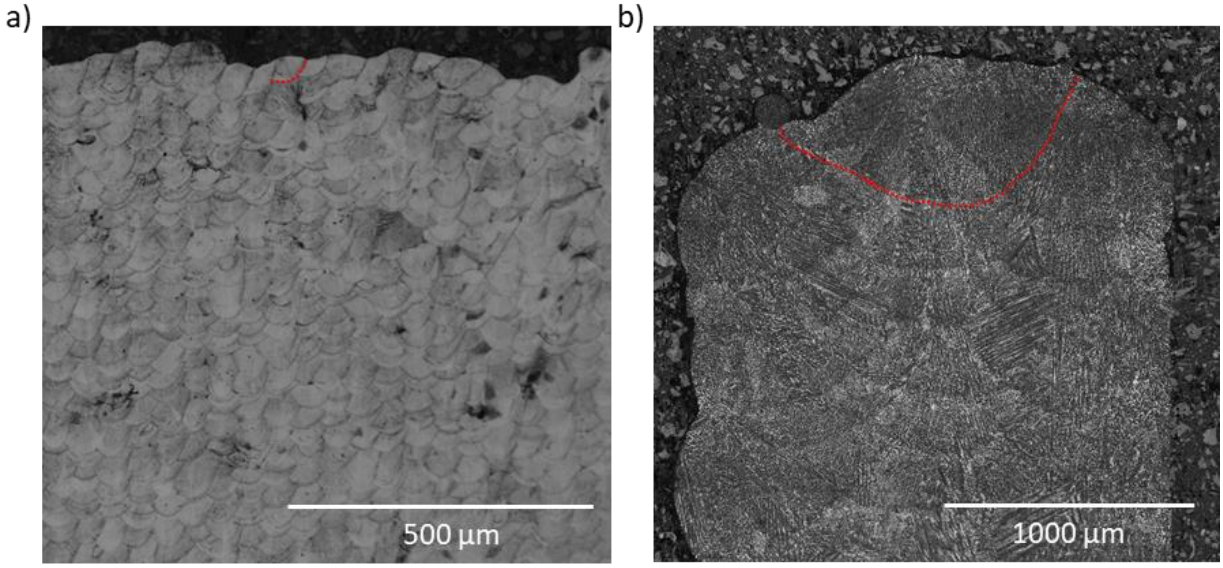

Figure 11-11: Low resolution optical micrographs of etched samples, with example melt pools outlined; a) L-PBF; b) L-DED

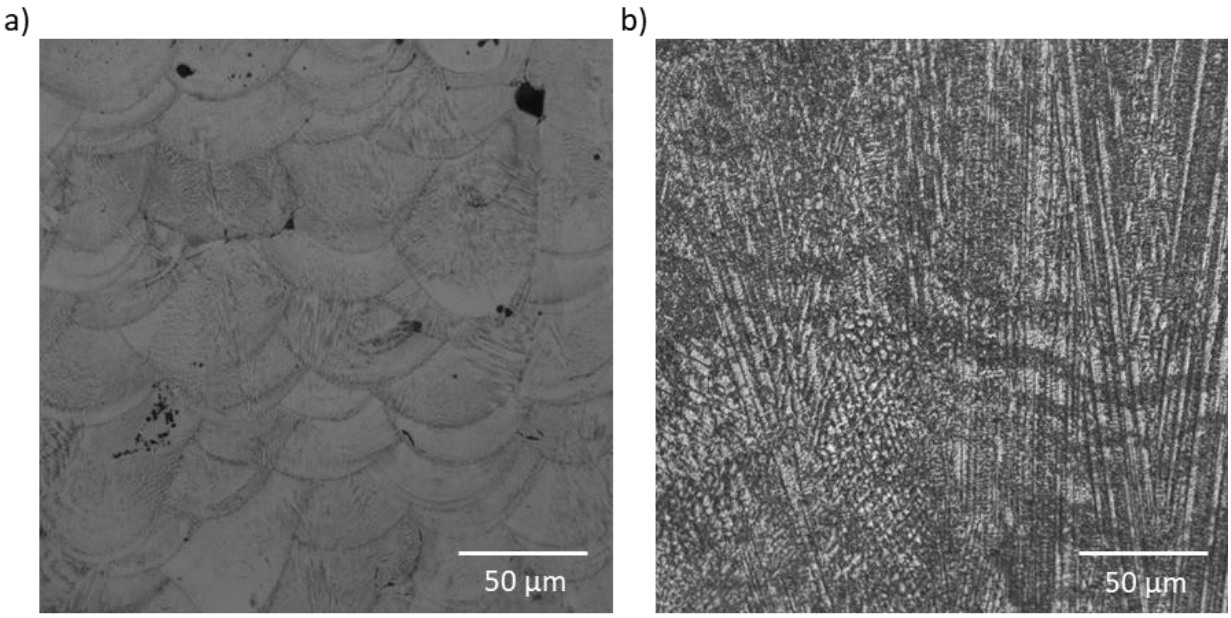

Figure 11-12: High resolution optical micrographs of etched samples, with the microstructure visible; a) L-PBF; b) L-DED

A summary of melt pool dimensions is shown in Table 11-4, with standard deviations in brackets. The melt pools in L-DED are both wider and deeper than in L-PBF and in both cases, the high heat input samples experience larger melt pools. Since only the central melt pool could be measured for the BeAM samples, the error is the measurement resolution rather than the standard deviation.

Table 11-4: Comparison of melt pool dimensions and PDAS between L-PBF and L-DED. Standard deviations in brackets, for BeAM samples, melt pool dimension errors are the measurement resolution

Sample	Melt Pool Width (µm)	Melt Pool Depth (µm)	λ_1 (µm)
Aconity_L	73.1 (14.0)	48.1 (12.5)	1.1 (0.1)
Aconity_H	78.7 (7.0)	112.1 (14.0)	1.0 (0.2)
BeAM_L	780 (1)	274 (1)	1.8 (0.5)
BeAM_H	973 (1)	406 (1)	3.0 (0.5)

The finer microstructure was revealed by etching, as seen in Figure 11-12; Table 11-4 shows that in L-PBF, the PDAS is much smaller than in L-DED and that there is little variation in PDAS with processing parameters. In L-DED, PDAS varies by 1.7x depending on the processing parameters with low heat input leading to a finer microstructural scale (but still larger than L-PBF).

11.4. Discussion

On the Aconity3D Mini, thermal monitoring is performed using a spot pyrometer, this effectively is a sensor which absorbs photons of a set wavelength range and the output signal (mV) is proportional to the intensity of the light hitting the sensor. The thermal intensity from the Basler camera on the BeAM Magic 2.0 is a sum of all the pixels in the image; effectively, this is what a spot pyrometer does. As such, the monitoring methods between the two processes are comparable. Their sensitivities may be different, but the measurement methodology is the same.

As already discussed in Chapter 6 and Chapter 9, the NE calculation ($\frac{P}{\sqrt{v}}$) appears to be more accurately match experimental results than NED ($\frac{P}{v}$). This was further emphasised by the experiments in this chapter, for both L-PBF (Figure 11-4) and L-DED (Figure 11-6), $\frac{P}{\sqrt{v}}$ was shown to more accurately correlate with the thermal signatures than $\frac{P}{v}$. Interestingly, in L-PBF, the lower heat input samples were found to reach a temperature plateau quicker than the high heat input samples; in L-DED there were no clear patterns in temperature plateau. This could potentially be explained by the relatively large heat source and the small number of hatches actually printed – in the full part, only 150 hatches are printed in L-DED, compared to over 20,000 hatches in L-PBF, allowing much more opportunity for steady state to be reached.

Both processes appear to show a similar response to both power and velocity despite, their melt pool sizes being almost an order of magnitude different (Table 11-4). Similar thermal trends are seen in both L-PBF and L-DED (Figure 10-25); the thermal signal increases with thickness for very thin components until a maximum which occurs at a width of 2-3 mm. From here, the thermal signal appears to drop and plateau, with any samples above 5 mm experiencing similar thermal

signals; at this point, the components can be considered bulk, so conduction is the dominant heat flow mechanism and sufficient conduction occurs that the component is no longer saturated with heat.

The melt pool dimensions in both processes follow the expected trends, being larger in the high heat input samples (Table 11-4). The large increase in melt pool depth in the Aconity_H sample is due to the keyholing regime being active; there was a bigger increase in the melt pool depth than width for the L-DED process as well. In terms of the microstructure, it is widely disputed whether cells or dendrites are seen in AM. In L-DED micrographs (Figure 10-19), dendritic perturbations can be seen, so these will be referred to as cellular dendrites; in L-PBF, no perturbations can be seen, so these will be referred to as cells. As shown in Section 2.4.1, increasing the thermal gradient leads to a transition from columnar dendritic structures to cellular structures [386]; this is a complex relationship, as cellular structures are possible at both low and high cooling rates [96,97]. The high cooling rates in L-PBF could explain why the microstructure in these samples is of a more cellular nature [386].

The exact relationship between microstructure, G, V and cooling rate ($\dot{T}$) is complex. There are many calculations for the PDAS (which should also hold for PCAS), but the general relation is $\lambda_1 \propto G^{-\frac{1}{2}}$ [98,387]. This may not hold for all temperatures, but seems to be applicable in Inconel 718 under similar conditions [99,295,388]. Fang et al. show that in their conditions, $\lambda_1 \propto \dot{T}$ [389], however, their PDAS is 5x larger than that measured in this work (which is a larger difference than that between L-PBF and L-DED in this work) and this has not been shown to hold under the conditions used in this work.

Using the measured PDAS, a cooling rate can be calculated using equations by Trivedi and Hunt [98,387], as summarised by Raghavan et al. for Inconel 718 [99]. Using both equations, a range of cooling rates of $9x10^4$-$7x10^5$ K/s are calculated for L-DED, with a range of $5x10^6$-$1x10^7$ K/s for L-PBF. These are higher than those predicted in literature [4], but given the simple nature of the calculations, they are as close to reported values as could be reasonably expected.

Despite similar increases in energy density, the PDAS range in L-DED is bigger than in L-PBF, this is due to the greater cooling rates in L-PBF – at high cooling rates, a bigger change in cooling rate is required for a specified change in PDAS. To increase the PDAS in L-PBF samples by 0.2 μm, a 30 % decrease in thermal gradient would be required; for L-DED, it was found that only a 16 % decrease in thermal gradient would be required for the same 0.2 μm increase in PDAS.

This explains the trend in PDAS summarised in Table 11-4; the structure size is larger in L-DED as the cooling rate and thermal gradient are much lower. The PDAS (Figure 10-22) decreased from 4.8 μm to 2.3 μm as sample width increased; this suggests that by increasing the width, the thermal gradient (and so the cooling rate) was increased. Additionally, this relationship explains why there is no change in structure size in L-PBF despite NE changing by 1.7x – at this PDAS, an enormous change in thermal gradient would be required to change the PDAS. The structure size in L-DED is slightly larger, so a 2x change in NE led to a 1.7x change in PDAS, the thermal gradients are lower and a smaller change in thermal gradient is required to change the PDAS.

There is a large range of grain structures possible within both processes as summarised in Figure 11-7. The range of structures shown for L-PBF ranges from small grains with weak texture to larger columnar grains of strong <100> texture; this is similar to the range of structures reported for 316L by Heiden et al. (Figure 11-2) [280]. In terms of L-DED structures, Chapter 10 shows the range of grain structures available with constant parameters, Figure 11-7 shows that a much finer grain

structure is also possible; the range of structures experienced is comparable to those reported in literature [180,285]. Neither of the L-DED samples in Figure 11-7 show a <112> (seen in Chapter 10); as only thin components are being compared in this chapter. We believe this not to be a factor in L-PBF, as the range of grain structures seen in this chapter is comparable to those reported in literature [94,390].

In both processes, a lower heat input resulted in a finer grain size; conventionally, this would be expected to result in a higher yield strength and so a harder material. This is the case in L-DED, however, in the case of L-PBF, the higher heat input results the harder sample (Table 11-3). Chapter 8 shows that there is a hardness variation between the centre and the edges of L-DED components. No trend was seen in the L-PBF maps; Choi et al. also found their hardness in L-PBF produced Inconel 718 to be homogenous [391]. This could be due to the much smaller melt pool size, potentially there is a hardness change at the very edges, but this could be only the outer 100 μm, which is below the spatial resolution of the hardness indenter.

Section 8.4 and Section 11.3.3 show that using area weighted grain average is more representative when analysing AM samples with complex, anisotropic structures than using a simple average. As such, ranges of area weighted average grain properties are shown in Figure 11-10, comparing the structures of L-PBF with those of L-DED. The average grain area in L-DED samples can be much greater than in L-PBF due to the larger melt pool, however, at low heat inputs, the L-DED sample had a smaller average grain area, this is likely due to the fact that the L-PBF parameters were not pushed to the lower limit of their processing window.

The Hall-Petch effect can be used to correlate yield strength to the grain size using $\sigma_y \propto d_g^{-1/2}$ where d_g is the grain diameter [354,355]. We have previously shown that the hardness is proportional to the yield strength [348,349], so $HV \propto d_g^{-1/2}$. If the grain diameter is small, then even a small change in grain diameter is sufficient to affect the hardness, as hardness is more sensitive to grain size changes in smaller grains. As such, we would expect changes in grain size in L-PBF to have a greater effect on the hardness values than changes in L-DED grain size. However, the increase in grain size in L-DED is so much larger than that in L-PBF, that we would expect this increase in grain sizes to lead to the increase in L-DED hardness to be 35 % greater than the hardness increase in L-PBF. The aspect ratios of both processes are relatively high, with the L-PBF having a much larger maximum aspect ratio, which is explained by the very columnar structure seen in Figure 11-7, similar structures have been reported in literature [93,94]. This was predicted by the location of the L-PBF process on the G-V plot (Figure 2-17), with L-PBF covering the mixed and columnar areas, whilst L-DED is closer to the equiaxed region.

The orientation maps in Figure 11-7 show that L-PBF has a strong tendency towards the <100>, this leads to the low anisotropy factor seen in Figure 11-10. The grain orientations in L-DED are seen to stray much further away from <100>, resulting in a higher anisotropy factor. For both processes, the low heat input samples had weak texture and so low maximum mud values; the Aconity_H sample had by far the strongest texture (<100> orientation) and so had the highest maximum mud. The average grain average misorientation (GAM) in the L-PBF samples was much greater than that in L-DED samples (Figure 11-10); this is an interesting observation, as within each sample (Figure 11-8), the larger grains had higher GAM values, so one might expect the larger grains in L-DED to have higher GAM values than in L-PBF.

Since the cooling rates in L-PBF are much higher than in L-DED, the structure is cellular rather than dendritic. Each grain contains many cells, which are misorientated with respect to one another, and importantly, the cell walls are made up of dislocations. This is demonstrated for 316L in Figure

11-13 [60], the high dislocation density at cell walls visible, the same phenomena are reported for Hastelloy X [392] and would be expected in Inconel 718. Given that L-PBF contains cells (unlike L-DED), this explains the higher GAM values measured when compared to L-DED.

As explained in Section 8.1, GAM can be used as an indicator of the dislocation density [336–339]. Since a grain boundary is a discontinuity in lattice orientations, grain boundaries are essentially areas of high dislocation density. If a grain is large and there is a variation in orientation within it, this means there are lattice imperfections such as dislocations present to accommodate this misorientation. Conversely, in small grains, only small regions of "perfect" lattice are needed, so small grains are much more likely to have low GAM values. This explains the trends seen in L-DED, with small grains having lower GAM values.

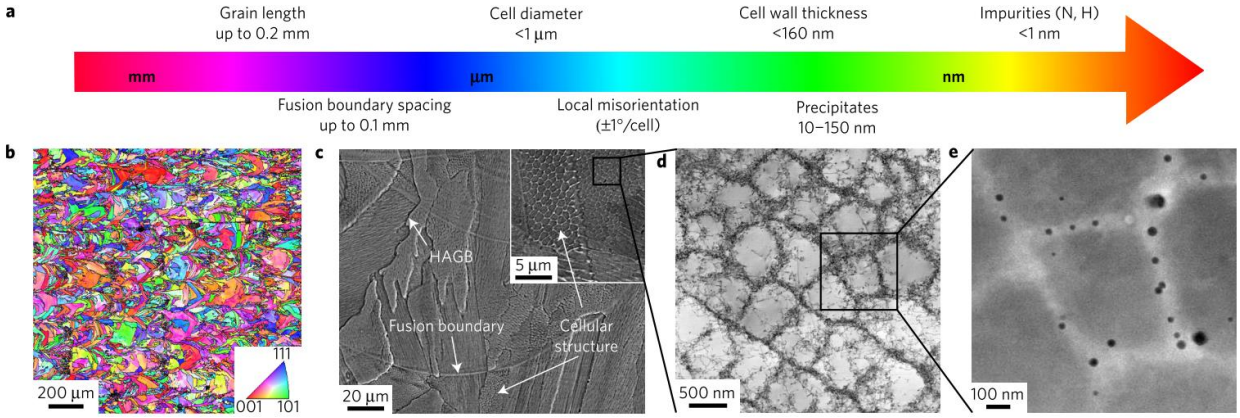

Figure 11-13: Multiscale microstructure of a 316L sample produced by L-PBF. a) schematic of length-scales; b) EBSD orientation map; c) SEM showing grain boundaries and cells; d) TEM of solidification cells; e) HAADF STEM image of a solidification cell. Reported by Morris Wang et al. [60]

This can be formalised by calculating the energy stored due to dislocations, $E_{dis} \propto \frac{\theta \rho_d}{D_{sub}}$, where θ is the misorientation angle (which is proportional to GAM), ρ_d is the dislocation density (also proportional to GAM) and D_{sub} is the subgrain diameter [393]. In the L-PBF samples, D_{sub} is the cell size, which is comparable between the two samples, so $E_{dislocations} \propto GAM^2$; since Aconity_H has a higher GAM than Aconity_L, it is expected to have a stored energy which is 34 % greater than Aconity_L. The high heat input sample also has larger grains, so in this case, the larger grains have higher misorientation and so a greater stored energy (which is essentially a higher strain). For the L-DED samples, PDAS changes mean that the energy stored remains within 2 % of one another for the high and low heat input samples, which is surprising, as large grains seem to show more misorientation (Figure 11-8d).

The thermal strain parameter, introduced in Section 5.1.7, $\varepsilon^* = \frac{\beta \Delta T}{EI} \frac{t}{F\sqrt{\rho}} {H_i}^{3/2}$ can be used to relate processing parameters to the strain in the final component [41]. Given than the geometry and material are the same throughout these samples, this can be simplified to $\varepsilon^* \propto \frac{t}{F} {H_i}^{3/2}$, where $F = \frac{\alpha t}{L^2}$; simplifying further to $\varepsilon^* \propto L^2 {H_i}^{3/2}$. As heat input increases, the melt pool size also increases, so for a high input sample, one would expect there to be a higher thermal strain. For L-PBF, where the dislocation density is higher, a higher thermal strain would be expected, which explains the higher stored energy calculated previously - that as dislocation density increases, thermal strain increases.

In L-DED, it is harder to calculate the stored energy due to dislocations, as it is hard to determine what the subgrain size is. Cells are surrounded by bunches of dislocation, whereas dendrites

generally form due to a compositional difference. However, the same thermal strain parameter calculations follow, so the higher heat input samples experience more thermal strain. Since these samples also have larger grains, it is not surprising that the larger grains have a higher GAM value as was initially observed in Chapter 8.

The GAM value for the Aconity_H sample is 11 % higher than for the Aconity_L sample, this suggests that the Aconity_H sample contains a significantly higher dislocation density than the Aconity_L sample. The principal behind work hardening is that as dislocation density increases, the dislocations repel one another, so the material is harder to deform [394]. The relationship $\sigma_y \propto \sqrt{\rho_d}$ has been widely reported [334,335]; since HV ~ σ_y /3 [348,349], $HV \propto \sqrt{\rho_d}$; Zhang et al. show that a hardness increase of 28 HV is possible in L-PBF [334], so it is concluded that the hardness increase measured in the Aconity3D L-PBF samples (19 HV) could be explained by the change in dislocation density (approximated using GAM).

Additionally, if precipitates are present, the higher the dislocation density, the more dislocations will interact with the precipitates and the hardness will further increase. The higher heat input would likely promote the nucleation/growth of γ" precipitates, so as well as there being more dislocations, there are likely to be more precipitates to interact with dislocations in Aconity_H. As such, the increased dislocation density in Aconity_H could explain the increased hardness exhibited when compared to Aconity_L.

Aconity_L has smaller grains than Aconity_H, which would increase the hardness, but also has a lower dislocation density, which would decrease the hardness. It's impossible to know which of these phenomena would dominate, but the increased precipitation potential and higher dislocation density in Aconity_H could explain the higher hardness measured. Overall, the Aconity (L-PBF) samples have both smaller grains and higher GAM values than the BeAM (L-DED) samples, which explains why the hardness values in the L-PBF samples are significantly higher than in the L-DED samples.

We have shown that the grain structures between L-PBF and L-DED are different, although there does seem to be some overlap where similar grain areas and textures can be achieved (Figure 11-10). Despite the fact that some of the properties overlap, it is likely to be impossible to create a sample with the same grain properties using both processes, as the grain properties are interlinked and so the combinations required may be mutually exclusive.

Table 11-3 shows that the mechanical properties of components made by the two processes are significantly different, with L-PBF samples being at least 17 % harder than L-DED samples. This difference relatively small, especially compared to the change in cooling rates, which are ~10^3x different; however, the hardness values are not comparable (Table 11-3). Even if most grain properties could be kept consistent between the processes, the difference in melt pool size and cooling rate completely changes the nature of the microstructure (cells vs dendrites) which in turn causes changes in the dislocation structure (related to GAM), which are not comparable between the processes. This conclusively shows that the properties of an additively manufactured component are strongly affected by the process used and casts doubts upon the idea of a process-agnostic alloy being developed (as discussed in Chapter 5).

The resultant microstructure and mechanical properties of a component are dependent on a combination of complex factors including:

- Laser power
- Laser beam size
- Laser velocity
- Powder size/composition
- Powder mass flow
- Component geometry
- Heat flow mechanisms
- Scan strategy and subsequent reheats

The combination in laser power and velocity lead to the NED in L-DED being ~75x larger than that in L-PBF (Table 11-1). This is equivalent to a ~15x increase in NE; either way, it is unsurprising that such a large difference in heat input results in a change in component properties. If the NED was comparable between the processes, then it may be possible to match melt pool sizes and cooling rates.

As discussed in Chapter 5 (initially introduced in Section 2.1.3), L-PBF is expected to experience rapid solidification and potentially solute trapping. If complete solute trapping were occurring, a planar interface would be expected [395], however, in L-PBF, cellular structures can be seen, so some solute trapping is occurring, but not complete solute trapping. Since regions of dendritic growth can be seen in L-DED, this is evidence of local segregation, which shows that no solute trapping occurs, however, rapid solidification is still occurring, as predicted in Chapter 5.

These factors are different between the two processes, so unfortunately, the final component properties are highly unlikely to be comparable. It has been shown that even if an AM component is heat treated, the mechanical properties are still dependent on the as-built microstructure (as discussed in Section 10.1.4) [67]. Even with heat-treatment, L-PBF components will behave differently to L-DED components, so the process must be selected with a specific application in mind. Finally, it much be concluded that even if process control is not perfect, any homogenisation of the as-built structure is beneficial, as it will result in a more homogenous final component; this is the case for both processes.

11.5. Summary

In this chapter, L-PBF and L-DED were compared, both in terms of thermal signatures, the resultant microstructures and the final mechanical properties. It was confirmed that for both processes, the relation $\frac{P}{\sqrt{v}}$ is a better fit to experimental results than $\frac{P}{v}$, as initially calculated in both Chapter 6 and in Chapter 9. In L-DED, the structure consists of columnar dendrites and the hardness is inversely proportional to grain area, as expected by the Hall-Petch effect; in both processes, the grain area decreases with increasing cooling rate. The microstructure is more complex in L-PBF, with each grain containing cells, which are surrounded by dislocations. In L-PBF, larger grains allow for more cells and so greater misorientation within a grain and a higher overall dislocation density. Additionally, Aconity_H experiences a higher heat input providing more opportunity for precipitation; the combination of these two factors is used to explain the higher hardness in the Aconity_H sample despite its' larger grain size.

The dendritic nature of the L-DED samples shows that local segregation occurs and so despite rapid solidification occurring, solute trapping does not occur. In L-DED, a higher heat input led to slower cooling and an increased PDAS. A similar effect was achieved in Chapter 11 by decreasing the sample width, which increased melt pool depth and decreased the cooling rate.

In L-PBF, we confirm that solute trapping occurs, as predicted in Chapter 5, resulting in a cellular microstructure. The higher heat input in Aconity_H allowed for more thermal strain to be developed, which was related to the energy stored due to dislocations (calculated using GAM). In L-DED, it is shown that higher heat input leads to larger grains, which experience more thermal strain – as shown by the higher GAM values; this explains the GAM trends seen in Chapter 8.

Despite the fact that the grain sizes seem to overlap between the processes, the two processes are still sufficiently different that the final components cannot be easily compared. The different thermal conditions during the process, which originate from the vastly different energy inputs, lead to very different thermal conditions and so microstructures. These changes are retained post heat-treatment, with differences in mechanical properties persisting. For a specific application, the desired properties must be specified and both the process and alloy must be selected specifically to match this. It is insufficient to select an alloy and assume that however it is produced, the final component will meet the required specifications (as explored in Chapter 5). The component must be built with homogeneity in mind, as heat treatment cannot completely remove anisotropy, so process control must continue to be improved until it is reliable enough to achieve industrial certification.

12. Conclusions and Future Work

12.1. Conclusions

At the start of this thesis, the scope of this project was defined as:

- What determines if an alloy will be easy to manufacture using AM? Does this depend on the process used? Can this be used to help develop new alloys?
- What can simple in-situ monitoring techniques tell us? Do the signals relate to the processing parameters?
- What advantage do advanced monitoring techniques give? Can cooling rates be accurately calculated? Can mechanical variations be explained by the thermal measurements?
- How do other factors, such as geometry, affect mechanical properties?
- Can thermal measurements be simplified? What are the key parameters which matter? By controlling these, is component homogeneity improved?
- How do the structures created by L-PBF and L-DED compare – do trends from one process follow in the other?

Throughout this thesis, the following conclusions were made:

1. A simple, yet comprehensive methodology was developed in Chapter 5 to predict the susceptibility of Nickel superalloys to various failure modes; these aligned with literature despite being significantly simpler. The differences between L-PBF and L-DED were interrogated, validating the advanced Thermo-Calc Scheil simulations. A quantitative comparison of the grain structures produced by both processes was shown in Chapter 11, which has not previously been reported. Fundamentally, the processes are shown to be similar, with melt pool sizes and thermal signals scaling with $\frac{P}{\sqrt{v}}$, however the mechanical properties are not comparable due to an order of magnitude change in melt pool sizes and 3 orders of magnitude difference in cooling rates. Hence alloys must be developed with a process in mind.
2. The L-PBF process is analysed in Chapter 6, validating the moving heat source models by correlating the predicted melt pool dimensions with experimental results; this allows for estimation of processing windows for new alloys. The observed swelling in L-PBF was investigated and a new swelling mechanism was hypothesised, originating from the divots caused by rapid solidification at the ends of laser hatches.
3. Thermal monitoring was explored in Chapter 7, comparing various cameras data acquisition rates and resolutions; greater detail was shown than that typically reported for L-DED. From side-on imaging, cooling rates were measured and correlated with melt pool length; this was shown to influence the microstructure and hardness, demonstrating that sufficient data can be acquired using low resolution monitoring of the melt pool for control of mechanical properties.
4. A new process control system was developed and integrated using coaxial monitoring as shown in Chapter 9, with both power and velocity controlled to keep the thermal intensity constant. Relatively low resolution monitoring was shown to contain sufficient data for measuring melt pool dimensions which can be used as a proxy for cooling rate. Process control is quantitatively shown to homogenise the grain structure, although the hardness was not found to be homogenised. A large disparity in melt pool depth was found despite

the coaxial melt pool image being consistent, this has not been previously reported and raises fundamental questions about using coaxial monitoring for process control.

5. Hardness is shown to vary when using constant processing parameters, with the hardness significantly reduced at the edges of the component. In Chapter 8, a moving heat source model was developed to show that the hardness variation stems from a change in γ" precipitation. Component thickness is shown to change the melt pool depth by 2.5x, which has not been previously reported and cannot be detected using coaxial monitoring. Chapter 10 explains how this change in melt pool shape leads to the different grain structures observed.

12.2. Future Work

The effect of melt pool shape in L-DED on the microstructure of the final component has been explored in this thesis. Industrial interest in L-DED is currently substantial and this study demonstrates that the process is controllable, paving the way for reliable turbine blade repair using Nickel superalloys. For this process control, it is likely that coaxial cameras will be used to achieve component homogeneity, which is likely to reach industrial certification within the next decade. Process control using dual wavelength cameras, which allow for temperature measurement, would enable better estimation of phase transitions and precipitate content – further improving process homogeneity.

New alloys will continue being developed and with time, higher temperature alloys with similar mechanical properties to CM247LC will be developed and manufactured using AM. These higher temperature alloys will extend applications of AM into higher temperature areas of aerospace engines, both in component repair and manufacturing of new components.

Further research in this area could focus on expanding the work from this thesis in the following areas:

Coaxial monitoring was determined to be the most applicable monitoring technique, however, only simple image analysis was performed, extracting the image sum and the melt pool dimensions. Chapter 9 and Chapter 10 showed that the melt pool depth varied greatly, even when the coaxial image was comparable. Further image analysis could be done to see whether the intensity gradients are different between shallow and deep melt pools. If they are, this would allow for much tighter process control, as the melt pool depth affects the grain orientation and is currently not measured in-situ. This could be investigated by concurrently monitoring the process from side-on and coaxially and correlating the signals; to determine whether or not the melt pool depth (measured side-on) can be predicted from the coaxial imagery. This would have the further advantage of validating coaxial monitoring, as the melt pool lengths could be compared between the two monitoring techniques. Alternatively, another monitoring technique such as laser-induced spectroscopy could be used to see if this would provide a greater insight into the melt pool depth.

In Chapter 8, the hardness of L-DED produced Inconel 718 was deduced to be dependent on the γ" precipitation, with more precipitation in the bulk of the component due to more reheating cycles. It was hypothesised that by rescanning the component edges with a lower power laser pass, precipitation at the component edges could be facilitated. This would theoretically allow for the components' hardness to be homogenised. The required rescan could be calculated using a moving heat source model and this could be tested to show that the additional precipitation potential due

to the rescan would result in a homogenous component hardness. Additionally, TEM analysis of the samples would allow for a definitive conclusion of the size and distribution of γ" precipitates.

Process control in L-DED was shown to be successful in terms of achieving a target thermal intensity (Chapter 9). Industrial applications could require different mechanical properties in different regions of a component. The control algorithm could easily be adapted to aim for different thermal intensity targets in different parts of the component. For example, a gear could be printed, with the central region being softer and the teeth being harder. Investigation of the effect of the control target on mechanical properties would be required, but overall, this would be an interesting extension as it would result in a proof of concept of a functionally graded component.

The control algorithm is alloy-agnostic, with only 4 small samples required for calibration of control parameters. Since Inconel 718 was shown to be relatively insensitive to changes in thermal intensity, It would be interesting to use process control on a more sensitive alloy, such as an Fe-Ni-Ti alloy, as used by Kürnsteiner et al [330]. Alternatively, alloys such as Ti-6Al-4V could be tested, as its structure has been shown to be controllable by adjusting processing parameters [376]. If an alloy is very sensitive to thermal conditions, process control would have a stronger homogenisation effect on it; this would be a rich seam of research to pursue.

Appendix A: Individual Susceptibility Values

Table A-1: Raw susceptibilities for the 10 susceptibilities for each of the 21 alloys

Alloy	HT1	HT2	HT3	HT4	TCP1	TCP2	TCP3	SAC1	SAC2	LC1
Inconel 718	0.30	173.0	1302	5.86	2.28	0.88	0.92	1.26	2.48	5.32
Inconel 625	0.91	201.8	1444	5.70	2.06	0.89	0.91	0.37	1.38	6.02
Hastelloy X	1.04	77.6	478	5.70	2.52	0.93	0.94	2.00	2.00	6.22
CM247LC	1.95	225.5	1037	5.48	2.06	0.90	0.98	6.19	6.43	2.63
CMSX-4	1.20	176.4	1090	5.53	1.95	0.87	0.97	6.44	7.08	2.21
Waspaloy	1.40	275.3	1499	5.49	2.21	0.89	0.94	3.92	3.13	6.04
ABD-850AM	1.16	334.4	2530	5.25	2.14	0.88	0.92	3.15	2.65	5.99
ABD-900AM	0.63	298.9	2177	5.47	2.29	0.89	0.95	4.12	4.05	5.61
AlloyDLD	1.30	253.9	1611	5.46	2.11	0.89	0.94	2.90	3.80	5.49
Rene41	0.88	198.9	1102	5.85	2.29	0.92	0.96	4.10	3.05	5.79
In738	1.70	279.5	1728	5.35	2.26	0.90	0.98	6.26	5.70	4.85
In713LC	1.74	205.9	1017	5.87	2.10	0.90	0.97	6.50	6.90	3.36
Udimet700	0.94	230.3	1930	5.71	2.55	0.92	0.99	7.19	6.00	5.00
RR1000	1.64	441.4	1754	5.85	2.45	0.91	0.98	6.02	5.10	5.00
Inconel939	1.26	334.8	1509	5.59	2.46	0.90	0.96	5.01	4.05	7.09
Haynes282	1.24	216.1	869	5.56	2.22	0.90	0.94	3.26	2.55	6.03
Udimet720	0.89	249.1	735	5.72	2.46	0.91	1.01	6.70	5.00	5.64
718+	0.39	216.3	645	5.93	2.51	0.88	0.91	2.92	3.98	5.71

Table A-2: Normalised susceptibilities for the 10 susceptibilities for each of the 21 alloys

Alloy	HT1	HT2	HT3	HT4	TCP1	TCP2	TCP3	SAC1	SAC2	LC1
Inconel 718	0.00	0.26	0.40	0.10	0.56	0.14	0.18	0.13	0.19	0.64
Inconel 625	0.37	0.34	0.47	0.34	0.19	0.34	0.08	0.00	0.00	0.78
Hastelloy X	0.45	0.00	0.00	0.33	0.94	1.00	0.35	0.24	0.11	0.82
CM247LC	1.00	0.41	0.27	0.66	0.18	0.42	0.77	0.85	0.89	0.09
CMSX-4	0.55	0.27	0.30	0.59	0.00	0.00	0.66	0.89	1.00	0.00
Waspaloy	0.66	0.54	0.50	0.65	0.44	0.21	0.35	0.52	0.31	0.79
ABD-850AM	0.52	0.71	1.00	1.00	0.32	0.11	0.18	0.41	0.22	0.77
ABD-900AM	0.20	0.61	0.83	0.67	0.56	0.27	0.45	0.55	0.47	0.70
AlloyDLD	0.60	0.48	0.55	0.69	0.28	0.31	0.31	0.37	0.42	0.67
Rene41	0.35	0.33	0.30	0.11	0.57	0.81	0.54	0.55	0.29	0.73
In738	0.85	0.55	0.61	0.85	0.52	0.42	0.71	0.86	0.76	0.54
In713LC	0.87	0.35	0.26	0.09	0.25	0.48	0.67	0.90	0.97	0.24
Udimet700	0.39	0.42	0.71	0.32	1.00	0.90	0.80	1.00	0.81	0.57
RR1000	0.81	1.00	0.62	0.12	0.83	0.72	0.72	0.83	0.65	0.57
Inconel939	0.58	0.71	0.50	0.50	0.86	0.49	0.55	0.68	0.47	1.00
Haynes282	0.57	0.38	0.19	0.54	0.46	0.55	0.33	0.42	0.21	0.78
Udimet720	0.36	0.47	0.12	0.30	0.85	0.64	1.00	0.93	0.64	0.70
718+	0.05	0.38	0.08	0.00	0.94	0.01	0.00	0.37	0.46	0.72

Table A-3: Comparison of different Thermo-Calc Scheil calculations for the main alloys being analysed. Shown are the results of the classic Scheil calculation along with Back Diffusion calculations and the Solute Trapping calculation - for both L-PBF and L-DED. The percentage differences compared to the classic Scheil calculation are shown

					Deviation from Scheil Calculation		
Material	Calculation	Freezing Range	Crack Susceptibility Coefficient	Kou Cracking Susceptibility	Freezing Range	Crack Susceptibility Coefficient	Kou Cracking Susceptibility
Inconel 718	Scheil	173.0	0.30	1301.9	N/A	N/A	N/A
Inconel 625	Scheil	201.8	0.91	1444.1	N/A	N/A	N/A
Hastelloy X	Scheil	77.6	1.04	478.4	N/A	N/A	N/A
CM247LC	Scheil	225.5	1.95	1036.6	N/A	N/A	N/A
CMSX-4	Scheil	176.4	1.20	1090.5	N/A	N/A	N/A
Waspaloy	Scheil	275.3	1.40	1499.1	N/A	N/A	N/A
ABD-850AM	Scheil	334.4	1.16	2529.8	N/A	N/A	N/A
ABD-900AM	Scheil	298.9	0.63	2177.1	N/A	N/A	N/A
AlloyDLD	Scheil	253.9	1.30	1610.9	N/A	N/A	N/A
Inconel 718	BD PBF	173.0	0.30	1301.5	0.00	0.00	0.00
Inconel 625	BD PBF	201.8	0.90	1446.6	0.00	-0.01	0.00
Hastelloy X	BD PBF	68.4	0.79	442.6	-0.12	-0.23	-0.07
CM247LC	BD PBF	222.8	1.91	1034.1	-0.01	-0.02	0.00
CMSX-4	BD PBF	175.1	1.19	1079.3	-0.01	-0.01	-0.01
Waspaloy	BD PBF	275.1	1.38	1491.8	0.00	-0.01	0.00
ABD-850AM	BD PBF	333.3	1.16	2547.2	0.00	0.00	0.01
ABD-900AM	BD PBF	298.8	0.62	2173.4	0.00	0.00	0.00
AlloyDLD	BD PBF	254.0	1.29	1619.6	0.00	0.00	0.01
Inconel 718	ST PBF	164.9	0.91	1374.0	-0.05	2.02	0.06
Inconel 625	ST PBF	201.4	0.92	1412.7	0.00	0.02	-0.02
Hastelloy X	ST PBF	69.2	1.43	350.0	-0.11	0.38	-0.27
CM247LC	ST PBF	182.0	1.73	929.1	-0.19	-0.11	-0.10
CMSX-4	ST PBF	162.4	1.36	953.5	-0.08	0.13	-0.13
Waspaloy	ST PBF	225.3	1.36	1074.3	-0.18	-0.02	-0.28
ABD-850AM	ST PBF	296.5	1.65	1981.7	-0.11	0.42	-0.22
ABD-900AM	ST PBF	298.8	0.62	2173.4	0.00	0.00	0.00
AlloyDLD	ST PBF	237.6	1.64	1356.7	-0.06	0.26	-0.16
Inconel 718	BD DED	173.0	0.30	1301.1	0.00	0.01	0.00
Inconel 625	BD DED	201.9	0.87	1460.4	0.00	-0.04	0.01
Hastelloy X	BD DED	63.8	0.74	388.4	-0.18	-0.29	-0.19
CM247LC	BD DED	213.6	1.76	1024.7	-0.05	-0.10	-0.01
CMSX-4	BD DED	169.0	1.13	1025.9	-0.04	-0.06	-0.06
Waspaloy	BD DED	274.0	1.33	1466.8	0.00	-0.05	-0.02
ABD-850AM	BD DED	333.1	1.17	2561.0	0.00	0.01	0.01
ABD-900AM	BD DED	298.5	0.62	2164.9	0.00	-0.01	-0.01
AlloyDLD	BD DED	254.0	1.26	1626.9	0.00	-0.03	0.01
Inconel 718	ST DED	172.0	0.32	1326.2	-0.01	0.07	0.02
Inconel 625	ST DED	196.6	1.26	971.2	-0.03	0.39	-0.33
Hastelloy X	ST DED	77.6	1.07	470.6	0.00	0.03	-0.02

CM247LC	ST DED	222.4	1.93	1029.9	-0.01	-0.01	-0.01
CMSX-4	ST DED	176.0	1.21	1084.6	0.00	0.01	-0.01
Waspaloy	ST DED	272.7	1.40	1510.7	-0.01	0.00	0.01
ABD-850AM	ST DED	326.5	1.15	2551.6	-0.02	-0.01	0.01
ABD-900AM	ST DED	296.9	0.64	2237.5	-0.01	0.02	0.03
AlloyDLD	ST DED	253.5	1.33	1594.9	0.00	0.03	-0.01

Appendix B: L-DED Heat Flow Model

In addition to the samples mentioned in Chapter 8, several wider walls were also printed with the same parameters; these are listed in Table B-1. For each of these, the thermal intensities are plotted in Figure B-1a (moving average with 100 frame window); the average thermal intensity in the top 1 mm of the wall is show in Figure B-1b.

To capture the cooling experienced in the walls the part was split into three temperature regions: molten, hot and cool. The laser scan strategy was followed for the top layer of each wall. The surface area for each temperature range was calculated. Dimensions and average temperatures for each category were taken from literature [295,396]. For simplicity, the molten region was modelled as a cuboid of dimensions 0.5 x 1.1 x 1.5 mm (depth x width x length) with a temperature range of 1600 – 3500 K. The melt pool extended 1 mm behind and 0.5 mm in front of the laser centre (Figure B-2). 1.1 mm was measured as single hatch wall width and was used as the melt pool width throughout; constant melt pool size was used for simplicity for all parameter sets.

Table B-1: Dimensions of additional walls

Number of hatches	Measured sample width (mm)
1	1.1 ± 0.05
2	1.3 ± 0.05
3	1.7 ± 0.05
4	2.1 ± 0.05
6	2.8 ± 0.05
8	3.6 ± 0.05
12	5.1 ± 0.05
16	6.6 ± 0.05
22	9.1 ± 0.05

The hot region was centred on the molten zone, extending 0.5 mm in front of the laser centre. Dimensions used were 2 x 3 x 5 mm (depth x width x length) and a temperature range of 700 – 1600 K (Figure B-2). The rest of the wall was modelled as cool, which covered temperatures of 350 – 700 K, 350 K being the assumed baseplate temperature.

The three main heat flow mechanisms were modelled as follows:

- Radiation from the exposed surfaces to the surrounding environment is frequently not modelled. Heat flow per unit time (W), $q_{rad} = A\varepsilon\sigma(T^4-T_{room}^4)$, was calculated; where A is surface area (m^2), ε is emissivity, σ is the Stefan Boltzmann constant ($5.67x10^{-8}$ $Wm^{-2}K^{-4}$), T and T_{room} are the surface temperature and the room temperature (298 K) respectively (in Kelvin). ε = 0.85 was selected, which is the emissivity of oxidised 718 [397] (in the local argon shielding, samples are still slightly oxidised).
- Conduction occurs from the outer surface to the surrounding Argon, where the heat is spread by convection. This will be referred to as convection. Heat flow per unit time (W); $q_{conv} = hA\Delta T$, where h is the heat transfer coefficient ($Wm^{-2}K^{-1}$), A is the surface area (m^2) and ΔT is the temperature difference between the surface and the atmosphere (298 K). h = 100 $Wm^{-2}K^{-1}$ [295]. Convection within the melt pool (due to Marangoni flow) was ignored because by averaging the melt pool temperature, the temperature variations are removed.
- Conduction through the part into the baseplate, which in this case will only be considered vertically. Heat flow per unit time (W); $q_{cond} = kA\Delta T/L$, where k is the thermal conductivity ($Wm^{-1}K^{-1}$), A is cross-sectional area (m^2), ΔT is the temperature difference between the elevated temperature area and the baseplate (baseplate temperature taken as 350 K) and L is the conduction distance. Room temperature thermal conductivity, k = 9.94 $Wm^{-1}K^{-1}$ was used [273]. 10 mm walls were built on a 5 mm thick baseplate which was clamped to a 40 mm steel table, the bottom of which was assumed to be at 298 K. So for conduction of the molten zone, conduction from 3500 K was calculated at 54 mm (hottest at top surface) and averaged with the conduction from 1600 K at 53.5 mm. This was repeated for all three regions as summarised in Table B-2.

For each temperature range, a heat flow per unit area was calculated as described for both the top and bottom of the temperature range (Table B-2). These were averaged to give a heat flow per unit area for each mechanism, summarised in Table B-3. This is a major simplification, but if done consistently, allows for a direct comparison between the different heat flow mechanisms. The surface areas of each region (per hatch) were divided by the scanning duration to give heat loss per unit time (W), shown in Table B-4. This allowed for 3 different heat flows (conduction, radiation and convection) to be calculated at each temperature range for each wall, which could be summed to give the total heat flow (Table B-4).

Cooling rates (Ks^{-1}) were also calculated, $\dot{T} = q/(V\rho c_p)$ where V is volume (m^3), ρ is density (8100 kgm^{-3} [396]) and c_p is specific heat capacity (425 $Jkg^{-1}K^{-1}$ [273]). Volume per second was calculated using a hatch volume (width 1.1 mm, depth 0.5 mm, length 20 mm) and dividing by hatch duration (0.6 s).

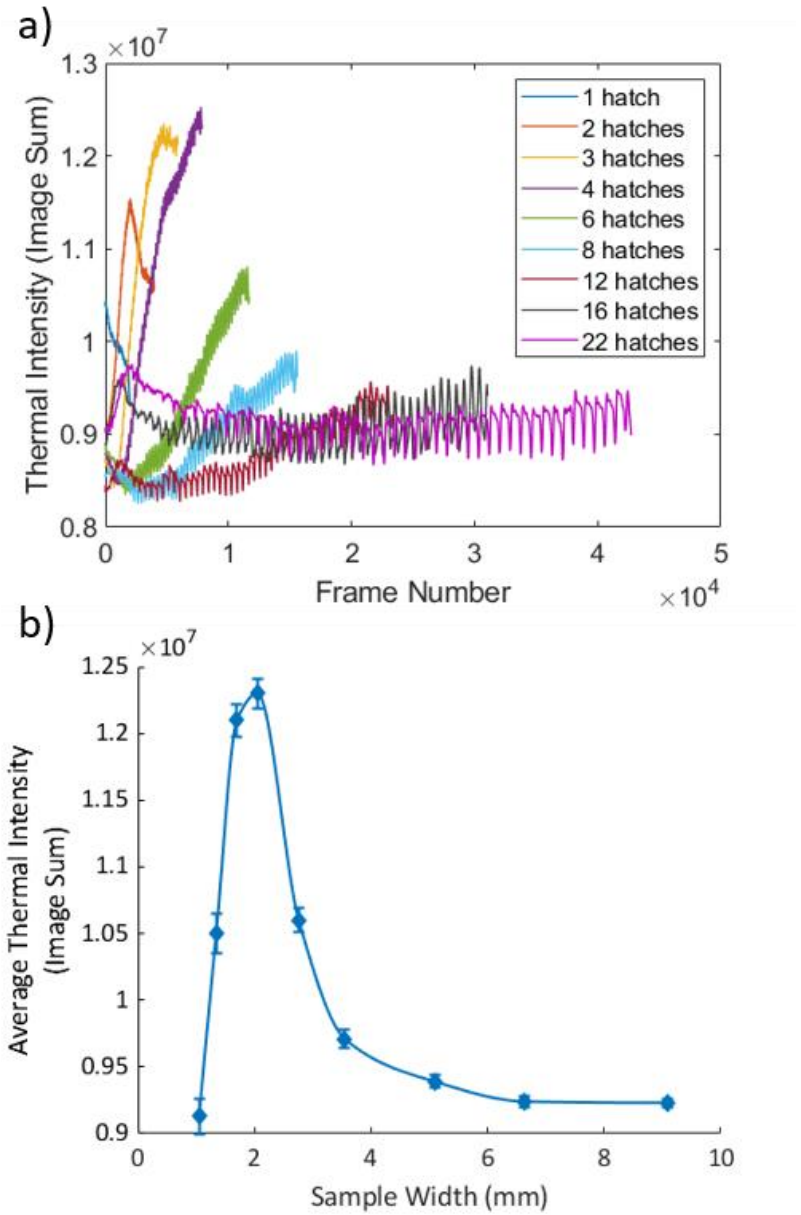

Figure B-1: Changes in thermal intensity for 9 wall thicknesses; a) variation with time; b) Average image intensity of top 1 mm plotted against sample width (standard error shown)

The various heat flow contributions are shown in Figure 10-24. Given that most thermal intensities hadn't reached a plateau, the heat flow must be lower than the input laser power (300 W). The calculated cooling is around 90 W, which is lower than expected. However, only conduction in the build direction is considered; in larger parts, lateral conduction in the other two axes will also be significant. This won't be as large as the build direction, but in combination could be expected to be of a similar magnitude. In addition, a flat melt pool surface is modelled, the addition of material actually leads to a semi cylindrical surface, which is around a factor of 2 larger when considering the melt pool shape due to laser recoil. Finally, radiation $\propto T^4$, so by averaging the heat flow due to radiation across regions of varying temperature, the increased cooling from the hottest regions will be ignored.

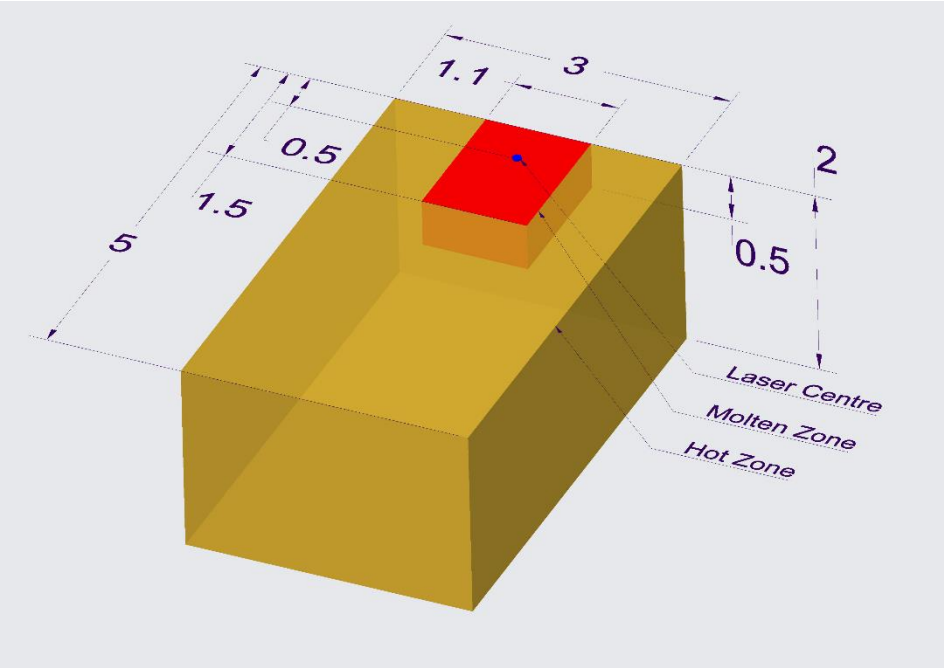

Figure B-2: Diagram showing dimensions of molten and hot zones

Table B-2: Breakdown of heat flow contributions at region limits. For conduction, different temperatures were experienced at different conduction distances; the pairs of values at limits of the same region are marked with the same symbol (^ “)*

Temperature (K)	Heat flow due to Radiation (W/m^2)	Heat flow due to Convection (W/m^2)		Heat flow due to Conduction at 54 mm (W/m^2)	Heat flow due to Conduction at Secondary Distance (W/m^2)	Secondary Distance (mm)
350	343.2	5200			* 11747.3	44
700	11192.1	40200		* 73997.8	^ 76843.8	52
1600	315487.4	130200		^ 239664.4	“ 44523665.0	53.5
3500	7232264.8	320200		“ 589405.2		

These model simplifications explain the low cooling values calculated and would bring them in line with the heat input. Both radiation and conduction areas are underestimated by a similar magnitude and both scale linearly with area, so the ratio of these isn’t expected to change significantly. Radiation is dominant in thin walls as the sides of the wall are hotter due to their proximity to the laser position, but this effect decays quickly with width. Temperature is expected to have an inverse relationship with cooling; this is seen when comparing Figure B-2b with total cooling from Figure 10-24, increasing confidence in the model.

Most models assume that conduction is the sole heat flow mechanism, in bulk parts this is assumption works, as conduction is dominant. However, Figure 10-24 suggests that in thin components, the other flow mechanisms are no longer insignificant, radiation adding a

significant heat loss contribution. The model predicts conduction to keep increasing with component size, which doesn't occur above 6 mm width. At this point, the width is sufficient that conduction could occur both laterally and vertically, so the effect of increasing the vertical conduction area becomes negligible.

Table B-3: Summary of final heat flows used for each region (averaged from Table B-2)

Zone	Temperature Range (K)	Heat flow due to Radiation (W/m^2)	Heat flow due to Convection (W/m^2)	Heat flow due to Conduction (W/m^2)
Cool	350 - 700	5767.655	22700	42872.5
Hot	700 - 1600	163339.8	85200	158254.1
Molten	1600 - 3500	3773876	225200	22556535.1

Cooling rates were calculated to be of the order 10^3 Ks^{-1} which is in line with literature [104,105]. Cooling rate decreases monotonically with increasing thermal intensity (Figure B-3). The image sums are shown to be proportional to both melt pool area and maximum intensity. The relationship in Figure B-3 confirms the monotonic trend between melt pool size and cooling rate as seen in literature.

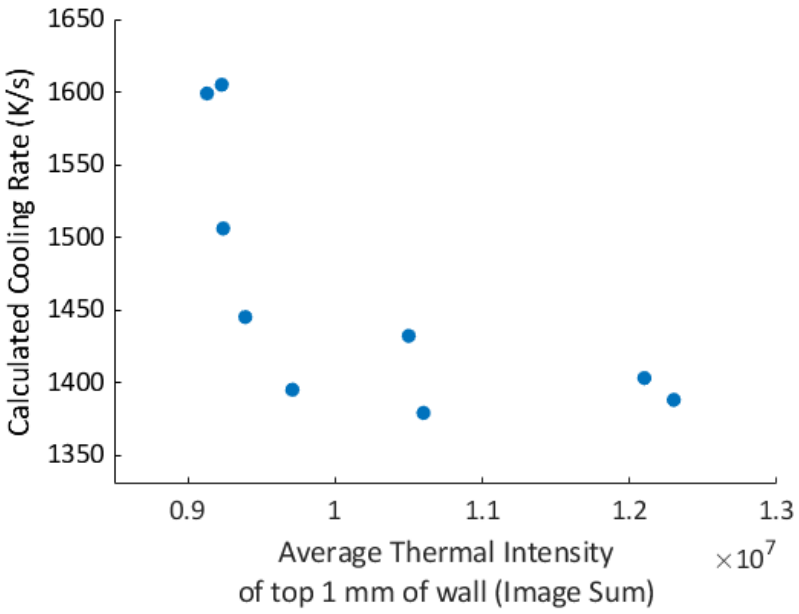

Figure B-3: Calculated cooling rates of walls plotted against the average image sums

Table B-4: Summary of component dimensions, surface areas of each region for each wall and the calculated heat loss by each heat loss mechanisms. Total cooling and calculated cooling rates also shown

Hatches	Width (mm)	Length (mm)	Height (mm)	Layer Duration (s)	Molten top area/hatch (mm^2)	Hot top area/hatch (mm^2)	Cool top area/hatch (mm^2)	Total Molten area/hatch (mm^2)	Total hot area/hatch (mm^2)	Total cool area/hatch (mm^2)	Total Convection (W)	Total Conduction (W)	Total Radiation (W)	Total Cooling (W)	Vol of hatch (m^3)	Cooling Rate of hatch (K/s)
1	1.1	20	10	0.61	1.62	3.10	13.29	3.13	20.06	415.81	19.5	52.7	28.8	100.9	0.018	1599
2	1.3	20	10	1.32	1.62	4.41	19.97	2.39	22.26	428.22	18.4	49.1	22.9	90.4	0.018	1432
3	1.7	20	10	2.04	1.62	6.01	26.37	2.15	24.28	441.57	18.5	48.5	21.5	88.6	0.018	1403
4	2.1	20	10	2.75	1.62	8.37	32.02	2.02	22.54	458.44	18.6	48.7	20.3	87.6	0.018	1388
6	2.8	20	10	4.18	1.62	9.27	47.12	1.90	19.17	492.13	19.0	49.2	18.9	87.0	0.018	1379
8	3.6	20	10	5.61	1.62	9.91	62.47	1.84	17.70	525.46	19.7	49.9	18.3	88.0	0.018	1395
12	5.1	20	10	8.47	1.62	10.56	93.83	1.78	16.24	589.78	21.5	51.7	18.1	91.2	0.018	1445
16	6.6	20	10	11.33	1.62	10.88	125.51	1.75	15.50	653.55	23.4	53.5	18.2	95.1	0.018	1506
22	9.1	20	10	15.62	1.62	11.14	173.24	1.72	14.90	750.97	26.3	56.3	18.7	101.3	0.018	1605

Bibliography

[1] Standard Terminology for Additive Manufacturing Technologies F2792, 2013. doi:10.1520/F2792-12A.2.

[2] J.-C. Andre, A. Le Mehaute, O. De Witte, Patent FR 2567668, FR 2567668, 1984.

[3] W.T. Carter, M.G. Jones, Direct Laser Sintering of Metals, Proceeding SFF Symp. (1993) 51–9. https://sffsymposium.engr.utexas.edu/Manuscripts/1993/1993-05-Carter.pdf.

[4] T. DebRoy, H.L. Wei, J.S. Zuback, T. Mukherjee, J.W. Elmer, J.O. Milewski, A.M. Beese, A. Wilson-Heid, A. De, W. Zhang, Additive manufacturing of metallic components – Process, structure and properties, Prog. Mater. Sci. 92 (2018) 112–224. doi:10.1016/j.pmatsci.2017.10.001.

[5] N. Guo, M.C. Leu, Additive manufacturing: Technology, applications and research needs, Front. Mech. Eng. 8 (2013) 215–243. doi:10.1007/s11465-013-0248-8.

[6] B. Blakey-Milner, P. Gradl, G. Snedden, M. Brooks, J. Pitot, E. Lopez, M. Leary, F. Berto, Metal additive manufacturing in aerospace : A review, Mater. Des. 209 (2021) 110008. doi:10.1016/j.matdes.2021.110008.

[7] T. DebRoy, T. Mukherjee, J.O. Milewski, J.W. Elmer, B. Ribic, J.J. Blecher, W. Zhang, Scientific, technological and economic issues in metal printing and their solutions, Nat. Mater. 18 (2019) 1026–1032. doi:10.1038/s41563-019-0408-2.

[8] GEAdditive, New manufacturing milestone: 30,000 additive fuel nozzles, (2018). https://www.ge.com/additive/stories/new-manufacturing-milestone-30000-additive-fuel-nozzles (accessed October 11, 2021).

[9] J. Scott, N. Gupta, C. Weber, S. Newsome, Additive manufacturing: Status and opportunities, Sci. Technol. Policy Inst. (2012) 1–19. https://cgsr.llnl.gov/content/assets/docs/IDA_AdditiveM3D_33012_Final.pdf.

[10] G. Tapia, A. Elwany, A Review on Process Monitoring and Control in Metal-Based Additive Manufacturing, J. Manuf. Sci. Eng. 136 (2014) 060801. doi:10.1115/1.4028540.

[11] S.K. Everton, M. Hirsch, P. Stravroulakis, R.K. Leach, A.T. Clare, Review of in-situ process monitoring and in-situ metrology for metal additive manufacturing, Mater. Des. 95 (2016) 431–445. doi:10.1016/j.matdes.2016.01.099.

[12] A.T. Clare, R.S. Mishra, M. Merklein, H. Tan, I. Todd, L. Chechik, J. Li, M. Bambach, Alloy design and adaptation for additive manufacture, J. Mater. Process. Technol. 299 (2022). doi:10.1016/j.jmatprotec.2021.117358.

[13] S.M. Thompson, L. Bian, N. Shamsaei, A. Yadollahi, An overview of Direct Laser Deposition for additive manufacturing; Part I: Transport phenomena, modeling and diagnostics, Addit. Manuf. 8 (2015) 36–62. doi:10.1016/j.addma.2015.07.001.

[14] W.J. Sames, K.A. Unocic, R.R. Dehoff, T. Lolla, S.S. Babu, F.A. List, S. Pannala, R.R. Dehoff, S.S. Babu, K.A. Unocic, R.R. Dehoff, T. Lolla, S.S. Babu, Thermal effects on microstructural heterogeneity of Inconel 718 materials fabricated by electron beam melting, J. Mater. Res. 29 (2014) 1920–1930. doi:10.1557/jmr.2014.140.

[15] E.A. Jägle, Z. Sheng, L. Wu, L. Lu, J. Risse, A. Weisheit, D. Raabe, Precipitation Reactions in Age-

Hardenable Alloys During Laser Additive Manufacturing, Jom. 68 (2016) 943–949. doi:10.1007/s11837-015-1764-2.

[16] K. Kempen, L. Thijs, B. Vrancken, J. Van Humbeeck, J.-P. Kruth, Producing Crack-Free, High Density M2 HSS Parts By Selective Laser Melting: Pre-Heating the Baseplate, Proc. 24th Int. Solid Free. Fabr. Symp. (2013) 131–139. http://utw10945.utweb.utexas.edu/Manuscripts/2013/2013-10-Kempen.pdf.

[17] T. Mukherjee, V. Manvatkar, A. De, T. DebRoy, Dimensionless numbers in additive manufacturing, J. Appl. Phys. 121 (2017). doi:10.1063/1.4976006.

[18] W. Kurz, R. Trivedi, Rapid solidification processing and microstructure formation, Mater. Sci. Eng. A. 179–180 (1994) 46–51. doi:10.1016/0921-5093(94)90162-7.

[19] M.J. Aziz, T. Kaplan, Continuous Growth Model for Interface Motion during Alloy Solidification, Acta Metall. Mater. 36 (1988) 2335–2347. doi:10.1016/0001-6160(88)90333-1.

[20] C. Arnold, M. Aziz, M. Schwarz, D. Herlach, Parameter-free test of alloy dendrite-growth theory, Phys. Rev. B - Condens. Matter Mater. Phys. 59 (1999) 334–343. doi:10.1103/PhysRevB.59.334.

[21] B. Giovanola, W. Kurz, Modeling of microsegregation under rapid solidification conditions, Metall. Trans. A. 21 (1990) 260–263. doi:10.1007/BF02656445.

[22] M. Zimmermann, M. Carrard, W. Kurz, Rapid solidification of Al-Cu eutectic alloy by laser remelting, Acta Metall. 37 (1989) 3305–3313. doi:10.1016/0001-6160(89)90203-4.

[23] N.J. Harrison, I. Todd, K. Mumtaz, Reduction of micro-cracking in nickel superalloys processed by Selective Laser Melting: A fundamental alloy design approach, Acta Mater. 94 (2015) 59–68. doi:10.1016/j.actamat.2015.04.035.

[24] H. Knoll, S. Ocylok, A. Weisheit, H. Springer, E. Jägle, D. Raabe, Combinatorial Alloy Design by Laser Additive Manufacturing, Steel Res. Int. 88 (2017) 1–11. doi:10.1002/srin.201600416.

[25] N. Shamsaei, A. Yadollahi, L. Bian, S.M. Thompson, An overview of Direct Laser Deposition for additive manufacturing; Part II: Mechanical behavior, process parameter optimization and control, Addit. Manuf. 8 (2015) 12–35. doi:10.1016/j.addma.2015.07.002.

[26] U. Scipioni Bertoli, G. Guss, S. Wu, M.J. Matthews, J.M. Schoenung, In-situ characterization of laser-powder interaction and cooling rates through high-speed imaging of powder bed fusion additive manufacturing, Mater. Des. 135 (2017) 385–396. doi:10.1016/j.matdes.2017.09.044.

[27] W. Kurz, D.J. Fisher, Dendrite Growth at the Limit of Stability: Tip Radius and Spacing, Acta Metall. 29 (1981) 11–20. doi:10.1016/0001-6160(81)90082-1.

[28] A.M. Mullis, R.F. Cochrane, N.J. Adkins, Estimation of Cooling Rates During Close-Coupled Gas Atomization using Secondary Dendrite Arm Spacing Measurement, Metall. Mater. Trans. B Process Metall. Mater. Process. Sci. 44 (2013) 992–999. doi:10.1186/1742-7622-5-2.

[29] V. Manvatkar, A. De, T. Debroy, Heat transfer and material flow during laser assisted multi-layer additive manufacturing, J. Appl. Phys. 116 (2014). doi:10.1063/1.4896751.

[30] T. Mukherjee, W. Zhang, T. DebRoy, An improved prediction of residual stresses and distortion in additive manufacturing, Comput. Mater. Sci. 126 (2017) 360–372. doi:10.1016/j.commatsci.2016.10.003.

[31] D. Rosenthal, The Theory of Moving Sources of Heat and Its Application to Metal Treatments, Trans. Am. Soc. Mech. Eng. 43 (1946) 849–866.

[32] M.F. Ashby, K.E. Easterling, The transformation hardening of steel surfaces by laser beams-I.

Hypo-eutectoid steels, Acta Metall. 32 (1984) 1935–1948. doi:10.1016/0001-6160(84)90175-5.

[33] M. Gäumann, C. Bezençon, P. Canalis, W. Kurz, Single-crystal laser deposition of superalloys: Processing-microstructure maps, Acta Mater. 49 (2001) 1051–1062. doi:10.1016/S1359-6454(00)00367-0.

[34] T.W. Eagar, N.S. Tsai, Temperature fields produced by traveling distributed heat sources, Weld. J. 62 (1983) 346–355.

[35] C.D. Boley, S.A. Khairallah, A.M. Rubenchik, Calculation of laser absorption by metal powders in additive manufacturing, Appl. Opt. 54 (2015) 2477. doi:10.1364/AO.54.002477.

[36] F. Dausinger, J. Shen, Energy Coupling Efficiency In Laser Surface Treatment, ISIJ Int. 33 (1993) 925–933. doi:10.2355/isijinternational.33.925.

[37] A. Rubenchik, S. Wu, S. Mitchell, I. Golosker, M. LeBlanc, N. Peterson, Direct measurements of temperature-dependent laser absorptivity of metal powders, Appl. Opt. 54 (2015) 7230. doi:10.1364/AO.54.007230.

[38] J. Trapp, A.M. Rubenchik, G. Guss, M.J. Matthews, In situ absorptivity measurements of metallic powders during laser powder-bed fusion additive manufacturing, Appl. Mater. Today. 9 (2017) 341–349. doi:10.1016/j.apmt.2017.08.006.

[39] M. Picasso, C.F. Marsden, J.D. Wagniere, A. Frenk, M. Rappaz, A simple but realistic model for laser cladding, Metall. Mater. Trans. B. 25 (1994) 281–291. doi:10.1007/BF02665211.

[40] A. Dass, A. Moridi, State of the art in directed energy deposition: From additive manufacturing to materials design, Coatings. 9 (2019) 1–26. doi:10.3390/COATINGS9070418.

[41] T. Mukherjee, J.S. Zuback, A. De, T. DebRoy, Printability of alloys for additive manufacturing, Sci. Rep. 6 (2016) 19717. doi:10.1038/srep19717.

[42] T. Mukherjee, T. DebRoy, Mitigation of lack of fusion defects in powder bed fusion additive manufacturing, J. Manuf. Process. 36 (2018) 442–449. doi:10.1016/j.jmapro.2018.10.028.

[43] A. Raghavan, H.L. Wei, T.A. Palmer, T. DebRoy, Heat transfer and fluid flow in additive manufacturing, J. Laser Appl. 25 (2013) 052006. doi:10.2351/1.4817788.

[44] T. DebRoy, W. Zhang, J. Turner, S.S. Babu, Building digital twins of 3D printing machines, Scr. Mater. 135 (2017) 119–124. doi:10.1016/j.scriptamat.2016.12.005.

[45] W. King, A.T. Anderson, R.M. Ferencz, N.E. Hodge, C. Kamath, S.A. Khairallah, Overview of modelling and simulation of metal powder bed fusion process at Lawrence Livermore National Laboratory, Mater. Sci. Technol. 31 (2015) 957–968. doi:10.1179/1743284714Y.0000000728.

[46] C. Körner, A. Bauereiß, E. Attar, Fundamental consolidation mechanisms during selective beam melting of powders, Model. Simul. Mater. Sci. Eng. 21 (2013) 1–18. doi:10.1088/0965-0393/21/8/085011.

[47] J. Li, C. Myant, B. Wu, The Current Landscape for Additive Manufacturing Research, Imp. Coll. Addit. Manuf. Netw. 2016 ICL A (2016) 1–83. https://spiral.imperial.ac.uk/handle/10044/1/39726.

[48] T.M. Pollock, A.J. Clarke, S.S. Babu, Design and Tailoring of Alloys for Additive Manufacturing, Metall. Mater. Trans. A Phys. Metall. Mater. Sci. 51 (2020) 6000–6019. doi:10.1007/s11661-020-06009-3.

[49] C. Körner, M. Ramsperger, C. Meid, D. Bürger, P. Wollgramm, M. Bartsch, G. Eggeler, Microstructure and Mechanical Properties of CMSX-4 Single Crystals Prepared by Additive

Manufacturing, Metall. Mater. Trans. A. (2018). doi:10.1007/s11661-018-4762-5.

[50] M. Ramsperger, C. Körner, Selective electron beam melting of the single crystalline nickel-base superalloy CMSX-4®: From columnar grains to a single crystal, in: Superalloys 2016 Proc. 13th Int. Symp. Superalloys, Seven Springs, Pennsylvania, 2016: pp. 341–349. doi:10.1002/9781119075646.ch37.

[51] Subhash Mahajan, Encyclopedia of Materials: Science and Technology - 1st Edition, Pergamon. (2001).

[52] X. Zhao, S. Li, M. Zhang, Y. Liu, T.B. Sercombe, S. Wang, Y. Hao, R. Yang, L.E. Murr, Comparison of the microstructures and mechanical properties of Ti-6Al-4V fabricated by selective laser melting and electron beam melting, Mater. Des. 95 (2016) 21–31. doi:10.1016/j.matdes.2015.12.135.

[53] ABD-900AM, Oxmet Technol. (2021). https://uploads-ssl.webflow.com/5beae18915bc0db1ee3fa25d/5dfb6119d19f967e1e57decb_OxMet Technologies - ABD-900AM datasheet.pdf.

[54] L.N. Carter, C. Martin, P.J. Withers, M.M. Attallah, The influence of the laser scan strategy on grain structure and cracking behaviour in SLM powder-bed fabricated nickel superalloy, J. Alloys Compd. 615 (2014) 338–347. doi:10.1016/j.jallcom.2014.06.172.

[55] K. Schmidtke, F. Palm, A. Hawkins, C. Emmelmann, Process and mechanical properties: Applicability of a scandium modified Al-alloy for laser additive manufacturing, Phys. Procedia. 12 (2011) 369–374. doi:10.1016/j.phpro.2011.03.047.

[56] Y.T. Tang, C. Panwisawas, J.N. Ghoussoub, Y. Gong, J.W.G. Clark, A.A.N. Németh, D.G. McCartney, R.C. Reed, Alloys-by-design: Application to new superalloys for additive manufacturing, Acta Mater. 202 (2021) 417–436. doi:10.1016/j.actamat.2020.09.023.

[57] J.O. Milwaki, Additive Manufacturing of Metals: From Fundamental Technology to Rocket Nozzles, Medical Implants, and Custom Jewelry, Springer International Publishing, 2017. doi:10.1007/978-3-319-58205-4.

[58] B. Zheng, J.C. Haley, N. Yang, J. Yee, K.W. Terrassa, Y. Zhou, E.J. Lavernia, J.M. Schoenung, On the evolution of microstructure and defect control in 316L SS components fabricated via directed energy deposition, Mater. Sci. Eng. A. 764 (2019) 138243. doi:10.1016/j.msea.2019.138243.

[59] A. Saboori, A. Aversa, G. Marchese, S. Biamino, M. Lombardi, P. Fino, Microstructure and mechanical properties of AISI 316L produced by directed energy deposition-based additive manufacturing: A review, Appl. Sci. 10 (2020). doi:10.3390/app10093310.

[60] Y.M. Wang, T. Voisin, J.T. McKeown, J. Ye, N.P. Calta, Z. Li, Z. Zeng, Y. Zhang, W. Chen, T.T. Roehling, R.T. Ott, M.K. Santala, P.J. Depond, M.J. Matthews, A. V. Hamza, T. Zhu, Additively manufactured hierarchical stainless steels with high strength and ductility, Nat. Mater. 17 (2018) 63–70. doi:10.1038/NMAT5021.

[61] R. Bowman (TMS), Superalloys: A Primer and History, 9th Int. Symp. Superalloys. (2000). http://www.tms.org/meetings/specialty/superalloys2000/superalloyshistory.html.

[62] M.J. Donachie, S.J. Donachie, Superalloys: A Technical Guide, 2nd ed., ASM International, 2002.

[63] C.T. Sims, N.S. Stoloff, W.C. Hagel, Superalloys II: High-Temperature Materials for Aerospace and Industrial Power, John Wiley & Sons, 1987.

[64] L.N. Carter, M.M. Attallah, R.C. Reed, Laser Powder Bed Fabrication of Nickel-Base Superalloys : Influence of Parameters ; Characterisation, Quantification and Mitigation of Cracking, Superalloys 2012. (2012) 577–586. doi:10.1002/9781118516430.ch64.

[65] M.M. Attallah, R. Jennings, X. Wang, L.N. Carter, Additive manufacturing of Ni-based superalloys: The outstanding issues, MRS Bull. 41 (2016) 758–764. doi:10.1557/mrs.2016.211.

[66] R.A. Rahman Rashid, S. Abaspour, S. Palanisamy, N. Matthews, M.S. Dargusch, Metallurgical and geometrical characterisation of the 316L stainless steel clad deposited on a mild steel substrate, Surf. Coatings Technol. 327 (2017) 174–184. doi:10.1016/j.surfcoat.2017.08.013.

[67] S. Sanchez, G. Gaspard, C.J. Hyde, I.A. Ashcroft, G.A. Ravi, A.T. Clare, The creep behaviour of nickel alloy 718 manufactured by laser powder bed fusion, Mater. Des. 204 (2021) 109647. doi:10.1016/j.matdes.2021.109647.

[68] Z. Song, W. Gao, D. Wang, Z. Wu, M. Yan, L. Huang, X. Zhang, Very-high-cycle fatigue behavior of inconel 718 alloy fabricated by selective laser melting at elevated temperature, Materials (Basel). 14 (2021) 1–16. doi:10.3390/ma14041001.

[69] K.T. Son, T.Q. Phan, L.E. Levine, K.S. Kim, K.A. Lee, M. Ahlfors, M.E. Kassner, The creep and fracture properties of additively manufactured inconel 625, Materialia. 15 (2021) 101021. doi:10.1016/j.mtla.2021.101021.

[70] G.E. Bean, D.B. Witkin, T.D. McLouth, D.N. Patel, R.J. Zaldivar, Effect of laser focus shift on surface quality and density of Inconel 718 parts produced via selective laser melting, Addit. Manuf. 22 (2018) 207–215. doi:10.1016/j.addma.2018.04.024.

[71] S. Sanchez, P. Smith, Z. Xu, G. Gaspard, C.J. Hyde, W.W. Wits, I.A. Ashcroft, H. Chen, A.T. Clare, Powder Bed Fusion of nickel-based superalloys: A review, Int. J. Mach. Tools Manuf. 165 (2021). doi:10.1016/j.ijmachtools.2021.103729.

[72] D. Deng, J. Moverare, R.L. Peng, H. Söderberg, Microstructure and anisotropic mechanical properties of EBM manufactured Inconel 718 and effects of post heat treatments, Mater. Sci. Eng. A. 693 (2017) 151–163. doi:10.1016/j.msea.2017.03.085.

[73] H. Qi, M. Azer, A. Ritter, Studies of standard heat treatment effects on microstructure and mechanical properties of laser net shape manufactured Inconel 718, Metall. Mater. Trans. A Phys. Metall. Mater. Sci. 40 (2009) 2410–2422. doi:10.1007/s11661-009-9949-3.

[74] I. Yadroitsev, L. Thivillon, P. Bertrand, I. Smurov, Strategy of manufacturing components with designed internal structure by selective laser melting of metallic powder, Appl. Surf. Sci. 254 (2007) 980–983. doi:10.1016/j.apsusc.2007.08.046.

[75] L.E. Murr, E. Martinez, S.M. Gaytan, D.A. Ramirez, B.I. MacHado, P.W. Shindo, J.L. Martinez, F. Medina, J. Wooten, D. Ciscel, U. Ackelid, R.B. Wicker, Microstructural architecture, microstructures, and mechanical properties for a nickel-base superalloy fabricated by electron beam melting, Metall. Mater. Trans. A Phys. Metall. Mater. Sci. 42 (2011) 3491–3508. doi:10.1007/s11661-011-0748-2.

[76] M. Rombouts, G. Maes, M. Mertens, W. Hendrix, Laser metal deposition of Inconel 625: Microstructure and mechanical properties, J. Laser Appl. 24 (2012) 052007. doi:10.2351/1.4757717.

[77] N.J. Marchand, R.M. Pelloux, B. Ilschner, A fracture mechanics criterion for thermal-mechanical fatigue crack growth of gas turbine materials, Eng. Fract. Mech. 31 (1988) 535–551. doi:10.1016/0013-7944(88)90095-1.

[78] Q. Han, R. Mertens, M.L. Montero-Sistiaga, S. Yang, R. Setchi, K. Vanmeensel, B. Van Hooreweder, S.L. Evans, H. Fan, Laser powder bed fusion of Hastelloy X: Effects of hot isostatic pressing and the hot cracking mechanism, Mater. Sci. Eng. A. 732 (2018) 228–239. doi:10.1016/j.msea.2018.07.008.

[79] S. Dryepondt, M. Kirka, F.A. List, Microstructure and Properties of Hastelloy X Fabricated by Additive Manufacturing Many Exciting Research Topics on Additive Manufacturing, 2017. https://www.netl.doe.gov/sites/default/files/netl-file/20180410_1600A_Presentation_FWP-FEAA119_ORNL.pdf.

[80] F. Wang, X.H. Wu, D. Clark, On direct laser deposited Hastelloy X: Dimension, surface finish, microstructure and mechanical properties, Mater. Sci. Technol. 27 (2011) 344–356. doi:10.1179/026708309X12578491814591.

[81] U. Scipioni Bertoli, A.J. Wolfer, M.J. Matthews, J.P.R. Delplanque, J.M. Schoenung, On the limitations of Volumetric Energy Density as a design parameter for Selective Laser Melting, Mater. Des. 113 (2017) 331–340. doi:10.1016/j.matdes.2016.10.037.

[82] M. Thomas, G.J. Baxter, I. Todd, Normalised model-based processing diagrams for additive layer manufacture of engineering alloys, Acta Mater. 108 (2016) 26–35. doi:10.1016/j.actamat.2016.02.025.

[83] W.E. King, H.D. Barth, V.M. Castillo, G.F. Gallegos, J.W. Gibbs, D.E. Hahn, C. Kamath, A.M. Rubenchik, Observation of keyhole-mode laser melting in laser powder-bed fusion additive manufacturing, J. Mater. Process. Technol. 214 (2014) 2915–2925. doi:10.1016/j.jmatprotec.2014.06.005.

[84] D.B. Hann, J. Iammi, J. Folkes, A simple methodology for predicting laser-weld properties from material and laser parameters, J. Phys. D. Appl. Phys. 44 (2011). doi:10.1088/0022-3727/44/44/445401.

[85] H.D. Baehr, K. Stephan, Heat and Mass Transfer, Second, Springer, 2006. doi:10.1017/CBO9781107415324.004.

[86] M. Tang, P.C. Pistorius, J.L. Beuth, Prediction of lack-of-fusion porosity for powder bed fusion, Addit. Manuf. 14 (2017) 39–48. doi:10.1016/j.addma.2016.12.001.

[87] D.J. Tillack, Nickel alloys and stainless steels for elevated temperature service : weldability considerations, Proc. from Mater. Solut. 97 Join. Repair Gas Turbine Components. (1997) 29–40.

[88] O. Hunziker, D. Dye, R.C. Reed, On the formation of a centerline grain boundary during fusion welding, Acta Mater. 48 (2000) 4191–4201. doi:10.1016/S1359-6454(00)00273-1.

[89] A. Vasinonta, J.L. Beuth, R. Ong, Melt Pool Size Control in Thin-Walled and Bulky Parts via Process Maps, Proc. 12th Solid Free. Fabr. Symp. (2001) 432–440. doi:10.26153/tsw/3337.

[90] A. Vasinonta, J. Beuth, Process Maps for Controlling Residual Stress and Melt Pool Size in Laser-Based SFF Processes, Proc. 2000 Solid Free. Fabr. Symp. Solid Free. Fabr. Symp. (2000) 200–208.

[91] S. Bontha, N.W. Klingbeil, Thermal Process Maps for Controlling Microstructure in Laser-Based Solid Freeform Fabrication, Solid Free. Fabr. Symp. (2003) 219–226. doi:10.26153/tsw/5557.

[92] S. Bontha, The Effect of Process Variables on Microstructure in Laser-Deposited Materials, Wright State University, 2006.

[93] S.H. Sun, T. Ishimoto, K. Hagihara, Y. Tsutsumi, T. Hanawa, T. Nakano, Excellent mechanical and corrosion properties of austenitic stainless steel with a unique crystallographic lamellar microstructure via selective laser melting, Scr. Mater. 159 (2019) 89–93. doi:10.1016/j.scriptamat.2018.09.017.

[94] O. Gokcekaya, T. Ishimoto, S. Hibino, J. Yasutomi, T. Narushima, T. Nakano, Unique crystallographic texture formation in Inconel 718 by laser powder bed fusion and its effect on mechanical anisotropy, Acta Mater. 212 (2021) 116876. doi:10.1016/j.actamat.2021.116876.

[95] C. Guévenoux, S. Hallais, A. Charles, E. Charkaluk, A. Constantinescu, Influence of interlayer dwell time on the microstructure of Inconel 718 Laser Cladded components, Opt. Laser Technol. 128 (2020) 106218. doi:10.1016/j.optlastec.2020.106218.

[96] W. Kurz, C. Bezençon, M. Gäumann, Columnar to equiaxed transition in solidification processing, Sci. Technol. Adv. Mater. 2 (2001) 185–191. doi:10.1016/S1468-6996(01)00047-X.

[97] W. Kurz, D.J. Fisher, Fundamentals of Solidification, 4th ed., Trans Tech Publications, 1998.

[98] R. Trivedi, Interdendritic Spacing: Part II. A Comparison of Theory and Experiment, Metall. Trans. A. 15 (1984) 977–982. doi:10.1007/BF02644689.

[99] N. Raghavan, S. Simunovic, R. Dehoff, A. Plotkowski, J. Turner, M. Kirka, S. Babu, Localized melt-scan strategy for site specific control of grain size and primary dendrite arm spacing in electron beam additive manufacturing, Acta Mater. 140 (2017) 375–387. doi:10.1016/j.actamat.2017.08.038.

[100] W. Wang, P.D. Lee, M. McLean, A model of solidification microstructures in nickel-based superalloys: Predicting primary dendrite spacing selection, Acta Mater. 51 (2003) 2971–2987. doi:10.1016/S1359-6454(03)00110-1.

[101] J.D. Hunt, Steady state columnar and equiaxed growth of dendrites and eutectic, Mater. Sci. Eng. 65 (1984) 75–83. doi:10.1016/0025-5416(84)90201-5.

[102] R.R. Dehoff, M.M. Kirka, W.J. Sames, H. Bilheux, A.S. Tremsin, L.E. Lowe, S.S. Babu, Site specific control of crystallographic grain orientation through electron beam additive manufacturing, Mater. Sci. Technol. 31 (2015) 931–938. doi:10.1179/1743284714Y.0000000734.

[103] N. Raghavan, R. Dehoff, S. Pannala, S. Simunovic, M. Kirka, J. Turner, N. Carlson, S.S. Babu, Numerical modeling of heat-transfer and the influence of process parameters on tailoring the grain morphology of IN718 in electron beam additive manufacturing, Acta Mater. 112 (2016) 303–314. doi:10.1016/j.actamat.2016.03.063.

[104] L. Chechik, N.A. Boone, L.R. Stanger, P. Honniball, F. Freeman, G. Baxter, J.R. Willmott, I. Todd, Variation of texture anisotropy and hardness with build parameters and wall height in directed-energy-deposited 316L steel, Addit. Manuf. 38 (2021) 101806. doi:10.1016/j.addma.2020.101806.

[105] W. Hofmeister, M. Griffith, M. Ensz, J. Smugeresky, Solidification in direct metal deposition by LENS processing, JOM. 53 (2001) 30–34. doi:10.1007/s11837-001-0066-z.

[106] A.A. Kazakov, Alloy Compositions for Semisolid Forming, Adv. Mater. Process. 157 (2000) 31–34.

[107] J. Lecomte-Beckers, A. Rassili, M. Carton, M. Robelet, Study of liquid fraction evolution of semi-solid steels for thixoforming, in: Proc. 8th ESAFORM Conf. Mater. Form., Cluj-Napoca, 2005: pp. 1087–1090.

[108] J. Lecomte-Beckers, A. Rassili, M. Carton, M. Robelet, R. Koeune, Study of the liquid fraction and thermophysical properties of semi-solid steels and application to the simulation of inductive heating for thixoforming, in: Adv. Methods Mater. Form., Springer, 2007: pp. 321–347. doi:10.1007/3-540-69845-0_20.

[109] D. Liu, H. V. Atkinson, H. Jones, Thermodynamic prediction of thixoformability in alloys based on the Al-Si-Cu and Al-Si-Cu-Mg systems, Acta Mater. 53 (2005) 3807–3819. doi:10.1016/j.actamat.2005.04.028.

[110] N. Boone, C. Zhu, C. Smith, I. Todd, J.R. Willmott, Thermal near infrared monitoring system for electron beam melting with emissivity tracking, Addit. Manuf. 22 (2018) 601–605.

doi:10.1016/j.addma.2018.06.004.

[111] Hamamatsu, ORCA-Flash4.0 V3 Technical Note, (2018). https://www.hamamatsu.com/content/dam/hamamatsu-photonics/sites/documents/99_SALES_LIBRARY/sys/SCAS0134E_C13440-20CU_tec.pdf.

[112] L. Michalski, K. Eckersdorf, J. Kucharski, J. McGhee, Temperature Measurement, Second, 2001.

[113] C. Hole, Cost and practicality of in-process monitoring for metal Additive Manufacturing, Met. Addit. Manuf. 2 (2016) 63–69.

[114] B.M. Lane, E.P. Whitenton, Calibration and Measurement Procedures for a High Magnification Thermal Camera, Natl. Inst. Stand. Technol. (2016). doi:10.6028/NIST.IR.8098.

[115] E. Rodriguez, J. Mireles, C.A. Terrazas, D. Espalin, M.A. Perez, R.B. Wicker, Approximation of absolute surface temperature measurements of powder bed fusion additive manufacturing technology using in situ infrared thermography, Addit. Manuf. 5 (2015) 31–39. doi:10.1016/j.addma.2014.12.001.

[116] F. Zhang, K. Yu, K. Zhang, Y. Liu, K. Xu, Y. Liu, An emissivity measurement apparatus for near infrared spectrum, Infrared Phys. Technol. 73 (2015) 275–280. doi:10.1016/j.infrared.2015.10.001.

[117] B. Lane, E. Whitenton, V. Madhavan, A. Donmez, Uncertainty of temperature measurements by infrared thermography for metal cutting applications, Metrologia. 50 (2013) 637–653. doi:10.1088/0026-1394/50/6/637.

[118] P.A. Hooper, Melt pool temperature and cooling rates in laser powder bed fusion, Addit. Manuf. 22 (2018) 548–559. doi:10.1016/j.addma.2018.05.032.

[119] C. Krishna, P. Vallabh, X. Zhao, Single-camera Two-Wavelength Imaging Pyrometry for Melt Pool Temperature Measurement and Monitoring in Laser Powder Bed Fusion based Additive Manufacturing, ArXiv Prepr. (2021).

[120] H. Schöpp, A. Sperl, R. Kozakov, G. Gött, D. Uhrlandt, G. Wilhelm, Temperature and emissivity determination of liquid steel S235, J. Phys. D. Appl. Phys. 45 (2012). doi:10.1088/0022-3727/45/23/235203.

[121] K. Jurrens, Measurement Science Roadmap for Metal-Based Additive Manufacturing, 2013. doi:10.1007/s13398-014-0173-7.2.

[122] P. Bidare, I. Bitharas, R.M. Ward, M.M. Attallah, A.J. Moore, Fluid and particle dynamics in laser powder bed fusion, Acta Mater. 142 (2018) 107–120. doi:10.1016/j.actamat.2017.09.051.

[123] W.J. Sames, F.A. List, S. Pannala, R.R. Dehoff, S.S. Babu, The metallurgy and processing science of metal additive manufacturing, Int. Mater. Rev. 61 (2016) 315–360. doi:10.1080/09506608.2015.1116649.

[124] J.C. Heigel, B.M. Lane, Measurement of the Melt Pool Length During Single Scan Tracks in a Commercial Laser Powder Bed Fusion Process, in: Proc. 2017 ASME Int. Conf. Manuf. Sci. Eng., Los Angeles, CA, 2017. doi:10.1115/MSEC2017-2942.

[125] M.H. Farshidianfar, A. Khajepour, A.P. Gerlich, Effect of real-time cooling rate on microstructure in Laser Additive Manufacturing, J. Mater. Process. Tech. 231 (2016) 468–478. doi:10.1016/j.jmatprotec.2016.01.017.

[126] Y.S. Lee, M.M. Kirka, R.B. Dinwiddie, N. Raghavan, J. Turner, R.R. Dehoff, S.S. Babu, Role of Scan Strategies on Thermal Gradient and Solidification Rate in Electron Beam Powder Bed Fusion Y.S.,

Addit. Manuf. (2018). doi:10.1016/j.addma.2018.04.038.

[127] H.R. Shercliff, M.F. Ashby, The prediction of case depth in laser transformation hardening, Metall. Trans. A. 22 (1991) 2459–2466. doi:10.1007/BF02665012.

[128] H. Krauss, T. Zeugner, M.F. Zaeh, Layerwise monitoring of the Selective Laser Melting process by thermography, Phys. Procedia. 56 (2014) 64–71. doi:10.1016/j.phpro.2014.08.097.

[129] R. Bernhard, P. Neef, T. Eismann, H. Wiche, C. Hoff, J. Hermsdorf, S. Kaierle, V. Wesling, Additive manufacturing of LMD nozzles for multi-material processing, Procedia CIRP. 94 (2020) 336–340. doi:10.1016/j.procir.2020.09.063.

[130] T.J. Rockstroh, J. Mazumder, Spectroscopic studies of plasma during cw laser materials interaction, J. Appl. Phys. 61 (1987) 917–923. doi:10.1063/1.338142.

[131] L. Song, J. Mazumder, Real time Cr measurement using optical emission spectroscopy during direct metal deposition process, IEEE Sens. J. 12 (2012) 958–964. doi:10.1109/JSEN.2011.2162316.

[132] P. Dryburgh, D. Pieris, F. Martina, R. Patel, S. Sharples, W. Li, A.T. Clare, S. Williams, R.J. Smith, Spatially resolved acoustic spectroscopy for integrity assessment in wire–arc additive manufacturing, Addit. Manuf. 28 (2019) 236–251. doi:10.1016/j.addma.2019.04.015.

[133] M.S. Hossain, H. Taheri, In Situ Process Monitoring for Additive Manufacturing Through Acoustic Techniques, J. Mater. Eng. Perform. 29 (2020) 6249–6262. doi:10.1007/s11665-020-05125-w.

[134] L. Scime, J. Beuth, Anomaly detection and classification in a laser powder bed additive manufacturing process using a trained computer vision algorithm, Addit. Manuf. 19 (2018) 114–126. doi:10.1016/j.addma.2017.11.009.

[135] C. Zhao, K. Fezzaa, R.W. Cunningham, H. Wen, F. De Carlo, L. Chen, A.D. Rollett, T. Sun, Real-time monitoring of laser powder bed fusion process using high-speed X-ray imaging and diffraction, Sci. Rep. 7 (2017) 3602. doi:10.1038/s41598-017-03761-2.

[136] N.P. Calta, A.A. Martin, J.A. Hammons, M.H. Nielsen, T.T. Roehling, K. Fezzaa, M.J. Matthews, J.R. Jeffries, T.M. Willey, J.R.I. Lee, Pressure dependence of the laser-metal interaction under laser powder bed fusion conditions probed by in situ X-ray imaging, Addit. Manuf. 32 (2020). doi:10.1016/j.addma.2020.101084.

[137] C.L.A. Leung, S. Marussi, R.C. Atwood, M. Towrie, P.J. Withers, P.D. Lee, In situ X-ray imaging of defect and molten pool dynamics in laser additive manufacturing, Nat. Commun. 9 (2018) 1–9. doi:10.1038/s41467-018-03734-7.

[138] S.J. Wolff, H. Wu, N. Parab, C. Zhao, K.F. Ehmann, T. Sun, J. Cao, In-situ high-speed X-ray imaging of piezo-driven directed energy deposition additive manufacturing, Sci. Rep. 9 (2019) 1–14. doi:10.1038/s41598-018-36678-5.

[139] Y. Chen, S.J. Clark, Y. Huang, L. Sinclair, C. Lun Alex Leung, S. Marussi, T. Connolley, O. V. Magdysyuk, R.C. Atwood, G.J. Baxter, M.A. Jones, I. Todd, P.D. Lee, In situ X-ray quantification of melt pool behaviour during directed energy deposition additive manufacturing of stainless steel, Mater. Lett. 286 (2021) 129205. doi:10.1016/j.matlet.2020.129205.

[140] M. Mani, B.M. Lane, M.A. Donmez, S.C. Feng, S.P. Moylan, A review on measurement science needs for real-time control of additive manufacturing metal powder bed fusion processes, Int. J. Prod. Res. 55 (2017) 1400–1418. doi:10.1080/00207543.2016.1223378.

[141] W.W. Liu, Z.J. Tang, X.Y. Liu, H.J. Wang, H.C. Zhang, A Review on In-situ Monitoring and Adaptive Control Technology for Laser Cladding Remanufacturing, Procedia CIRP. 61 (2017) 235–240.

doi:10.1016/j.procir.2016.11.217.

[142] T. Craeghs, F. Bechmann, S. Berumen, J.P. Kruth, Feedback control of Layerwise Laser Melting using optical sensors, Phys. Procedia. 5 (2010) 505–514. doi:10.1016/j.phpro.2010.08.078.

[143] E. Vasileska, A.G. Demir, B.M. Colosimo, B. Previtali, Layer-wise control of selective laser melting by means of inline melt pool area measurements, J. Laser Appl. 32 (2020) 022057. doi:10.2351/7.0000108.

[144] L. Tang, R.G. Landers, Melt pool temperature control for laser metal deposition processes-part II: Layer-to-layer temperature control, J. Manuf. Sci. Eng. Trans. ASME. 132 (2010) 0110111–0110119. doi:10.1115/1.4000883.

[145] C. Meacock, R. Vilar, Laser powder microdeposition of CP2 Titanium, Mater. Des. 29 (2008) 353–361. doi:10.1016/j.matdes.2007.01.033.

[146] L. Tang, R.G. Landers, Melt pool temperature control for laser metal deposition processes-part I: Online temperature control, J. Manuf. Sci. Eng. Trans. ASME. 132 (2010) 0110101–0110109. doi:10.1115/1.4000882.

[147] L. Song, V. Bagavath-Singh, B. Dutta, J. Mazumder, Control of melt pool temperature and deposition height during direct metal deposition process, Int. J. Adv. Manuf. Technol. 58 (2012) 247–256. doi:10.1007/s00170-011-3395-2.

[148] A.R. Nassar, J.S. Keist, E.W. Reutzel, T.J. Spurgeon, Intra-layer closed-loop control of build plan during directed energy additive manufacturing of Ti-6Al-4V, Addit. Manuf. 6 (2015) 39–52. doi:10.1016/j.addma.2015.03.005.

[149] J.T. Hofman, B. Pathiraj, J. Van Dijk, D.F. De Lange, J. Meijer, A camera based feedback control strategy for the laser cladding process, J. Mater. Process. Tech. 212 (2012) 2455–2462. doi:10.1016/j.jmatprotec.2012.06.027.

[150] M.L. Griffith, W.H. Hofmeister, G.A. Knorovsky, D.O. Maccallum, E. Schlienger, J.E. Smugeresky, Direct Laser Additive Fabrication System with Image Feedback Control, US 6459951 B1, 2002.

[151] M.H. Farshidianfar, F. Khodabakhshi, A. Khajepour, A.P. Gerlich, Closed-loop control of microstructure and mechanical properties in additive manufacturing by directed energy deposition, Mater. Sci. Eng. A. 803 (2021) 140483. doi:10.1016/j.msea.2020.140483.

[152] S. Donadello, M. Motta, A.G. Demir, B. Previtali, Monitoring of laser metal deposition height by means of coaxial laser triangulation, Opt. Lasers Eng. 112 (2018) 136–144. doi:10.1016/j.optlaseng.2018.09.012.

[153] J.-P. Kruth, J. Deckers, E. Yasa, R. Wauthlé, Assessing and comparing influencing factors of residual stresses in selective laser melting using a novel analysis method, Proc. Inst. Mech. Eng. Part B J. Eng. Manuf. 226 (2012) 980–991. doi:10.1177/0954405412437085.

[154] H.K. Lee, Effects of the cladding parameters on the deposition efficiency in pulsed Nd:YAG laser cladding, J. Mater. Process. Technol. 202 (2008) 321–327. doi:10.1016/j.jmatprotec.2007.09.024.

[155] Y. Lu, S. Wu, Y. Gan, T. Huang, C. Yang, L. Junjie, J. Lin, Study on the microstructure, mechanical property and residual stress of SLM Inconel-718 alloy manufactured by differing island scanning strategy, Opt. Laser Technol. 75 (2015) 197–206. doi:10.1016/j.optlastec.2015.07.009.

[156] S. Catchpole-Smith, N. Aboulkhair, L. Parry, C. Tuck, I.A. Ashcroft, A. Clare, Fractal scan strategies for selective laser melting of 'unweldable' nickel superalloys, Addit. Manuf. 15 (2017) 113–122. doi:10.1016/j.addma.2017.02.002.

[157] C. Körner, H. Helmer, A. Bauereiß, R.F. Singer, Tailoring the grain structure of IN718 during selective electron beam melting, MATEC Web Conf. 14 (2014) 08001. doi:10.1051/matecconf/20141408001.

[158] T. Scharowsky, V. Juechter, R.F. Singer, C. Körner, Influence of the Scanning Strategy on the Microstructure and Mechanical Properties in Selective Electron Beam Melting of Ti-6Al-4V, Adv. Eng. Mater. 17 (2015) 1573–1578. doi:10.1002/adem.201400542.

[159] H.L. Wei, J. Mazumder, T. DebRoy, Evolution of solidification texture during additive manufacturing, Sci. Rep. 5 (2015) 16446. doi:10.1038/srep16446.

[160] S.L. Mccracken, X. Yu, Y.C. Lim, D.F. Farson, S.S. Babu, Grain Structure Refinement in Nickel Alloy Welds by Magnetic Arc Stirring, Proc. ASME 2011 Press. Vessel. Pip. Div. Conf. (2011) 1–13.

[161] Y.C. Lim, X. Yu, J.H. Cho, J. Sosa, D.F. Farson, S.S. Babu, S. McCracken, B. Flesner, Effect of magnetic stirring on grain structure refinement: Part 1 – Autogenous nickel alloy welds, Sci. Technol. Weld. Join. 15 (2010) 583–589. doi:10.1179/136217110X12720264008277.

[162] Y. Xiong, X. Ying Wei, J. Du, A. Yang, L. Liu, D. Zeng, Grain refinement of superalloy IN718C by the addition of inoculants, Metall. Mater. Trans. A. 35 (2004) 2111–2114. doi:10.1007/s11661-004-0159-8.

[163] W. Jin, F. Bai, T. Li, G. Yin, Grain refinement of superalloy IN100 under the action of rotary magnetic fields and inoculants, Mater. Lett. 62 (2008) 1585–1588. doi:10.1016/j.matlet.2007.09.028.

[164] C.J. Todaro, E. M.A., D. Qui, D. Zhang, M.J. Bermingham, E.W. Lui, M. Brandt, D.H. StJohn, M. Qian, Grain structure control during metal 3D printing by high-intensity ultrasound, Nat. Commun. 11 (2020) 1–9. doi:10.1038/s41467-019-13874-z.

[165] N. Kalentics, E. Boillat, P. Peyre, S. Ćirić-Kostić, N. Bogojević, R.E. Logé, Tailoring residual stress profile of Selective Laser Melted parts by Laser Shock Peening, Addit. Manuf. 16 (2017) 90–97. doi:10.1016/j.addma.2017.05.008.

[166] N. Kalentics, E. Boillat, P. Peyre, C. Gorny, C. Kenel, C. Leinenbach, J. Jhabvala, R.E. Logé, 3D Laser Shock Peening – A new method for the 3D control of residual stresses in Selective Laser Melting, Mater. Des. 130 (2017) 350–356. doi:10.1016/j.matdes.2017.05.083.

[167] Aconity3D, Aconity3D Configurator, (n.d.). https://configurator.aconity3d.com/EN/units/AconityMINI (accessed April 21, 2022).

[168] F.S.H.B. Freeman, B. Thomas, L. Chechik, I. Todd, Multi-faceted monitoring of powder flow rate variability in directed energy deposition, Addit. Manuf. Lett. 2 (2022) 100024. doi:10.1016/j.addlet.2021.100024.

[169] L. Chechik, L-DED Printing of 316L Steel Cylinders, (2022). doi:10.5281/zenodo.6760037.

[170] L. Chechik, Scripts for thermal monitoring, EBSD Analysis and Melt Pool Modelling of L-DED, (2022). doi:10.5281/zenodo.6760054.

[171] S. Baraldo, A. Vandone, A. Valente, E. Carpanzano, Closed-Loop Control by Laser Power Modulation in Direct Energy Deposition Additive Manufacturing, Springer International Publishing, 2020. doi:10.1007/978-3-030-46212-3_9.

[172] EMCO TEST Universal Hardness Tester, (n.d.). https://www.directindustry.com/prod/emco-test-pruefmaschinen/product-34502-888975.html (accessed April 21, 2021).

[173] ASTM, ASTM E384-17: Standard Test Method for Microindentation Hardness of Materials, Annu.

B. ASTM Stand. (2010) 1–42. doi:10.1520/E0384-17.

[174] F. Bachmann, R. Hielscher, H. Schaeben, Texture analysis with MTEX- Free and open source software toolbox, Solid State Phenom. 160 (2010) 63–68. doi:10.4028/www.scientific.net/SSP.160.63.

[175] P. Lehto, H. Remes, T. Saukkonen, H. Hänninen, J. Romanoff, Influence of grain size distribution on the Hall-Petch relationship of welded structural steel, Mater. Sci. Eng. A. 592 (2014) 28–39. doi:10.1016/j.msea.2013.10.094.

[176] NIST, Weighted Standard Deviation, DATAPLOT Ref. Man. (1996). http://itl.nist.gov/div898/software/dataplot/refman2/ch2/weightsd.pdf.

[177] M.T. Hutchings, P.J. Withers, T.M. Holden, T. Lorentzen, Introduction to the Characterization of Residual Stress By Neutron Diffraction, 2005.

[178] J.C. Stinville, C. Tromas, P. Villechaise, C. Templier, Anisotropy changes in hardness and indentation modulus induced by plasma nitriding of 316L polycrystalline stainless steel, Scr. Mater. 64 (2011) 37–40. doi:10.1016/j.scriptamat.2010.08.058.

[179] J.J. Roa, G. Fargas, A. Mateo, E. Jiménez-Piqué, Dependence of nanoindentation hardness with crystallographic orientation of austenite grains in metastable stainless steels, Mater. Sci. Eng. A. 645 (2015) 188–195. doi:10.1016/j.msea.2015.07.096.

[180] Y.C. Yeoh, G. Macchi, E. Jain, B. Gaskey, S. Raman, G. Tay, D. Verdi, A. Patran, A.M. Grande, M. Seita, Multiscale microstructural heterogeneity and mechanical property scatter in Inconel 718 produced by directed energy deposition, J. Alloys Compd. 887 (2021) 161426. doi:10.1016/j.jallcom.2021.161426.

[181] MTEX, Grain Orientation Parameters, (n.d.). https://mtex-toolbox.github.io/GrainOrientationParameters.html (accessed June 10, 2022).

[182] Mathworks, k-means clustering, (n.d.). https://uk.mathworks.com/help/stats/kmeans.html (accessed May 3, 2022).

[183] R.C. Reed, The Superalloys fundamentals and applications, 2006. doi:10.1017/CBO9780511541285.

[184] M. Durand-Charre, The Microstructure of Superalloys, Gordon and Breach Science Publishers, 1997.

[185] B.D. Conduit, T. Illston, S. Baker, D.V. Duggappa, S. Harding, H.J. Stone, G.J. Conduit, Probabilistic neural network identification of an alloy for direct laser deposition, Mater. Des. 168 (2019) 107644. doi:10.1016/j.matdes.2019.107644.

[186] M.C. Hardy, C. Argyrakis, H.S. Kitaguchi, A.S. Wilson, R.C. Buckingham, K. Severs, S. Yu, C. Jackson, E.J. Pickering, S.C.H. Llewelyn, C. Papadaki, K.A. Christofidou, P.M. Mignanelli, A. Evans, D.J. Child, H.Y. Li, N.G. Jones, C.M.F. Rae, P. Bowen, H.J. Stone, Developing alloy compositions for future high temperature disk rotors, Proc. 14th Int. Symp. Superalloys. (2021). doi:10.1007/978-3-030-51834-9_2 This.

[187] H. International, HAYNES® 282® alloy brochure, Haynes Int. (2021).

[188] ATI, ATI 718Plus® technical data sheet, 1 (2013) 1–5.

[189] M. Segersäll, Nickel-Based Single-Crystal Superalloys temperature properties, Linkoping University, 2013.

[190] T.M. Smith, N.M. Senanayake, C.K. Sudbrack, P. Bonacuse, R.B. Rogers, P. Chao, J. Carter,

Characterization of nanoscale precipitates in superalloy 718 using high resolution SEM imaging, Mater. Charact. 148 (2019) 178–187. doi:10.1016/j.matchar.2018.12.018.

[191] American Welding Society (AWS), Standard Welding Terms and Definitions, 2010.

[192] H. Naffakh Moosavy, M.R. Aboutalebi, S.H. Seyedein, C. Mapelli, Microstructural, mechanical and weldability assessments of the dissimilar welds between γ′- And γ″-strengthened nickel-base superalloys, Mater. Charact. 82 (2013) 41–49. doi:10.1016/j.matchar.2013.04.018.

[193] T. Illston, Developments in Additive Manufacturing of Nickel Superalloys for Aerospace Applications, Int. Conf. Addit. Manuf. 2012. (2012). http://materialssolutions.co.uk/wp-content/uploads/2014/08/Trevor-Illston-AM-Conf-2012.pdf.

[194] M.H. Haafkens, J.H.G. Matthey, A New Approach to the Weldability of Nickel-Base, As-Cast and Powder Metallurgy Superalloys, in: Maint. Serv. High Termperature Parts. Agard Conf. Proc. No. 317, 1981.

[195] D. Dye, O. Hunziker, R.C. Reed, Numerical analysis of the weldability of superalloys, Acta Mater. 49 (2001) 683–697. doi:10.1016/S1359-6454(00)00361-X.

[196] H.N. Moosavy, M.R. Aboutalebi, S.H. Seyedein, M. Khodabakhshi, C. Mapelli, New approach for assessing the weldability of precipitation-strengthened nickel-base superalloys, Int. J. Miner. Metall. Mater. 20 (2013) 1183–1191. doi:10.1007/s12613-013-0853-x.

[197] M.B. Henderson, D. Arrell, R. Larsson, M. Heobel, G. Marchant, Nickel based superalloy welding practices for industrial gas turbine applications, Sci. Technol. Weld. Join. 9 (2004) 13–21. doi:10.1179/136217104225017099.

[198] S. Kou, Welding Metallurgy, Second, Wiley Interscience, 2003. doi:10.1016/j.theochem.2007.07.017.

[199] G.J. Davies, J.G. Garland, Solidification Structures and Properties of Fusion Welds, Int. Metall. Rev. 20 (1975) 83–108. doi:10.1179/imtlr.1975.20.1.83.

[200] N. Coniglio, C.E. Cross, Initiation and growth mechanisms for weld solidification cracking, Int. Mater. Rev. 58 (2013) 375–397. doi:10.1179/1743280413Y.0000000020.

[201] D.G. Eskin, L. Katgerman, A quest for a new hot tearing criterion, Metall. Mater. Trans. A Phys. Metall. Mater. Sci. 38 A (2007) 1511–1519. doi:10.1007/s11661-007-9169-7.

[202] T.W. Clyne, G.J. Davies, Comparison between experimental data and theoretical predictions relating to dependence of solidification cracking on composition, in: Solidif. Cast. Met., Sheffield, 1977: pp. 275–278.

[203] M. Rappaz, J.-M. Drezet, M. Gremaud, A New Hot-Tearing Criterion M., Metall. Mater. Trans. A. 30 (1999) 449–455. doi:10.1007/s11661-999-0334-z.

[204] B.G. Thomas, Modeling of Hot Tearing and Other Defects in Casting Processes, ASM Handb. 22 (2009) 362–374.

[205] J. Zhang, R.F. Singer, Hot tearing of nickel-based superalloys during directional solidification, Acta Mater. 50 (2002) 1869–1879. doi:10.1016/S1359-6454(02)00042-3.

[206] L. Katgerman, A Mathematical Model for Hot Cracking of Aluminium Alloys during DC Casting, Essent. Readings Light Met. 3 (1982) 907–911. doi:10.1002/9781118647783.ch114.

[207] S. Kou, A criterion for cracking during solidification, Acta Mater. 88 (2015) 366–374. doi:10.1016/j.actamat.2015.01.034.

[208] E.D. Manson-Whitton, I.C. Stone, J.R. Jones, P.S. Grant, B. Cantor, Isothermal grain coarsening of spray formed alloys in the semi-solid state, Acta Mater. 50 (2002) 2517–2535. doi:10.1016/S1359-6454(02)00080-0.

[209] M. Rappaz, I. Farup, J.-M. Drezet, Study and Modeling of Hot Tearing Formation, Mert. C. Flemings Symp. Solidif. Mater. Process. (2000) 213–22. http://infoscience.epfl.ch/record/62662.

[210] H.N. Moosavy, M.R. Aboutalebi, S.H. Seyedein, An analytical algorithm to predict weldability of precipitation-strengthened nickel-base superalloys, J. Mater. Process. Technol. 212 (2012) 2210–2218. doi:10.1016/j.jmatprotec.2012.06.010.

[211] S.A. David, J.M. Vitek, S.S. Babu, L.A. Boatner, R.W. Reed, Welding of nickel base superalloy single crystals, Sci. Technol. Weld. Join. 2 (1997) 79–88. doi:10.1179/stw.1997.2.2.79doi.org/10.1179/stw.1997.2.2.79.

[212] Y. Zhou, A. Volek, Effect of carbon additions on hot tearing of a second generation nickel-base superalloy, Mater. Sci. Eng. A. 479 (2008) 324–332. doi:10.1016/j.msea.2007.06.076.

[213] J. Grodzki, N. Hartmann, R. Rettig, E. Affeldt, R.F. Singer, Effect of B, Zr, and C on Hot Tearing of a Directionally Solidified Nickel-Based Superalloy, Metall. Mater. Trans. A Phys. Metall. Mater. Sci. 47 (2016) 2914–2926. doi:10.1007/s11661-016-3416-8.

[214] A. Després, S. Antonov, C. Mayer, C. Tassin, M. Veron, J.J. Blandin, P. Kontis, G. Martin, On the role of boron, carbon and zirconium on hot cracking and creep resistance of an additively manufactured polycrystalline superalloy, Materialia. 19 (2021). doi:10.1016/j.mtla.2021.101193.

[215] M.S. Lewandowski, R.A. Overfelt, High temperature deformation behavior of solid and semi-solid alloy 718, Acta Mater. 47 (1999) 4695–4710. doi:10.1016/S1359-6454(99)00252-9.

[216] M. Braccini, C. Martin, M. Suery, Relation Between mushy zone rheology and hot tearing phenomena in Al-Cu alloys, Model. Cast. Weld. Adv. Solidif. Process. IX. (2000) 18–24.

[217] G.A. Young, T.E. Capobianco, M. a. Penik, B.W. Morris, J.J. McGee, The mechanism of ductility dip cracking in nickel-chromium alloys, Weld. J. 87 (2008) 31S-43S. http://www.aws.org/wj/supplement/WJ_2008_02_s31.pdf.

[218] P. Mercelis, J. Kruth, Residual stresses in selective laser sintering and selective laser melting, Rapid Prototyp. J. 12 (2006) 254–265. doi:10.1108/13552540610707013.

[219] R. Deffley, Development of processing strategies for the additive layer manufacture of aerospace components in Inconel 718, University of Sheffield, 2012.

[220] J. Hunt, F. Derguti, I. Todd, Selection of steels suitable for additive layer manufacturing, Ironmak. Steelmak. 41 (2014) 254–256. doi:10.1179/0301923314Z.000000000269.

[221] E.A. Ott, J. Groh, H. Sizek, Metals affordability initiative: Application of allvac Alloy 718Plus® for aircraft engine static structural components, Proc. Int. Symp. Superalloys Var. Deriv. (2005) 35–45. doi:10.7449/2005/superalloys_2005_35_45.

[222] R.L. Dreshfield, Estimation of gamma phase composition in nickel-base superalloys (based on geometric analysis of a four-component phase diagram), NASA Tech. Note. (1970).

[223] H.J. Murphy, C.T. Sims, A.M. Beltran, PHACOMP revisited, Superalloys 1968. (1968) 47–66. doi:10.1007/BF03378761.

[224] E.S. Machlin, J. Shao, SIGMA-SAFE: A phase diagram approach to the sigma phase problem in ni base superalloys, Metall. Trans. A. 9 (1978) 561–568. doi:10.1007/BF02646413.

[225] Calculation of Electron Vacancy Number in Superalloys, SAE International, 2017.

[226] M.J. Cieslak, G.A. Knorovsky, T.J. Headley, A.D. Romig, The use of new PHACOMP in understanding the solidification microstructure of nickel base alloy weld metal, Metall. Trans. A. 17 (1986) 2107–2116. doi:10.1007/BF02645909.

[227] H.L. Wei, T. Mukherjee, W. Zhang, J.S. Zuback, G.L. Knapp, A. De, T. DebRoy, Mechanistic models for additive manufacturing of metallic components, Prog. Mater. Sci. 116 (2021). doi:10.1016/j.pmatsci.2020.100703.

[228] M. Marty, G. Hug, A. Walder, Influence of Chromium and Molybdenum on the Structural Stability of a High Strength Damage Tolerant P/M Nickel Based Alloy for Turbine Disks, Mater. Res. Soc. Symp. Proc. 186 (1991) 401–406.

[229] J.S. Zhang, Z.Q. Hu, Y. Murata, M. Morinaga, N. Yukawa, Design and Development of Hot Corrosion-Resistant Nickel-Base Single-Crystal Superalloys by the d-Electrons Alloy Design Theory : Part II . Effects of Refractory Metals Ti , Ta , and Nb on Microstructures and Properties, Metall. Trans. A. 24 (1993) 2451–2464.

[230] B. Mondal, T. Mukherjee, T. DebRoy, Crack free metal printing using physics informed machine learning, Acta Mater. 226 (2022) 117612. doi:10.1016/j.actamat.2021.117612.

[231] C.L. Frederick, Control of Grain Structure in Selective-Electron Beam Melting of Nickel-based Superalloys, (2018) 1–143. https://trace.tennessee.edu/utk_graddiss/4952.

[232] J.O. Andersson, T. Helander, L. Höglund, P. Shi, B. Sundman, Thermo-Calc & DICTRA, computational tools for materials science, Calphad Comput. Coupling Phase Diagrams Thermochem. 26 (2002) 273–312. doi:10.1016/S0364-5916(02)00037-8.

[233] Y. Sato, Representation of the viscosity of molten alloy as a function of the composition and temperature, Jpn. J. Appl. Phys. 50 (2011) 15–18. doi:10.1143/JJAP.50.11RD01.

[234] M. Morinaga, N. Yukawa, H. Adachi, H. Ezaki, New Phacomp and its Applications to Alloy Design, Superalloys 1984 (Fifth Int. Symp. (1984) 523–532. doi:10.7449/1984/Superalloys_1984_523_532.

[235] EOS, 30 years of EOS, (2019). http://30years.eos.info/en (accessed April 20, 2020).

[236] M. Schmidt, M. Merklein, D. Bourell, D. Dimitrov, T. Hausotte, K. Wegener, L. Overmeyer, F. Vollertsen, G.N. Levy, Laser based additive manufacturing in industry and academia, CIRP Ann. - Manuf. Technol. 66 (2017) 561–583. doi:10.1016/j.cirp.2017.05.011.

[237] D. Buchbinder, W. Meiners, N. Pirch, K. Wissenbach, J. Schrage, Investigation on reducing distortion by preheating during manufacture of aluminum components using selective laser melting, J. Laser Appl. 26 (2014) 012004. doi:10.2351/1.4828755.

[238] B. Cheng, S. Shrestha, K. Chou, Stress and deformation evaluations of scanning strategy effect in selective laser melting, Addit. Manuf. 12 (2016) 240–251. doi:10.1016/j.addma.2016.05.007.

[239] E. Yasa, J. Deckers, T. Craeghs, M. Badrossamay, J. Kruth, Investigation on Occurence of Elevated Edges in Selective Laser Melting, in: Solid Free. Fabr., 2009: pp. 180–192.

[240] H. Chen, T. Cheng, Z. Li, Q. Wei, W. Yan, Is high-speed powder spreading really unfavourable for the part quality of laser powder bed fusion additive manufacturing?, Acta Mater. 231 (2022) 117901. doi:10.1016/j.actamat.2022.117901.

[241] K.A. Mumtaz, P. Erasenthiran, N. Hopkinson, High density selective laser melting of Waspaloy®, J. Mater. Process. Technol. 195 (2008) 77–87. doi:10.1016/j.jmatprotec.2007.04.117.

[242] M.J. Matthews, G. Guss, S.A. Khairallah, A.M. Rubenchik, P.J. Depond, W.E. King, Denudation of

metal powder layers in laser powder bed fusion processes, Acta Mater. 114 (2016) 33–42. doi:10.1016/j.actamat.2016.05.017.

[243] I. Yadroitsev, I. Smurov, Surface morphology in selective laser melting of metal powders, Phys. Procedia. 12 (2011) 264–270. doi:10.1016/j.phpro.2011.03.034.

[244] S. Clijsters, T. Craeghs, S. Buls, K. Kempen, J.P. Kruth, In situ quality control of the selective laser melting process using a high-speed, real-time melt pool monitoring system, Int. J. Adv. Manuf. Technol. 75 (2014) 1089–1101. doi:10.1007/s00170-014-6214-8.

[245] Y. Tian, D. Tomus, P. Rometsch, X. Wu, Influences of processing parameters on surface roughness of Hastelloy X produced by selective laser melting, Addit. Manuf. (2017). doi:10.1016/j.addma.2016.10.010.

[246] P. Bidare, R.R.J. Maier, R.J. Beck, J.D. Shephard, A.J. Moore, An open-architecture metal powder bed fusion system for in-situ process measurements, Addit. Manuf. 16 (2017) 177–185. doi:10.1016/j.addma.2017.06.007.

[247] T. Craeghs, S. Clijsters, E. Yasa, F. Bechmann, S. Berumen, J.P. Kruth, Determination of geometrical factors in Layerwise Laser Melting using optical process monitoring, Opt. Lasers Eng. 49 (2011) 1440–1446. doi:10.1016/j.optlaseng.2011.06.016.

[248] L. Newton, N. Senin, C. Gomez, R. Danzl, F. Helmli, L. Blunt, R. Leach, Areal topography measurement of metal additive surfaces using focus variation microscopy, Addit. Manuf. 25 (2019) 365–389. doi:10.1016/j.addma.2018.11.013.

[249] W. Di, Y. Yongqiang, S. Xubin, C. Yonghua, Study on energy input and its influences on single-track,multi-track, and multi-layer in SLM, Int. J. Adv. Manuf. Technol. 58 (2012) 1189–1199. doi:10.1007/s00170-011-3443-y.

[250] M.C. Taylor, T.H.. Childs, C. Hauser, Morphology of direct SLS-processed stainless steel layers, 13th Solid Free Form Fabr. Proc. 44 (2002) 530–537. http://utwired.engr.utexas.edu/lff/symposium/proceedingsArchive/pubs/Manuscripts/2002/2002-60-Taylor.pdf.

[251] M.A. Groeber, E. Schwalbach, S. Donegan, K. Chaput, T. Butler, J. Miller, Application of characterization, modelling, and analytics towards understanding process-structure linkages in metallic 3D printing, IOP Conf. Ser. Mater. Sci. Eng. 219 (2017). doi:10.1088/1757-899X/219/1/012002.

[252] I. Yadroitsev, I. Yadroitsava, A. Du Plessis, E. MacDonald, eds., Fundamentals of Laser Powder Bed Fusion of Metals, Elsevier, 2021. doi:10.1016/c2020-0-01200-4.

[253] C. Tang, K.Q. Le, C.H. Wong, Physics of humping formation in laser powder bed fusion, Int. J. Heat Mass Transf. 149 (2020). doi:10.1016/j.ijheatmasstransfer.2019.119172.

[254] S.A. Khairallah, A.A. Martin, J.R.I. Lee, G. Guss, N.P. Calta, J.A. Hammons, M.H. Nielsen, K. Chaput, E. Schwalbach, M.N. Shah, M.G. Chapman, T.M. Willey, A.M. Rubenchik, A.T. Anderson, Y.M. Wang, M.J. Matthews, W.E. King, Controlling interdependent meso-nanosecond dynamics and defect generation in metal 3D printing, Science (80-.). 368 (2020) 660–665. doi:10.1126/science.aay7830.

[255] R. Cunningham, C. Zhao, N. Parab, C. Kantzos, J. Pauza, K. Fezzaa, T. Sun, A.D. Rollett, Keyhole threshold and morphology in laser melting revealed by ultrahigh-speed x-ray imaging, Science (80-.). 363 (2019) 849–852. doi:10.1126/science.aav4687.

[256] A.A. Martin, N.P. Calta, S.A. Khairallah, J. Wang, P.J. Depond, A.Y. Fong, V. Thampy, G.M. Guss, A.M. Kiss, K.H. Stone, C.J. Tassone, J.N. Weker, M.F. Toney, T. Van Buuren, M.J. Matthews, Dynamics of

pore formation during laser powder bed fusion additive manufacturing, Nat. Commun. 10 (2019) 1–10. doi:10.1038/s41467-019-10009-2.

[257] M. Pothen, K. Winands, F. Klocke, Compensation of scanner based inertia for laser structuring processes, J. Laser Appl. 29 (2017) 012017. doi:10.2351/1.4974906.

[258] Raylase, SP-ICE-3 User's Manual 1.29.0, (2017).

[259] T.M. Wischeropp, C. Emmelmann, M. Brandt, A. Pateras, Measurement of actual powder layer height and packing density in a single layer in selective laser melting, Addit. Manuf. 28 (2019) 176–183. doi:10.1016/j.addma.2019.04.019.

[260] H.W. Mindt, M. Megahed, N.P. Lavery, M.A. Holmes, S.G.R. Brown, Powder Bed Layer Characteristics: The Overseen First-Order Process Input, Metall. Mater. Trans. A Phys. Metall. Mater. Sci. 47 (2016) 3811–3822. doi:10.1007/s11661-016-3470-2.

[261] D.J. Dagel, G.D. Grossetete, D.O. Maccallum, S.P. Korey, Four-color imaging pyrometer for mapping temperatures of lase-based metal processes, Sandia Natl. Lab. (2016).

[262] M. Pavlov, M. Doubenskaia, I. Smurov, Pyrometric analysis of thermal processes in SLM technology, 5 (2010) 523–531. doi:10.1016/j.phpro.2010.08.080.

[263] M. Doubenskaia, M. Pavlov, S. Grigoriev, E. Tikhonova, I. Smurov, Comprehensive Optical Monitoring of Selective Laser Melting, J. Laser Micro/Nanoengineering. 7 (2012). doi:10.2961/j1mn.2012.03.001.

[264] T. Craeghs, S. Clijsters, J. Kruth, Detection of process failures in Layerwise Laser Melting with optical process monitoring, Phys. Procedia. 39 (2012) 753–759. doi:10.1016/j.phpro.2012.10.097.

[265] W.E. King, A.T. Anderson, R.M. Ferencz, N.E. Hodge, C. Kamath, S.A. Khairallah, A.M. Rubenchik, Laser powder bed fusion additive manufacturing of metals; physics, computational, and materials challenges, Appl. Phys. Rev. 2 (2015) 041304. doi:10.1063/1.4937809.

[266] G.L. Knapp, T. Mukherjee, J.S. Zuback, H.L. Wei, T.A. Palmer, A. De, T. DebRoy, Building blocks for a digital twin of additive manufacturing, Acta Mater. 135 (2017) 390–399. doi:10.1016/j.actamat.2017.06.039.

[267] D.M. Collins, H.J. Stone, A modelling approach to yield strength optimisation in a nickel-base superalloy, Int. J. Plast. 54 (2014) 96–112. doi:10.1016/j.ijplas.2013.08.009.

[268] A.J. Dunbar, E.R. Denlinger, M.F. Gouge, P. Michaleris, Experimental validation of finite element modeling for laser powder bed fusion deformation, Addit. Manuf. (2016). doi:10.1016/j.addma.2016.08.003.

[269] Autodesk Netfabb Local Simulation 2020.0, (2020).

[270] S. Tammas-Williams, H. Zhao, F. Léonard, F. Derguti, I. Todd, P.B. Prangnell, Materials Characterization XCT analysis of the in fl uence of melt strategies on defect population in Ti – 6Al – 4V components manufactured by Selective Electron Beam Melting, Mater. Charact. 102 (2015) 47–61. doi:10.1016/j.matchar.2015.02.008.

[271] Kleiber, Kleiber Pyrometer Operation Manual, (n.d.). https://kleiberinfrared.com/images/stories/pdf/data/Anleitungen/Manual_740_LO.pdf.

[272] Martin Baiker, Alicona file format reader (al3D), (2016). https://uk.mathworks.com/matlabcentral/fileexchange/37018-alicona-file-format-reader-al3d.

[273] A.S. Agazhanov, D.A. Samoshkin, Y.M. Kozlovskii, Thermophysical properties of Inconel 718 alloy,

J. Phys. Conf. Ser. 1382 (2019). doi:10.1088/1742-6596/1382/1/012175.

[274] F.S.H.B. Freeman, A. Lincoln, J. Sharp, A. Lambourne, I. Todd, Exploiting thermal strain to achieve an in-situ magnetically graded material, Mater. Des. 161 (2019) 14–21. doi:10.1016/j.matdes.2018.11.011.

[275] P. Nie, O.A. Ojo, Z. Li, Numerical modeling of microstructure evolution during laser additive manufacturing of a nickel-based superalloy, Acta Mater. 77 (2014) 85–95. doi:10.1016/j.actamat.2014.05.039.

[276] P. Bajaj, J. Wright, I. Todd, E.A. Jägle, Predictive process parameter selection for Selective Laser Melting Manufacturing: Applications to high thermal conductivity alloys, Addit. Manuf. 27 (2019) 246–258. doi:10.1016/j.addma.2018.12.003.

[277] B.A. Fisher, B. Lane, H. Yeung, J. Beuth, Toward determining melt pool quality metrics via coaxial monitoring in laser powder bed fusion, Manuf. Lett. 15 (2018) 119–121. doi:10.1016/j.mfglet.2018.02.009.

[278] C.H. Yu, R.L. Peng, V. Luzin, M. Sprengel, M. Calmunger, J.E. Lundgren, H. Brodin, A. Kromm, J. Moverare, Thin-wall effects and anisotropic deformation mechanisms of an additively manufactured Ni-based superalloy, Addit. Manuf. 36 (2020) 101672. doi:10.1016/j.addma.2020.101672.

[279] Q.B. Nguyen, M.L.S. Nai, Z. Zhu, C.N. Sun, J. Wei, W. Zhou, Characteristics of Inconel Powders for Powder-Bed Additive Manufacturing, Engineering. 3 (2017) 695–700. doi:10.1016/J.ENG.2017.05.012.

[280] M.J. Heiden, S.C. Jensen, J.R. Koepke, D.J. Saiz, S.M. Dickens, B.H. Jared, Process and feedstock driven microstructure for laser powder bed fusion of 316L stainless steel, Materialia. 21 (2022) 101356. doi:10.1016/j.mtla.2022.101356.

[281] Q.B. Nguyen, D.N. Luu, S.M.L. Nai, Z. Zhu, Z. Chen, J. Wei, The role of powder layer thickness on the quality of SLM printed parts, Arch. Civ. Mech. Eng. 18 (2018) 948–955. doi:10.1016/j.acme.2018.01.015.

[282] W. Li, M. Soshi, Modeling analysis of the effect of laser transverse speed on grain morphology during directed energy deposition process, Int. J. Adv. Manuf. Technol. (2019) 3279–3291. doi:10.1007/s00170-019-03690-6.

[283] L.E. Criales, Y.M. Arısoy, B. Lane, S. Moylan, A. Donmez, T. Özel, Laser powder bed fusion of nickel alloy 625: Experimental investigations of effects of process parameters on melt pool size and shape with spatter analysis, Int. J. Mach. Tools Manuf. 121 (2017) 22–36. doi:10.1016/j.ijmachtools.2017.03.004.

[284] H.L. Wei, J. Mazumder, T. DebRoy, Evolution of solidification texture during additive manufacturing, Sci. Rep. 5 (2015) 1–7. doi:10.1038/srep16446.

[285] G.P. Dinda, A.K. Dasgupta, J. Mazumder, Texture control during laser deposition of nickel-based superalloy, Scr. Mater. 67 (2012) 503–506. doi:10.1016/j.scriptamat.2012.06.014.

[286] L.L. Parimi, G. Ravi, D. Clark, M.M. Attallah, Microstructural and texture development in direct laser fabricated IN718, Mater. Charact. 89 (2014) 102–111. doi:10.1016/j.matchar.2013.12.012.

[287] S. Chen, G. Guillemot, C.A. Gandin, Three-dimensional cellular automaton-finite element modeling of solidification grain structures for arc-welding processes, Acta Mater. 115 (2016) 448–467. doi:10.1016/j.actamat.2016.05.011.

[288] G.P. Dinda, A.K. Dasgupta, S. Bhattacharya, H. Natu, B. Dutta, J. Mazumder, Microstructural

characterization of laser-deposited Al 4047 alloy, Metall. Mater. Trans. A Phys. Metall. Mater. Sci. 44 (2013) 2233–2242. doi:10.1007/s11661-012-1560-3.

[289] G. Bi, A. Gasser, Restoration of nickel-base turbine blade knife-edges with controlled laser aided additive manufacturing, Phys. Procedia. 12 (2011) 402–409. doi:10.1016/j.phpro.2011.03.051.

[290] D.R. Feenstra, V. Cruz, X. Gao, A. Molotnikov, N. Birbilis, Effect of build height on the properties of large format stainless steel 316L fabricated via directed energy deposition, Addit. Manuf. 34 (2020) 101205. doi:10.1016/j.addma.2020.101205.

[291] M.L. Griffith, M.T. Ensz, J.D. Puskar, C. V. Robino, J.A. Brooks, J.A. Philliber, J.E. Smugeresky, W.H. Hofmeister, Understanding the Microstructure and Properties of Components Fabricated by Laser Engineered Net Shaping (LENS), MRS Proc. 625 (2000) 9. doi:10.1557/PROC-625-9.

[292] A. Aversa, A. Saboori, E. Librera, M. [de Chirico], S. Biamino, M. Lombardi, P. Fino, The Role of Directed Energy Deposition Atmosphere Mode on the Microstructure and Mechanical Properties of 316L Samples, Addit. Manuf. 34 (2020) 101274. doi:https://doi.org/10.1016/j.addma.2020.101274.

[293] S. Chen, Y. Miyahara, A. Nomoto, Crystallographic orientation dependence of nanoindentation hardness in austenitic phase of stainless steel, Philos. Mag. Lett. 98 (2018) 473–485. doi:doi.org/10.1080/09500839.2019.1577997.

[294] E. Broitman, Indentation Hardness Measurements at Macro-, Micro-, and Nanoscale: A Critical Overview, Tribol. Lett. 65 (2017) 1–18. doi:10.1007/s11249-016-0805-5.

[295] S.J. Wolff, Z. Gan, S. Lin, J.L. Bennett, W. Yan, G. Hyatt, K.F. Ehmann, G.J. Wagner, W.K. Liu, J. Cao, Experimentally validated predictions of thermal history and microhardness in laser-deposited Inconel 718 on carbon steel, Addit. Manuf. 27 (2019) 540–551. doi:10.1016/j.addma.2019.03.019.

[296] G. Bi, A. Gasser, K. Wissenbach, A. Drenker, R. Poprawe, Characterization of the process control for the direct laser metallic powder deposition, Surf. Coatings Technol. 201 (2006) 2676–2683. doi:10.1016/j.surfcoat.2006.05.006.

[297] J. Yu, X. Lin, J. Wang, J. Chen, W. Huang, Mechanics and energy analysis on molten pool spreading during laser solid forming, Appl. Surf. Sci. 256 (2010) 4612–4620. doi:10.1016/j.apsusc.2010.02.060.

[298] T.G. Spears, S.A. Gold, In-process sensing in selective laser melting (SLM) additive manufacturing, Integr. Mater. Manuf. Innov. 5 (2016) 16–40. doi:10.1186/s40192-016-0045-4.

[299] Additive Manufacturing, Concept Laser: In-situ Quality Assurance with QMmeltpool 3D Coaxial Inspection with QMmeltpool 3D, (2015). https://additivemanufacturing.com/2015/07/02/concept-laser-in-situ-quality-assurance-with-qmmeltpool-3d-coaxial-inspection-with-qmmeltpool-3d/ (accessed April 14, 2022).

[300] T. Hua, C. Jing, L. Xin, Z. Fengying, H. Weidong, Research on molten pool temperature in the process of laser rapid forming, J. Mater. Process. Technol. 198 (2008) 454–462. doi:10.1016/j.jmatprotec.2007.06.090.

[301] D. Hu, R. Kovacevic, Sensing, modeling and control for laser-based additive manufacturing, Int. J. Mach. Tools Manuf. 43 (2003) 51–60. doi:10.1016/S0890-6955(02)00163-3.

[302] L. Chechik, Comparison of Monitoring Methods during L-DED of Inconel 718, (2022). doi:10.5281/zenodo.6760221.

[303] Hamamatsu, lnGaAs camera C12741-03, (n.d.).

https://www.hamamatsu.com/resources/pdf/sys/SCAS0111E_C12741-03.pdf (accessed June 19, 2020).

[304] F. Sakuma, S. Hattori, Establishing a practical temperature standard by using a narrow-band radiation thermometer with a silicon detector, in: Temp. Meas. Control Sci. Ind. Vol. 5, 1982: pp. 421–427.

[305] C. Zhu, M.J. Hobbs, R.C. Masters, C. Rodenburg, J.R. Willmott, An Accurate Device for Apparent Emissivity Characterisation in Controlled Atmospheric Conditions up to 1423 K, IEEE Trans. Instrum. Meas. 69 (2019) 4210. doi:10.1109/TIM.2019.2944504.

[306] P. Saunders, D.R. White, Physical basis of interpolation equations for radiation thermometry, Metrologia. 40 (2003) 195–203. doi:10.1088/0026-1394/40/4/309.

[307] H. Fukuyama, H. Higashi, H. Yamano, Thermophysical Properties of Molten Stainless Steel Containing 5 mass % B4C, Nucl. Technol. 205 (2019) 1154–1163. doi:10.1080/00295450.2019.1578572.

[308] R. V. Tompson, G.K. Tushar, H. Jo, S.K. Loyalka, K. Sridharan, D.S. Viswanath, Long-term prediction of emissivity of structural materals for high temperature reactor systems, 2018. doi:10.2172/1463106.

[309] P. Pichler, B.J. Simonds, J.W. Sowards, G. Pottlacher, Measurements of thermophysical properties of solid and liquid NIST SRM 316L stainless steel, J. Mater. Sci. 55 (2020) 4081–4093. doi:10.1007/s10853-019-04261-6.

[310] G. Bi, C.N. Sun, A. Gasser, Study on influential factors for process monitoring and control in laser aided additive manufacturing, J. Mater. Process. Technol. 213 (2013) 463–468. doi:10.1016/j.jmatprotec.2012.10.006.

[311] P. Saunders, Radiation thermometry: Fundamentals and applications in the petrochemical industry, 2007. doi:10.1117/3.741687.

[312] J.T. Black, R.A. Kosher, Degramo's Materials and Processes in Manufacturing, 2012. doi:10.1017/CBO9781107415324.004.

[313] C. Slama, M. Abdellaoui, Structural characterization of the aged Inconel 718, J. Alloys Compd. 306 (2000) 277–284. doi:10.1016/S0925-8388(00)00789-1.

[314] A. Niang, B. Viguier, J. Lacaze, Some features of anisothermal solid-state transformations in alloy 718, Mater. Charact. 61 (2010) 525–534. doi:10.1016/j.matchar.2010.02.011.

[315] W.J. Sames, K.A. Unocic, G.W. Helmreich, M.M. Kirka, F. Medina, R.R. Dehoff, S.S. Babu, Feasibility of in situ controlled heat treatment (ISHT) of Inconel 718 during electron beam melting additive manufacturing, Addit. Manuf. 13 (2017) 156–165. doi:10.1016/j.addma.2016.09.001.

[316] Y. Tian, D. McAllister, H. Colijn, M. Mills, D. Farson, M. Nordin, S. Babu, Rationalization of microstructure heterogeneity in Inconel 718 builds made by the direct laser additive manufacturing process, Metall. Mater. Trans. A Phys. Metall. Mater. Sci. 45 (2014) 4470–4483. doi:10.1007/s11661-014-2370-6.

[317] R.Y. Zhang, H.L. Qin, Z.N. Bi, J. Li, S. Paul, T.L. Lee, S.Y. Zhang, J. Zhang, H.B. Dong, Temperature-Dependent Misfit Stress in Gamma Double Prime Strengthened Ni-Base Superalloys, Metall. Mater. Trans. A Phys. Metall. Mater. Sci. 51 (2020) 1860–1873. doi:10.1007/s11661-020-05627-1.

[318] A. Devaux, L. Nazé, R. Molins, A. Pineau, A. Organista, J.Y. Guédou, J.F. Uginet, P. Héritier, Gamma double prime precipitation kinetic in Alloy 718, Mater. Sci. Eng. A. 486 (2008) 117–122.

doi:10.1016/j.msea.2007.08.046.

[319] H.E. Huang, C.H. Koo, Characteristics and Mechanical Properties of Polycrystalline CM 247 LC Superalloy Casting, Mater. Trans. 45 (2004) 562–568. doi:10.2320/matertrans.45.562.

[320] I.L. Svetlov, N. V Petrushin, D. V Shchegolev, K.K. Khvatskiy, Anisotropy of Mechanical Properties of Single Crystal in Fourth Generation Ni-Based Superalloy, 9th Liege Conf. Mater. Adv. Power Eng. 2010. (2010) 1–6. https://www.osti.gov/etdeweb/servlets/purl/21588215.

[321] B. Saleem, H. Dong, Phase Characterization of CRA Fastener INCONEL718 in Relation of Hydrogen Assisted Cracking, Mater. Today Proc. 2 (2015) S383–S392. doi:10.1016/j.matpr.2015.05.053.

[322] S.L. Semiatin, N.C. Levkulich, R. Larsen, J.S. Tiley, K.N. Wertz, F. Zhang, T.M. Smith, R.Y. Zhang, H.B. Dong, P. Gadaud, J. Cormier, The Application of Differential Scanning Calorimetry to Investigate Precipitation Behavior in Nickel-Base Superalloys Under Continuous Cooling and Heating Conditions, Metall. Mater. Trans. A Phys. Metall. Mater. Sci. 52 (2021) 3706–3726. doi:10.1007/s11661-021-06362-x.

[323] Y. Tian, J.A. Muñiz-Lerma, M. Brochu, Nickel-based superalloy microstructure obtained by pulsed laser powder bed fusion, Mater. Charact. 131 (2017) 306–315. doi:10.1016/j.matchar.2017.07.024.

[324] N. Saunders, Z. Guo, A.P. Miodownik, J.-P. Schillé, Modelling the Material Properties and Behaviour of Multicomponent Alloys, 22nd CAD-FEM Users. (2004) 1–8. http://sentesoftware.co.uk/media/2497/cad-fem.pdf.

[325] A. Balan, M. Perez, T. Chaise, S. Cazottes, D. Bardel, F. Corpace, F. Pichot, A. Deschamps, F. De Geuser, D. Nelias, Precipitation of γ″ in Inconel 718 alloy from microstructure to mechanical properties, Materialia. 20 (2021) 101187. doi:10.1016/j.mtla.2021.101187.

[326] A.M. Kamara, S. Marimuthu, L. Li, A numerical investigation into residual stress characteristics in laser deposited multiple layer waspaloy parts, J. Manuf. Sci. Eng. Trans. ASME. 133 (2011) 1–10. doi:10.1115/1.4003833.

[327] C. Kumara, D. Deng, F. Hanning, M. Raanes, J. Moverare, P. Nylén, Predicting the Microstructural Evolution of Electron Beam Melting of Alloy 718 with Phase-Field Modeling, Metall. Mater. Trans. A Phys. Metall. Mater. Sci. 50 (2019) 2527–2537. doi:10.1007/s11661-019-05163-7.

[328] C. Kumara, A. Segerstark, F. Hanning, N. Dixit, S. Joshi, J. Moverare, P. Nylén, Microstructure modelling of laser metal powder directed energy deposition of alloy 718, Addit. Manuf. 25 (2019) 357–364. doi:10.1016/j.addma.2018.11.024.

[329] W.J. Sames, K.A. Unocic, R.R. Dehoff, T. Lolla, S.S. Babu, Thermal effects on microstructural heterogeneity of Inconel 718 materials fabricated by electron beam melting, J. Mater. Res. 29 (2014) 1920–1930. doi:10.1557/jmr.2014.140.

[330] P. Kürnsteiner, M.B. Wilms, A. Weisheit, B. Gault, E.A. Jägle, D. Raabe, High-strength Damascus steel by additive manufacturing, Nature. 582 (2020). doi:10.1038/s41586-020-2409-3.

[331] X. Chen, C. Qiu, In-situ development of a sandwich microstructure with enhanced ductility by laser reheating of a laser melted titanium alloy, Sci. Rep. 10 (2020) 1–12. doi:10.1038/s41598-020-72627-x.

[332] D. Li, H. Huang, C. Chen, S. Liu, X. Liu, X. Zhang, K. Zhou, Additive manufacturing of high strength near β titanium alloy Ti-55511 by engineering nanoscale secondary α laths via in-situ heat treatment, Mater. Sci. Eng. A. 814 (2021) 141245. doi:10.1016/j.msea.2021.141245.

[333] T.R. Smith, J.D. Sugar, C. San Marchi, J.M. Schoenung, Strengthening mechanisms in directed energy deposited austenitic stainless steel, Acta Mater. 164 (2019) 728–740. doi:10.1016/j.actamat.2018.11.021.

[334] S. Zhang, X. Lin, L. Wang, X. Yu, Y. Hu, H. Yang, L. Lei, W. Huang, Strengthening mechanisms in selective laser-melted Inconel718 superalloy, Mater. Sci. Eng. A. 812 (2021) 141145. doi:10.1016/j.msea.2021.141145.

[335] J.E. Bailey, P.B. Hirsch, The dislocation distribution flow stress and stored energy in cold worked crystalline silver, Philos. Mag. 5 (1960). file://ce/rd_organisation/PTA-MAD/Common/10 Literature2008/Recov_Rex_GrainGrowth/Stored energy/Bailey (1945) # The dislocation distribution flow stress and stored energy in cold worked crystalline silver.pdf.

[336] P.J. Konijnenberg, S. Zaefferer, D. Raabe, Assessment of geometrically necessary dislocation levels derived by 3D EBSD, Acta Mater. 99 (2015) 402–414. doi:10.1016/j.actamat.2015.06.051.

[337] M. Calcagnotto, D. Ponge, E. Demir, D. Raabe, Orientation gradients and geometrically necessary dislocations in ultrafine grained dual-phase steels studied by 2D and 3D EBSD, Mater. Sci. Eng. A. 527 (2010) 2738–2746. doi:10.1016/j.msea.2010.01.004.

[338] Z. Zribi, H.H. Ktari, F. Herbst, V. Optasanu, N. Njah, EBSD, XRD and SRS characterization of a casting Al-7wt%Si alloy processed by equal channel angular extrusion: Dislocation density evaluation, Mater. Charact. 153 (2019) 190–198. doi:10.1016/j.matchar.2019.04.044.

[339] I. Carneiro, S. Simoes, Recent Advances in EBSD Characterization of Metals, Metals (Basel). 10 (2020). doi:10.3390/met10081097.

[340] C. Moussa, M. Bernacki, R. Besnard, N. Bozzolo, About quantitative EBSD analysis of deformation and recovery substructures in pure Tantalum, IOP Conf. Ser. Mater. Sci. Eng. 89 (2015). doi:10.1088/1757-899X/89/1/012038.

[341] V. Juechter, T. Scharowsky, R.F. Singer, C. Körner, Processing window and evaporation phenomena for Ti-6Al-4V produced by selective electron beam melting, Acta Mater. 76 (2014) 252–258. doi:10.1016/j.actamat.2014.05.037.

[342] R. Sampson, R. Lancaster, M. Sutcliffe, D. Carswell, C. Hauser, J. Barras, An improved methodology of melt pool monitoring of direct energy deposition processes, Opt. Laser Technol. 127 (2020). doi:10.1016/j.optlastec.2020.106194.

[343] Z. Tang, W. Liu, Y. Wang, K.M. Saleheen, Z. Liu, A review on in situ monitoring technology for directed energy deposition of metals, Int. J. Adv. Manuf. Technol. (2020).

[344] J.W. Martin, Precipitation Hardening, Second, Butterworth Heinemann, 1998. doi:10.1016/c2009-0-24506-5.

[345] A.J. Goodfellow, E.I. Galindo-Nava, C. Schwalbe, H.J. Stone, The role of composition on the extent of individual strengthening mechanisms in polycrystalline Ni-based superalloys, Mater. Des. 173 (2019) 107760. doi:10.1016/j.matdes.2019.107760.

[346] J. Xu, H. Gruber, R. Boyd, S. Jiang, R.L. Peng, J.J. Moverare, On the strengthening and embrittlement mechanisms of an additively manufactured Nickel-base superalloy, Materialia. 10 (2020) 100657. doi:10.1016/j.mtla.2020.100657.

[347] R.W. Kozar, A. Suzuki, W.W. Milligan, J.J. Schirra, M.F. Savage, T.M. Pollock, Strengthening mechanisms in polycrystalline multimodal nickel-base superalloys, Metall. Mater. Trans. A Phys. Metall. Mater. Sci. 40 (2009) 1588–1603. doi:10.1007/s11661-009-9858-5.

[348] J.R. Cahoon, W.H. Broughton, A.R. Kutzak, The determination of yield strength from hardness

measurements, Metall. Trans. 2 (1971) 1979–1983. doi:10.1007/BF02913433.

[349] M.O. Lai, K.B. Lim, On the prediction of tensile properties from hardness tests, J. Mater. Sci. 26 (1991) 2031–2036. doi:10.1007/BF00549163.

[350] Q. Wang, Z. Li, S. Pang, X. Li, C. Dong, P.K. Liaw, Coherent precipitation and strengthening in compositionally complex alloys: A review, Entropy. 20 (2018). doi:10.3390/e20110878.

[351] Maher, Alloy 718 Data Sheet, (n.d.) 1–5. https://www.maher.com/media/pdfs/718-datasheet.pdf.

[352] J.M. Oblak, D.F. Paulonis, D.S. Duvall, Coherency strengthening in Ni base alloys hardened by DO22 γ′ precipitates, Metall. Trans. 5 (1974) 143–153. doi:10.1007/BF02642938.

[353] H.A. Roth, C.L. Davis, R.C. Thomson, Modeling solid solution strengthening in nickel alloys, Metall. Mater. Trans. A Phys. Metall. Mater. Sci. 28 (1997) 1329–1335. doi:10.1007/s11661-997-0268-2.

[354] J.P. Hirth, J. Lothe, T. Mura, Theory of Dislocations (2nd ed.), J. Appl. Mech. 50 (1983). doi:10.1115/1.3167075.

[355] E.O. Hall, The deformation and ageing of mild steel: III Discussion of results, Proc. Phys. Soc. Sect. B. 64 (1951) 747–753. doi:10.1088/0370-1301/64/9/303.

[356] J. William D. Callister, Fundamentals of Materiales Science and Engineering, 2001. doi:10.1007/978-981-10-2529-7_2.

[357] J.S. Keist, T.A. Palmer, Development of strength-hardness relationships in additively manufactured titanium alloys, Mater. Sci. Eng. A. 693 (2017) 214–224. doi:10.1016/j.msea.2017.03.102.

[358] R.P. Mudge, N.R. Wald, Laser engineered net shaping advances additive manufacturing and repair, Weld. J. (Miami, Fla). 86 (2007) 44–48.

[359] A. Gisario, M. Kazarian, F. Martina, M. Mehrpouya, Metal additive manufacturing in the commercial aviation industry: A review, J. Manuf. Syst. 53 (2019) 124–149. doi:10.1016/j.jmsy.2019.08.005.

[360] ATI, INSIGHT 08 - Additive Manufacturing – Applications in Aerospace, Insight. (2018) 1–16. https://www.ati.org.uk/media/sogpibd0/insight08-additive-manufacturing.pdf.

[361] S. Sreekanth, Laser-Directed Energy Deposition: Influence of Process Parameters and Heat-Treatments, University West, 2020.

[362] B.C. Salzbrenner, J.M. Rodelas, J.D. Madison, B.H. Jared, L.P. Swiler, Y.L. Shen, B.L. Boyce, High-throughput stochastic tensile performance of additively manufactured stainless steel, J. Mater. Process. Technol. 241 (2017) 1–12. doi:10.1016/j.jmatprotec.2016.10.023.

[363] H. Wang, W. Liu, Z. Tang, Y. Wang, X. Mei, K.M. Saleheen, Z. Wang, H. Zhang, Review on adaptive control of laser-directed energy deposition, Opt. Eng. 59 (2020) 1–18. doi:10.1117/1.OE.59.7.070901.

[364] A.G. Medrano Tellez, Fibre Laser Metal Deposition with Wire : Parameters Study and Temperature Control, 2010.

[365] T. Purtonen, A. Kalliosaari, A. Salminen, Monitoring and adaptive control of laser processes, Phys. Procedia. 56 (2014) 1218–1231. doi:10.1016/j.phpro.2014.08.038.

[366] B.T. Gibson, Y.K. Bandari, B.S. Richardson, W.C. Henry, E.J. Vetland, T.W. Sundermann, L.J. Love, Melt pool size control through multiple closed-loop modalities in laser-wire directed energy

deposition of Ti-6Al-4V, Addit. Manuf. 32 (2020) 100993. doi:10.1016/j.addma.2019.100993.

[367] J. Mazumder, D. Dutta, N. Kikuchi, A. Ghosh, Closed loop direct metal deposition: Art to Part, Opt. Lasers Eng. 34 (2000) 397–414. doi:10.1016/S0143-8166(00)00072-5.

[368] J.C. Haley, B. Zheng, U.S. Bertoli, A.D. Dupuy, J.M. Schoenung, E.J. Lavernia, Working distance passive stability in laser directed energy deposition additive manufacturing, Mater. Des. 161 (2019) 86–94. doi:10.1016/j.matdes.2018.11.021.

[369] L. Tang, R.G. Landers, Melt pool temperature modeling and control for laser metal deposition processes, Proc. Am. Control Conf. (2009) 4791–4796. doi:10.1109/ACC.2009.5160415.

[370] M.H. Farshidianfar, A. Khajepour, A. Gerlich, Real-time control of microstructure in laser additive manufacturing, Int. J. Adv. Manuf. Technol. 82 (2016) 1173–1186. doi:10.1007/s00170-015-7423-5.

[371] F. Wirth, K. Wegener, A physical modeling and predictive simulation of the laser cladding process, Addit. Manuf. 22 (2018) 307–319. doi:10.1016/j.addma.2018.05.017.

[372] K.A. Sofinowski, S. Raman, X. Wang, B. Gaskey, M. Seita, Layer-wise engineering of grain orientation (LEGO) in laser powder bed fusion of stainless steel 316L, Addit. Manuf. 38 (2021) 101809. doi:10.1016/j.addma.2020.101809.

[373] M.M. Kirka, D.A. Greeley, C. Hawkins, R.R. Dehoff, Effect of anisotropy and texture on the low cycle fatigue behavior of Inconel 718 processed via electron beam melting, Int. J. Fatigue. 105 (2017) 235–243. doi:10.1016/j.ijfatigue.2017.08.021.

[374] S. Ghorbanpour, S. Sahu, K. Deshmukh, E. Borisov, T. Riemslag, E. Reinton, V. Bertolo, Q. Jiang, A. Popovich, A. Shamshurin, M. Knezevic, V. Popovich, Effect of microstructure induced anisotropy on fatigue behaviour of functionally graded Inconel 718 fabricated by additive manufacturing, Mater. Charact. 179 (2021) 111350. doi:10.1016/j.matchar.2021.111350.

[375] S. Gribbin, S. Ghorbanpour, N.C. Ferreri, J. Bicknell, I. Tsukrov, M. Knezevic, Role of grain structure, grain boundaries, crystallographic texture, precipitates, and porosity on fatigue behavior of Inconel 718 at room and elevated temperatures, Mater. Charact. 149 (2019) 184–197. doi:10.1016/j.matchar.2019.01.028.

[376] G. Zhang, X. Lu, J. Li, J. Chen, X. Lin, M. Wang, H. Tan, W. Huang, In-situ grain structure control in directed energy deposition of Ti6Al4V, Addit. Manuf. 55 (2022) 102865. doi:10.1016/j.addma.2022.102865.

[377] L.C. Wei, L.E. Ehrlich, M.J. Powell-Palm, C. Montgomery, J. Beuth, J.A. Malen, Thermal conductivity of metal powders for powder bed additive manufacturing, Addit. Manuf. 21 (2018) 201–208. doi:10.1016/j.addma.2018.02.002.

[378] J. Pistor, C. Breuning, C. Körner, A single crystal process window for electron beam powder bed fusion additive manufacturing of a cmsx-4 type ni-based superalloy, Materials (Basel). 14 (2021). doi:10.3390/ma14143785.

[379] D.E. Jodi, T. Kitashima, Y. Koizumi, T. Nakano, M. Watanabe, Manufacturing single crystals of pure nickel via selective laser melting with a flat-top laser beam, Addit. Manuf. Lett. 3 (2022) 100066. doi:10.1016/j.addlet.2022.100066.

[380] L. Wang, S. Felicelli, Analysis of thermal phenomena in LENS™ deposition, Mater. Sci. Eng. A. 435–436 (2006) 625–631. doi:10.1016/j.msea.2006.07.087.

[381] J.C. Heigel, Thermo-Mechanical Modeling of Thin Wall Builds using Powder Fed Directed Energy Deposition, 1st ed., Elsevier Inc., 2018. doi:10.1016/B978-0-12-811820-7.00010-0.

[382] R. Rai, J.W. Elmer, T.A. Palmer, T. Debroy, Heat transfer and fluid flow during keyhole mode laser welding of tantalum, Ti-6Al-4V, 304L stainless steel and vanadium, J. Phys. D. Appl. Phys. 40 (2007) 5753–5766. doi:10.1088/0022-3727/40/18/037.

[383] A. Alhuzaim, S. Imbrogno, M.M. Attallah, Controlling Microstructural and Mechanical Properties of Direct Laser Deposited Inconel 718 via Laser Power, J. Alloys Compd. (2020). doi:10.1016/j.jallcom.2021.159588.

[384] I. Tabernero, A. Lamikiz, S. Martínez, E. Ukar, J. Figueras, Evaluation of the mechanical properties of Inconel 718 components built by laser cladding, Int. J. Mach. Tools Manuf. 51 (2011) 465–470. doi:10.1016/j.ijmachtools.2011.02.003.

[385] I. Serrano-Munoz, T. Mishurova, T. Thiede, M. Sprengel, A. Kromm, N. Nadammal, G. Nolze, R. Saliwan-Neumann, A. Evans, G. Bruno, The residual stress in as-built Laser Powder Bed Fusion IN718 alloy as a consequence of the scanning strategy induced microstructure, Sci. Rep. 10 (2020) 1–15. doi:10.1038/s41598-020-71112-9.

[386] H. Jones, Rapid Solidification of Metals and Alloys, Institution of Metallurgists, London, 1983.

[387] J.D. Hunt, Cellular and primary Dendrite Spacings, in: Solidif. Cast. Met., The Metals Society, Sheffield, 1979: p. 3.

[388] P. Promoppatum, S.C. Yao, P.C. Pistorius, A.D. Rollett, A Comprehensive Comparison of the Analytical and Numerical Prediction of the Thermal History and Solidification Microstructure of Inconel 718 Products Made by Laser Powder-Bed Fusion, Engineering. 3 (2017) 685–694. doi:10.1016/J.ENG.2017.05.023.

[389] L. Fang, L. Cheng, J.A. Glerum, J. Bennett, J. Cao, G.J. Wagner, Data-driven analysis of process, structure, and properties of additively manufactured Inconel 718 thin walls, Npj Comput. Mater. 8 (2022) 1–15. doi:10.1038/s41524-022-00808-5.

[390] V.A. Popovich, E. V. Borisov, A.A. Popovich, V.S. Sufiiarov, D. V. Masaylo, L. Alzina, Functionally graded Inconel 718 processed by additive manufacturing: Crystallographic texture, anisotropy of microstructure and mechanical properties, Mater. Des. 114 (2017) 441–449. doi:10.1016/j.matdes.2016.10.075.

[391] J.-P. Choi, G.-H. Shin, S. Yang, D.-Y. Yang, J.-S. Lee, M. Brochu, J.-H. Yu, Densification and microstructural investigation of Inconel 718 parts fabricated by selective laser melting, Powder Technol. 310 (2017) 60–66. doi:10.1016/j.powtec.2017.01.030.

[392] C. Yu, Anisotropic Mechanical Behaviours and Thin-wall Effects of Additively Manufactured Austenitic Alloys, Linköping University, n.d. doi:10.3384/9789179293154.

[393] A. Rollett, F. Humphreys, G.S. Rohrer, M. Hatherly, Recrystallization and Related Annealing Phenomena: Second Edition, 2004. doi:10.1016/B978-0-08-044164-1.X5000-2.

[394] D. Hull, D.J. Bacon, Introduction to Dislocations, 2011. doi:10.1016/C2009-0-64358-0.

[395] T. Pinomaa, A. Laukkanen, N. Provatas, Solute trapping in rapid solidification, MRS Bull. 45 (2020) 910–915. doi:10.1557/mrs.2020.274.

[396] H.L. Wei, G.L. Knapp, T. Mukherjee, T. DebRoy, Three-dimensional grain growth during multi-layer printing of a nickel-based alloy Inconel 718, Addit. Manuf. 25 (2019) 448–459. doi:10.1016/j.addma.2018.11.028.

[397] M. Balat-Pichelin, J.L. Sans, E. Bêche, V. Flaud, J. Annaloro, Oxidation and emissivity of Inconel 718 alloy as potential space debris during its atmospheric entry, Mater. Charact. 127 (2017) 379–390. doi:10.1016/j.matchar.2017.02.016.